

AD-A041 849 GENERAL ELECTRIC CO CINCINNATI OHIO AIRCRAFT ENGINE GROUP F/G 20/1
HIGH VELOCITY JET NOISE SOURCE LOCATION AND REDUCTION. TASK 4. --ETC(U)
FEB 77 W S CLAPPER, E J STRINGAS DOT-05-30034

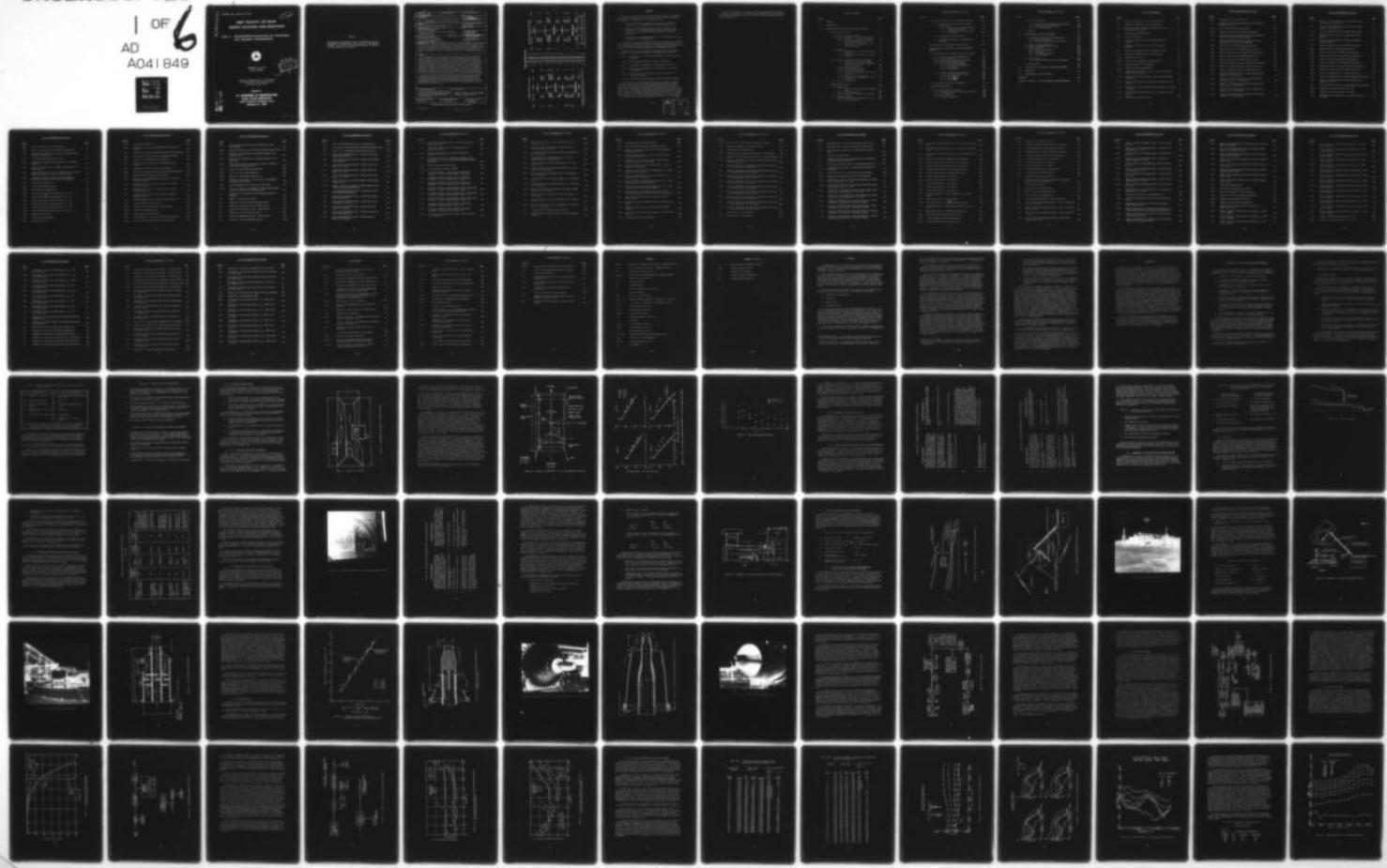
UNCLASSIFIED

1 OF 6
ADI
A041849

R77AEG189

FAA-RD-76-79-4

NL





849

ADA 041849

REPORT NO. FAA-RD-76-79,IV

**HIGH VELOCITY JET NOISE
SOURCE LOCATION AND REDUCTION**

**TASK 4 - DEVELOPMENT/EVALUATION OF TECHNIQUES
FOR 'INFLIGHT' INVESTIGATION**



**FEBRUARY 22, 1977
FINAL REPORT**



Document is available to the U.S. public through
the National Technical Information Service,
Springfield, Virginia 22161.

Prepared for

**U.S. DEPARTMENT OF TRANSPORTATION
FEDERAL AVIATION ADMINISTRATION
Systems Research & Development Service
Washington, D.C. 20590**

NU.
DOC FILE COPY.

NOTICE

This document is disseminated under the sponsorship of the Department of Transportation in the interest of information exchange. The United States Government assumes no liability for its contents or use thereof.

(9) Final rep't.

1. Report No. (10) 4 FAA-RD-76-79 IV	2. Government Accession No. (11)	3. Recipient's Catalog No.
4. Title and Subtitle High Velocity Jet Noise Source Location and Reduction. Task 4 • Development/Evaluation of Techniques for Inflight Investigation.		5. Report Date (22) February 22, 1977
6. Author(s) W.S. Clapper (Task 4 Technical Director and Editor), et al. E.J. Stringas (Technical Project Manager)		6. Performing Organization Code
7. Performing Organization Name and Address General Electric Company Advanced Engineering and Technology Programs Department Aircraft Engine Group Cincinnati, Ohio 45215		8. Performing Organization Report No. R77AEG189
9. Sponsoring Agency Name and Address U.S. Department of Transportation Federal Aviation Administration Systems Research and Development Services Washington, D.C. 20590		10. Work Unit No.
11. Contract or Grant No. DOT-OS-30034		12. 13. Type of Report and Period Covered Task 4 Final Report February, 1977
14. Sponsoring Agency Code ARD-550		15. Supplementary Notes This report is in partial fulfillment of the subject program. Related documents to be issued in the course of the program include final reports of the following Tasks: Task 1 - Activation of Facilities and Validation of Source Location Techniques; Task 1 Supplement - Certification of the General Electric Jet Noise Anechoic Test Facility; Task 2 - Theoretical Developments and Basic Experiments; Task 3 - Experimental Investigation of Suppression Principles; Task 5 - Investigation of "Inflight" Aero-Acoustic Effects; Task 6 - Noise Abatement Nozzle Design Guide.
16. Abstract This report presents the results of Task 4 as conducted under the subject program over a period of 30 months. Task 4 was formulated to identify and evaluate several inflight simulation techniques, select the most promising technique for demonstration and validation, and employ that technique in testing under Task 5 of the program. Techniques evaluated include closed-circuit wind tunnels, free jets, rocket sleds, and high speed trains. Pertinent results from the evaluation phase and rationale which led to selection of the free jet simulation technique are discussed, including advantages and disadvantages. The results of a theoretical study aimed at relating the noise signature obtained in a free jet facility for simulation of forward flight effects on jet noise with the noise signature in true flight are presented. Transformation is carried out by extracting static directivity of the noise after correcting for refraction, turbulent scattering, and absorption effects, and then employing a suitable multipole source decomposition to evaluate the proper dynamic effect. A flowchart describing the details of the transformation procedure and a listing of the computer program are included.		
Acoustic results from the Learjet and NASA-Lewis F-106 Aircraft Flyovers and the French Aerotrain Tests, taken with a baseline, 8-lobe, and 104-tube nozzle were used to formulate a data base for verification of the free jet simulation technique. Detailed directivity and spectra comparisons between aerotrain data and transformed free jet data are presented for three primary jet velocities and two flight velocities for the three nozzle types. It is concluded that the validity of the free jet technique and associated transformation procedure has been satisfactorily demonstrated.		
17. Key Words (Suggested by Author(s)) Jet Noise, Inflight Jet Noise Effects, Closed and Open Throat Wind Tunnels, High Speed Trains, Aircraft Flyover Noise, Measurement Techniques, Simulated Flight Noise Signatures, Baseline and Suppressor Nozzles		18. Distribution Statement Document is available to the public through the National Technical Information Service, Springfield, Virginia, 22151
19. Security Classif. (of this report) Unclassified	20. Security Classif. (of this page) Unclassified	21. No. of Pages 556 568
22. Price*		

* For sale by the National Technical Information Service, Springfield, Virginia 22151

403 468

METRIC CONVERSION FACTORS

Approximate Conversions to Metric Measures

Symbol	When You Know	Multiply by	To Find	Symbol
<u>LENGTH</u>				
in	inches	.25	centimeters	mm
ft	feet	30	centimeters	cm
yd	yards	0.9	meters	m
mi	miles	1.6	kilometers	km
<u>AREA</u>				
in ²	square inches	6.5	square centimeters	cm ²
ft ²	square feet	0.09	square meters	m ²
yd ²	square yards	0.8	square kilometers	km ²
mi ²	square miles	2.6	hectares	ha
	acres	0.4		
<u>MASS (weight)</u>				
oz	ounces	.28	grams	g
lb	pounds	0.45	kilograms	kg
	short tons (2000 lb)	0.9	tonnes	t
<u>VOLUME</u>				
tsbp	teaspoons	5	milliliters	ml
tbsp	tablespoons	15	milliliters ¹	ml
fl oz	fluid ounces	30	milliliters	ml
c	cups	0.24	liters	l
pt	pints	0.47	liters	l
qt	quarts	0.95	liters	l
gal	gallons	3.8	cubic meters	m ³
ft ³	cubic feet	0.03	cubic meters	m ³
yd ³	cubic yards	0.76	cubic meters	m ³
<u>TEMPERATURE (exact)</u>				
°F	Fahrenheit temperature	5/9 (after subtracting 32)	Celsius temperature	°C

i i

Approximate Conversions from Metric Measures

Symbol	When You Know	Multiply by	To Find	Symbol
<u>LENGTH</u>				
in	millimeters	0.04	inches	in
in	centimeters	0.4	inches	in
ft	meters	3.3	feet	ft
yd	meters	1.1	yards	yd
mi	kilometers	0.6	miles	mi
<u>AREA</u>				
in ²	square centimeters	0.16	square inches	in ²
yd ²	square meters	1.2	square yards	yd ²
mi ²	square kilometers	0.4	square miles	mi ²
	hectares (10,000 m ²)	2.5	acres	
<u>MASS (weight)</u>				
oz	grams	0.035	ounces	oz
kg	kilograms	2.2	pounds	lb
t	tonnes (1000 kg)	1.1	short tons	
<u>VOLUME</u>				
ml	milliliters	0.03	fluid ounces	fl oz
ml	liters	2.1	pints	pt
ml	liters	1.06	quarts	qt
ml	cubic meters	0.26	gallons	gal
ml	cubic meters	35	cubic feet	ft ³
ml	cubic meters	1.3	cubic yards	yd ³
<u>TEMPERATURE (exact)</u>				
°C	Celsius temperature	9/5 (then add 32)	Fahrenheit temperature	°F
<u>Temperature (approx.)</u>				
°F	Fahrenheit temperature	-40	-40	-40
		32	0	0
		40	20	20
		50	30	30
		60	40	40
		70	50	50
		80	60	60
		90	70	70
		100	80	80
		212	100	100
		212	212	212

*1 in = 2.54 (exactly). For other exact conversions and more detailed tables, see NBS Mon. Publ. 236.

Units of Weights and Measures, Price \$2.25, SD Catalog No. C1310266.

PREFACE

This report describes the work performed under Task 4 of the DOT/FAA High Velocity Jet Noise Source Location and Reduction Program (Contract DOT-OS-30034). The objectives of the contract were:

- Investigation of the aerodynamic and acoustic mechanisms of various jet noise suppressors, including scaling effects.
- Analytical and experimental studies of the acoustic source distribution in such suppressors, including identification of source location, nature and strength, and noise reduction potential.
- Investigation of inflight effects on the aerodynamic and acoustic performance of these suppressors.

The results of these investigations led to the preparation of a design guide report for predicting the overall characteristics of suppressor concepts from models to full-scale static, to in-flight conditions, as well as a quantitative and qualitative prediction of the phenomena involved.

The work effort in this program was organized under the following major Tasks, each of which is reported in a separate Final Report:

Task 1 - Activation of Facilities and Validation of Source Location Techniques.

Task 2 - Theoretical Developments and Basic Experiments.

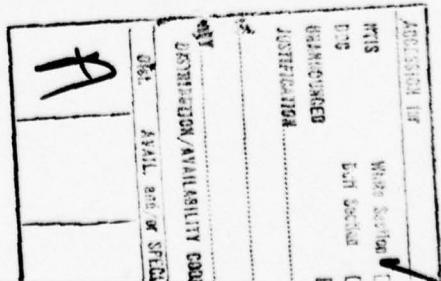
Task 3 - Experimental Investigation of Suppression Principles.

Task 4 - Development and Evaluation of Techniques for "Inflight" Investigation.

Task 5 - Investigation of "Inflight" Aero-Acoustic Effects on Suppressed Exhausts.

Task 6 - Preparation of Noise Abatement Nozzle Design Guide Report.

Task 1 was an investigative and survey effort designed to identify acoustic facilities and test methods best suited to jet noise studies. Task 2 was a theoretical effort complemented by theory verification experiments which extended across the entire contract period of performance. Task 3 represented a substantial contract effort to gather various test data on a wide range of High Velocity Jet Nozzle suppressors. These data, intended to help identify several "optimum" nozzles for "in-flight" testing under Task 5, provide an extensive high quality data bank useful to preparation of the Task 6 design guide, as well as to future studies.



Task 4, the subject of the present report, was formulated to develop a technique for evaluating the in-flight noise signature of a given arbitrary suppressor design without the need to perform time consuming and relatively costly flight tests.

TABLE OF CONTENTS

<u>Section</u>	<u>Page</u>
1.0 SUMMARY	1
2.0 INTRODUCTION	4
3.0 EVALUATION OF FIXED- AND MOVING-FRAME TECHNIQUES	5
3.1 Fixed-Frame Facilities	6
3.1.1 Closed-Circuit Wind Tunnels	9
3.1.1.1 NASA-Ames 7 x 10-Foot Wind Tunnel	9
3.1.1.2 NASA-Ames 40 x 80-Foot Wind Tunnel	15
3.1.1.3 FluiDyne Engineering Corporation 66 x 66-Inch Wind Tunnel	15
3.1.1.4 NASA-Lewis 8 x 6-Foot and 9 x 15- Foot Wind Tunnels	18
3.1.2 Free Jets	19
3.1.2.1 NASA-Langley Aircraft Noise Reduction Laboratory	21
3.1.2.2 General Electric Anechoic Jet Noise Facility	23
3.1.3 "As-is" Assessment of Free Jet Technique	29
3.1.3.1 Test Setup and Nozzle Hardware Description for "As-is" Assessment of Free Jet Technique	29
3.1.3.2 Data Acquisition	37
3.1.3.3 Data Reduction Methods	46
3.1.3.4 Data Scaling Procedure	48
3.1.3.5 Test Matrix Description and Acoustic Results	55
3.1.3.6 Free Jet Tests, Assessment	86
3.1.3.7 General Electric/NASA-Lewis Free Jet Comparison	96
3.1.4 Electronic Simulation	103
3.2 Moving-Frame Facilities	108
3.2.1 Rocket Sleds	108
3.2.1.1 Rocket Sled Background Noise Measure- ments	108
3.2.1.2 Sled Design Study	126
3.2.1.3 Acoustic Data Acquisition Procedure	132
3.2.2 High Speed Trains	139
3.2.2.1 DOT High Speed Ground Test Center	139
3.2.2.2 Bertin Aerotrain	139

TABLE OF CONTENTS (Continued)

<u>Section</u>	<u>Page</u>
3.3 Statistical Analysis of Moving-Source Problem	143
3.3.1 Applying Confidence Limits to Moving- Source Data	143
3.3.1.1 Model for the Statistical Error in Moving-Source Data	147
3.3.1.2 Confidence Statements on Single Data Records	149
3.3.2 Independence of Data Records	151
3.3.3 Statistical Comparison of Moving-Source Data Sets	158
3.4 Analytical Transformation Screening Study	161
4.0 SURVEY LEADING TO SELECTION OF INFLIGHT SIMULATION TECHNIQUE	173
4.1 Fixed-Frame Free Jet Demonstration Test Program	174
4.1.1 Test Setup and Nozzle Configurations	174
4.1.2 Acoustic Test Matrix	176
4.1.3 Data Acquisition and Data Reduction	176
4.1.4 Acoustic Data Analysis/Results	189
4.1.5 Laser Velocimeter Measurements	212
4.1.5.1 Test Setup and Conditions	215
4.1.5.2 Data Analysis	218
4.1.5.3 Conclusions	238
4.1.6 Ellipsoidal Mirror Measurements	238
4.1.6.1 Test Setup and Conditions	243
4.1.6.2 Data Reduction	243
4.1.6.3 Data Analysis	252
4.1.6.4 Conclusions	265
4.2 Recommended Analytical Transformation	266
5.0 FLIGHT ASSURANCE TESTING	295
5.1 Gates Learjet-25C Test Program	295
5.1.1 Configuration Description and Test Matrix	295
5.1.2 Data Acquisition	299
5.1.3 Data Reduction	306
5.1.4 Learjet Data Analysis	330

TABLE OF CONTENTS (Concluded)

<u>Section</u>	<u>Page</u>
5.2 F-106 Test Program	345
5.2.1 Configuration Description and Test Matrix	345
5.2.2 Test Setup and Data Reduction	349
5.2.3 F-106 Data Analysis	349
5.3 Summary	371
6.0 MOVING-FRAME VALIDATION TEST PROGRAM	372
6.1 Configuration Description and Test Matrix	372
6.1.1 Aerotrain Facility	372
6.1.2 Nozzle Configuration and Test Matrix	372
6.2 Impact of Background Noise	379
6.3 Impact of Extraneous Noise Sources	396
6.4 Data Acquisition	414
6.4.1 Acoustic Measurements	414
6.4.2 Trajectory	415
6.4.3 Aerodynamic Parameters	415
6.4.4 Test Procedures	418
6.5 Data Reduction	422
6.5.1 Ground Reflection Correction Procedure	422
6.6 Data Analysis	425
7.0 VERIFICATION OF THE INFLIGHT SIMULATION TECHNIQUE	459
8.0 CONCLUSIONS	508
9.0 RECOMMENDATIONS FOR FUTURE WORK	511
REFERENCES	513
APPENDIX - LISTING OF FLIGHT TRANSFORMATION COMPUTER PROGRAM	517

LIST OF ILLUSTRATIONS

<u>Figure</u>		<u>Page</u>
3-1.	Schematic of NASA-Ames 7 x 10-ft Wind Tunnel.	10
3-2.	Schematic of NASA-Ames 7 x 10-ft Wind Tunnel.	12
3-3.	Effect of Acoustic Treatment on NASA-Ames 7 x 10-ft Wind Tunnel Hall Radius.	13
3-4.	Directional Microphone Results.	14
3-5.	Free Jet Technique.	20
3-6.	Interior of General Electric Jet Noise Anechoic Facility.	24
3-7.	Schematic of General Electric Free Jet Anechoic Facility.	28
3-8.	Free Jet Critical Aero-Acoustic Design Criteria.	30
3-9.	Schematic of JENOTS Facility Acoustic Arena.	31
3-10.	JENOTS Acoustic Arena.	32
3-11.	Schematic of Coannular-Flow JENOTS Facility.	34
3-12.	Free Jet/Coannular Plenum Chamber.	35
3-13.	JENOTS Coannular Plenum Chamber.	36
3-14.	JENOTS Free Jet/Coannular Plenum - Acoustic Validation of Primary Nozzle Only.	38
3-15.	Schematic of 3.56-Inch Diameter Primary Nozzle Assembly with Shroud.	39
3-16.	3.56-Inch Diameter Nozzle Installed on JENOTS Dual Flow Facility.	40
3-17.	Schematic of 2-Inch Internal Diameter STA Nozzle with Free Jet Shroud.	41
3-18.	2-Inch Diameter STA Nozzle Installed on JENOTS Dual Flow Facility.	42
3-19.	JENOTS Data Acquisition System.	44

LIST OF ILLUSTRATIONS (Continued)

<u>Figure</u>		<u>Page</u>
3-20.	Data Reduction System Flow Chart.	47
3-21.	Comparison of Air Attenuation Models at 50% Relative Humidity and 68° F.	49
3-22.	Data Reduction Operations Flow Chart.	50
3-23.	Details of Full-Scale Data Reduction Program.	52
3-24.	Electronic Noise Floor Spectra of the 90° Microphone System with Shorted Cathode Follower.	53
3-25.	Electronic Noise Floor Spectra of the 90° System with Microphone Covered by Pistonphone.	54
3-26.	Ambient and Free Jet OASPL Characteristics.	58
3-27.	Ambient and Free Jet 1/3 OBSPL Characteristics.	59
3-28.	Ambient and Free Jet Power Spectra Characteristics.	60
3-29.	Ambient and Primary Jet OASPL Characteristics.	62
3-30.	Ambient and Primary Jet OBSPL Characteristics.	63
3-31.	Ambient and Primary Jet Power Spectra Characteristics.	64
3-32.	Effects of Forward Velocity on OASPL Directivity.	65
3-33.	Effects of Forward Velocity on OASPL Directivity.	66
3-34.	Effects of Forward Velocity on Sound Pressure Level Spectra at $V_J = 800$ ft/sec.	68
3-35.	Effects of Forward and Velocity on Sound Pressure Level Spectra at $V_J = 1115$ ft/sec.	69
3-36.	Effects of Forward Velocity on Sound Pressure Level Spectra at $V_J = 1270$ ft/sec.	70
3-37.	Effects of Forward Velocity on Sound Pressure Level Spectra at $V_J = 1480$ ft/sec.	71
3-38.	Effects of Forward Velocity on Sound Pressure Level Spectra at $V_J = 1640$ ft/sec.	72

LIST OF ILLUSTRATIONS (Continued)

<u>Figure</u>		<u>Page</u>
3-39.	Effects of Forward Velocity on Sound Pressure Level Spectra at $V_J = 1870$ ft/sec.	73
3-40.	Effects of Forward Velocity on Sound Pressure Level Spectra at $V_J = 2090$ ft/sec.	74
3-41.	Effects of Forward Velocity on Power Level Spectra.	75
3-42.	Effects of Forward Velocity on Sound Power Level Spectra.	76
3-43.	Effects of Forward Velocity on OASPL and OAPWL Vs. Primary Velocity.	77
3-44.	OASPL and OAPWL Variation with Relative Velocity.	78
3-45.	Ambient and Free Jet OASPL Characteristics.	80
3-46.	Ambient and Free Jet 1/3 OBSPL Characteristics.	81
3-47.	Ambient and Free Jet Power Spectra Characteristics.	82
3-48.	Ambient and Primary Jet OASPL Characteristics.	83
3-49.	Ambient and Primary Jet 1/3 OBSPL Characteristics.	84
3-50.	Ambient and Primary Jet Power Spectra Characteristics.	85
3-51.	Effects of Forward Velocity on OASPL Directivity.	87
3-52.	Effects of Forward Velocity on OASPL Directivity.	88
3-53.	Effect of Forward Velocity on Sound Pressure Level Spectra.	89
3-54.	Effect of Forward Velocity on Sound Pressure Level Spectra, $\theta_I = 90^\circ$.	90
3-55.	Effect of Forward Velocity on Power Spectra Characteristics.	91
3-56.	Comparison of Free Jet Spectra, $\theta_I = 90^\circ$.	93
3-57.	Comparison of Free Jet Spectra, $\theta_I = 140^\circ$.	94
3-58.	Comparison of Free Jet Spectra from Other References, $\theta_I = 90^\circ$.	95

LIST OF ILLUSTRATIONS (Continued)

<u>Figure</u>		<u>Page</u>
3-59.	Free Jet Installation with STA Nozzle.	97
3-60.	Effect of Diameter Ratio on Pressure Distribution.	98
3-61.	Comparison of Wind Tunnel and Free Jet Pressure Distributions of STA Nozzle.	99
3-62.	Free Jet/Primary Nozzle Test Set-Ups.	100
3-63.	Comparison of JENOTS and NASA-Lewis Static 1/3 OBSPL Spectra.	101
3-64.	Effect of Forward Flight on JENOTS and NASA-Lewis 1/3 OBSPL Spectra.	102
3-65.	Geometric Construction Used to Determine Number of Fixed Microphones Required to Simulate Source Motion.	105
3-66.	Geometric Construction Used to Determine Number of Microphones Required in Moving Source Simulation.	106
3-67.	Clean Sled Configuration.	110
3-68.	Alternate Sled Configuration.	111
3-69.	Holloman AFB Microphone Array.	112
3-70.	Typical Sled Spectra Characteristics, $\theta_I = 25^\circ$.	114
3-71.	Typical Sled Spectra Characteristics, $\theta_I = 40^\circ$.	115
3-72.	Typical Sled Spectra Characteristics, $\theta_I = 70^\circ$.	116
3-73.	Typical Sled Spectra Characteristics, $\theta_I = 120^\circ$.	117
3-74.	Typical Sled Spectra Characteristics, $\theta_I = 140^\circ$.	118
3-75.	Typical Sled Spectra Characteristics, $\theta_I = 160^\circ$.	119
3-76.	Normalized Max. OASPL.	120
3-77.	Normalized Spectra Shape.	121
3-78.	Typical Directivity.	122

LIST OF ILLUSTRATIONS (Continued)

<u>Figure</u>		<u>Page</u>
3-79.	B-52 Sled Configuration.	123
3-80.	Comparison of Predicted and Measured B-52 Sled Noise Spectra.	124
3-81.	Comparison of Predicted and Measured B-52 Sled Directivity.	125
3-82.	Sled System, Jet Nozzle Design Performance Envelope.	127
3-83.	Schematic of Proposed Nozzle Test System.	129
3-84.	Preliminary Layout Drawing of Sled/Exhaust Nozzle System.	130
3-85.	Estimated Sled Velocity Profile and Staging.	131
3-86.	Generalized Configuration Used for Sled Noise Prediction.	133
3-87.	Estimated Maximum Background Noise Level.	134
3-88.	Predicted Sled Background Noise Estimates at 50-Foot Measuring Position.	135
3-89.	Estimated Conical Nozzle Noise Levels at a 100-Foot Measuring Position.	138
3-90.	Estimated Conical Nozzle Noise Levels at a 50-Foot Measuring Position.	138
3-91.	Estimated Conical Nozzle Noise Levels at a 25-Foot Measuring Position.	138
3-92.	Estimated Upper Limit of Frequency Range Capability.	141
3-93.	Bertin Aerotrain Test Facility.	142
3-94.	Principle of Measurement and Synchronization.	144
3-95.	Effects of Integration Time.	145
3-96.	Moving-Frame Data Repeatability.	146
3-97.	Single Channel of a 1/3-Octave Band Analysis System.	148
3-98.	Points on Chi Square Curve Used in Equation (3).	150

LIST OF ILLUSTRATIONS (Continued)

<u>Figure</u>		<u>Page</u>
3-99.	95% Confidence Interval Curves as a Function of Data Record Number.	152
3-100.	Typical Microphone Array for Moving Source Data Acquisition.	153
3-101.	Condition for Independence of Microphone Signals from Different Poles.	153
3-102.	Condition for Independence of Microphone Signal for the Same Poles.	155
3-103.	95% Confidence Rejection Limits for D_1-D_2 $k_i =$ Number of 0.125-second Integrations in D_i .	160
3-104.	Free Jet to Wind Tunnel Transformation.	162
3-105.	Free Jet to Static Transformation.	163
3-106.	Definition of Retarded Coordinate, θ_R .	166
3-107.	Schematic Illustrations of Free Jet Flow Field Relative to Primary Nozzle Plume.	166
3-108.	Scaled Representation of GE Free Jet Flow Field.	168
3-109.	Ability of Free Jet - Wind Tunnel - Flight Transformation to Predict Flight Noise from Reference 4.	172
4-1.	Procedure for Verification of the Inflight Simulation Technique.	175
4-2.	JENOTS - Free Jet Test Facility.	177
4-3.	Schematic of Free Jet 3.56-Inch Conical Nozzle.	178
4-4.	Schematic of Free Jet 2.0-Inch Conical Nozzle.	179
4-5.	Fixed Frame Demonstration Test - Conical Nozzle.	180
4-6.	Schematic of Free Jet/8-Lobe Nozzle.	181
4-7.	Fixed Frame Demonstration Test - 8-Lobe Nozzle.	182
4-8.	Schematic of Free Jet/104-Tube Nozzle.	183

LIST OF ILLUSTRATIONS (Continued)

<u>Figure</u>		<u>Page</u>
4-9.	Fixed Frame Demonstration Test - 104-Tube Nozzle.	184
4-10.	Data Reduction Operations/Fixed Frame Demonstration Tests.	191
4-11.	Typical Free Jet Background Noise Characteristics.	192
4-12.	Fixed Frame Demonstration Test - Conical Nozzle Peak OASPL Characteristics.	193
4-13.	Fixed Frame Demonstration Test - Conical Nozzle OASPL Directivities.	194
4-14.	Fixed Frame Demonstration Test - Conical Nozzle SPL Spectra, $\theta_I = 140^\circ$.	196
4-15.	Fixed Frame Demonstration Test - Conical Nozzle SPL Spectra, $\theta_I = 90^\circ$.	197
4-16.	Fixed Frame Demonstration Test - Conical Nozzle SPL Spectra, $\theta_I = 50^\circ$.	198
4-17.	Effect of Free Jet Area Ratio on OASPL Forward Flight Characteristics.	199
4-18.	Effect of Free Jet Area Ratio on Sound Pressure Level Forward Flight Characteristics.	200
4-19.	Fixed Frame Demonstration Test - 8-Lobe Daisy Nozzle Peak OASPL Characteristics.	202
4-20.	Fixed Frame Demonstration Test - 8-Lobe Daisy Nozzle OASPL Directivities.	203
4-21.	Fixed Frame Demonstration Test - 8-Lobe Daisy Nozzle SPL Spectra - $\theta_I = 50^\circ$.	204
4-22.	Fixed Frame Demonstration Test - 8-Lobe Nozzle SPL Spectra - $\theta_I = 140^\circ$.	205
4-23.	Fixed Frame Demonstration Test - 104-Tube Nozzle Peak OASPL Characteristics.	206
4-24.	Fixed Frame Demonstration Test - 104-Tube Nozzle OASPL Directivities.	207

LIST OF ILLUSTRATIONS (Continued)

<u>Figure</u>		<u>Page</u>
4-25.	Fixed Frame Demonstration Test - 104-Tube Nozzle SPL Spectra, $\theta_I = 140^\circ$.	208
4-26.	Fixed Frame Demonstration - 104-Tube Nozzle SPL Spectra, $\theta_I = 140^\circ$.	209
4-27.	Fixed Frame Demonstration - 104-Tube Nozzle SPL Spectra, $\theta_I = 50^\circ$.	210
4-28.	Supercritical Velocity - Temperature Dependency Noise Characteristics of Conical and 104-Tube Nozzles, Static and Flight.	213
4-29.	Laser Velocimeter Optics Package.	214
4-30.	Laser Velocimeter Set-Up at JENOTS.	216
4-31.	Histogram Validation of Mean Velocity Traversing Technique - 3.56-in. Conical Nozzle - $X/D_8 = 0.1$.	219
4-32.	Histogram Validation of Mean Velocity Traversing Technique - 3.56-in. Conical Nozzle - $X/D_8 = 3.0$.	220
4-33.	Histogram Validation of Mean Velocity Traversing Technique - 3.56-in. Conical Nozzle - $X/D_8 = 6.0$.	221
4-34.	Histogram Validation of Wind-On Mean Velocity Traversing Technique - 3.56-in. Conical Nozzle - $X/D_8 = 0.1$.	222
4-35.	Histogram Validation of Wind-On Mean Velocity Traversing Technique - 3.56-in. Conical Nozzle - $X/D_8 = 3.0$.	223
4-36.	Histogram Validation of Wind-On Mean Velocity Traversing Technique - 3.56-in. Conical Nozzle - $X/D_8 = 6.0$.	224
4-37.	Histogram Validation of Mean Velocity Traversing Technique - 104-Tube Nozzle - $X/D_8 = 2.0$.	225
4-38.	Histogram Validation of Mean Velocity Traversing Technique - 104-Tube Nozzle - $X/D_8 = 1.0$.	226
4-39.	Centerline Velocity Decay for 3.56-in. Conical Nozzle, $V_J = 1130 \text{ ft/sec}$.	227

LIST OF ILLUSTRATIONS (Continued)

<u>Figure</u>		<u>Page</u>
4-40.	Velocity Profiles for 3.56-in. Conical Nozzle, $V_J = 1130$ ft/sec, $V_o = 0$.	228
4-41.	Velocity Profiles for 3.56-in. Conical Nozzle, $V_J = 1130$ ft/sec, $V_o = 150$ ft/sec.	230
4-42.	Centerline Velocity Decay for 3.56-in. Conical Nozzle, $V_J = 2200$ ft/sec.	231
4-43.	Centerline Velocity Near Nozzle Exit for 3.56-in. Conical Nozzle, $V_J = 2200$ ft/sec.	232
4-44.	Velocity Profiles for 8-Lobe Daisy Nozzle, $V_J = 1130$ ft/sec, $V_o = 0$.	233
4-45.	Velocity Profiles for 8-Lobe Daisy Nozzle, $V_J = 1130$ ft/sec, $V_o = 150$ ft/sec.	234
4-46.	Axial Velocity Traverse Behind a Lobe - 8-Lobe Nozzle, $V_J = 1130$ ft/sec.	235
4-47.	Velocity Profiles for 104-Tube Nozzle, $V_J = 1130$ ft/sec, $V_o = 0$.	236
4-48.	Velocity Profiles for 104-Tube Nozzle, $V_J = 1130$ ft/sec, $V_o = 150$ ft/sec.	237
4-49.	Axial Velocity Traverse Behind an Outer Tube, 104-Tube Nozzle, $V_J = 1130$ ft/sec.	239
4-50.	Centerline Velocity Decay for 2.0-in. STA Nozzle, $V_J = 1130$ ft/sec.	240
4-51.	Velocity Profiles for 2.0-in. STA Nozzle, $V_J = 1130$ ft/sec, $V_o = 0$.	241
4-52.	Velocity Profiles for 2.0-in. STA Nozzle, $V_J = 1130$ ft/sec, $V_o = 150$ ft/sec.	242
4-53.	Test Set-Up for Ellipsoidal Mirror Surveys.	244
4-54.	18-Inch Diameter Shallow Dish EM with a 9-Foot Working Distance.	245

LIST OF ILLUSTRATIONS (continued)

<u>Figure</u>		<u>Page</u>
4-55.	Ellipsoidal Mirror Set-Up at JENOTS.	246
4-56.	Gain of the 18-Inch Diameter Ellipsoidal Mirror.	249
4-57.	Width of "Collection Volume" for the 18-Inch Diameter Ellipsoidal Mirror.	251
4-58.	Integral Closure Check for 3.56-in. Conical Nozzle, $V_J = 2253 \text{ ft/sec}$, $V_o = 0$.	253
4-59.	Integral Closure Check for 3.56-in. Conical Nozzle, $V_J = 2205 \text{ ft/sec}$, $V_o = 150 \text{ ft/sec}$.	254
4-60.	Integral Closure Check for 8-Lobe Nozzle, $V_J = 2154$ ft/sec, $V_o = 278 \text{ ft/sec}$.	255
4-61.	Integral Closure Check for 104-Tube Nozzle, $V_J = 2203$ ft/sec, $V_o = 295 \text{ ft/sec}$.	256
4-62.	Integral Closure Check for 2.0-in. STA Nozzle, $V_J =$ 2213 ft/sec , $V_o = 152 \text{ ft/sec}$.	257
4-63.	Axial Location of Peak Source Regions for 2.0-in. STA, 8-Lobe Daisy and 104-Tube Nozzles.	258
4-64.	Axial Location of Peak Source Regions for 2.0-in. STA, 104-Tube, and 3.56-in. Conical Nozzles.	259
4-65.	Axial Location of Peak Source Regions for 3.56-in. Conical, 8-Lobe Daisy, 104-Tube, and 20-in. STA Nozzles.	260
4-66.	Axial Location of Peak Source Regions for 3.56-in. Conical Nozzle.	261
4-67.	Axial Location of Peak Source Regions for 8-Lobe Daisy Nozzle.	262
4-68.	Axial Location of Peak Source Regions for 104-Tube Nozzle.	263
4-69.	Axial Location of Peak Source Regions for 2.0-in. STA Nozzle.	264
4-70.	Absorption of Sound by Turbulence.	273

LIST OF ILLUSTRATIONS (continued)

<u>Figure</u>		<u>Page</u>
4-71.	The Problem of Transforming From Static to Flight.	274
4-72.	Example of Synthesis of Exhaust Arc Noise.	274
4-73.	Recombination of Singularities.	275
4-74.	Example of the Recommendation Procedure - Aft Quadrant.	279
4-75.	Example of the Recommendation Procedure - Forward Quadrant.	280
4-76.	Impact of Refraction and Turbulence Absorption Corrections, on OASPL Directivity.	282
4-77.	Impact of Refraction and Turbulence Absorption Corrections, $f = 250$ and 500 Hz, Conical Nozzle.	283
4-78.	Impact of Refraction and Turbulence Absorption Corrections, $f = 1000$ and 2000 Hz, Conical Nozzle.	284
4-79.	Impact of Refraction and Turbulence Absorption Corrections, $f = 4000$ and 8000 Hz, Conical Nozzle.	285
4-80.	Impact of Refraction and Turbulence Absorption Corrections, $f = 250$ and 500 Hz, 8-Lobe Nozzle.	286
4-81.	Impact of Refraction and Turbulence Absorption Corrections, $f = 1000$ and 2000 Hz, 8-Lobe Nozzle.	287
4-82.	Impact of Refraction and Turbulence Absorption Corrections, $f = 4000$ and 8000 Hz, 8-Lobe Nozzle.	288
4-83.	Impact of Refraction and Turbulence Absorption Corrections, $f = 250$ and 500 Hz, 104-Tube Nozzle.	289
4-84.	Impact of Refraction and Turbulence Absorption Corrections, $f = 1000$ and 2000 Hz, 104-Tube Nozzle.	290
4-85.	Impact of Refraction and Turbulence Absorption Corrections, $f = 4000$ and 2000 Hz, 104-Tube Nozzle.	291
5-1.	Gates Learjet - Conical Nozzle.	296
5-2.	Gates Learjet - 8-Lobe Nozzle.	297

LIST OF ILLUSTRATIONS (Continued)

<u>Figure</u>		<u>Page</u>
5-3.	Microphone Array - Learjet Conical Nozzle Flight Test.	300
5-4.	Microphone Array - Learjet 8-Lobe Nozzle Flight Test.	301
5-5.	General Electric Acoustic Van - Gates Learjet Flyover Test.	302
5-6.	Interior of Acoustic Van.	303
5-7.	Equipment Schematic for Data Acquisition and Processing - General Electric Acoustic Van.	304
5-8.	A Typical Fiber Optics Trace for Overhead Determination.	307
5-9.	Information Flow Diagram - Flyover Data Processing and Adjustment.	310
5-10.	Learjet Static Data - Ground Reflection Corrections.	312
5-11.	Comparison of Measured and Free Field Flight Data.	316
5-12.	Comparison of Classical Free Field Corrections for 8-Lobe Nozzle Flight Data - $\theta_I = 100^\circ$.	317
5-13.	Comparison of Classical Free Field Corrections for 8-Lobe Nozzle Flight Data - $\theta_I = 140^\circ$.	318
5-14.	Comparison of Flush Mounted and 20-Foot Microphone 8-Lobe Nozzle Free Field Flight Data - $\theta_I = 100^\circ$.	319
5-15.	Comparison of Flush Mounted and 20-Foot Microphone 8-Lobe Nozzle Free Field Flight Data - $\theta_I = 140^\circ$.	320
5-16.	Comparison of Measured and Free Field Corrected - 4-Foot Microphone Flight Spectra - 400-Foot Altitude.	325
5-17.	Comparison of Measured and Free Field Corrected - 4-Foot Microphone Flight Spectra - 1000-Foot Altitude.	326
5-18.	Comparison of Measured and Free Field Corrected - 20-Foot Microphone Flight Spectra - 400-Foot Altitude.	327
5-19.	Comparison of Measured and Free Field Corrected - 20-Foot Microphone Flight Spectra - 1000-Foot Altitude.	328

LIST OF ILLUSTRATIONS (continued)

<u>Figure</u>		<u>Page</u>
5-20.	Peak OASPL and PNL Characteristics - Gates Learjet Flyover Test.	332
5-21.	90° OASPL and PNL Characteristics - Gates Learjet Flyover Test.	333
5-22.	50° OASPL and PNL Characteristics - Gates Learjet Flyover Test.	334
5-23.	Learjet Conical Nozzle OASPL Directivity Patterns.	335
5-24.	Learjet Conical Nozzle PNL Directivity Patterns.	336
5-25.	Learjet 8-Lobe Nozzle OASPL Directivity Patterns.	337
5-26.	Learjet 8-Lobe Nozzle PNL Directivity Patterns.	338
5-27.	Learjet Conical Nozzle - Maximum Angle Spectra.	339
5-28.	Learjet Conical Nozzle - 90° Spectra.	340
5-29.	Learjet Conical Nozzle - 50° Spectra.	341
5-30.	Learjet 8-Lobe Nozzle - 130° Spectra.	342
5-31.	Learjet 8-Lobe Nozzle - 90° Spectra.	343
5-32.	Learjet 8-Lobe Nozzle - 40° Spectra.	344
5-33.	F-106 Test Vehicle; J75 Main Powerplant; J85's Under Wings.	346
5-34.	F-106 Flyover Test - Baseline Nozzle.	347
5-35.	F-106 Flyover Test - 104-Tube Suppressor Nozzle.	348
5-36.	Microphone Set-Up - F-106/J85 Baseline Nozzle Flyover Test.	351
5-37.	NASA Sound Field for F-106/104-Tube Nozzle Test.	355
5-38.	F-106 Peak OASPL and PNL Characteristics.	357
5-39.	F-106 90° OASPL and PNL Characteristics.	358
5-40.	F-106 50° OASPL and PNL Characteristics.	359

LIST OF ILLUSTRATIONS (continued)

<u>Figure</u>		<u>Page</u>
5-41.	Schematic of F-106 Baseline Nozzle.	360
5-42.	F-106 Baseline Nozzle OASPL Directivity Patterns.	361
5-43.	F-106 Baseline Nozzle PNL Directivity Patterns.	362
5-44.	F-106/104-Tube Nozzle OASPL Directivity Patterns.	363
5-45.	F-106/104-Tube Nozzle PNL Directivity Patterns.	364
5-46.	F-106 Baseline Nozzle Max. Angle Spectra.	365
5-47.	F-106 Baseline Nozzle 90° Spectra.	366
5-48.	F-106 Baseline Nozzle 50° Spectra.	367
5-49.	F-106/104-Tube Nozzle Max. Angle Spectra.	368
5-50.	F-106/104-Tube Nozzle 90° Spectra.	369
5-51.	F-106/104-Tube Nozzle 50° Spectra.	370
6-1.	Schematic of the Test Track and Acoustic Measurement Arena for the Bertin Aerotrain.	373
6-2.	Aerotrain Test Facility.	374
6-3.	Bertin Aerotrain Conical Nozzle.	375
6-4.	Bertin Aerotrain 8-Lobe Daisy Nozzle.	376
6-5.	Bertin Aerotrain 104-Tube Nozzle.	377
6-6.	Aerotrain Background Noise - Static Conditions.	380
6-7.	Impact of Aerotrain Background Noise - Static Conditions, $\theta_I = 30^\circ, \theta_I = 60^\circ$.	381
6-8.	Impact of Aerotrain Background Noise - Static Conditions, $\theta_I = 90^\circ, 120^\circ$.	382
6-9.	Impact of Aerotrain Background Noise - Static Conditions, $\theta_I = 150^\circ$.	383
6-10.	Impact of Aerotrain Background Noise on Flight OASPL Directivity Patterns.	384

LIST OF ILLUSTRATIONS (Continued)

<u>Figure</u>		<u>Page</u>
6-11.	Impact of Aerotrain Background Noise - Conical Nozzle, $\theta_I = 30^\circ$.	386
6-12.	Impact of Aerotrain Background Noise - 8-Lobe and 104-Tube Nozzles, $\theta_I = 30^\circ$.	387
6-13.	Impact of Aerotrain Background Noise - Conical Nozzle, $\theta_I = 60^\circ$.	388
6-14.	Impact of Aerotrain Background Noise - 8-Lobe and 104-Tube Nozzles, $\theta_I = 60^\circ$.	389
6-15.	Impact of Aerotrain Background Noise - Conical Nozzle, $\theta_I = 90^\circ$.	390
6-16.	Impact of Aerotrain Background Noise - 8-Lobe and 104-Tube Nozzles, $\theta_I = 90^\circ$.	391
6-17.	Impact of Aerotrain Background Noise - Conical Nozzle, $\theta_I = 120^\circ$.	392
6-18.	Impact of Aerotrain Background Noise - 8-Lobe and 104-Tube Nozzles, $\theta_I = 120^\circ$.	393
6-19.	Impact of Aerotrain Background Noise - Conical Nozzle, $\theta_I = 150^\circ$.	394
6-20.	Impact of Aerotrain Background Noise - 8-Lobe and 104-Tube Nozzles, $\theta_I = 150^\circ$.	395
6-21.	Combustor Noise Spectra (from Reference 40).	397
6-22.	Impact of Extraneous Noise Sources on Aerotrain Data at 90° .	399
6-23.	Comparison of Aerotrain Data with J85 Core Engine Noise, (Reference 41).	400
6-24.	Modified Predictions of Combustion Noise Spectra for 8-Lobe and 104-Tube Nozzles (Based on Reference 41).	402
6-25.	Impact of Extraneous Noise Sources on Aerotrain Data at Maximum Noise Angles.	403
6-26.	Impact of Extraneous Noise Sources on Aerotrain OASPL Directivity Data (Conical Nozzle).	404

LIST OF ILLUSTRATIONS (Continued)

<u>Figure</u>		<u>Page</u>
6-27.	Impact of Extraneous Noise on Aerotrain OASPL Directivity Data (8-Lobe Nozzle).	405
6-28.	Impact of Extraneous Noise Sources on Aerotrain OASPL Directivity (104-Tube Nozzle).	406
6-29.	Impact of Extraneous Noise Sources on Aerotrain Spectra at Maximum Noise Angle.	408
6-30.	Impact of Extraneous Noise Sources on Aerotrain Spectra at 90° Angle.	409
6-31.	Impact of Extraneous Noise Sources on Aerotrain Spectra at 50° Angle.	410
6-32.	Impact of Extraneous Noise Sources on Aerotrain Spectra at Maximum Noise Angle.	411
6-33.	Impact of Extraneous Noise Sources on Aerotrain Spectra at 90° Angle.	412
6-34.	Impact of Extraneous Noise Sources on Aerotrain Spectra at 50° Angle.	413
6-35.	Aerotrain Microphone Array.	416
6-36.	Aerotrain Synchronization Procedure.	417
6-37.	Monitoring Locations of Cycle Parameters.	419
6-38.	Schematic of Aerotrain Operating Procedure.	420
6-39.	Summary of Peak PNL Characteristics.	426
6-40.	Summary of Peak OASPL Characteristics.	427
6-41.	Bertin Aerotrain - PNL Directivity Patterns, $V_J = 2200$ ft/sec, Conical.	428
6-42.	Bertin Aerotrain - PNL Directivity Patterns, $V_J = 2200$ ft/sec, 8-Lobe.	429
6-43.	Bertin Aerotrain - PNL Directivity Patterns, $V_J = 2200$ ft/sec, 104-Tube.	430
6-44.	Bertin Aerotrain - PNL Directivity Patterns, $V_J = 1830$ ft/sec, Conical.	431

LIST OF ILLUSTRATIONS (Continued)

<u>Figure</u>		<u>Page</u>
6-45.	Bertin Aerotrain - PNL Directivity Patterns, $V_J = 1830$ ft/sec, 8-Lobe.	432
6-46.	Bertin Aerotrain - PNL Directivity Patterns, $V_J = 1830$ ft/sec, 104-Tube.	433
6-47.	Bertin Aerotrain - PNL Directivity Patterns, $V_J = 1440$ ft/sec, Conical.	434
6-48.	Bertin Aerotrain - PNL Directivity Patterns, $V_J = 1440$ ft/sec, 8-Lobe.	435
6-49.	Bertin Aerotrain - PNL Directivity Patterns, $V_J = 1440$ ft/sec, 104-Tube.	436
6-50.	Bertin Aerotrain - OASPL Directivity Patterns, $V_J = 2200$ ft/sec, Conical.	437
6-51.	Bertin Aerotrain - OASPL Directivity Patterns, $V_J = 2200$ ft/sec, 8-Lobe.	438
6-52.	Bertin Aerotrain - OASPL Directivity Patterns, $V_J = 2200$ ft/sec, 104-Tube.	439
6-53.	Bertin Aerotrain - OASPL Directivity Patterns, $V_J = 1830$ ft/sec, Conical.	440
6-54.	Bertin Aerotrain - OASPL Directivity Patterns, $V_J = 1830$ ft/sec, 8-Lobe.	441
6-55.	Bertin Aerotrain - OASPL Directivity Patterns, $V_J = 1830$ ft/sec, 104-Tube.	442
6-56.	Bertin Aerotrain - OASPL Directivity Patterns, $V_J = 1440$ ft/sec, Conical.	443
6-57.	Bertin Aerotrain - OASPL Directivity Patterns, $V_J = 1440$ ft/sec, 8-Lobe.	444
6-58.	Bertin Aerotrain - OASPL Directivity Patterns, $V_J = 1440$ ft/sec, 104-Tube.	445
6-59.	Summary of OASPL Characteristics, $\theta_I = 90^\circ$.	446
6-60.	Summary of OASPL Characteristics, $\theta_I = 50^\circ$.	447

LIST OF ILLUSTRATIONS (Continued)

<u>Figure</u>		<u>Page</u>
6-61.	Comparison of Static and Flight Spectra, $\theta_I = 130^\circ$, $V_J = 2200$ ft/sec.	448
6-62.	Comparison of Static and Flight Spectra, $\theta_I = 130^\circ$, $V_J = 1800$ ft/sec.	449
6-63.	Comparison of Static and Flight Spectra, $\theta_I = 130^\circ$, $V_J = 1400$ ft/sec.	450
6-64.	Comparison of Static and Flight Spectra, $\theta_I = 90^\circ$, $V_J = 2200$ ft/sec.	451
6-65.	Comparison of Static and Flight Spectra, $\theta_I = 90^\circ$, $V_J = 1800$ ft/sec.	452
6-66.	Comparison of Static and Flight Spectra, $\theta_I = 90^\circ$, $V_J = 1400$ ft/sec.	453
6-67.	Comparison of Static and Flight Spectra, $\theta_I = 50^\circ$, $V_J = 2200$ ft/sec.	454
6-68.	Comparison of Static and Flight Spectra, $\theta_I = 50^\circ$, $V_J = 1800$ ft/sec.	455
6-69.	Comparison of Static and Flight Spectra, $\theta_I = 50^\circ$, $V_J = 1400$ ft/sec.	456
7-1.	Comparison of Flight Assurance and Aerotrain Peak Noise Characteristics.	460
7-2.	Comparison of Flight Assurance and Aerotrain Peak Noise Characteristics.	461
7-3.	Comparison of Aerotrain and Flight Assurance Data.	463
7-4.	Comparison of Aerotrain and Flight Assurance Data.	464
7-5.	Comparison of Aerotrain and Flight Assurance Data.	465
7-6.	Comparison of Aerotrain and Learjet Data - 8-Lobe Nozzle.	466
7-7.	Comparison of 8-Lobe Nozzle Aerotrain and Learjet Data.	467
7-8.	Comparison of 8-Lobe Nozzle Aerotrain and Learjet Data.	468

LIST OF ILLUSTRATIONS (continued)

<u>Figure</u>		<u>Page</u>
7-9.	Comparison of Aerotrain and F-106 Data - 104-Tube Nozzle.	470
7-10.	Comparison of Aerotrain and F-106 Data - 104-Tube Nozzle.	471
7-11.	Comparison of Aerotrain and F-106 Data - 104-Tube Nozzle.	472
7-12.	One-Third-Octave Directivity Comparisons - Conical Nozzle.	473
7-13.	One-Third-Octave Directivity Comparisons - 104-Tube Nozzle.	474
7-14.	One-Third-Octave Directivity Comparisons - 8-Lobe Nozzle.	475
7-15.	Comparison of Conical Nozzle OASPL Directivity Patterns, $V_J = 2200 \text{ ft/sec.}$	477
7-16.	Comparison of Conical Nozzle OASPL Directivity Patterns, $V_J = 1800 \text{ ft/sec.}$	478
7-17.	Comparison of Conical Nozzle OASPL Directivity Patterns, $V_J = 1400 \text{ ft/sec.}$	479
7-18.	Comparison of Conical Nozzle PNL Directivity Patterns, $V_J = 2200 \text{ ft/sec.}$	480
7-19.	Comparison of Conical Nozzle PNL Directivity Patterns, $V_J = 1800 \text{ ft/sec.}$	481
7-20.	Comparison of Conical Nozzle PNL Directivity Patterns, $V_J = 1400 \text{ ft/sec.}$	482
7-21.	Comparison of Conical Nozzle Δ OASPL Directivity Patterns.	483
7-22.	Comparison of Conical Nozzle Δ PNL Directivity Patterns.	484
7-23.	Comparison of 8-Lobe Nozzle OASPL Directivity Patterns, $V_J = 2200 \text{ ft/sec.}$	485
7-24.	Comparison of 8-Lobe Nozzle OASPL Directivity Patterns, $V_J = 1800 \text{ ft/sec.}$	486
7-25.	Comparison of 8-Lobe Nozzle PNL Directivity Patterns, $V_J = 2200 \text{ ft/sec.}$	487
7-26.	Comparison of 8-Lobe Nozzle PNL Directivity Patterns, $V_J = 1800 \text{ ft/sec.}$	488
7-27.	Comparison of 8-Lobe Δ OASPL Directivity Patterns.	489

LIST OF ILLUSTRATIONS (Concluded)

<u>Figure</u>		<u>Page</u>
7-28.	Comparison of 8-Lobe Nozzle Δ PNL Directivity Patterns.	490
7-29.	Comparison of 104-Tube Nozzle OASPL Directivity Patterns, $V_J = 2200 \text{ ft/sec.}$	492
7-30.	Comparison of 104-Tube Nozzle OASPL Directivity Patterns, $V_J = 1800 \text{ ft/sec.}$	493
7-31.	Comparison of 104-Tube Nozzle PNL Directivity Patterns, $V_J = 2200 \text{ ft/sec.}$	494
7-32.	Comparison of 104-Tube Nozzle PNL Directivity Patterns, $V_J = 1800 \text{ ft/sec.}$	495
7-33.	Comparison of 104-Tube Nozzle Δ OASPL Directivity Patterns.	496
7-34.	Comparison of 104-Tube Nozzle Δ PNL.	497
7-35.	Comparison of Conical Nozzle Spectra, $V_J = 2200 \text{ ft/sec.}$, $\theta_I = 120^\circ.$	498
7-36.	Comparison of Conical Nozzle Spectra, $V_J = 2200 \text{ ft/sec.}$, $\theta_I = 90^\circ.$	499
7-37.	Comparison of Conical Nozzle Spectra, $V_J = 2200 \text{ ft/sec.}$, $\theta_I = 50^\circ.$	500
7-38.	Comparison of 8-Lobe Nozzle Spectra, $V_J = 2200 \text{ ft/sec.}$, $\theta_I = 120^\circ.$	501
7-39.	Comparison of 8-Lobe Nozzle Spectra, $V_J = 2200 \text{ ft/sec.}$, $\theta_I = 90^\circ.$	502
7-40.	Comparison of 8-Lobe Nozzle Spectra, $V_J = 2200 \text{ ft/sec.}$, $\theta_I = 50^\circ.$	503
7-41.	Comparison of 104-Tube Nozzle Spectra, $V_J = 2200 \text{ ft/sec.}$, $\theta_I = 120^\circ.$	505
7-42.	Comparison of 104-Tube Nozzle Spectra, $V_J = 2200 \text{ ft/sec.}$, $\theta_I = 90^\circ.$	506
7-43.	Comparison of 104-Tube Nozzle Spectra, $V_J = 2200 \text{ ft/sec.}$, $\theta_I = 50^\circ.$	507

LIST OF TABLES

<u>Table No.</u>		<u>Page</u>
3-I	Summary of Fixed-Frame Facilities Initially Considered in this Program.	7
3-II	Fixed-Frame Acoustic Requirements.	8
3-III	Fixed-Frame Aerodynamic Performance Requirements.	8
3-IV	Evaluation of NASA-Ames 7 x 10-ft Wind Tunnel.	16
3-V	Evaluation of NASA-Ames 40 x 80-ft Wind Tunnel.	17
3-VI	Aerodynamic Evaluation of FluiDyne Engineering Corporation 66 x 66-inch Wind Tunnel	18
3-VII	Acoustic Evaluation of the NASA-Lewis 9 x 15-ft Wind Tunnel and Aerodynamic Evaluation of the NASA-Lewis 8 x 6-ft Wind Tunnel.	19
3-VIII	Description of Free Jet Facilities.	22
3-IX	Evaluation of NASA-Langley Free Jet/Jet Noise Facility.	25
3-X	Anechoic Jet Noise Facility Test Capabilities.	29
3-XI	JENOTS Free Jet Capability.	33
3-XII	Acoustic Test Matrix, Aerodynamic Test Conditions, Free Jet Area Ratio = 11.6.	56
3-XIII	Acoustic Test Matrix, Aerodynamic Test Conditions, Free Jet Area Ratio = 35.	57
3-XIV	Comparison of Max-Min OASPL's With Free Jet Velocity.	61
3-XV	Inlet Angle Minimum Number of Microphones.	107
3-XVI	Rocket Sled Facility Evaluation.	109
3-XVII	Typical Angular Resolution for Data Versus Measuring Distances and Playback Speeds.	140
3-XVIII	Confidence Limits as a Function of Sideline Distance and Record/Playback Ratio.	140

LIST OF TABLES (continued)

<u>Table No.</u>		<u>Page</u>
4-I	Fixed-Frame Demonstration Test, 3.56-in. Conical Nozzle.	185
4-II	Fixed-Frame Demonstration Test, 2.00-in. STA Nozzle.	186
4-III	Fixed-Frame Demonstration Test, 8-Lobe Nozzle.	187
4-IV	Fixed-Frame Demonstration Test, 104-Tube Nozzle.	188
4-V	Range of Test Variables.	189
4-VI	JENOTS Ground Reflection Corrections (Δ dBs to be added to SPL's).	190
4-VII	Test Matrix for Laser Velocimeter Measurements.	217
4-VIII	Test Matrix for Ellipsoidal Mirror Surveys.	247
4-IX	Algorithm Description.	267
4-X	Example of Source Decomposition.	277
4-XI	Typical Examples of Source Decomposition by Nozzle Fixed Uncorrelated Point Singularities.	293
5-I	Learjet Test Conditions Matrix, 8-Lobe Daisy Suppressor Nozzle.	298
5-II	Comparison of Fiber Optics and Laser-Tracker Overhead Determination.	308
5-III	Comparison of Fiber-Optics and Camera System Overhead Determination.	309
5-IV	Learjet Conical Nozzle Static Ground Reflection Corrections.	313
5-V	Learjet 8-Lobe Nozzle Static Ground Reflection Corrections.	314
5-VI	Learjet Flight Ground Reflection Correction.	321
5-VII	Learjet Flight Ground Reflection Corrections.	322

LIST OF TABLES (concluded)

<u>Table No.</u>		<u>Page</u>
5-VIII	Learjet Flight Ground Reflection Corrections.	323
5-IX	Learjet Flight Ground Reflection Corrections.	324
5-X	NASA/F-106 Test Matrix.	350
5-XI	F-106 Baseline Nozzle Static Ground Reflection Corrections.	352
5-XII	F-106 104-Tube Nozzle Static Ground Reflection Corrections.	353
5-XIII	F-106 104-Nozzle Flight Ground Reflection Corrections.	354
6-I	Aerotrain Test Matrix Conical Nozzle.	378
6-II	Examples of Aerotrain Flight Velocity Variation Through the Acoustic Arena.	421
6-III	One-Third-Octave Comparisons - Δ dB Static Minus Flight.	458

SYMBOLS

OASPL	Overall Sound Pressure Level, dB re: 0.0002 dynes/cm ²
SPL	Sound Pressure Level, dB re: 0.0002 dynes/cm ²
PNL	Perceived Noise Level, PNdB
P _{T8} /P _o	Total nozzle exhaust pressure over ambient pressure
P _o	Ambient Pressure, 1bf/in. ²
LV	Laser Velocimeter
EM	Ellipsoidal Mirror
α	Effective Absorption Coefficient
RH	Relative Humidity
PWL	Power Level (10^{-13} watts)
fD/V	Strouhal Number (Frequency \times Diameter over Velocity)
V _j , V _J	Jet velocity, isentropic, fully expanded, ft/sec
V _o	Airplane velocity, ft/sec
EGA	Extra Ground Attenuation
OAPWL	Overall Power Level
θ_I	Angle Referenced to the Inlet
f	Frequency
V(8)	Core (primary) velocity
V(28)	Fan (secondary) velocity
V _R	Relative velocity, V _J - V _o
1/3 OBSPL	One-Third-Octave Band Sound Pressure Level
T _{T8}	Exhaust Gas Total Temperature, ° R
A ₈ , A _j	Exhaust Nozzle Area, in. ²
M _o	Mach Number

SYMBOLS (concluded)

ρ_j	Fully expanded jet density, lbm/ft^3
ρ_{ISA}	Ambient density, lbm/ft^3
ω	Density ratio exponent
R	Source-to-observer distance, ft
D_j	Exhaust nozzle diameter, in.

1.0 SUMMARY

The DOT High Velocity Jet Noise Source Location and Reduction Program, Contract DOT-OS-30034, was conceived to bring analytical and experimental knowledge to bear on understanding the fundamentals of jet noise for simple and complex suppressor nozzles.

One key program objective was to evaluate techniques for investigating the effect that flight motion has on the noise signature of any arbitrary suppressor nozzle. The intent was to investigate methods of performing fixed-frame* and moving-frame** experiments under Task 4 of the contract and to then apply one selected method in Tasks 3 and 5 to gather data and resolve the most effective means of accounting for inflight effects without the costly and relatively imprecise requirement to actually conduct flight tests.

The technical method of approach was to explore a wide range of possible methods to attain the objectives. The methods evaluated were:

- Closed-circuit wind tunnels
- Free jets
- Rocket sleds
- High-Speed trains

The evaluation, during the first eleven months of the contract, resulted in identifying the advantages and disadvantages of the several fixed- and moving-frame techniques. Closed-circuit wind tunnels were found in general to be incapable of long-duration operation at elevated temperature. Similarly, the use of rocket sled tracks for moving-frame acoustic testing represented a high technical risk in terms of developing a sled to actually yield high quality data. Logistics associated with the remoteness of the test site plus the relatively costly and time consuming test procedures also made the cost effectiveness of the rocket sled method very low.

A new technical approach, which offered lower technical risk and significantly improved data quality, was ultimately chosen. The implementation

*"Fixed frame" refers to an experimental system in which the source (jet nozzle) is stationary relative to the observer (microphone).

**"Moving frame" refers to an experimental system in which the source is in motion relative to the observer just as in an actual flight test.

of this new approach was enhanced by the General Electric Company's development of an anechoic facility with free jet* capability in an existing test cell at the Evendale, Ohio, plant.

The new method of approach combines anechoic free jet tests with analytical transformations to effectively create the inflight effect in a fixed-frame test environment. The description and verification of this method are the subject of this report.

The details of a theoretical study aimed at relating noise signatures obtained in a free jet facility for simulation of forward flight effects on jet noise with the noise signature recorded in true flight is presented. The transformation is carried out by extracting the "static directivity" of the noise after correcting for refraction, turbulent scattering and absorption effects and then employing a suitable multipole source decomposition to evaluate the proper dynamic effect. The source decomposition indicates that the jet noise sources are primarily dipole and quadropole in nature. The impact of the turbulence absorption correction is found only to be important at frequencies above 2000 Hz.

The assessment of the technique consisted of testing three nozzles, conical, 8-lobe, and 104-tube, on a free jet facility and transforming the data to represent the inflight condition. These nozzles were chosen because they include a baseline nozzle with no suppression plus both a simple and an extremely complex suppressor nozzle design. Two approaches were used to provide a data base of actual moving-frame test results with which to compare the transformed free jet results for the same three suppressor designs in order to verify the inflight simulation technique. These included flight assurance testing using a Gates Learjet and an F-106 aircraft plus a highly controlled moving-frame validation test program using the Bertin Aerotrain.

The nozzle configurations evaluated on the free jet were one-third scale models of the nozzles evaluated on the Learjet, F-106, and Aerotrain. In the flight assurance and moving-frame validation testing, multiple passes, as well as multiple microphones, were used to assure an adequate data sampling. For both static and flight test, freestream velocities from static to 420 ft/sec were covered. In addition, nozzles were operated at both subsonic and supersonic exhaust conditions to assess the impact of shock noise. On the free jet facility, measurements were made using the laser velocimeter to determine the effect of freestream velocity on the turbulent mixing characteristics of all three configurations. The results of these test programs and the contents of this report are unique in the following respect:

*A free jet is, in effect, a wind tunnel without walls which provides a freestream flow of finite diameter to simulate the immersion of a jet in moving air.

- An adequate high quality data base has been made available for the first time to compare actual flight test data with highly controlled moving-frame test results, (i.e., Learjet and F-106 versus Aerotrain).
- The suppressor geometries evaluated are representative of simple and extremely complex suppressor nozzle designs and are complemented by a simple conical nozzle design. The data base for evaluation of the inflight simulation is, therefore, broad in the scope of potential suppressor configurations.
- The suppressor nozzles evaluated on the free jet were exact one-third scale models of the flight test hardware, thus, providing a unique data base for evaluation of the inflight simulation technique.

The Aerotrain test results on the basis of OASPL as a function of V_j , show that peak noise reduction relative to static levels for a conical nozzle increases with increasing flight velocity and increases with decreasing jet velocity. Suppressors, in contrast, demonstrate inflight noise reduction to be only a function of forward velocity. The inflight directivity characteristics in the forward quadrant appear insensitive to nozzle geometry for the range of conditions evaluated. The reduction at angle of peak noise for each of the three nozzle configurations does not extend to angles in the forward quadrant or at the 90° point. The 90° spectra revealed little or no change from static to flight for all three configurations over the range of conditions evaluated, indicative of no pure source noise reduction. One possible explanation for this lack of reduction at 90° is that the jet noise signature may be contaminated by combustion noise. Combustion noise predictions were made based on available semi-empirical techniques to assess the impact of combustion noise. The comparison of predicted combustion noise and flight noise spectra show that, for these configurations, the insensitivity of 90° spectra to flight were not due to combustion noise.

Using this data, extensive comparisons are presented for the three nozzles to illustrate the ability of the inflight simulation technique to predict the proper trends on the basis of peak OASPL, PNL, directivity characteristics, and spectrum shape.

It is concluded that the validity of the free jet technique and associated transformation procedure has been satisfactorily demonstrated.

This report describes the advantages and disadvantages of each type of simulation technique as well as the reasoning which led to the selection of the free jet technique. The free jet demonstration test program and the development of the transformation are also presented. The flight tests and the Aerotrain test are described, and the detailed verification analysis is presented. Finally, comparisons are presented between the Aerotrain and transformed free jet data to demonstrate the validity of the inflight simulation technique. It is then recommended that this technique be utilized in executing Task 5 of the program, thus providing data to use as a basis for incorporation into the Task 6 design guide.

2.0 INTRODUCTION

During the past two decades, extensive static testing has been conducted to determine the mechanisms of jet noise generation for simple and complex exhaust nozzle systems. An experimental data base has resulted that assists the designer. Design criteria have been formulated in the past using this data base to meet suppression goals for all types of exhaust nozzle systems. When prototype exhaust systems were designed and tested under actual flight conditions, however, the effectiveness of the suppressor nozzle system was observed to be much less than the projected static test results would predict. This apparent inability of static measurements to be accurately projected to flight has produced a critical problem for the acoustic designer.

One solution to this problem would be to develop a technique that would enable the inflight noise signature of any arbitrary suppressor nozzle to be determined using a ground-based facility and scale model test hardware with no more complexity than that currently being used for static testing. Once developed, this type of facility would provide a flexible and economical way to develop inflight design criteria. In addition, certain types of ground-based facilities (such as free jet, acoustic wind tunnels) would provide additional advantages, such as diagnostic measurement techniques, which could be utilized to optimize nozzle geometry plus provide data to evaluate the assumptions in proposed analytical models. Using conventional flight test techniques to accomplish this goal is impractical due to cost and due to the fact that the specific cycle of the engine test vehicle limits the application of the results. In addition, current types of diagnostic measurement techniques, such as laser velocimeters and ellipsoidal mirrors, cannot yet be practically applied on flight test vehicles.

This report presents the results of Task 4 of the High Velocity Jet Noise Source Location and Reduction program, DOT-OS-30034. Task 4 was formulated to evaluate several inflight simulation techniques which had to be identified and to select the most promising one for demonstration and validation in order that the selected technique, if successful, could be employed in the testing under Task 5 of the program.

3.0 EVALUATION OF FIXED- AND MOVING-FRAME TECHNIQUES

One approach to evaluate the flight noise signature of any exhaust nozzle system is by actual flight testing. Careful analysis of flight test procedures, however, reveals the following limitations of this technique:

- The inability to differentiate one effect from another.
- Acoustic propagation path lengths are long and atmospheric attenuations can have a significant effect.
- Obtaining accurate definition of the aircraft relative to the microphone location is difficult.
- The inability to use existing source location techniques to determine the changes in the mechanisms of jet noise due to inflight effects.
- Fabrication of flight weight hardware requires a long lead time and does not have the flexibility for parametric variation typical of scale model systems.
- Excessive costs are involved in flight test programs sufficient to preclude ever developing the insight necessary to systematically design nozzles with good inflight suppression characteristics.
- Test conditions are limited to the specific engine cycle, resulting in an inadequate vehicle for parametric testing.

The above limitations of flight testing provided the impetus to search for a more flexible and economical way to determine the flight noise signature of any exhaust nozzle configuration. Section 3 describes the survey and results of an investigation conducted as the initial work element of Task 4 of the High Velocity Jet Noise Program (DOT-OS-30034). Its purpose was to identify existing fixed-frame and moving-frame test facilities and to document each facility's capability relative to a set of established requirements.

This portion of Task 4 represents a logical extension of the facility surveys conducted under Task 1 of this contract. It was incorporated in Task 4 because it focuses only on those facilities which might be applicable to the study of "inflight" effects.

Section 3.1 covers the fixed-frame investigations and Section 3.2 presents the moving-frame survey results.

Section 3.3 presents a statistical analysis of the moving source problem by showing the statistically expected accuracy band of two different sets of data through an error analysis technique.

Section 3.4 documents the screening study survey conducted as an initial step in the process of developing an analytical transformation technique.

3.1 FIXED-FRAME FACILITIES

The purpose of Task 4 was the selection, evaluation, and validation of a method for determining the effects of flight, including relative velocity changes and dynamic effects, on the acoustic and aerodynamic characteristics of any given exhaust nozzle configuration.

A fixed reference-frame technique is a necessary element to consider in the program because it provides a practical capability of determining the inflight effects on thrust and aerodynamic flow fields. The advantages of using a fixed-frame facility for acoustic measurements are summarized as follows:

- Continuous operation at a given freestream condition allows the measurement of statistically adequate samples with an unsteady signal.
- No free-field corrections are required if the delta is measured in an anechoic environment.
- The background noise in a well designed acoustically-treated tunnel would be lower than the self noise level of a moving-frame vehicle, thus, increasing the potential exhaust velocity range that can be investigated.
- The nozzle test conditions in a closed-return wind tunnel or a free jet facility can be controlled precisely and are unaffected by the external environment.
- The capability exists for making detailed aerodynamic investigation such as laser velocimeter measurements, or other noise source location measurements.

The disadvantages of the various fixed-frame techniques assessed in this program are dependent on the type of facility chosen (closed-circuit wind tunnels or free jets). Therefore, they are presented in the sections describing each facility. A summary of the facilities reviewed is presented in Table 3-1. The facilities are divided into the two fixed-frame categories of closed-circuit wind tunnels and free jets.

Table 3-I. Summary of Fixed-Frame Facilities Initially Considered in this Program.

Wind Tunnels	Free Jet Facilities
<ul style="list-style-type: none"> ● NASA-Ames 7 by 10-Foot ● NASA-Ames 40 by 80-Foot ● FluiDyne 66 by 66-inch Transonic ● NASA-Lewis 8 by 6-Foot and 9 by 15-Foot ● NASA-Langley 30 by 60-Foot* 	<ul style="list-style-type: none"> ● Naval Ship Research and Development Center ● MIT (2) ● United Technologies Research Center ● NASA-Lewis ● NASA-Langley ● General Electric Anechoic Facility

*Facility was dropped from consideration during the preliminary evaluation because impractical modifications were required.

In comparing the facilities, two sets of requirements were identified which must be met in order to successfully demonstrate a fixed reference frame technique. One pertains to acoustic measurements, and the other to aerodynamic performance measurements. These requirements are summarized in Tables 3-II and 3-III, respectively.

Of the facilities investigated (Table 3-I), only a few are remotely capable of meeting the acoustic and/or aerodynamic performance requirements.

Summaries of the evaluations of the most promising wind tunnel and the free jet facilities are presented in Sections 3.1.1 and 3.1.2, respectively, followed in Section 3.1.3 by an evaluation of an idea to use an electronic simulation technique for correcting fixed-frame data to the inflight condition.

Table 3-II. Fixed-Frame Acoustic Requirements.

1. Sufficient model airflow is necessary to continuously supply a 4 to 6-inch throat diameter nozzle at a pressure ratio, P_{T8}/P_0 , of 4.0 at ambient flow temperature, or approximately 18 to 39 lbm/sec at $T_8 = 520^\circ R$, $P_0 = 14.7$ psia.
2. The facility must be capable of withstanding exhaust gas temperatures of $2500^\circ R$ for a period of 4 hours.
3. The facility should be anechoic in the 200 Hz to 40,000 Hz range.
4. Model external flow velocity must be variable between 0 and 350 ft/sec to simulate aircraft velocities from the start of the takeoff roll through the community noise measuring point.
5. The facility must allow an isolated, clear field of view of the exhaust plume for at least 25 exit diameters downstream of the nozzle exit plane in order to properly conduct laser velocimeter surveys.
6. The facility must be available for heavy utilization.

Table 3-III. Fixed-Frame Aerodynamic Performance Requirements.

1. Sufficient model airflow capacity to supply a 6-inch throat diameter nozzle to a pressure ratio, P_{T8}/P_0 , of 4.0 at ambient temperature. Unlike the acoustic requirement, the flow must be available only long enough to set the desired conditions and record data, thus, permitting the use of a "blowdown" model air supply.
2. All aerodynamic performance measurements may be conducted at ambient temperature conditions.
3. Model external flow velocity should be variable between 0 and 400 ft/sec.
4. A force and flow measuring system is required that is capable of determining static thrust coefficient and discharge coefficient to $\pm 1/2\%$, spanning a nozzle pressure ratio of $2.0 < P_{T8}/P_0 < 4.0$.
5. Availability of the facility corresponds to the acoustic requirement.

3.1.1 Closed-Circuit Wind Tunnels

Closed-circuit wind tunnels have been used for many years for aero-dynamic performance measurements. There would be a significant cost advantage if these same facilities could be used for acoustic measurements. Closed-circuit wind tunnels also have two inherent advantages over free jet type facilities:

- The medium through which the sound is propagating is in the correct reference frame. Dynamic effect corrections are therefore unnecessary. A doppler shift correction must be applied, however.
- Shear layer corrections that are necessary in a free jet facility are not required in a wind tunnel, because the microphones are placed inside the flow stream.

The acceptability of a closed-circuit wind tunnel must be determined relative to three additional criteria, however, as noted in Reference 1. These criteria are stated as follows:

- Impact of tunnel drive background noise, flow noise, and pseudo-sound contamination of the microphone measurements on the noise signature that is being measured.
- The contamination of the measured acoustic signature by reverberation.
- The ability to make measurements in a region where extrapolations to representative distances may be accomplished using inverse square law and appropriate air attenuations.

It is important to note that these criteria are in addition to those of Table 3-II and are relevant only to closed-circuit wind tunnels. Based on these criteria, four of the five facilities listed in Table 3-I were selected for a detailed evaluation. The evaluation results are presented in Sections 3.1.1.1 through 3.1.1.4.

3.1.1.1 NASA-Ames 7 x 10-Foot Wind Tunnel

Two 7 x 10 foot wind tunnels were the first built at Moffett Field (1939-40). NASA owns both tunnels and operates Tunnel No. 1. Tunnel No. 2 is operated by the U.S. Army Mobility Research and Development Laboratory at Moffett Field, California. Tunnel No. 1 was considered for modification and use in evaluation of in-flight effects (aircraft forward velocity) on jet noise and jet noise suppression.

A schematic of the wind tunnel is shown in Figure 3-1. The tunnel is of a fairly standard design, featuring a 14:1 contraction ratio nozzle, a 5 degree included angle diffuser, and a return section. The tunnel is closed circuit with some capability for air exchange. The 7 x 10-foot test section

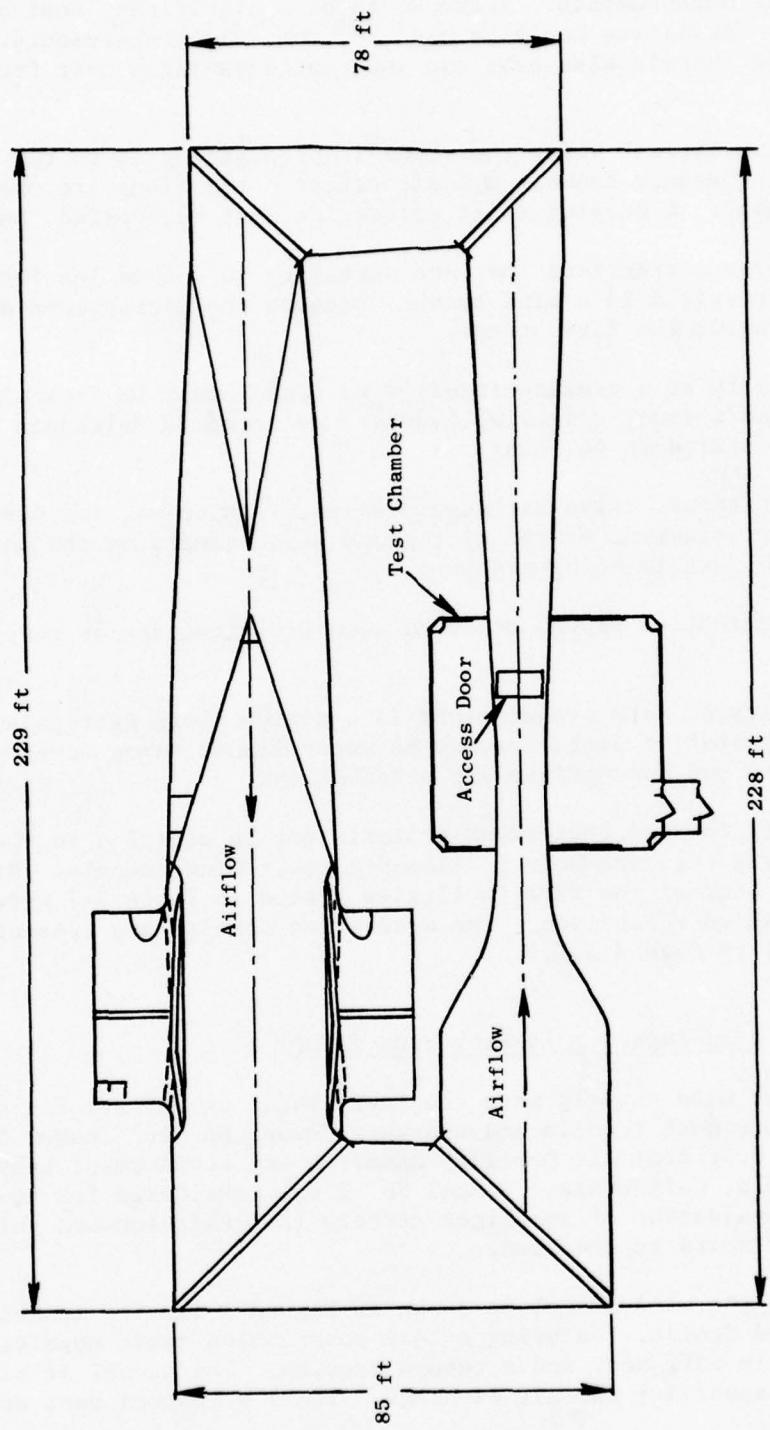


Figure 3-1. Schematic of NASA-Ames 7 x 10-ft Wind Tunnel.

is capable of test velocities up to 380 ft/sec. Tunnel No. 1 has large 5 x 7-foot glass windows in the test section wall which could provide access for Laser Velocimeter plume measurements or for flow visualization equipment.

The tunnel instrumentation includes a thrust table which is linked mechanically to readout scales. The pressure recording equipment includes 12 Scanivalves on separate channels plus 80 other channels for temperature, etc. The data is recorded on punched paper tape, compatible with the SEL 840 computer which provides timely data reduction. A high pressure air source is available (90 to 150 psia depending on nearby transonic tunnel operation) with flow capability of 3 to 6 pounds per second, dependent on size of test nozzle being supplied. An auxiliary air supply is available which can supply 25 lbm/sec at a compressor discharge pressure of approximately 50 psia.

The NASA-Ames 7 x 10-foot facility has had the test section acoustically treated to minimize the reverberation effects. A test program was conducted to evaluate the effectiveness of treating the wind tunnel. A schematic of the treated test section and the measurement locations are presented on Figure 3-2. Several microphone locations were used to determine the hall radius* of the wind tunnel and the tunnel background noise levels. The results of the survey indicated that the treatment did not effectively increase the hall radius of the wind tunnel. The reason for the ineffectiveness of the treatment was due to a relatively thick face plate. Following these initial series of tests, another series of measurements were conducted using no face plate. The results of these measurements, presented on Figure 3-3, indicated that the hall radius of the wind tunnel was increased from approximately 4 feet to 12 feet.

Directional microphone measurements were also conducted to determine the location of the significant noise source. The porous-strip microphone used is described in detail in Reference 2. These data are summarized in Figure 3-4. The directional microphone was placed 55 inches downstream from the source and was first aimed at the radiating source (0°) thereby measuring the incident noise, then the microphone was rotated 180° , thereby measuring the reflected noise from the end of the tunnel. This showed the reflected noise to be approximately 20 dB lower than the incident noise for the frequency region where measurements with the directional microphone were valid (1.6 to 10 kHz). When this microphone was aimed at the sidewall (at first reflecting point), it measured SPL's which were approximately 10 dB down from those measured at 0° . Taking into account that there are four walls, however, this difference would be 4 dB. Thus, the effectiveness of the acoustic treatment is of significant importance in the design of a wind tunnel for acoustic measurements.

*Hall radius is defined as the point where the level of the reverberant field and the direct field are equal.

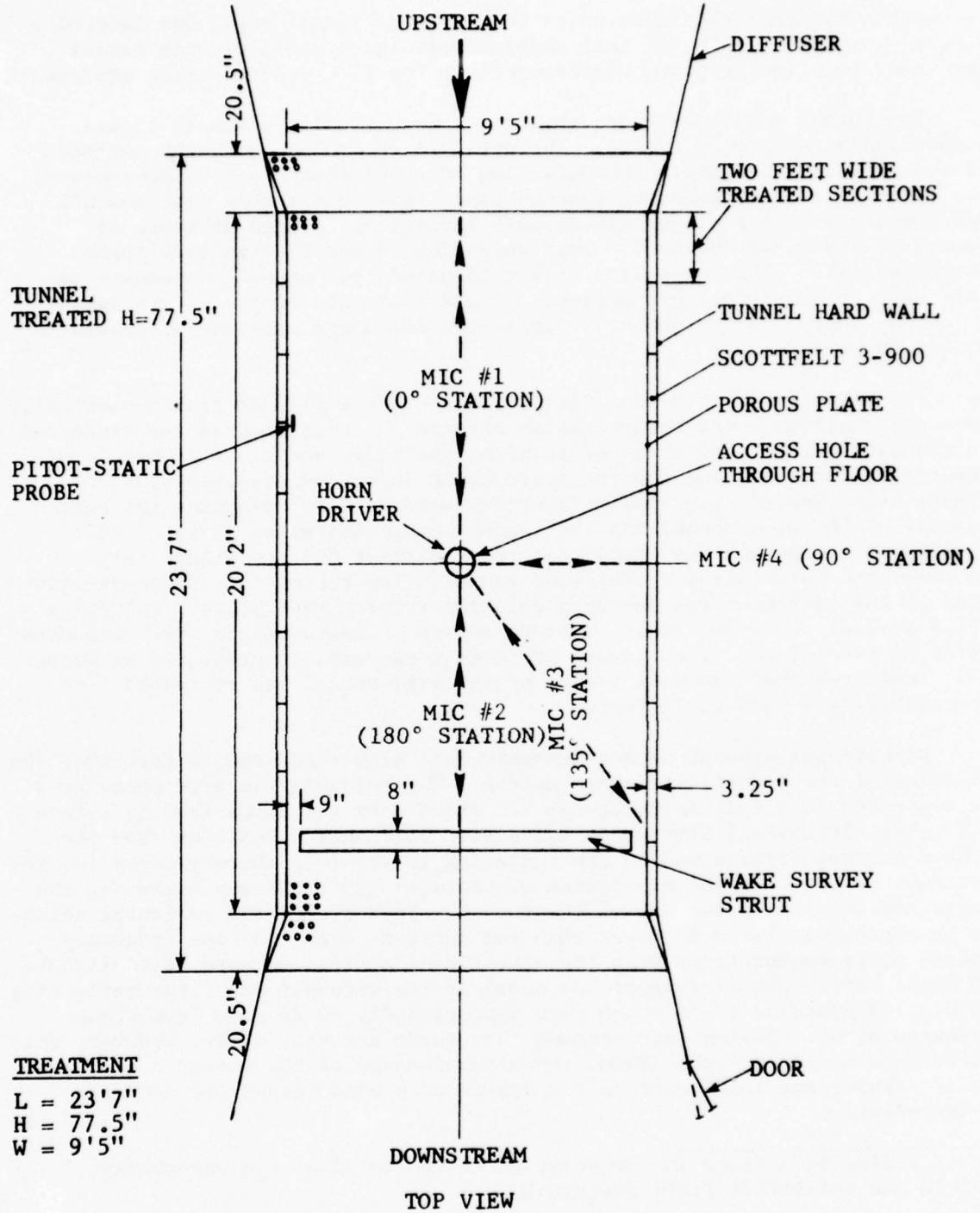


Figure 3-2. Schematic of NASA-Ames 7 x 10-ft Wind Tunnel Test Section.

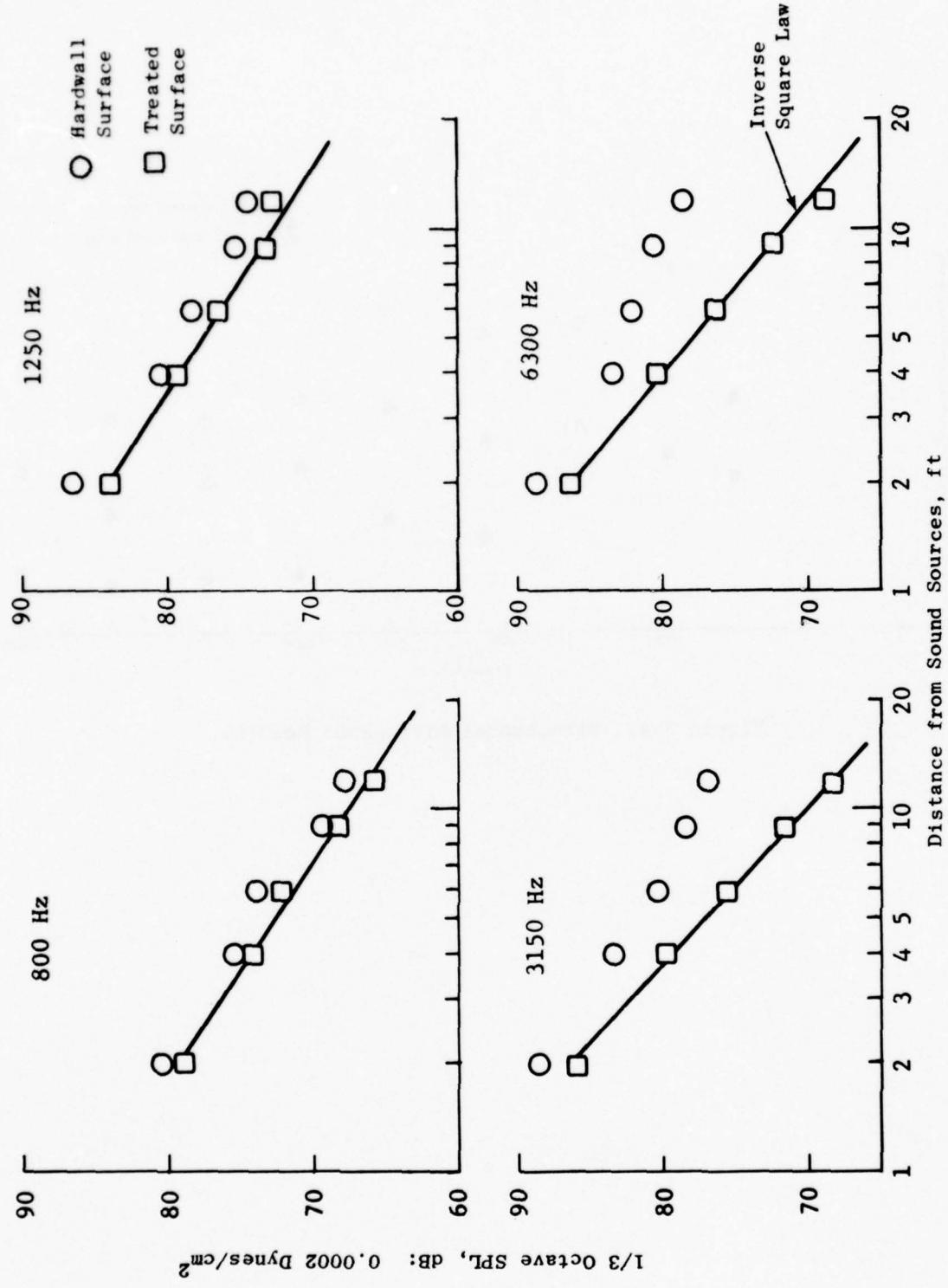


Figure 3-3. Effect of Acoustic Treatment on NASA-Ames 7 x 10-ft Wind Tunnel Hall Radius.

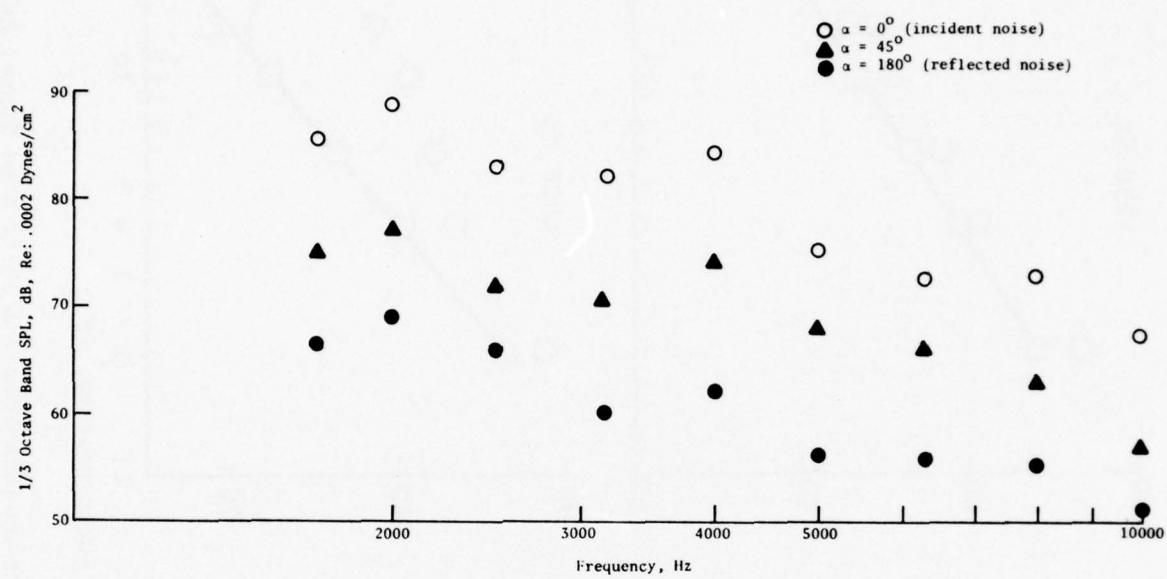


Figure 3-4. Directional Microphone Results.

In summary, the assessment of the 7 x 10-foot wind tunnel indicates that acoustic treatment is an effective way to minimize reverberation effects. However, the 7 x 10-foot wind tunnel can be operated only with a nozzle at ambient temperature. It would also require modifications before it could be used for performance measurements. The 7 x 10-foot Ames facility acoustic and aerodynamic performance measurement capabilities are compared to the requirements of Tables 3-II and 3-III in Table 3-IV.

The most severe limitation of the Ames 7 x 10-foot tunnel is the limited air supply, followed closely by the inability of the facility to withstand elevated exhaust gas temperatures. It should be noted that the requirements expressed in Table 3-II and 3-III are stringent and applicable to jet noise testing only. The inability to meet these requirements does not mean that the facility is not acceptable to perform other types of diagnostic acoustic measurements.

3.1.1.2 NASA-Ames 40 x 80-Foot Wind Tunnel

The NASA-Ames 40 x 80-foot wind tunnel has undergone extensive development for acoustic testing. Initial calibration of this facility was done as described in Reference 3. This facility has been demonstrated to be an acceptable facility for acoustic measurements on full-scale systems as described in Reference 4 and 5. Reference 3 presents a detailed discussion on the impact of background noise and reverberation effects on the noise measurements made in this facility. However, during the time period of this evaluation, the facility had not been utilized for scale-model jet noise measurement. The evaluation of the facility relative to the criteria presented in Tables 3-II and 3-III is presented on Table 3-V.

In summary, the NASA-Ames 40 x 80-foot wind tunnel would require extensive modification to meet the objectives of the proposed scale-model test program. Once these modifications were completed, test time would be a severe problem because of the high facility demand and utilization.

3.1.1.3 FluiDyne Engineering Corporation 66 x 66-Inch Wind Tunnel

The FluiDyne Channel 10 Facility is a transonic wind tunnel having a 66 x 66-inch slotted-wall test section. This is an induction-type tunnel in which atmospheric air is drawn through the test section using air ejectors to reduce the downstream pressure. The required test section Mach number is obtained by controlling the mass flow to the ejectors.

Thrust data is obtained by direct force measurement using a strain gage force balance system. This balance permits the measurement of net installed nozzle thrust during tests with external flow around the model. The model is located just upstream of the test nozzle in the support tube. The test nozzle is structurally isolated from the upstream (grounded) portion of the balance system by a thin elastic membrane. The force on the model assembly downstream of the seal was transmitted via the balance strain gage elements to a digital readout system.

Table 3-IV. Evaluation of NASA-Ames 7 x 10-ft Wind Tunnel.

<u>Acoustic Evaluation</u>	<u>Aerodynamic Evaluation</u>
1. Model airflow capacity was found to be inadequate. The rental of auxiliary compressors was investigated. A contractor could have supplied machines capable of 28 lbm/sec output at 325 psig, however, the cost was considered to be prohibitive.	1. Did not meet airflow requirements. Auxiliary air supply provided mass flow, but not enough pressure.
2. The facility could not withstand continuous, elevated temperatures for long periods of time without significant modification, thus making LV measurements difficult.	2. Met all aero performance measurement requirements.
3. The tunnel is partially anechoic between 800 Hz and 2000 Hz; the effective absorption coefficient, α , is 0.75.	3. Met external flow velocity requirements.
4. Met external flow velocity requirements.	4. The existing under floor thrust table has not been used for exhaust system performance testing. An extensive development program would have to be undertaken to modify the system to handle large airflows across the balance system and to calibrate out unwanted forces (such as friction and pressure loads on the model strut and support tube assembly). An alternative would be to buy an exhaust nozzle thrust/flow measuring system which is internal to the model support tube. The tunnel therefore does not meet the aerodynamic measuring requirements.
5. Met exhaust plume viewing requirements assuming cold flow testing.	5. Meets availability requirements.
6. Met availability requirements.	

Table 3-V. Evaluation of NASA-Ames 40 x 80-ft Wind Tunnel.

<u>Acoustic Evaluation</u>	<u>Aerodynamic Evaluation</u>
1. The air supply system is capable of 25 lbm/sec airflow and a pressure ratio of 3.5. However, the pressure ratio available to the nozzle would be somewhat less because 70 ft of pipe would be required to route this flow to the model.	1. The facility meets the weight flow requirements, but the maximum attainable pressure ratio is approximately $P_{T8}/P_0 = 3.0$.
2. The current combustor capability is from ambient to 1600° R.	2. Met external flow requirements.
3. The test section is partially treated. The half radius is large enough so that reverberation effects may be minimized and has been increased by a factor of three due to the addition of the acoustic treatment.	3. Freestream velocity range is 0 to 325 ft/sec.
4. Freestream velocity range is 0 to 325 ft/sec.	4. Force balance system would have to be modified to determine nozzle thrust coefficient.
5. The laser velocimeter system would need to be installed inside the wind tunnel. This would be a costly and high risk modification.	5. If all modifications were accomplished, facility availability for performance testing did not appear to be a problem.
6. Availability limited to approximately 9 weeks per year.	

The test data consisted of measurements of airflow rate, balance force, nozzle surface pressures, model total pressure, ambient pressure, meter total temperature and inlet pressures necessary to calculate the stream thrust entering the metric (floating) portion of the model assembly. Pressures were measured with mercury and water manometer banks and Bourdon-tube gages and recorded on Polaroid camera film. Temperatures were measured with iron/ constantan thermocouples and recorded on chart recorders.

This facility was found to be unsuitable for acoustic measurements, but was included as a means of obtaining aerodynamic performance data. This facility is evaluated basically on the aerodynamic requirements of Table 3-III in Table 3-VI.

Table 3-VI. Aerodynamic Evaluation of FluiDyne Engineering Corporation 66 x 66-Inch Wind Tunnel.

1. Maximum airflow capacity is 20 lbm/sec, limiting models to 4-inch throat diameters.
2. Met temperature requirement.
3. Minimum tunnel velocity is about 220 ft/sec, depending on model configuration. FluiDyne estimates that velocities can be lowered by "spoiling" the inlet flow with screens and adjusting tunnel mass flow with the downstream ejectors.
4. Met requirements for force and flow measuring systems.
5. Met facility availability requirements.

This facility would conditionally qualify for aerodynamic performance measurements, providing model throat diameter limited to 4 inches is acceptable and problems associated with controlling Mach number to speeds less than 220 ft/sec are resolved.

3.1.1.4 NASA-Lewis 8 x 6-Foot and 9 x 15-Foot Wind Tunnels

The NASA-Lewis 8 x 6-foot test section has been successfully used by General Electric for aerodynamic performance testing during the Supersonic Transport Noise Reduction Technology Program, Phase II, and was evaluated relative to the aerodynamic performance criteria in Table 3-III. The NASA Lewis 9 x 15-foot wind tunnel was evaluated relative to the acoustic criteria and Table 3-II. The results are presented in Table 3-VII.

Table 3-VII. Acoustic Evaluation of the NASA-Lewis 9 x 15-Foot Wind Tunnel and Aerodynamic Evaluation of the NASA-Lewis 8 x 6-Foot Wind Tunnel.

<u>Acoustic Evaluation (9 x 15-ft Wind Tunnel)</u>	<u>Aerodynamic Evaluation (8 x 6-ft Wind Tunnel)</u>
1. Met model airflow requirements.	1. Met airflow requirements.
2. No temperature capability.	2. Met temperature requirements.
3. Does not meet requirements.	3. Steady-state operation at 400 ft/sec is possible with transient data during tunnel stabilization period.
4. Velocity range limited to ft/sec.	4. Met accuracy requirements. 220
5. Extensive modifications	5. Met availability requirements.
6. Met availability requirements.	

The 8 x 6-foot tunnel was considered a strong candidate for performance testing, but the 9 x 15-foot wind tunnel was unacceptable as a jet noise acoustic test facility.

3.1.2 Free Jets

Free jet and closed-circuit wind tunnels are known to provide equivalent aerodynamic nozzle performance data, Reference 6. The free jet facility is a viable and cost effective system for aerodynamic and acoustic performance testing. Changes in the turbulent structure of a jet nozzle plume due to external flow are exactly simulated, if the area of the free jet is adequate, and are those experienced during flight. These attractive characteristics made it worthwhile that a free jet system be explored for its potential as a simulated "inflight effects" acoustic test facility.

The free jet technique, Figure 3-5, can in principle provide most of the relevant features of flight noise generation, without resorting to actual flyovers. Advantages are:

- Static and flight scale-model configurations can be identical.
- Freestream conditions can be precisely controlled for evaluating both far field acoustic characteristics and changes in jet turbulence structure.

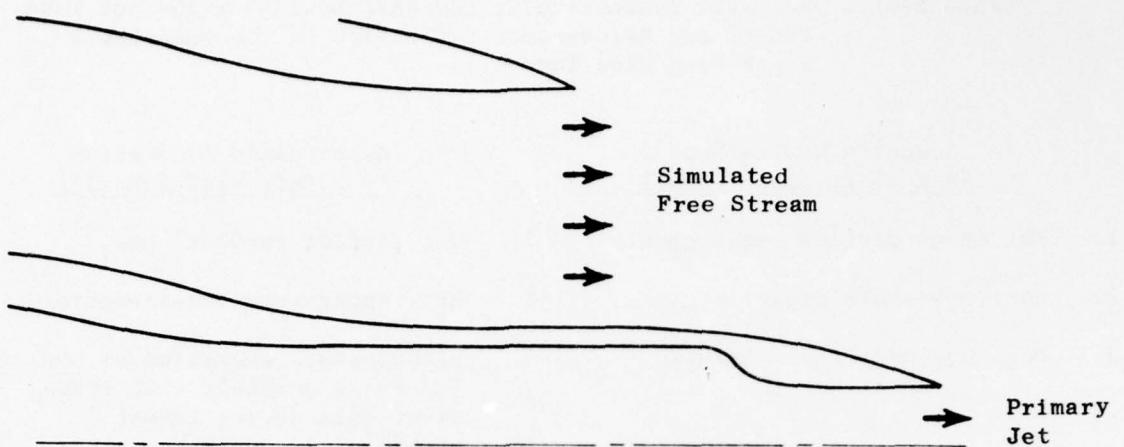


Figure 3-5. Free Jet Technique.

- Corrections to free field are not required (if in an anechoic environment).
- Detailed laser velocimeter measurements, as well as other in-jet noise source measurement techniques, can be utilized.

The free jet only provides partial results for the determination of inflight effects because the medium for sound propagation outside of the free jet boundary is stationary in relation to the source (whereas it is moving in the flight case).

During evaluation of fixed-frame testing techniques, available free jets and open-throat wind tunnels were examined relative to their potential in accommodating and conducting simulated wind-on acoustic tests. Table 3-VIII lists the candidate facilities assessed during the late 1973 period.

Although "free jet" capability was available, the potential for conducting jet noise testing under this wind-on environment was either just being planned or in the process of being checked out.

The following sections describe the NASA-Langley and General Electric Anechoic facilities, considered the most promising free jet candidates.

3.1.2.1 NASA-Langley Aircraft Noise Reduction Laboratory

During the evaluation phase described above, considerable attention was given to looking in depth at the new NASA-Langley free jet/jet noise facility to assess its applicability to the type and range of nozzles and the acoustic test matrix envisioned for evaluation not only in Task 4 but in the remaining phases of the DOT/FAA High Velocity Jet Noise Program.

This new acoustic research facility is primarily intended for fundamental studies and component research. The research air supply system, the anechoic chamber, and the reverberant chamber are elements which constitute part of the facility. These test chambers are acoustically and mechanically isolated so that other parts of the facility and other surrounding facilities cannot affect the anechoic and reverberant chambers and vice-versa.

The research air supply system consists of two separate sources which are humidity and temperature controlled. One is an 86,000-cfm source which supplies flow rates up to 150 ft/sec for a 4-foot diameter vertically mounted nozzle (this condition was used to specify the noise level of the facility). The other one is a 42,000-cfm source which supplies flow rates up to 700 ft/sec for a 1-ft², horizontally mounted nozzle.

Table 3-VIII. Description of Free Jet Facilities.

• Circa 1973

Facility	Freestream Velocity Capability, ft/sec	Test Section	Farfield Acoustic Environment	Jet Nozzle Test Capability	Comments
• NSRDC, Carderock Anechoic Facility	~ 200	Large (~ 60 ft ²)	Anechoic	No	Undergoing checkout at time of study, new operational - specifically being utilized for non-jet noise activities.
• MIT, Cambridge Low Noise, Low Turbulence Wind Tunnel	~ 180	Small (~ 1.6 ft ²)	Anechoic	No	Operational, acoustic, and vibrations work.
• UTRC Acoustic Research Tunnel	~ 700	Variable (~ 4 to 10 ft ²)	Anechoic	No (Yes)*	Operational, *Co-annular hot jet flow capability added since then ($V_J \approx 2000$ ft/sec).
• MIT V/STOL Noise Open Jet Wind Tunnel	~ 120	Large (~ 38 ft ²)	Anechoic	No	Operational, very low velocities.
• NASA Lewis Free Jet	~ 260	Small (~ 1.2)	Outdoor	Yes	Operational, cold flow jet only ($V_J \approx 1000$ ft/sec).
• NASA Langley Aircraft Noise Reduction Laboratory Free Jet	~ 700	Variable (~ 1 to 13 ft ²)	Anechoic	Yes	Not operational during study, currently being check out.

The anechoic chamber is a double-wall structure consisting of a steel-framed box mounted on springs within a concrete building. A 36-inch air space is provided between the steel-framed box and the concrete building. The inside of the steel-framed box is lined with 34-inch long (base to tip) fiberglass wedges which are covered to prevent flaking and are 99 percent absorptive at 100 Hz. The chamber dimensions inside the wedge tips are 20 ft x 30 ft x 30 ft high. It is intended to leave the test-level removable floor grating in place during testing except for those tests involving very high frequencies. There is a large collector in the ceiling to exhaust airflow from the vertical nozzle and small holes along the base of the walls to allow air seepage to help reduce turbulence caused by collector aspiration. One of the walls contains a collector/intake for the horizontal air nozzle.

The reverberant chamber is also of double-wall construction, i.e., a concrete box within a concrete building with the inner chamber mounted on springs. There is a 10-inch air gap between the chambers. All the inner surfaces of this chamber are of smooth hard concrete with the interior walls and ceiling splayed. The nominal inside dimensions are 20 ft by 28 ft by 14 ft high.

The model air supply limits continuous operation to nozzles of two-inch throat size. Although the anechoic chamber is capable of withstanding high exhaust gas temperatures, no provision is available for heating the air supply.

In order to meet the acoustic and aerodynamic requirements of Task 4, facility modifications would be required. Referring to Tables 3-II and 3-III, the facility acoustic and aerodynamic capabilities are compared to requirements in Table 3-IX.

This facility was omitted from further consideration because the air supply for scale-model acoustic testing was severely limited.

3.1.2.2 General Electric Anechoic Jet Noise Facility

This section describes the anechoic jet noise facility designed and constructed by the General Electric Company to conduct acoustic tests of baseline and suppressor nozzles. Plans are also under way to modify this existing anechoic facility to permit simulated wind-on testing. The "as is" assessment of the JENOTS free jet test setup, to be discussed in the next section (3.1.2.1), basically provided the design criteria for the proposed anechoic facility modification.

The General Electric Anechoic Test Facility was built in an existing engine test cell exhaust stack measuring 42 feet in diameter and 72 feet in height. A photograph of the interior of the facility is shown in Figure 3-6.

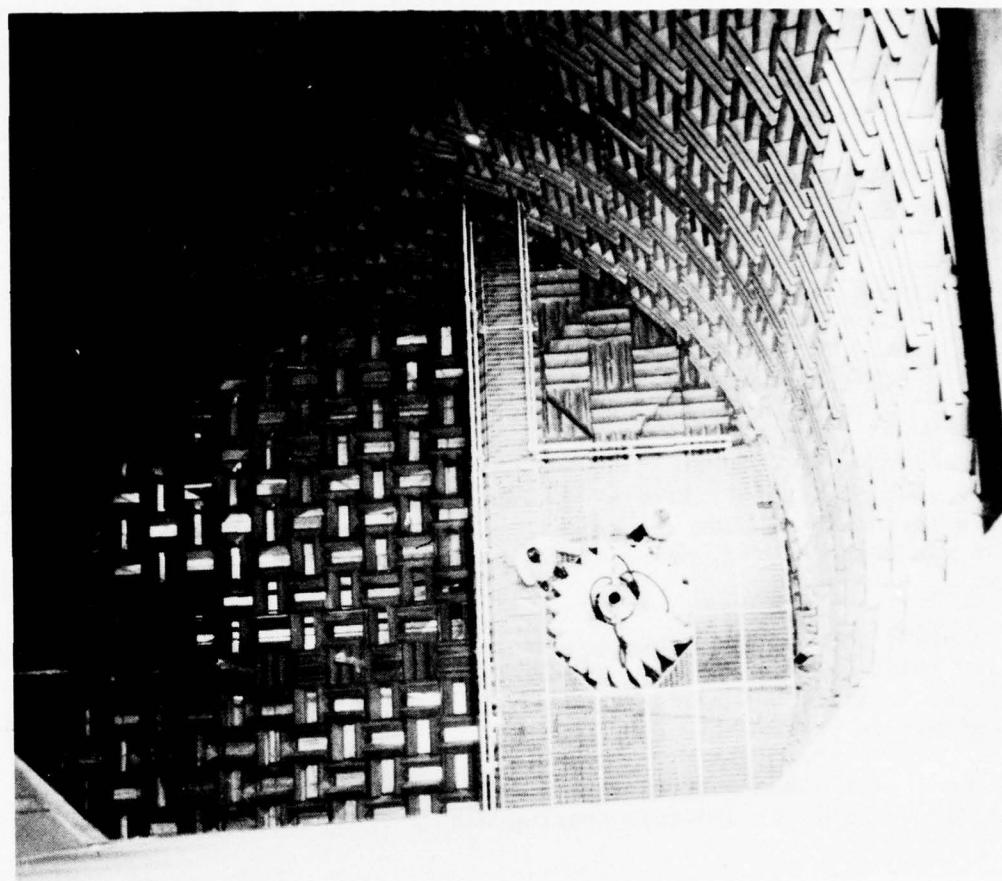


Figure 3-6. Interior of General Electric Jet Noise Anechoic Facility.

Table 3-IX. Evaluation of NASA Langley Free Jet/Jet Noise Facility.

<u>Acoustic Evaluation</u>	<u>Aerodynamic Evaluation</u>
1. A significant increase in the model air supply capacity would have been required. NASA Langley investigated this possibility and estimated it could have been done at a substantial cost. An investment of this magnitude was not considered as being cost effective at that time.	1. The air supply was capable of providing 17 lbm/sec for approximately 30 sec. This would have been enough to run a 4-inch throat diameter nozzle to a nozzle pressure ratio of 4.0 and allow the acquisition of aerodynamic performance data.
2. A burner system would have to be installed to meet the requirements.	2. Met temperature requirements.
3. Met anechoic requirements.	3. Met external flow velocity requirements.
4. Met external flow velocity requirements.	4. No system for measuring thrust was available in the present facility.
5. An observation window was provided and should have given an adequate field of view for the LV with minor modifications.	5. Meeting current Task 4 schedule would have been dependent on the time required to make facility operational.
6. Other than the air supply problem, the facility could have met program schedules with some initial slippage, and assuming no main operational development and check out delays.	

The chamber inner surfaces are lined with Owens Fiberglas "Intermediate Service Board" which is a lightweight (3 lb/ft^3) insulation composed of fiberglass fibers bonded together in semirigid board-like form with a special high temperature binder satisfactory for temperatures up to 850° F . In regions of the facility where the wedges may be exposed to degradation due to flow impingement, the wedges are wrapped in glass fiber cloth. The wedge assemblies are 8 inch x 24 inch x 19 inch deep (3 per module) in blocks 2 ft x 2 ft mounted on 18-gage steel base frames which are mounted on steel tracks fastened to the wall with a 3-inch air space giving an overall wedge top-to-wall surface distance of 22 inches. This installation is designed to meet a low frequency cut-off requirement of below 220 Hz and 0.99 absorption coefficient above 220 Hz. The flooring around the test section is removed for all acoustic testing.

To satisfy the aspiration effect of the test models, two air inlet ducts, 13 ft 4 in. x 16 ft x 12 ft, are located at the base of the test chamber. Air is drawn through the ducts into two separate acoustically lined plenums and then through the false floor where the middle wedges are omitted (34% open), and into the chamber (Reference Figure 3-7) to maintain low noise levels in the chamber during other test cell operations.

The two air ducts contain silence baffles using Owen Corning impregnated fiberglass which has a relatively low water absorption rate and a fill density of 4 lb/ft^3 . Each baffle is bent so as to prevent "line of sight" into or out of the lower chamber area (tail canted down $8-1/2^\circ$ with the horizontal). Each inlet silencer is designed for a maximum pressure differential (ΔP) of 0.4 inches of water at 400 lb/sec maximum total combined airflow at standard atmospheric conditions.

To meet OSHA near field, plant boundary, and local community allowable sound pressure levels, an exhaust stack "T" silencer system at the top of the chamber is used. Exhaust gases from the test model are collected at the base of the "T" and exhausted out the two exhaust ducts (13 ft x 13 ft x 7 ft) at the top of the "T". The exhaust silencers contain baffles using Owens Corning nonimpregnated fiberglass which has a relatively low water absorption rate and a density of 6 lb/ft^3 . Each baffle is bent to prevent "line of sight" into and out of the chamber. Each silencer is designed for a maximum pressure differential (ΔP) of 0.27 inches of water corresponding to 770 lb/sec maximum total combined airflow.

The chamber will accommodate both single-flow and dual-flow models within the following operating capabilities:

- Turbojet models - single flow
 - Maximum size, 6-inch diameter conical nozzle (28.3 in.^2)
 - Maximum pressure ratio, 4.0
 - Exhaust gas temperature, 560° R to 3000° R
 - Airflow, 38 - 18 lb/sec

- Turbofan models - dual flow

- Conical nozzle of 10.5-inch diameter (86.6 in.^2) (equivalent to the largest coannular nozzle to be used at a maximum pressure ratio of 2.0)

	<u>Cold</u>	<u>Hot</u>
Temperature	560° R	1960° R
Airflow	57 lb/sec	30 lb/sec

- Conical nozzle of 6-inch diameter (28.3 in.^2) equivalent to largest coannular nozzle to be used at a maximum pressure ratio of 4.0

	<u>Cold</u>	<u>Hot</u>
Temperature	560° R	1960° R
Airflow	42 lb/sec	22.5 lb/sec

Acoustic data is recorded in a central data acquisition/reduction area on a Sangamo/Sabre IV recorder operating with IRIG wideband group I electronics at 120 in./sec giving an operating range of 0 to 125 kHz. Three different sound-field configurations are used to record these data.

1. Far Field - 13 microphones positioned at acoustic angles of 40° to 160° (in respect to the nozzle inlet) along the ceiling, wall, and floor. Figure 3-6 shows the 40° to 60° microphone positions.
2. Near Field - one microphone which can be translated anywhere in a plane between the nozzle and far-field microphones.
3. Ellipsoidal Mirror - one microphone mounted at the focal point in an ellipsoidal mirror. The mirror can be traversed parallel to the jet flow to a height of 20 ft above the exit plane of the test nozzle.

As previously mentioned, plans to design and modify this facility to accommodate wind-on testing are currently underway. Figure 3-7 schematically depicts the proposed facility modifications which will permit testing of single- and dual-flow nozzle systems within a 13-foot-square free jet test section simulating velocities up to $M_0 = 0.30$. (See Table 3-X).

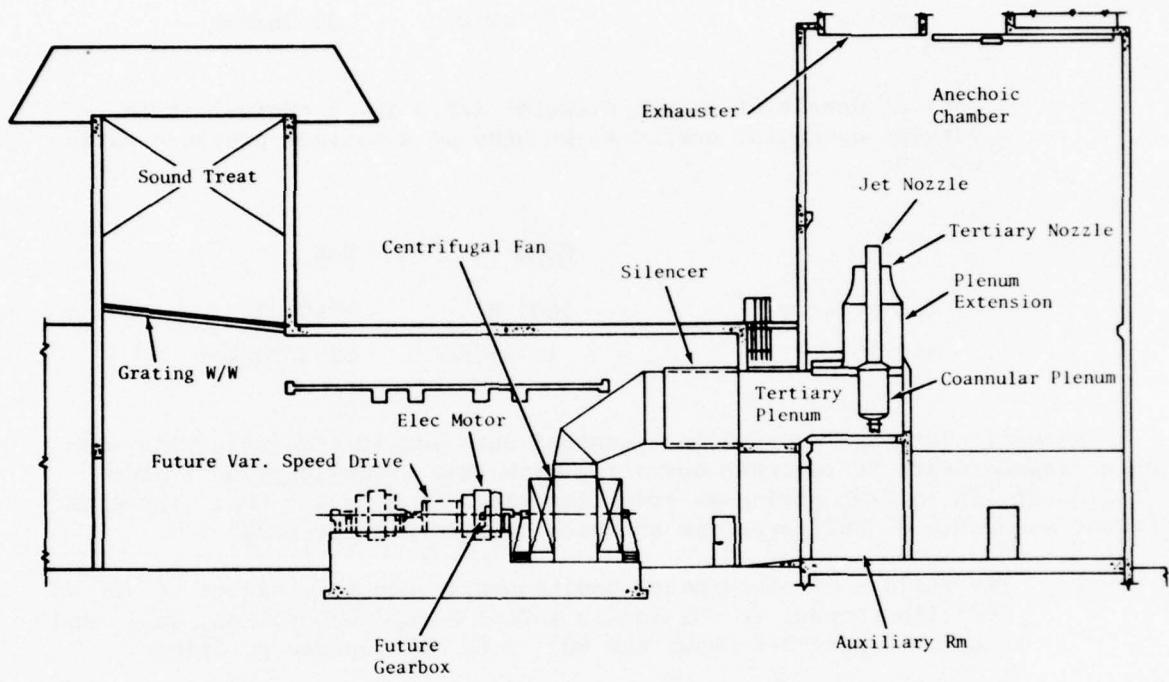


Figure 3-7. Schematic of General Electric Free Jet Anechoic Facility.

3.1.3 "As-Is" Assessment of Free Jet Technique

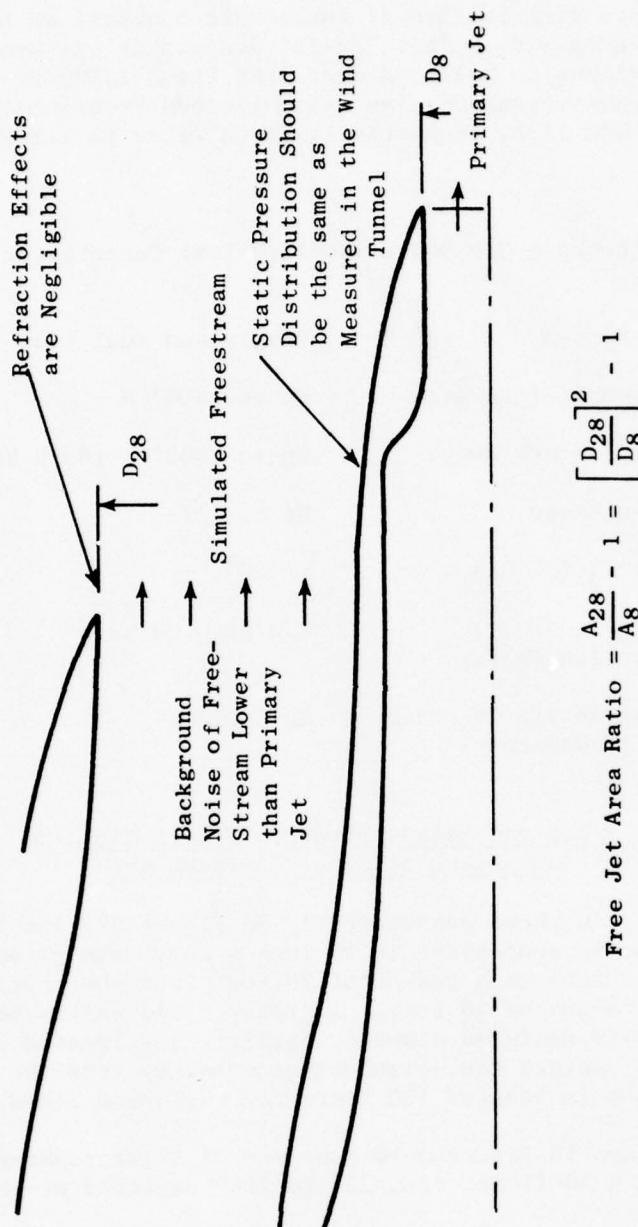
A program of analytical and experimental studies was conducted to determine: (1) the most acceptable free jet-to-nozzle area ratio, (2) the effect of noise produced by the simulated freestream, and (3) the duplication of external pressure distribution of the nozzle boattail as measured in the wind tunnel (see Figure 3-8). This "as-is" assessment was conducted at the General Electric Jet Engine Noise Outdoor Test Stand (JENOTS) using 2.0- and 3.56-inch diameter convergent nozzles which yielded free jet-to-nozzle exit area ratios of 35 and 11.6, respectively (area ratio is illustrated in Figure 3-8).

Table 3-X. Anechoic Jet Noise Facility Test Capabilities.

3.1.3.1 Test Setup and Nozzle Hardware Description for "As-Is" Assessment of Free Jet Technique

The JENOTS facility is shown schematically in Figure 3-9 and pictorially in Figure 3-10. The nozzle centerline is 55 inches above the ground plane which is composed of concrete to a radius of 20 feet from the nozzle exit and then crushed rock to a radius of 40 feet. A grassy field exists beyond the acoustic arena. Specially designed acoustic barriers are located 60 feet from the sound field to protect the neighboring community from the high sound levels. The control room is located 100 feet from the sound field.

The sound field shown in Figure 3-10 consists of 14 microphones arranged on 10° intervals around a 40-ft arc from 30° to 160° centered at the nozzle discharge plane.



$$\text{Free Jet Area Ratio} = \frac{A_{28}}{A_8} - 1 = \left[\frac{D_{28}}{D_8} \right]^2 - 1$$

Figure 3-8. Free Jet Critical Aero - Acoustic Design Criteria.

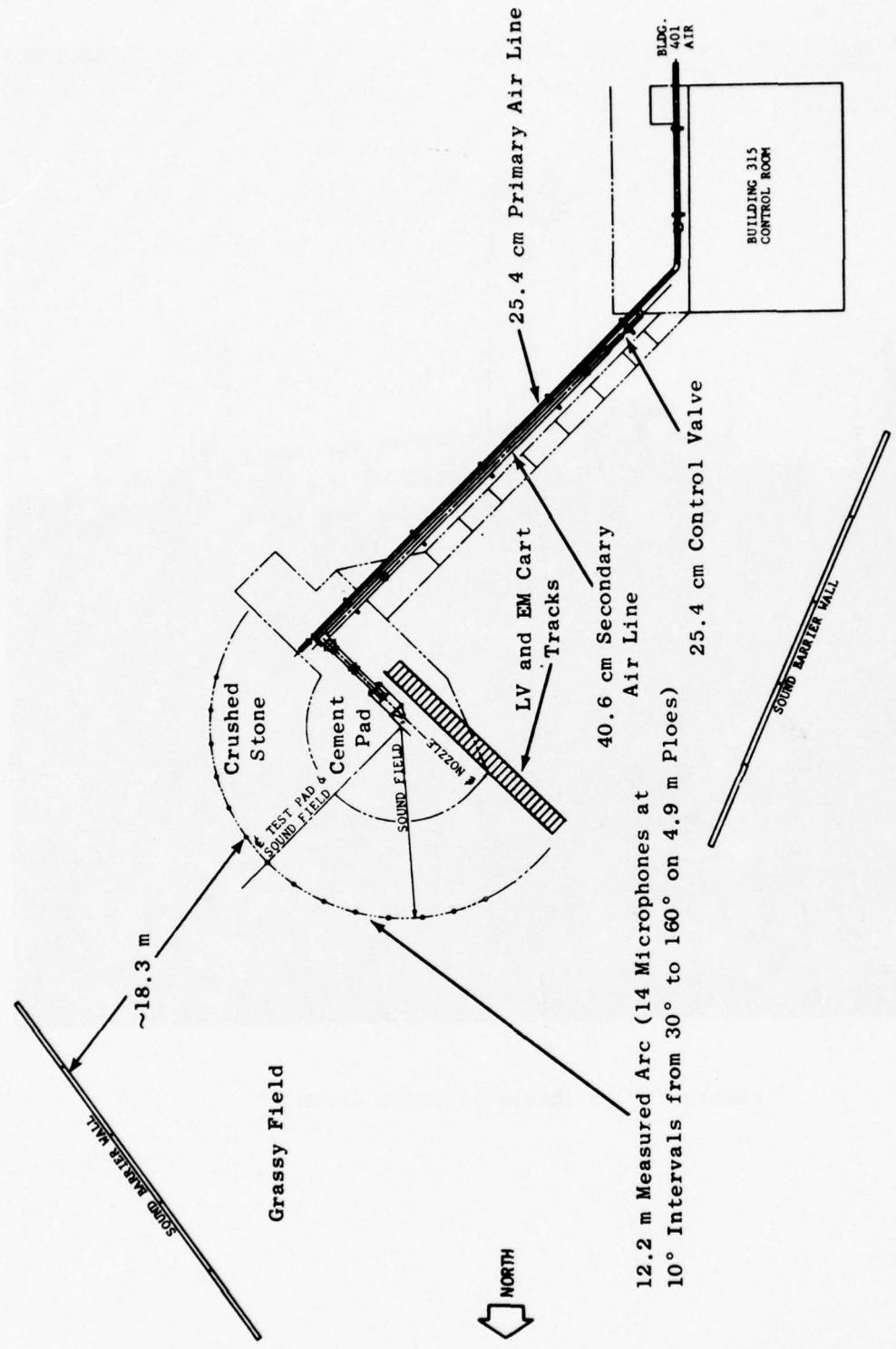


Figure 3-9. Schematic of JENOTS Facility Acoustic Arena.



Figure 3-10. JENOTS Acoustic Arena.

The microphones are elevated 16 feet above the ground on specially designed "goose neck" mounts to minimize the influence of reflections.

The outdoor arena is subject to ambient weather conditions. Outside air temperature, barometric pressure, and wet- and dry-bulb temperatures are recorded throughout a test. This information is used to correct the sound data to standard day. Wind speed and direction also are recorded.

Acoustic testing is conducted only during dry conditions, at wind levels below 10 mph.

The free jet (which is essentially a coannular facility) at JENOTS is shown schematically in Figure 3-11 and pictorially in Figure 3-12. Air for the primary and free jet (secondary) streams is supplied from the Evendale central air supply system through 10-inch and 16-inch air lines, respectively. The plenum chamber, to which the test models are attached, is shown schematically in Figure 3-13. It serves a two-fold purpose: (1) gives the flow a uniform velocity profile, and (2) eliminates any high-frequency system noise through the use of acoustically treated baffles located in the secondary and primary streams.

Flow conditions for the primary and free jet (secondary) streams are controlled separately, with the airflows being measured using an orifice-plate system coupled with pressure and thermocouple rakes. Rig instrumentation data are converted to digital punched tape and displayed in engineering units through the use of a time-sharing computer program. Burner systems located in the air supply lines prior to the plenum chamber provide heated streams. The range of conditions under which the free jet facility operates is presented in Table 3-XI.

Table 3-XI. JENOTS Free Jet Capability.

Free jet total temperature	Ambient
Primary flow total temperature	Ambient to 1800° R
Primary flow pressure ratio	1.05 → 4.0
Free jet velocity	0 → 420 ft/sec
Free jet weight flow	0 → 90 lb/sec
Primary stream weight flow	0 → 30 lb/sec

The outer shroud, which serves as the free jet nozzle, is attached downstream of the coannular plenum flange (Figure 3-13). Shroud outer diameter and geometry were varied from 12.0- to 12.6-inch diameter to accommodate the 2- and 3.56-inch diameter primary nozzles.

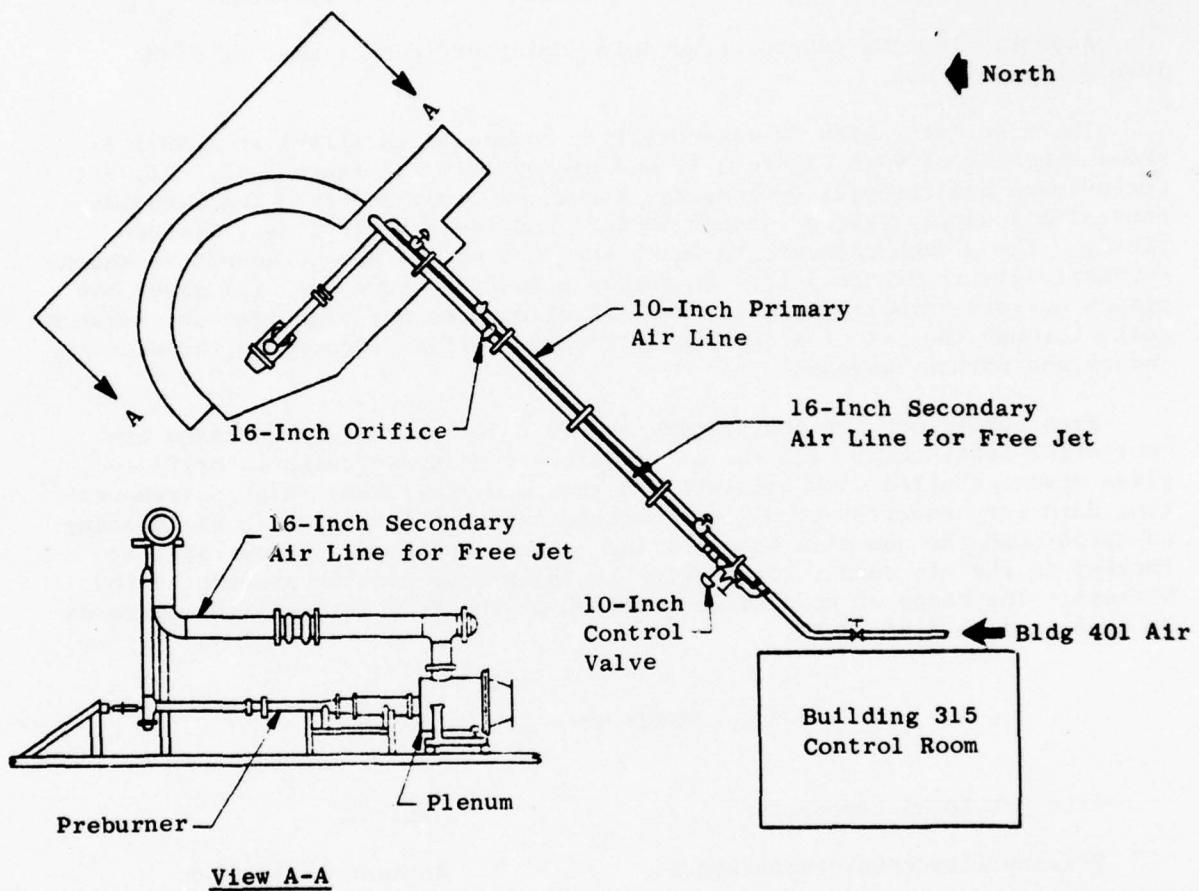


Figure 3-11. Schematic of Coannular-Flow JENOTS Facility.

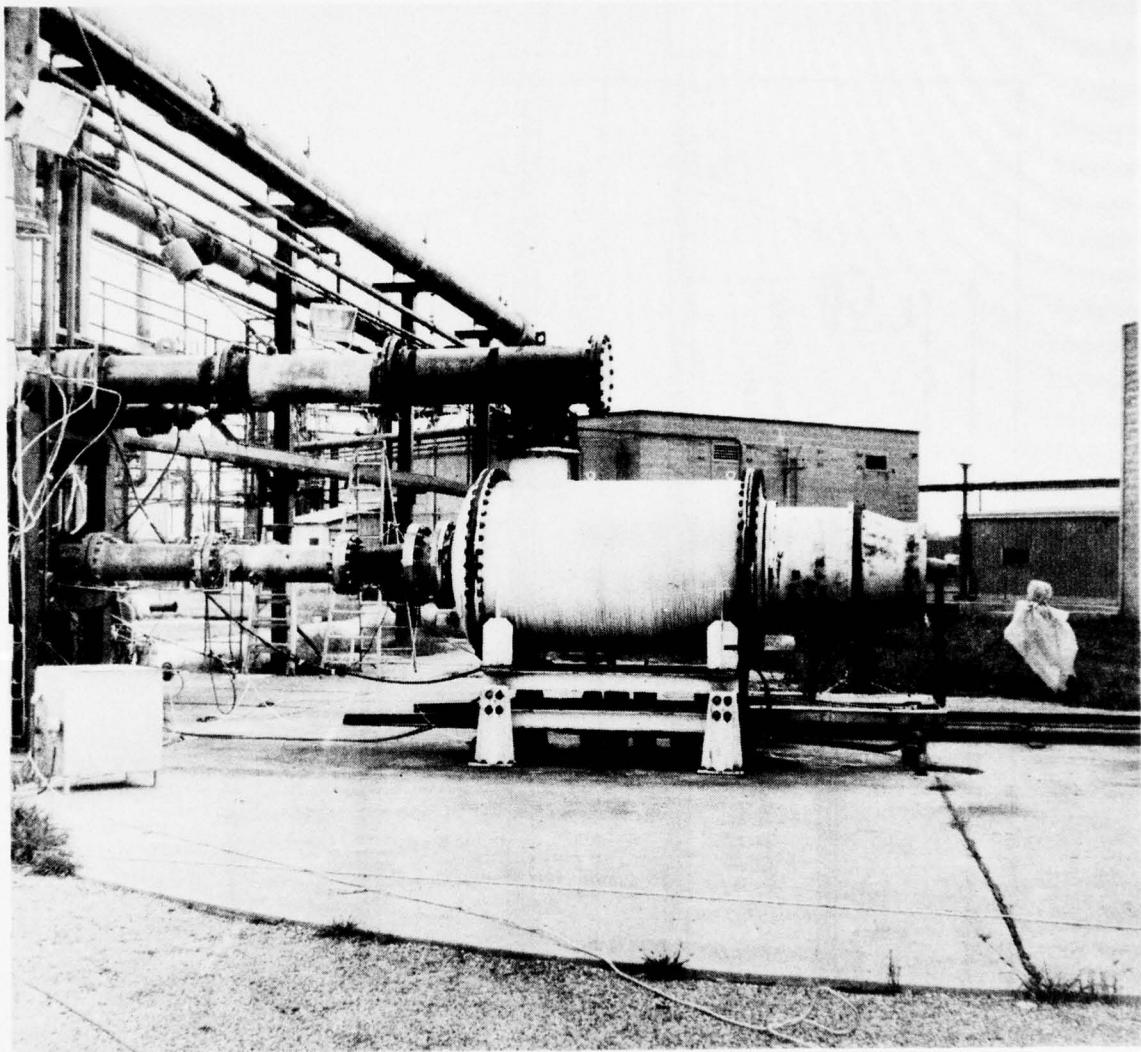


Figure 3-12. Free Jet/Coannular Plenum Chamber.

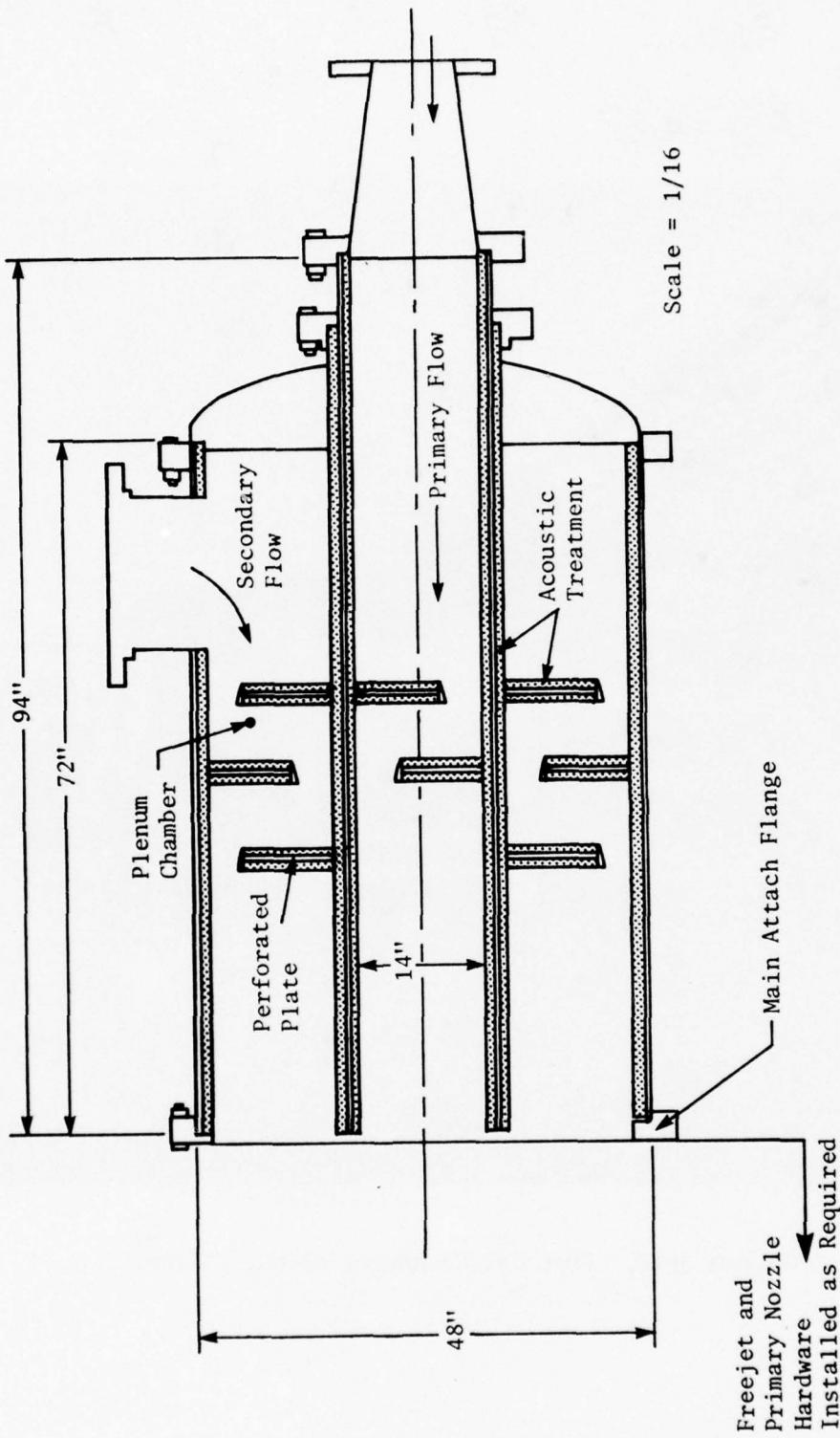


Figure 3-13. JENOTS Coannular Plenum Chamber.

Several precautions were taken to eliminate all extraneous noise emanating from the facility itself through the primary nozzle. All air supply pipe lines, including the secondary which provides flow for the free jet, were wrapped with sheet lead to prevent piping noise from escaping through the walls of the air supply lines. All elbows in the lines were lined with acoustically absorbing material to minimize the generation of turbulent noise. A pretest checkout of the primary nozzle was conducted at velocities along constant temperature lines, and the normalized overall sound pressure level at the 90° station was compared to the appropriate power law. Variations of less than 1 dB were accepted as uncontaminated data. The data were corrected for the effect of ground reflection by semiempirical correction factors as evolved during Task 1 of this program and described in depth in the Task 1 Final Report (Reference 7). The comparison was made by normalizing the parameters in terms of the semiempirical scaling laws which have been proposed by Hoch, et al. (Reference 8). Figure 3-14 illustrates how these data compare to both the proposed NASA-Lewis, (Reference 9), and SAE A21 committee, (Reference 10), jet noise prediction models.

It was concluded that the primary flow of the coannular facility provides clean jet noise down to approximately 600 ft/sec and upwards of 2500 ft/sec, which is well within the requirements outlined in the Task 4 work plan.

It should be noted that noise from the secondary or free jet stream was treated as background noise in the course of these tests and is therefore included in the discussion of test data.

Two primary nozzle configurations were tested on the JENOTS free jet setup. The 3.56-inch diameter nozzle was evaluated with a 12.6-inch diameter outer shroud which resulted in a free jet/nozzle area ratio of 11.6 (see Figures 3-15 and 3-16). The other primary nozzle was a 2-inch diameter version of the Supersonic Tunnel Association (STA) nozzle, which was also utilized in assessing the effect of free jet-to-primary nozzle area ratio on afterbody pressure distribution. The STA nozzle (Figure 3-17) was tested with a 12.0-inch free jet shroud providing a free jet-to-primary nozzle area ratio of 35 (Figure 3-18).

3.1.3.2 Data Acquisition

All the free jet facility data and additional pressure and temperatures for various test model instrumentation requirements are recorded on a digital data acquisition system.

A total of 125 pressure lines, 96 CA T/C circuits, and 21 IR T/C circuits are available for use with the digital system.

One hundred pressure lines out of the 125 connect to a bank of 8 scanner valves containing 25 psia transducers. Each scanner valve can measure 11 pressures per transducer for a total of 88 pressures in the 0 to 25 psia

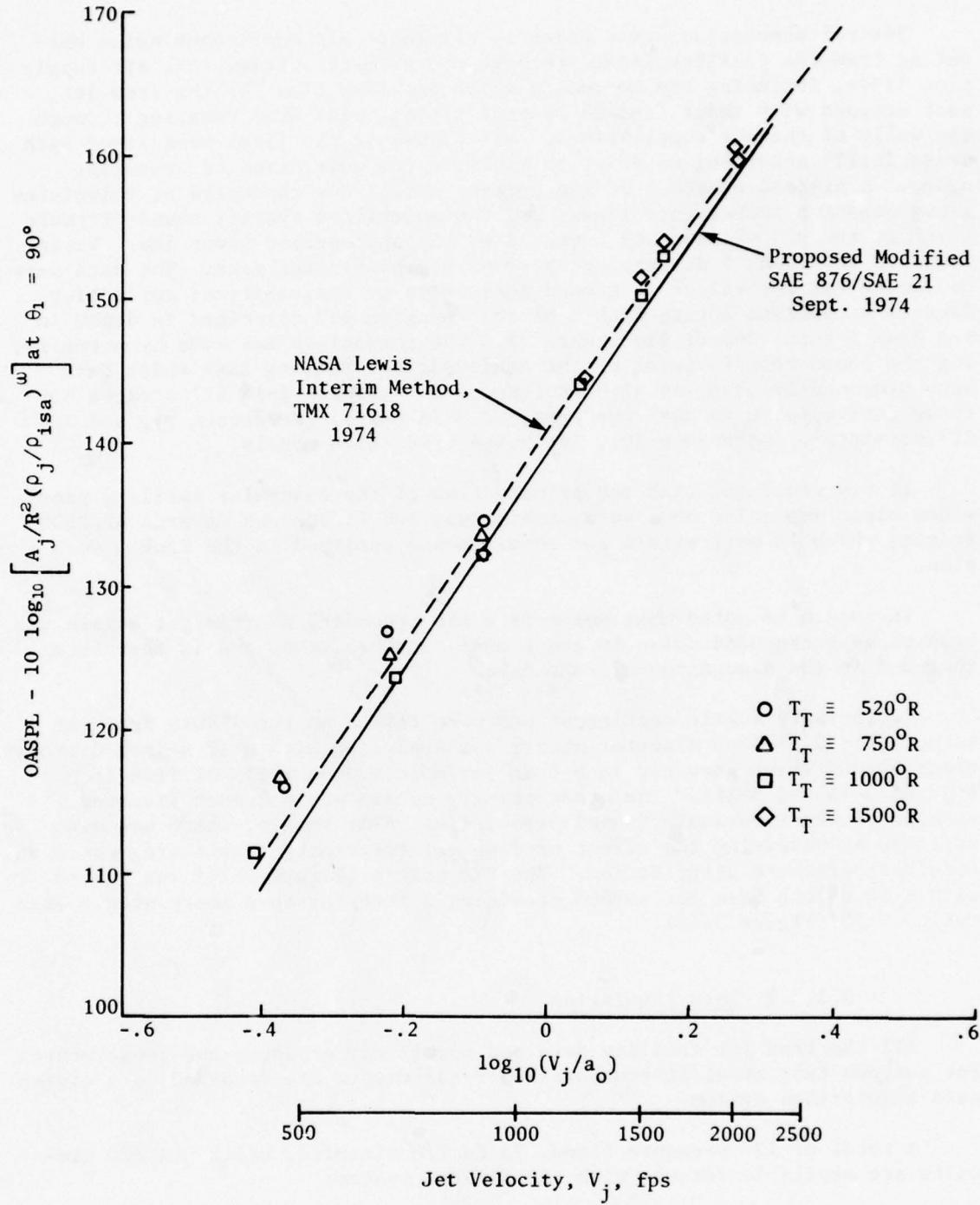


Figure 3-14. JENOTS Free Jet/Coannular Plenum - Acoustic Validation of Primary Nozzle Only.

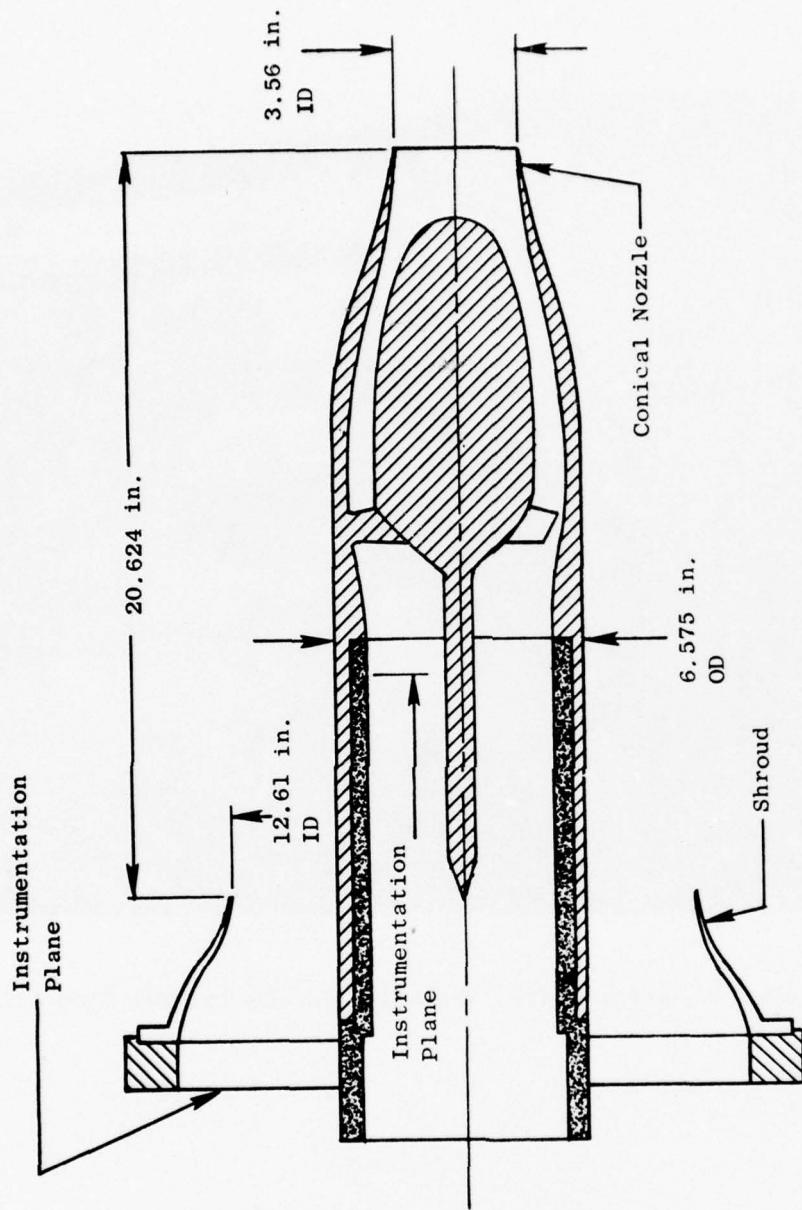


Figure 3-15. Schematic of 3.56-inch Diameter Primary Nozzle Assembly with Shroud.



Figure 3-16. 3.56-Inch Diameter Nozzle Installed on JENOTS Dual Flow Facility.

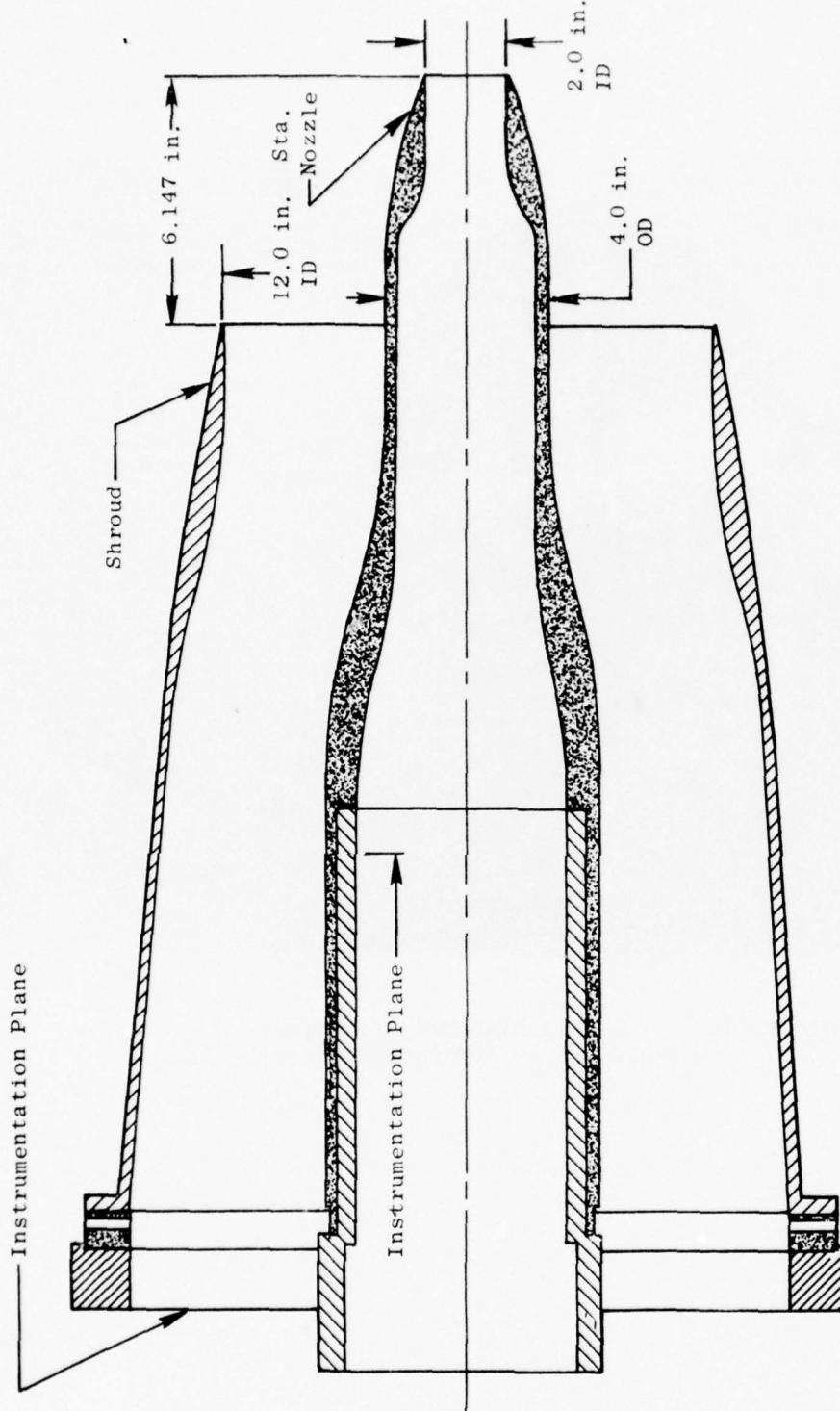


Figure 3-17. Schematic of 2-inch Internal Diameter STA Nozzle with Free Jet Shroud.

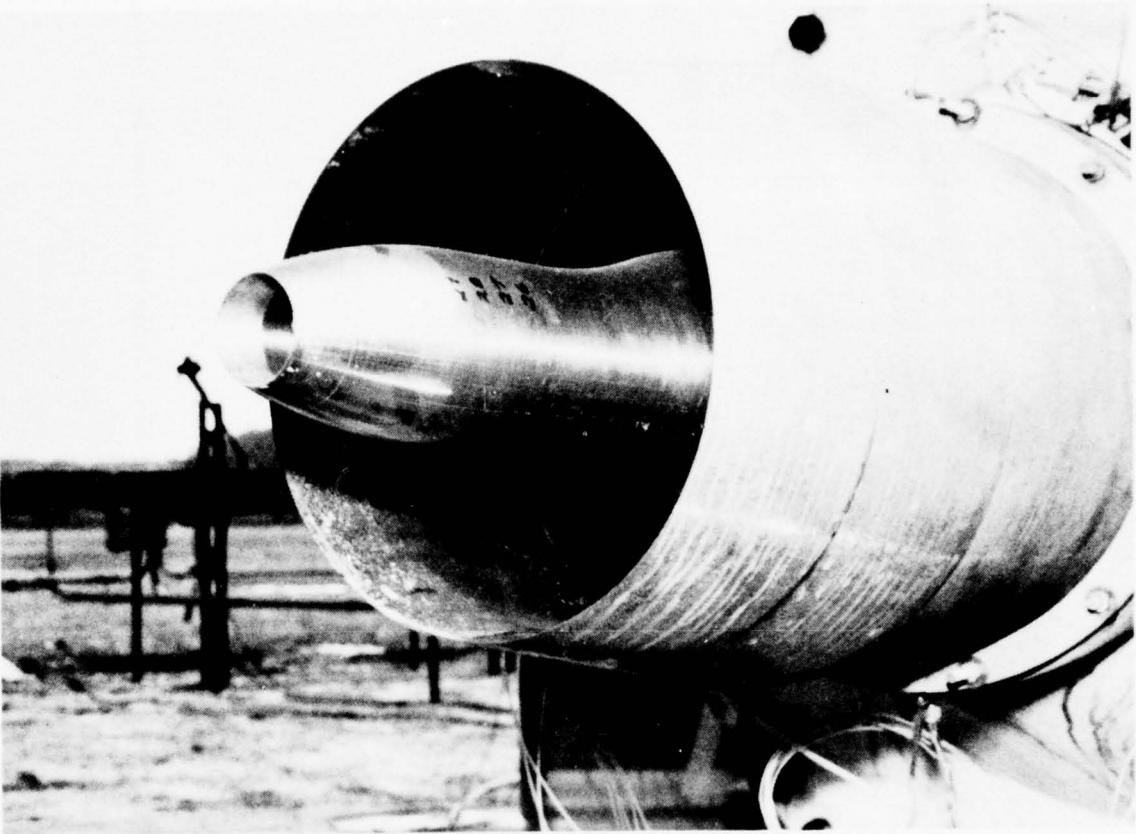


Figure 3-18. 2-Inch Diameter STA Nozzle
Installed on JENOTS Dual Flow Facility.

range. Twenty-five pressure lines are routed to a cabinet containing five individual transducers that handle pressures of 0, 50, 100, and 500 psia but can be changed to meet specific requirements. The 8 scanners are used for measuring model pressures, while the individual transducers measure facility airflow data.

The CA T/C's are used to measure main airflow temperature and various skin temperatures on the models. These signals are then fed into an automatic switching unit in an ordered manner and conducted through digital amplifiers to a digital printer and a digital punch. The printer stamps respective digital position numbers and parameters in "counts" on a ribbon paper that can be correlated, with the aid of a "hookup" sheet, to readings in engineering units. The punch unit perforates digital punch tape which is used for inputting the time-sharing teletype system for processing to engineering units and calculations, (i.e., weight flow, ideal velocity, mean total temperature, and total pressure ratio, etc.).

The acoustic data collection system at JENOTS is shown schematically in Figure 3-19. It is composed of a B&K microphone/cathode follower powered and conditioned by a B&K 2801 power supply followed by three feet of line to a specially designed 10-dB, fixed-gain preamplifier which drives 150 feet of cable terminating at the variable-gain, differential-input amplifiers to the Sangamo/Sabre IV tape recorder. The signal is recorded on tape for future playback in the data reduction room.

The microphones used were the B&K 4133, 1/2-inch free-field microphones. These free-field microphones are designed such that the microphone diaphragm resonance is over-damped in such a way that the normal incidence free-field pressure increase is compensated by the decrease of pressure sensitivity of the microphone cartridge. All the free jet tests were conducted with 1/2-inch microphones since acoustic data was required in the 250 Hz to 40 kHz range.

The cathode follower used most often is the B&K 2615 preamplifier, although B&K 2619's are also used. The purpose of the cathode follower is to give a very high input impedance with small load to the microphone and a low output impedance allowing the connection of long cables between the preamplifier and relatively low impedance amplifiers in the circuit. The B&K 2619 uses a field-effect transistor to give higher input impedance and lower inherent noise than the B&K Type 2615. The cathode follower also supplies the microphone with a 200-volt polarization from the power supply.

The B&K 2801 power supply is operated in the direct output mode to avoid sensitivity loss. The frequency response of the various preamplifiers is not influenced by the power supply when used in this position. This power supply does have optional 50 Ω and 200 Ω transformer output for use in eliminating amplifier oscillation and dampening RC resonance. The JENOTS systems, however, are free of such problems due to the unloading of the power supply by the preamplifier.

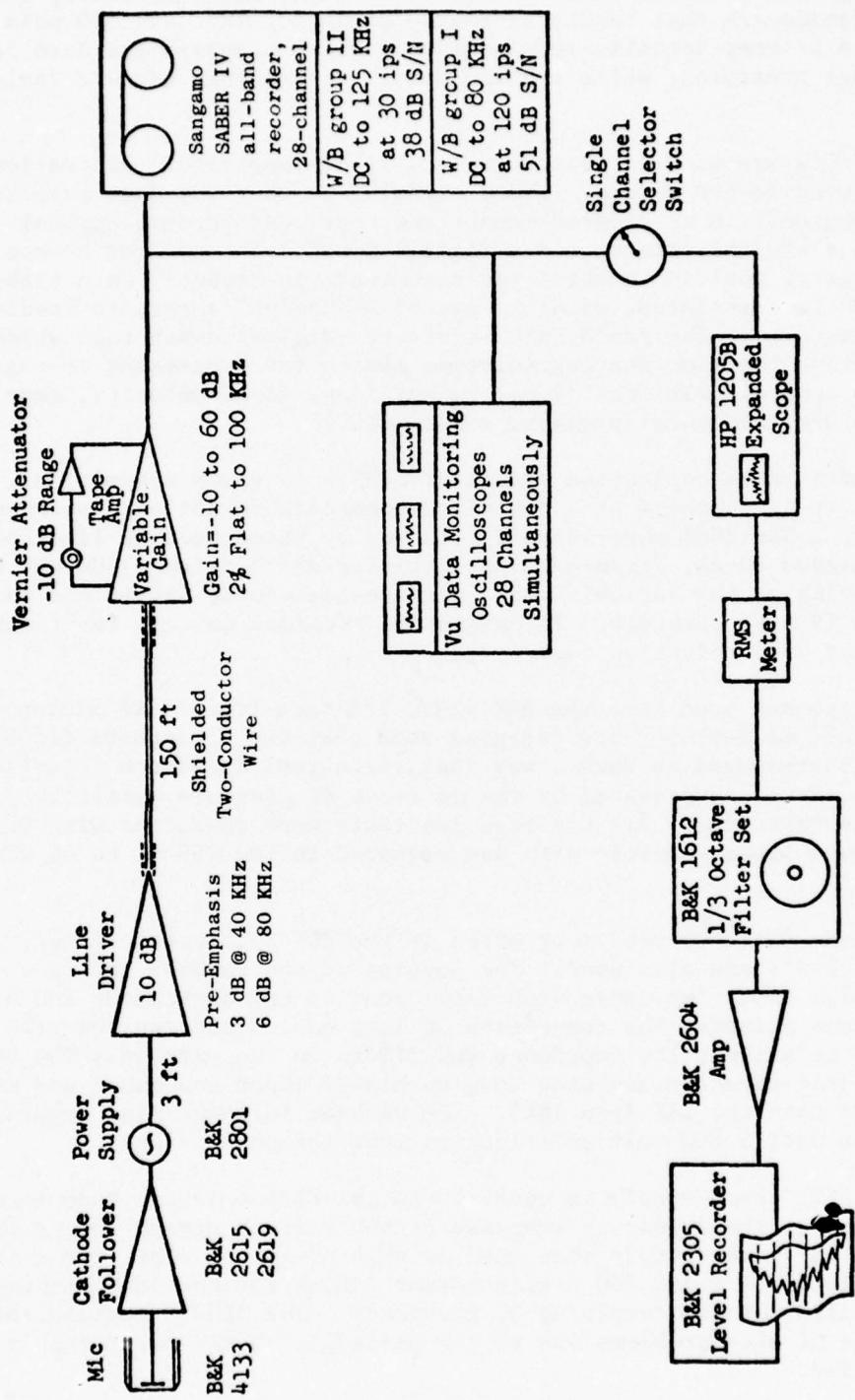


Figure 3-19. JENOTS Data Aquisition System.

Three feet from the output of the power supply is a fixed 10-dB amplifier for driving the signal to the tape recorder amplifier. The amplifier was designed by the General Electric AEBG* Electronic Instrumentation Group and built from high quality components by Random Electronics, a Cincinnati firm. In anticipation of the low sound levels experienced at high frequency, the circuitry was designed with a frequency response that "preemphasized" the high frequency signals such that it has a 3-dB increase at 40 kHz and an additional 3-dB increase between 40 to 80 kHz. This feature is optional and can easily be removed if one expects high sound levels at high frequency and desires a flat frequency response throughout the spectra.

Two-conductor, shielded wire was chosen for the 150 feet of lead from the line driver to the tape recorder amplifier. This design was favored over the conventional coaxial cable because of the susceptibility of coaxial cable toward pick-up of stray signals such as radio stations. The two-conductor, shielded wire is also more rugged than the coaxial cable and lasts longer giving lower maintenance and replacement cycles. The cable introduces an effective 0.0458- μ f capacitance to the circuit.

The amplifier at the tape recorder has a variable gain from -10 dB to +60 dB. The amplifier delivers a 4-volt, peak-to-peak signal to the tape recorder electronics at the normal calibration signal level. This setting will allow 6 dB over range without distortion. The amplifiers are flat within 5% from 5 Hz to 100 Hz. Each amplifier has an adjustable vernier attenuation which can give any desired measure of attenuation between 0 and 10 dB. During test calibration, this vernier is usually adjusted to make the 124-dB pistonphone calibration signal the full-scale (1.4 Vrms) input to the tape recorder. The 10-dB steps in the tape recorder amplifier then directly correspond to 10-dB steps in OASPL from 124 dB. The vernier can be moved to the fixed position, in which case the signal goes directly into the 10-dB step tape recorder amplifier. The output of each amplifier channel has a Vu-Data Monitoring oscilloscope for continual inspection of all signals for any clipping or deterioration of the signal due to excessive crest factor (peak value/rms).

The Sangamo/Sabre IV, 4930 magnetic tape recorder/reproducer has IRIG wideband, and RM wideband Group I and Group II capability. In normal JENOTS operation, all data are recorded on one-inch tape Wideband Group II at 30 ips having a flat frequency response in excess of 100 kHz when used in conjunction with the B&K 4135 microphone. The voice channel is recorded direct.

The JENOTS recorder was modified to record 28 tracks and to improve its signal-to-noise dynamic range from the normal 32 dB to 39 dB overall frequencies. This lower noise floor was obtained by individual channel tuning by the Sangamo Electric Company at the factory. Playback capability of two data channels + voice for on-site data investigation is also available.

*AEBG - Aircraft Engine Business Group

On-line data reduction and monitoring capability is available in the JENOTS control room. As shown in Figure 3-19, a signal-channel selector switch can route any microphone signal parallel to the tape recorder for expanded waveform presentation of a HPI205 B oscilloscope. The overall sound level of the selected channel can be read out on a calibrated rms meter. The signal can then be passed through a B&K 1612 band-pass filter set, amplified by a B&K 2604 amplifier, and recorded on a B&K 2305 level recorder. The filter set can be dialed to 1/3-octave frequencies from 12.5 Hz to 40 kHz; octave frequencies from 16 Hz to 31.5 Hz; or linear, "A", "B", and "C" weighted networks from 20 Hz to 45 kHz.

3.1.3.3 Data Reduction Methods

Standard data reduction is conducted in the General Electric Instrumentation and Data Room (IDR). As shown in Figure 3-20, the data tapes are played back on a CEC3700B tape deck with electronics capable of reproducing signal characteristics within the specifications indicated for Wideband Group I and Group II. An automatic shuttling control is incorporated in the system. In normal operation, a tone is inserted on the recorder and the time slot designed for data analysis. The tape control automatically shuttles the tape initiating an integration-start signal to the analyzer at the tone as the tape moves in its forward motion. This motion continues until a complete integration is received from the analyzer at which time the tape direction is reversed and, at the tone, the tape restarts in the forward direction advancing the channel to be analyzed until all the channels have been processed. A time-code generator also is utilized to signal tape position of the readings as directed by the computer program control. After each total reading is complete, the number of tape channels at each point is advanced to the next reading.

All 1/3-octave analyses are performed on a General Radio 1921 1/3-octave analyzer. Normal integration time is set for 32 seconds to ensure good integration for the low-frequency content. The analyzer has a 1/3-octave filter set for 12.5 Hz to 100 kHz and has a rated accuracy of $\pm 1/4$ dB in each band. Each data channel is passed through an interface to the GEPAC 30 computer where the data are corrected for the frequency response of the microphone and the data acquisition system and corrected to standard day (59° F, 70% RH) atmospheric attenuation conditions per SAE ARP866 Standards to 8 kHz and GE corrections from 10 kHz to either 40 or 80 kHz. The output of the computer is passed to a Terminet 300 console where the corrected SPL's can be punched out on paper tape and printed out on sheets for "quick-look" analysis. For calculation of acoustic power, corrections for ground reflections to free field, scaling to other nozzle sizes, or extrapolations to different far-field distances, the data are sent to the Honeywell 6000 computer for data processing. This step can either be accomplished by storing the SPL's on punched paper tape and/or transmitting via direct time-share link to the 6000 computer through a 1200 Band Modem. In the 6000 computer, the data are processed through the Full-Scale Data Reduction (FSDR) Program, where the appropriate calculations are performed. The data printout is accomplished on a high speed "remote" terminal. A magnetic tape can be written for CALCOMP plotting of the data.

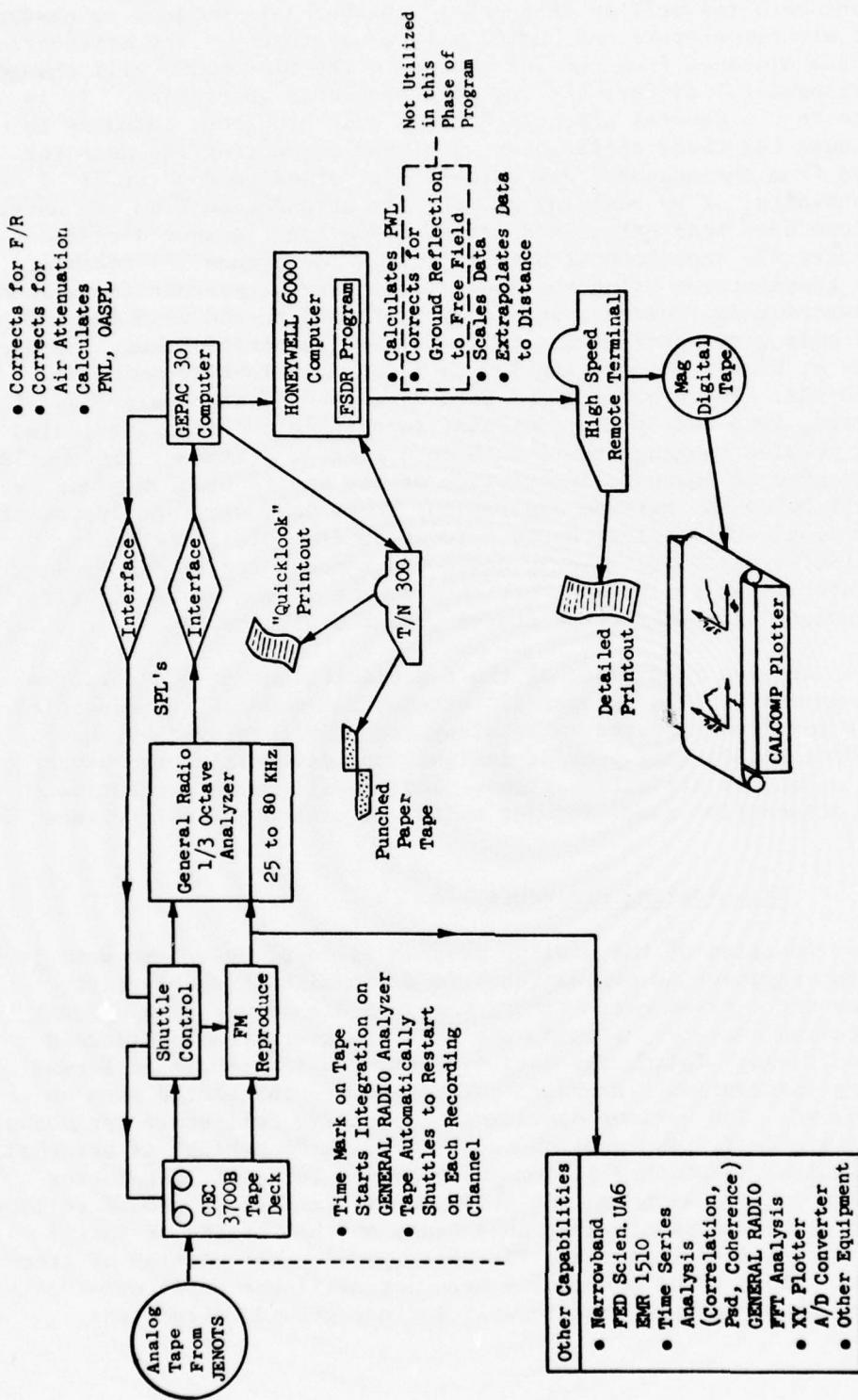


Figure 3-20. Data Reduction System Flow Chart.

Testing outdoors (as well as in anechoic chambers) is subject to changes in the ambient air temperature and humidity from day to day. The attenuation of sound over the distance from the jet source to the microphone will change with these environmental differences due to atmospheric absorption. It is common practice in the General Electric Company and throughout industry to attempt to account for these differences by either correcting the data for air attenuation from the measured day values to a "standard day" of 77° F and 70% relative humidity, or by removing all the air attenuation from the data. These corrections have been calculated using ARP866 for the last decade. This work extended the experimental data of Harris (Reference 11) taken at 20° C to other temperatures using the theoretical work of Knesner (Reference 12); Harris' experiments, however, were only performed to the 12.5 kHz narrowband, so he only gives corrections to the 8 kHz 1/3-octave band. The need for corrections at higher frequencies led to a General Electric Company extension to 80 kHz. These corrections were developed by extrapolations of the ARP866 curves, tempered by the continual experience of comparing scaled jet spectra of nozzles ranging from 1 inch to 4 feet in diameter. Knesner's theory does not give an adequate description of the entire problem since, at frequencies well below the maximum absorption, there is a distinct systematic deviation from single-relaxation theory. To reconcile this discrepancy, Evans, et al. (Reference 13), recently developed a model for predictions at 20° C for frequencies up to 100 kHz, but they do not recommend that their model be extrapolated to other temperatures beyond a 5° C spread.

Figure 3-21 shows a comparison of the two predictions at 50% relative humidity. The question of the proper air attenuation model for frequencies above 20 kHz is far from answered. The study recently completed by the University of Mississippi will provide insight into determining the proper values of high frequency air attenuations. Additional comments relative to the proper air attenuation model for jet noise are presented in Reference 7.

3.1.3.4 Data Scaling Procedure

The primary function of the scaling program is to present test data in a useful form for engineering evaluation. To accomplish this objective, three operations are carried out. First, the data are adjusted to account for test calibration factors. Second, the data are corrected to standard atmospheric conditions. Third, the data are arranged in a specific format with identifying information. Standard parameters are calculated such as PNL, OASPL, and PWL. The various operations to achieve full-scale jet noise are shown in Figure 3-22. The scaling technique is a "matching" of Strouhal numbers (fD/V) which, assuming V is common, provides for a scaling factor based on diameter ratio. Although not shown in Figure 3-22, a ground reflection correction procedure is now available based on the results of Task 1 "Activation of Facilities" (Reference 7), which permits calculation of free-field jet noise. Since these procedures were not available until mid-1974, all the acoustic data presented herein will include ground reflections.

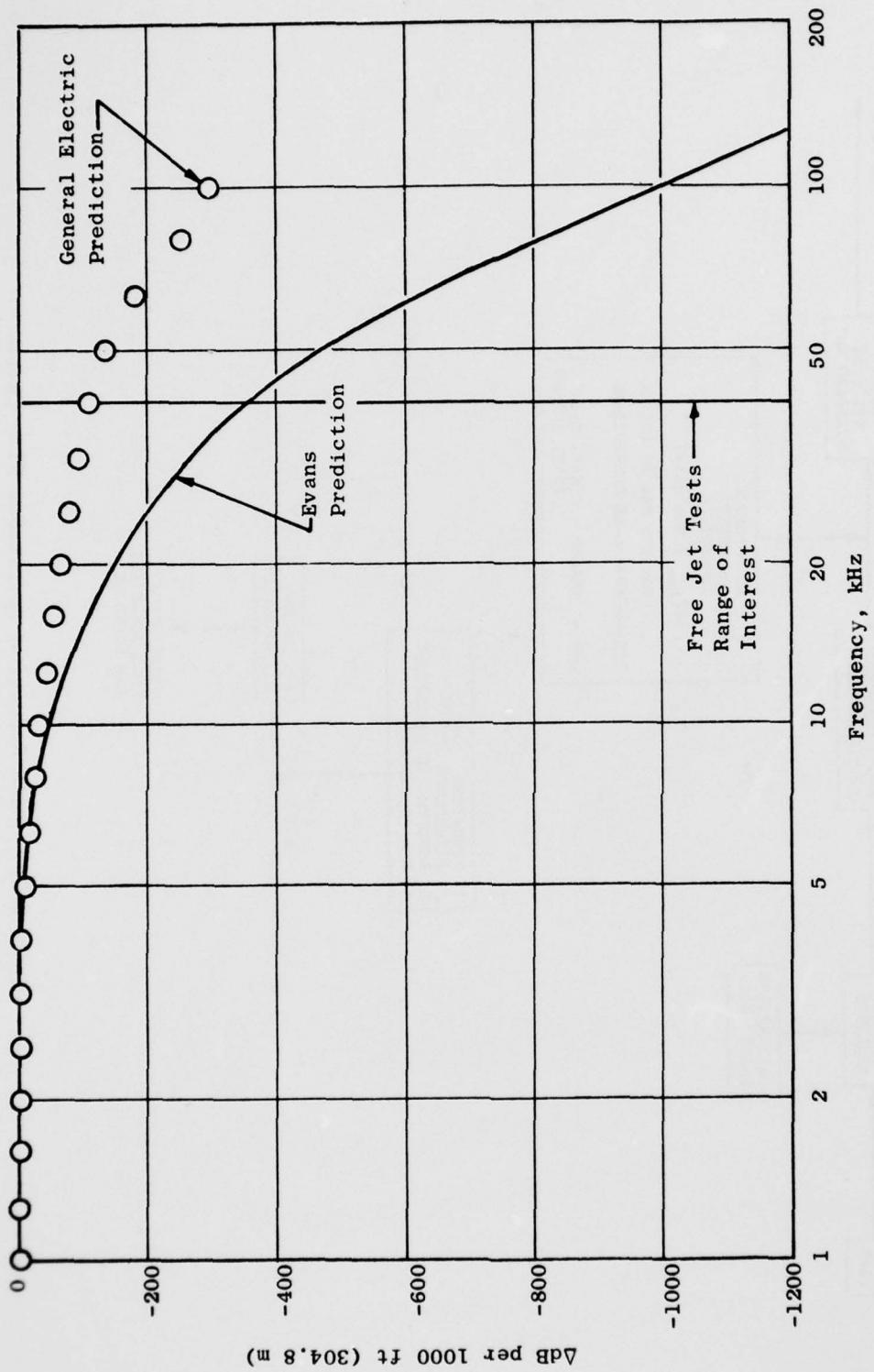


Figure 3-21. Comparison of Air Attenuation Models
at 50% Relative Humidity and 68°F.

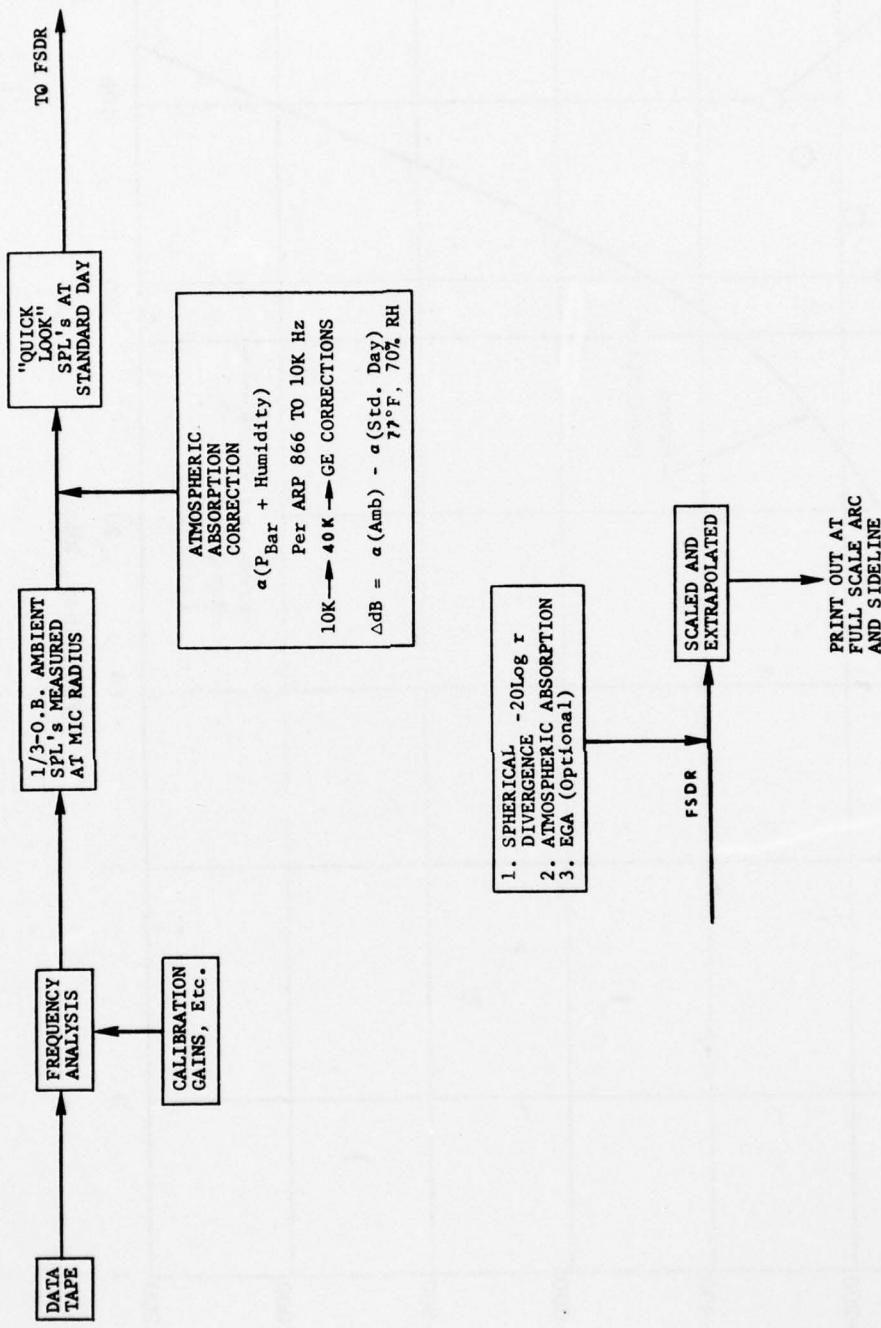


Figure 3-22. Data Reduction Operations Flow Chart.

The weight flow adder, applied to all SPL's, is based on the assumption that the ratio of diameter squared is the same as airflow ratio. Details of the Full-Scale Data Reduction (FSDR) Program are outlined in Figure 3-23.

Model data are corrected for atmospheric absorption and for assumed scattering losses or EGA at the input arc spectrum. After frequency shifts and application of the weight flow adder, projection to the desired sideline or flyover path is accomplished using inverse square law distance effect, absorption, and EGA. The EGA is calculated per Figure 4 of SAE specification AIR 923.

There are some limitations of the data acquisition and reduction systems which are attributable to electronic noise. Typical results obtained from investigations of electronic noise floor spectral shape are shown in Figure 3-24. These represent the frequency distribution of the electronic noise floor for the JENOTS electronic system. It was obtained by removing the microphone from the cathode follower and replacing it with a shorting cap.

Several distinct characteristics are apparent. The first is the relatively constant level from 50 Hz to 400 Hz and from 1600 Hz to 10 kHz. The fact that this flat region shifts uniformly with the 10-dB-gain steps and vanishes at the highest setting indicates that this portion of the spectra is associated with the tape recorder electronics. The second characteristic is the peculiar peaking occurring in the bands from 500 Hz to 1250 Hz. The fact that the shape is maintained and shifted uniformly with amplifier gain, and that it tends to "sink into the mud" at the highest gain, implies that the phenomenon is also associated with the tape recorder electronics. The third spectral characteristic is the 6-dB-per-octave ramp occurring at high frequency. As the tape recorder gain is increased, more of this ramp is uncovered and the upswing occurs at an earlier frequency. This is believed to be electronic noise from the cathode follower, power supply, and line drivers responding to the preemphasis built into the line driver frequency response. Of the three sources, the cathode follower is the noisiest. In similar tests, B&K 4135 1/4-inch microphones were left on the cathode follower and the microphones were covered by a pistonphone calibrator. Similar characteristics were observed, as seen in Figure 3-25. The low frequency portion of the spectra is dominated by ambient acoustic signals which are leaking into the piston phone.

Given the nominal values for noise floor quoted in the equipment specifications, one sees that the tape recorder 38-dB dynamic range is the limiting floor at most gain settings used for jet noise work. A few of the test points were taken with the gain setting below the point where a higher gain should have been used. However, this deteriorated dynamic range only affected the 40 kHz data and caused no perceptible change in sound power level (<<0.5 dB).

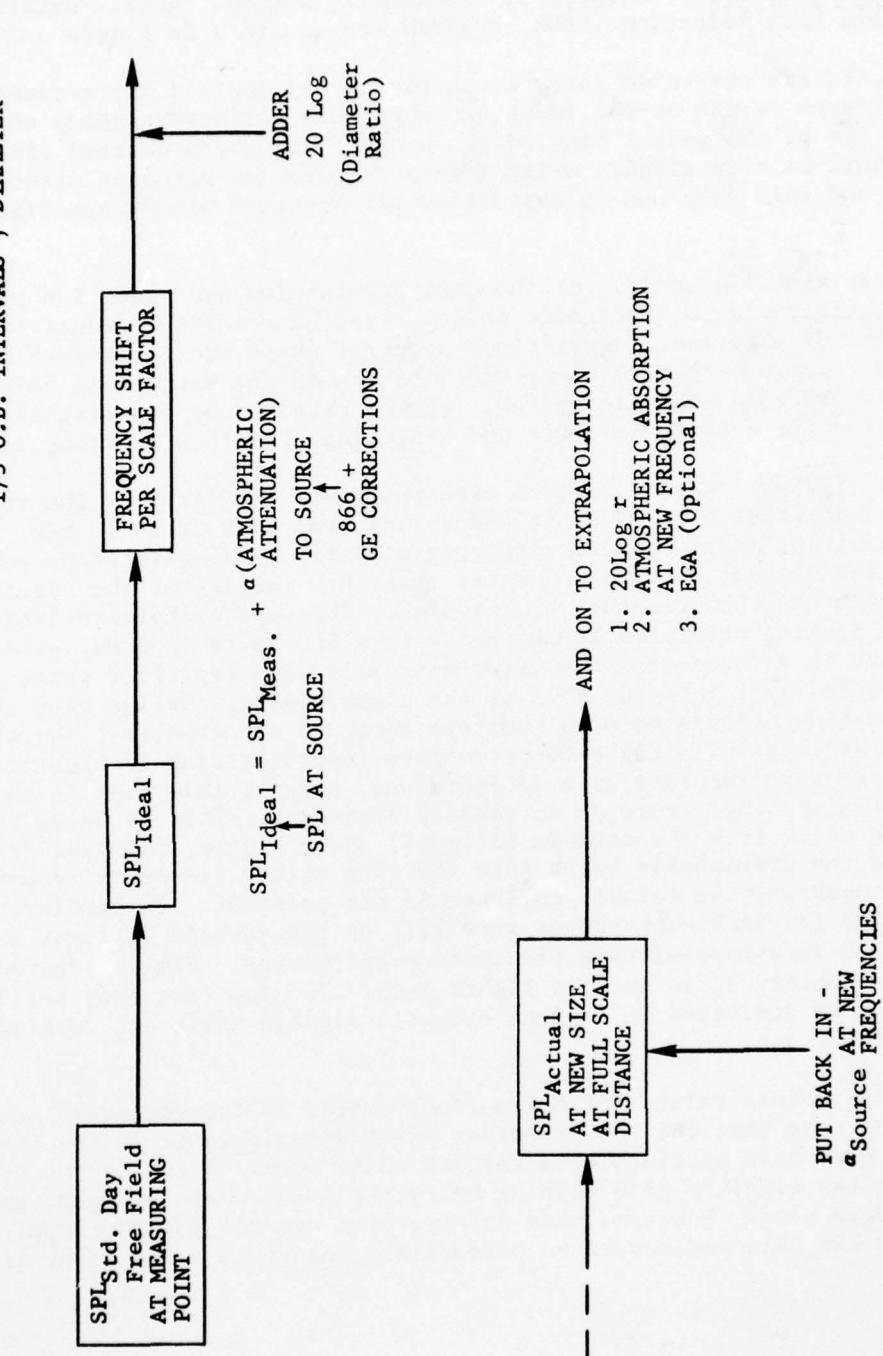


Figure 3-23. Details of Full-Scale Data Reduction Program.

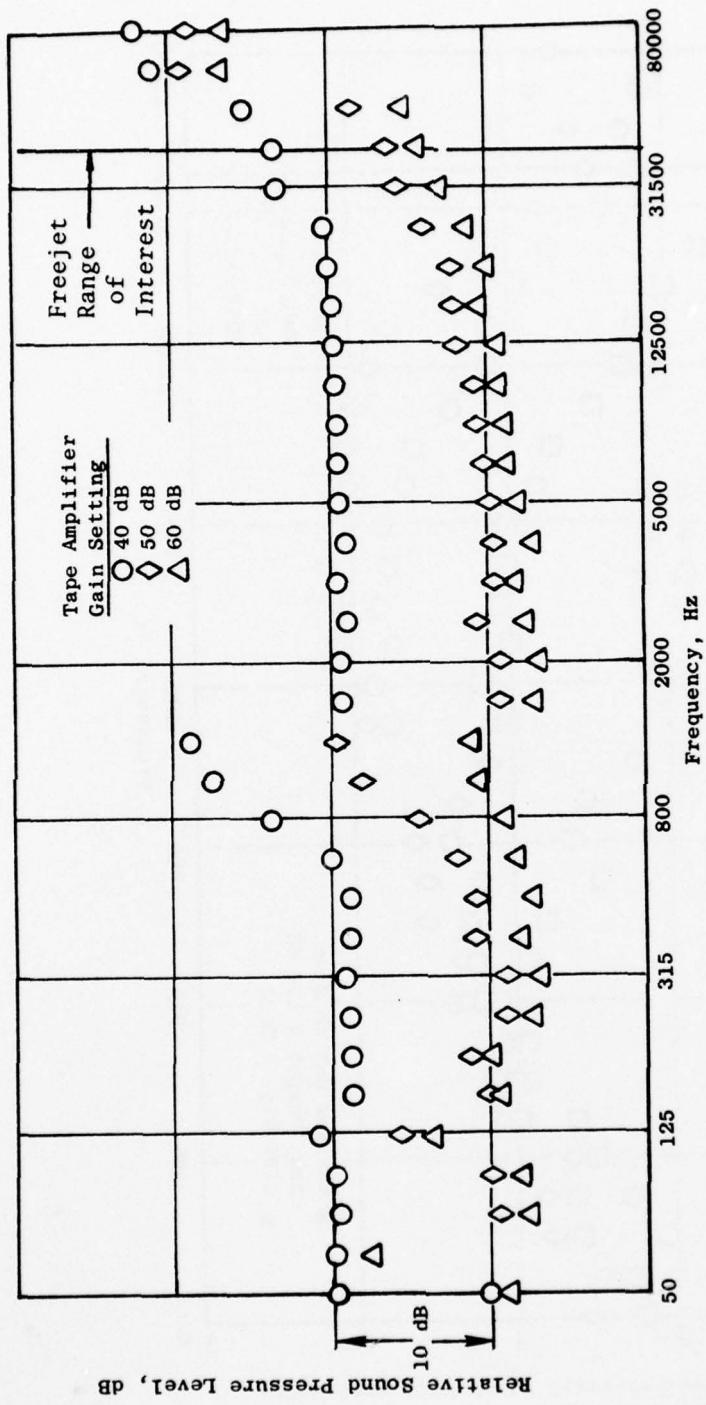


Figure 3-24. Electronic Noise Floor Spectra of the 90° Microphone System with Shorted Cathode Follower.

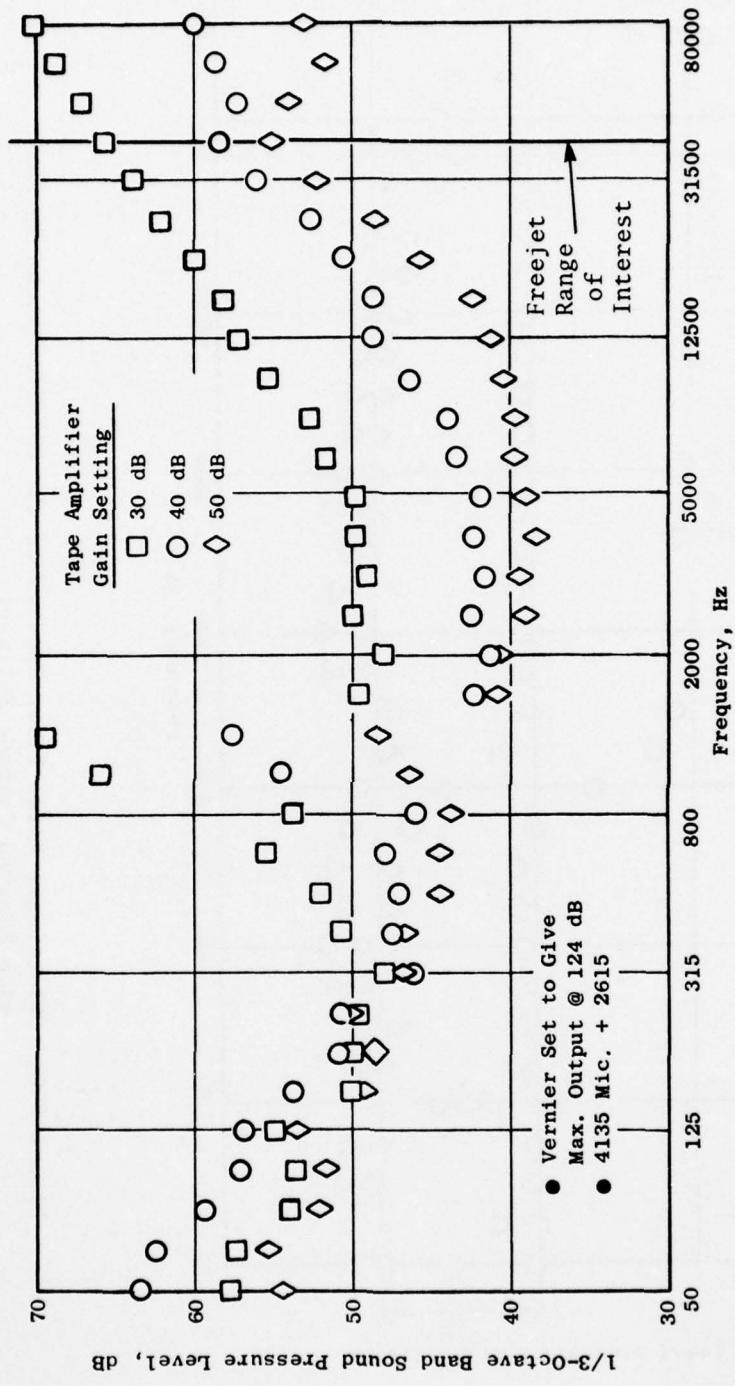


Figure 3-25. Electronic Noise Flow Spectra of the 90° System with Microphone Covered by Pistonphone.

3.1.3.5 Test Matrix Description and Acoustic Results

This section presents the results obtained at the JENOTS facility utilizing two convergent nozzles having free jet area ratios of 11.6 and 35.0. Acoustic data are presented for primary flow with/without free jet flow and free jet alone (to assess its contribution to the far field). Also included are some comparisons with previously published NASA-Lewis free jet results. Some ancillary aerodynamic analyses dealing with boattail pressure distributions and their variation with free jet area ratio are also provided.

The parametric acoustic test matrix was selected to provide data which were indicative of the velocity range of the J85 engine (i.e., $V_{j,max} \approx 2100$ ft/sec) and for simulated free-stream velocities near 400 ft/sec. Generally- 4 free-stream or free-jet velocities (including a static run) were covered in both series of free jet tests. Details of the test matrix are shown in Tables 3-XII and 3-XIII, respectively, for the 3.55-inch and 2.00-inch STA diameter nozzle/free jet configurations.

In each case, the acoustic tests were run systematically varying free jet velocity (with the primary nozzle leaking to avoid any internal dead-air regions) to obtain the noise signature of the free jet in the far field and permit separation of the free jet noise from the primary jet noise during dual-flow operation. The primary nozzle velocity was varied alone to document primary jet noise. Finally, the free jet and primary nozzles were run simultaneously through a wide range of useful combinations to determine the influence of the external flow on primary-nozzle jet noise characteristics.

The acoustic data to be presented are at model scale, with ground reflections, corrected to a standard day (59° F, 70% RH), and on a 40-foot arc.

Acoustic data at the test conditions delineated in Table 3-XIII are presented in computer-plot form. The computer plots include: power spectra, 1/3-octave sound pressure level, overall power level, and overall sound pressure level directivities. One-third-octave sound pressure level spectra are shown for inlet angles of 60°, 90°, 120°, and 140° taken on the 40-foot arc and corrected to standard day.

Figures 3-26 through 3-28 are typical plots taken with the 12-inch free jet operating with essentially no flow through the primary nozzle, (just enough to assure a "flowing-full" condition so as not to alter the noise signature of free jet flow). The directivities, sound pressure, and power spectra are shown for free-stream velocities of 75, 165, 265, and 365 ft/sec. The spectra shown in Figure 3-27 were utilized during the forward velocity testing to correct the far-field data taken to preclude contamination of this free jet noise on the primary jet noise. As will be seen in the following paragraphs, the main area of consideration will be below the frequency range of 400 Hz.

Table 3-XII. Acoustic Test Matrix, Aerodynamic Test Conditions, Free Jet Area Ratio = 11.6.

- $D_8 = 3.56"$
(Primary)
- $D_{28} = 12.61"$
(Free Jet)
- Free Jet Area Ratio =

$$\left(\frac{D_{28}}{D_8}\right)^2 - 1 = 11.6$$

Data Point	P_{T8}/P_0	T_{T8} °R	V_8 ft/sec	P_{T28}/P_0	T_{T28} °R	V_{28} ft/sec
2	1.001	459	46	1.005	529	95
3	1.003	459	67	1.023	530	203
4	1.003	459	68	1.045	528	282
7	1.180	1205	818	1.000	ambient	0
8	1.373	1249	1142	1.000	ambient	0
9	1.488	1270	1282	1.000	ambient	0
10	1.672	1345	1490	1.000	ambient	0
11	1.806	1400	1622	1.000	ambient	0
12	2.09	1521	1872	1.000	ambient	0
13	2.275	1695	2077	1.000	ambient	0
15	1.174	1191	802	1.046	507	279
16	1.173	1204	804	1.02	509	186
17	1.170	1200	979	1.005	492	92
18	1.365	1238	1127	1.005	508	93
19	1.367	1250	1135	1.019	510	181
20	1.366	1251	1133	1.046	506	279
23	1.478	1271	1273	1.046	508	279
24	1.479	1267	1272	1.021	508	190
25	1.483	1265	1275	1.005	508	93
26	1.663	1343	1482	1.005	512	94
27	1.663	1344	1482	1.02	510	186
28	1.665	1340	1482	1.047	508	282
31	1.825	1401	1636	1.048	523	289
32	1.815	1401	1629	1.022	531	199
33	1.828	1414	1646	1.003	545	75
34	2.095	1520	1874	1.003	554	76
35	2.092	1514	1868	1.022	532	199
36	2.082	1519	1866	1.05	524	295
39	2.230	1708	2063	1.042	528	272
40	2.29	1718	2029	1.022	529	199
41	2.27	1688	2070	1.005	572	99

**Table 3-XIII. Acoustic Test Matrix, Aerodynamic Test Conditions,
Free Jet Area Ratio = 35.**

• $D_8 = 2.00"$
(Primary)

• $D_{28} = 12.00"$
(Free Jet)

• Free Jet Area Ratio =

$$\left(\frac{D_{28}}{D_8} \right)^2 - 1 = 35$$

Data Point	<u>P_{T8/P_Q}</u>	<u>T_{T8 ° R}</u>	<u>V_{8 ft/sec}</u>	<u>P_{T28/P_Q}</u>	<u>T_{T28 ° R}</u>	<u>V_{28 ft/sec}</u>
2	1.004	494	84	1.011	505	138
3	1.010	501	129	1.03	508	227
4	1.017	504	171	1.054	508	302
5	1.022	517	197	1.092	513	391
7	1.171	1211	802	1.000	ambient	0
8	1.354	1247	1117	1.000	ambient	0
9	1.479	1261	1269	1.000	ambient	0
10	1.646	1349	1471	1.000	ambient	0
11	1.809	1408	1629	1.000	ambient	0
12	2.099	1513	1872	1.000	ambient	0
13	2.289	1694	2084	1.000	ambient	0
14	1.169	1208	797	1.078	513	362
15	1.169	1205	796	1.041	518	267
16	1.172	1208	803	1.015	523	163
17	1.168	1192	789	1.002	528	60
18	1.362	1248	1128	1.003	535	74
19	1.345	1237	1100	1.015	532	165
20	1.357	1252	1123	1.037	530	257
21	1.352	1235	1109	1.079	530	370
22	1.479	1281	1279	1.079	532	371
23	1.477	1268	1270	1.04	538	268
24	1.478	1264	1269	1.014	543	161
25	1.479	1262	1269	1.003	548	75
26	1.653	1338	1471	1.003	556	76
27	1.672	1351	1493	1.015	544	167
28	1.658	1348	1480	1.04	541	269
29	1.658	1343	1478	1.084	540	385
30	1.812	1425	1641	1.078	539	371
31	1.811	1418	1636	1.04	540	269
32	1.812	1418	1637	1.016	544	172
33	1.807	1409	1628	1.003	564	76
34	2.082	1525	1870	1.003	566	76
35	2.083	1523	1869	1.015	519	163
36	2.093	1509	1866	1.04	522	264
37	2.094	1521	1874	1.078	506	359
38	2.28	1702	2084	1.078	509	360
39	2.298	1693	2087	1.048	531	291
40	2.308	1688	2089	1.027	535	221
41	2.301	1693	2089	1.012	538	148
42	1.18	508	531	1.092	517	393
43	1.371	510	727	1.093	519	396
44	1.491	511	814	1.093	519	396
45	1.666	513	915	1.093	520	396
46	1.821	513	985	1.094	520	398
47	2.09	514	1083	1.094	520	398
48	2.289	515	1142	1.095	521	400
49	1.009	510	125	1.007	515	111
50	1.024	511	204	1.024	517	205
51	1.047	513	284	1.047	519	285
52	1.082	513	371	1.092	520	394

- 2.00 Inch Prim. Nozzle Diam.
- 40 Foot Radius, 59° F, 70% R.H.

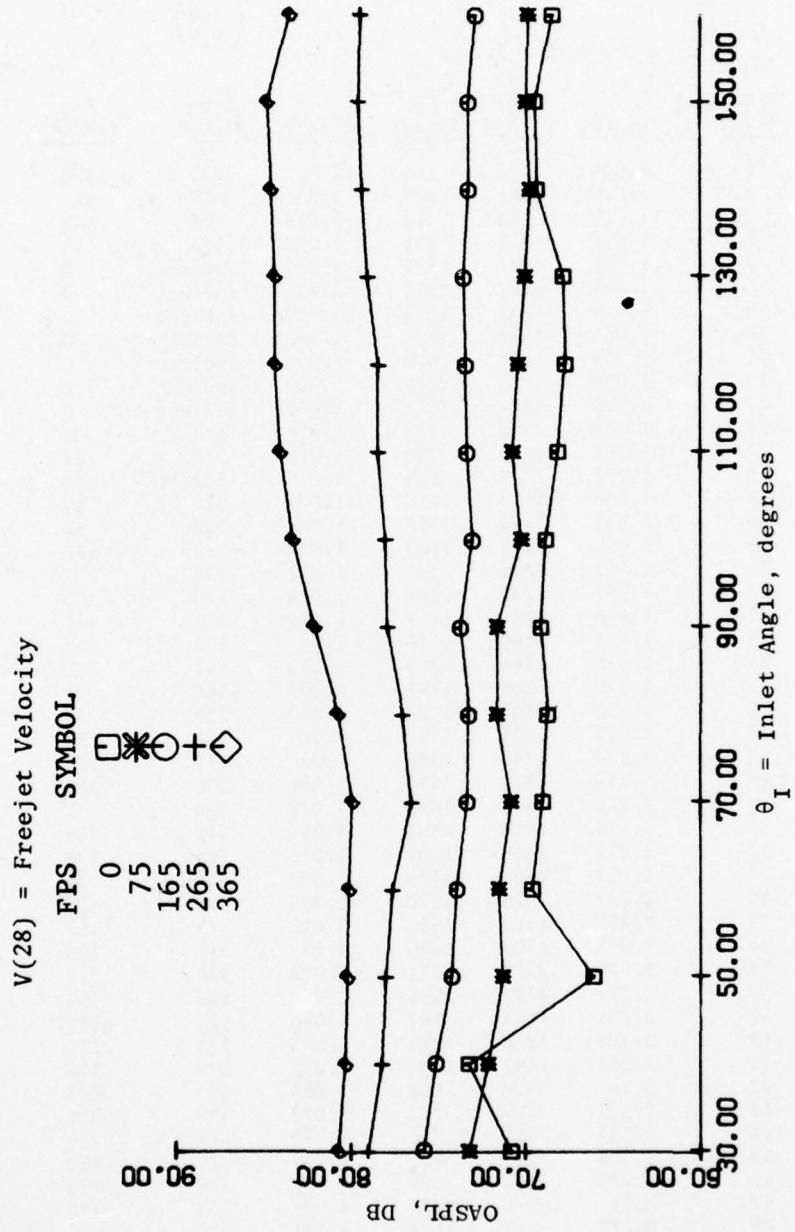


Figure 3-26. Ambient and Free Jet OASPL Characteristics.

2.00 INCH PRIM. NOZZLE DIAM.
40 FOOT RADIUS, 59° F., 70% R.H.

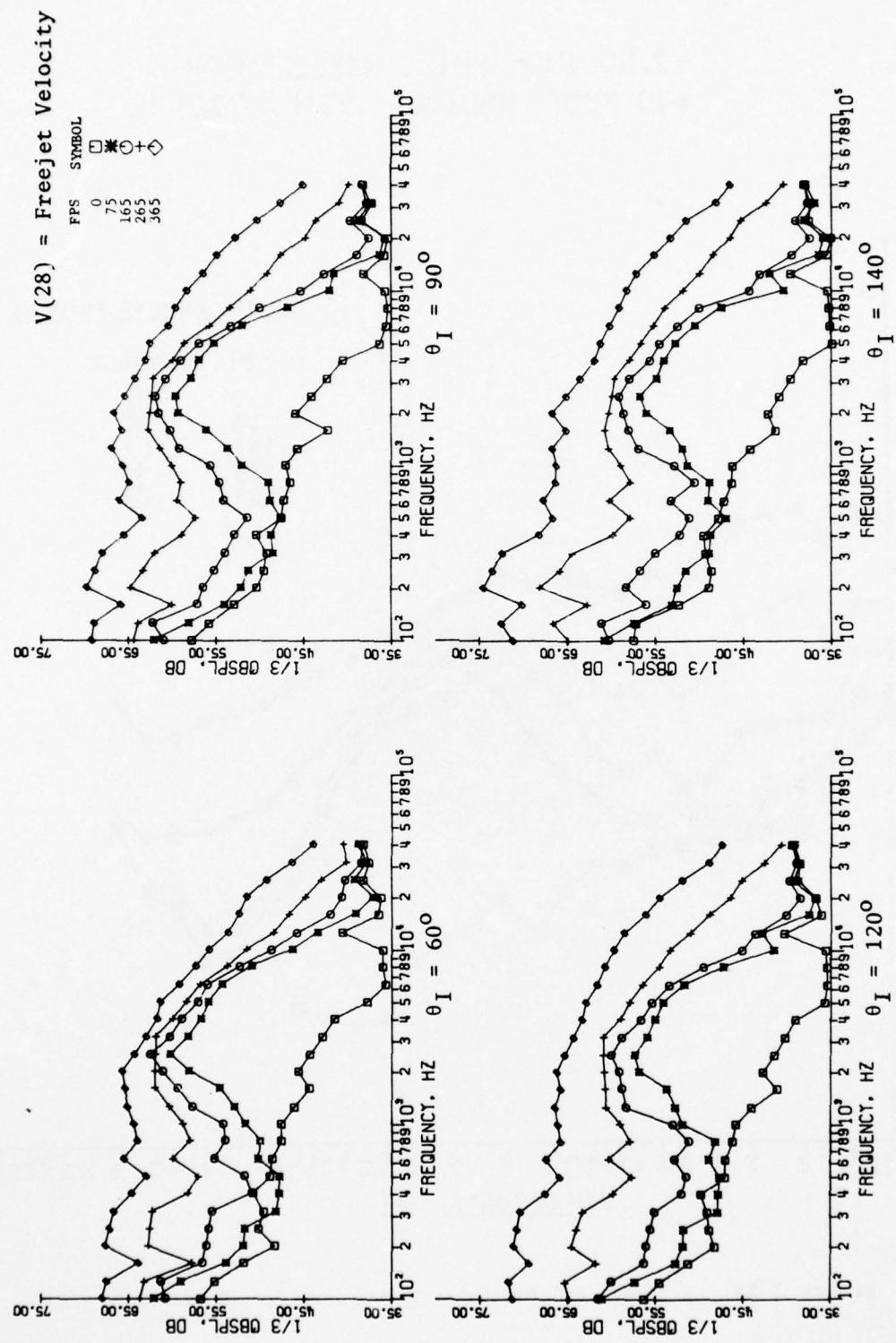


Figure 3-27. Ambient and Free Jet 1/3 OBSPL Characteristics.

- 2.00 INCH PRIM. NOZZLE DIAM.
- 40 FOOT RADIUS, 59°F, 70%R.H.

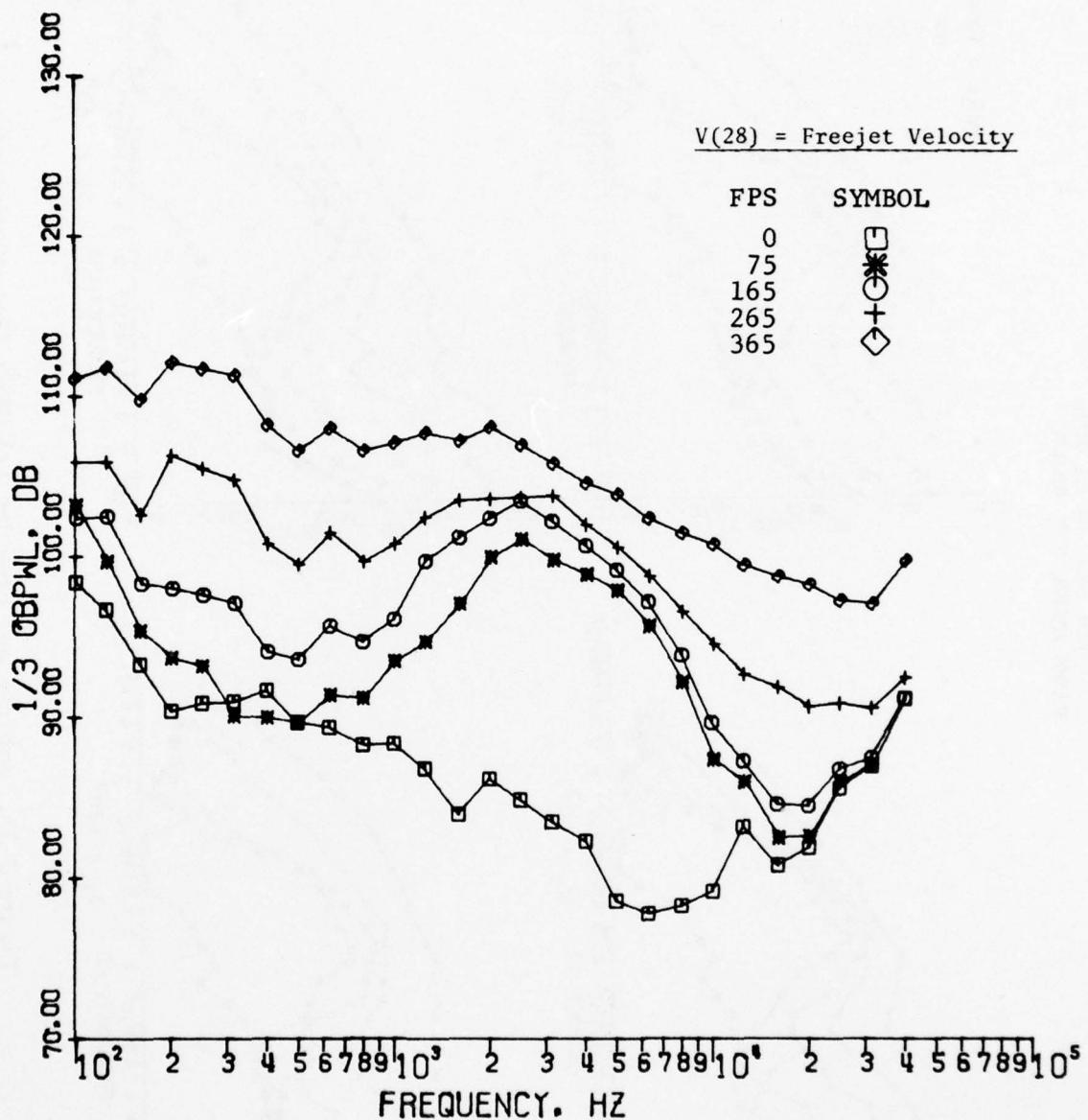


Figure 3-28. Ambient and Free Jet Power Spectra Characteristics.

The primary nozzle noise characteristics operating statically (zero forward velocity) are presented in Figures 3-29 through 3-31, respectively. The directivity plots of Figure 3-29 show the typical jet noise trends to be expected in the velocity range of 800 to 2090 ft/sec. The dropoff between peak noise to the noise at the extreme forward angles is seen to be more pronounced with increasing velocity, while the angle of peak noise tends to occur at lower inlet angles with increasing velocity.

The sound pressure level spectra for four typical inlet angles are shown in Figure 3-30 at primary velocities of 800 to 2090 ft/sec. Spectral shape is seen to be typical of that previously observed for conical nozzles, increasing in level with increasing jet velocity at any given directivity angle. Strouhal scaling (i.e., $fD/V \approx 0.2$) is observed at angles near the peak noise lobe as noted on the $\theta_I \approx 140^\circ$ plot of Figure 3-30. For completeness of presentation, Figure 3-31 summarizes the sound level spectra characteristics of the 2-inch primary nozzle. Again, it can be seen that peak PWL frequency increases with increasing primary jet velocity.

The influence of forward velocity is illustrated in the OASPL directivity plots of Figures 3-32 and 3-33 for the entire range of primary and free jet velocities covered. Also included in each plot is the free jet-only directivity for a velocity of 365 ft/sec since the data presented have not been corrected for this effect. Thus, it is obvious that the data for the 800 ft/sec jet velocity case is indeed contaminated and not indicative of the true forward velocity effects. It is also evident from these results that the reduction in OASPL with increasing free jet velocity is, to all intents and purposes, essentially independent of angle from the inlet. This is especially noted for velocities up to 1480 ft/sec (Figure 3-32) where the attenuation is seen to remain constant up to angles of about 130° . Above this near-peak noise region, the reduction appears to increase with increasing inlet angle. Above 1480 ft/sec (Figure 3-33), the trends remain essentially the same except for the apparent closing of the forward velocity directivity curves in the 90° to 130° range.

This insensitivity of noise reduction with inlet angle can also be illustrated by comparing the differences between (maximum - minimum) OASPL values. Table 3-XIV presents such a tabulation for 3 free jet and 3 primary jet velocities.

Table 3-XIV. Comparison of Max.-Min. OASPL's
With Free Jet Velocity.

[Δ (OASPL) @ 40° Arc]

Primary Jet Velocity (ft/sec)	V(28) Free Jet Velocity		
	0	165 ft/sec	365 ft/sec
1115	14.0	13.5	11.0
1480	17.5	17.5	16.5
1870	19.5	19.5	19.5

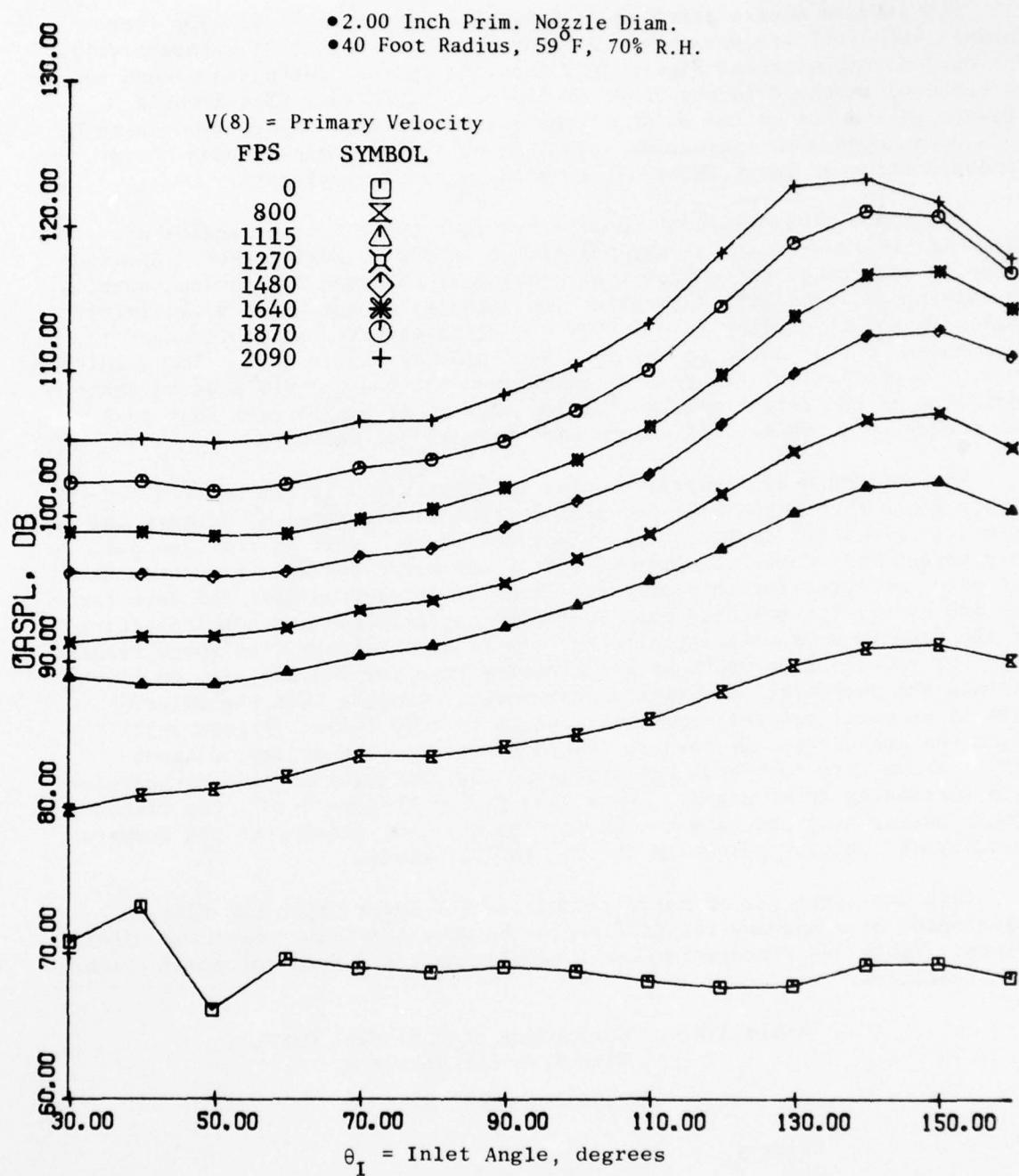


Figure 3-29. Ambient and Primary Jet OASPL Characteristics.

AD-A041 849

GENERAL ELECTRIC CO CINCINNATI OHIO AIRCRAFT ENGINE GROUP F/G 20/1
HIGH VELOCITY JET NOISE SOURCE LOCATION AND REDUCTION. TASK 4. --ETC(U)
FEB 77 W S CLAPPER, E J STRINGAS DOT-OS-30034

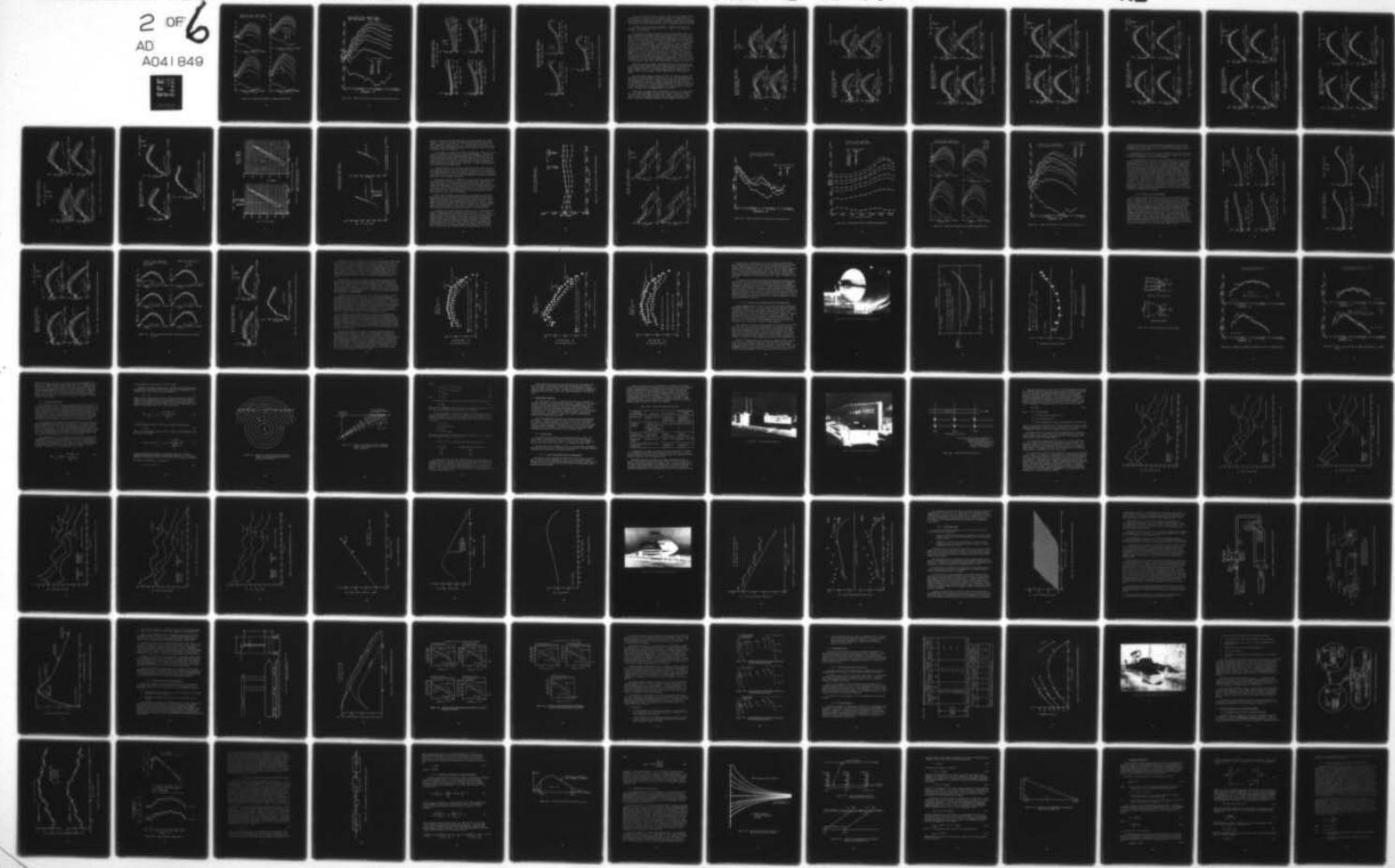
UNCLASSIFIED

2 OF 6
AD
A041 849

R77AEG189

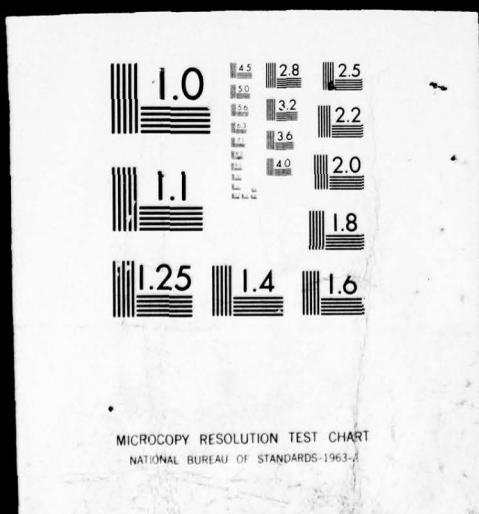
FAA-RD-76-79-4

NL



IFIED
2 OF 6
AD

A041 849



● 2.00 Inch Prim. Nozzle Diam.
 ● 40 Foot Radius, 59° F, 70% R.H.

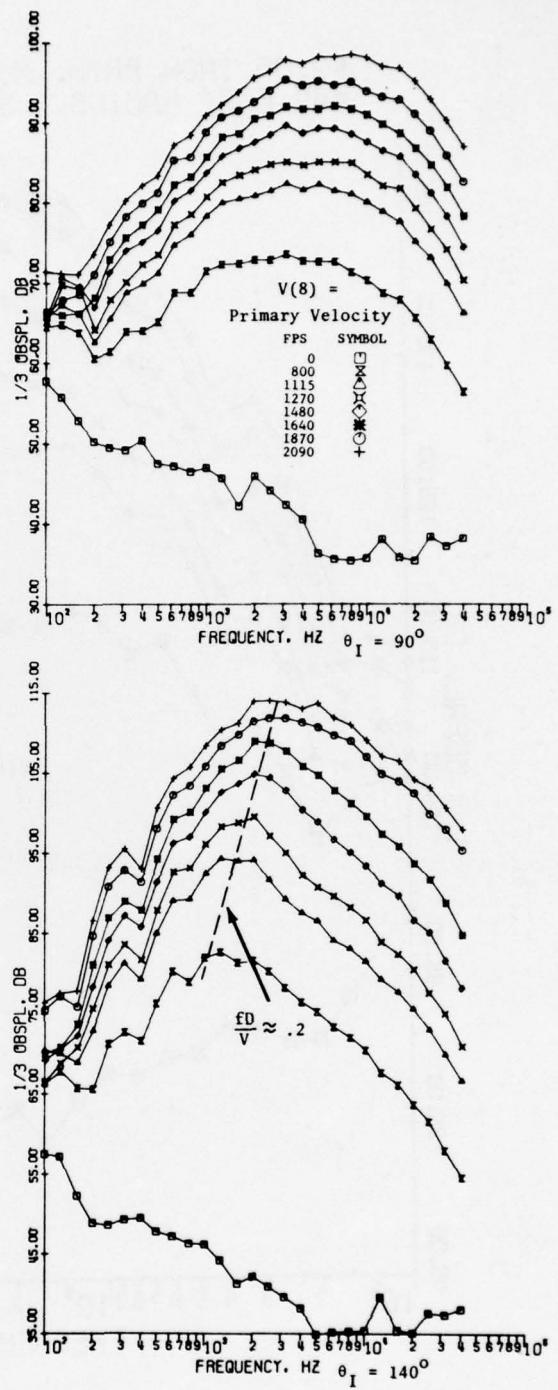
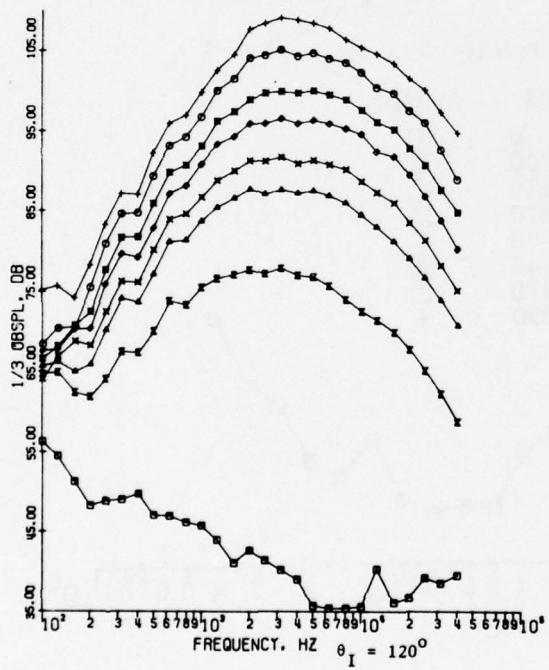
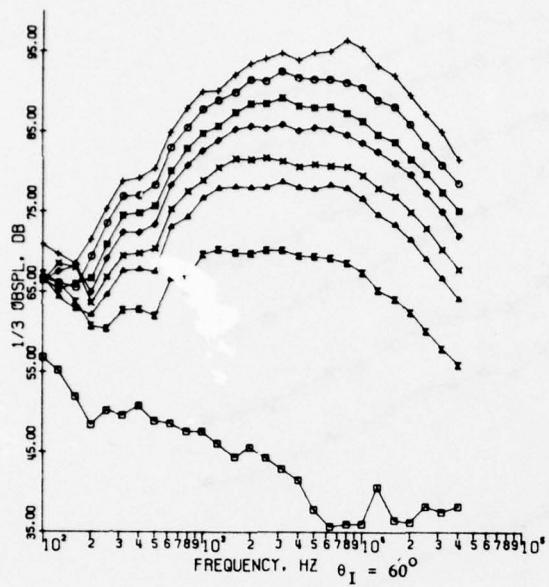


Figure 3-30. Ambient and Primary Jet OBSPL Characteristics.

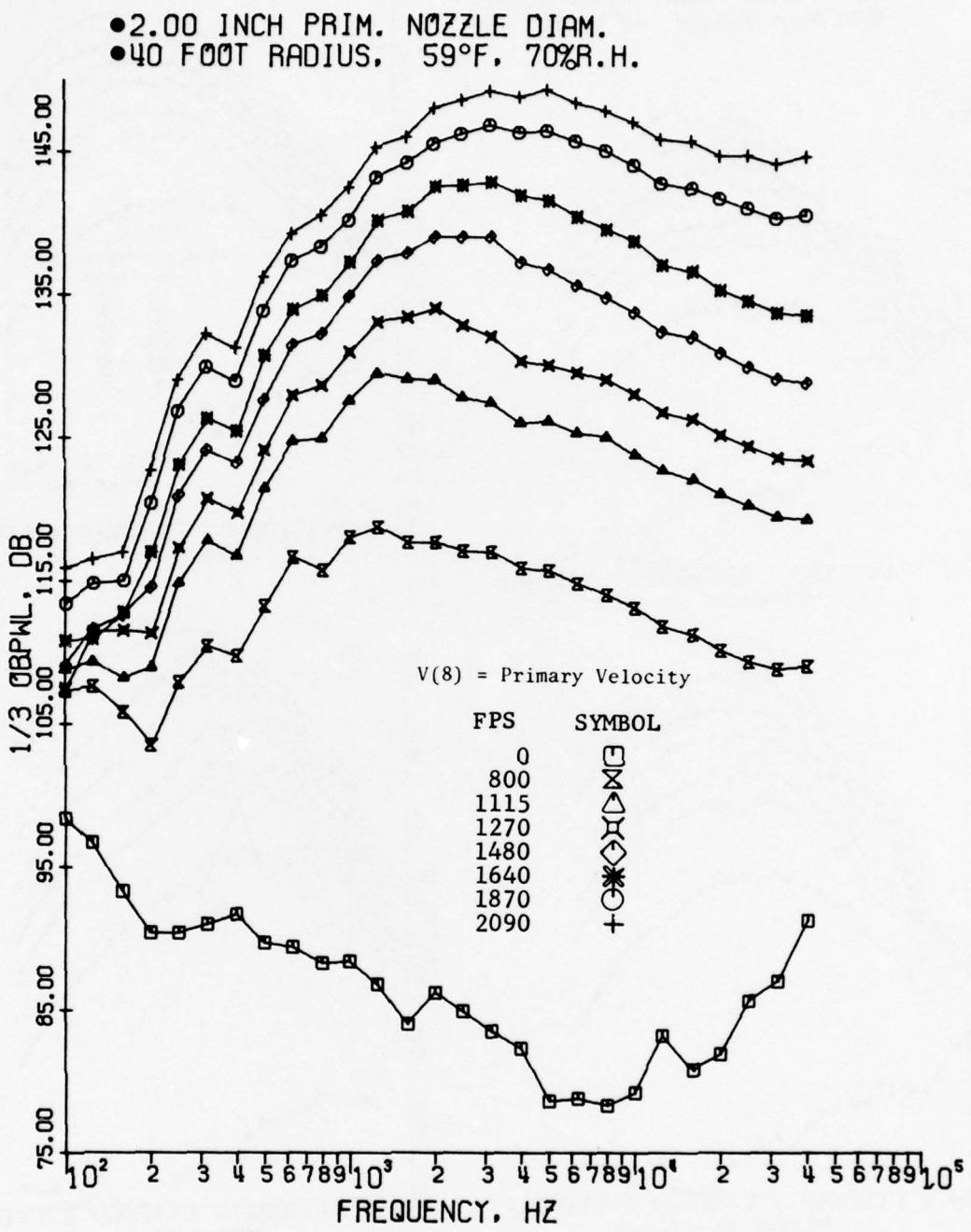
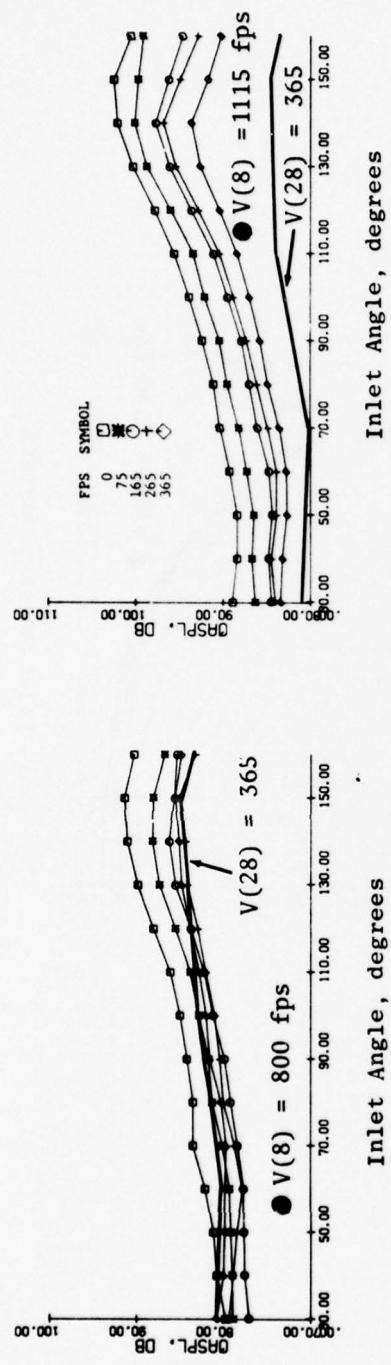


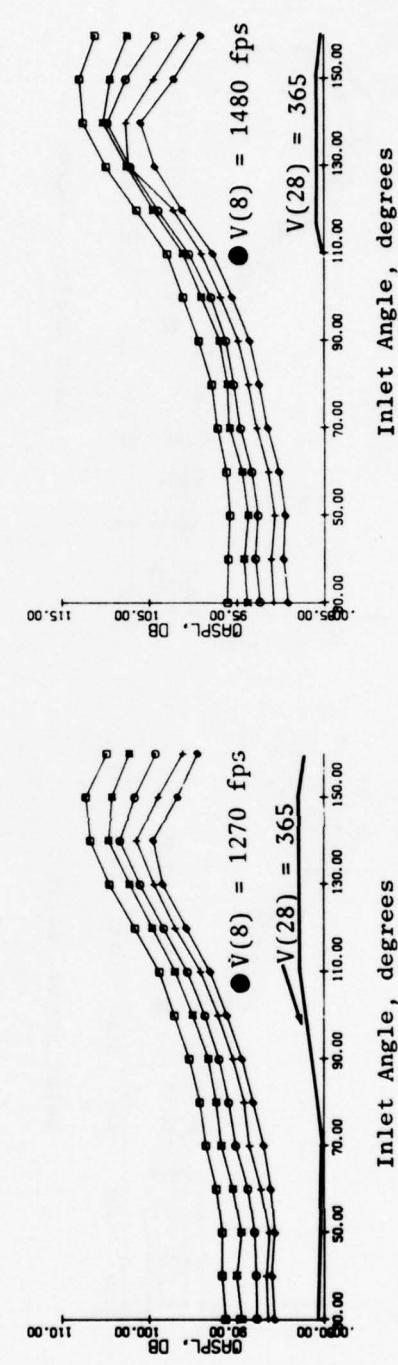
Figure 3-31. Ambient and Primary Jet Power Spectra Characteristics.

● 2.00 Inch Prim. Nozzle Diam.
 ● 40 Foot Radius, 59° F., 70% R.H.

V(28) = Free Jet Velocity



Inlet Angle, degrees



Inlet Angle, degrees

Figure 3-32. Effects of Forward Velocity on OASPL Directivity.

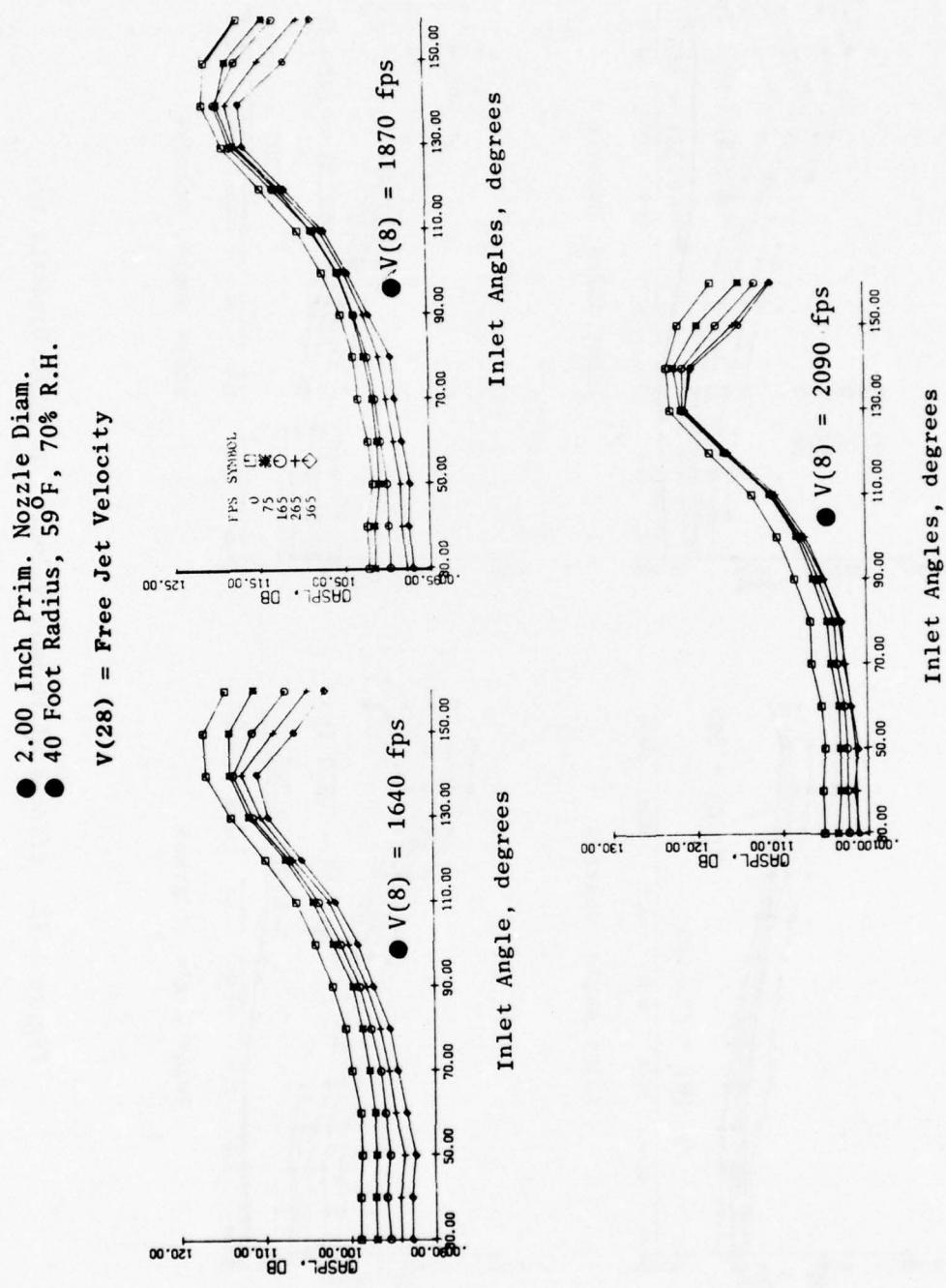


Figure 3-33. Effects of Forward Velocity on OASPL Directivity.

The data presented on Table 3-XIV shows that, at the two highest primary jet velocities, Δ OASPL's are only slightly affected by forward velocity, indicating that the shape of the directivity pattern is essentially unchanged by the addition of free-stream velocity. The lowest primary jet velocity does show change in directivity pattern from static to simulated-flight conditions.

The effect of the free jet also appears to translate the peak noise region to a shallower inlet angle (i.e., $\Delta \theta_I \approx -10^\circ$) for all primary and free jet flow conditions.

The variation of sound pressure level spectra with forward velocity is shown in Figures 3-34 through 3-40 for inlet angles of 60° , 90° , 120° , and 140° . Based on the directivity characteristics previously discussed, sound pressure levels are seen to decrease with increasing free jet velocity at all primary nozzle velocities with the reduction being essentially broadband in nature (i.e., at all frequencies). The data is "as is", e.g., not corrected for free jet (background) noise, as noted previously. However, examination of the spectra, level and shape, for both free jet alone and the free jet/primary reveals that the contamination is minimal and primarily restricted to velocities in the order of 800 ft/sec. This fact is illustrated by superimposing the free jet-only spectra at 365 ft/sec on each of the plots in Figures 3-34 to 3-40. Except for the 800 ft/sec condition, which obviously needs to be corrected since the data are about 3 to 4 dB apart, examination of the spectral plots shows that at velocities up to about 1480 ft/sec, only frequencies in the 250 to 400 Hz region are contaminated. Above this velocity range, the spectral data is essentially unaffected by the free jet except for the shallower angles where some contamination is evident below 200 Hz.

Peak noise frequency remains essentially unaffected by forward velocity at all inlet angles. Additionally, for primary velocities below 1870 ft/sec, peak frequency is generally the same for inlet angles up to 120° but decreases slightly at 140° . At the high primary velocity (2090 ft/sec) condition, however, peak frequency location decreases with increasing inlet angle.

The power spectra shown in Figures 3-41 and 3-42 basically exhibit the same trend as the sound pressure level spectra (e.g., decreasing level with increasing free jet velocity). Again, the 365 ft/sec free jet-alone spectrum is superimposed to illustrate its impact on the resultant measured noise. Only the 800 ft/sec spectra are really influenced by the free jet across the frequency range while at velocities above 1115 ft/sec, frequencies below 250 Hz are affected; and the spectrum reduction with forward velocity increase tends to decrease with increasing primary jet velocity.

The effect of forward flight is summarized in terms of near peak angle ($\theta_I \approx 140^\circ$) OASPL and OAPWL in Figures 3-43 and 3-44 in terms of primary velocity, $V(8)$, and relative velocity [$V(8) - V(28)$], respectively. Examination of Figure 3-43 shows the same trends observed by the directivity plots, namely that suppression relative to the primary nozzle alone (i.e.,

- 2.00 Inch Prim. Nozzle Diam.
- 40 Foot Radius, 59° F., 70% R.H.
- $V(8) = 800$ ft/sec

$V(28)$ = Free Jet Velocity

FPS SYMBOL

0	□
75	■
165	○
265	+
365	◊

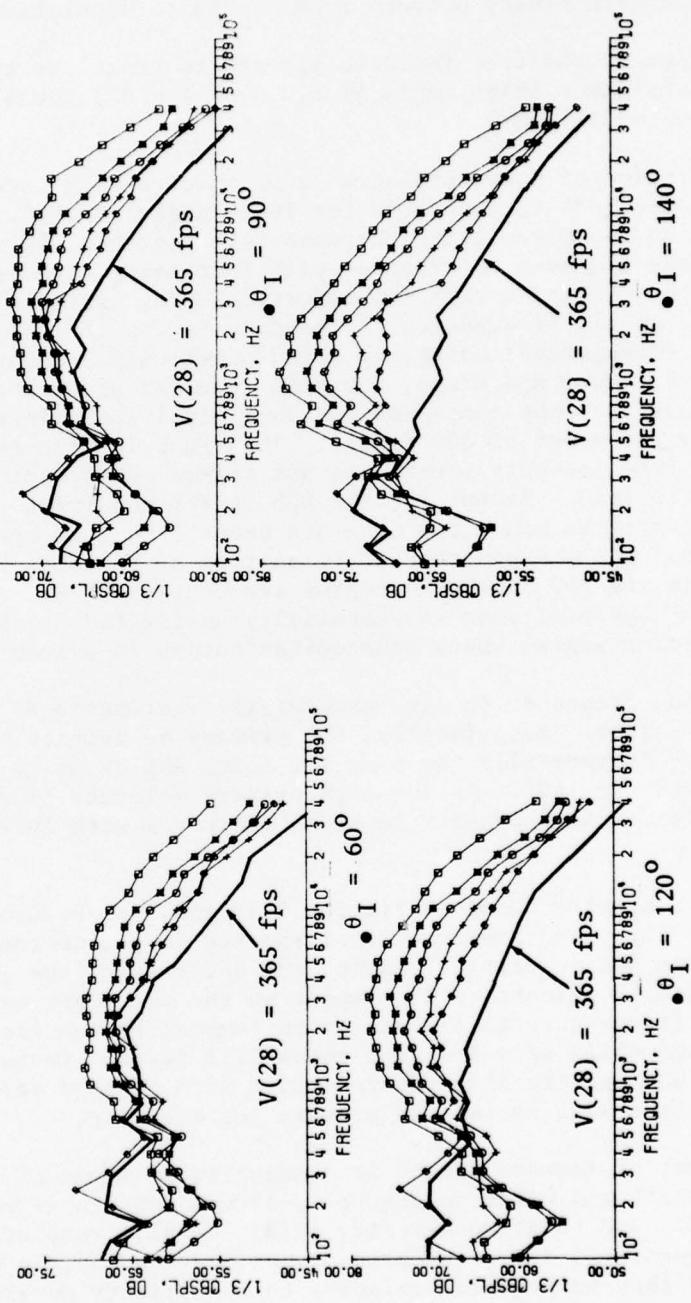


Figure 3-34. Effects of Forward Velocity on Sound Pressure Level Spectra
at $V_J = 800$ ft/sec.

- 2.00 Inch Prim. Nozzle Diam.
- 40 Foot Radius, 59° F., 70% R.H.
- $V(8) = 1115 \text{ ft/sec}$

$V(28) = \text{Free Jet Velocity}$

FPS SYMBOL

- 0
- 75
- 165
- 265
- ◇ 365

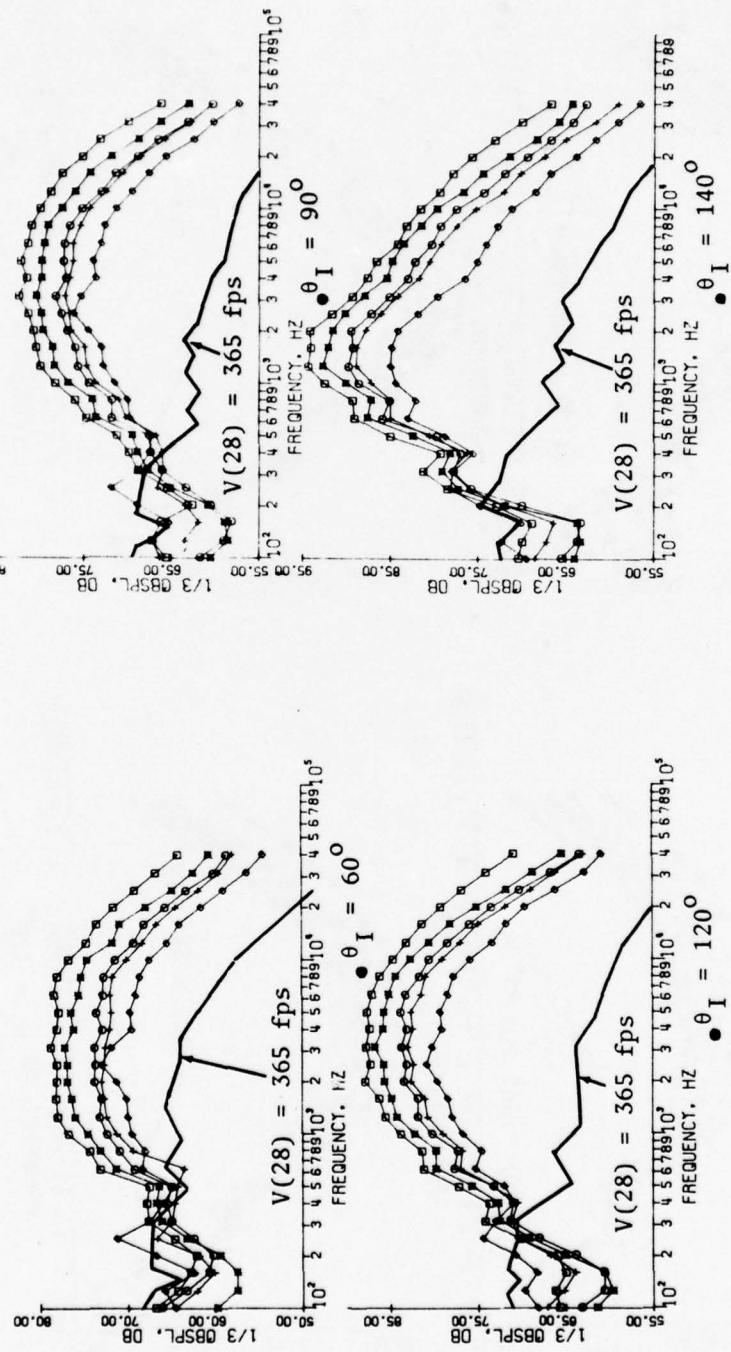


Figure 3-35. Effects of Forward Velocity on Sound Pressure Level Spectra
at $V_J = 1115 \text{ ft/sec}$.

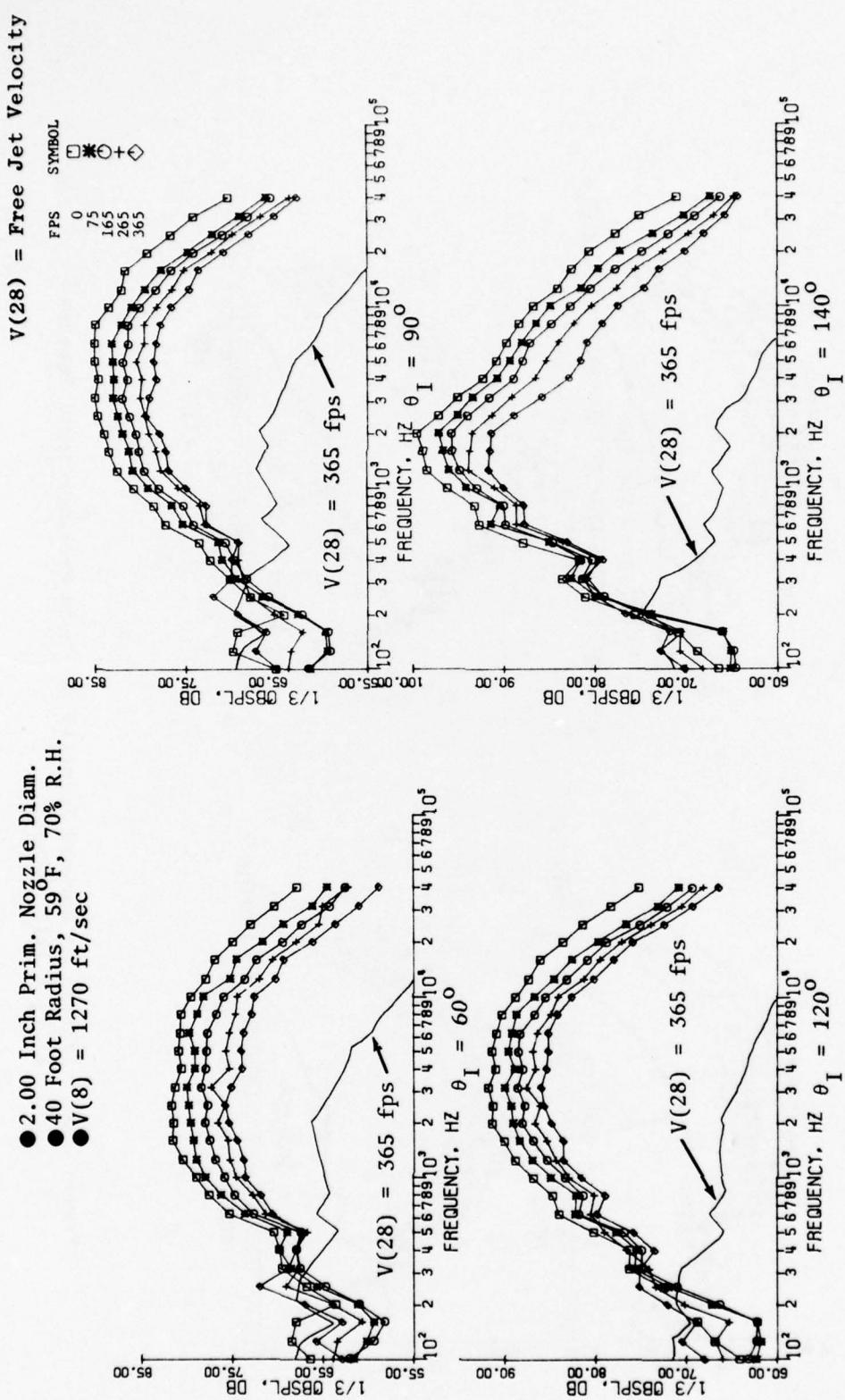


Figure 3-36. Effects of Forward Velocity on Sound Pressure Level Spectra
at $V_J = 1270$ ft/sec.

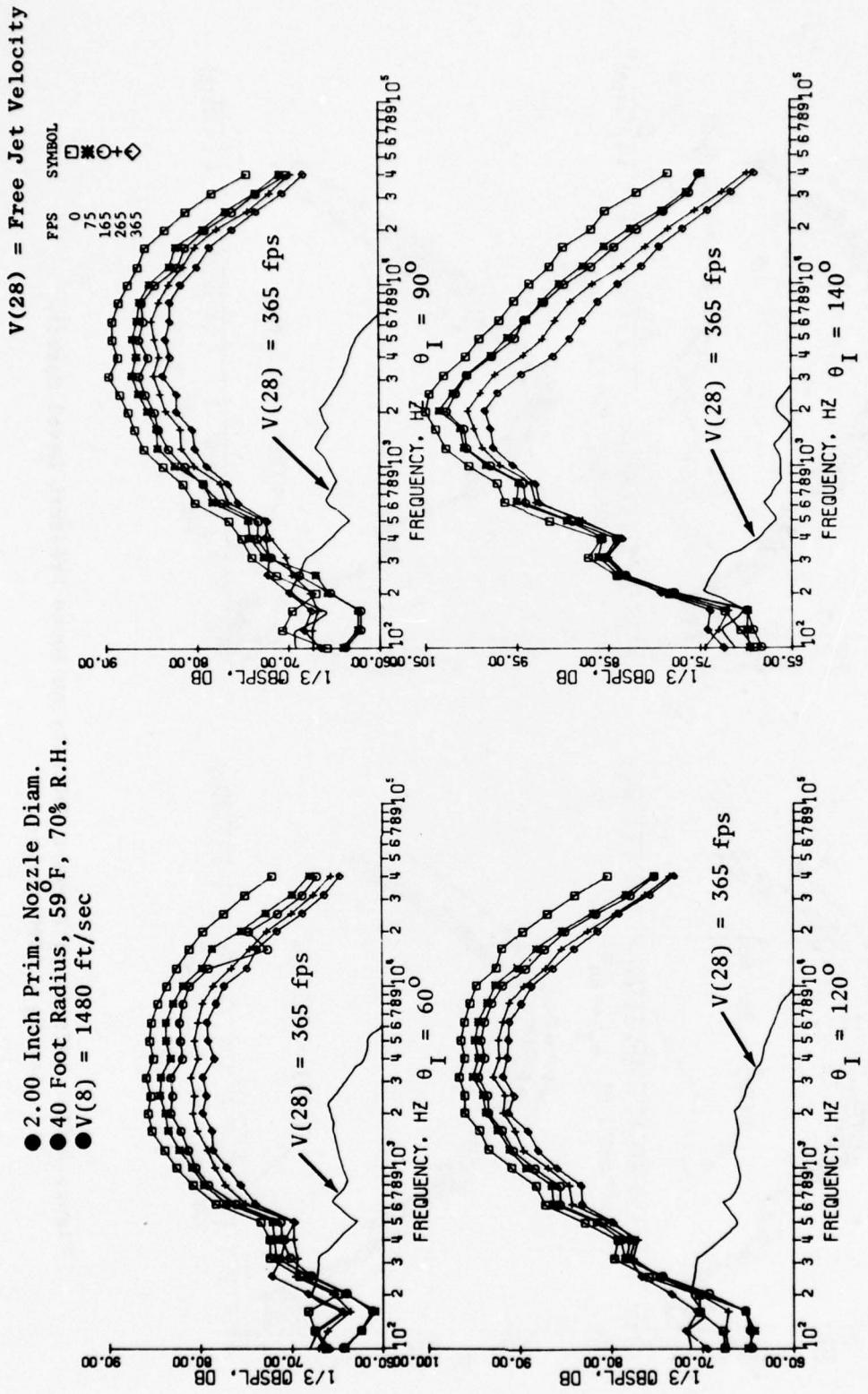


Figure 3-37. Effects of Forward Velocity on Sound Pressure Level Spectra at $V_J = 1480 \text{ ft/sec.}$

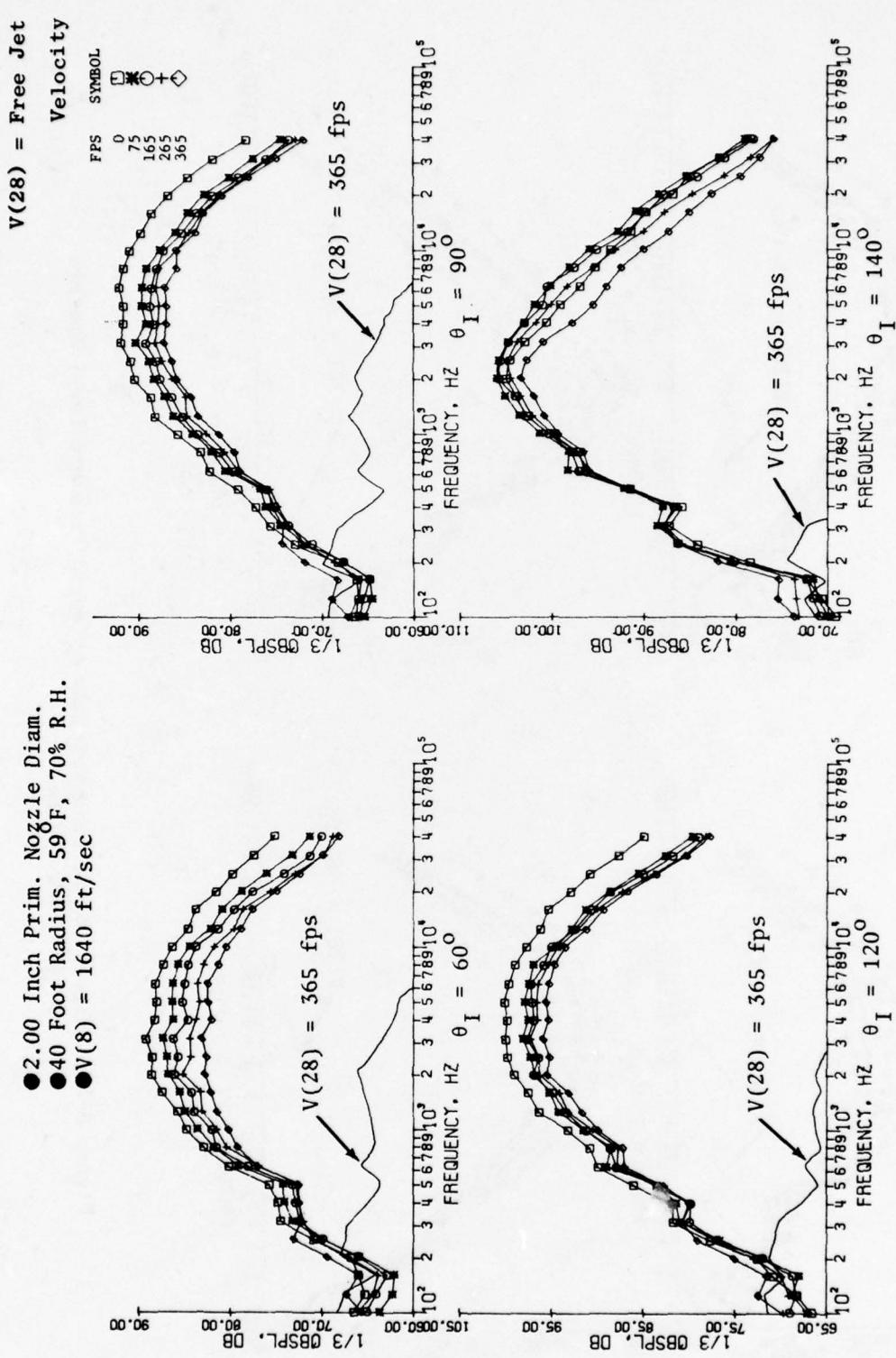


Figure 3-38. Effects of Forward Velocity on Sound Pressure Level Spectra
 at $V_J = 1640$ ft/sec.

- 2.00 Inch Prim. Nozzle Diam.
- 40 Foot Radius, 59° F., 70% R.H.
- $V(8) = 1870 \text{ ft/sec}$

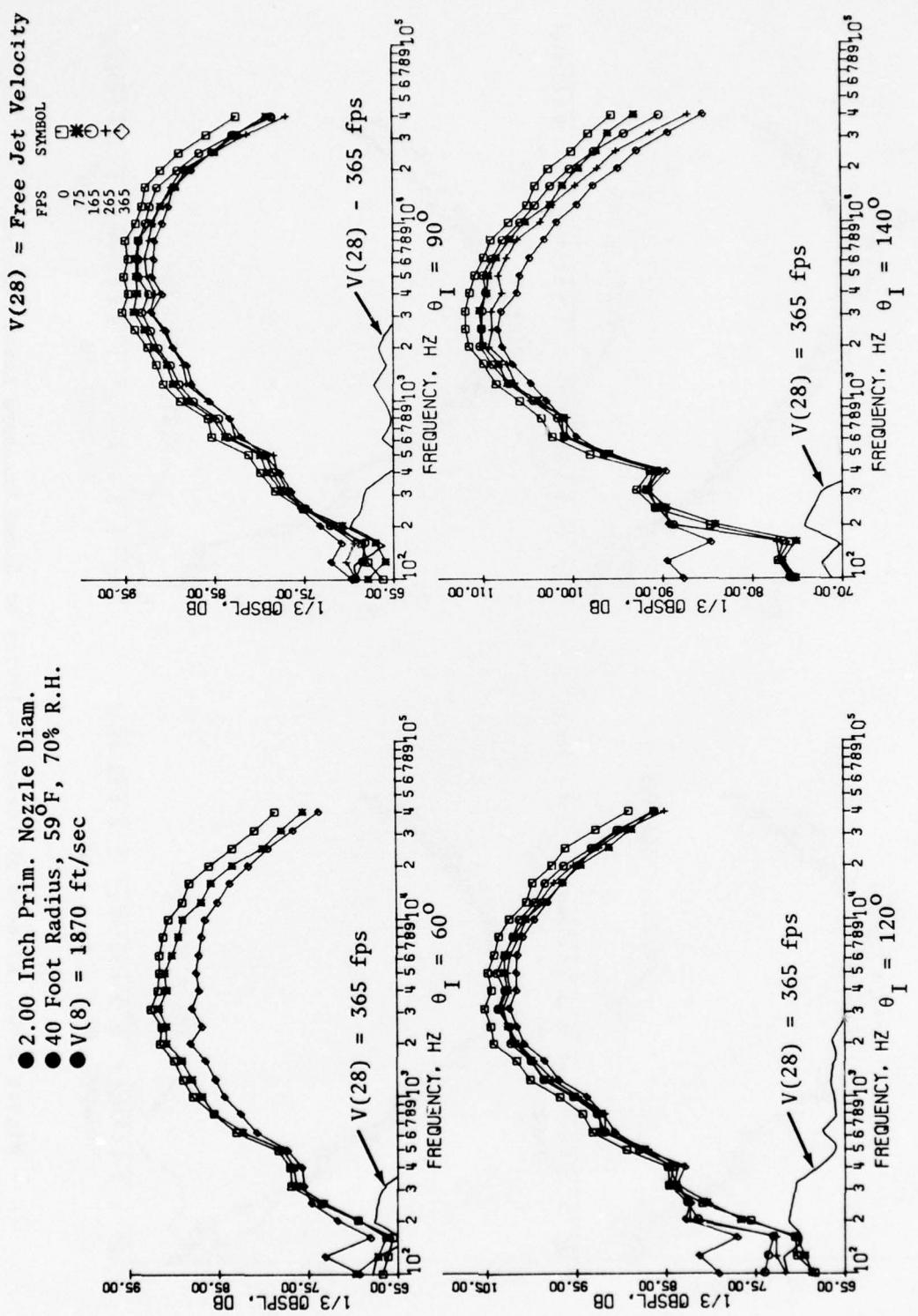


Figure 3-39. Effects of Forward Velocity on Sound Pressure Level Spectra
at $V_J = 1.870 \text{ ft/sec.}$

● 2.00 Inch Prim. Nozzle Diam.
 ● 40 Foot Radius, 59° F., 70% R.H.
 ● $V(8)$ = 2090 ft/sec

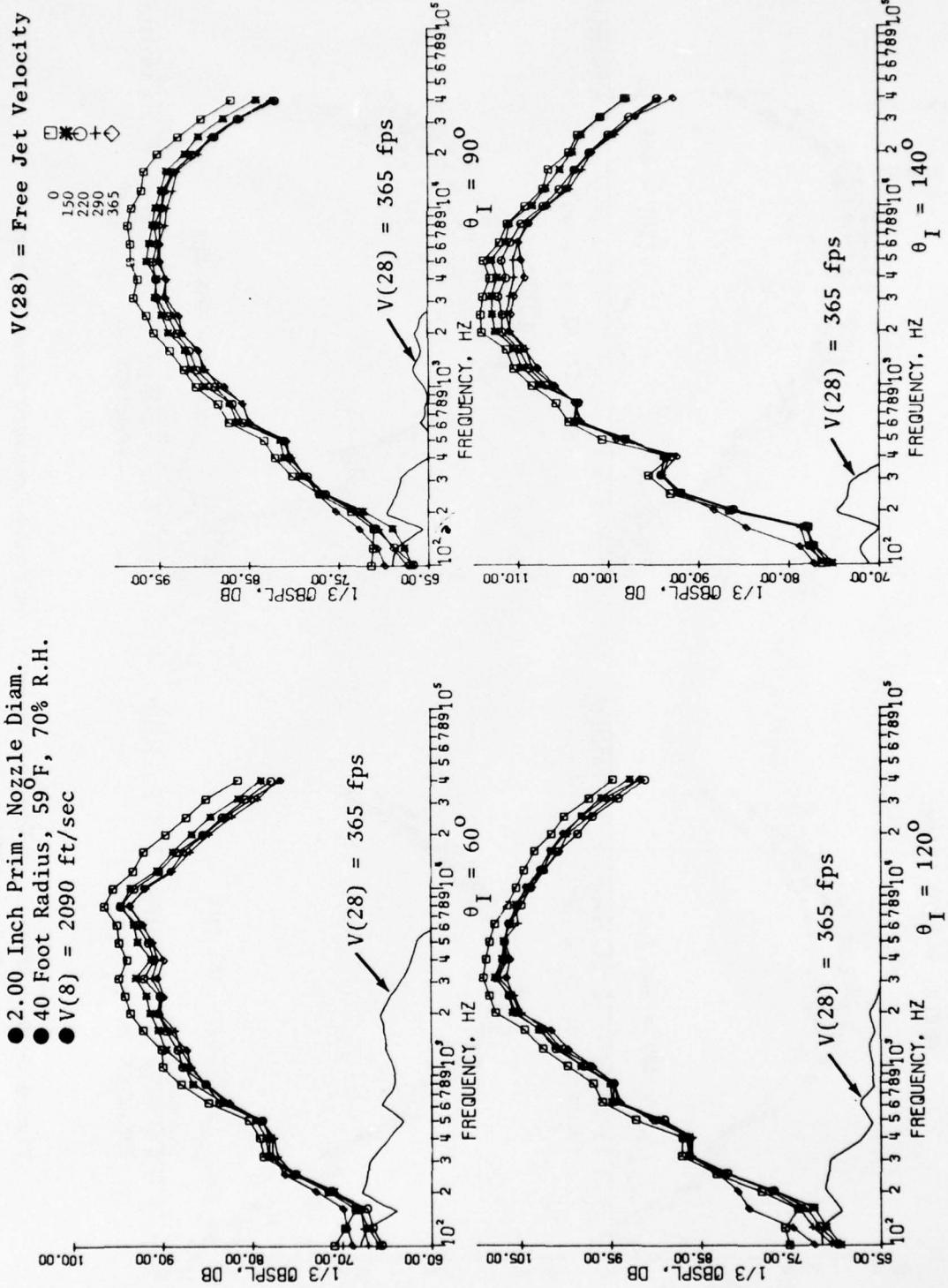


Figure 3-40. Effects of Forward Velocity on Sound Pressure Level Spectra
at $V_J = 2090$ ft/sec.

- 2.00 Inch Prim. Nozzle Diam.
- 40 Foot Radius, 59° F, 70% R.H.

$V(28) = \text{Free Jet Velocity}$

FPS	SYMBOL
0	□
75	*
165	○
265	+
365	◊

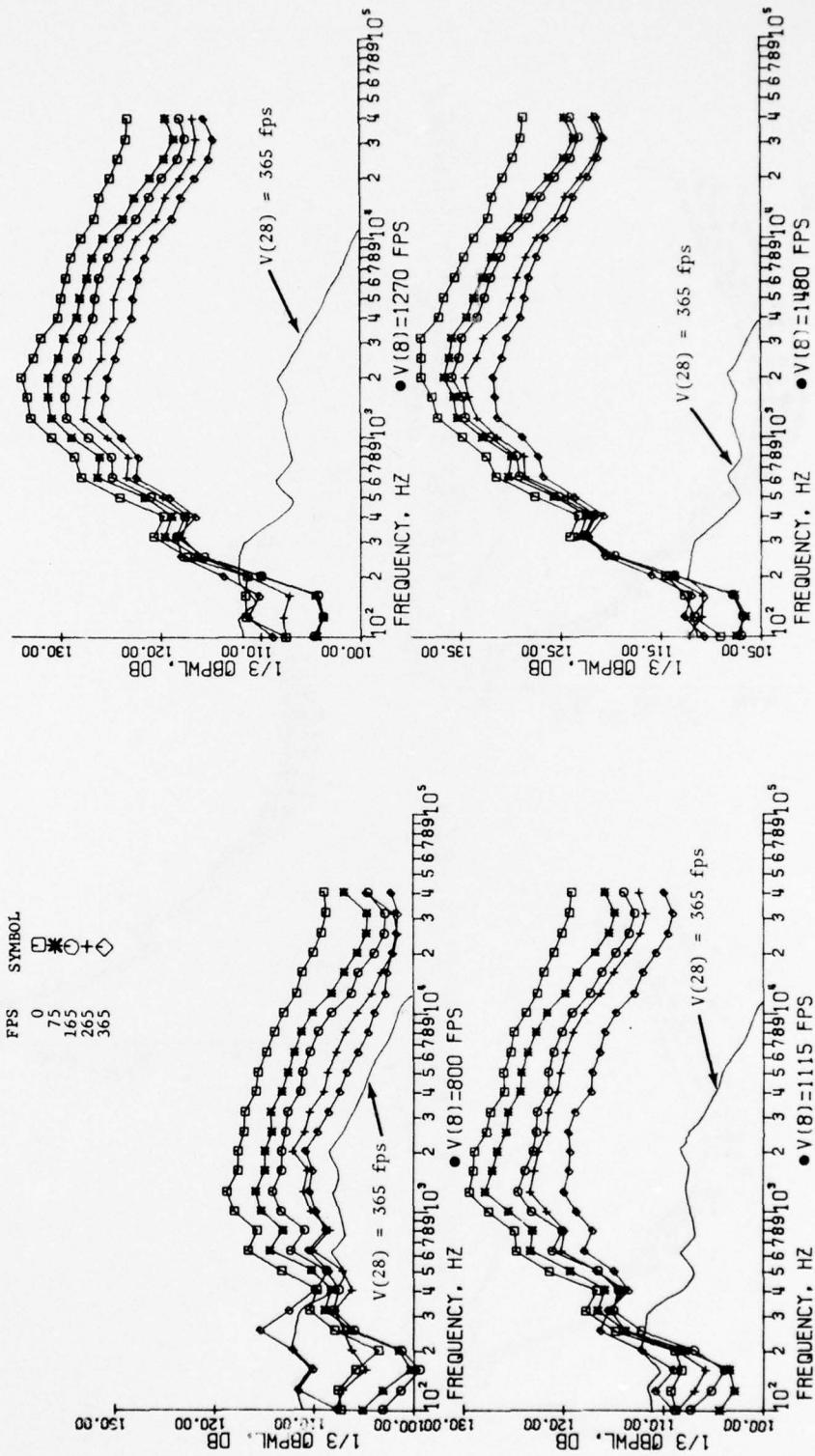


Figure 3-41. Effect of Forward Velocity on Sound Power Level Spectra.

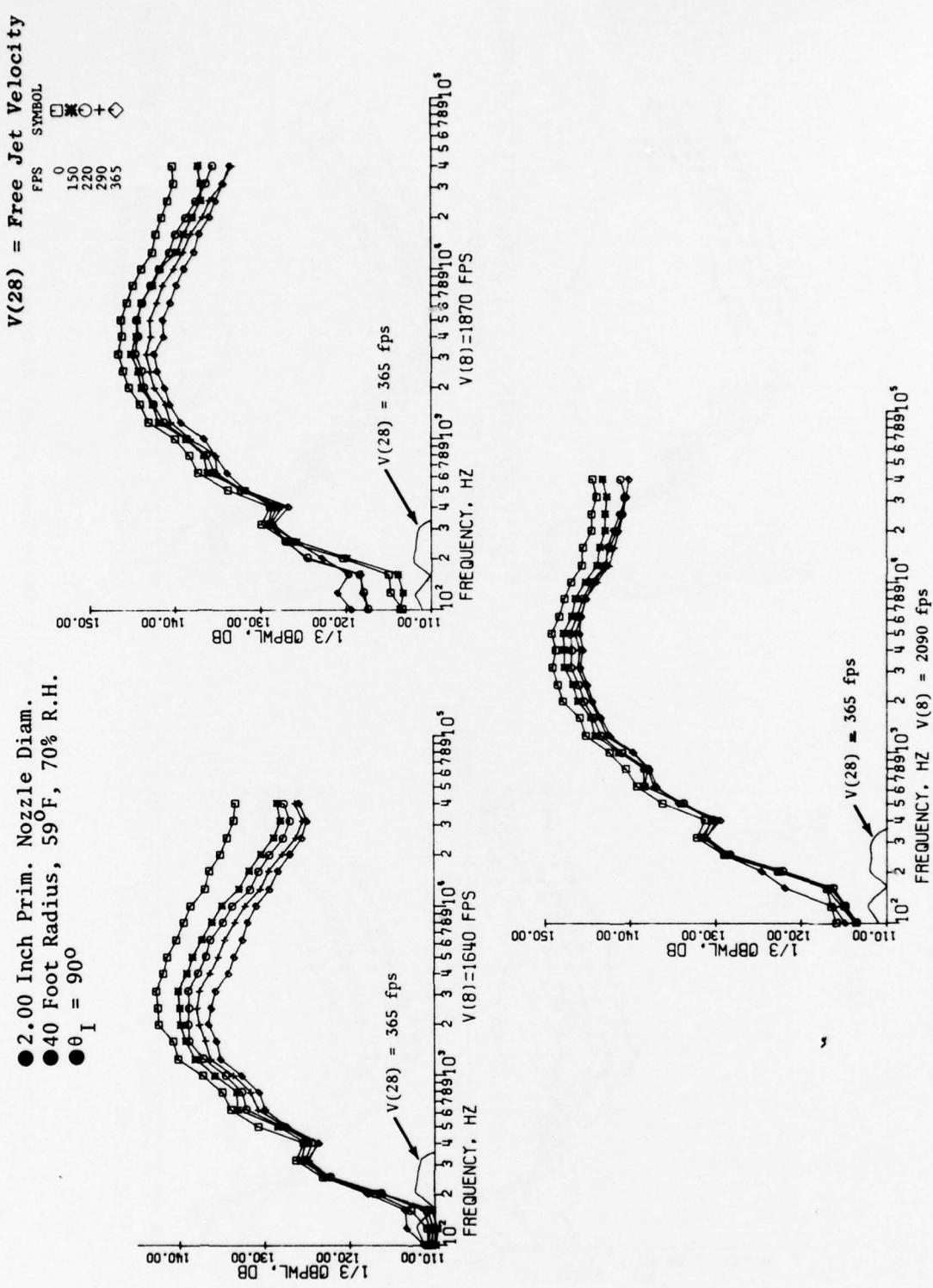


Figure 3-42. Effect of Forward Velocity on Sound Power Level Spectra.

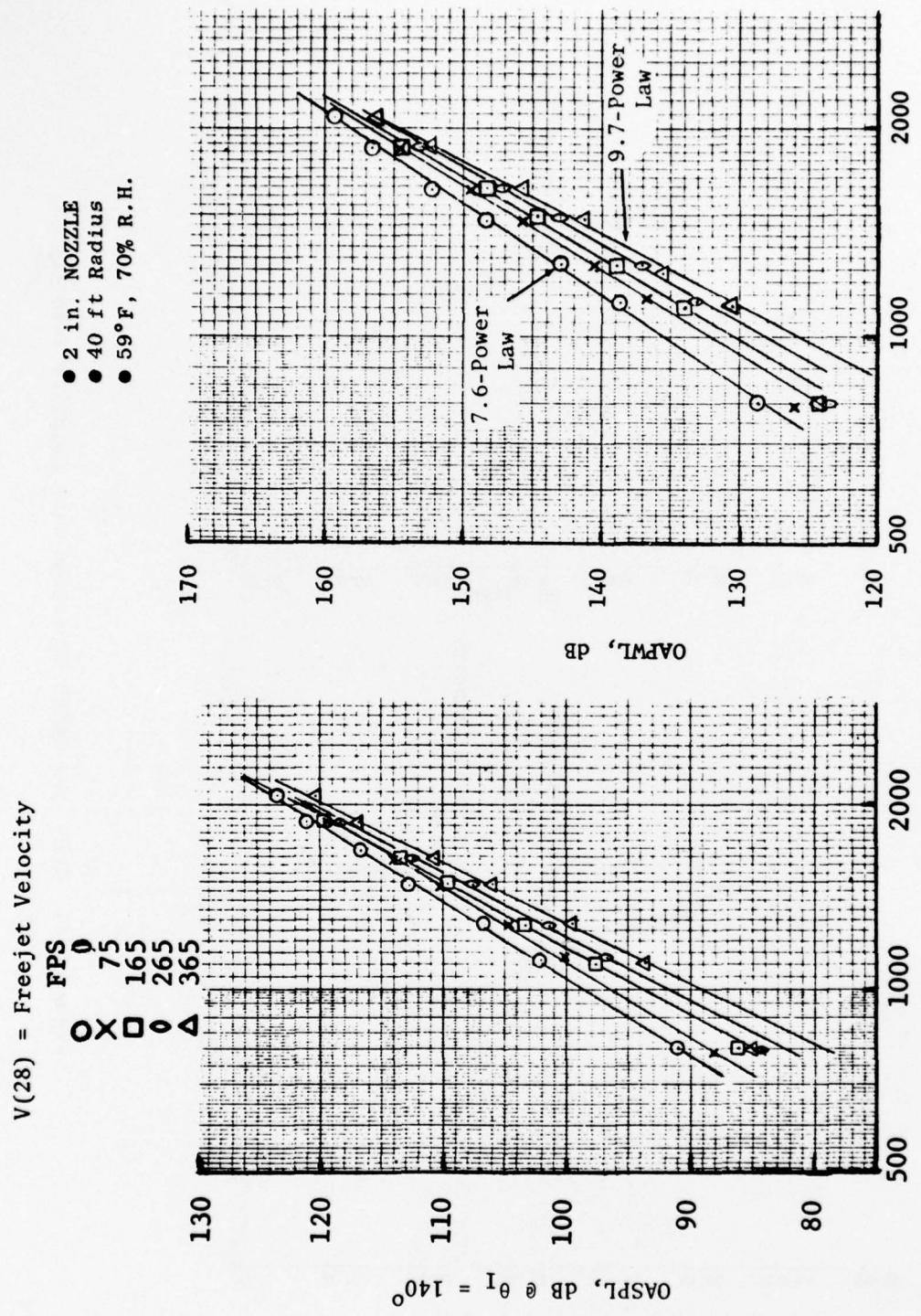


Figure 3-43. Effects of Forward Velocity on OASPL and OAPWL Vs. Primary Velocity.

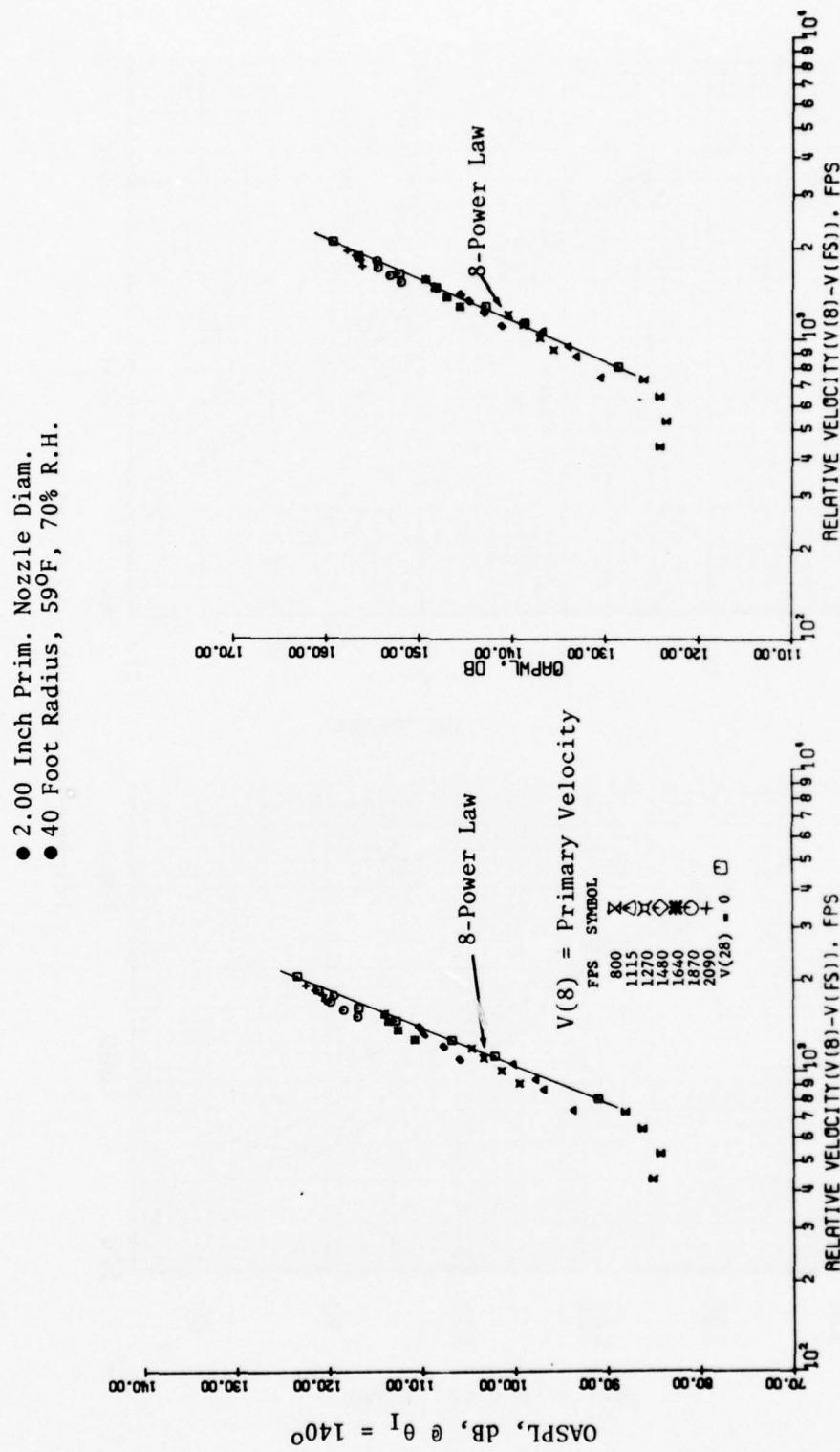


Figure 3-44. OASPL and OAPWL Variation with Relative Velocity.

static) increases with increasing forward velocity and decreasing primary velocity. It is also obvious from these plots that the 800 to 1115 ft/sec region is affected by the free jet. It is interesting to note that the static OAPWL data conforms to about the 7.6-power law, which is well within the range of other experimental evidence, but increases to about 9.7 at the high free jet velocity condition.

In an attempt to collapse these OASPL and OAPWL data, (Figure 3-44), the relative velocity was utilized as the correlating parameter. Although the static data, $V(28) = 0$, is in good agreement with the 8-power law, the reduction in OASPL and OAPWL levels with increasing free jet velocity do not coincide with the static results. Generally, the slope of the data at any primary velocity is less steep (lower slope) than its static counterpart. These findings are not unique and are only shown to verify trends previously put forth by other experimentalists.

A similar series of tests, as just described for the 2-inch nozzle, was also conducted utilizing the 3.56-inch nozzle with another free jet shroud (12.6-inch dia) which resulted in a free jet area ratio of 11.6. Generally, the trends are similar to those described previously for the 35 free jet area ratio tests so the discussion to follow will highlight those data considered pertinent to the following comparisons.

Figures 3-45 through 3-47 summarize the directivity sound pressure level and power spectra of the free jet with the primary nozzle leaking, as previously discussed, to eliminate any effect due to an inner wake region. Levels when compensated for the difference in free jet flow area, as well as trends, are quite similar to those described for the 12.0-inch diameter free jet shroud. As will be shown later, these data will be utilized to assess the contribution and frequency separation of free jet and primary nozzle during velocity (e.g., dual flow) testing.

Overall sound pressure level directivity, sound pressure, and sound power spectra for the primary nozzle operating statically are depicted in Figures 3-48 through 3-50. The directivity plots exhibit the usual peaked directivity characteristic associated with increasing jet velocity. The higher velocity points (1640, 1870, and 2080 ft/sec) also show the expected shift of peak noise angle to lower values. Examination of the SPL and PWL spectra shown in Figures 3-49 and 3-50 are typical of those exhibited by conical nozzles and previously described under the 2-inch STA nozzle.

In general, the results obtained from these series of tests were quite similar to those reported upon for the 2-inch STA nozzle. At the onset, however, it was known that the smaller effective area of the free jet and the larger diameter of the primary jet would tend to decrease the separation peak frequencies (free jet going to a higher frequency, primary moving toward a lower frequency) while increasing the difference in peak noise levels between the two streams which in turn would tend to minimize the contribution of the free jet to the far-field acoustic signature during dual-flow operation. On the questionable side, however, the low free jet area ratio may not permit adequate external flow simulation of the jet

- 3.56 in. Prim. Nozzle Dia
- 40 ft Radius, 59°F, 70% R.H.

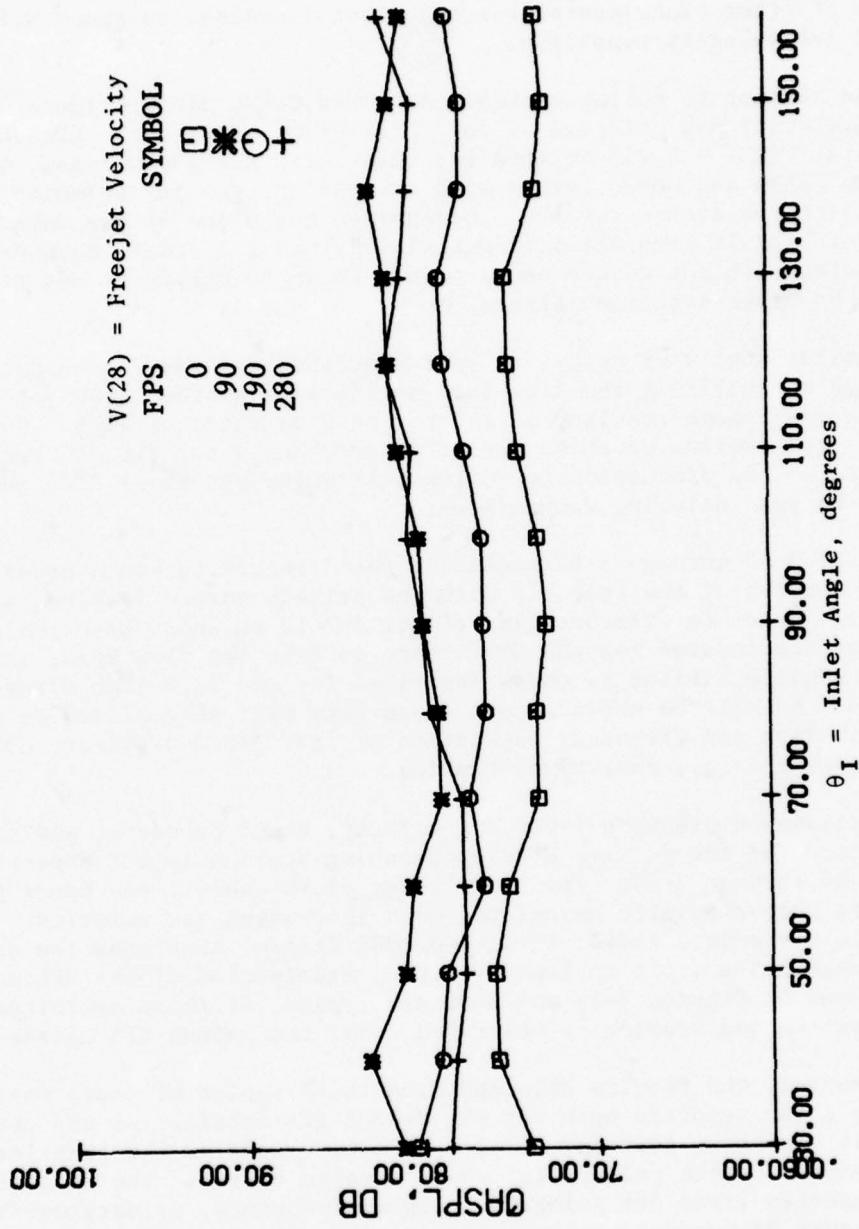


Figure 3-45. Ambient and Free Jet OASPL Characteristics.

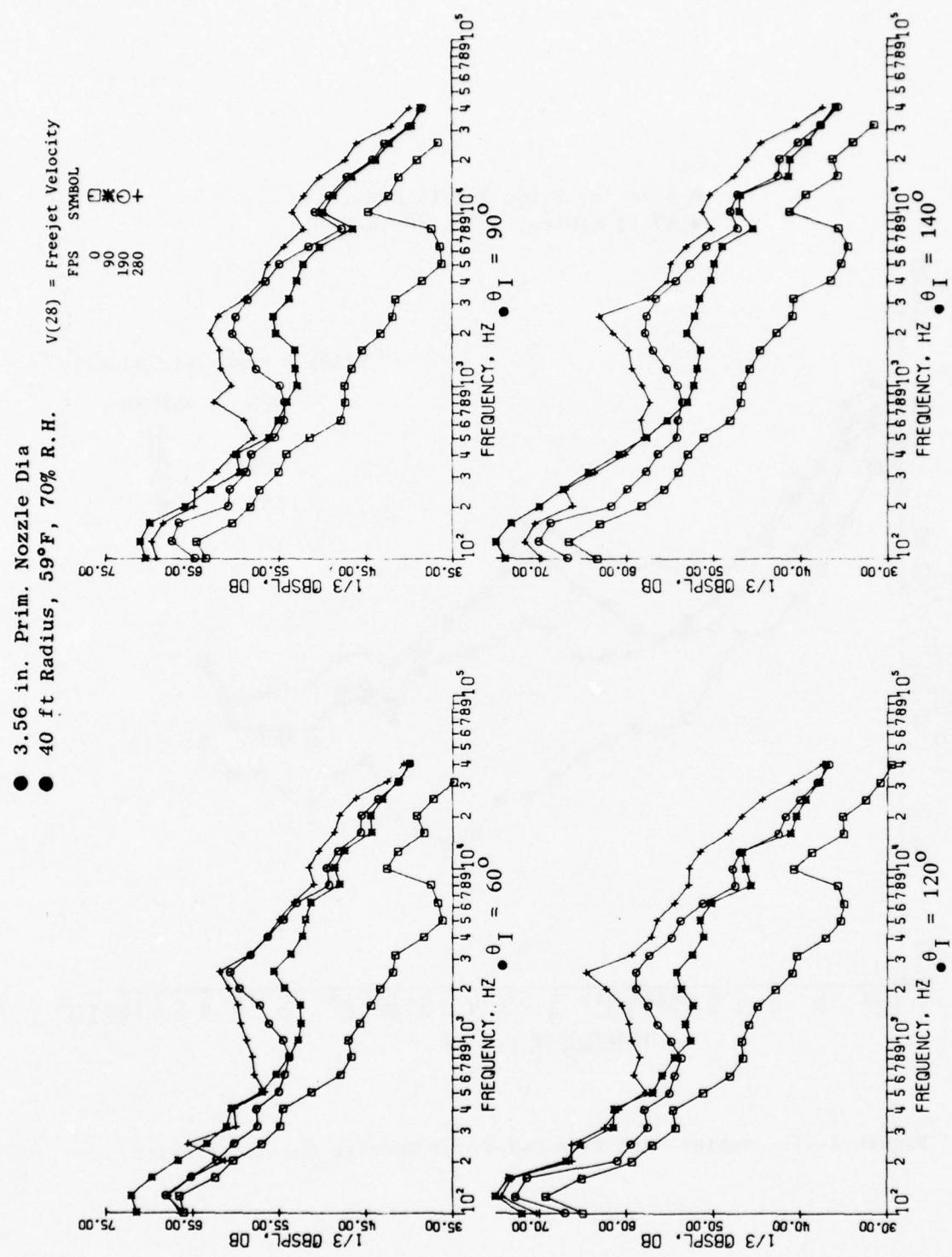


Figure 3-46. Ambient and Free Jet 1/3 OB SPL Characteristics.

● 3.56 in. Prim. Nozzle Dia
● 40 ft Radius, 59°F, 70% R.H.

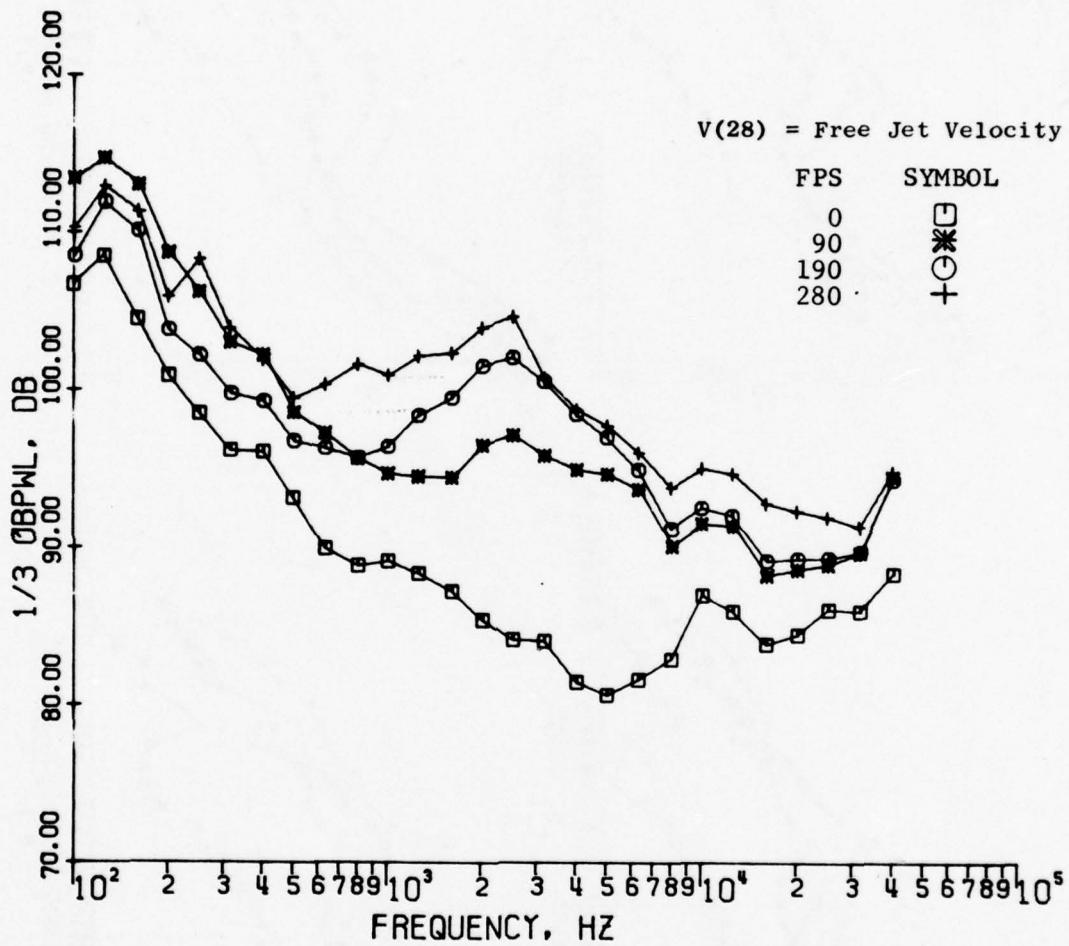


Figure 3-47. Ambient and Free Jet Power Spectra Characteristics.

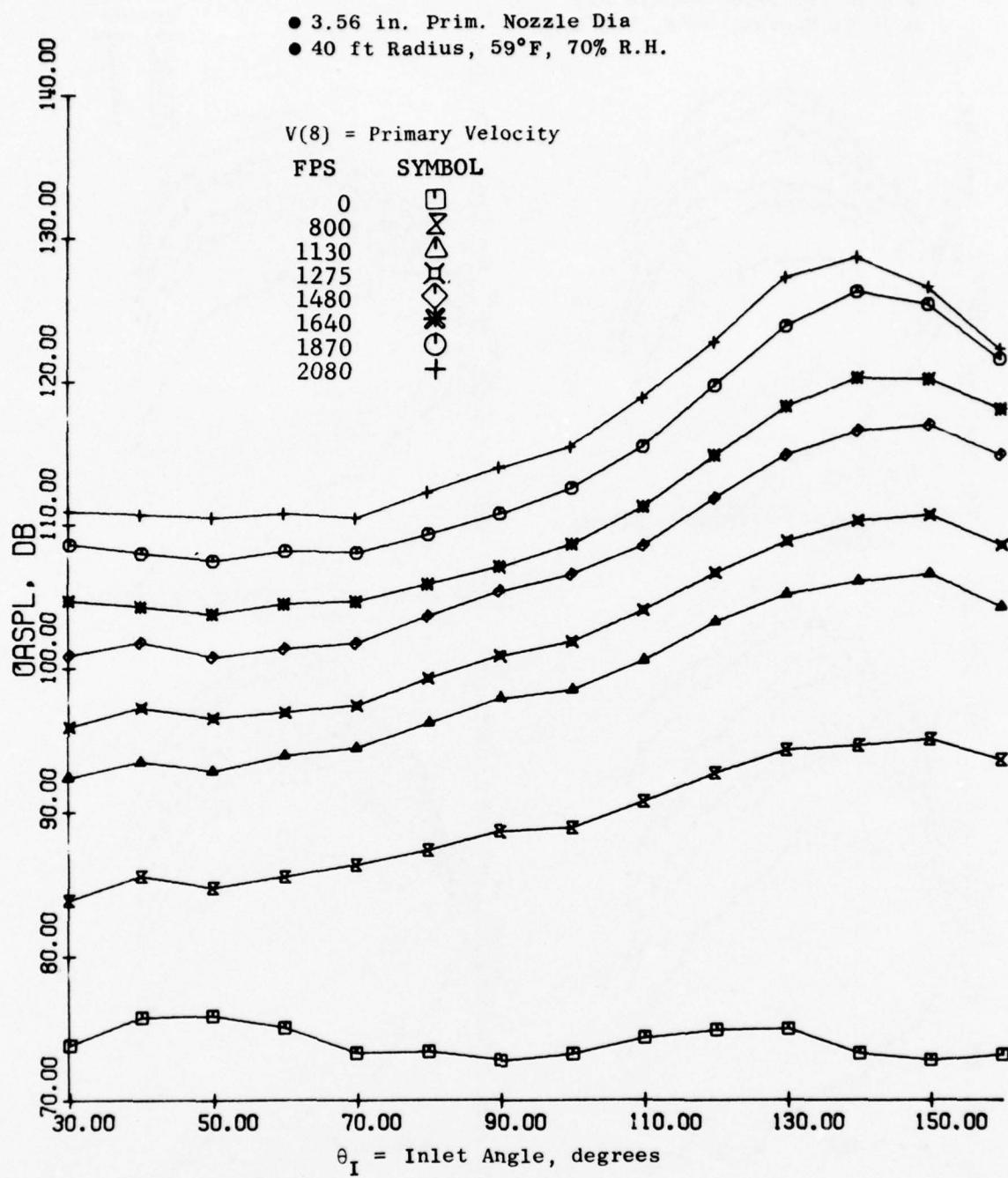


Figure 3-48. Ambient and Primary Jet OASPL Characteristics.

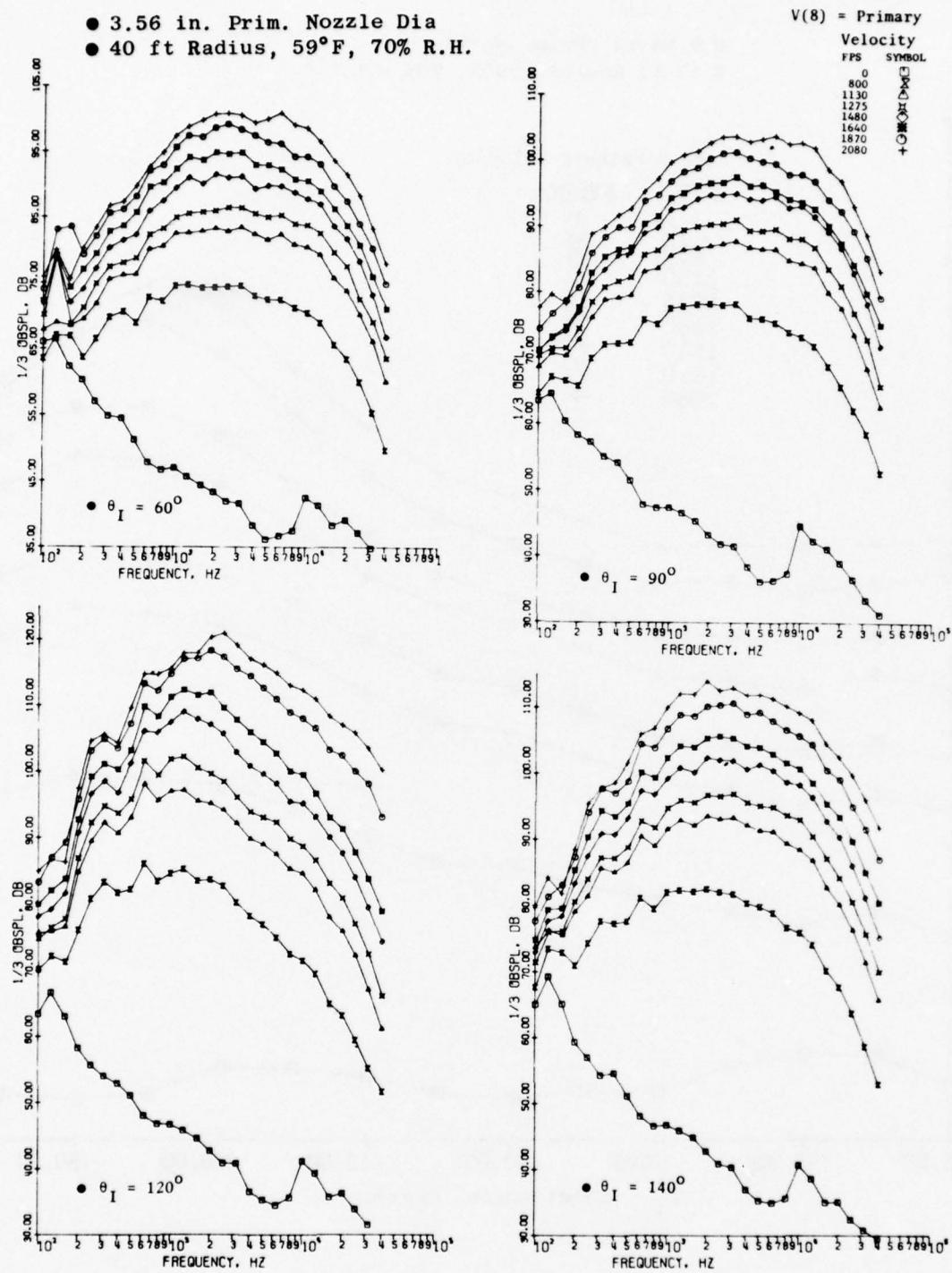


Figure 3-49. Ambient and Primary Jet 1/3 OBSPL Characteristics.

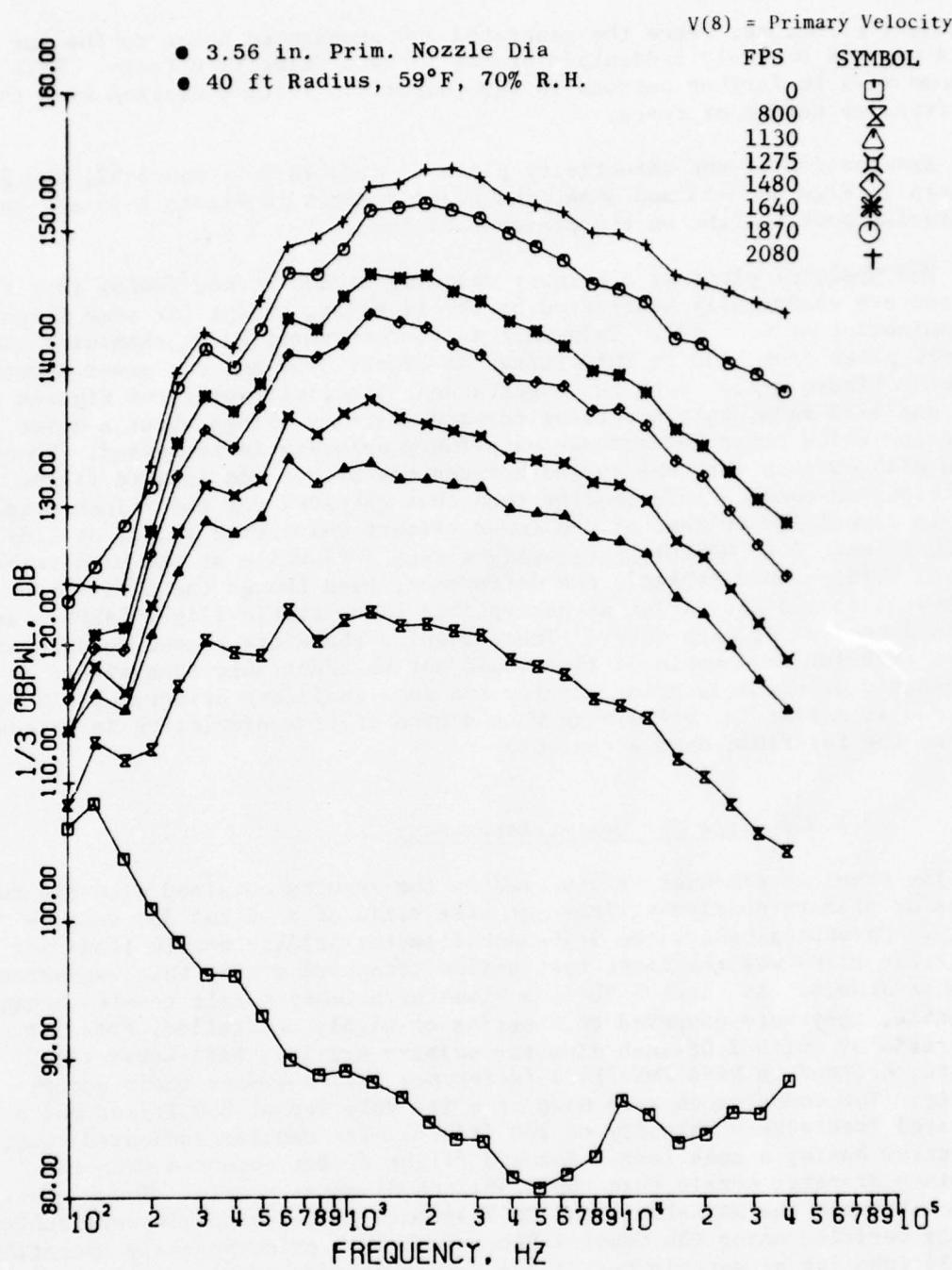


Figure 3-50. Ambient and Primary Jet Power Spectra Characteristics.

turbulent structure, hence the generated and propagated noise to the far field may not be truly indicative of the forward velocity effects. This dilemma will be further pursued in the comparison section dealing with the two free jet series of tests.

Examination of the directivity plots of Figures 3-51 and 3-52, the SPL spectra in Figures 3-53 and 3-54, and power spectra in Figure 3-55 all tend to provide some insight on the previous comments.

The spectral plots at a primary velocity of 800 ft/sec reveal that the spectra are essentially unaffected by the free jet, except for some slight contamination at $\theta_I \approx 60^\circ$. This fact is further verified by examining the 90° SPL plots from 1130 to 2080 ft/sec in Figure 3-54 and the power spectra shown in Figure 3-55. Both the spectra and directivity plots of Figures 3-51 and 3-52 show that increasing forward velocity brings about a noise reduction which tends to decrease as primary velocity is increased. However, it is also obvious that the spread between the static and forward flight conditions is considerably smaller than that recorded for the 2-inch nozzle. This is especially evident at the lower primary velocities [e.g., at $V(8) \approx 1120$ ft/sec, $\Delta (\Delta OASPL)(Static-Flight)Peak \approx 4$] while at the high velocity end [$V(8) \approx 2080$ ft/sec], the difference, even though the Δ difference is about 1 to 1.5 dB, is not as perceptible since static-flight OASPL's are within 2 to 3 dB of each other. These results therefore tended to suggest that a free jet area ratio of 11.6 would not be acceptable from either an aerodynamic or acoustic point of view and some ancillary criteria would be required to assist in determining what degree of flow simulation is necessary to make the far-field data acceptable.

3.1.3.6 Free Jet Tests, Assessment

The previous discussions centered on the results obtained with the two series of primary nozzles at free jet area ratio of 11.6 and 35, respectively. Chronologically, the 3.56-inch diameter primary nozzle (free jet area ratio 11.6) was the first test series conducted during this assessment phase at JENOTS. As these 3.56-inch diameter primary nozzle results became available, they were compared to a series of highly controlled, free jet area ratio 39 (with 2.06-inch diameter primary nozzle), NASA-Lewis test results reported in NASA TMX-71438 (Reference 14) to assess their acceptability. The comparisons were made at a jet velocity of 800 ft/sec and a simulated free-stream velocity of 300 ft/sec. The results indicated that, on a spectrum basis, a much larger forward flight effect occurred with the 2.06-inch diameter nozzle than the 3.56-inch diameter nozzle. These observations between the NASA-Lewis and GE 3.56-inch diameter nozzle were subsequently verified using the General Electric 2-inch primary nozzle operating in a 35 free jet area-ratio test setup. This difference was noted previously during the results/analysis of the 3.56-inch diameter nozzle.

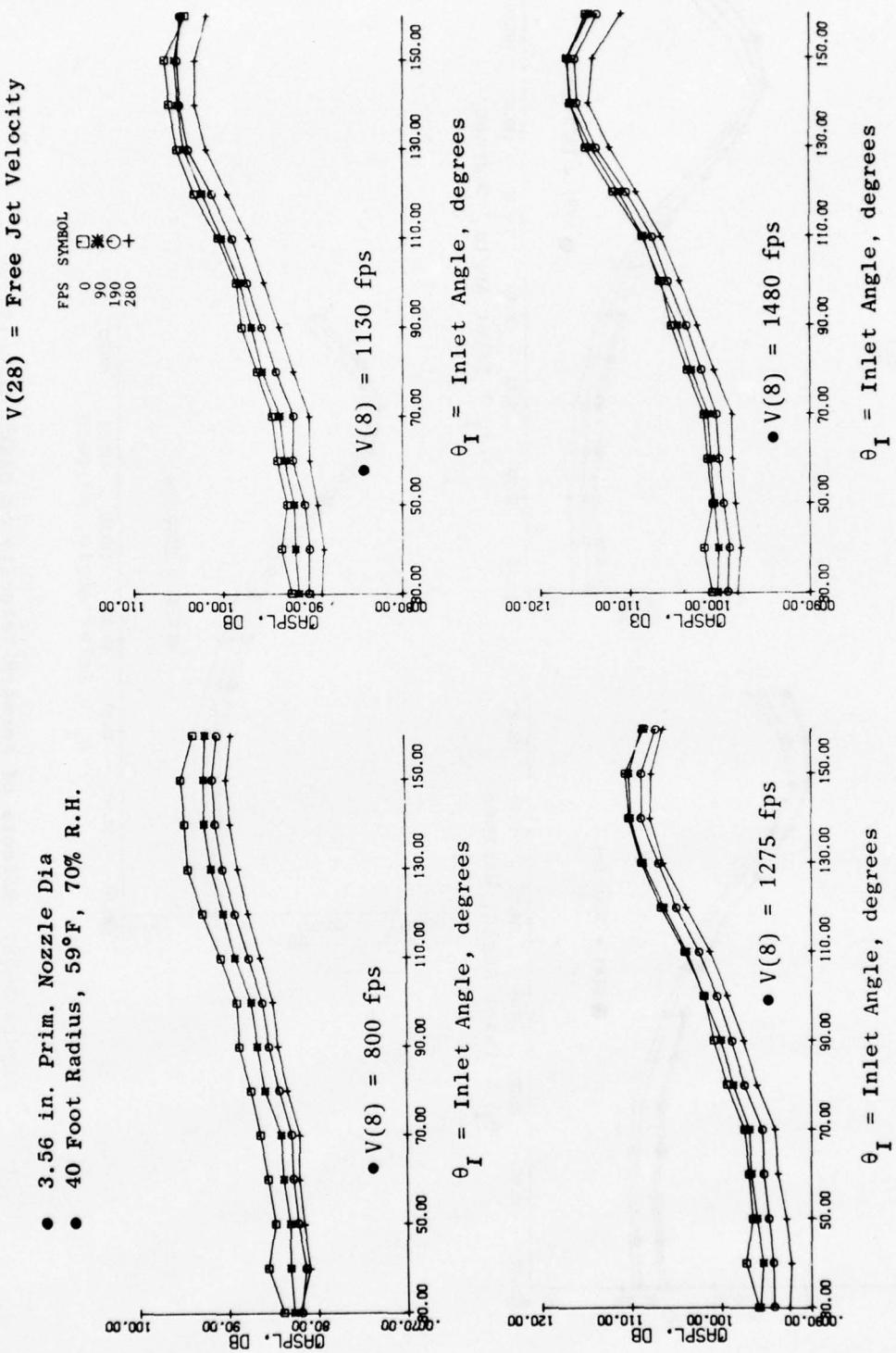


Figure 3-51. Effects of Forward Velocity on OASPL Directivity.

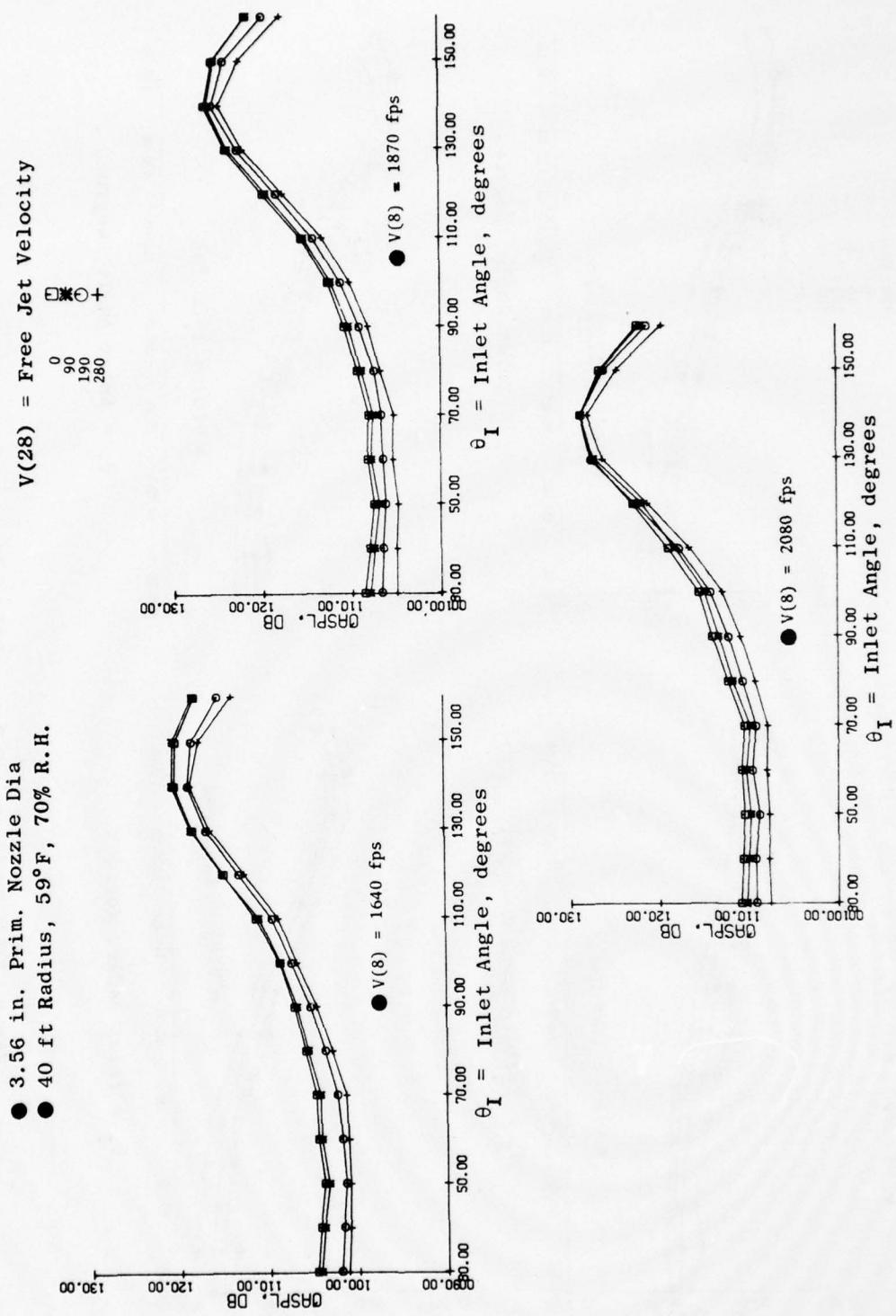


Figure 3-52. Effects of Forward Velocity on OASPL Directivity.

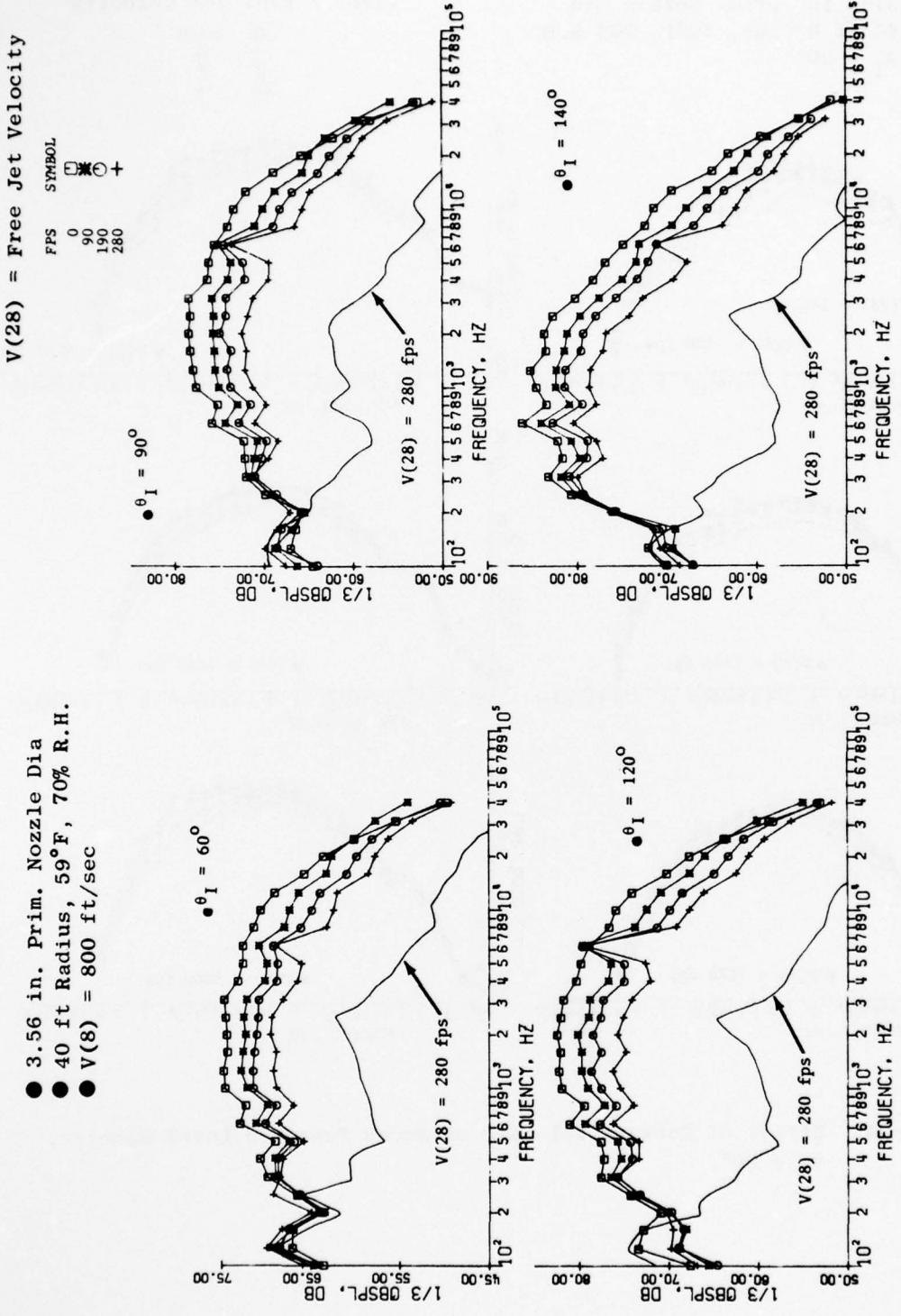


Figure 3-53. Effect of Forward Velocity on Sound Pressure Level Spectra.

- 3.56 in. Prim. Nozzle Dia
- 40 ft Radius, 59°F, 70% R.H.
- $\theta_I = 90^\circ$

$V(28) = \text{Free Jet Velocity}$

FPS	SYMBOL
0	+
90	○
190	■
280	□

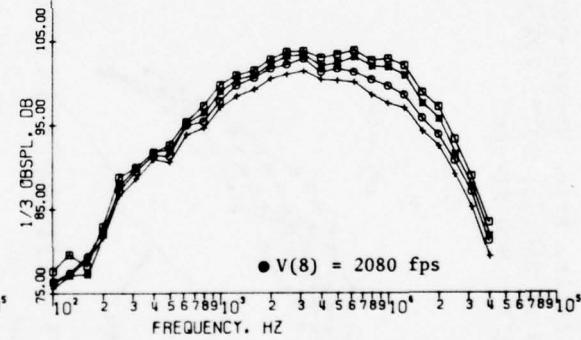
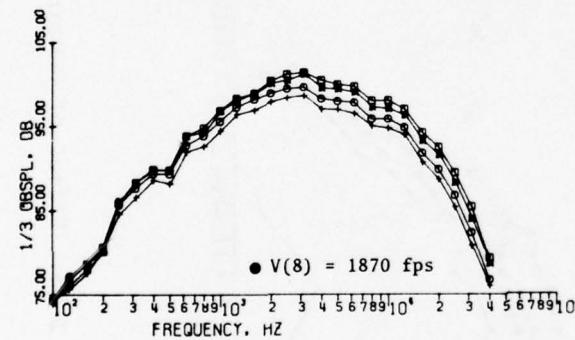
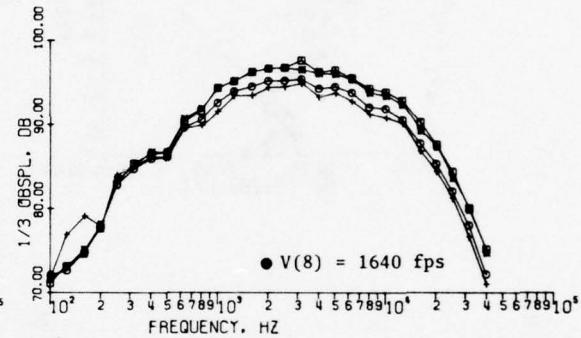
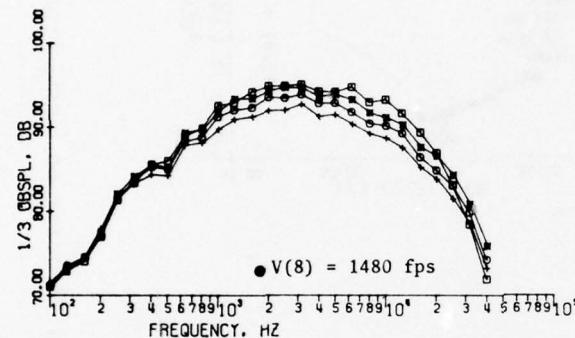
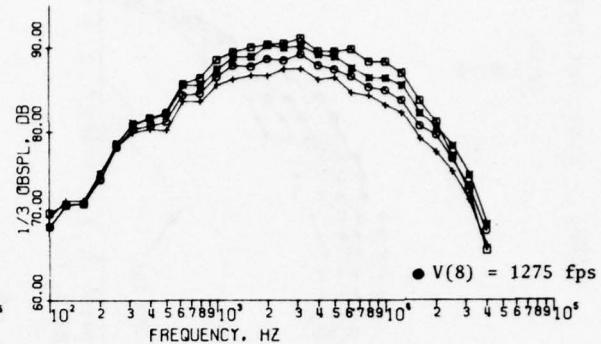
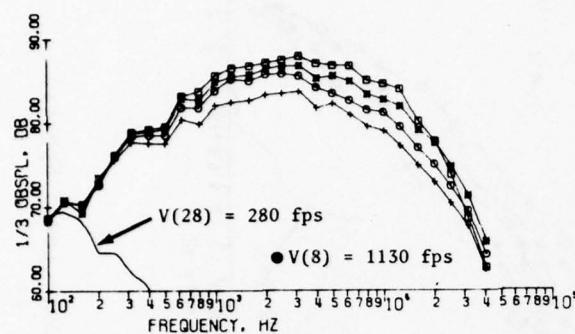


Figure 3-54. Effect of Forward Velocity on Sound Pressure Level Spectra,
 $\theta_I = 90^\circ$.

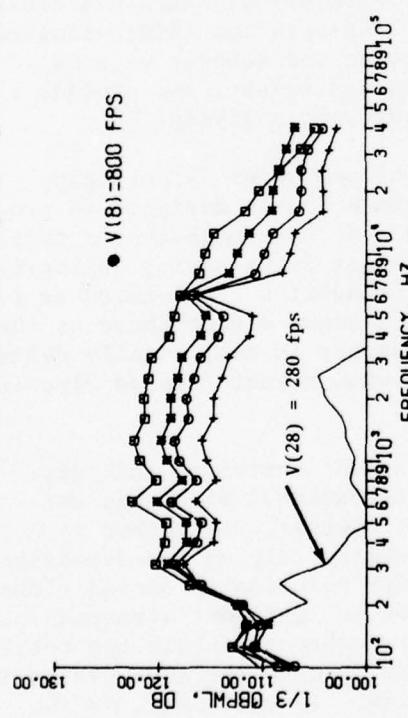
● 3.56 Inch Prim. Nozzle Diam.
 ● 40 Foot Radius, 59° F, 70% R.H.

) = Free Jet Velocity
 FPS SYMBOL

0
 90
 190
 280

● V(8)=1130 FPS
 1/3 GBDPL, DB

● V(8)=800 FPS



● V(8)=280 FPS
 1/3 GBDPL, DB

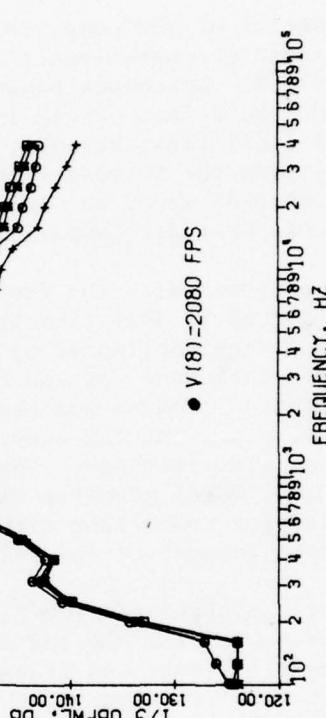
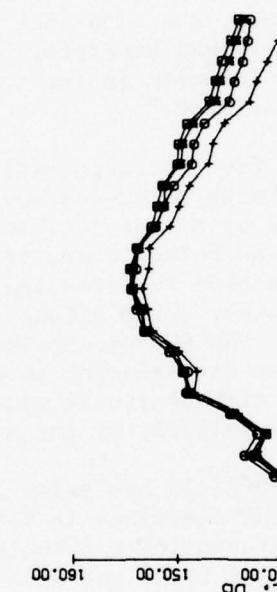


Figure 3-55. Effect of Forward Velocity on Power Spectra Characteristics.

Figures 3-56 and 3-57 compare the static and forward flight [$V(28) = 280$ ft/sec] results of the two General Electric series of tests with the 2-inch data scaled up to the larger nozzle for a typical primary velocity [$V(8) = 1273$ ft/sec]. The static data for the two nozzles compare quite favorably as illustrated; however, the wind-on results strongly suggest that the larger area-ratio free jet permits a better simulated-flight flow environment in which to immerse the nozzle. This is especially evident for the broadside comparison (Figure 3-56) which, acoustically speaking, is essentially indicative of changes in the jet turbulence intensity characteristics.

Results of the comparison of these GE and previously mentioned NASA-Lewis sound-pressure-levels are summarized for the 90° angle position in Figure 3-58. Agreement between the GE and NASA-Lewis static and wind-on data for the 2-inch nozzle is well within the measurement accuracy of both outdoor facilities; however, the 3.56-inch diameter nozzle data is obviously not enjoying the forward-flight benefits. Further details on this phase of the assessment study are included in the section entitled "General Electric/NASA-Lewis Free Jet Comparisons."

Concurrent with the free jet area ratio acoustic assessment, a study was conducted to analytically determine how well inflight aerodynamic parameters are duplicated by a free jet, thus, providing further substantiation and confidence for the 2-inch diameter nozzle noise data. A potential-flow computer program was used to investigate how changes in the free jet boundary, e.g., annulus area, would affect the external pressure distribution of the nozzle afterbody. The Supersonic Tunnel Association (STA) standard wind tunnel model geometry was selected to provide the referee external pressures for comparison with available wind tunnel results and provide a basis for judgment of the validity of the aerodynamic analysis.

The computerized flow-field analysis, developed under NASA-Langley Contract No. NAS1-10804 and described in Reference 15, is designed to predict the flow (sub- and transonic) around long and short high-bypass ratio fan-duct nacelles with inlet flows and with exhaust flows having appropriate aerothermodynamic properties. The flow-field boundaries are located as far upstream and downstream as necessary to obtain minimum disturbances at the boundary. The far-field lateral flow-field boundary is analytically defined to exactly represent free flight conditions or wind tunnel (closed circuit and open throat) effects.

The solution technique is based on a Streamtube Curvature Analysis. The Streamtube Curvature Method (STC) of solving external flows has not been discussed significantly in the literature; however, the method is a very natural one. For example, engineers frequently rely on one-dimensional, compressible-flow relationships for a first-order solution to ducted flows. The STC approach is similar except that a number of confluent streamtubes, with slightly different properties, are added together to obtain the total flow in the channel. Each streamtube is handled in much the same way as is the one streamtube in the one-dimensional problem. In the limit, as the size of the individual streamtubes approaches zero, the STC method satisfies the inviscid equations of motion exactly.

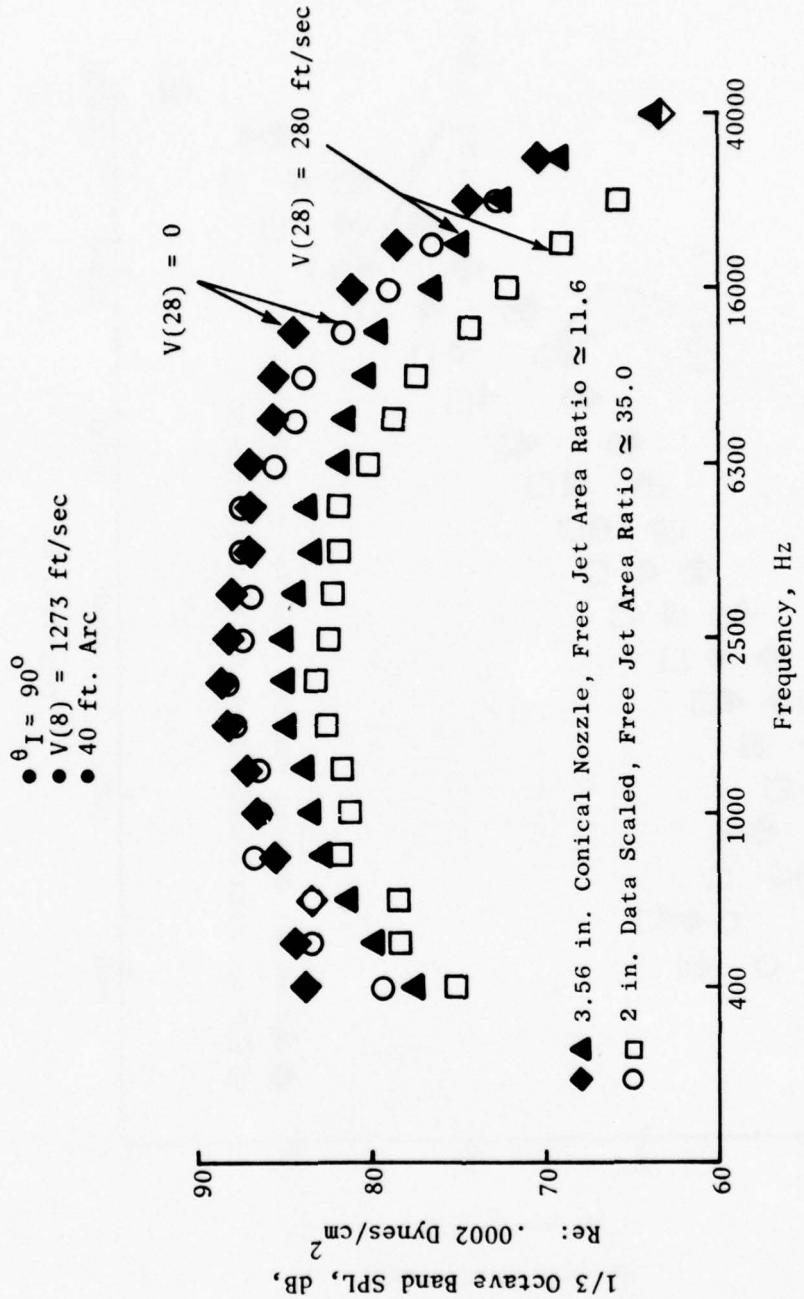


Figure 3-56. Comparison of Free Jet Spectra, $\theta_1 = 90^\circ$.

- $\theta_1 = 140^\circ$
- $V(8) = 1273 \text{ ft/sec}$
- 40 ft. Arc

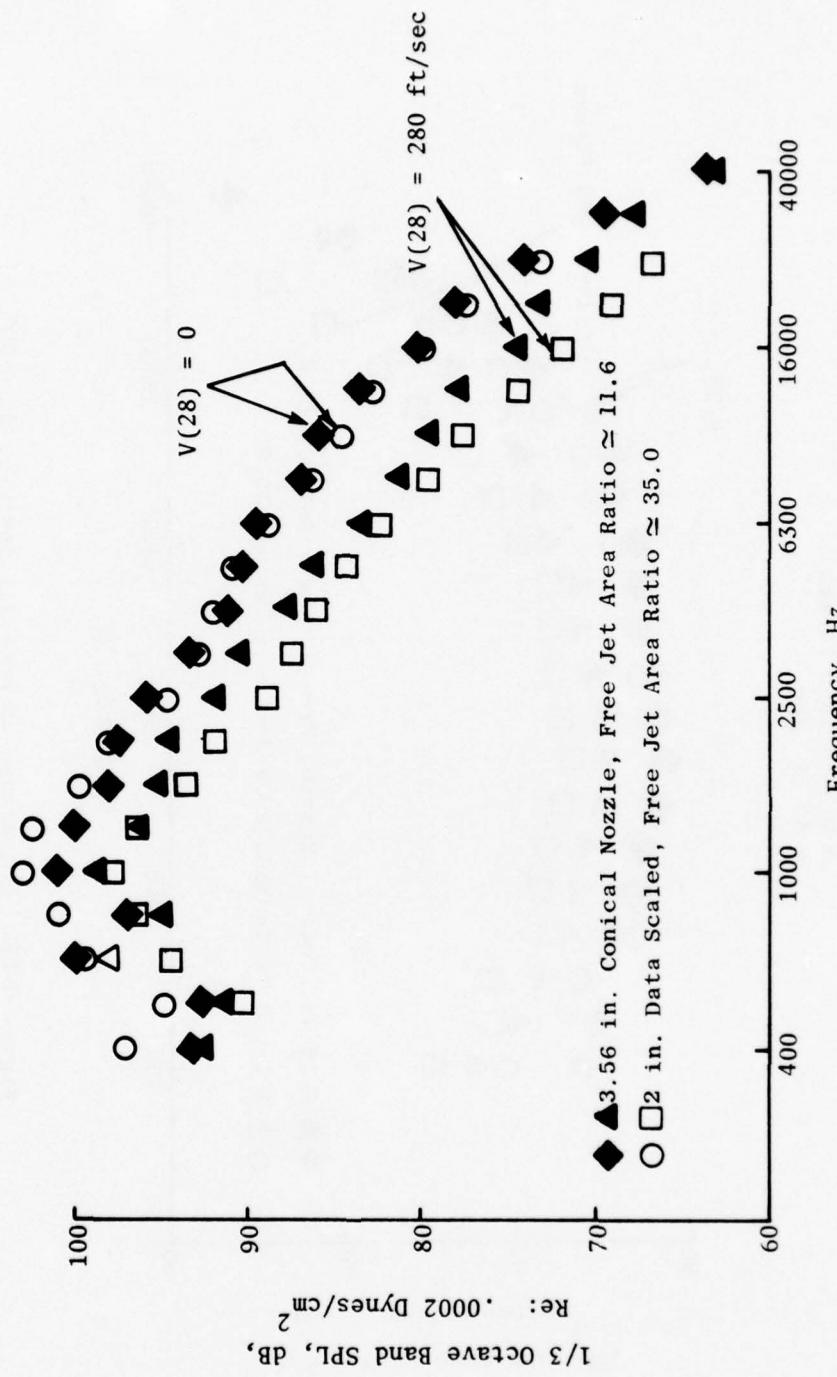


Figure 3-57. Comparison of Free Jet Spectra, $\theta_1 = 140^\circ$.

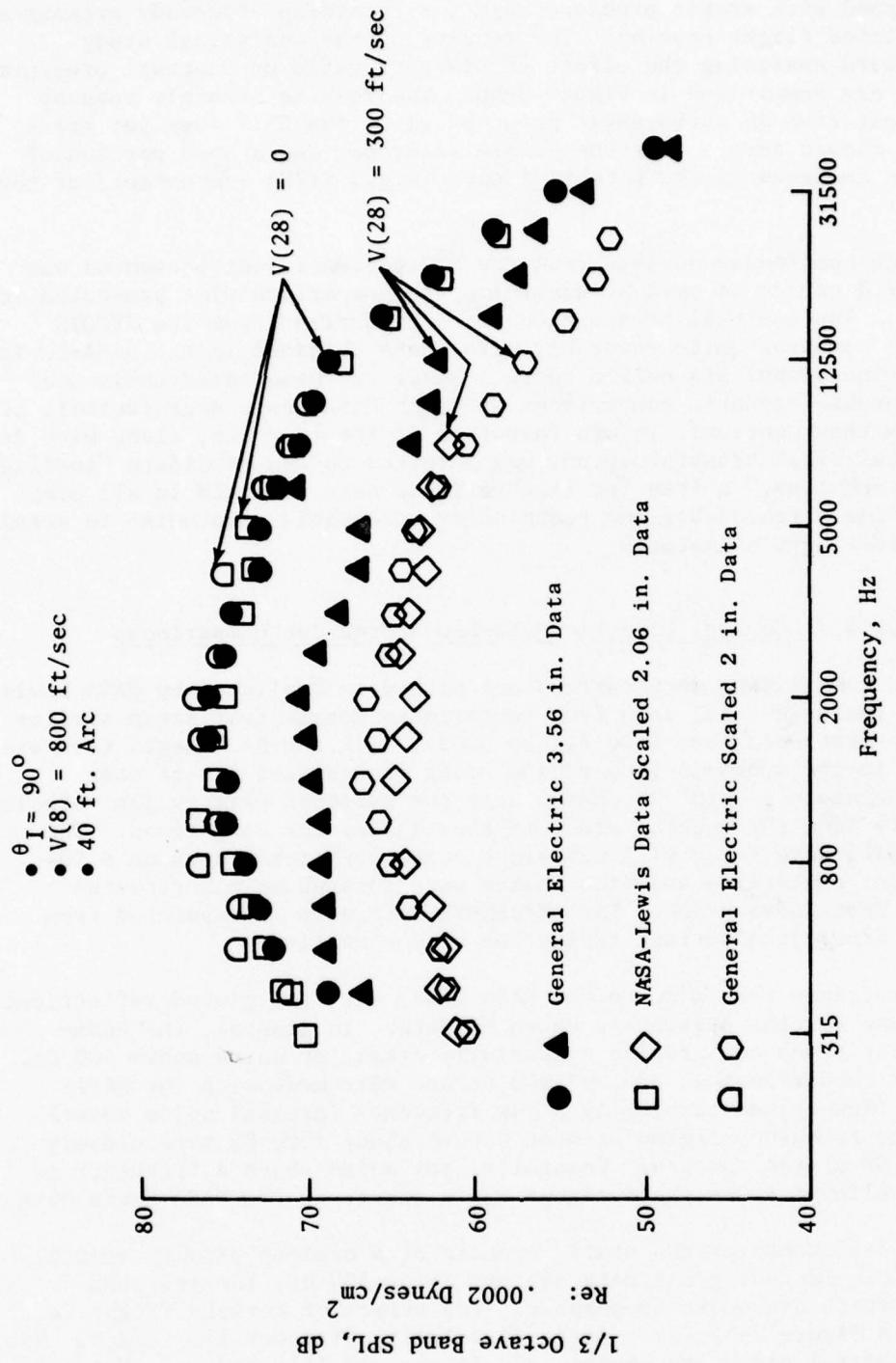


Figure 3-58. Comparison of Free Jet Spectra from Other References, $\theta_1 = 90^\circ$.

Figure 3-59 is a photograph of the free jet installation with STA nozzle equipped with static pressure taps for recording afterbody pressures during simulated-flight testing. The results of the analytical study directed toward assessing the effect of diameter ratio on boattail pressure coefficient are summarized in Figure 3-60. The results strongly suggest that, at least from an aerodynamic point of view, the 35:1 free jet area-ratio setup should assure that the nozzle afterbody and a good portion of the plume is immersed in the potential core [e.g., $V(28) \approx \text{constant}$] of the free jet.

The high confidence derived from the STC analyses just presented was well justified as can be seen by examining the comparison plot presented in Figure 3-61. The boattail pressure coefficient derived from the JENOTS measurements compares quite favorably with those obtained in the NASA-Lewis 6 x 8-foot wind tunnel STA nozzle tests. Based on these aerodynamic data and the favorable acoustic comparisons with the NASA-Lewis data (details of which follow this section), it was felt that if the free jet, along with its companion analytical transformation, was selected as the candidate "in-flight simulation technique," a free jet area ratio of near 40 would in all probability provide a reasonable and technically acceptable compromise to attaining simulated-flight signatures.

3.1.3.7 General Electric/NASA-Lewis Free Jet Comparisons

Limited comparisons were carried out with data published by NASA-Lewis (TMX-71438) (Reference 14) in a free jet/primary nozzle test setup similar to the above-mentioned test (see Figure 3-62). All the NASA-Lewis work was carried out in the subsonic flow regime using pressurized air at near ambient temperature ($\sim 520^\circ \text{R}$), hence only one subsonic primary jet velocity was available from the General Electric test series for comparison. The NASA-Lewis data were taken with 0.50-inch condenser microphones on a 10-foot arc. Jet centerline and microphones were located on a horizontal plane 12.75 feet above grade. The GE/JENOTS data were extrapolated from the 40-foot arc to the 10-foot radius for easy comparison.

No corrections were made to the NASA-Lewis data for ground reflections, as in the case for the previously shown GE data. In general, the NASA-Lewis free jet setup can provide essentially clean jet noise above 400 Hz. The velocity comparisons at 835 and 940 ft/sec were made with the NASA-Lewis noisy flow system (basically a low frequency internal noise source) since the low frequency region between 400 to about 1500 Hz more closely matched the GE static spectra. Generally, jet noise above a frequency of 1500 Hz is believed to be the dominant noise source in the NASA-Lewis data.

Figure 3-63 compares the static spectra at a nominal primary velocity of 835 ft/sec. Excluding the data scatter below 500 Hz, the spectrum levels and trends are quite comparable. The effect of forward flight is summarized in Figure 3-64 for a free jet velocity of about 170 ft/sec. Two GE/JENOTS spectral plots are shown: 800 ft/sec and 1115 ft/sec. Using an eighth-power law dependency, both velocities were point corrected to a

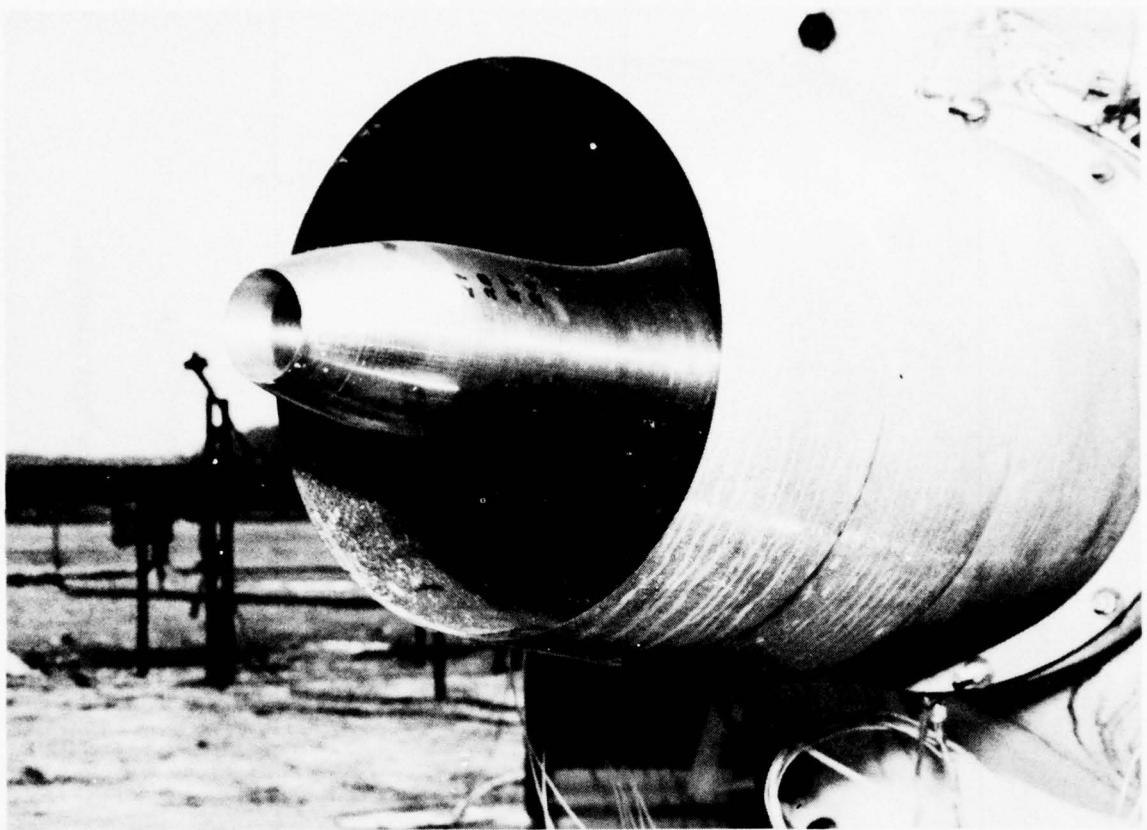


Figure 3-59. Free Jet Installation with STA Nozzle.

•STC Results

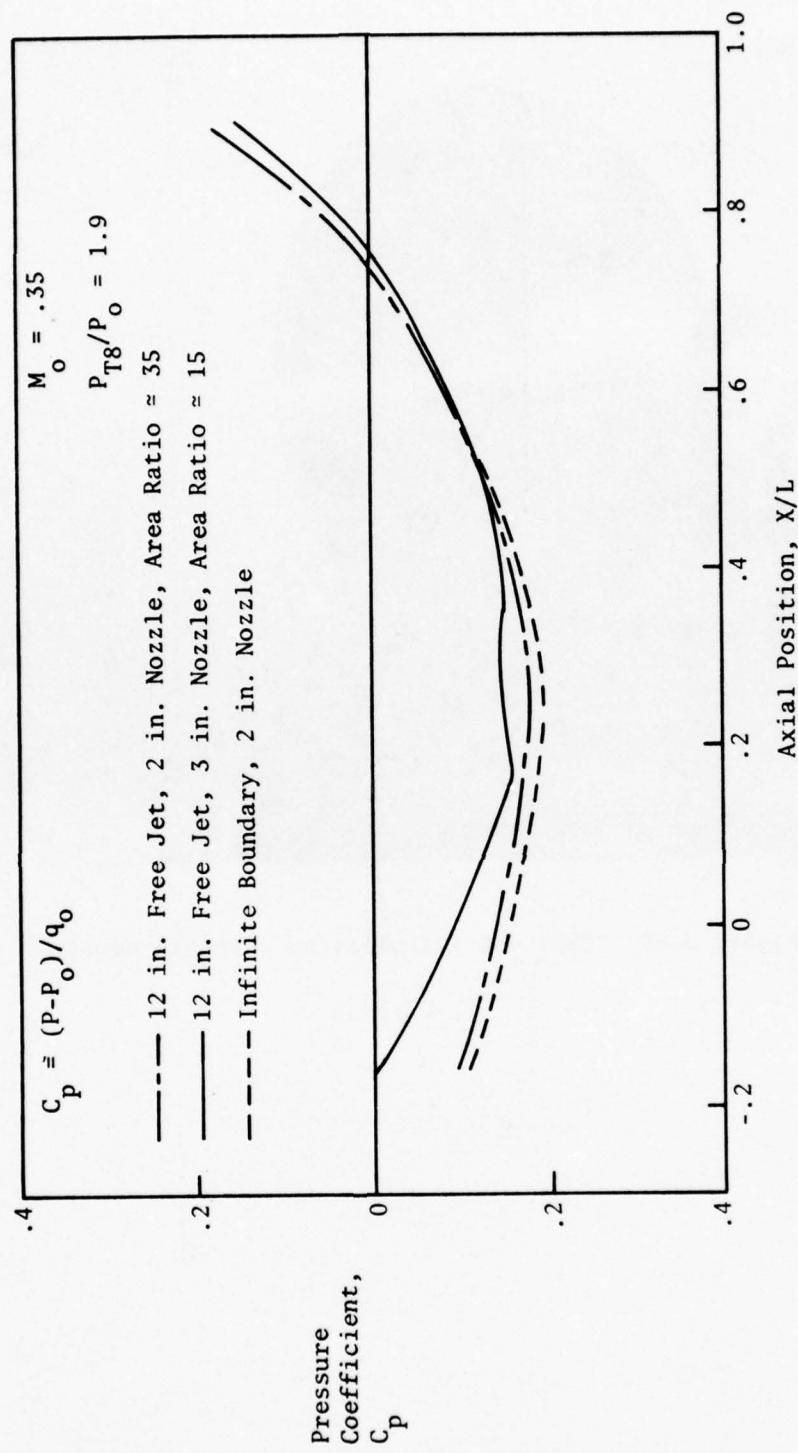


Figure 3-60. Effect of Diameter Ratio on Pressure Distribution.

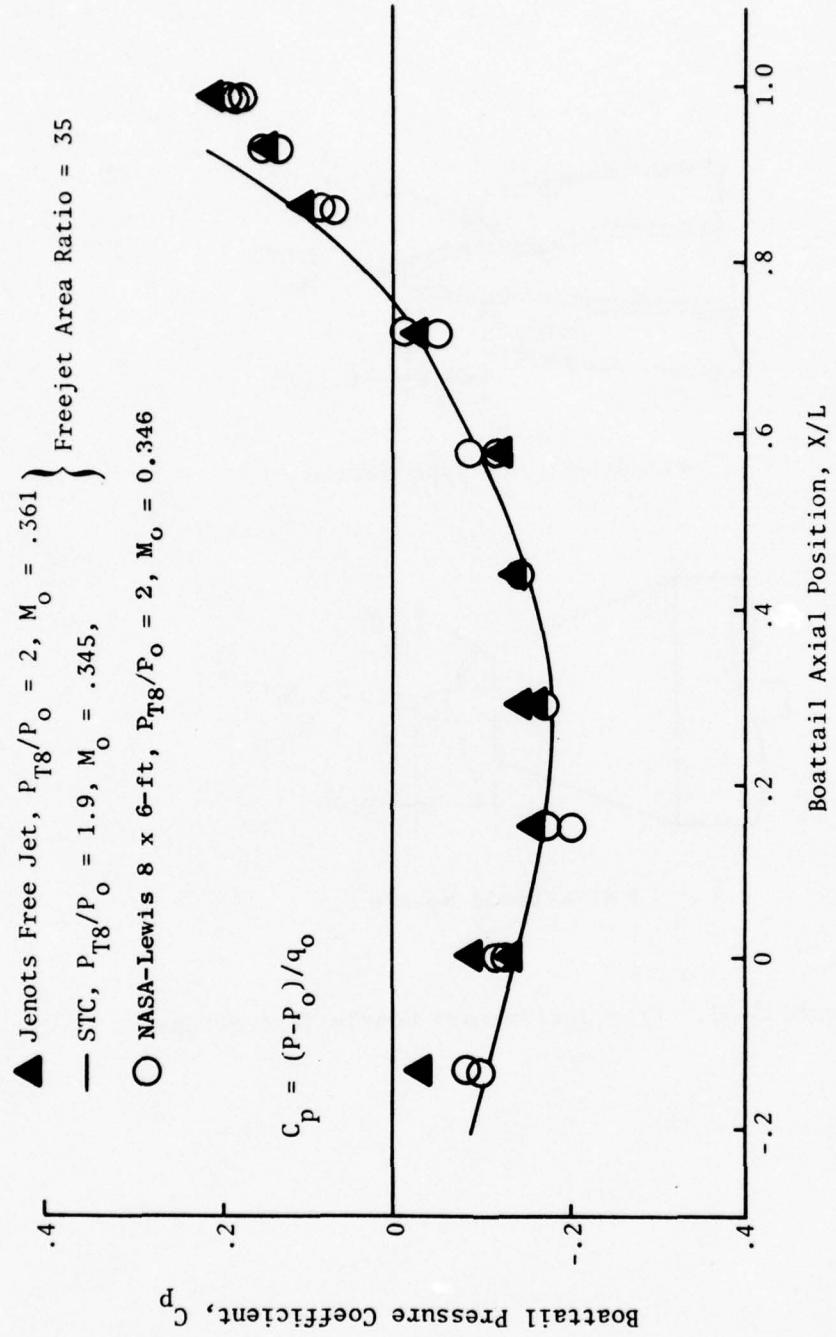
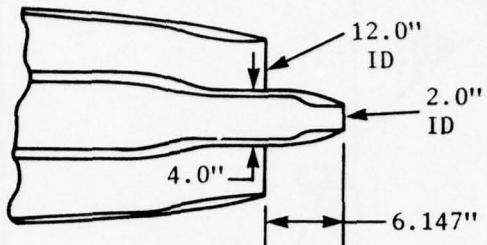
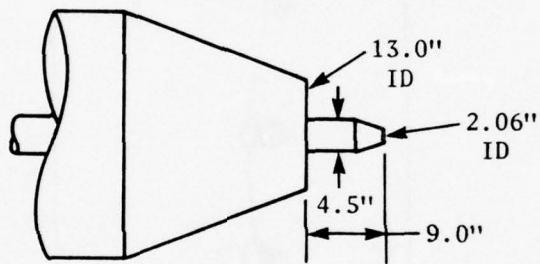


Figure 3-61. Comparison of Wind Tunnel and Free Jet Pressure Distributions of STA Nozzle.



● GE/Jenots Sta Type Nozzle



● NASA-Lewis Nozzle

Figure 3-62. Free Jet/Primary Nozzle Test Setups.

- 2 Inch Prim. Nozzle Diam; $V(28) = 0$
- 10 Foot Radius, 59°F , 70% R.H.

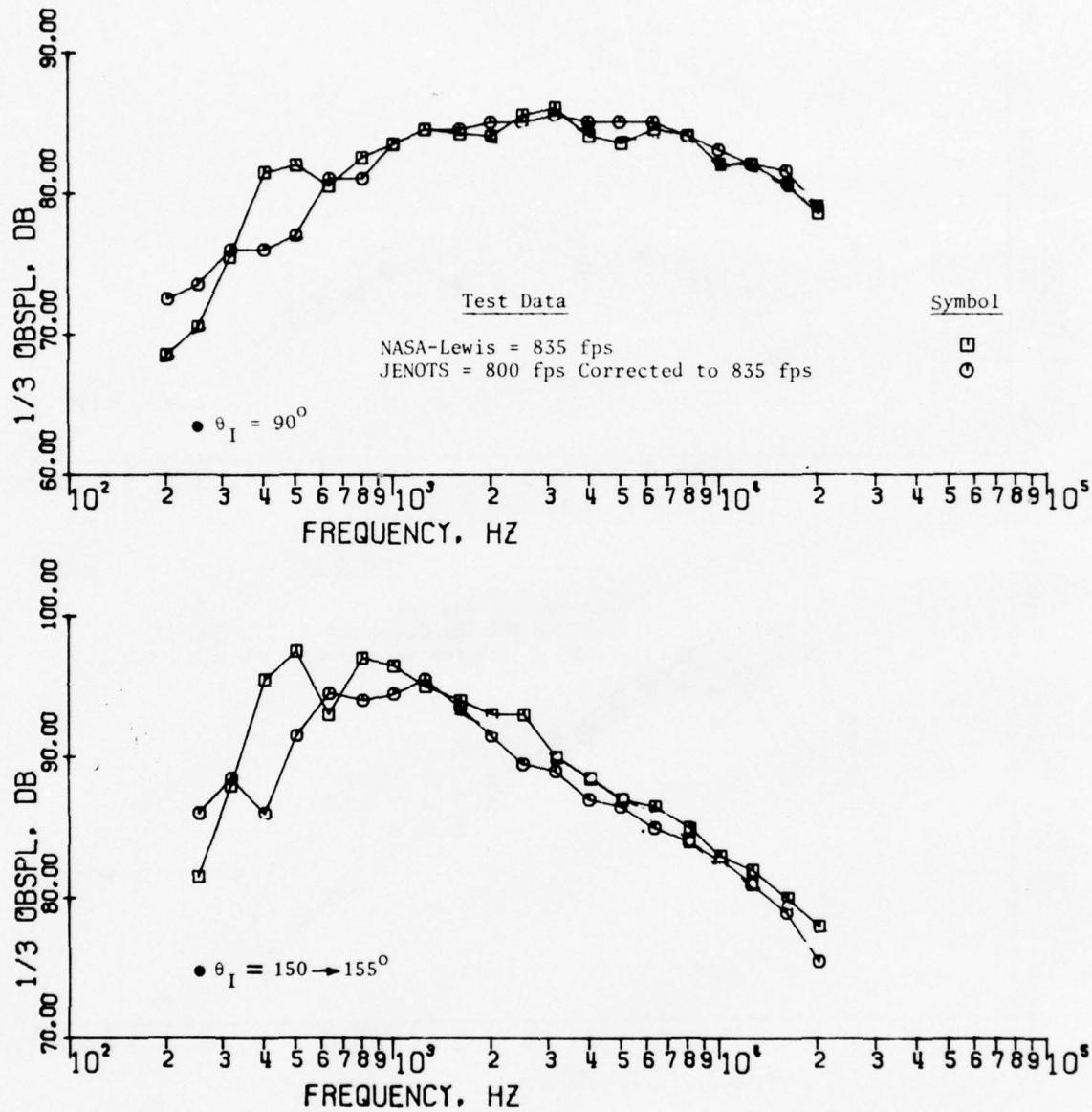


Figure 3-63. Comparison of JENOTS and NASA-Lewis Static 1/3 OBSPL Spectra.

- 2 Inch Prim. Nozzle Diam.; $V(28) = 170$ fps
- 10 Foot Radius, 59°F , 70% R. H.

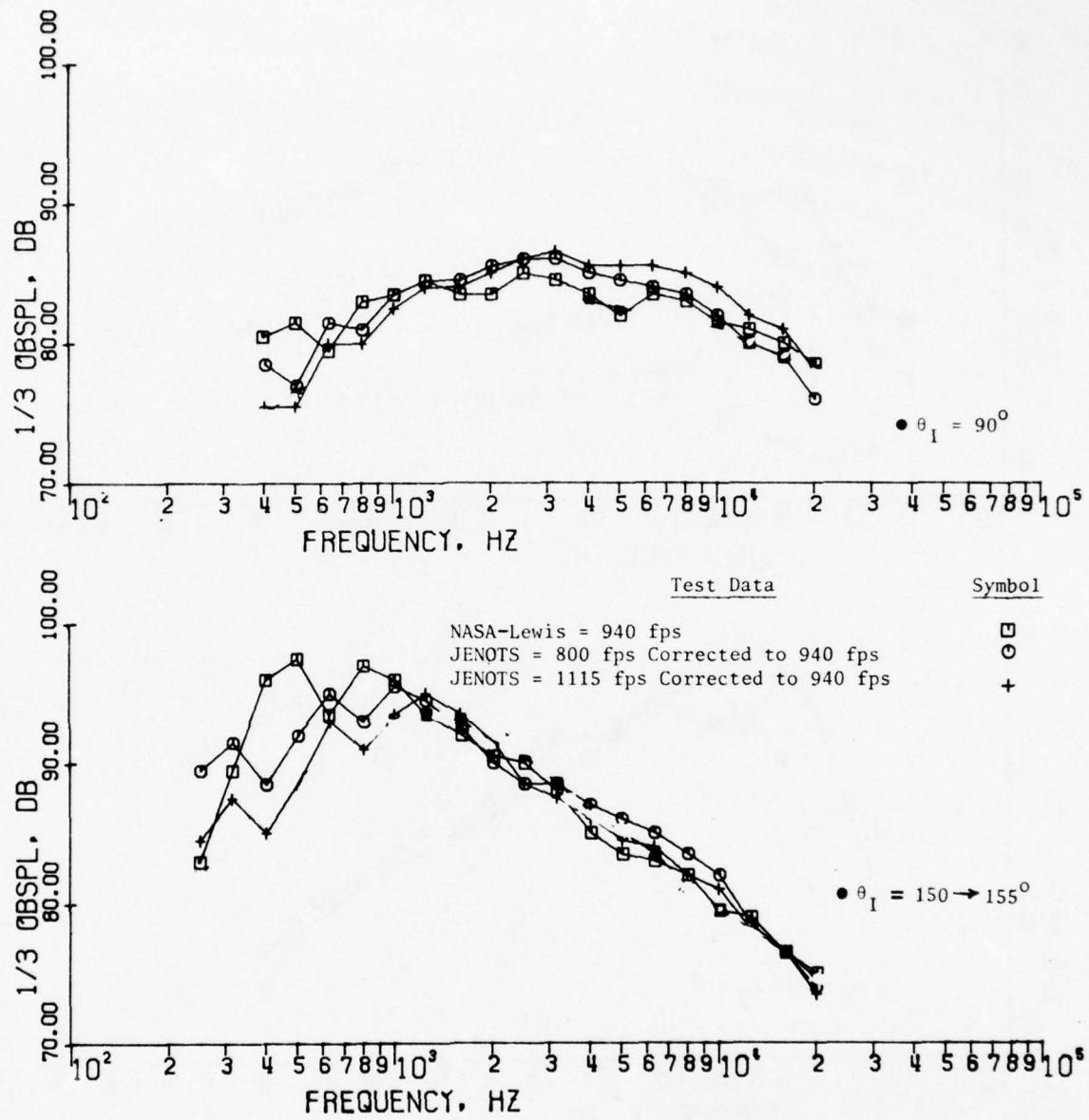


Figure 3-64. Effect of Forward Flight on JENOTS and NASA-Lewis $1/3$ OBSPL Spectra.

primary velocity of 940 ft/sec for comparison with the NASA-Lewis data. Again the two JENOTS conditions agree quite well, with the NASA-Lewis data above 1000 to 1500 Hz being somewhat on the high side. Considering the difference in free jet setups as well as in nozzle geometry, heated (GE) versus unheated (NASA-Lewis) primary jet flows, the spectral comparisons are well within measurement accuracy and indeed provide added confidence that a free jet can, to all intents and purposes, adequately simulate a flight flow environment for the immersed jet nozzle from which "inflight effects" may be derived.

3.1.4 Electronic Simulation

One proposed method of correcting fixed-frame data for the effects of motion was to place a series of fixed microphones along the trajectory. If it is assumed that the proper microphone sequencing would simulate a moving medium through which sound is propagating, this equivalent "moving" source signal could be constructed from simultaneously recording the family of fixed-microphone outputs. This synthetic moving-source signal would then be subjected to the same analysis procedure used to reduce actual moving-frame data. The advantage of this technique is that an actual signal is obtained which may be directly compared to "real" moving-frame data.

A sufficiently large number of microphones must be used to obtain an adequate approximation to a moving-source signal. If the number of microphones required is very large, the technique becomes impractical to implement. It is felt that if the number of microphones required exceeds 40, the cost and complexity of the recording and data-combining system precludes the use of this technique. We will show that this limitation negates the use of the multiple-microphone technique as a generally applicable method for correcting fixed-frame data for the effects of motion.

The required number of microphones may be determined by applying the "sampling theorem" of statistical communication theory. This theorem states that a signal may be represented by a set of its equispaced samples if its spectrum is band-limited. The original, continuous signal may be reconstructed by expanding the sampled version in a series of $\sin(x)/x$ functions. Specifically, the sampling theorem says that:

$$x(+)=\sum_{n=-\infty}^{\infty} x(nT_s) \frac{\sin(\pi(\frac{t}{T_s} - n))}{\pi(\frac{t}{T_s} - n)} \quad (1)$$

if the spectrum of $x(t)$, $S_{xx}(\omega) = 0$ for $|\omega| > \frac{\pi}{T_s}$.

Consider the diagram in Figure 3-65. Here we show wave fronts propagating from a point source whose time fluctuations are described by the function, $x(t)$. The spacing of the wave fronts is

$$r_s = c T_s \quad (2)$$

where c is the speed of sound. The "o's" indicate where these concentric circles cross a straight line trajectory distance, d , from the source. Suppose T_s is chosen to meet the conditions of eq (2) and $q_n(t)$ are the outputs of microphones stationed at the "o's", then the time signal at any point x on the trajectory, $s(x, t)$, must be given by:

$$s(x, t) = \sum_{n=-\infty}^{\infty} q_n(t) \frac{\sin [\pi(\frac{x}{r_s} - n)]}{\pi(\frac{x}{r_s} - n)} \quad (3)$$

To simulate motion along the trajectory, we make the substitution

$$x = v_o t \quad (4)$$

where v_o is the synthetic source velocity. Thus, the "moving source" signal, $x_v(t)$, is given by

$$x_v(t) = s(vt, t) = \sum_{n=-\infty}^{\infty} q_n(t) \frac{\sin [\pi(\frac{v_o t}{r_s} - n)]}{\pi(\frac{v_o t}{r_s} - n)} \quad (5)$$

Let us now determine the number of microphones required to obtain a T second data record centered about a measurement angle of θ_0 . We use the geometric construction in Figure 3-66 to write the following relationships:

The number of microphones, n , is given by

$$n = (r_2 - r_1)/r_s + 1 \quad (6)$$

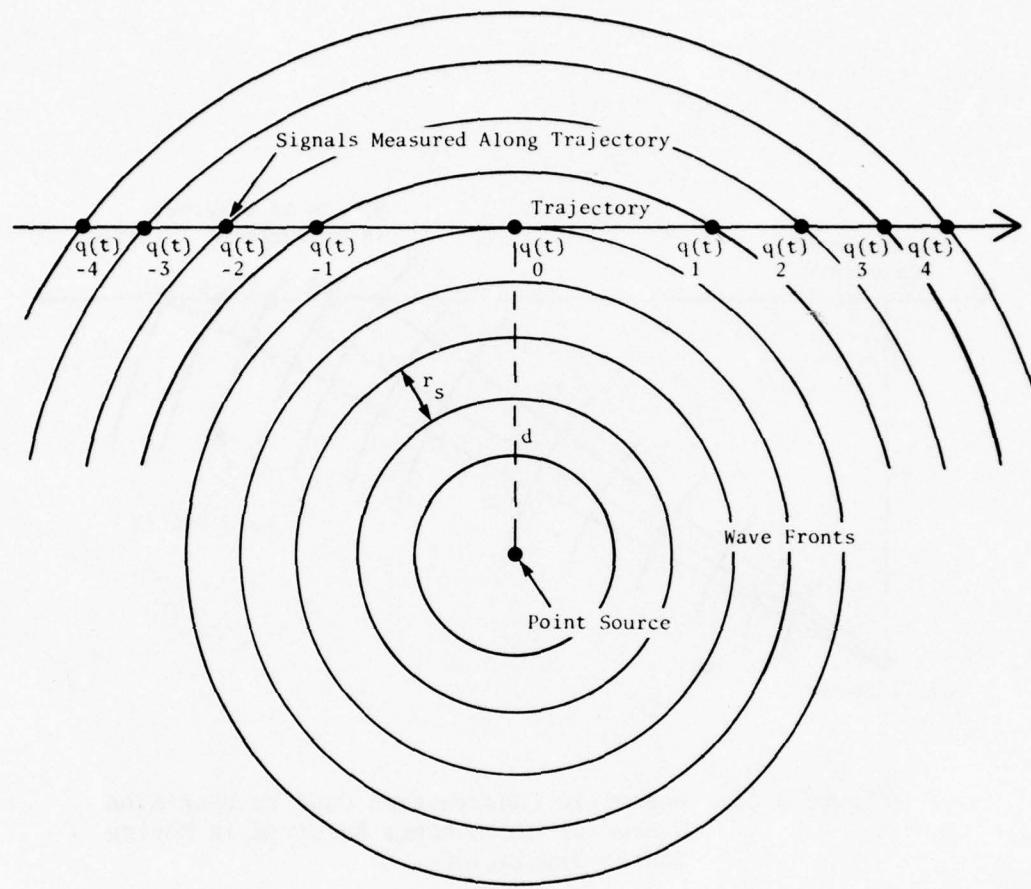


Figure 3-65. Geometric Construction Used to Determine Number of Fixed Microphones Required to Simulate Source Motion.

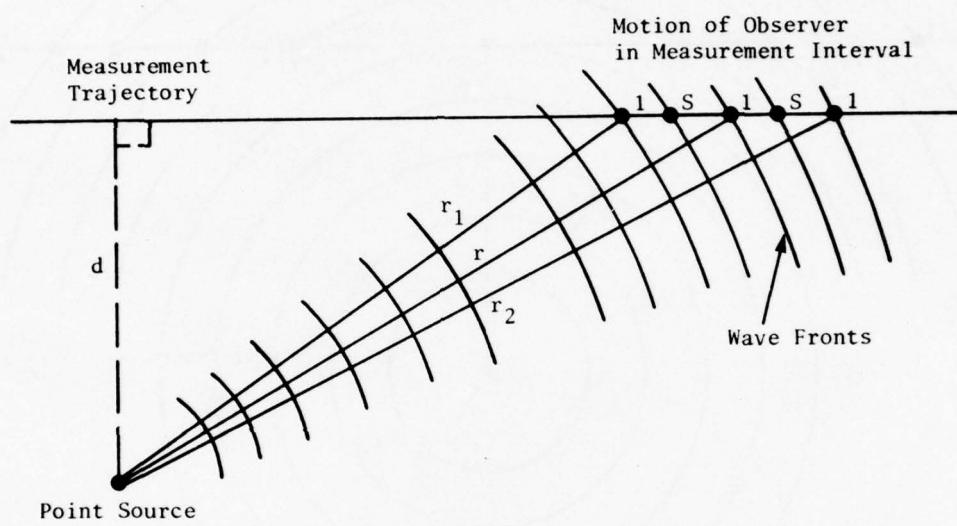


Figure 3-66. Geometric Construction Used to Determine Number of Microphones Required in Moving Source Simulation.

where

$$r_1 = [r^2 + \delta^2 - r\delta\cos\theta_o]^{1/2} \quad (7)$$

$$r_2 = [r^2 + \delta^2 + 2r\delta\cos\theta_o]^{1/2} \quad (8)$$

$$r = d/\sin\theta_o \quad (9)$$

and $\delta = V_o T/2.$ (10)

The equation for r_s is given in eq (2) which may also be written as

$$r_s = \frac{C}{2f_M} \quad (11)$$

where f_M is the frequency above which the source power is negligible. Note that f_M is not maximum frequency required in the analysis.

It is now possible to determine the number of microphones required to add the effects of motion to data taken under typical conditions. As an example, consider the case where the multiple-microphone technique is used to correct data taken from a free jet at 8:1 scale. Typical test conditions are:

$$d = 27 \text{ feet}$$

$$V_o = 350 \text{ feet/second}$$

$$f_M = 40 \text{ kHz}$$

$$T = 0.125 \text{ seconds}$$

The number of microphones required to correct data taken at inlet angles of 20° , 50° , and 90° is shown in Table 3-XV:

Table 3-XV. Inlet Angle Minimum Number of Microphones.

Inlet Angle	Minimum Number of Microphones
20°	2937
50°	1791
90°	1104

For this typical case at least 1100 microphones and simultaneous recording channels are required. All of these signals would then have to be combined using the time-varying weighting function in eq (5). This operation would have to be realized by special hardware or by simultaneous sampling (in time) the 1100+ channels and evaluating eq (5) with a digital computer. The resulting time series would then have to be analyzed to obtain 1/3-octave values, OASPL, etc.

This example illustrates the fact that the multiple microphone technique does not provide a general method for simulating motion effects. This is because a prohibitively large number of microphones are required to properly sample the source signal. The approach may be useful, however, in some special applications, particularly when the bandwidth of the data is small.

3.2 MOVING-FRAME FACILITIES

The second general class of techniques that have been considered for inflight simulation is the moving-frame technique. Examples of this type of facility are high speed trains, rocket sleds, and spinning rigs. When evaluating moving-frame facilities relative to fixed-frame techniques, it is important to note the advantages and disadvantages of each type of technique plus the risk and technical complexity involved in the development of each facility. The ability of the chosen technique to produce the required acoustic data bank in a timely and economical fashion must be assessed and realistically evaluated.

This section presents the results of evaluating several moving-frame facilities. It should be noted that these facilities have been rated on the criteria of being acceptable "test beds" for jet noise work, which depends on quite different criteria than most of those for which the facilities were initially designed. The negative aspects rated herein for these facilities should, therefore, be viewed specifically as applicable when considering the respective facilities for jet acoustic tests.

3.2.1 Rocket Sleds

Two rocket sled facilities were evaluated during the program: The test tracks at Holloman AFB, Alamogordo, New Mexico, and Naval Weapons Center, China Lake, California. Both of these facilities were visited and found to have many similar capabilities, as summarized on Table 3-XVI.

The results of this assessment, as well as the exploratory experimental work required, which led to a preliminary sled design and projected operating procedures, are described in the following sections.

3.2.1.1 Rocket Sled Background Noise Measurements

One of the initial questions in determining the feasibility of obtaining "inflight" jet noise measurements from a scale-model nozzle mounted aboard a moving test bed concerned the magnitude of background noise produced by flow over the sled surface and its level relative to those noise levels produced by the test model.

Sufficient information was not available for making this evaluation because the sleds had not been designed or used for noise tests. Preliminary acoustic measurements were, therefore, obtained during sled testing performed by the Air Force Special Weapons Center located at Holloman Air Force Base, New Mexico, and by the Naval Weapons Center, China Lake, California. While this data was obtained at single sled velocities and on configurations that were not aerodynamically clean, it did indicate that the background noise levels could represent a potential problem. Proper design of "acoustic" sled configurations operating at different velocities, however, might overcome this "noise floor problem".

Table 3-XVI. Rocket Sled Facility Evaluation.

Facility Requirements	Objective	Holloman AFB	Naval Weapons Center
Payload Sled	Utilize available sled	Available but would need modifications	Available but would need modifications
Telemetry Systems	Adequate to provide accurate sled velocity and location relative to MIC locations	Meets objective	Meets objective
Terrain for Acoustic Arena	Flat surface Hard ground	Needs modification	Needs modification
Background Noise	OASPL = 90 dB	OASPL = 113.3 dB	OASPL = 111.1 dB
Type of Weather Conditions	59° F, 70% RH	Low absolute humidity	Low absolute humidity

Arrangements were made with Holloman test track personnel for acquisition of additional data from sled configurations operating over a range of velocities typical of those desired for the proposed test program on vehicles having a relatively clean aerodynamic design.

Additional data were obtained on the sled configurations shown on Figures 3-67 and 3-68 at sled velocities of 300, 225, and 137 ft/sec with the test setup shown schematically on Figure 3-69. Tracking information in the form of time, displacement, and sled velocity were provided and used in conjunction with the acoustic data acquisition and reduction, enabling accurate determination of the acoustic angle at each data measuring position.

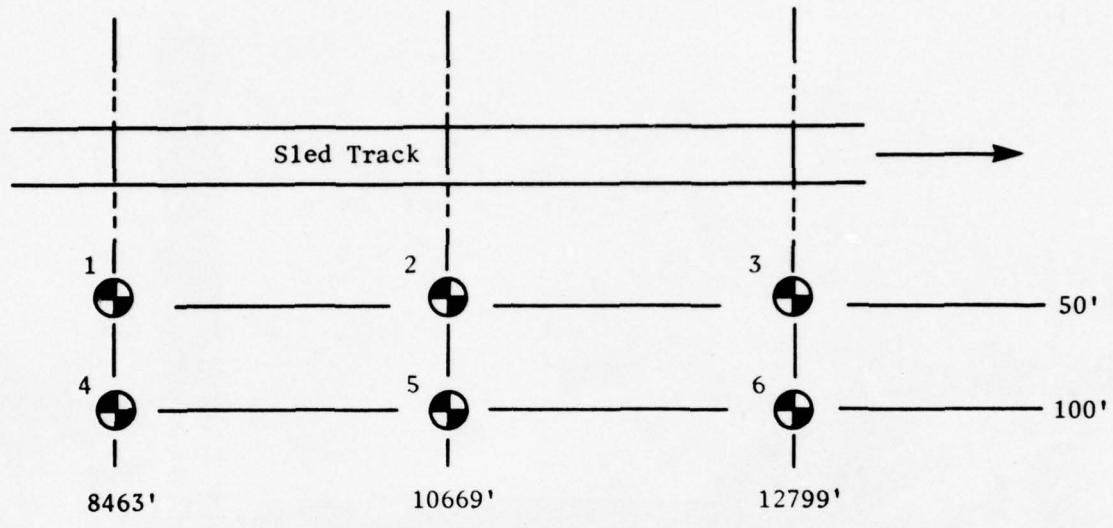
LENGTH 207" NOSE: 16° HALF A_{ANGLE}
HEIGHT 48" 78" LONG
WIDTH 42"
FRONTRAL AREA 16.5 SQ FT
WEIGHT 3877 LBS



Figure 3-67. Clean Sled Configuration.



Figure 3-68. Alternate Sled Configuration.



Test Notes:

- Rocket Fired from 5000' Pos.
- Motor Braked @ 6000' Pos.
- Sound Field Generally Flat and Clear of Bushes, However, a Ditch Ran Parallel to the track at \approx 25' Position.

Figure 3-69. Holloman AFB Microphone Array.

Some resulting spectra for the 50-foot sideline measurements are shown for equivalent angles for the three sled velocities on Figures 3-70 through 3-75. The data show a strong ground-effect influence with dissimilar effects at different measuring locations attributed to the nonuniform terrain at each measuring location. If the ground effect oscillations in the data are smoothed, a spectrum roll-off of approximately 3-4 dB per octave is observed for most angles at the three velocity conditions. The absence of high frequency tones in the spectra is indicative of no runner noise contamination. Normalizing the data in terms of Strouhal Number:

$$SN = \frac{f D}{V} \quad (12)$$

where: SN = Strouhal Number

f = 1/3-octave center frequency (Hz)

V = sled velocity (ft/sec)

D = smaller dimension of obstacle perpendicular to the flow (ft)

results in essentially parallel lines for each sled velocity with an average separation indicating an acoustic level increasing as $V^{3.5}$, similar to the V^4 dependence normally found with a monopole type noise mechanism.

The same directivity, when corrected for ground effects, is found to be quite similar for all sled velocities and frequencies over the range of available data, with a peak occurring in the $120^\circ - 130^\circ$ area and a roll-off of about 11 dB at the extreme angles.

This information is presented in Figures 3-76 to 3-78 in normalized form to be used as a guide for predicting OASPL and spectrum shape. The data were normalized for size by $10 \log_{10}$ [frontal area]. The spectrum shape has the roll-off characteristics similar to the classical Strouhal shape; however, the range of available data was insufficient to define the peak frequency, estimated to be in the 5-10 Hz area.

As a check on the validity of this approach, a set of data was obtained at one velocity, 100 ft/sec on a sled used for B-52 simulated ejection-seat testing, as shown on Figure 3-79. While this particular sled was something less than ideal (because of multiple openings in the roof and partially open cockpit), it did represent a vehicle having approximately 10 times the frontal area of the smaller sled. Figures 3-80 and 3-81 show the prediction, based on the small sled, compared to the actual B-52 data. The results indicate the spectrum shape and directivity to be similar to prediction, but the level to be higher, relative to prediction, with this difference attributed to the poor aerodynamic configuration. As was the case of the smaller sled, no runner noise was apparent.

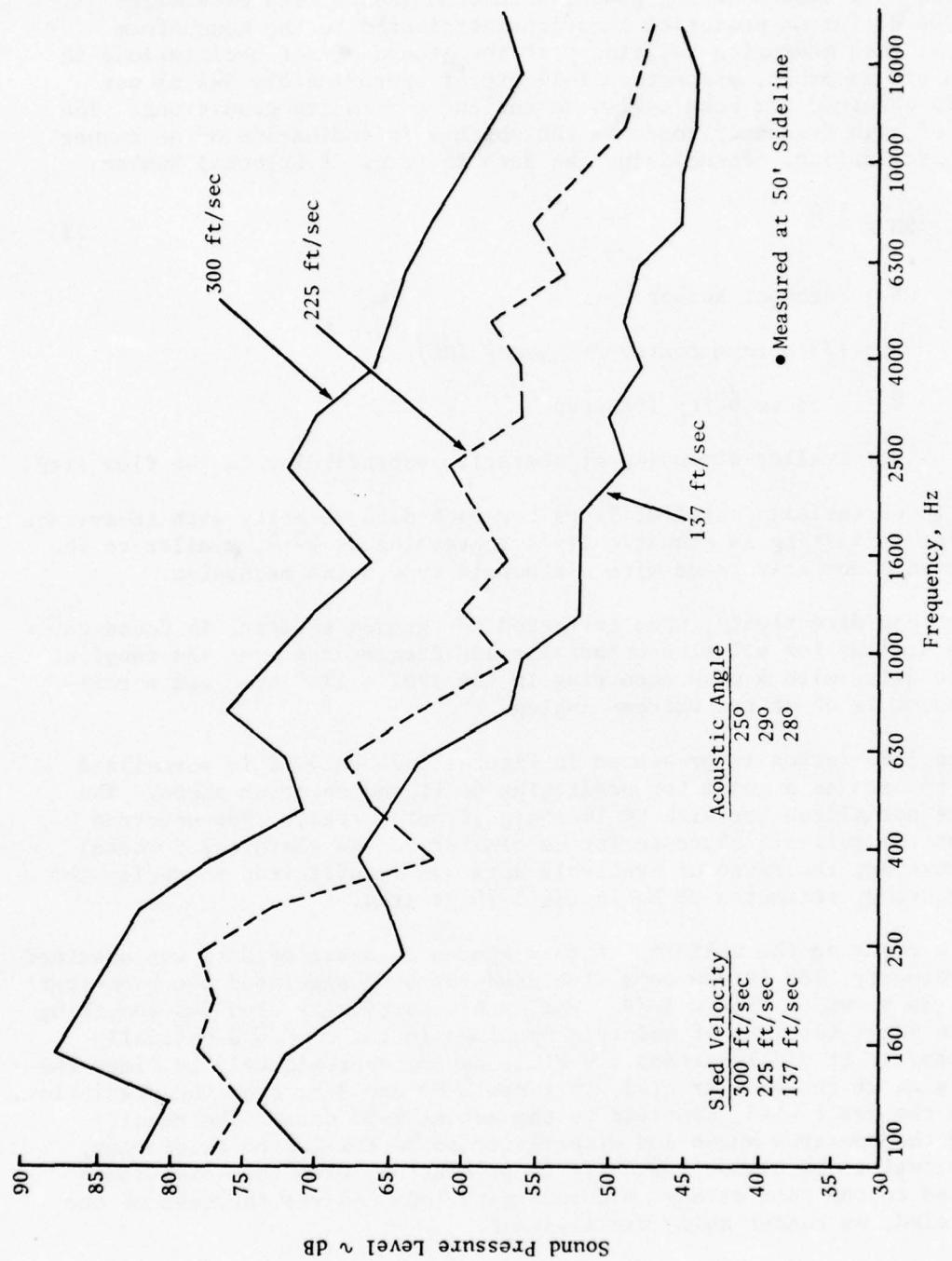


Figure 3-70. Typical Sled Spectra Characteristics, $\theta_1 = 25^\circ$.

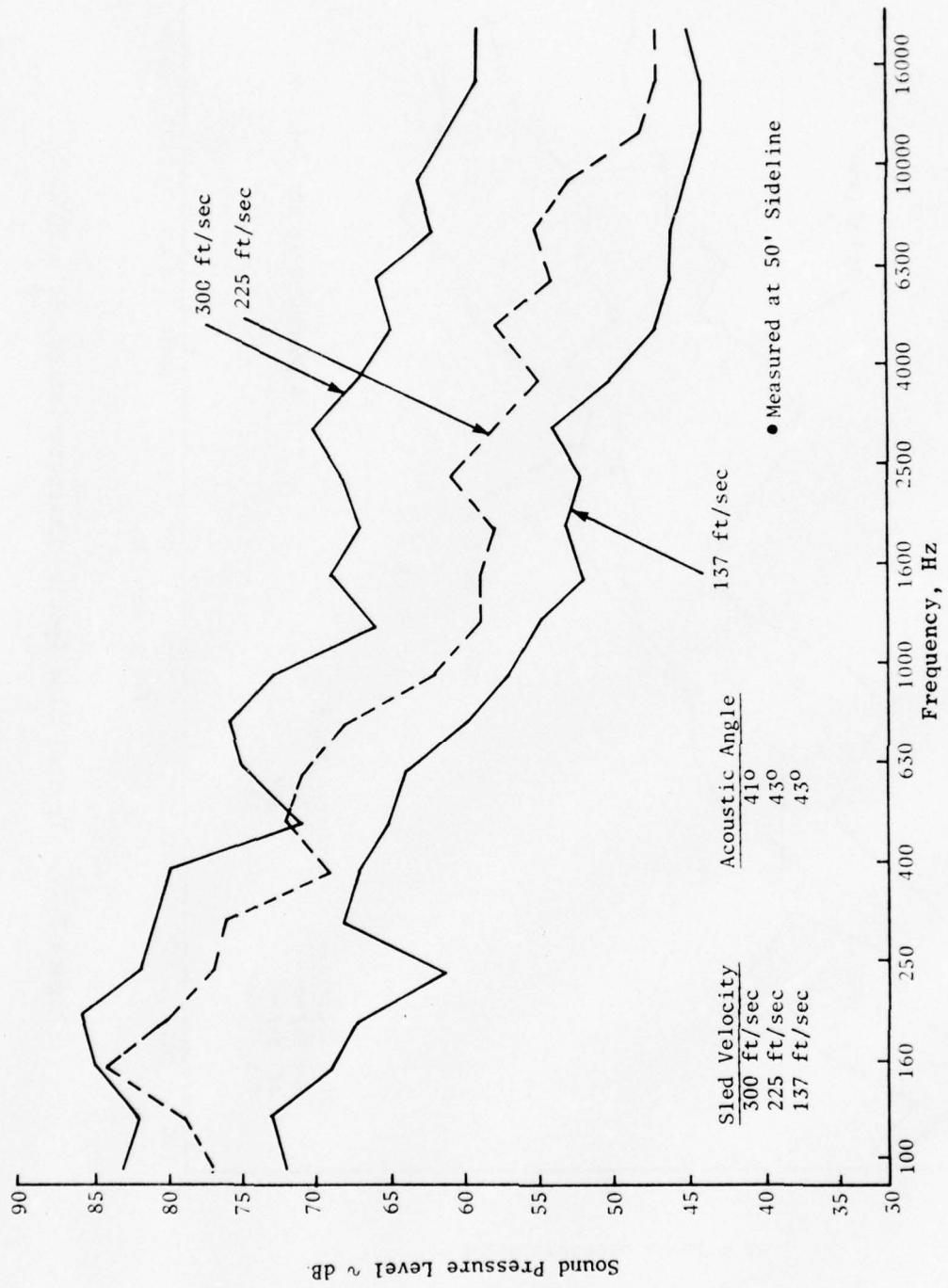


Figure 3-71. Typical Sled Spectra Characteristics, $\theta_1 = 40^\circ$.

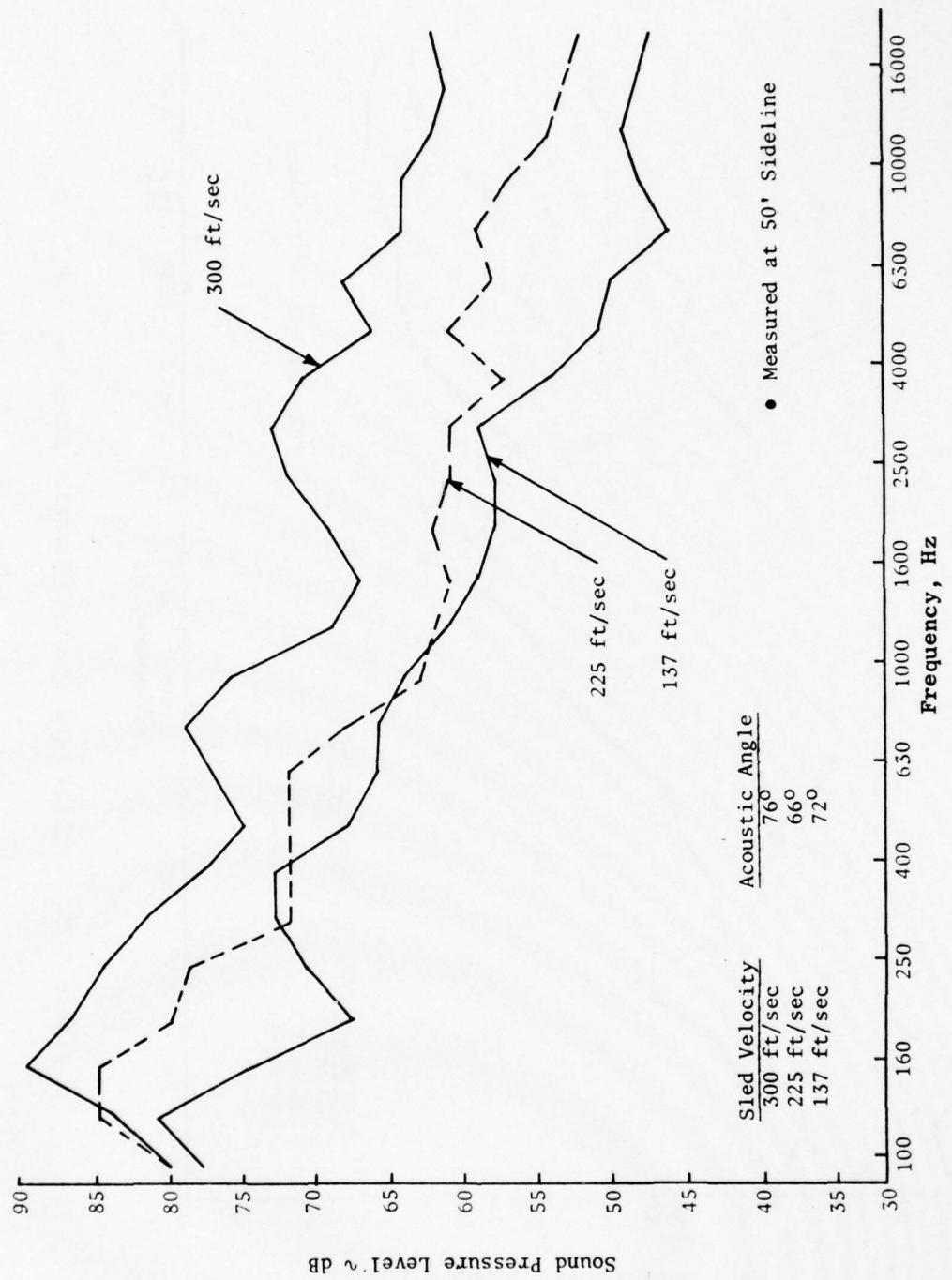


Figure 3-72. Typical Sled Spectra Characteristics, $\theta_1 = 70^\circ$.

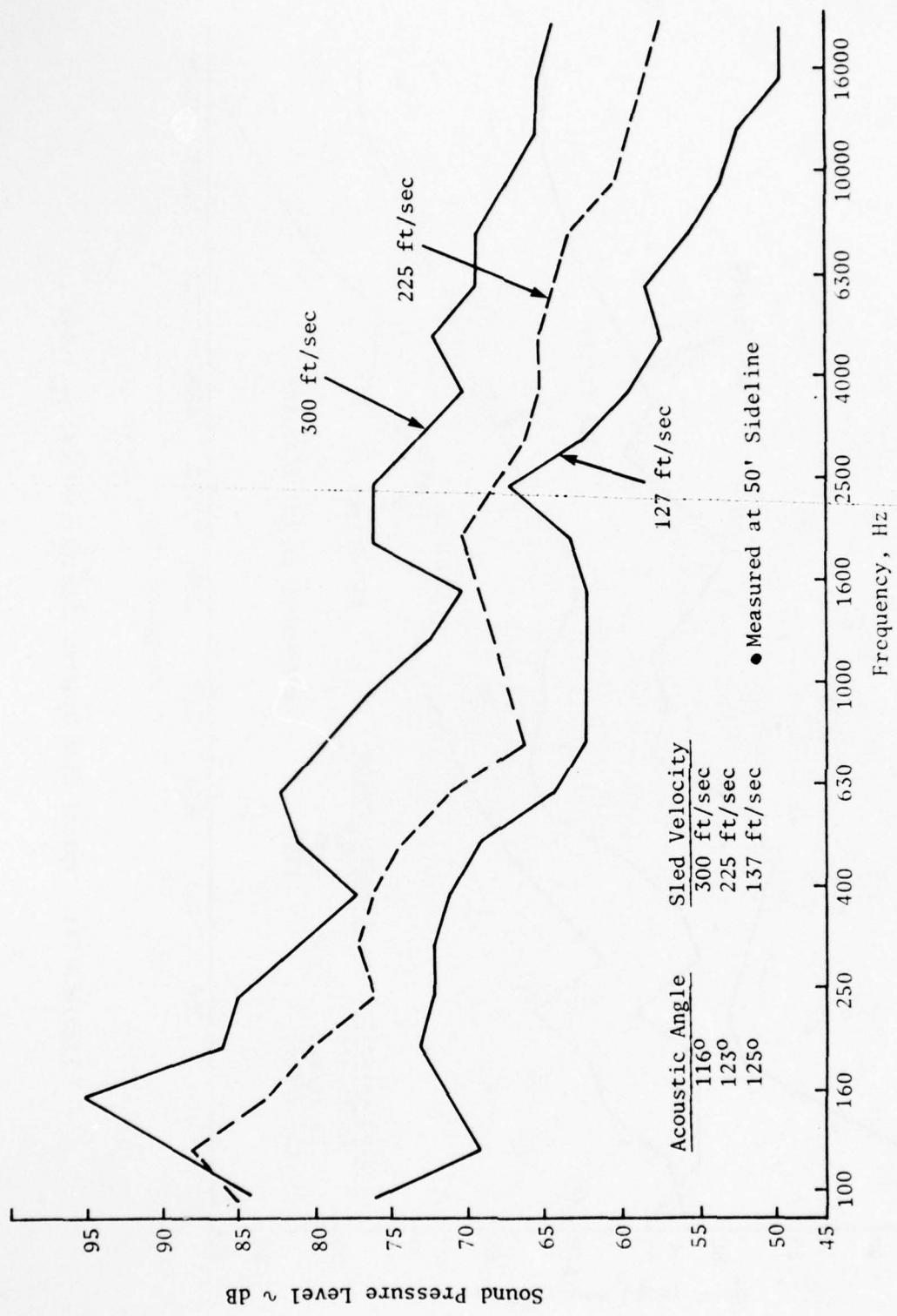


Figure 3-73. Typical Sled Spectra Characteristics, $\theta_1 = 120^\circ$.

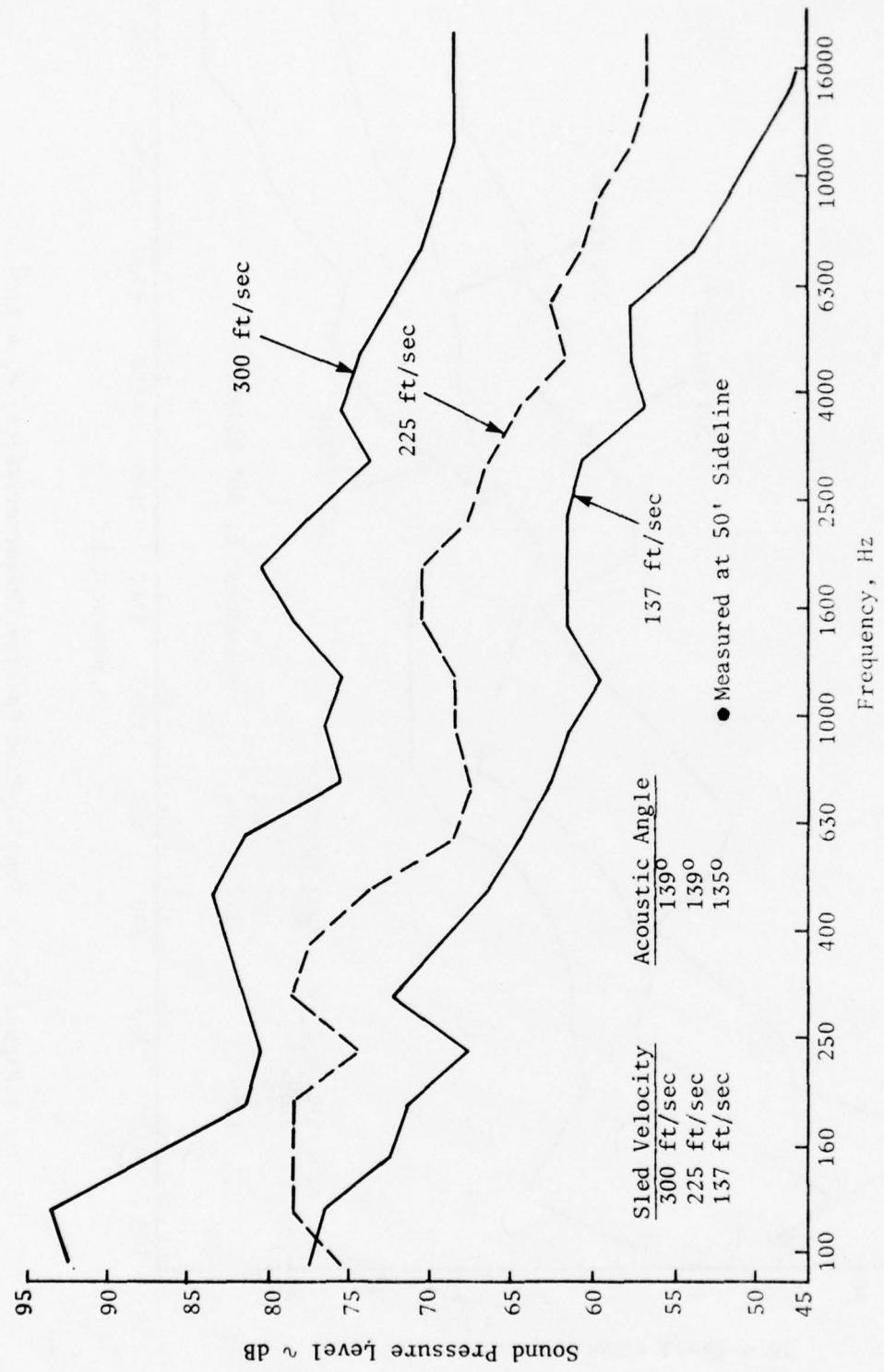


Figure 3-74. Typical Sled Spectra Characteristics, $\theta_1 = 140^\circ$.

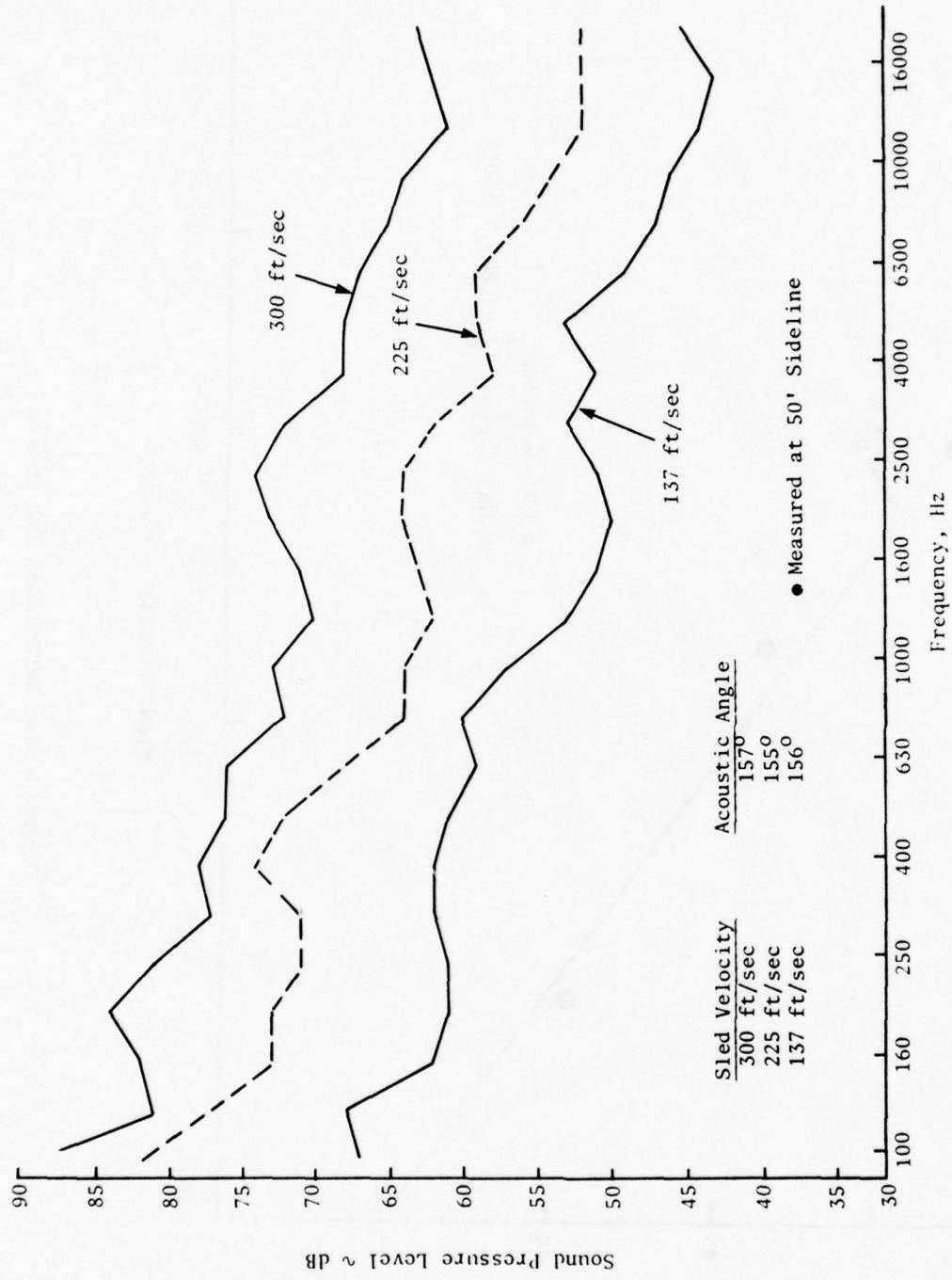


Figure 3-75. Typical Sled Spectra Characteristics, $\theta_1 = 160^\circ$.

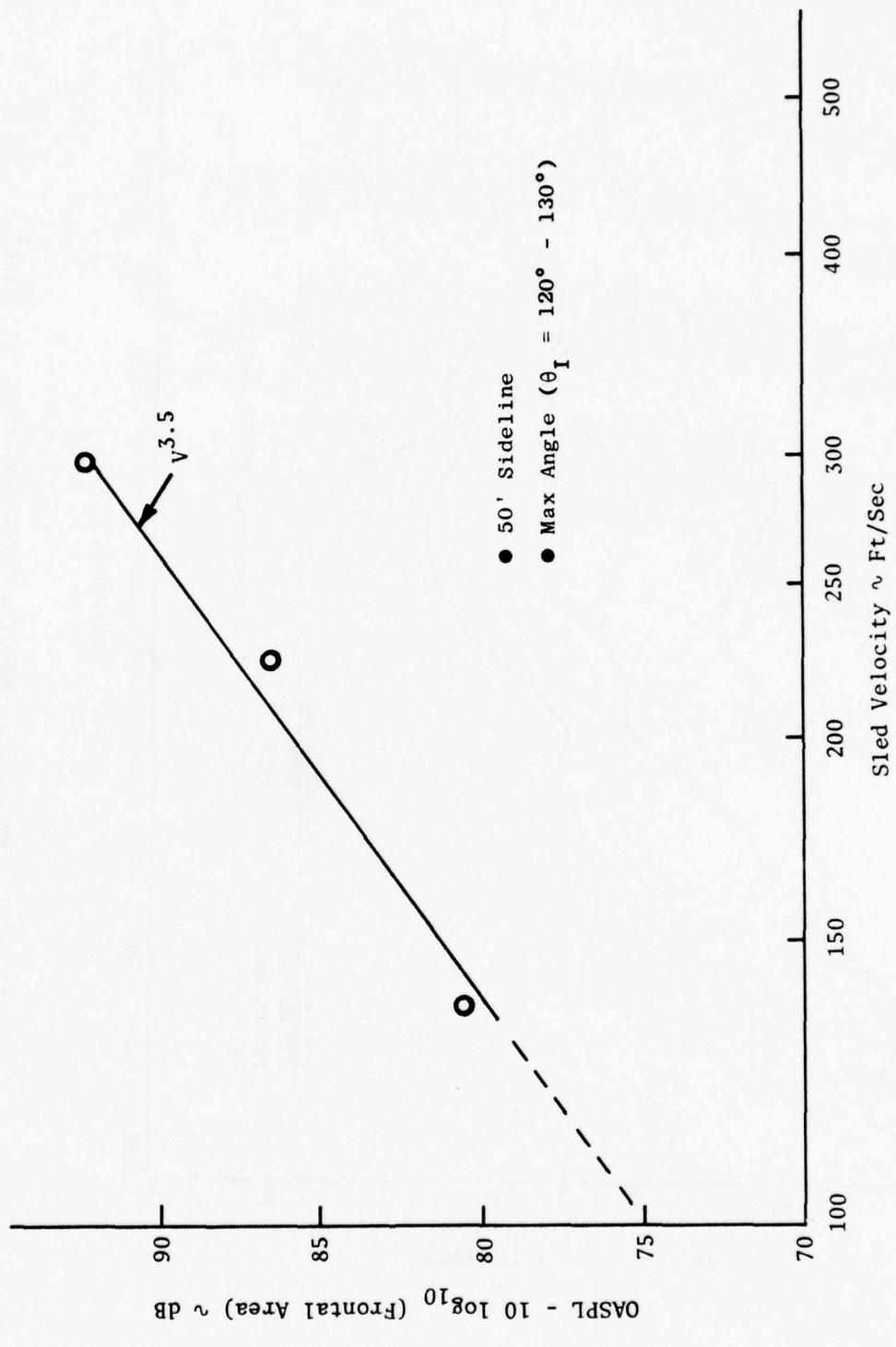


Figure 3-76. Normalized Max OASPL.

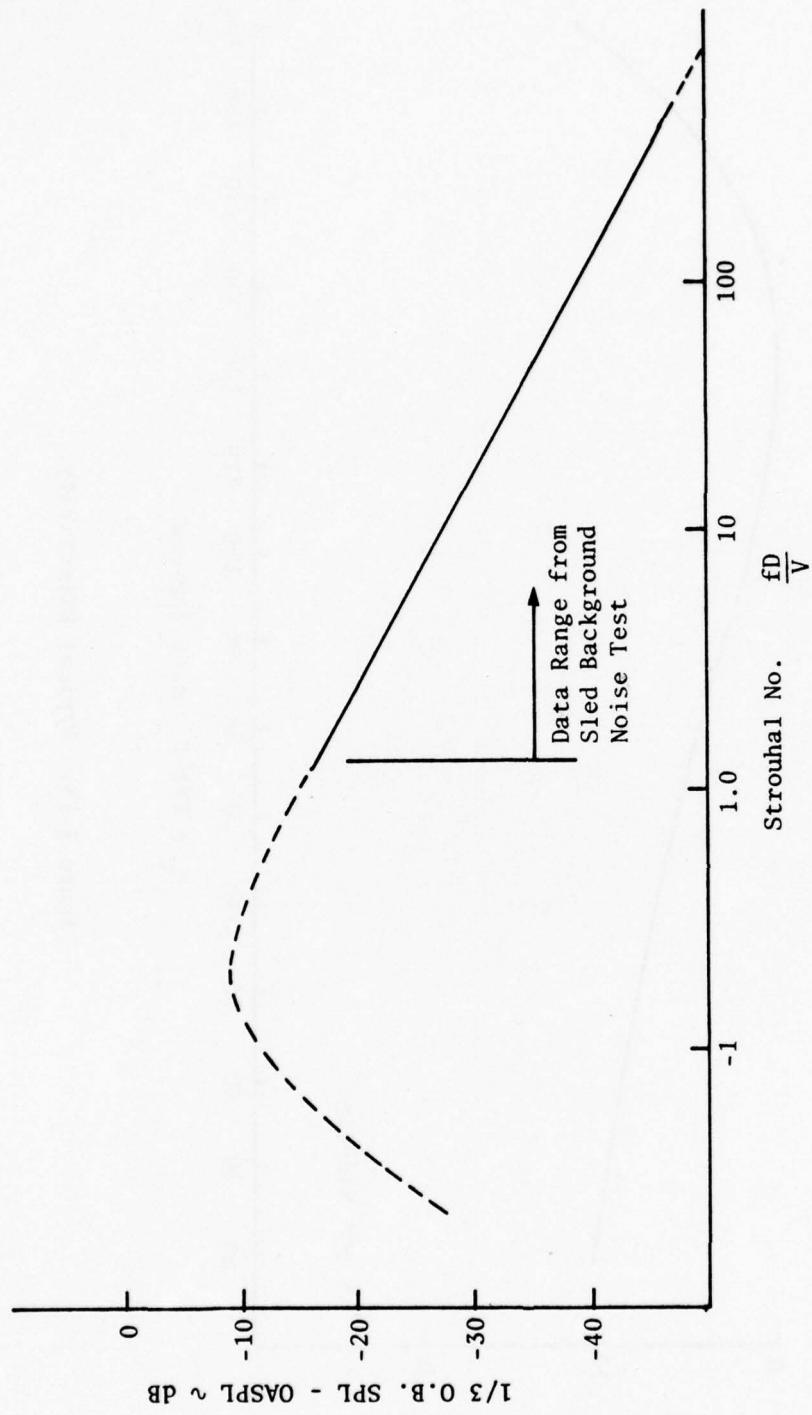


Figure 3-77. Normalized Spectra Shape.

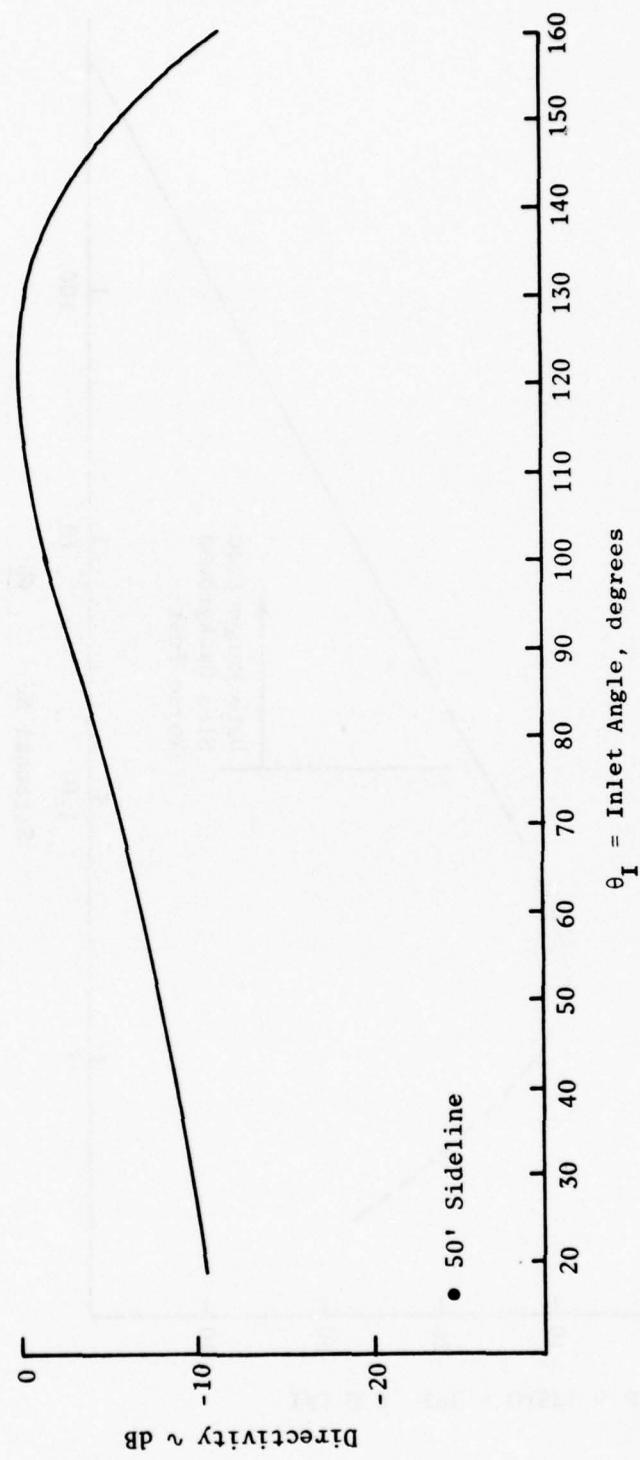


Figure 3-78. Typical Directivity.

LENGTH 36'
HEIGHT 15'
WIDTH 10'
WEIGHT 12,000 LBS



Figure 3-79. B-52 Sled Configuration.

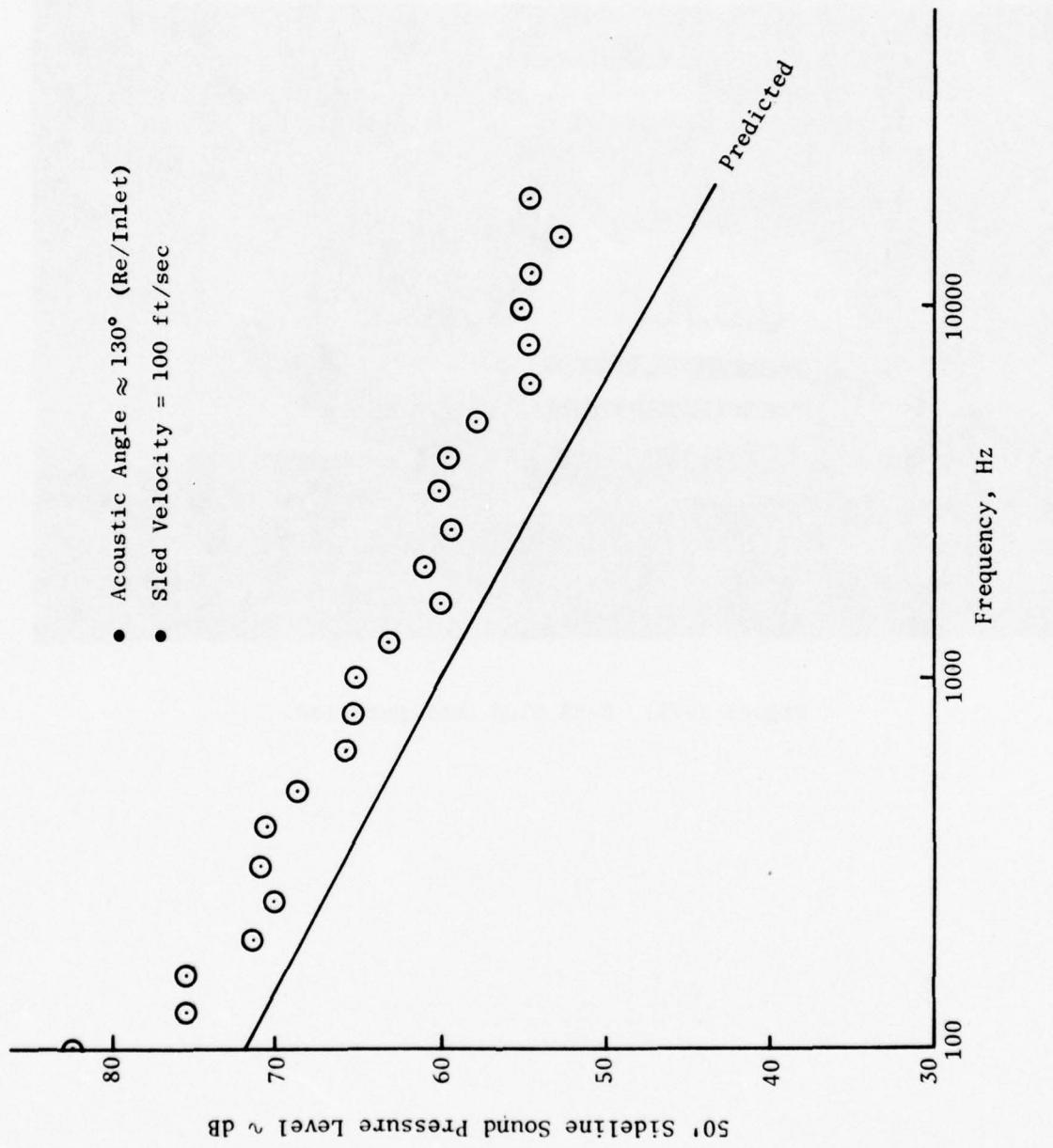


Figure 3-80. Comparison of Predicted and Measured B-52 Sled Noise Spectra.

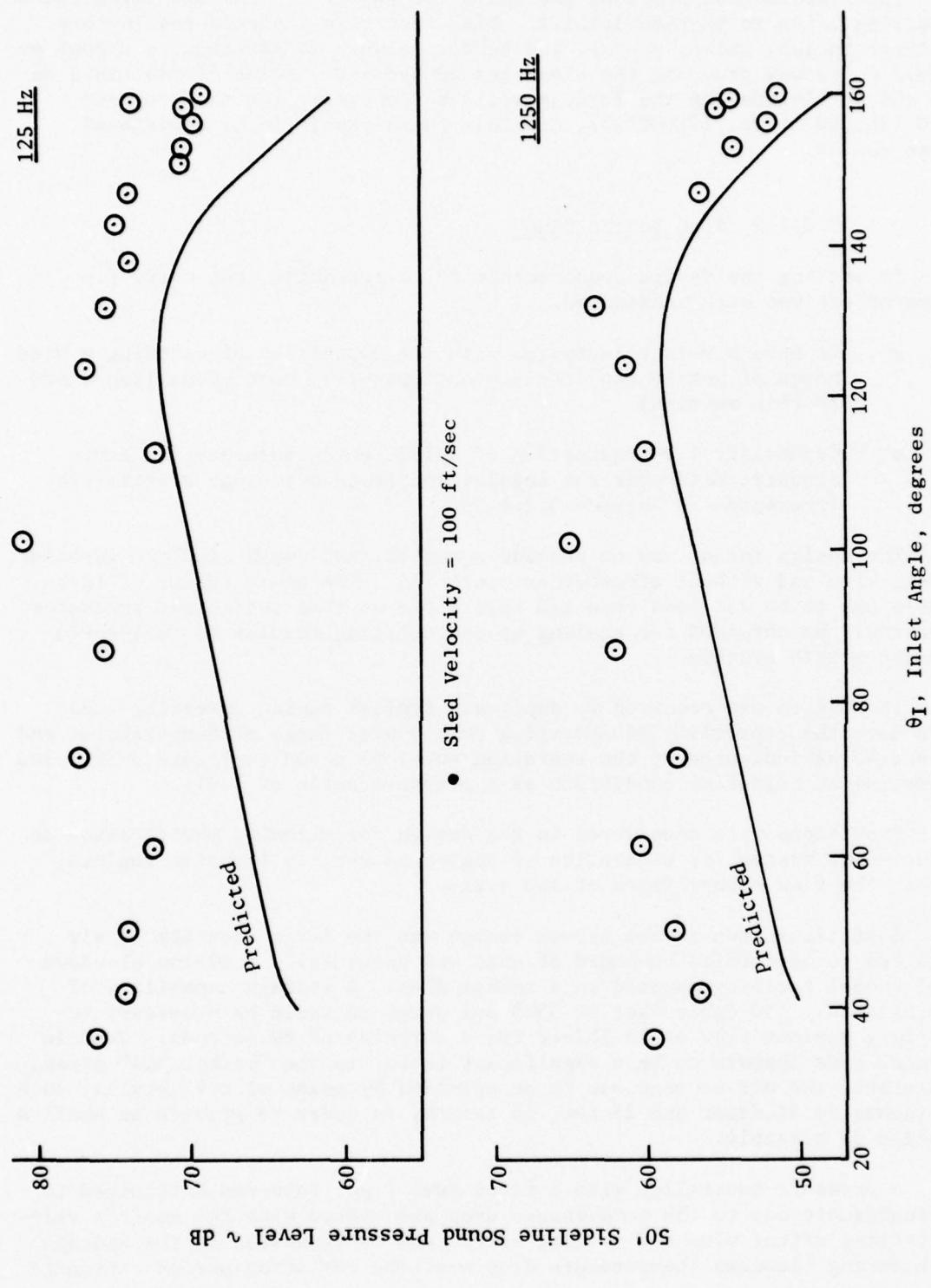


Figure 3-81. Comparison of Predicted and Measured B-52 Sled Directivity.

This information provides the basis for the test sled noise predictions appearing later in Section 3.2.1.2. Risk factors not considered in this estimate include valve, piping, and burner noise. In addition, although no runner noise was present, the sleds tested had low loading (lb/sq. in.) on the shoes. Increasing the loading would be necessary for the proposed sled (38,000 lb vs. 12,000 lb), and this could result in an additional noise source.

3.2.1.2 Sled Design Study

In setting the design requirements for a jet-noise test sled, two prime objectives were considered.

- To have a versatile system with the capability of covering a wide range of nozzle applications and operating conditions (described in this section)
- Capability for acquisition of sufficiently accurate far field acoustic data over the angular and frequency range of interest (presented in Section 3.2.1.3)

The design intent was to provide a system that could simulate turbojet models with and without afterburner operation. The scale factor of these models was to be not less than 1/8 full scale so that sufficient frequency data could be obtained for scaling up and relating results to full-scale exhaust nozzle systems.

The system was required to duplicate typical engine operating lines plus have the capability of operating over a wide range of temperatures and pressures as indicated by the operating envelope shown on Figure 3-82 (plus operating at cold flow conditions at a pressure ratio of 4.0).

Provisions were considered in the design for allowing modification to a dual-flow system for simulation of high-bypass-ratio turbofan engines, within the flow capabilities of the system.

A critical item in the system design was the large quantity of air required to be carried on-board of what was essentially a 20-ton blowdown wind tunnel facility mounted on a rocket sled. A storage capability of approximately 150 cubic feet at 3500 psi pressure would be necessary to supply a maximum flow of 30 lb/sec for a duration of 60 seconds. Vehicle frontal area appears to be a significant factor in the "background" noise; therefore, the air storage was to be provided by means of six vessels, each 16 inches in diameter and 25 feet in length, in order to provide as small a profile as possible.

A pressure controller with a fixed fuel input rate was determined to be inadequate due to the temperature drop associated with the control valve throttling effect plus the cooling effect due to expansion in the storage tank during blowdown (temperature drop over the operating period estimated

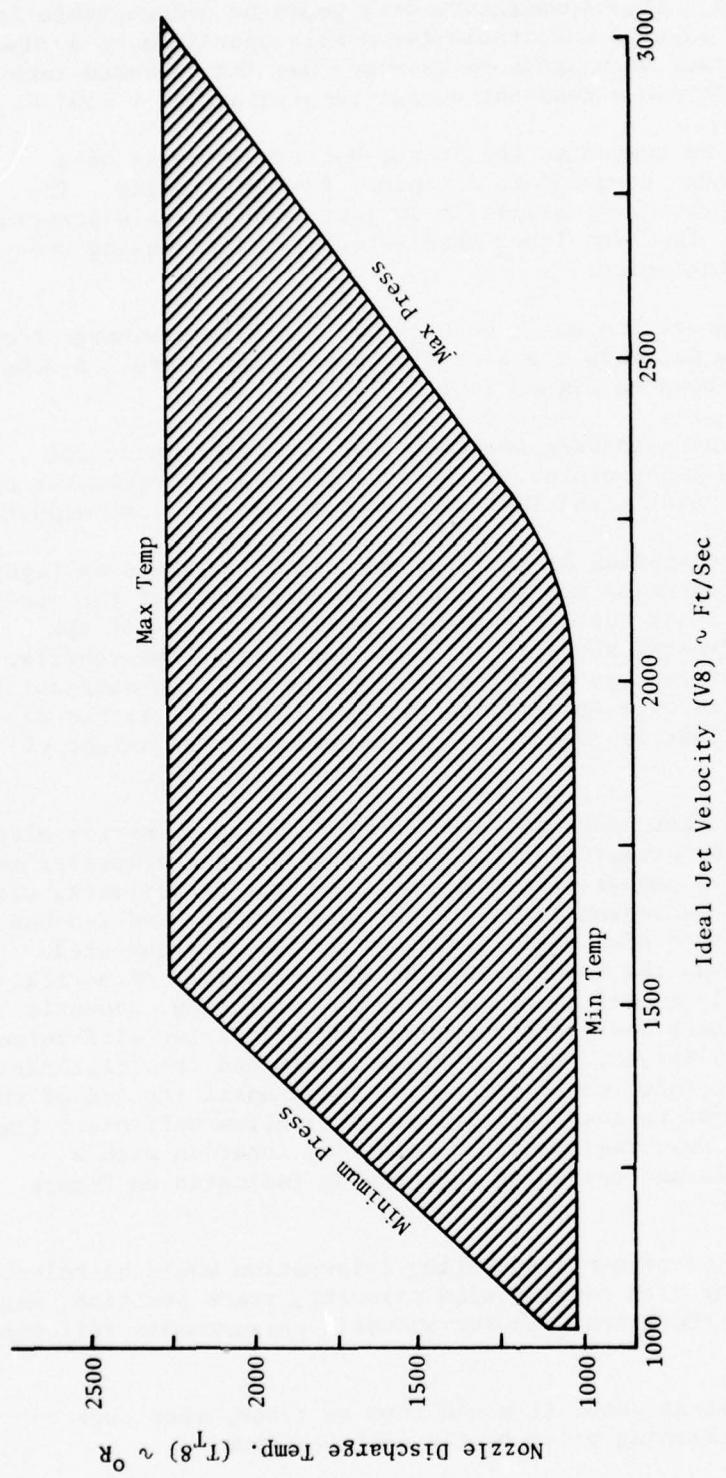


Figure 3-82. Sled System, Jet Nozzle Design Performance Envelope.

at approximately 200° F). This temperature drop would be unacceptable for flow control, and would also be unsuitable for stable operation of a JP-4 burner system. A preburner using gaseous hydrogen was incorporated into the system design to maintain a constant output temperature of \approx 150° F.

The airflow was to be routed to the burner section by means of a multitube pylon arrangement to maintain a minimal frontal profile. The test nozzle was to be mounted approximately 10 feet over the main structure to prevent wake effects, from the lower structure, from influencing the nozzle operating characteristics.

The combustor would operate on JP-4 fuel with a nozzle discharge temperature feedback control to maintain a preset discharge temperature. A schematic of the system is shown on Figure 3-83.

Flow straighteners and acoustic treatment for removing piping and combustor noise would be incorporated in the area between the combustor and the nozzle to minimize system noise influence on test nozzle noise signature.

A preliminary layout drawing of the proposed system is shown on Figure 3-84 indicating the placement of some of the major components of the system. As can be seen, the air bottles represent a major portion of the system and dictate the general shape of the lower portion of the vehicle. To minimize the effect of induced noise caused by flow over the surface(s), the structures are covered by a streamlined fairing. The vehicle has an overall length of approximately 33 feet and an estimated gross weight of 38,000 pounds.

During testing, the test model would be mounted aboard a carrier sled. The firing sequence would consist of the carrier sled being accelerated to a speed of 400 ft/sec by a pusher sled using solid-rocket propellants, with an acceleration rate not exceeding 5 g's. After the carrier sled reached maximum velocity, the pusher sled would disengage and the carrier sled would continue to move down the track with a deceleration rate of approximately 10 ft/sec to obtain a maximum of information per firing, acoustic data would be taken at track positions corresponding to carrier sled velocities of 300, 200, and 100 ft/sec, with locations determined from calibration runs. Firing of the test model would not be initiated until the end of the acceleration phase in order to conserve air but still allow sufficient time for stabilization before reaching the first measuring location with a predicted velocity profile and operating sequence as indicated on Figure 3-85.

During testing, the aerodynamic operating information would be telemetered and recorded along with carrier sled velocity, track position, and timing information for correlation with the acoustic measurements following testing.

After the vehicle was at rest, it would then be transported back to the firing area for refurbishing prior to the next test run.

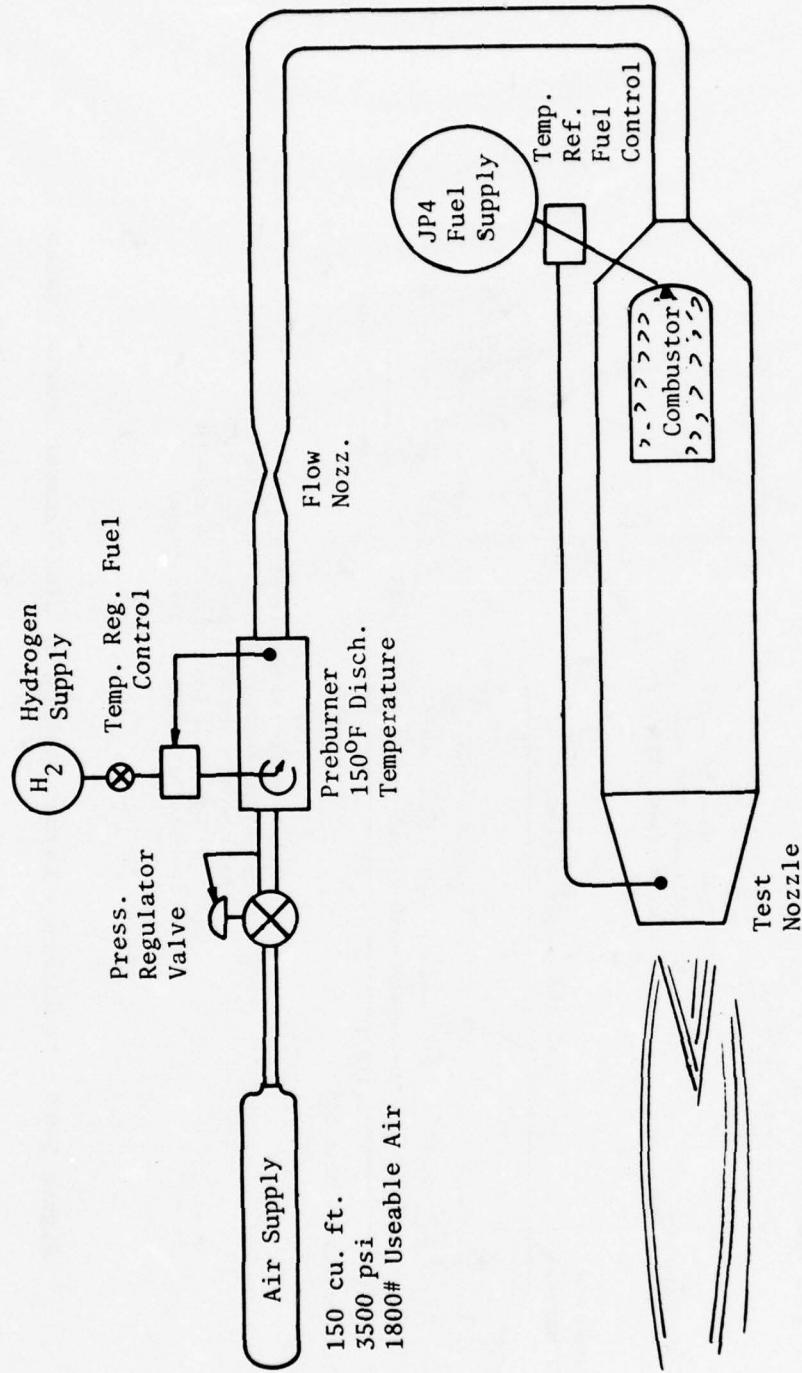


Figure 3-83. Schematic of Proposed Nozzle Test System.

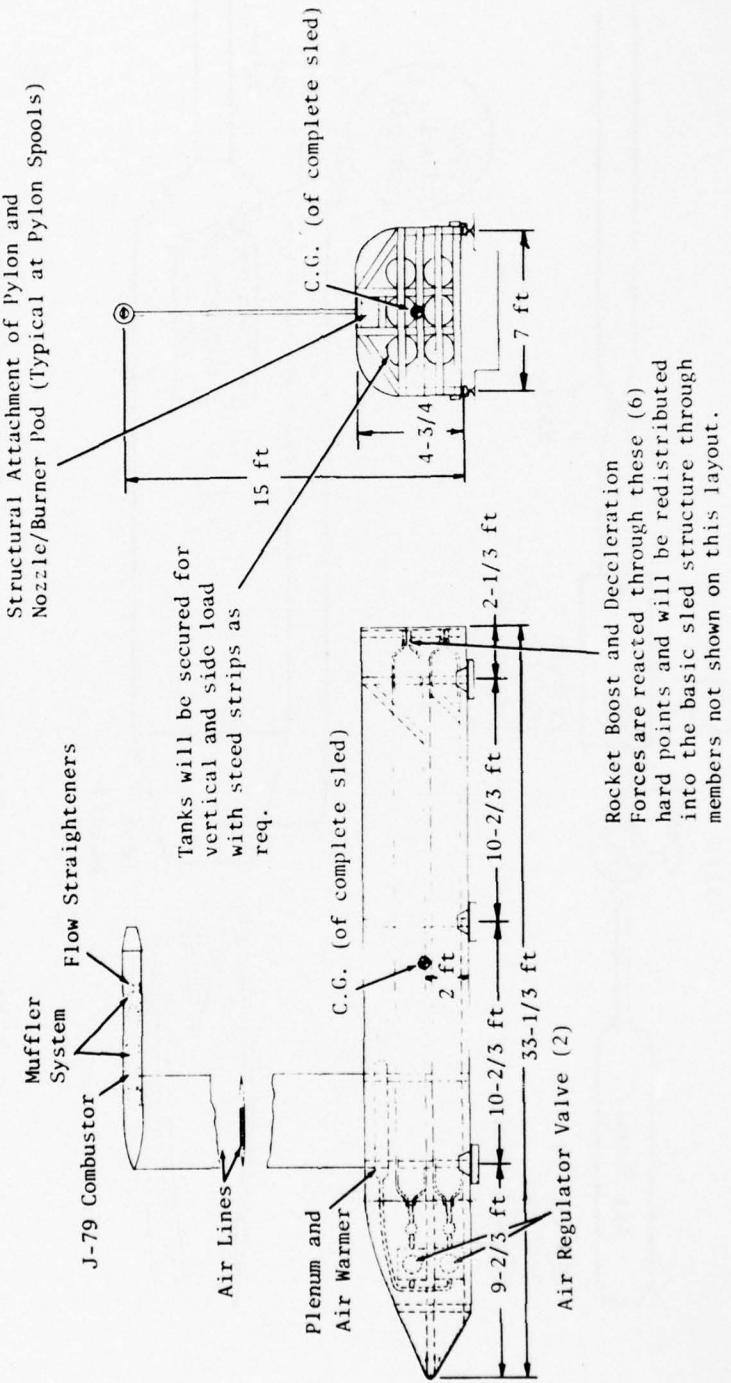


Figure 3-84. Preliminary Layout Drawing of Sled/Exhaust Nozzle System.

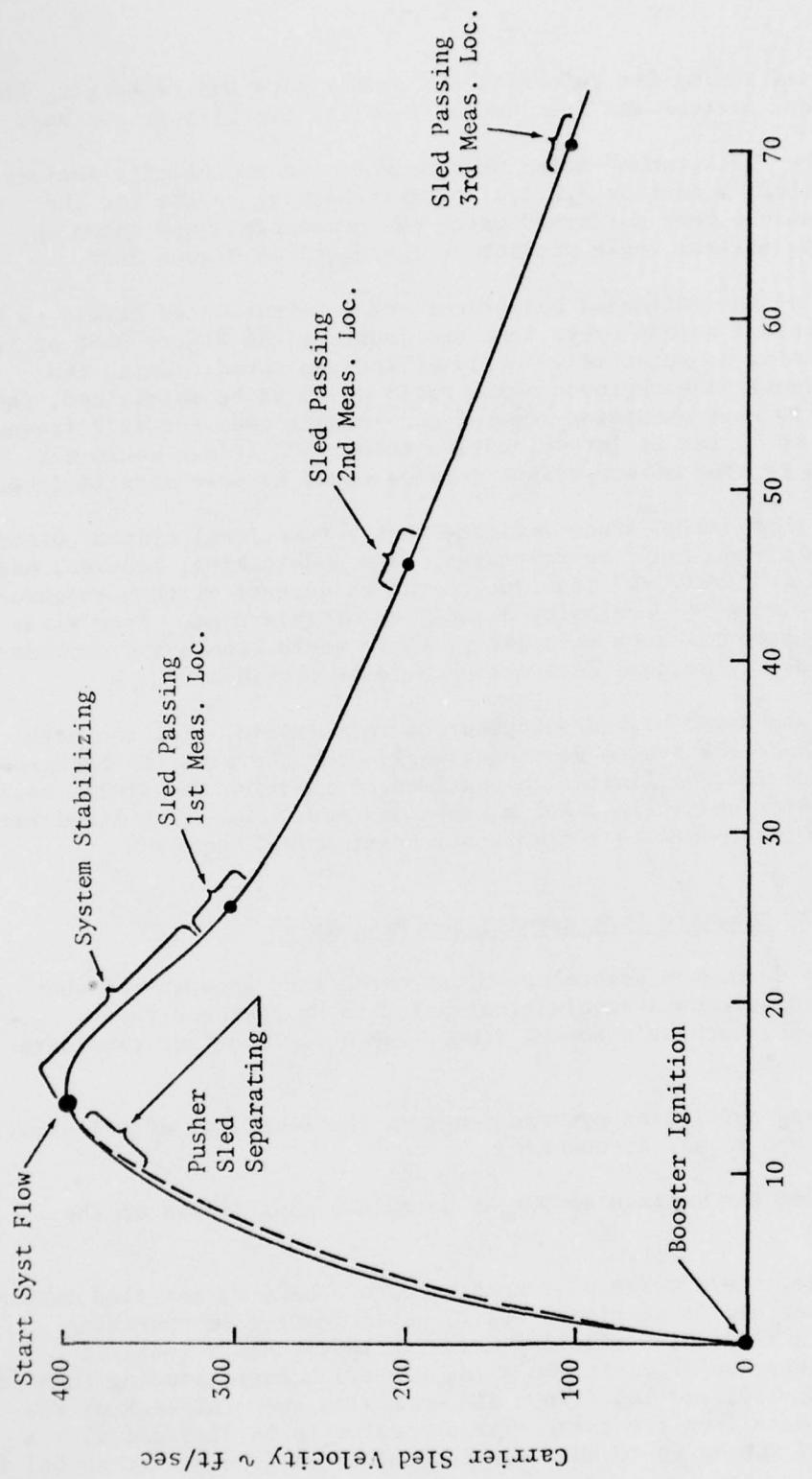


Figure 3-85. Estimated Sled Velocity Profile and Staging.

The estimated timing for reloading the pusher sled and recharging the air tanks and fuel systems was four hours, enabling two firings per day.

Based on the "background" noise measurements and empirically derived relations described in Section 3.2.1.1, estimated noise levels for the proposed test vehicle were performed using the geometric shape shown on Figure 3-86, with maximum angle prediction indicated on Figure 3-87.

Comparison of the estimated background noise versus noise levels to be expected from conical nozzle operations are indicated on Figure 3-88 at jet velocities (assuming no relative velocity effect) as noted. Using the criteria that signal to background noise ratio of 10 dB be maintained, the estimate indicates that obtaining conical nozzle data over the full frequency range of 400 Hz to 40 kHz at jet velocities below 1600 ft/sec would not be feasible, and testing of suppressor nozzles would be even more limited.

Results of this design study indicate that a functional system, meeting the program objectives, could be developed. Its undertaking, however, had to be considered a "high risk" item due to the uniqueness of this endeavor and limited experience in developing a facility of this type. Even after a successful development of such a facility, there would remain the considerable risk that the operational test costs would be prohibitive.

The costs associated with development of this system, plus the high operating costs once the system was functional, combined with the background noise restrictions and the limitation that source location techniques (such as laser-velocimeter and ellipsoidal microphone) could not be utilized led to the conclusion that this is a high-risk, uneconomical approach.

3.2.1.3 Acoustic Data Acquisition Procedure

This section documents several problems which were encountered when considering an acoustic data acquisition system to be operated from a moving test vehicle, such as a rocket sled. The most important considerations are:

- Obtaining sufficient dynamic range in the recording at all sideline angles and at all frequencies
- Obtaining the maximum amount of data in a single pass of the vehicle

As an example, the problem of recording data from a rocket sled facility as previously described in Section 3.2.1.2, would involve an operating model mounted on a sled, with sideline acoustic measurements required during sled deceleration at positions along the track corresponding to sled velocities of 300, 200, and 100 ft/sec for each sled run. At each of the three positions, data from the three microphones would be recorded with a frequency range of 200 Hz to 40 kHz, (corresponding to 5000 Hz for an 8:1 full-scale model).

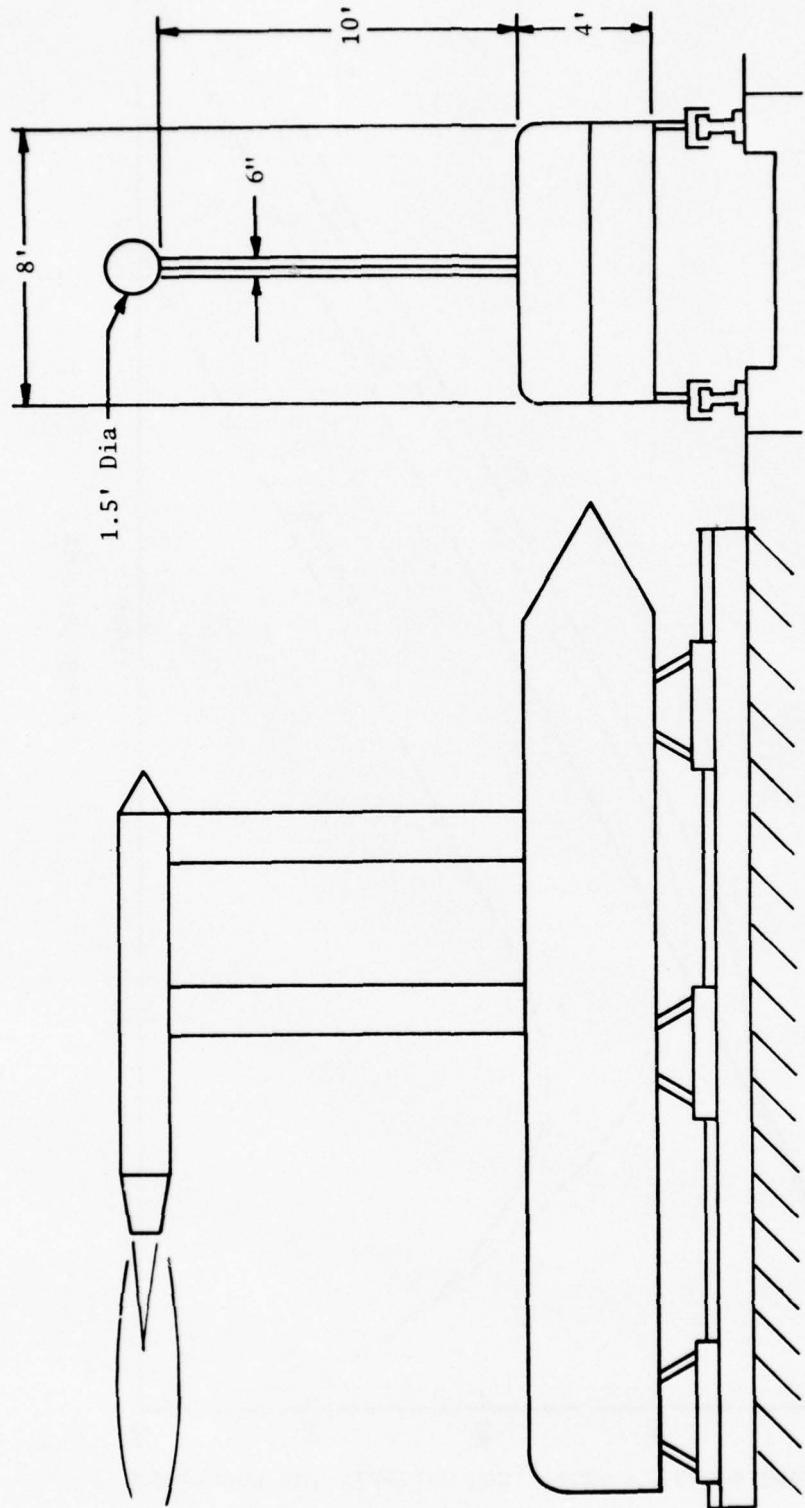


Figure 3-86. Generalized Configuration Used for Sled Noise Prediction.

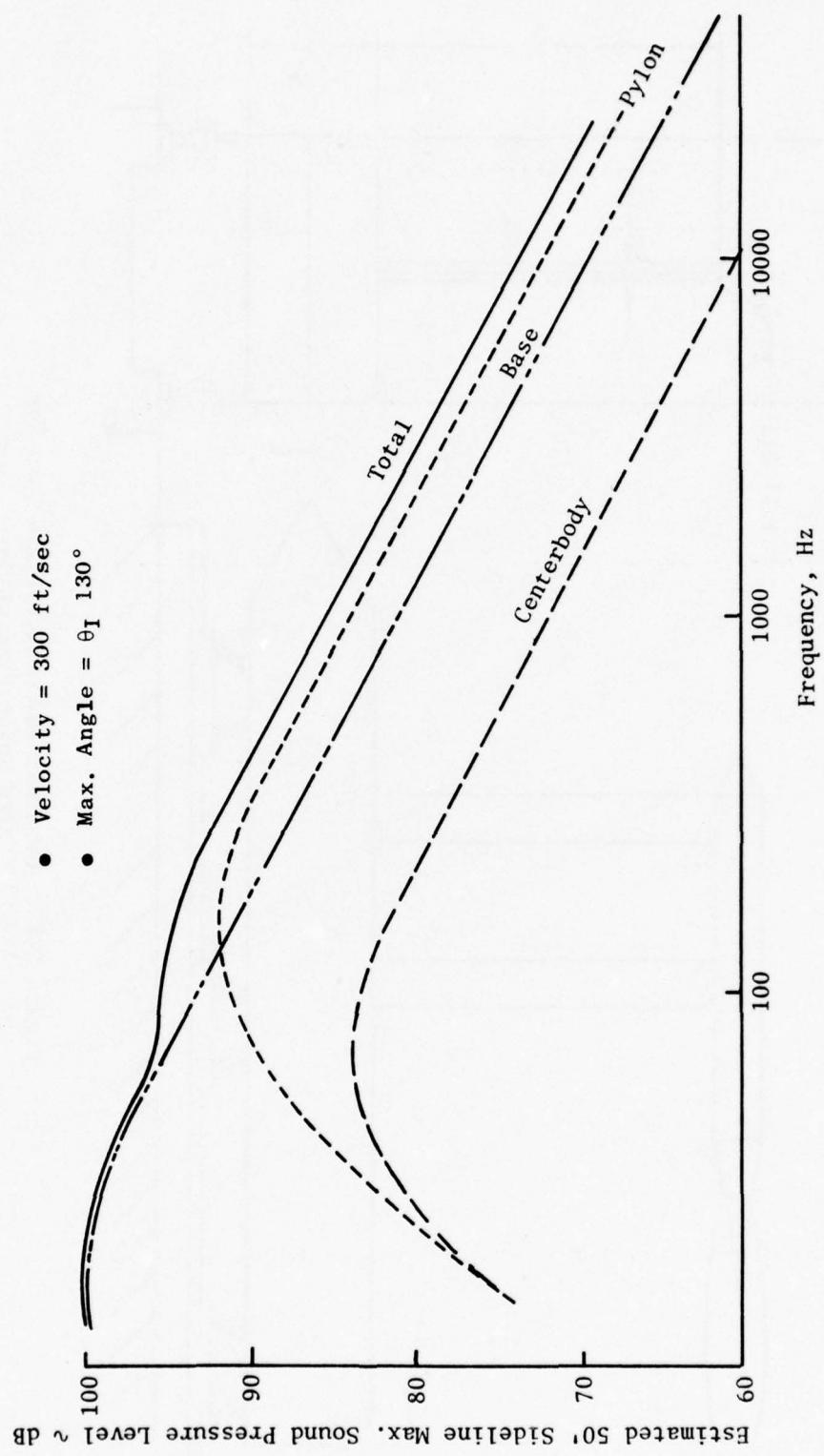


Figure 3-87. Estimated Maximum Background Noise Level.

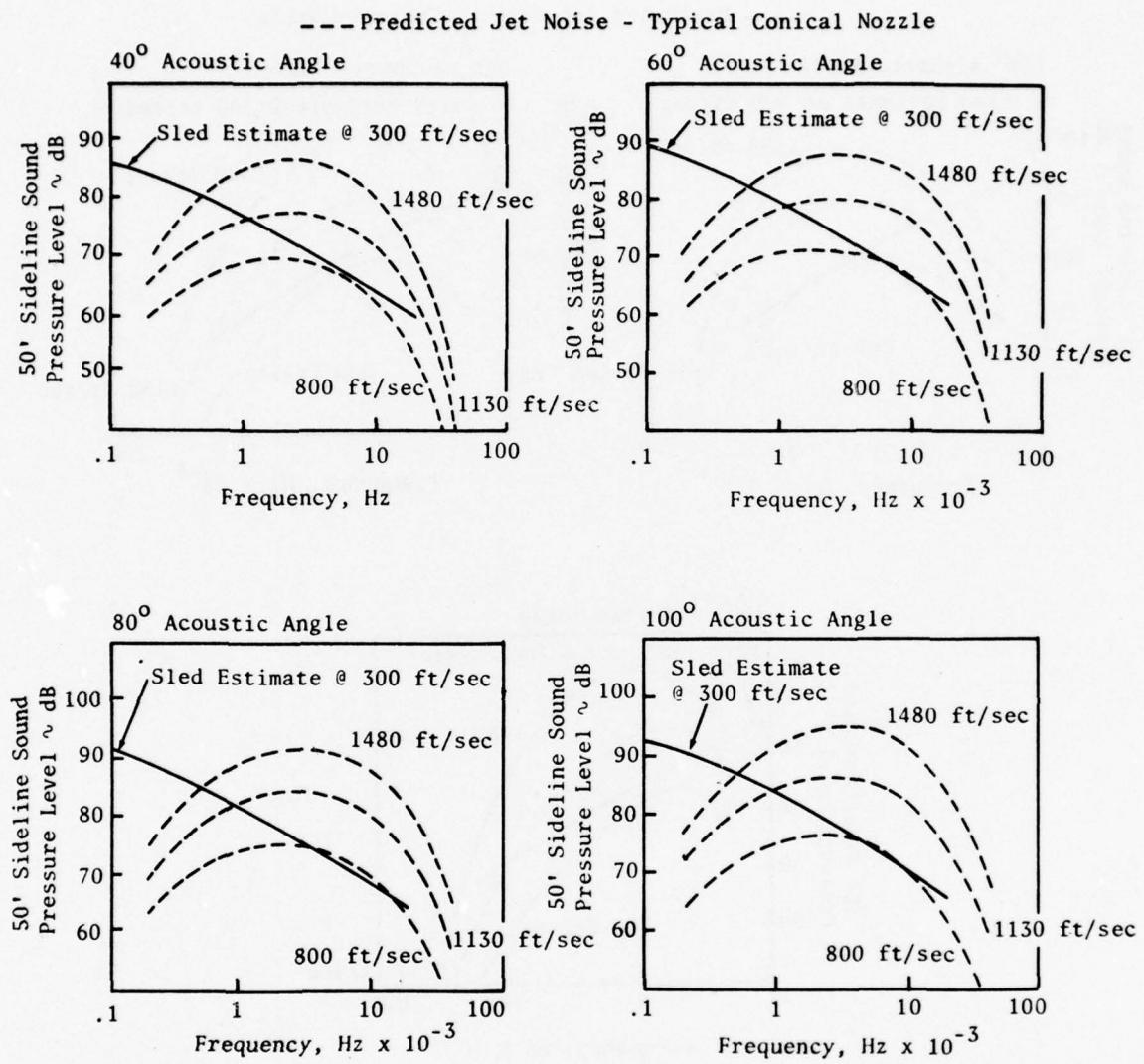


Figure 3-88. Predicted Sled Background Noise Estimates at 50-Foot Measuring Position.

--- Predicted Jet Noise - Conical Nozzle

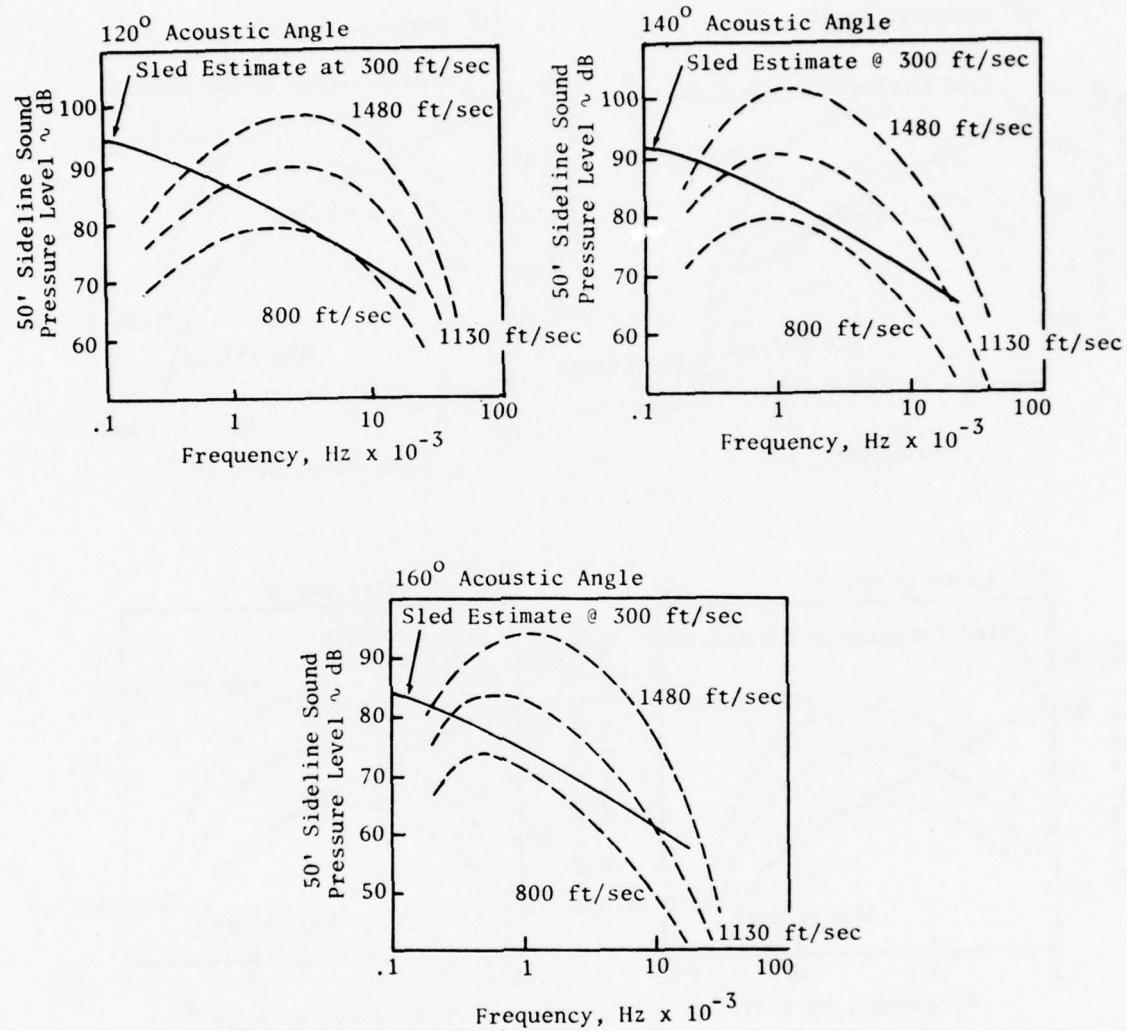


Figure 3-88. Predicted Sled Background Noise Estimates
at 50-Foot Measuring Position (Concluded).

The sideline distance at which measurements are taken must be resolved because this will have a pronounced effect on the duration of time that the sled is within the area of interest (acoustic angles of 20° to 160°). This in turn influences directly the number of samples, data accuracy, and related acquisition problems.

Using 100-foot sideline as a starting point (corresponding to an 800-foot flyover for a full-scale model), a duration of 1.83 seconds would be experienced with the sled moving at 300 ft/sec. Assuming 1/8-second integration (the fastest available on the G.R. analyzer), 14 pieces (spectra) of data could be obtained from the pass. An estimate of the levels to be encountered is shown on Figure 3-89. It is apparent that when the system is set for recording the maximum overall level, a dynamic range on the order of 100 dB would be required to pick up high frequency data. The high frequency levels are low because of the high atmospheric absorption rate at these "large" distances due to the extreme angles. This is far in excess of the normal recording range ability of 40 to 50 dB.

If the microphone location was chosen at a 50-foot distance (Figure 3-90), a benefit would be realized in terms of the dynamic range required and in terms of possible problems with the ambient noise floor. The duration of the event would be reduced to 0.9 seconds, however, thus providing only 7 pieces of data at 1/8-second integration. Similar benefits and disadvantages would be derived if the distance were further reduced to 25 feet (Figure 3-91), resulting in three pieces of data from about a 0.45-second duration.

The dynamic range requirement can partially be resolved by recording each microphone on three channels through three amplifiers adjusted to record maximum level, max. - 10 dB, and max. - 20 dB, respectively. This type of arrangement (3 channels/microphone × 3 microphones/location × 3 locations = 27 channels) would fill the capacity of the 28-track recorder while increasing the effective dynamic range to 60 to 70 dB. Final data would be a composite of these three systems.

The limitation on the number of data pieces per event which results from the 1/8-second minimum integration time could be resolved by changing the ratio of recording speed/playback speed from 1 to 2 (or possibly 4) and maintaining the 1/8-second integration; in effect giving 1/16 or 1/32-second integration time. The disadvantage of this method however, is a reduction in data reliability.

In conclusion:

- If high frequencies (to 40 kHz) are required, a close distance, fast integration time (with resulting loss of reliability in the lower frequencies) is required.
- If lower frequencies are deemed more important, better low frequency reliability can be obtained with increased sideline distance and slower integration times.

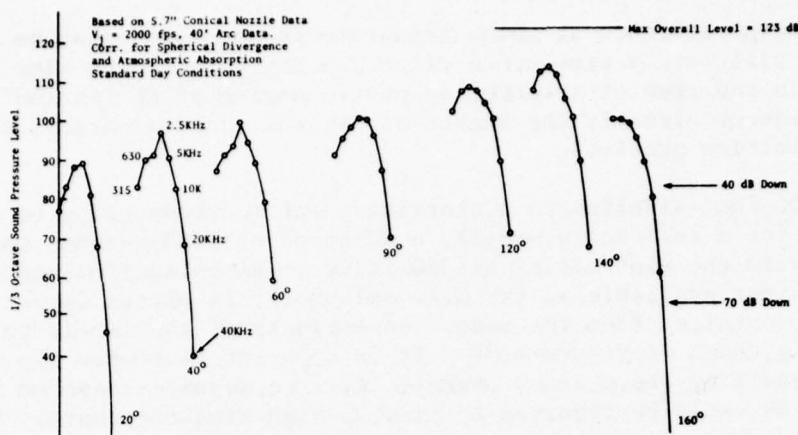


Figure 3-89. Estimated Conical Nozzle Noise Levels at a 100-Foot Measuring Position.

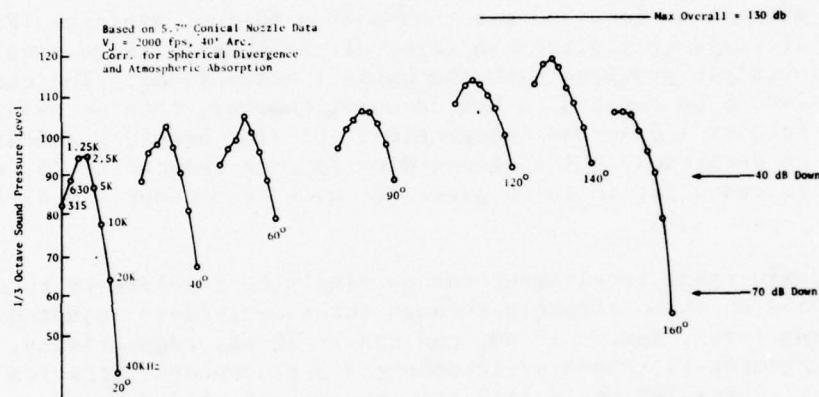


Figure 3-90. Estimated Conical Nozzle Noise Levels at a 50-Foot Measuring Position.

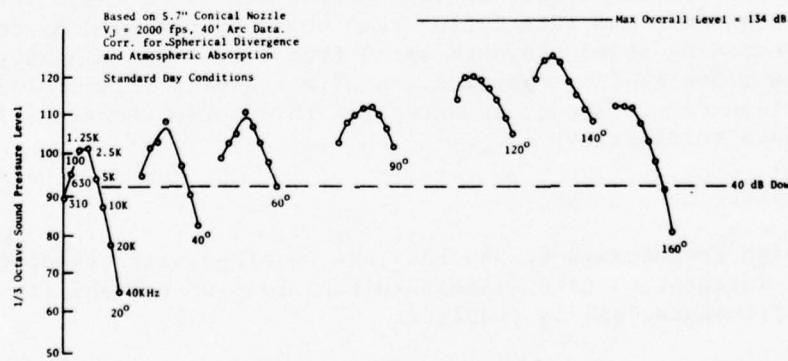


Figure 3-91. Estimated Conical Nozzle Noise Levels at a 25-Foot Measuring Position.

- A good compromise might be a 50-foot measurement with a 2:1 playback and 1/8 second (1/16 second effective) on the G.R. analyzer. This would provide a minimum of 14 samples, as indicated on Tables 3-XVII and 3-XVIII, with an upper frequency limit as indicated on Figure 3-92.

3.2.2 High Speed Trains

Two high speed train facilities meet the general requirements of a moving-frame facility in terms of operational velocity capability. These are the Linear Induction Motor Research Vehicle at the DOT High Speed Ground Test Center located at Pueblo, Colorado, and the Bertin Aerotrain in Goemetz, France. The evaluation of these facilities, with the nozzle test module either carried aboard or towed behind the vehicle, is presented in the following sections.

3.2.2.1 DOT High Speed Ground Test Center

The Linear Induction Motor Research Vehicle (LIMRV) was developed as an experimental test vehicle at the DOT High Speed Ground Test Center.

The LIMRV utilizes a T64 turboshaft gas turbine engine as a main power source and can attain speeds of approximately 290 ft/sec. In addition, boost power generated by two J52 turbojet engines allows the vehicle to attain a top speed of 360 ft/sec.

Use of the J52 engines for the proposed acoustic testing was not considered viable, however, because the noise they generate would mask the acoustic signals from any test nozzle. The added weight of the nozzle test module (estimated at 15,000 lb), without the added power of the J52 engines, would limit the maximum attainable speed to an estimated 240 ft/sec to 300 ft/sec if required to meet program objectives.

Utilization of this high speed train on this program was not pursued further.

3.2.2.2 Bertin Aerotrain

The Bertin Aerotrain is illustrated on Figure 3-93. This vehicle was developed as an acoustic test bed by the French engine company SNECMA. The vehicle is operated on a 6 km track and is equipped with a J85 turbojet engine for propulsion. Because the vehicle was chosen for further demonstration testing, a detailed description is presented in Section 6.1. The evaluation of this vehicle which led to its selection for further demonstration is presented in this section.

Table 3-XVII. Typical Angular Resolution for Data Versus Measuring Distances and Playback Speeds.

Measurement Distance, ft	Record/Playback Ratio	Measurement Distance, ft	Record/Playback Ratio	Measurement Distance, ft	Record/Playback Ratio
100	1:1				
50	2:1	50	1:1	25	1:1
25	4:1	25	2:1		
		21.3°			
		24.6	22.9		26.9
		28.9			
		34.2	31.6		
		43.3			
		55.6	48.9		63.6
		72.8			
		93.7	83.0		
		113.8		122.1	
		129.2			
		140.0	144.0		
		147.5			
		152.8			
		156.7	154.8		
		159.6			

Table 3-XVIII. Confidence Limits as a Function of Sideline Distance and Record/Playback Ratio.

Sideline Measuring Distance (ft)	Record to Playback Ratio	Nc. Spectra Available 20° to 160°	90% Confidence Interval for Average of 3 Points 400 Hz to 4000 Hz	Spectrum Analyzer
100	1:1	15	-1.0 to +1.4 dB ±0.4 dB	
50	2:1	15	-1.8 to +2.2 dB ±0.6	
25	4:1	15	-2.2 to +3.3 dB ±0.8	

(Assumes 1/8-sec integration on 1/3-octave analyzer)

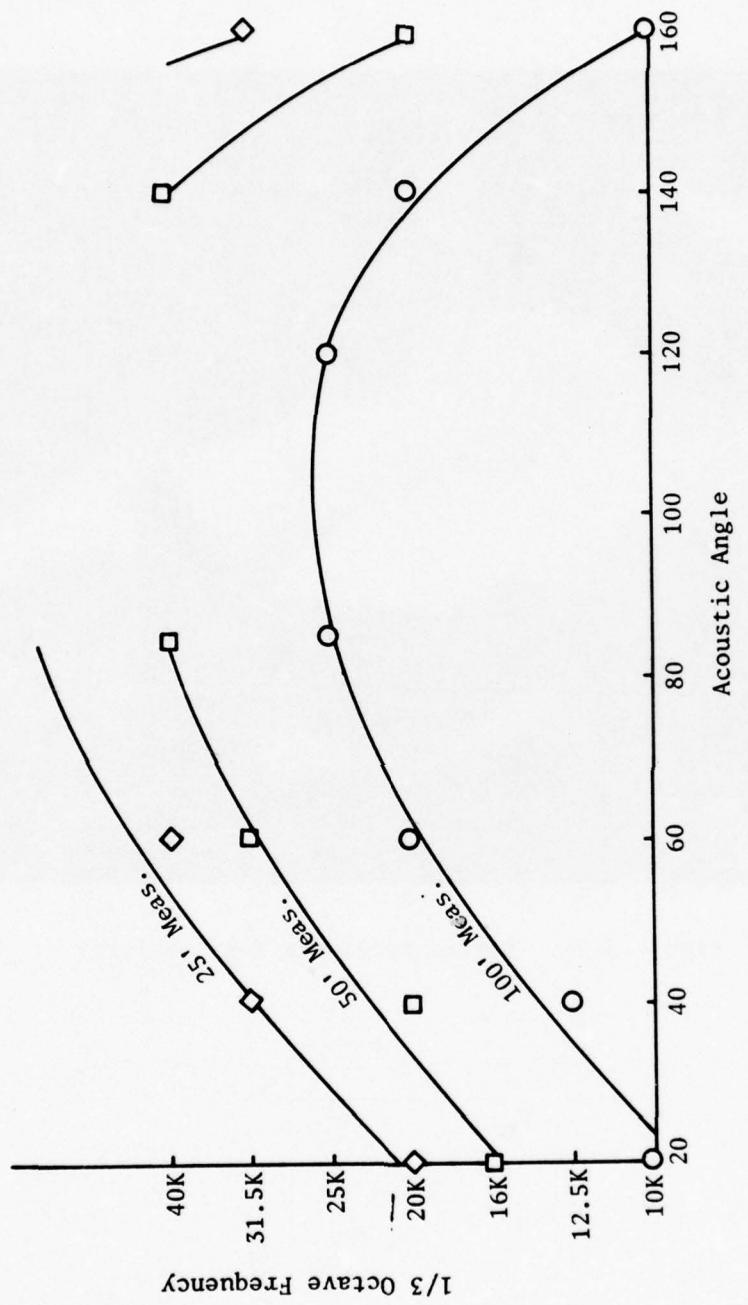


Figure 3-92. Estimated Upper Limit of Frequency Range Capability.

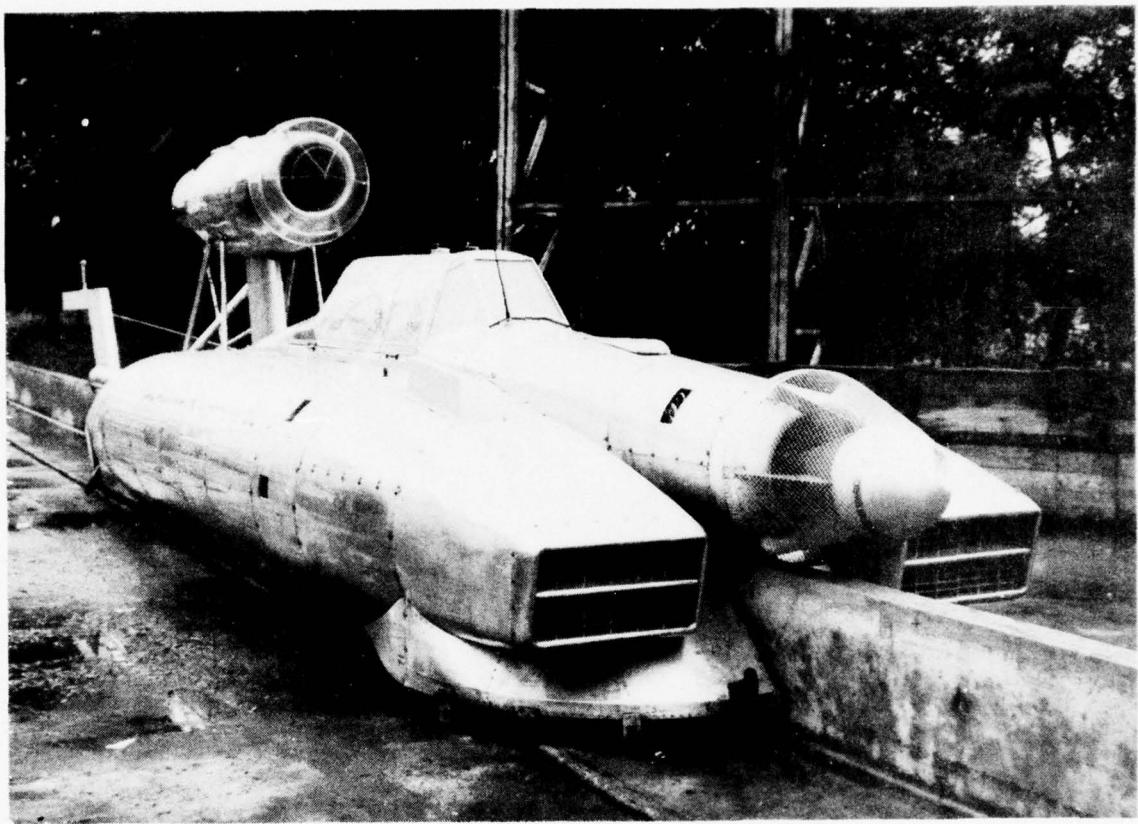


Figure 3-93. Bertin Aerotrain Test Facility.

Y

Five key items were considered in the Aerotrain evaluation:

1. Exact definition of noise source relative to the microphone
2. Background noise levels relative to expected suppressor nozzle noise levels
3. Duration of acoustic signal/data repeatability
4. Free-field correction
5. Consistency of moving-frame results with respect to other data sources

The first item was resolved by the synchronization procedure illustrated on Figure 3-94 and fully described in Section 6.4. The second item was evaluated by using the background noise data presented in Section 6.2 and was found to have minimal impact. The third item has been discussed in-depth during the rocket sled discussion as to the proper tradeoffs between measurement distance and integration time. An example of the impact of integration time is presented on Figure 3-95. The corresponding repeatability of actual acoustic data using this setup is summarized relative to OASPL and spectra and presented on Figure 3-96. The data fall within a ± 2 dB band.

The major Aerotrain shortcomings were that (1) scale-model hardware could not be utilized, (2) the cycle conditions investigated were only along a J85 operating line (and therefore no parametric variations of cycle condition could be conducted), and (3) the maximum vehicle speed was 275 ft/sec (significantly less than the goal of 400 ft/sec).

The Aerotrain/J85 vehicle, however, could be easily fitted with existing suppressor systems previously flight-tested by NASA-Lewis and General Electric. Two suppressors were chosen: a 104-tube nozzle and an 8-lobe nozzle. These two nozzles were representative of a simple, moderate suppressor already in commercial service and a complex exhaust suppressor system.

As a result of this hardware availability and the advanced state of development of the vehicle, the Aerotrain was selected to be used for the moving-frame validation test series described in Section 6.0.

3.3 STATISTICAL ANALYSIS OF MOVING-SOURCE PROBLEM

3.3.1 Applying Confidence Limits to Moving-Source Data

Confidence limits are important because they indicate the expected repeatability of data from independent, identical experiments. They constitute an error analysis in the sense that any statistical variation in the performance of an experiment is taken into account. Physical differences

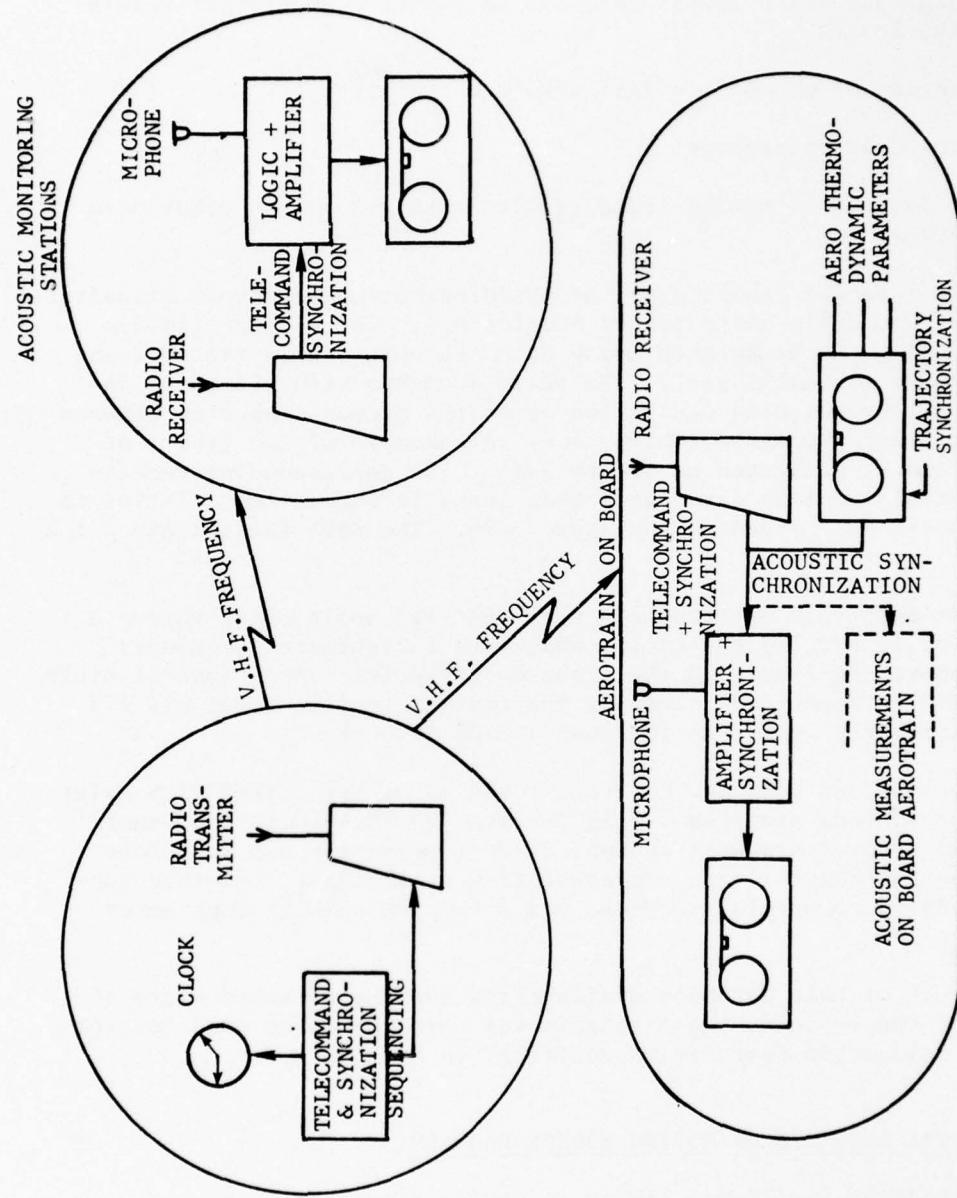


Figure 3-94. Principle of Measurement and Synchronization.

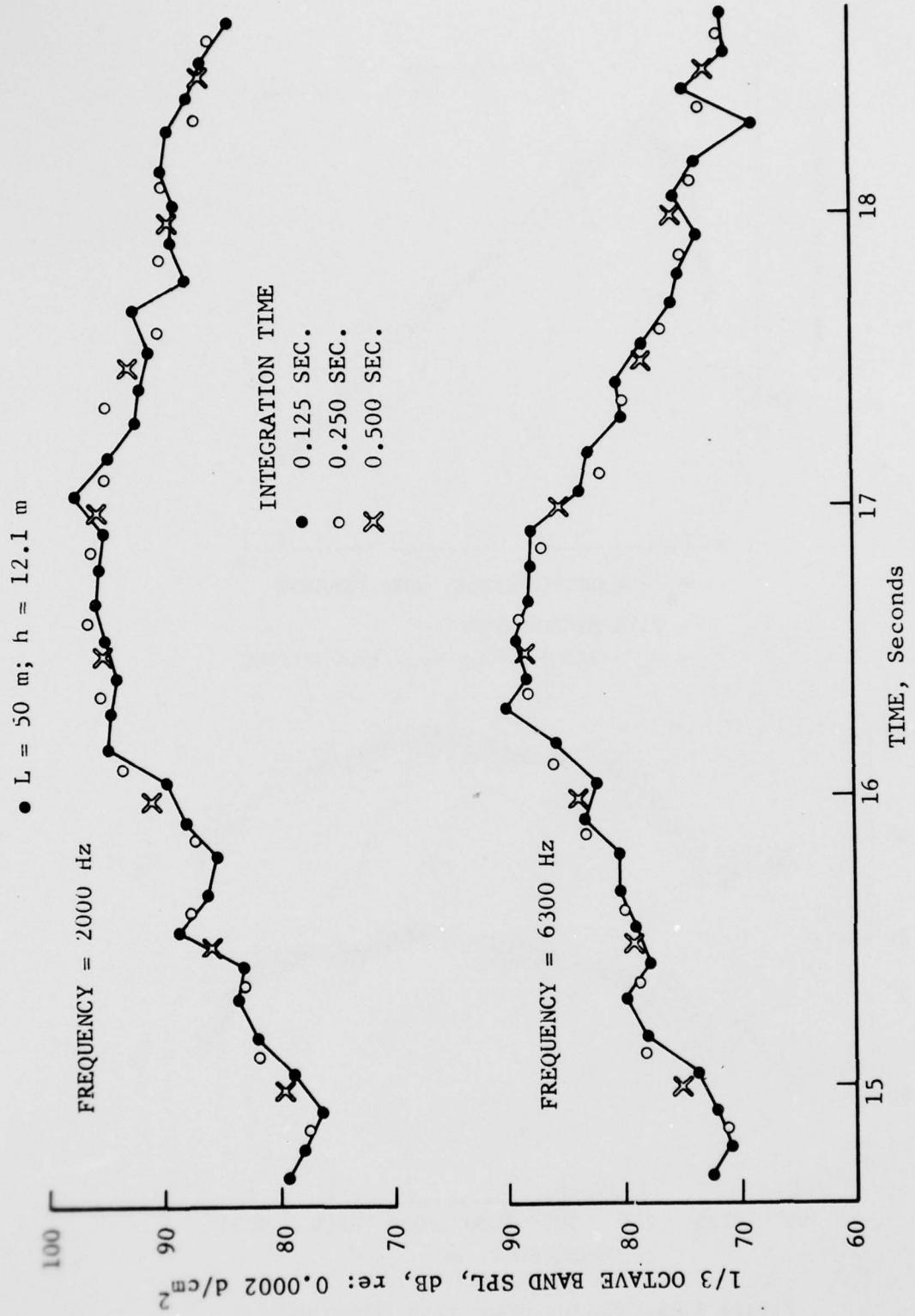


Figure 3-95. Effects of Integration Time.

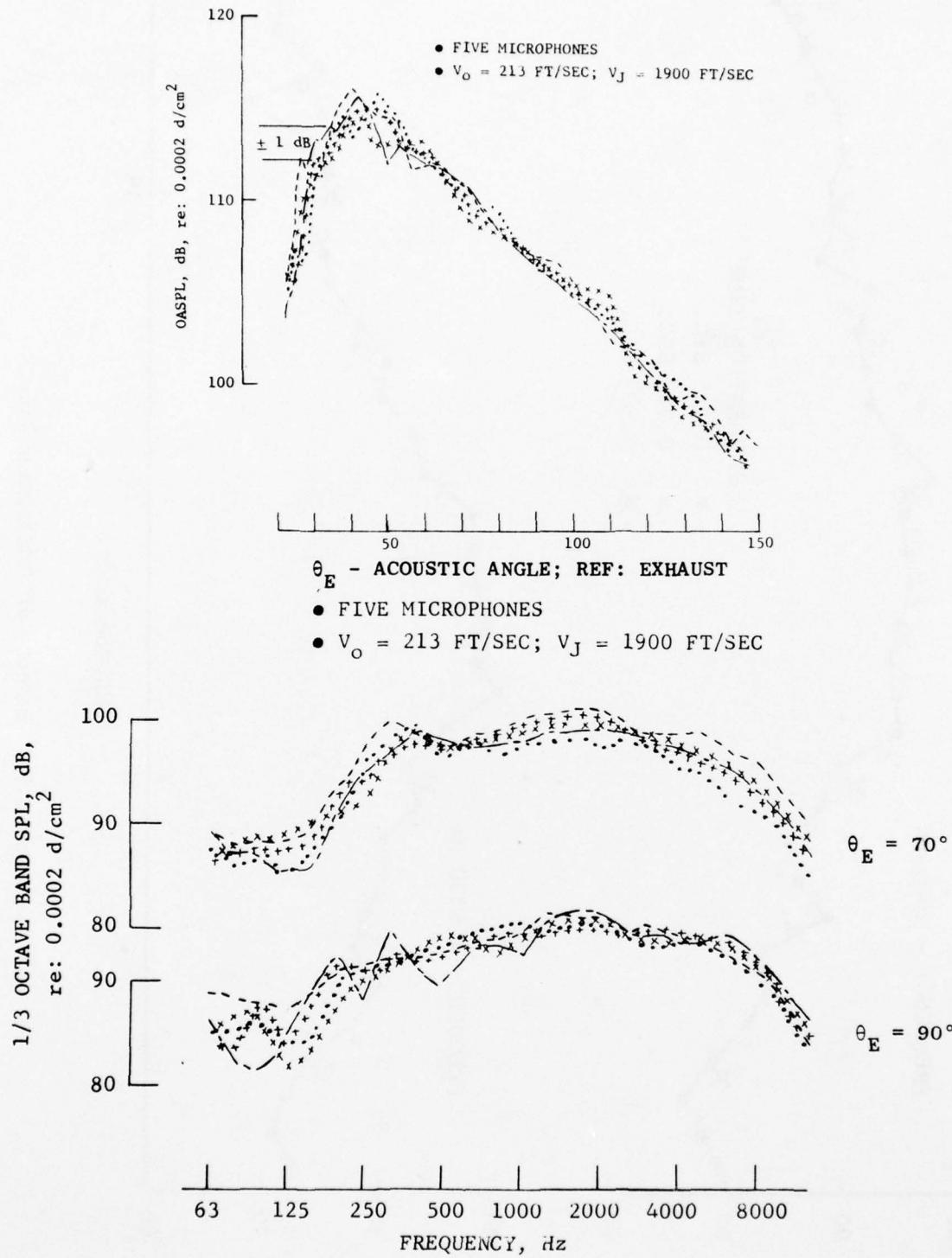


Figure 3-96. Moving Frame Data Repeatability.

between experiments are not treated by confidence limits, so that one expects data from experiments that are physically different to disagree if the confidence limits are tight enough. In this case, confidence limits provide a means of telling how much of the difference between two data sets may be attributed to the statistical fluctuations in the data. If the difference between two data sets is small enough, the experiments may be considered equivalent for engineering purposes even though a hypothesis test fails at a prescribed level of confidence. A major advantage of looking at confidence limits is that they can often show that large variations between data sets may be attributed to statistical variation and that despite wide variations between data, the mean results of the experiments may be identified. In such a case, more data is required to distinguish between the two experiments.

3.3.1.1 Model for the Statistical Error in Moving-Source Data

Confidence limits will be used throughout this report as a measure of the statistical error in data obtained from various moving-source and free jet experiments. It is prudent, therefore, to state the statistical basis for the confidence limits to be used. All confidence statements are based on some model of (and therefore on some assumption about) the randomness in the data. The fundamental assumption to be made is that the acoustic pressure fluctuations follow a Gaussian probability distribution. This assumption is justified by the Central Limit Theorem of probability theory. This theorem asserts that the Gaussian probability distribution "will result quite generally from the sum of a large number of independent variables acting together" (Reference 16, page 66). Since the sound pressure fluctuations at a microphone result from the random motion of a large number of gas molecules, the central limit theorem can be invoked and the acoustic pressure, $p(t)$, can be assumed to follow a Gaussian distribution.

Consider one channel of a 1/3-octave band analysis system as shown in Figure 3-97. If $p(t)$ is a Gaussian random variable representing a microphone signal, it is known that the output of the 1/3-octave filter, $p_{BW}(t)$, will also be a Gaussian variable. Therefore, the output of the squaring circuit will follow a Chi-Square distribution. The sum of several Chi-Square random variables is also a Chi-Square variable. Thus, the output of the finite time integrator, p^2_{BW} , is a Chi-Square variable. Associated with a Chi-Square variable is a number called its "degrees of freedom(n)". The number of degrees of freedom can be interpreted as the "number of independent pieces of data" in the Chi-Square variable. Bendat and Piersol (Reference 16) state that " p^2_{BW} has

$$n = 2B_w T \quad (13)$$

degrees of freedom, where B_w is the bandwidth of the 1/3-octave filter and T is the total integration time". Note that the output of a 1/3-octave analyzer is often expressed in dB, obtained by dividing p^2_{BW} by a reference mean square pressure and taking ten times the logarithm. This

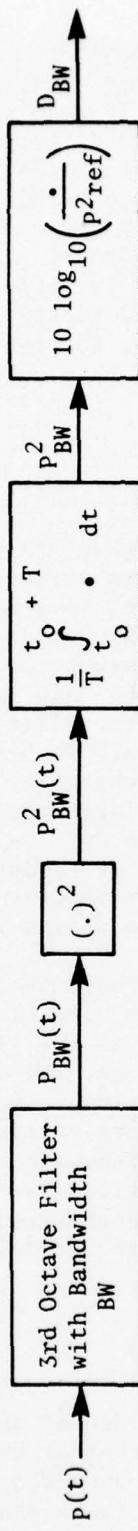


Figure 3-97. Single Channel of 1/3-Octave Band Analysis System.

value, D_{BW} , does not follow a Chi-Square distribution. Therefore, to combine two analyses where the finite time integrals are over disjointed time intervals, one must convert the dB values to mean square pressure values before coaveraging the data sets. Given k data sets, each integrated for time, T, the resulting average will be a Chi-Square variable and have

$$n = 2B_W T k \quad (14)$$

degrees of freedom.

3.3.1.2 Confidence Statements on Single Data Records

Suppose a measured value of p^{-2}_{BW} with n degrees of freedom was obtained. It would be hopefully close to the actual mean square pressure σ^2_{BW} . Given some probability level, it can be stated how close the true mean square pressure is to the measured value of p^{-2}_{BW} . This is a confidence statement in statistical terminology. For the Chi-Square density, it can be written that

$$P_{rob} \left\{ x_{.025, n}^2 < \frac{\bar{p}_{BW}^2 n}{\sigma_{BW}^2} < x_{.975, n}^2 \right\} = .95 \quad (15)$$

where $x_{.025, n}^2$ and $x_{.975, n}^2$ are points on the Chi-Square density curve with n degrees of freedom, as defined in Figure 3-98. The probability statement above is equivalent (by rearranging the inequality) to the following:

$$P_{rob} \left\{ \frac{\bar{p}_{BW}^2 n}{x_{.025, n}^2} > \sigma_{BW}^2 > \frac{\bar{p}_{BW}^2 n}{x_{.975, n}^2} \right\} = .95 \quad (16)$$

This confidence statement may be written as: "The true value of the mean square pressure, σ_{BW}^2 , must lie between $\bar{p}_{BW}^2 n/x_{.975, n}^2$ and $\bar{p}_{BW}^2 n/x_{.025, n}^2$ with a probability of 0.95 (or 95% confidence). Generally, mean square pressure data are presented in dB. Since the logarithm is a monotonically increasing function, eq (16) can be written as

$$P_{rob} \left\{ \hat{D}_{BW} + 10 \log_{10} \left[\frac{n}{x_{.025, n}^2} \right] > D_{BW} > \hat{D}_{BW} + 10 \log_{10} \left[\frac{n}{x_{.975, n}^2} \right] \right\} = .95 \quad (17)$$

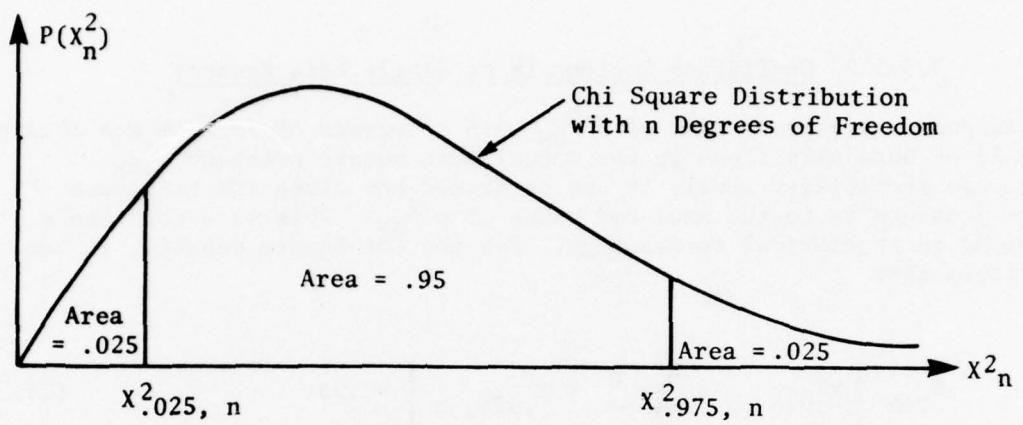


Figure 3-98. Points on Chi Square Curve Used in Eq. (3).

where

$$D_{BW} = 10 \log_{10} \left[\frac{\sigma_{BW}^2}{\bar{P}_{ref}^2} \right] \quad (18)$$

and $D_{BW} = 10 \log_{10} (\bar{P}_{BW})^2 (\bar{P}_{ref})^2$ is the true value of the mean square pressure in dB. For convenience, a plot of $10 \log_{10}(n/x^2 0.025, n)$ as a function of 1/3-octave band center frequency is used in the analysis. The plot is for various values of k (the number of data records in the average) assuming 0.125-second integration time. These curves are shown in Figure 3-99. Note that the statistical error expected in a data sample can be determined before any data is taken. This fact is very useful in planning acoustic tests.

3.3.2 Independence of Data Records

In the previous section (3.3.1), procedures were developed for determining confidence limits for 1/3-octave band data obtained from moving-source measurements. These results were expressed as a set of curves for the average of k statistically independent data sets where the integration time was 0.125 seconds for each analysis. To use these results, techniques must be developed for determining when data sets are independent and for treating partially dependent data.

There are two ways in which independent data may be obtained. Repeated passes of the vehicle at the same test condition result in independent data records. Data from k passes may be averaged (by converting the dB values to mean square pressure, arithmetically averaging, and converting the result to dB), and the confidence curve for k records can then be used to describe the statistical error in the average. Multiple microphones may also be used to obtain independent data records. This is done by spacing them so that the time histories used in the analysis at a particular measurement angle are taken when the vehicle is in disjointed segments of its trajectory. When acquiring moving-source data, the microphones are usually placed on several poles spaced distance, x, apart on a line distance, d, from and parallel to the vehicle trajectory. Also, more than one microphone is often placed on the same pole, spaced h units apart. The typical test setup is shown in Figure 3-100. The conditions necessary for these microphones to yield independent data records will now be derived.

Consider the geometric construction in Figure 3-101. For the signal observed at microphone pole 1 to be independent from the signal obtained at microphone pole 2 at a common measurement angle, θ , the trajectory segments on which these signals were generated must not overlap. The length of these segments is given as the vehicle-velocity multiplied by the analysis time. The analysis time is equal to the integration time used plus the

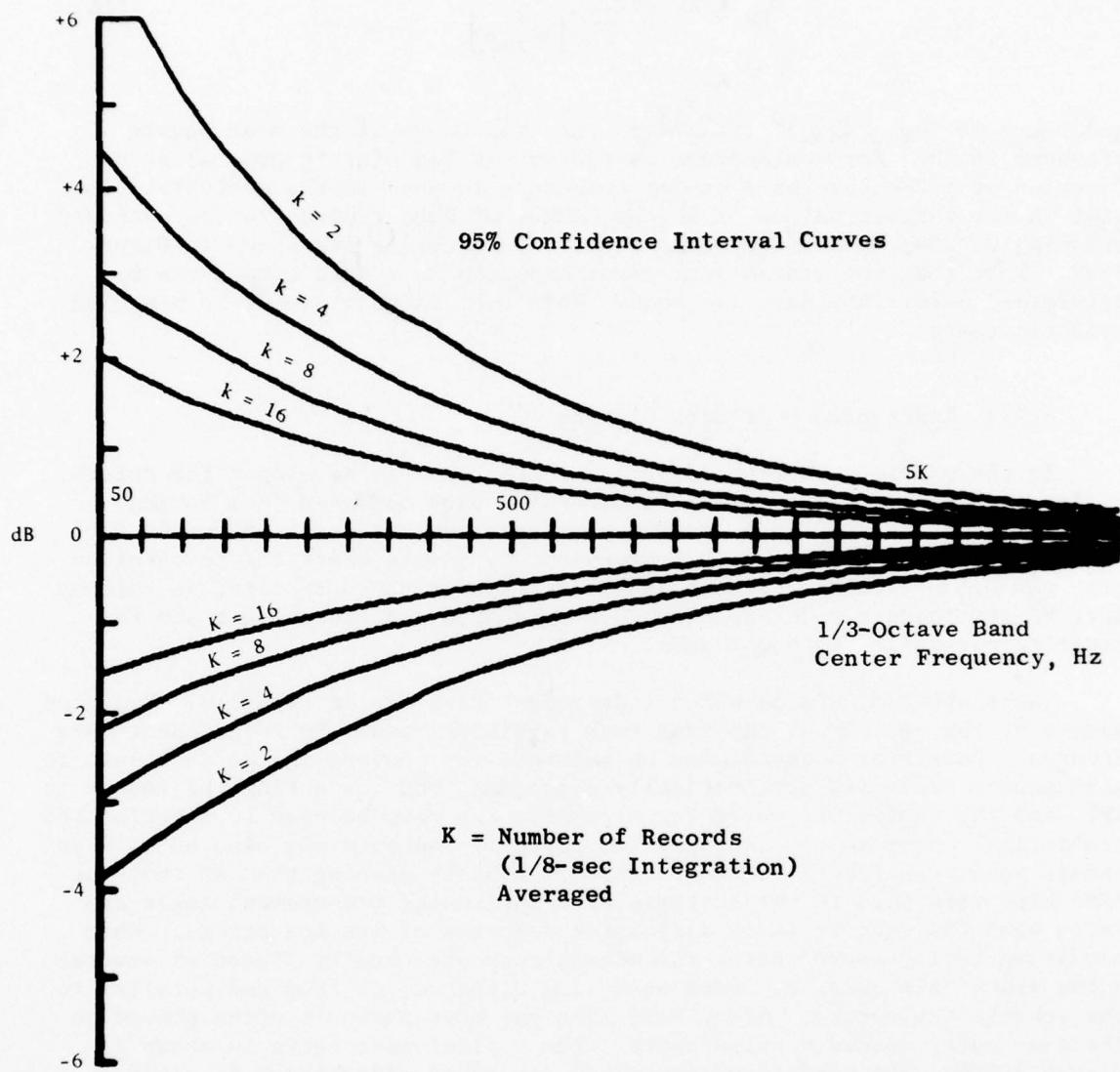


Figure 3-99. 95% Confidence Interval Curves as a Function of Data Record Number.

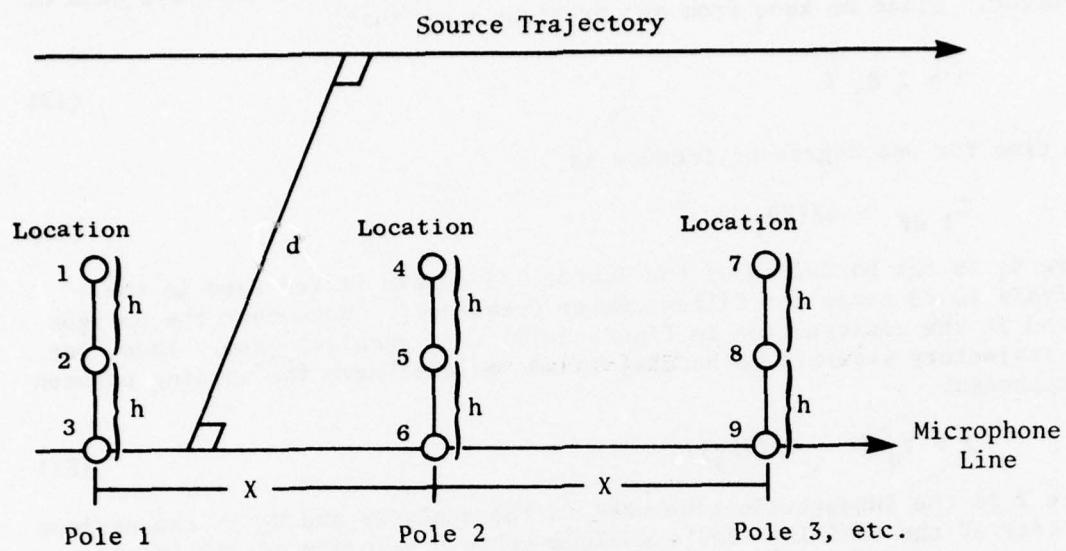


Figure 3-100. Typical Microphone Array for Moving Source Data Acquisition.

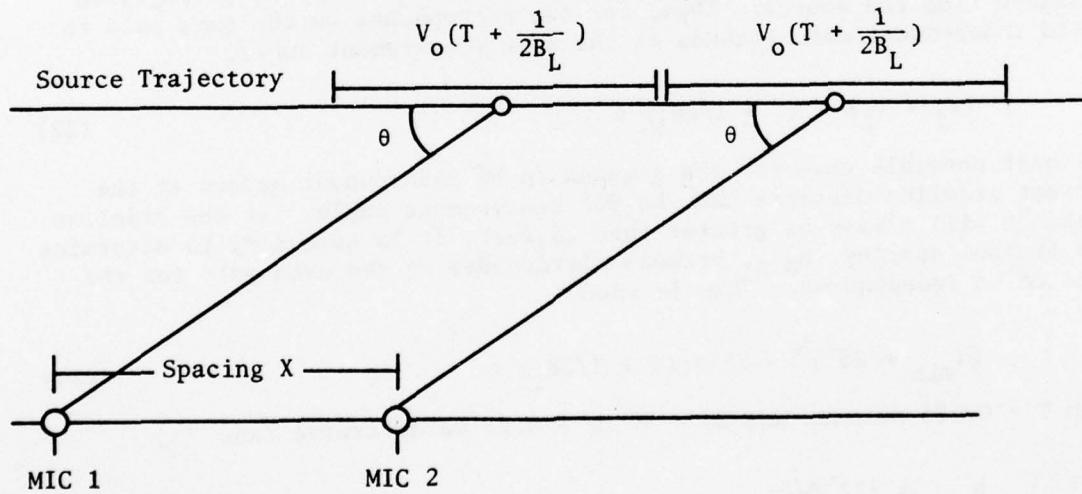


Figure 3-101. Condition for Independence of Microphone Signals from Different Poles.

time equivalent to one degree of freedom for the lowest 1/3-octave band of interest. Since we know from our previous work that

$$n = 2 B_1 T \quad (19)$$

the time for one degree of freedom is

$$T_{1 df} = 1/(2B_1) \quad (20)$$

where B_1 is the bandwidth of the lowest 1/3-octave filter used in the analysis (0.23 times the filter center frequency). Note that the polygon formed in the construction in Figure 3-101 is a parallelogram. Thus, for the trajectory segments to be disjointed, we must have the spacing between microphones,

$$x > V_o (T + 1/(2B_1)) \quad (21)$$

where T is the integration time used in the analysis and V_o is the maximum velocity of the vehicle. For a maximum vehicle velocity of 350 ft/sec, an integration time of 0.125 seconds, and a lowest frequency of interest of 50 Hz, the distance between poles must be $x > 59$ foot (18 meters) for the microphones to yield independent data samples.

To determine the requirement for microphones on the same pole to yield independent data records, consider the construction in Figure 3-102. Since the trajectory segment is the same for both microphones, the only delay between the signal each records is due to the difference in propagation distance from the source. Thus, for two microphones on the same pole to yield independent data records at the same measurement angle,

$$(r_1 - r_2) > (T + 1/2B_1) c \quad (22)$$

The best possible case for the signals to be independent occurs at the closest sideline distance and the 90° measurement angle. If the sideline distance will always be greater than 25 feet, it is necessary to determine the minimum spacing, h_{min} , between microphones on the same pole for the data to be independent. This is when

$$(h_{min} + 25^2)^{1/2} - 25 = (T + 1/2B_1) c \quad (23)$$

With $T = 0.125$ seconds and $B_1 = 50$ Hz \times 0.23 we determine that

$$h_{min} = 212 \text{ feet} \quad (24)$$

Consequently, microphones on the same pole usually will not yield independent data records.

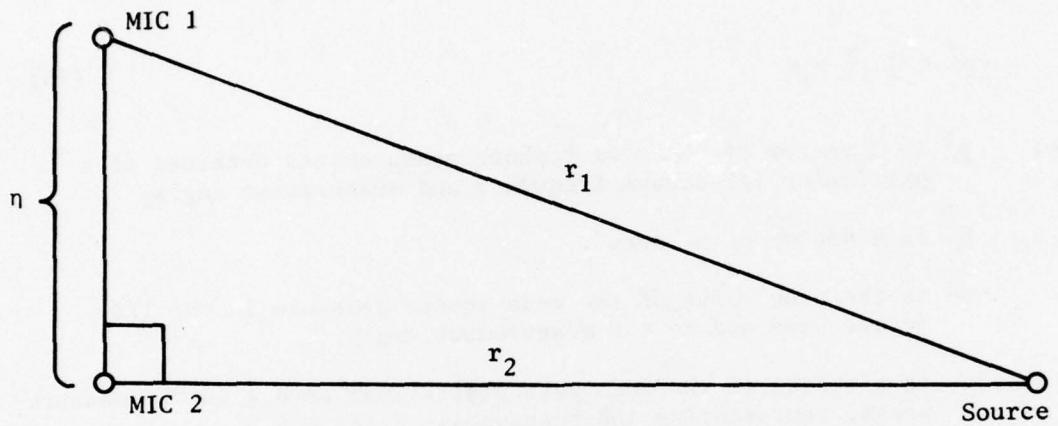


Figure 3-102. Condition for Independence of Microphone Signal for the Same Poles.

Averaging Data Records:

The analysis above shows that moving-source test runs will generate a mixture of correlated and independent data records. The questions of how to combine the data to obtain the best estimate (in the minimum variance sense) of the mean square pressure in a particular 1/3-octave band, and how to determine the effective number of data records in the estimate so that the appropriate confidence limit curve can be chosen involve estimation theory. The solutions may be obtained as shown below.

Consider the following model for a moving source data run:

$$\underline{p}^2 = \underline{U} \sigma^2 + \underline{\varepsilon} \quad (25)$$

where: \underline{p}^2 is a vector of the m microphone measurements obtained at a particular 1/3-octave frequency and measurement angle.

\underline{U} is a vector of m "ones".

σ^2 is the true value of the mean square pressure in the 1/3-octave band and at the measurement angle.

and $\underline{\varepsilon}$ is a vector of the zero mean statistical errors in the measurements, representing the randomness, $E\{\underline{\varepsilon}\} = \underline{0}$.

Let $R = E\{\underline{\varepsilon} \underline{\varepsilon}^T\}$, the covariance matrix of the error. This matrix equals the covariance matrix of \underline{p}^2 , the measurement vector. If an estimate of σ^2 from the data \underline{p}^2 is desired, Reference 17 shows that the unbiased estimate of σ^2 , (with minimum variance) which will be designated $\hat{\sigma}^2$, is given by:

$$\hat{\sigma}^2 = \Sigma \underline{U}^T R^{-1} \underline{p}^2 \quad (26)$$

where

$$\Sigma = [\underline{U}^T R^{-1} \underline{U}]^{-1} \quad (27)$$

is the variance of $\hat{\sigma}^2$, the estimate.

To evaluate the above, the error covariance matrix, R must be determined. Each measurement value, p_i^2 , has a variance which may be expressed in terms of its degrees of freedom and the true mean pressure because the individual measurements are related to Chi-Square variables. The variance is:

$$VAR\{p_i^2\} = 2\sigma^4/n \quad (28)$$

where n is the number of degrees of freedom associated with a single 1/3-octave integration. Thus, it is possible to write the error covariance matrix as

$$R = \frac{2\sigma^4}{n} \begin{bmatrix} 1 & \rho_{12}, & - & - & - & \rho_{1,m} \\ \rho_{21} & 1 & & & & \\ \rho_{31} & & 1 & & & \\ & & & 1 & & \\ & & & & 1 & \rho_{m-1,m} \\ \rho_{m,1} & \rho_{m,2} & - & - & - & \rho_{m,m-1} \end{bmatrix} = \frac{2\sigma^4}{n} \Phi \quad (29)$$

where ρ_{ij} is the correlation coefficient between the i^{th} and j^{th} measurement. If the data sets are independent, $\rho_{ij} = 0$, if the data is perfectly correlated (as is usually the case with data obtained from two microphones on the same pole) $\rho_{ij} \approx 1$. If the trajectory segments partially overlap, it is possible to show that ρ_{ij} equals the fraction of overlap when the 1/3-octave integration times are equal. The required estimate of the mean square pressure in a particular 1/3-octave band can be written as:

$$\hat{\sigma}^2 = [\underline{U}^T \phi^{-1} \underline{U}]^{-1} \underline{U}^T \phi^{-1} \underline{P}^2 \quad (30)$$

Note that the estimate depends only on the correlation coefficients and does not require the variance of each measurement. The variance of the estimate is:

$$\Sigma = \frac{2\sigma^4}{n[\underline{U}^T \phi^{-1} \underline{U}]} \quad (31)$$

since $\underline{U}^T \phi^{-1} \underline{U}$ is a scalar. Because $\hat{\sigma}^2$ is a Chi-Square variable, $E\{\hat{\sigma}^2\} = \sigma^2$, its number of degrees of freedom must be

$$n\hat{\sigma}^2 = [\underline{U}^T \phi^{-1} \underline{U}] n \quad (32)$$

Thus, the equivalent number of data records, k , used to choose the confidence interval for the estimate is

$$k = \underline{U}^T \phi^{-1} \underline{U} \quad (33)$$

where \underline{U} is an m vector of "ones" and ϕ is the matrix of correlation coefficients of the m individual measurements.

3.3.3 Statistical Comparison of Moving-Source Data Sets

Comparison between data from two different tests such as flight and high-speed train runs can be performed using a statistical hypothesis test. A hypothesis test is a method for determining whether the differences between the data sets can be attributed to the natural statistical variations in the data or result from physical differences between the experiments. The hypothesis test can only reject the hypothesis that the differences between data records are due to statistical variation. The result of a hypothesis test can not confirm the hypothesis that the experiments are identical. Therefore, it is important that sufficient data be available from each experiment so that the accuracies of the tests are acceptable in an engineering sense. A rejection of the hypothesis that the data sets are equivalent should be examined with engineering judgment. If the differences between the data are small enough for a particular purpose, there is no reason for not assuming that the underlying experiments are equivalent in that context. Hypothesis testing provides a method for attributing unacceptably large differences between data sets to either statistical variation (in which case, more data is required to determine if there is a difference between the experiments) or to a physical difference between the experiments.

To test the hypothesis that two sets of 1/3-octave band data are equivalent, the ratio between the average pressure squared values at each frequency must be computed. Since the average pressure squared values, P_{Bw1}^2 and P_{Bw2}^2 , are Chi-Square random variables, we know from statistical theory that the ratio follows the F distribution. Associated with the F distribution are two degrees of freedom, N_1 and N_2 . N_1 is the number of degrees of freedom associated with the Chi-Square variable in the numerator of the ratio, and N_2 corresponds to the number of degrees of freedom associated with the denominator. Thus, averaged outputs of a particular 1/3-octave analysis channel results in:

$$F_{N_1, N_2} = \frac{\bar{P}_{1, N_1}^2}{\bar{P}_{2, N_2}^2} \quad (34)$$

where $N_1 = 2k_1 T_1 B_w$

and $N_2 = 2k_2 T_2 B_w$

and $T_i =$ The integration time used in the analysis of the records in data set i .

$k_i =$ The number of data records integrated for time T_i in data set i .

AD-A041 849

GENERAL ELECTRIC CO CINCINNATI OHIO AIRCRAFT ENGINE GROUP F/G 20/1
HIGH VELOCITY JET NOISE SOURCE LOCATION AND REDUCTION, TASK 4. --ETC(U)
FEB 77 W S CLAPPER, E J STRINGAS

DOT-05-30034

UNCLASSIFIED

3 OF 6
AD
A041 849

R77AEG189

FAA-RD-76-79-4

NL





849

B_w = The bandwidth of the 1/3-octave filter ($B_w = 0.23$ times the filter center frequency)

The confidence interval for the F random variable may now be computed for the 95% confidence interval as follows:

$$P_{rob} \left\{ F_{N_1, N_2, .025} < \frac{\bar{P}_{1, N_1}^2}{\bar{P}_{2, N_2}^2} < F_{N_1, N_2, .975} \right\} = .95 \quad (35)$$

where $F_{N_1, N_2, .025}$ and $F_{N_1, N_2, .975}$ are the points on the F distribution curve, N_1 and N_2 degrees of freedom, chosen in a manner similar to those used to define the single record confidence interval. One-third-octave band data is generally expressed in dB. Since the logarithm is a monotonically increasing function, the confidence interval can be written as

$$\text{Prob} \{ 10 \log_{10} (F_{N_1, N_2, .025}) < D_1 - D_2 < 10 \log_{10} (F_{N_1, N_2, .975}) \} = .95 \quad (36)$$

where D_i is the 1/3-octave band output in dB from data set i:

$$(D_i = 10 \log_{10} (\bar{P}_{i, N_i}^2 / P_{ref}^2)) \quad (37)$$

The hypothesis test may be stated as follows: "If the difference in dB between the two data sets falls outside the inequality in brackets above, reject the hypothesis that the data sets come from equivalent experiments with 95% confidence." Note that if different amounts of data (i.e., $k_1 \neq k_2$ or $T_1 \neq T_2$) are used to generate the data from the two experiments, different test limits result for $D_1 - D_2$ and for $D_2 - D_1$. To simplify the comparison of data presented in this report, the test rejection limits are plotted in Figure 3-103 for various values of k_1 and k_2 (the number of records in each average) assuming the integration times, T_1 and T_2 , are 0.125 seconds.

It is important to note the limits for the hypothesis test do not depend on the values of the measured data. Therefore, if experiments are to be conducted for the purpose of comparing two different measurement techniques, the curves in Figure 3-103 can be used to determine the amount of data required to make an adequate comparison before the experiments are performed. This result is a valuable tool in the planning of efficient test programs.

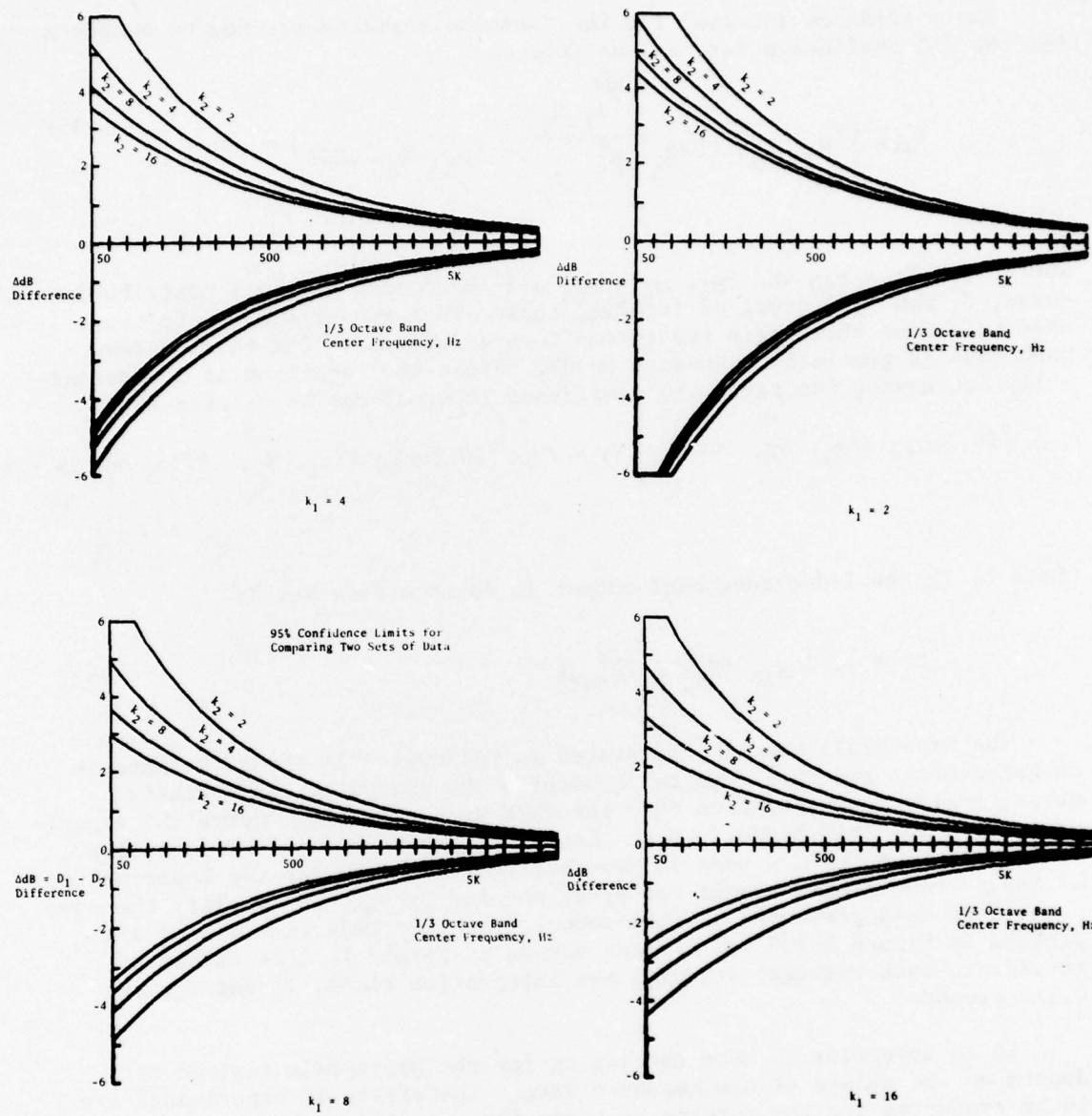


Figure 3-103. 95% Confidence Rejection Limits for $D_1 - D_2$
 k_i = number of .125 Second Integrations in D_i .

3.4 Analytical Transformation Screening Study

This section describes various approaches that have been suggested for the problem of transforming data acquired in a free jet facility to flight conditions. At the outset, it is pertinent to note the following. So long as measurements in the free jet facility are confined to conventional far-field measurements (in the sense of SPL spectra measurements on a fixed set of microphones on a given arc or sideline far from the free jet), and if the free jet-to-primary-nozzle area ratio is of the order of 50 or so, there is no absolutely defensible, perfectly rigorous procedure of carrying out this transformation. The reason is that, in general for a given frequency band, the transformation must depend on the type of sources producing the flight noise. There is no unique procedure of estimating such source distributions from measurements of sound pressure levels alone in the far field. The more popular approach to this transformation that has been adopted by various investigators (References 18, 19, and 20) is schematically shown in Figure 3-104. The free jet is assumed to provide an acoustic environment corresponding to a parallel-flow, doubly infinite jet. In fact, most investigations have gone a step further and treated the parallel-flow jet as a slug-flow jet. Investigators have first sought to answer the question of what noise signature would be produced by the same distribution of sources in an acoustic environment where the "jet" flow is now a parallel, slug flow of infinite radius, i.e., an infinitely large wind tunnel (with the microphones now immersed in the wind). What has not been clarified is under what circumstances such an exercise can be carried out to be independent of source type or independent of source frequency.

Once this transformation from "free jet" to wind tunnel is achieved, it is a trivial matter to rigorously transform from the wind tunnel frame to the flight condition since the flight frame of reference is related to the wind tunnel frame by a straightforward Galilean transformation.

A second approach is also possible based on the following philosophy. As illustrated in Figure 3-105, it is arguable that, with free jet-to-primary-nozzle area ratios of 50 or so and with the free jet exit plane displaced upstream of the primary nozzle exit plane (to enable acquisition of inlet arc data), what the free jet achieves is a proper simulation of the relative velocity environment insofar as simulation of the primary nozzle plume aerodynamics goes but very little of the acoustic simulation of uniform flow over the sources. Of course, at extremely shallow angles to the jet exhaust axis, we may expect an acoustic impact of the free jet in the sense of a refractive effect. Based on this notion, one may first attempt a transformation of the free jet data to a static frame somewhat analogous to the manner in which Professor Ribner's group has sought to separate jet noise directivity into a combination of refractive, convective, and "basic" directivity effects. Once such a "basic" directivity has been extracted, we can attempt a static-to-flight transformation. This, again, cannot be accomplished without attempting to say something about the nature of the sources. Section 4.2 will give the details of this source decomposition procedure.

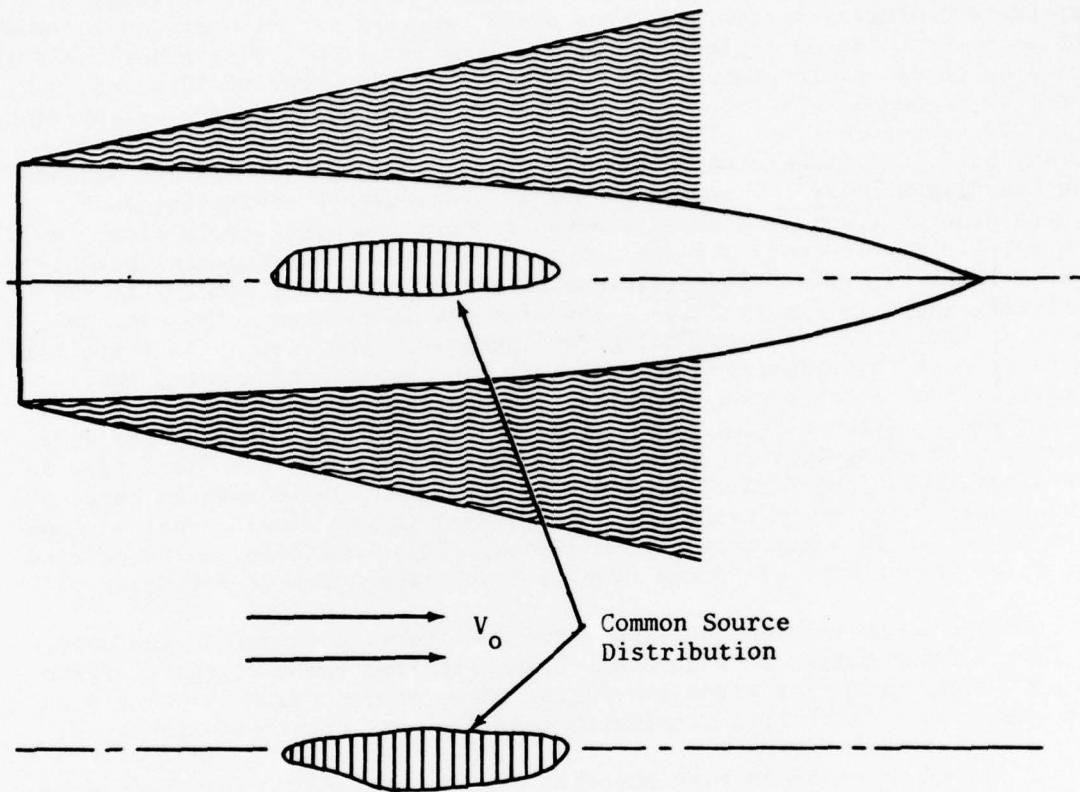


Figure 3-104. Free Jet to Wind Tunnel Transformation.

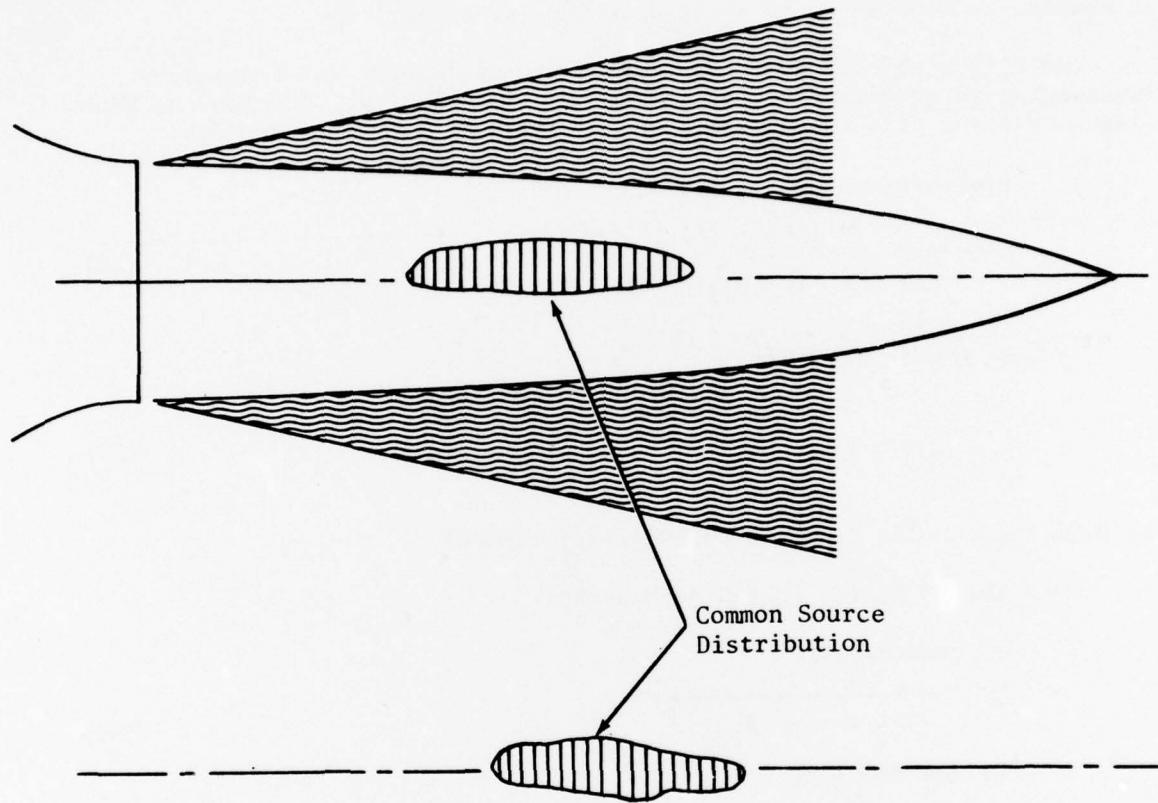


Figure 3-105. Free Jet to Static Transformation.

For purposes of the screening study, it is instructive to examine theoretical solutions for typical point singularities in the situations of flight, static and in a free jet. In the free jet, the results depend on the frequency, flow profile and location of the source. At low frequencies, we assume a plug-flow model, while at high frequencies a parallel sheared flow is assumed. Only asymptotic low and high frequency limits are presented; we assume the sources to be located on the jet centerline.

The flight and static results are quite well-known and frequency-independent so we will first state the free jet results. The low and high frequency asymptotic results for various types of singularities are:

1. pressure source:

$$p' \sim \frac{1}{R(1 - M \cos(\theta_{FJ}))^2} \quad (38)$$

at low frequencies

$$p' \sim \frac{1}{R(1 - M \cos(\theta_{FJ}))} \quad (39)$$

at high frequencies (outside the zone of silence).

Note that M is the flight Mach number.

2. xx quadrupole:

$$p' \sim \frac{1}{(1 - M \cos(\theta_{FJ}))^2} \quad (40)$$

at low frequencies

$$p' \sim \frac{\cos^2(\theta_{FJ})}{[1 - M \cos(\theta_{FJ})]} \quad (41)$$

at high frequencies (outside the zone of silence).

3. xr quadrupole:

$$p' \sim \frac{2 \cos(\theta_{FJ}) \sin(\theta_{FJ})}{[1 + (1 - M \cos \theta_{FJ})^2]} \quad (42)$$

at low frequencies

$$p' \sim \frac{\cos(\theta_{FJ}) \sqrt{(1 - M \cos \theta_{FJ})^2 - \cos^2 \theta_{FJ}}}{(1 - M \cos \theta_{FJ})} \quad (43)$$

at high frequencies outside the zone of silence.

4. rr quadrupole:

$$p' \sim \frac{2 \sin^2 (\theta_{FJ})}{[1 + (1 - M \cos \theta_{FJ})^2]} \quad (44)$$

at low frequencies

$$p' \sim \frac{[(1 - M \cos \theta_{FJ})^2 - \cos^2 \theta_{FJ}]}{(1 - M \cos \theta_{FJ})} \quad (45)$$

at high frequencies and outside the zone of silence.

The results of x and r dipoles are not given explicitly and can easily be deduced from the above.

The high frequency results have been given outside the zone of silence. Inside the zone of silence, they would all be modified by an exponential attenuation factor (for p') as:

$$\exp(-k \int_0^{r_\sigma} f dr) \quad (46)$$

where $f(r) = |(1 - M(r) \cos \theta_{FJ})^2 - \cos^2 \theta_{FJ}|^{1/2}$ and r_σ is uniquely defined (depending on θ_{FJ}) as the radius at which $f(r_\sigma) = 0$. $k = \omega/c$, where ω is the source frequency in radians/second and c the speed of sound.

In terms of a retarded radius R and retarded angle θ_R (Figure 3-106), the corresponding flight results (frequency-independent) are:

1. pressure source:

$$p' \sim \frac{1}{R(1 + M \cos \theta_R)} \quad (47)$$

2. xx quadrupoles:

$$p' \sim \frac{\cos^2 (\theta_R)}{(1 + M \cos \theta_R)^3} \quad (48)$$

3. xr quadrupoles:

$$p' \sim \frac{\sin (\theta_R) \cos (\theta_R)}{(1 + M \cos \theta_R)^3} \quad (49)$$

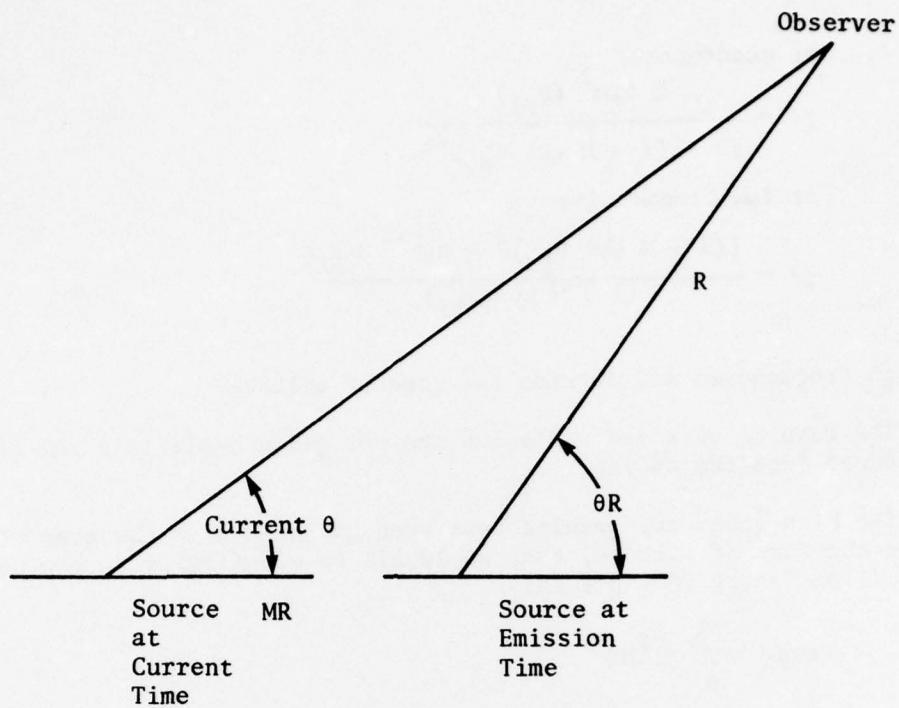


Figure 3-106. Definition of Retarded Coordinate, θ_R .

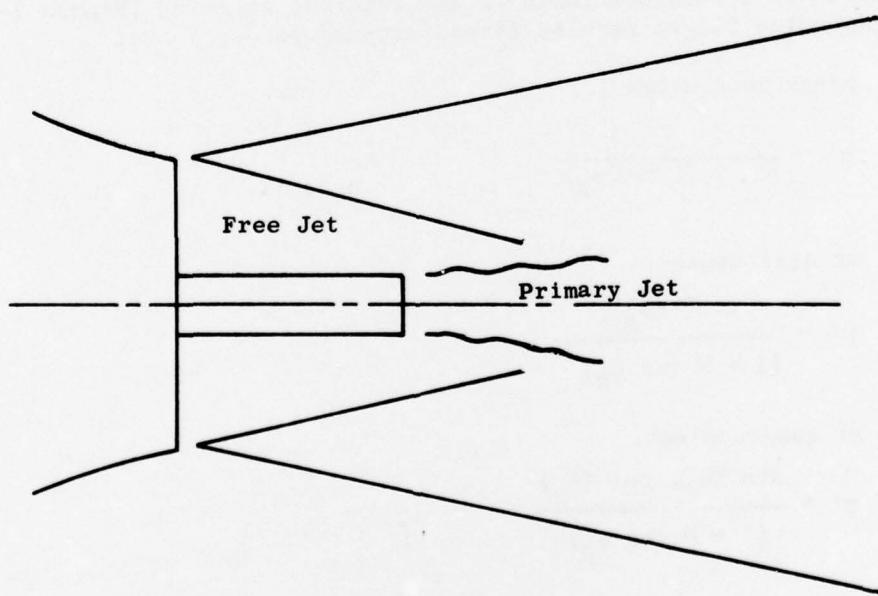


Figure 3-107. Schematic Illustrations for Free Jet Flow Field Relative to Primary Nozzle Plume.

4. rr quadrupoles:

$$p' \sim \frac{\sin^2(\theta_R)}{(1 + M \cos \theta_R)^3} \quad (50)$$

The zone of silence for the free jet of Figure 3-106 is the region $0 < \theta_{FJ} < \cos^{-1}(1/1 + M)$.

The approach to the problem of transforming free jet data to wind tunnel conditions may be explained in terms of Figure 3-108. Here the approach of Reference 18 is illustrated. The free jet is assumed to be large enough relative to the primary jet such that the evolution of plane waves from the source region is complete and also large enough so that the outgoing part of these plane waves is assumed to be the same as if the primary jet were in a wind tunnel. Then Reference 18 points out that this outgoing wave will be (1) refracted at the interface of the free jet and still-air and (2) suffer some form of transmission amplification or loss as it negotiates the free-jet, still-air interface. To take account of the refractive effect, Reference 18 points out that we may expect the signal emerging at θ_{FJ} in the free jet experiment to correspond to one emerging at a lesser angle, θ_R , in the flight case where θ_{FJ} and θ_R are related by

$$\cos \theta_{FJ} = \frac{\cos \theta_R}{1 + M \cos \theta_R} \quad (51)$$

It is a characteristic feature of such methods (References 18, 19, and 20) that no use is made in these methods of free jet data within the zone of silence (i.e., no real value of θ_R is related to θ_{FJ} for the above relation for $\theta_{FJ} < \cos^{-1}(1/1 + M)$ and conversely no real value of θ_{FJ} corresponds to $\theta_R > (\pi - \cos^{-1}(1/1 + M))$ and also one-to-one correspondence between free jet and flight data cannot be used to infer flight data for $\theta_R > \pi - \cos^{-1}(1/1 + M)$). The latter is an almost trivial restriction since we rarely even acquire flight data to angles from the jet exhaust axis as high as $(\pi - \cos^{-1}(1/1 + M))$. The former aspect is philosophically bothersome as there is a great deal of free jet data in the zone of silence especially at the lower frequencies which is not being used in this method.

To take account of effect (2), Reference 18 uses the Ribner-Miles (Reference 21 and 22) solution to the problem of transmission of plane waves across a vortex sheet to infer the transmission coefficient. The net result is a procedure to correct free jet data to flight by means of an angle shift formula as expressed above by the $\theta_{FJ} - \theta_R$ relation and an amplitude correction formula as expressed by the Ribner-Miles solution in Reference 18. The amplitude correction formula in Reference 18 is frequency or source-type independent and generally calls for applying a negative correction (in dB) to the exhaust arc free jet data ($\theta_R \geq 90^\circ$) and a positive correction (in dB) to the inlet arc free jet data to correct it to flight. Such amplitude corrections are clearly in the right direction as evidenced by cursory visual comparison of flight and free jet data. It is their source type and frequency independence that needs reexamination.

Turbulent Mixing Studies

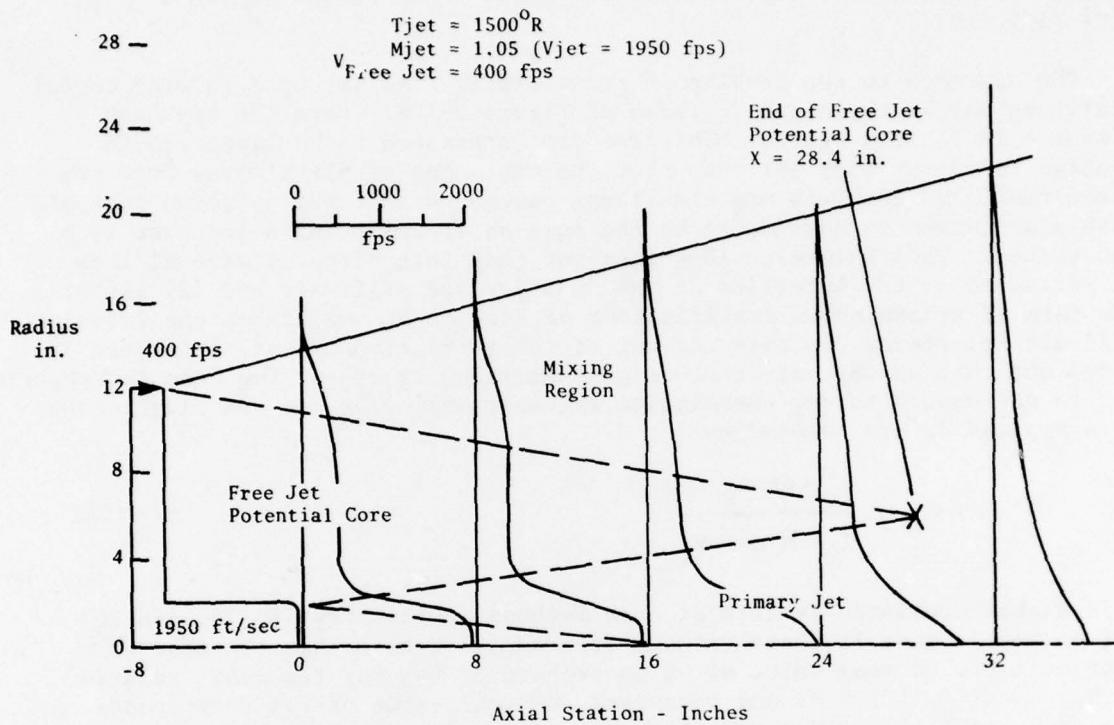


Figure 3-108. Scaled Representation of GE Free Jet Flow Field.

What are the prospects of rendering the free jet-flight transformation independent of source type and source frequency by means of an angle-shift, amplitude-correction formula? The previously tabulated basic solutions for various types of singularities in free jet and flight at low and high frequencies should be of great help in deciding this. Considering first the frequency dependence, using the angle shift formula, the ratio of amplitudes [$p'_{\text{flight}} : p'_{\text{free jet}}$] at the same far-field radius for a pressure source works out to $1/(1 + M \cos \theta_R)$ at low frequencies and $1/(1 + M \cos \theta_R)^2$ at high frequencies. This clearly shows that the amplitude correction factor has to be frequency dependent, being generally greater at low rather than high frequencies. The above amplitude ratios apply not only to pressure sources but all purely axial singularities (i.e., the monopole, x-dipole, xx quadrupole, etc.).

Consider next the amplitude ratio ($p'_{\text{flight}} : p'_{\text{free jet}}$) after using the angle shift formula and at the same far-field radius for xr quadrupole. The ratio is

$$\frac{[1 + (1 + M \cos \theta_R)^2] \sin (\theta_R)}{2 [1 + M \cos \theta_R]^3 \sqrt{[1 + M \cos \theta_R]^2 - \cos^2 (\theta_R)}}$$

at low frequencies which may be rewritten (at low frequencies) as:

$$(\text{press. amplitude correction for pressure source}) \times \frac{[1 + (1 + M \cos \theta_R)^2]}{2} \times \frac{\sin (\theta_R)}{\sqrt{[1 + M \cos \theta_R]^2 - \cos^2 \theta_R}}$$

At high frequencies, the ratio is $1/(1 + M \cos \theta_R)^2$ which is identical to that for a pressure source.

Finally, for the rr quadrupole, the ratio of amplitudes for the free jet and flight are again the same as for a pressure source at high frequencies, but for low frequencies, the ratio is:

$$(\text{Ratio for pressure source}) \times \left[\frac{1 + (1 + M \cos \theta_R)^2}{2} \right] \times \frac{\sin^2 (\theta_R)}{[(1 + M \cos \theta_R)^2 - \cos^2 (\theta_R)]}$$

The above exercise establishes two facts. At high frequencies, the transformation from free jet to flight by means of an angle shift and amplitude correction (equal to $(1 + M \cos \theta_R)^{-2}$ for the pressure) should work out to be independent of source type. At low frequencies, study of the ratios ($p'_{\text{flight}} : p'_{\text{free jet}}$) after applying the angle shift, show that the ratio ($p'_{\text{flight}} : p'_{\text{free jet}}$) is lesser for an xr or rr quadrupole than that for a pressure source in the exhaust arc and greater than that for a pressure source in the inlet arc. Clearly the corrections of all the

purely axial singularities (pressure source, monopole, axial dipole, xx quadrupole, etc.) are identical to that for a pressure source at all frequencies. Thus, for arbitrary frequencies in general, the correction cannot be independent of source type. Moreover, using a source-type independent correction can lead to overestimation of rear arc flight noise and underestimation of flight noise in the inlet arc. A similar error will result if, as in (References 18, 19, and 20), a high frequency result is supplied in a frequency-independent manner.

Consider now the prospects for a transformation to static conditions without using any angle shift formula. At low frequencies, the ratio ($p'_{FJ} : p'_{\text{static}}$) at fixed θ , R is:

$$\frac{1}{(1 - M \cos \theta)^2}$$

for the axial singularities and

$$\frac{1}{[\frac{1}{2} + \frac{1}{2}(1 - M \cos \theta)^2]}$$

for transverse singularities. To small order in $(M \cos \theta)$ (valid for the flight transformation problem since $M \geq 0.3$ usually) the latter is $(1 - M \cos \theta)^{-1}$. There is, therefore, some difference between corrections for transverse and axial singularities but the error is not great in using a source-type independent correction procedure (roughly 2 dB at $M = 0.3$). At high frequencies, the ratios [$p_{\text{free jet}} : p_{\text{static}}$] for various types of singularities are:

$$\{\text{axial singularities}\} \frac{(\text{exponential shielding factor})}{(1 - M \cos \theta)}$$

where (exponential shielding factor) stands for the previously mentioned shielding factor in the zone of silence and the factor is unity outside the zone of silence.

$$\{\text{xr quadrupole}\} \frac{[\sqrt{(1 - M \cos \theta)^2 - \cos^2 \theta}]}{\sin \theta}$$

x (correction for axial singularities)

$$\{\text{rr quadrupole}\} \frac{(1 - M \cos \theta)^2 - \cos^2 \theta}{\sin^2 \theta}$$

x (correction for axial singularities)

The fact that the ratio tends to zero as θ tends to the ray of silence $\cos^{-1} (1/1 + M)$ at high frequencies should not be taken too seriously as the asymptotic high frequency theory is actually not uniformly valid as θ tends to $\cos^{-1} 1/1 + M$.

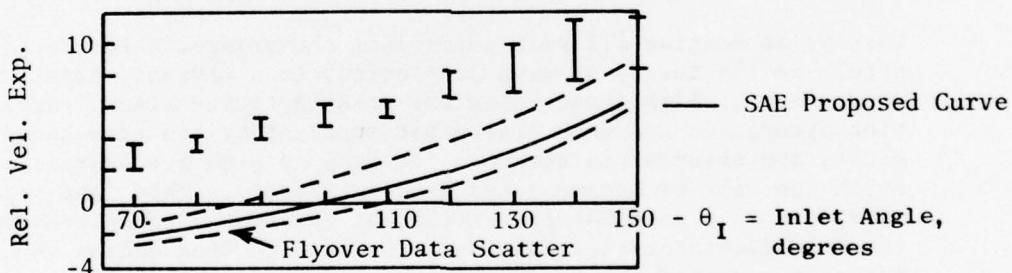
Thus, in contrast to the free jet flight transformation via the wind tunnel, the free jet-to-flight transformation is reasonably independent of source type (to an error of about 2 dB at $M = 0.3$) for low frequencies. It is not independent of source type at high frequencies, but there are several mitigating factors to be considered here:

1. Within the zone of silence, the ratio [p' free jet : p' static] is essentially dominated by the exponential shielding factor which is independent of singularity type.
2. The nonuniform validity of the high frequency expansion as $\theta \rightarrow \cos^{-1} (1/1 + M)$ has already been noted. Of more concern is the possibility of large values of the ratio $\{\sqrt{(1 - M \cos \theta)^2} - \cos^2 \theta \div \sin \theta\}$ as $\theta \rightarrow \pi$. But we usually do not acquire data beyond $\theta = 5\pi/6$ and, also at these angles, the transverse singularities would not be expected to contribute much either in the free jet or statically.
3. At high frequencies, in attempting to subtract out the shielding or refractive effect of the flow, it may be wiser to treat the source region as extensive (especially in view of the earlier noted fact that the free jet flow environment, while adequate aerodynamically, may be quite inadequate acoustically - see Figure 3-108 in this regard which is a scale drawing of the GE hybrid or free jet facility) and apply the correction factor for the Green's function or that for the pressure source.
4. Lastly, as Section 4.2 will point out, the prospects for relying purely on the theory of wave propagation in a laminar, parallel, shear flow at high frequencies are actually quite bleak. Refraction saturation and some absorption of sound by the turbulent eddies are observed in the free jet data at high frequencies which can only be accommodated semiempirically. This last feature mitigates to a considerable extent any apparent difficulties with the free jet-to-static transformation at high frequencies in terms of a dependence on source type.

The basic "theoretical" conclusions of this screening study can be summarized as follows. The problem of attempting to extract from conventional free jet data, the data to be expected if either the uniform flow region is infinitely extensive or if the free jet flow is absent acoustically (the static case) cannot be resolved in an absolutely rigorous manner. There are four reasons one should choose to adopt the route of first attempting to infer the "static" signature. Section 4.2 will deal comprehensively with how General Electric tackled the problem of transforming the data from "static" to flight conditions. First, with area ratios of 50 or so and

with the free jet exit plane offset to be substantially upstream of the primary nozzle exit plane as Figure 3-107 shows, at least in the GE free jet facility, the free jet appeared to provide adequate simulation of relative velocity from the point of primary-nozzle plume aerodynamic evolution but hardly much of a uniform flow environment from an acoustic point of view (in the sense of a uniform flow region much greater than the extent of source region). This suggested a transition of the data first to a static frame of reference. Second, philosophically the procedure adopted herein seems preferable to those of (References 18, 19, and 20) inasmuch as those procedures do not use all of the data taken in a free jet experiment and are also unable to predict flight data for an angle exceeding $\cos^{-1}(\cos(\theta_{FJ})/(1 - M \cos \theta_{FJ}))$ where θ_{FJ} is the largest angle from the jet exhaust axis for which free jet data is taken. Third, study of point singularity solutions indicate a modest advantage in trying to carry out the free jet - static transformation in terms of independence of source type.

The fourth (and perhaps most important) reason why we prefer the present approach is that (as explained in Reference 20) the approaches of (References 18 and 19) was, in fact, the approach that we employed first. Comparisons with flight data essentially revealed a problem similar to that reported in References 19 and especially 23, that such an approach considerably underestimates the inlet flight noise data as shown in Figure 3-109 where the effective velocity exponent for the OASPL for a conical nozzle is shown. Figure 3-109 is actually taken from Reference 23. Apparently employing a correction for the total noise signature based only on the correction for purely axial singularities causes an underestimation of the correction needed in the inlet arc, as might be expected from the study of point singularities in a free jet and in flight which did demonstrate (at low frequencies) that transverse singularities need a greater correction than axial singularities.



$$\bullet V_J = 1000 \text{ to } 1669 \text{ fps}, T_j = 900^{\circ}\text{F}$$

Figure 3-109. Ability of Free Jet-Wind Tunnel- Flight Transformation to Predict Flight Noise from Reference 4.

4.0 SURVEY LEADING TO SELECTION OF INFLIGHT SIMULATION TECHNIQUE

The objective of Task 4 was to evaluate techniques for investigating the effect that flight motion has on both the noise source characteristics and on the noise propagation to the observer. The intent was to investigate alternative methods of performing fixed and moving experiments and to then apply the best method in the remaining portion of the program (Tasks 3 and 5) to gather data and, hopefully, resolve the most effective means of accounting for "inflight effects" without resorting to costly and relatively imprecise flight tests.

As shown in Section 3, the technical method of approach was to explore a wide range of possible methods to achieve this objective. This study identified the advantages and disadvantages of several fixed- and moving-frame facilities. Where possible, meaningful exploratory experimental work was performed to aid in the decision making.

Several closed-circuit wind tunnels, specifically NASA-Lewis, NASA-Ames, and NASA-Langley, were high on the potential list. These facilities were rejected after being subjected to the rather severe acoustic and aerodynamic requirements (Section 3.1). Limited capabilities plus the necessity for extensive modifications ultimately eliminated each facility.

The (NSRDC) anechoic, open-throat (free jet) wind tunnel was also dropped from consideration primarily due to the practical fact that any government desire to perform the necessary additions plus the actual time involved in adding the required air capacity would extend beyond the current program time period.

The Holloman AFB and Naval Test Station rocket sled facilities were examined in depth. Developing these vehicles for moving-frame acoustic testing, however, represented a very high technical risk in terms of obtaining a satisfactory sled with an appropriate heated air supply to yield high quality acoustic data. The logistics associated with the remoteness of the test sites plus the relatively costly and time consuming test procedures made the cost effectiveness of the rocket sled method marginal at best. High Speed Trains, such as the DOT LIMRV* and Bertin Aerotrain, were also rejected because of their inherent inflexibility, remoteness of site, and expensive test costs for the sustained parametric investigations envisioned.

The free jet assessment discussed in Section 3.2, suggested that this technique would provide adequate simulation of jet turbulence properties during forward flight. It was deficient, however, in that the microphones would be fixed relative to the medium of sound propagation. This is in direct contrast to the true flight condition, where the microphones are positioned in the outer airstream and the noise source is in relative motion to

* LIMRV - Linear Induction Motor Research Vehicle

both. It can be said, therefore, that the free jet technique fails to simulate the correct medium of sound propagation.

An analytical effort was initiated concurrently, however, in the belief that a theoretical technique could be evolved which would analytically correct the aforementioned deficiency. Various analytical approaches were screened in order to satisfactorily transform free jet data to flight conditions (Section 3.4). The method finally defined and used effectively simulates the flight effect when combined with free jet data. The combined use of free jet test data from a fixed-frame facility and the analytical transformation was dubbed the "hybrid" technique. The Task 4 activity validated the "hybrid" technique. Aerodynamic performance testing will be conducted at the NASA-Lewis 6 x 8-foot wind tunnel as part of Task 3 of the contract.

The free jet demonstration tests utilized exact 1/3-scale duplicates of the J85 suppressor nozzles. The two flight assurance tests utilized a Gates Learjet and an F-106 with pod-mounted J85 engines tested with conical, 8-lobe, and 104-tube nozzles. The Bertin Aerotrain test used the same physical suppressor hardware as was tested on the F-106 and Gates Learjet. The analytical transformation was ultimately validated by transforming the fixed-frame demonstration data and then comparing it to the Aerotrain results. Figure 4-1 illustrates how these various activities interfaced.

This section, as well as the remainder of this report, presents the results of each element of this effort.

4.1 FIXED-FRAME FREE JET DEMONSTRATION TEST PROGRAM

A series of free jet tests was formulated to provide a set of highly controlled far-field acoustic data for scale models of a conical, 8-lobe daisy, and 104-tube nozzle. The data were subsequently scaled, transformed, and compared with the Bertin Aerotrain data to verify the chosen "hybrid" inflight simulation technique.

Laser velocimeter plume surveys and ellipsoidal mirror microphone axial traverses were also made to demonstrate the feasibility of using source measurement techniques for determining changes in the turbulent mixing and noise source locations within the exhaust plume due to external flow.

4.1.1 Test Setup and Nozzle Configurations

The fixed-frame demonstration testing was conducted at the GE JENOTS outdoor facility (described in Section 3.1.2.1) using a free jet shroud (25.6 in. ID) which permitted evaluating the nozzles in a free jet to exhaust nozzle flow area ratio of nominally between 40 or 50 to 1. The free jet incorporated a modest contraction ratio which resulted in measured turbulence levels in the potential core of the free jet of approximately 3 to 4 percent. Velocity uniformity across the free jet exit area was held to less than 4 percent for the free jet velocity range of zero to 350 ft/sec.

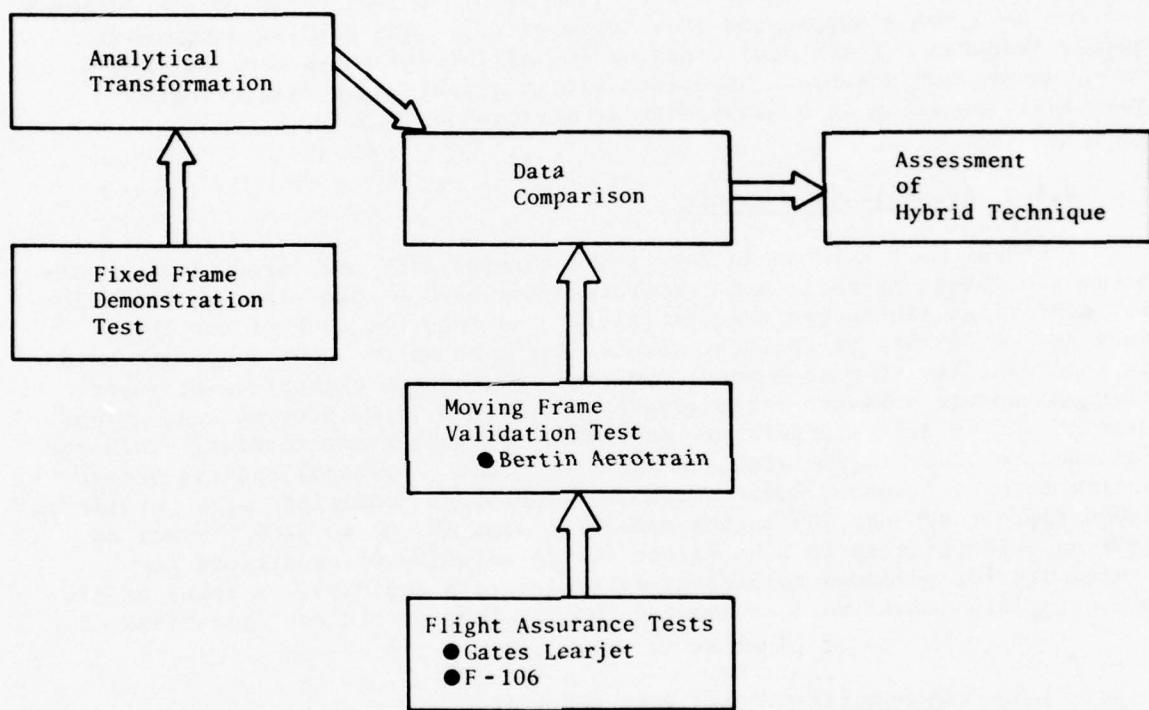


Figure 4-1. Procedure for Verification of the Inflight Simulation Techniques.

The 2-inch STA nozzle utilized in the "as-is" assessment portion of the program (Section 3.1.2.1) was also evaluated with this same shroud to assess the effect of free jet area ratio since its use resulted in an area ratio of 163 to 1.

Figure 4-2 is a photograph of the free jet setup at JENOTS. The 18-inch diameter ellipsoidal mirror (described later in Section 4.1.6) is also visible in the picture. Figures 4-3 through 4-9 present schematics and photographs of the two conical nozzles (3.56 inch and 2.00 inch) and the two suppressor nozzles (8-lobe daisy and 104-tube). The two suppressor configurations were selected because they were representative of a simple suppressor and a complex suppressor. The conical nozzles were the same ones evaluated during the "as-is" assessment phase. The simple 8-lobe daisy nozzle (Figures 4-6 and 4-7) has a suppressor area ratio of 2.1. The complex suppressor nozzle (Figures 4-8 and 4-9) contains 104 elliptical tubes divided into 5 rows, mounted on a conical baseplate with the tube major axis oriented radially, resulting in a suppressor area ratio* of 2.8.

4.1.2 Acoustic Test Matrix

The test matrix shown in Tables 4-I through 4-IV consisted of 14 combinations of pressure ratio and temperature for each of four free-stream velocity conditions [including the static ($V_o = 0$) run] for each of the three nozzles. A summary of the test variables are shown in Table 4-V. Included in this test series were several constant temperature excursions at supercritical nozzle pressure ratio ($P_{T8}/P_0 \approx 2.5$ to 3.5) to provide some assessment of the velocity-temperature dependency of suppressor nozzles. This was included to study shock-related noise (tonal and broadband) and its effect during forward flight. These pressure-temperature conditions were considered adequate to cover the J85 engine operating line (V_j up to 2200 ft/sec) as well as velocities up to 2600 ft/sec (representative of conditions now envisioned for advanced technology multiple-cycle engines). A total of 274 acoustic data points were documented for the four nozzle configurations.

4.1.3 Data Acquisition and Data Reduction

The acoustic data reported herein were acquired and processed, with one modification, using the acoustic and aerodynamic instrumentation systems described in depth in Section 3.1.2.1. The modification basically exercised a ground reflection option included in the GE data reduction system flow diagram (Figure 3-23).

The ground plane at JENOTS affects the propagation of noise due to reflection and absorption. The approach to converting the measured noise data to the "free field" was based on theoretical analysis of the ideal case of an infinitely hard surface, a point source of broadband noise, and a

*Suppressor area ratio is defined as the physical area based on the maximum physical diameter divided by the flow area.



Figure 4-2. JENOTS - Free Jet Test Facility.

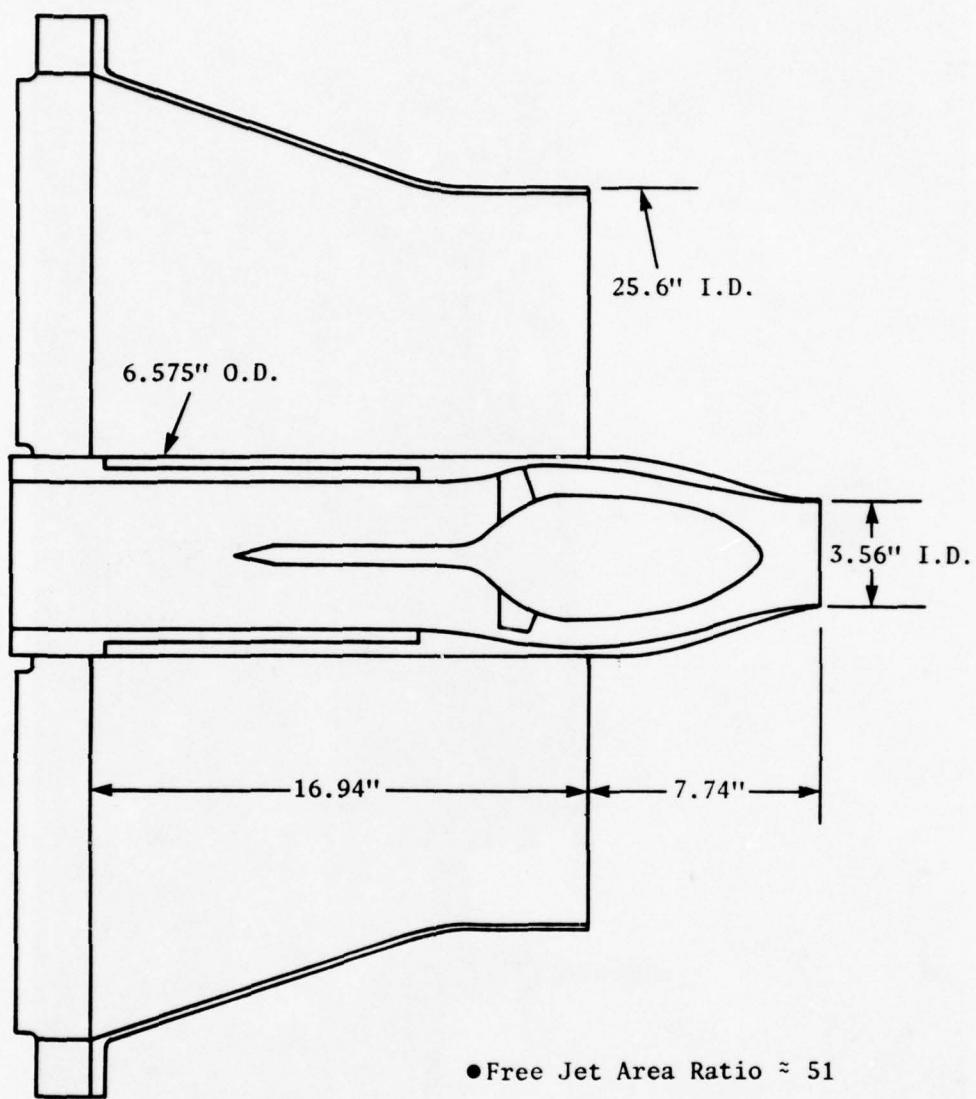


Figure 4-3. Schematic of Free Jet 3.56 Inch Conical Nozzle.

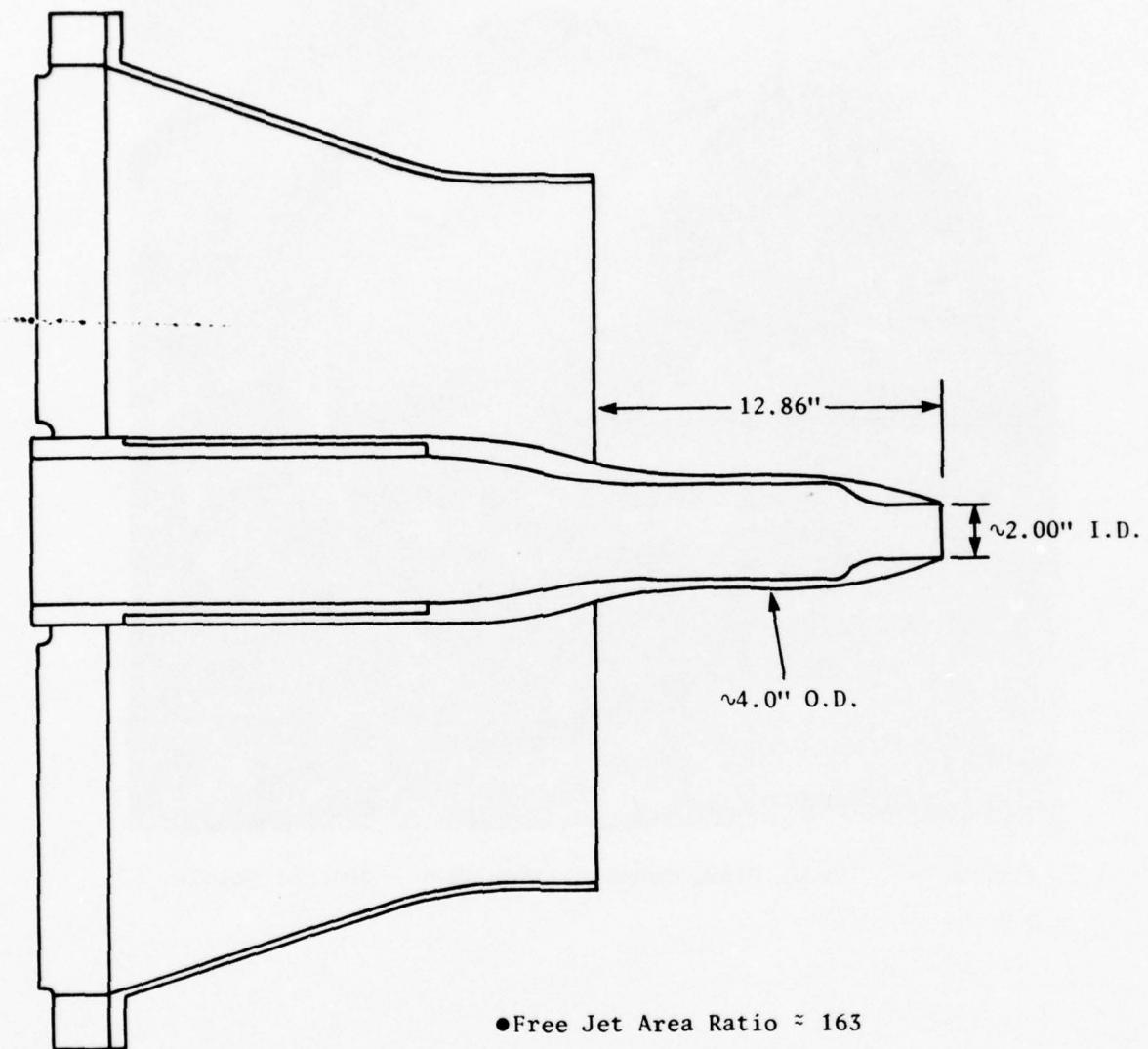


Figure 4-4. Schematic of Free Jet 2.0 Inch Conical Nozzle.

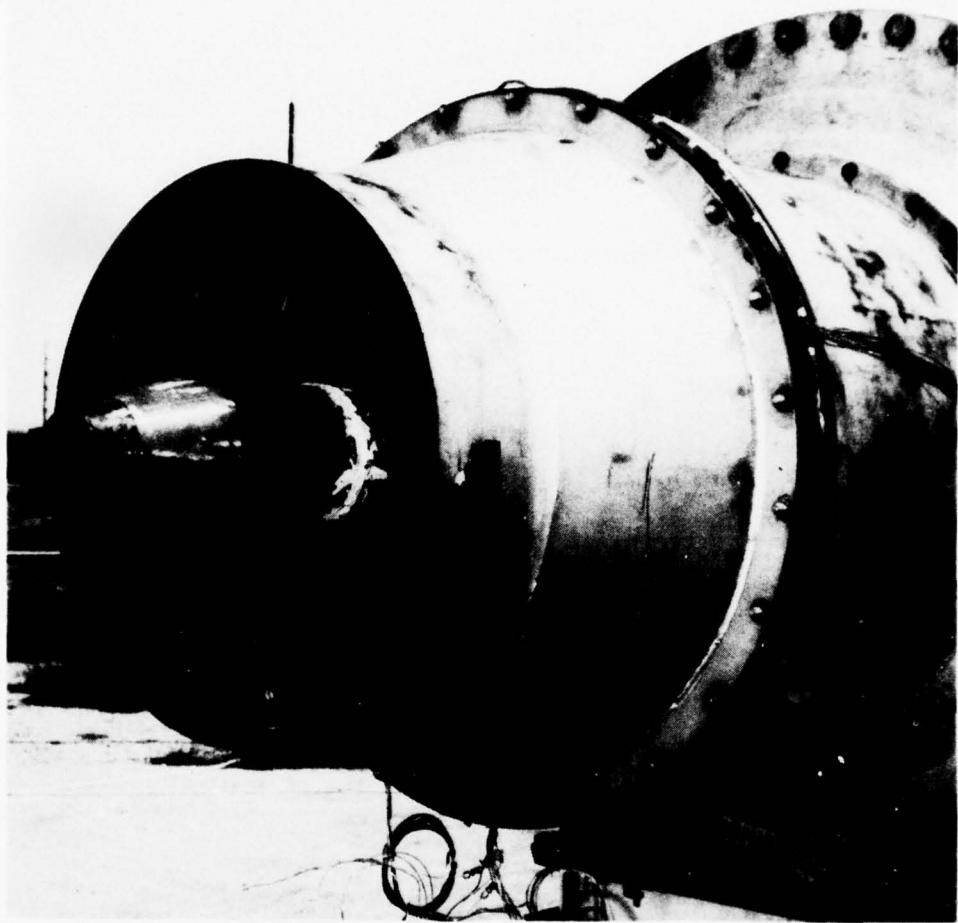


Figure 4-5. Fixed Frame Demonstration Test - Conical Nozzle.

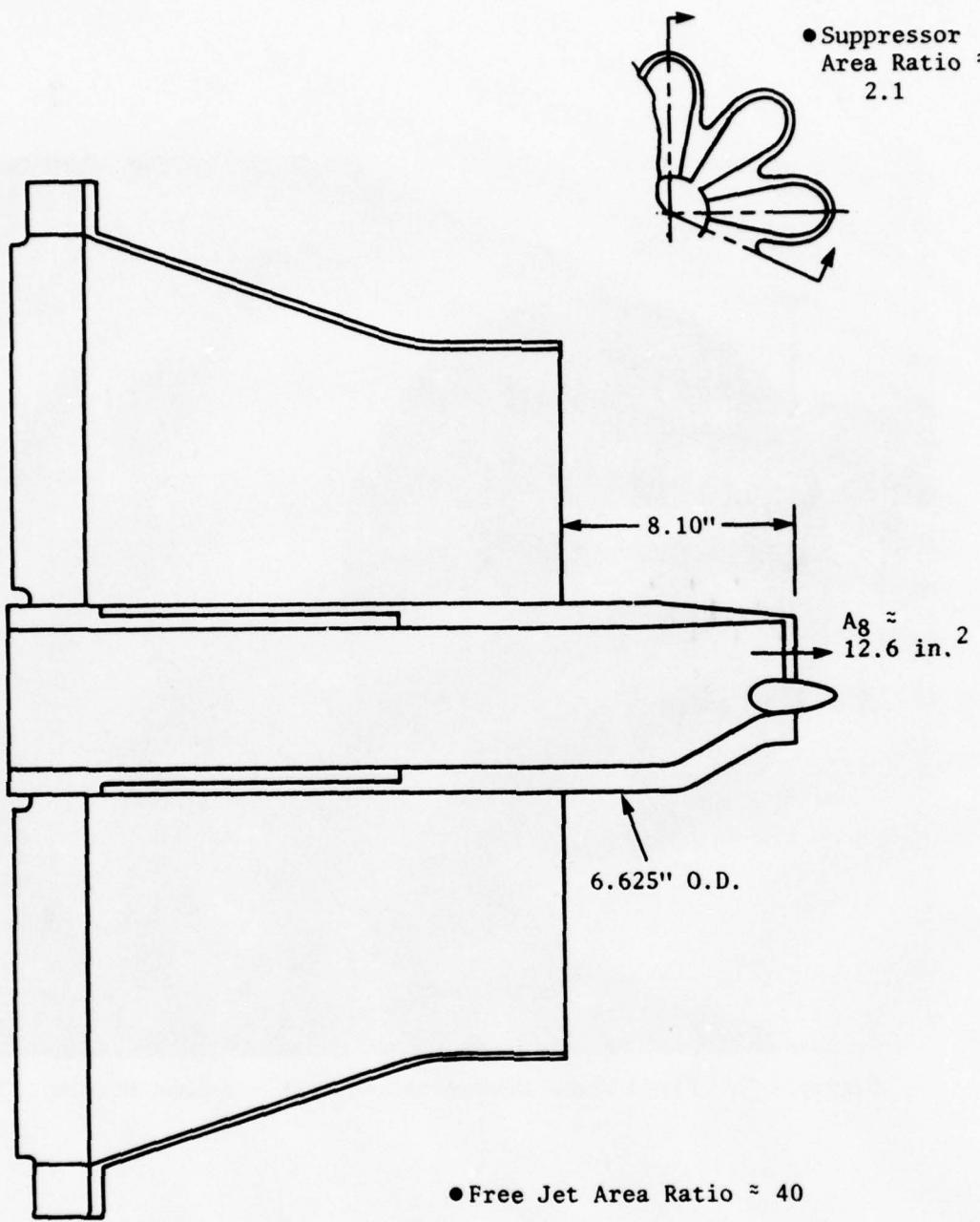


Figure 4-6. Schematic of Free Jet/8-Lobe Nozzle.

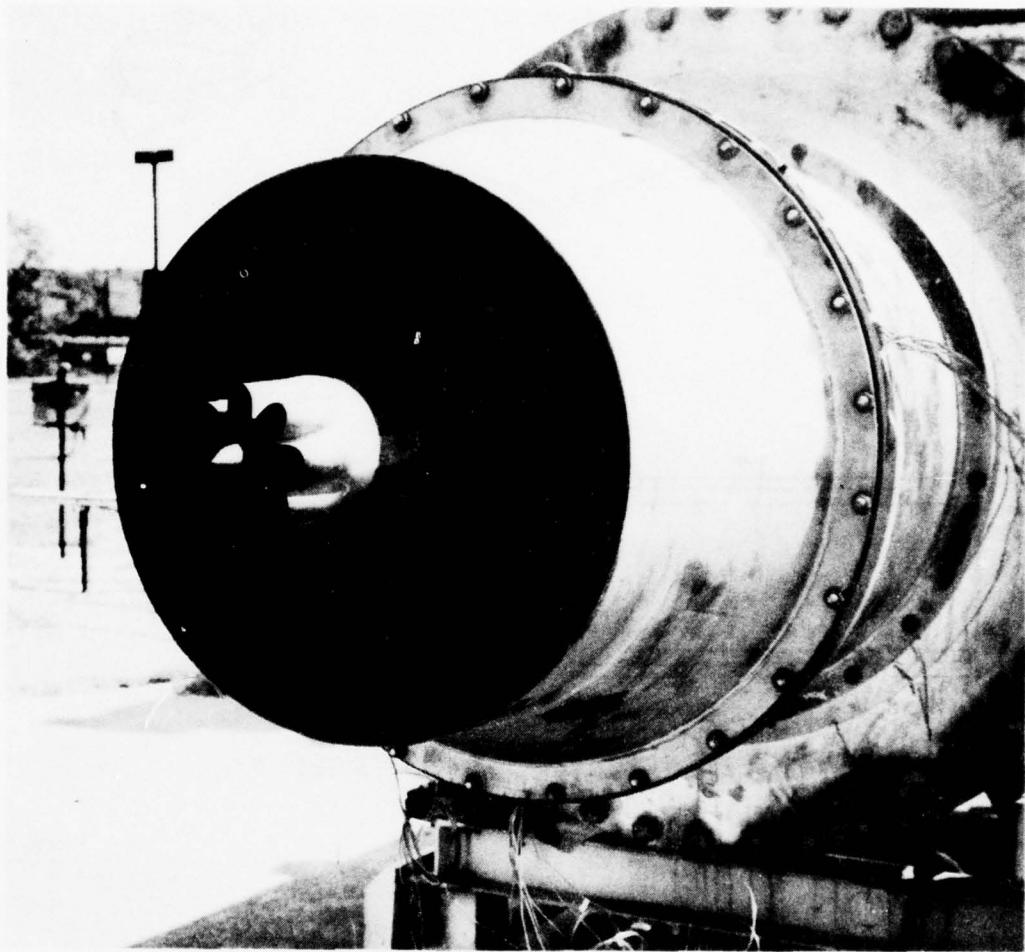


Figure 4-7. Fixed Frame Demonstration Test - 8-Lobe Nozzle.

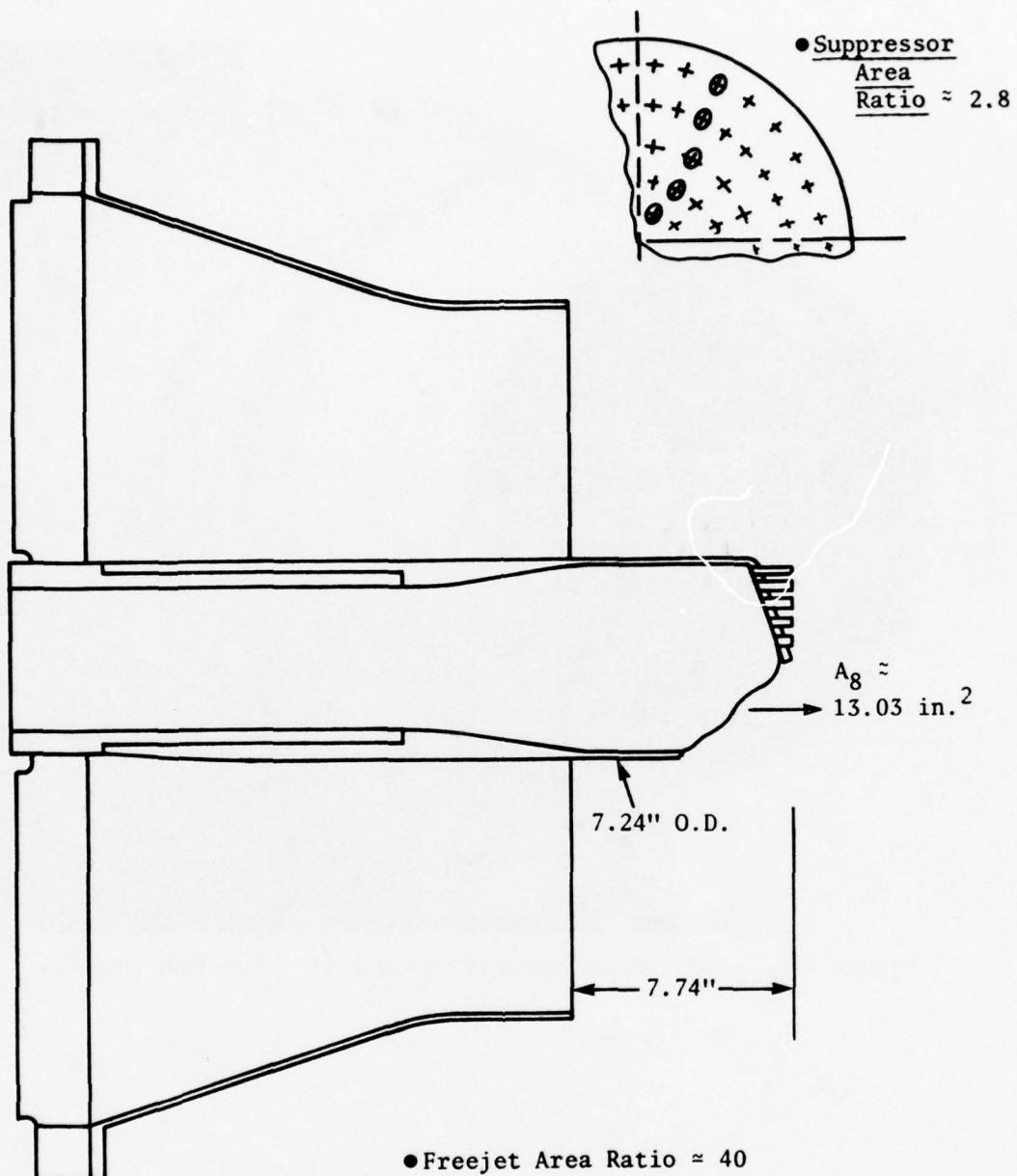


Figure 4-8. Schematic of Free Jet/104-Tube Nozzle.

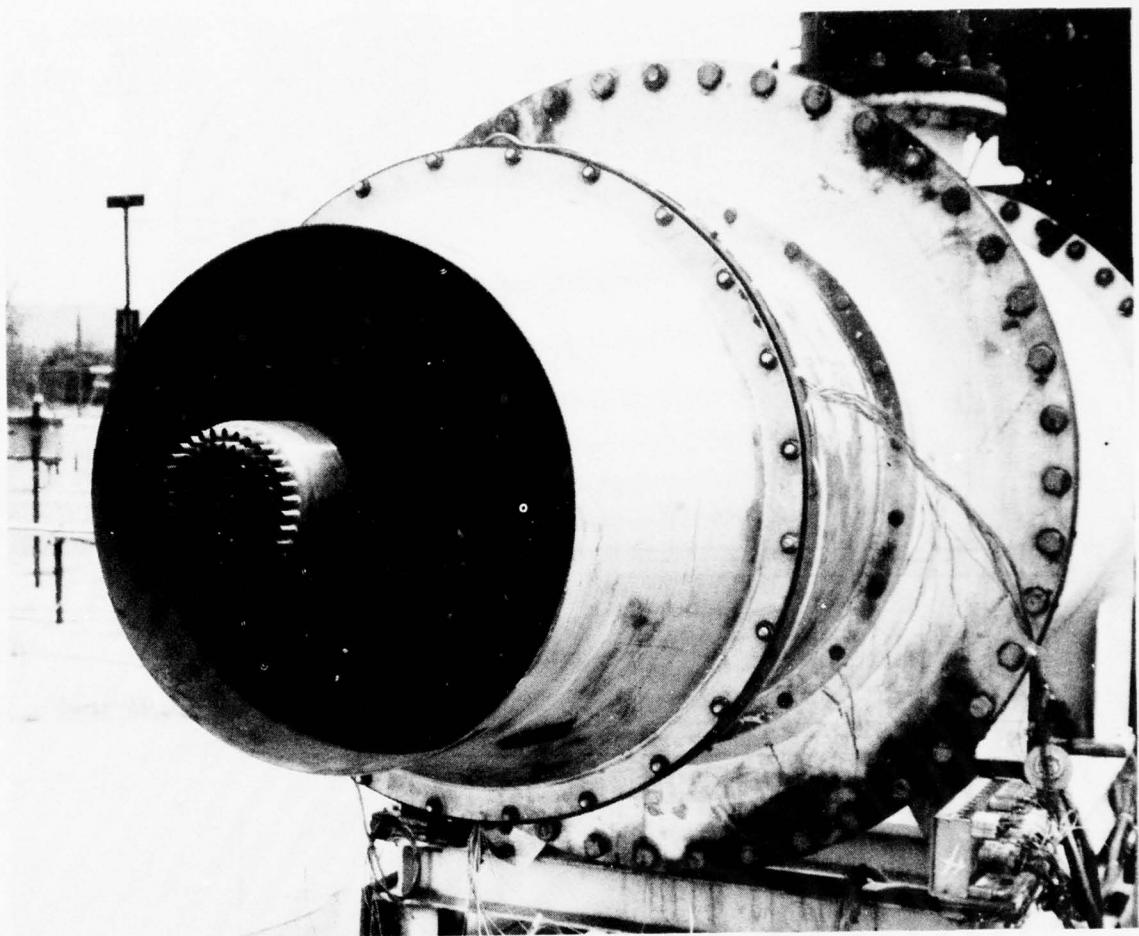


Figure 4-9. Fixed Frame Demonstration Test - 104-Tube Nozzle.

Table 4-I. Fixed-Frame Demonstration Test.

DATA PT. NO.	P_{T8}/P_0	T_{T8} °R	A_8 IN^2	V_8 FT/SEC	V_0 FT/SEC	$\log_{10}(V_j/A_0)$	$10 \log_{10}[(\rho_j/\rho_{ISA})^w A_j/R^2]$
1	1.171	1204	9.95	799	0	-.1526	-41.39
2	1.352	1255		1118		-.0072	-43.94
3	1.475	1262		1265		.0466	-45.03
4	1.605	1435		1481		.1151	-47.25
5	1.957	1464		1760		.1899	-48.50
6	2.000	1582		1857		.2133	-49.41
7	2.278	1697		2080		.2626	-49.83
8	2.447	1844		2253		.2971	-50.42
9	3.128	1687		2390		.3229	-49.02
10	3.442	1704		2486		.3399	-48.88
11	3.740	1799		2627		.3638	-49.18
12	1.589	1435		1466		.1107	-47.16
13	1.983	1561		1834		.2079	-49.26
14	2.455	1837		2252		.2470	-50.37
15	1.163	1194		779	153	-.1638	-41.22
16	1.355	1246		1118	150	-.0072	-43.92
17	1.474	1262		1264	134	.0463	-45.03
18	1.586	1429		1461	139	.1090	-47.10
19	1.947	1460		1751	152	.1878	-48.46
20	1.965	1570		1829	148	.2065	-49.32
21	2.269	1684		2068	145	.2599	-49.77
22	2.392	1809		2205	150	.2879	-50.29
23	3.146	1679		2390	146	.3228	-48.96
24	3.448	1703		2846	153	.3400	-48.87
25	3.765	1797		2630	146	.3644	-49.15
26	1.578	1428		1452	154	.1066	-47.04
27	1.965	1576		1832	152	.2074	-49.36
28	2.406	1817		2216	152	.2902	-50.32
29	1.164	1187		780	267	-.1639	-41.22
30	1.361	1259		1131	267	-.0019	-44.06
31	1.467	1267		1259	268	.0466	-45.01
32	1.636	1453		1518	267	.1259	-47.56
33	1.940	1466		1751	266	.1876	-48.50
34	1.946	1545		1801	265	.2001	-49.12
35	2.259	1680		2060	263	.2584	-49.76
36	2.353	1744		2146	264	.2261	-50.00
37	3.183	1690		2396	264	.3238	-49.03
38	3.440	1703		2484	263	.3397	-48.88
39	3.738	1794		2622	263	.3631	-49.16
40	1.644	1458		1529	266	.1287	-47.64
41	1.957	1551		1812	267	.2026	-49.17
42	2.371	1753		2160	266	.2790	-50.02
43	2.492	997		1660	0	.1644	-44.43
44	2.987	999		1796		.1987	-44.26
45	3.483	997		1896		.2223	-43.94
46	2.492	1400		1974		.2398	-47.90
47	2.995	1399		2136		.2741	-47.40
48	3.491	1402		2258		.2982	-47.03
52	2.482	998		1657	269	.1637	-44.44
53	2.987	996		1793	271	.1981	-44.23
54	3.480	995		1894	272	.2218	-43.93
55	2.467	1392		1958	268	.2364	-47.87
56	2.990	1395		2132	270	.2732	-47.38
57	3.478	1402		2255	272	.2977	-47.04
61	3.143	1696		2401	315	.3249	-49.06
62	2.312	1692		2094	313	.2654	-49.77
63	2.137	1580		1934	316	.2310	-49.36
64	1.941	1471		1754	319	.1884	-48.54
65	1.014	537		160	141	-.8514	-41.24
66	1.023	554		209	263	-.7381	-41.12
67	1.044	551		283	309	-.6013	-41.17
501	1.093	1681		713	156	-.2026	-40.35
502	1.118	1690		799	155	-.1528	-41.38
503	1.177	1693		964	154	-.0714	-43.27
504	1.242	1698		1110	153	-.0103	-44.91
505	1.304	1697		1223	151	.0321	-46.14
506	1.375	1698		1336	153	.0734	-47.27
507	1.429	1696		1411	152	.0938	-47.93
508	1.492	1701		1491	153	.1181	-48.61
509	1.634	1688		1637	150	.1584	-49.46
510	1.753	1696		1746	153	.1865	-49.94
511	1.217	1503		994	153	-.0578	-43.37
512	1.271	1246		998	152	-.0566	-43.00
513	1.353	991		993	149	-.0583	-42.48
514	1.507	738		991	144	-.0597	-41.83
515	1.783	566		1018	155	-.0677	-41.20
517	3.446	738		1625	161	.1554	-41.37
518	2.417	992		1630	157	.1568	-44.39
519	1.985	1240		1633	159	.1573	-46.61
520	1.752	1495		1637	149	.1585	-48.37
521	1.104	1704		757	0	-.1767	-40.88
522	1.187	1689		988		-.0612	-43.53
523	1.311	1682		1230		.0344	-46.16
524	1.498	1689		1494		.1186	-48.57
525	1.767	1700		1759		.1899	-50.00

3.56 Inch
Conical Nozzle

Table 4-II. Fixed-Frame Demonstration Test, 2.00-Inch STA Nozzle.

DATA PT. NO.	P _{T8} /P ₀	T _{T8} °R	A ₈ IN ²	V ₈ FT/SEC	V ₀ FT/SEC	log ₁₀ (V _j /A ₀)	10 log ₁₀ [(c ^p _j /c ^p _{ISA}) ^w A _j /R ²]
202	1.155	1202	3.14	765	0	-.1723	-44.10
203	1.346	1256		1110		-.0101	-43.90
204	1.467	1274		1263		.0458	-45.07
205	1.575	1287		1375		.0829	-45.85
206	1.805	1418		1632		.1573	-47.87
207	1.968	1509		1794		.1982	-48.87
208	2.262	1700		2074		.2613	-49.86
209	2.536	1694		2194		.2858	-49.56
210	3.125	1691		2392		.3233	-49.04
211	1.177	1174		802	139	-.1513	-41.40
2111	1.165	1224		794	151	-.1560	-41.33
212	1.357	1257		1125	149	-.0043	-44.01
213	1.469	1266		1261	154	.0451	-45.02
214	1.590	1448		1474	151	.1130	-47.28
215	1.940	146		1749	155	.1874	-48.49
216	1.965	157		1833	153	.2076	-49.37
217	2.259	1692		2067	155	.2599	-49.82
218	2.397	1818		2213	152	.2894	-50.33
219	3.141	1693		2398	161	.3244	-49.04
220	1.160	1218		780	296	-.1632	-41.23
221	1.359	1253		1126	295	-.0040	-44.01
222	1.466	1278		1264	296	.0461	-45.09
223	1.639	1455		1522	295	.1270	-47.59
224	1.944	1461		1750	295	.1874	-48.47
225	2.024	1551		1853	295	.2123	-49.20
226	2.366	1709		2130	293	.2729	-49.80
227	2.497	1767		2225	291	.2920	-49.98
228	3.335	1662		2427	284	.3296	-48.73
229	1.023	581		210	155	-.7278	-40.91
230	1.034	548		252	283	-.6571	-41.18
231	1.135	507		466	0	-.3877	-41.60
232	1.293	506		657	0	-.2384	-41.52
233	1.873	534		1027	0	.3449	-41.03
236	1.233	1193		915	0	-.0946	-42.28

Table 4-III. Fixed-Frame Demonstration Test, 8-Lobe Nozzle.

DATA PT. NO.	P_{T8}/P_0	T_{T8} °R	A_{82} IN ²	V_8 FT/SEC	V_0 FT/SEC	$\log_{10}(V_j/A_0)$	$10 \log_{10} [(C_j/I_{ISA})^{\omega} A_j/R^2]$
68	1.189	1199	12.56	835	0	-.1339	-41.67
69	1.383	1246		1153		.0063	-44.19
70	1.501	1263		1292		.0558	-45.22
71	1.613	1294		1412		.0944	-46.10
72	1.818	1403		1632		.1573	-47.77
73	1.990	1497		1800		.1997	-48.79
74	2.285	1686		2077		.2619	-49.76
75	2.559	1689		2200		.2870	-49.51
76	3.152	1689		2398		.3244	-49.01
77	3.465	1699		2487		.3402	-48.84
78	3.746	1791		2621		.3630	-49.14
79	1.575	1290		1377		.0834	-45.87
80	1.991	1490		1796		.1988	-48.74
81	2.528	1687		2186		.2842	-49.53
82	1.165	1194		785	124	-.1614	-41.26
83	1.359	1250		1124	123	-.0044	-43.99
84	1.480	1264		1272	152	.0487	-45.08
85	1.606	1291		1405	161	.0921	-46.04
86	1.809	1405		1628	159	.1560	-47.76
87	2.012	1501		1815	169	.2034	-48.83
88	2.270	1691		2072	157	.2610	-49.80
89	2.574	1698		2212	166	.2893	-49.54
90	3.176	1692		2408	169	.3260	-49.01
91	3.496	1696		2492	169	.3411	-48.80
92	3.801	1785		2629	168	.3642	-49.07
93	1.570	1293		1374	158	.0824	-45.87
94	1.970	1498		1788	157	.1969	-48.78
95	2.550	1690		2197	158	.2864	-49.52
96	1.161	1206		780	278	-.1641	-41.21
961	1.156	1176		758	203	-.1758	-41.05
962	1.187	1198		830	296	-.1381	-41.63
97	1.360	1245		1124	276	-.0049	-43.97
971	1.343	1248		1103	327	-.0131	-43.82
98	1.476	1267		1269	278	.0478	-45.08
99	1.569	1385		1422	281	.0973	-46.63
100	1.809	1405		1628	279	.1560	-47.76
101	1.903	1570		1788	280	.1969	-49.27
102	2.276	1681		2069	277	.2603	-49.74
103	2.316	1786		2154	280	.2778	-50.25
104	3.153	1690		2399	300	.3246	-49.02
105	3.467	1702		2490	302	.3407	-48.85
106	3.777	1802		2636	306	.3655	-49.17
107	1.550	1392		1407	294	.0928	-46.57
108	1.890	1581		1786	297	.1963	-49.34
109	2.312	1789		2155	278	.2777	-50.27
110	2.501	993		1658	0	.1642	-44.39
111	2.994	988		1788		.1967	-44.15
112	3.479	991		1890		.2209	-43.89
113	2.503	1394		1974		.2397	-47.84
114	2.992	1386		2125		.2718	-47.32
115	3.485	1398		2254		.2973	-47.01
119	2.496	997		1660	277	.1667	-44.43
120	3.032	996		1803	299	.2006	-44.21
121	3.499	996		1898	301	.2228	-43.93
122	2.499	1404		1979	305	.2410	-47.92
123	2.999	1396		2135	305	.2738	-47.38
124	3.515	1399		2261	312	.2987	-47.00
128	3.199	1692		2414	340	.3272	-48.99
129	2.596	1692		2217	342	.2903	-49.49
130	2.010	1505		1816	340	.2037	-48.86
131	1.841	1414		1655	343	.1632	-47.91
132	1.009	518		129	164	-.9545	-41.39
133	1.029	579		237	290	-.6790	-40.94
134	1.043	552		281	340	-.6057	-41.16
260	1.598	1395		1454	0	.1070	-46.88
261	1.952	1584		1828	0	.2065	-49.41
262	2.333	1782		2160	0	.2790	-50.22
263	1.535	1365		1379	154	.0839	-46.25
264	1.934	1563		1804	152	.2008	-49.24
265	2.257	1793		2129	152	.2726	-50.34
266	2.564	1691		2204	0	.2876	-49.52

Table 4-IV. Fixed-Frame Demonstration Test, 104-Tube Nozzle.

DATA PT. NO.	P_{T8}/P_0	T_{T8} OR	A_{8^2} IN ²	V_8 FT/SEC	V_0 FT/SEC	$\log_{10}(V_j/A_0)$	$10 \log_{10}[(\rho_j/\rho_{ISA})^w A_j/R^2]$
135	1.176	1204	13.03	811	122	-.1469	-41.47
136	1.365	1246		1130	0	-.0022	-44.02
137	1.490	1255		1277		.0507	-45.08
138	1.589	1303		1396		.0895	-46.06
139	1.820	1406		1636		.1532	-47.80
140	1.985	1495		1795		.1986	-48.77
141	2.277	1686		2073		.2610	-49.77
142	2.551	1686		2195		.2859	-49.50
143	3.149	1692		2400		.3247	-49.03
144	3.439	1696		2479		.3387	-48.84
145	3.743	1787		2617		.3624	-49.12
146	1.600	1278		1393		.0883	-45.90
147	1.992	1507		1807		.2014	-48.87
148	2.548	1688		2195		.2860	-49.52
149	1.178	1199		814	168	-.1456	-41.49
150	1.371	1252		1141	167	.0017	-44.11
151	1.491	1266		1284	168	.0529	-45.17
152	1.597	1299		1401	168	.0911	-46.06
153	1.823	1392		1629	171	.1565	-47.68
154	1.990	1499		1801	168	.2000	-48.80
155	2.296	1681		2079	172	.2623	-49.72
156	2.556	1697		2205	170	.2878	-49.56
157	3.167	1694		2406	170	.3258	-49.03
158	3.465	1699		2488	170	.3402	-48.84
159	3.772	1793		2629	169	.3642	-49.13
160	1.592	1290		1392	172	.0882	-45.96
161	2.000	1464		1785	171	.1962	-48.54
162	2.557	1685		2197	171	.2863	-49.49
1621	2.499	1271		1881	470	.2189	-46.94
163	1.092	1205		599	272	-.2773	-39.62
164	1.358	1249		1123	273	-.0052	-43.97
166	1.581	1297		1387	289	.0863	-45.96
167	1.813	1412		1634	275	.1578	-47.83
1671	1.817	1403		1632	281	.1572	-47.77
168	1.979	1498		1793	297	.1982	-48.79
169	2.284	1689		2078	294	.2621	-49.78
170	2.558	1694		2203	295	.2875	-49.54
1701	2.542	1690		2194	277	.2857	-49.53
171	3.157	1685		2397	290	.3241	-48.99
1711	3.162	1705		2413	278	.3270	-49.10
172	3.468	1709		2496	291	.3417	-48.89
173	3.773	1802		2636	267	.3654	-49.18
1731	3.776	1799		2634	290	.3651	-49.16
1732	3.779	1502		2400	296	.3247	-47.47
174	1.547	1309		1361	279	.0784	-45.87
176	2.531	1694		2192	297	.2854	-49.56
177	2.493	991		1655	0	.1631	-44.37
178	2.996	987		1787		.1966	-44.14
179	3.485	991		1891		.2211	-43.89
180	2.498	1389		1968		.2385	-47.82
181	3.001	1399		2138		.2744	-47.40
182	3.482	1399		2254		.2974	-47.02
183	2.497	1698		2181		.2831	-49.62
186	2.510	1001		1668	168	.1667	-44.47
187	3.002	1007		1807	169	.2013	-44.33
189	2.510	1384		1969	170	.2387	-47.78
1891	2.512	1395		1977	288	.2406	-47.84
190	3.009	1398		2139	170	.2747	-47.38
1901	2.997	1394		2133	288	.2734	-47.37
1861	2.508	996		1663	288	.1654	-44.42
1871	2.995	994		1793	291	.1981	-44.21
188	3.507	997		1900	286	.2233	-43.93
191	3.499	1387		2248	289	.2961	-46.93
195	3.160	1703		2411	425	.3267	-49.08
196	2.556	1694		2202	433	.2874	-49.54
197	1.821	1687		1795	439	.1986	-50.01
198	2.078	1515		1861	436	.2143	-48.94
199	1.016	616		185	170	-.7929	-40.65
200	1.056	543		318	292	-.5537	-41.24
2001	1.027	540		224	246	-.7094	-41.24
201	1.053	598		323	388	-.5443	-40.82
280	2.458	1800		2229	0	.2927	-50.19
281	1.491	1570		1431	159	.1002	-47.57
282	2.318	1770		2145	155	.2760	-50.17
521	1.093	1701		716	0	-.2000	-40.40
522	1.187	1688		987		-.0613	-43.52
523	1.320	1678		1243		.0391	-46.29
524	1.503	1683		1496		.1195	-48.57
525	1.769	1684		1753		.1882	-49.90

Table 4-V. Range of Test Variables.

Free Stream Velocity	0 to 350 ft/sec
Primary Jet Velocity	800 ft/sec to 2600 ft/sec
Primary Nozzle Pressure Ratio	1.2 to 3.75
Exhaust Gas Stagnation Temperature	1000° R to 1800° R

stable homogeneous medium. The analysis was modified by a series of tests and parametric studies conducted in Task 1 of this contract (Reference 7). It involves the determination of the ground impedance phase factor and reflection coefficient, an estimate of the scattering phenomenon, and a correction for the distributed source effects of the jet. The resulting calculations are shown in Table 4-VI. These values were incorporated into the data reduction program as standard corrections for JENOTS data as shown in Figure 4-10.

All the acoustic data presented herein have been corrected for ground reflections (corrected to free field), corrected for free jet background noise (where applicable), scaled to J85 size ($A_8 \approx 108.6 \text{ in.}^2$), and extrapolated to 400-foot sideline for a standard hot day (77° F, 70% relative humidity). The acoustic data to follow have been selected to point out those areas considered pertinent to free jet testing of baseline and suppressor nozzles. All the data taken on the free jet are included in the verification of simulated inflight technique (Section 7.0), transformed and compared to the Aerotrain results.

4.1.4 Acoustic Data Analysis/Results

The free jet setup discussed in Section 4.1.1 was operated in essentially "free jet alone" mode, with the primary nozzle flow leaking (to eliminate any undesirable acoustic effects that might be attributed to an internal wake region) to document its noise contribution as well as its effect on the nozzle far-field jet noise signature. Just as in the "as-is", assessment phase (Section 3.1.2.1), free jet background noise primarily affects the low frequency region (less than 200 Hz) of the jet noise spectrum. Figure 4-11 superimposes typical "free jet alone" spectra for velocities up to 309 ft/sec on conical and 104-tube nozzle spectra at jet velocities up to 2195 ft/sec. In general, conical nozzle jet noise data were found to be acoustically acceptable at higher simulated flight speeds down to jet velocities of about 1500 ft/sec while the 104-tube nozzle jet velocity range was acceptable down to about 1600 ft/sec.

Figures 4-12 and 4-13 present peak OASPL and OASPL directivity characteristics for the 3.56-inch conical nozzle and show the same trend previously discussed in Section 3.1.2.1 (noise level relative to the static jet noise

Table 4-VI. JENOTS Ground Reflection Corrections (Δ dBs to be added to SPLs).

Frequency (Hz)	Angles													
	30	40	50	60	70	80	90	100	110	120	130	140	150	160
50	-4.99	-4.97	-4.93	-4.88	-4.82	-4.75	-4.66	-4.55	-4.41	-4.24	-4.03	-3.77	-3.46	-3.1
63	-4.45	-4.41	-4.35	-4.29	-4.21	-4.1	-3.98	-3.82	-3.64	-3.42	-3.16	-2.86	-2.52	-2.19
80	-4.0	-4.0	-3.34	-3.23	-3.1	-2.95	-2.76	-2.53	-2.27	-1.96	-1.61	-1.22	-0.83	-0.47
100	-4.0	-4.0	-3.0	-3.0	-2.0	-0.7	-0.34	-0.07	0	0	1.6	2.11	2.54	
125	-3.5	-4.0	-3.5	-2.0	-2.5	-0.5	1.7	1.0	1.0	2.0	2.9	3.8	2.8	
160	0	01.5	-2.5	-0.5	-1.0	1.5	2.7	1.5	3.0	2.0	3.0	3.2	2.2	
200	-2.0	-1.5	-1.5	-1.0	-1.0	0.5	0	0.5	1.0	-0.17	-0.65	-1.03	0	
250	0	0	-0.5	-1.5	-1.5	-1.5	-2.5	-2.5	1.5	-1.0	-2.0	-4.48	-4.58	-2.39
315	1.5	0	-1.5	-1.5	-1.5	-1.8	-4.0	-1.5	-3.0	-3.0	-4.9	-5.09	-2.0	
400	-2.0	-4.2	-4.1	-4.1	-3.5	-3.2	-3.1	-2.34	-1.85	-1.34	-4.9	-0.37	-0.7	-4.3
500	-1.0	-1.0	0	-1.3	-1.1	-1.2	-1.1	-1.35	-1.14	-1.87	-2.1	+1.8	-0.5	
630	-1.64	-1.5	-1.0	-2.5	-2.0	-3.2	-2.1	-2.09	-2.03	-3.5	-3.5	-1.64	-1.3	-0.9
800	-1.55	-1.35	-1.12	-1.12	-1.0	-2.0	-2.0	-2.1	-0.88	-1.22	-0.5	-1.05	-0.5	+2.2
1000	-1.0	-2.44	-1.3	-2.36	-2.3	-2.13	-2.13	-1.9	-1.72	-1.47	-1.22	-2.1	-0.71	-0.8
1250	-1.97	-2.03	-2.10	-2.17	-2.24	-2.28	-2.28	-2.3	-2.24	-2.18	-2.12	-2.08	-2.04	-2.2
1600	-2.17	-1.5	-2.06	-1.98	-1.90	-1.83	-1.8	-1.83	-1.93	-2.07	-2.23	-2.36	-2.45	-2.5
2000	-0.74	-2.0	-2.8	-0.92	-1.11	-1.37	-1.7	-1.90	-2.05	-2.10	-2.06	-1.97	-1.88	-1.8
2500	-1.5	-2.0	-1.8	-2.84	-2.70	-2.52	-2.35	-2.29	-2.31	-2.37	-2.45	-2.51	-2.54	-2.56
3150	-2.57	-2.60	-2.66	-2.78	-2.93	-3.1	-3.14	-3.07	-2.91	-2.75	-2.65	-2.6	-2.59	
4000	-2.80	-2.78	-2.74	-2.66	-2.58	-2.55	-2.60	-2.67	-2.72	-2.72	-2.72	-2.72	-2.71	
5000	-2.69	-2.72	-2.77	-2.84	-2.90	-2.85	-2.60	-2.41	-2.36	-2.44	-2.52	-2.56	-2.58	-2.59
6300	-2.70	-2.68	-2.64	-2.59	-2.56	-2.64	-2.90	-2.97	-2.85	-2.72	-2.68	-2.66	-2.66	
8000	-2.76	-2.76	-2.75	-2.73	-2.67	-2.60	-2.60	-2.80	-2.78	-2.74	-2.72	-2.71	-2.7	
10000	-2.69	-2.69	-2.68	-2.67	-2.67	-2.71	-2.80	-2.70	-2.60	-2.63	-2.65	-2.65	-2.65	
12500	-2.70	-2.71	-2.69	-2.69	-2.69	-2.70	-2.70	-2.70	-2.66	-2.66	-2.66	-2.66	-2.66	
16000	-2.61	-2.61	-2.60	-2.58	-2.58	-2.56	-2.70	-2.60	-2.57	-2.57	-2.57	-2.57	-2.57	
20000	-2.63	-2.63	-2.62	-2.62	-2.61	-2.61	-2.70	-2.56	-2.60	-2.60	-2.59	-2.59	-2.59	
25000	-2.71	-2.71	-2.70	-2.70	-2.70	-2.69	-2.70	-2.68	-2.68	-2.68	-2.67	-2.67	-2.67	-2.66
31500	-2.74	-2.73	-2.73	-2.73	-2.72	-2.72	-2.72	-2.71	-2.71	-2.70	-2.70	-2.69	-2.69	-2.69
40000	-2.71	-2.71	-2.71	-2.71	-2.70	-2.70	-2.70	-2.69	-2.68	-2.68	-2.67	-2.67	-2.67	
50000	-2.73	-2.73	-2.73	-2.72	-2.72	-2.72	-2.72	-2.71	-2.71	-2.70	-2.70	-2.69	-2.69	
63000	-2.70	-2.70	-2.69	-2.69	-2.68	-2.68	-2.68	-2.67	-2.67	-2.67	-2.66	-2.66	-2.66	
80000	-2.72	-2.72	-2.72	-2.71	-2.71	-2.71	-2.70	-2.70	-2.69	-2.69	-2.68	-2.68	-2.68	

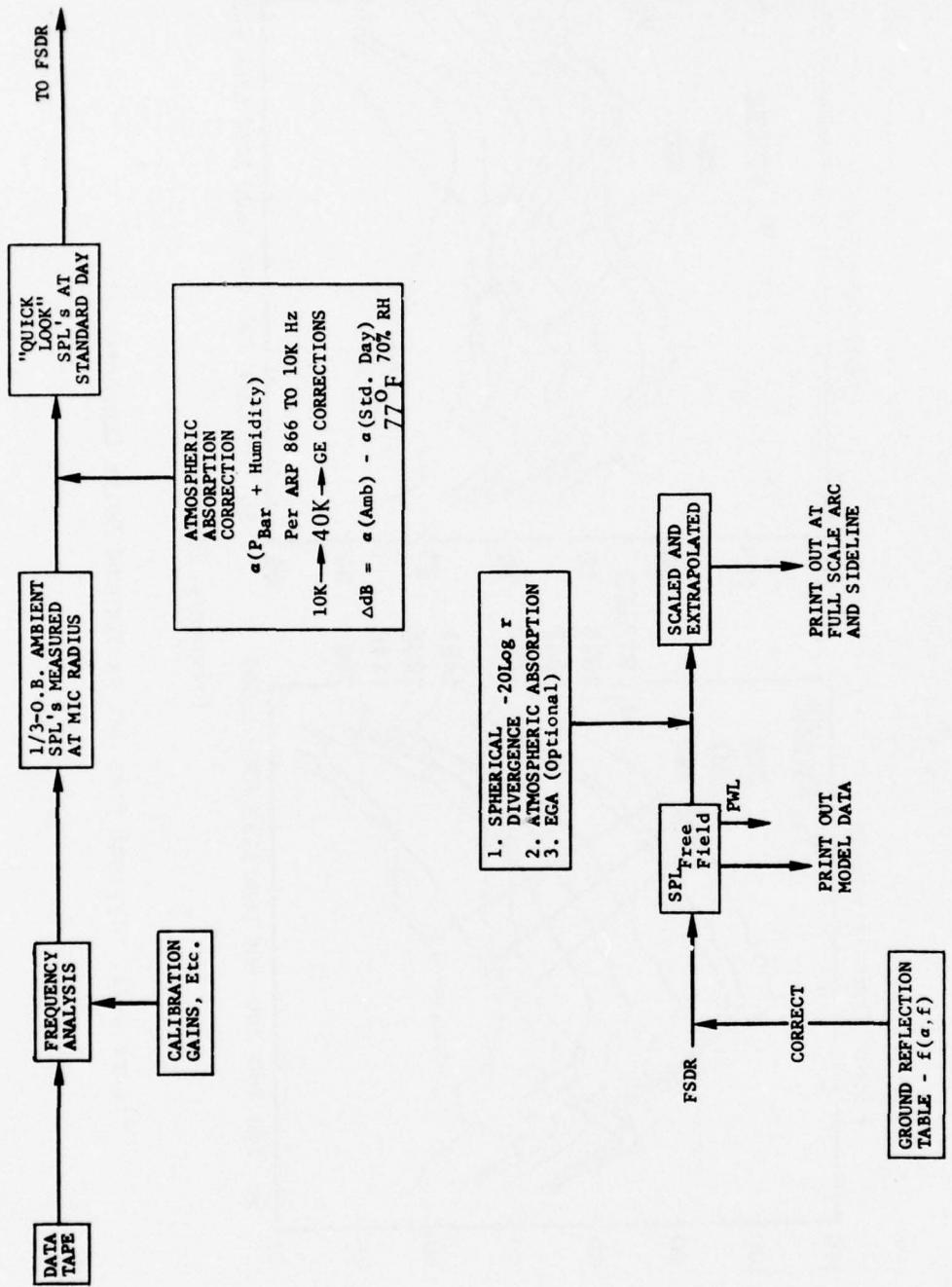


Figure 4-10. Data Reduction Operations/Fixed Frame Demonstration Tests.

- 400 ft. Sideline
- No EGA, Free Field
- 77°F, 70% R.H.
- $A_8 = 108.6 \text{ in.}^2$
- $\theta_1 = 130^\circ$

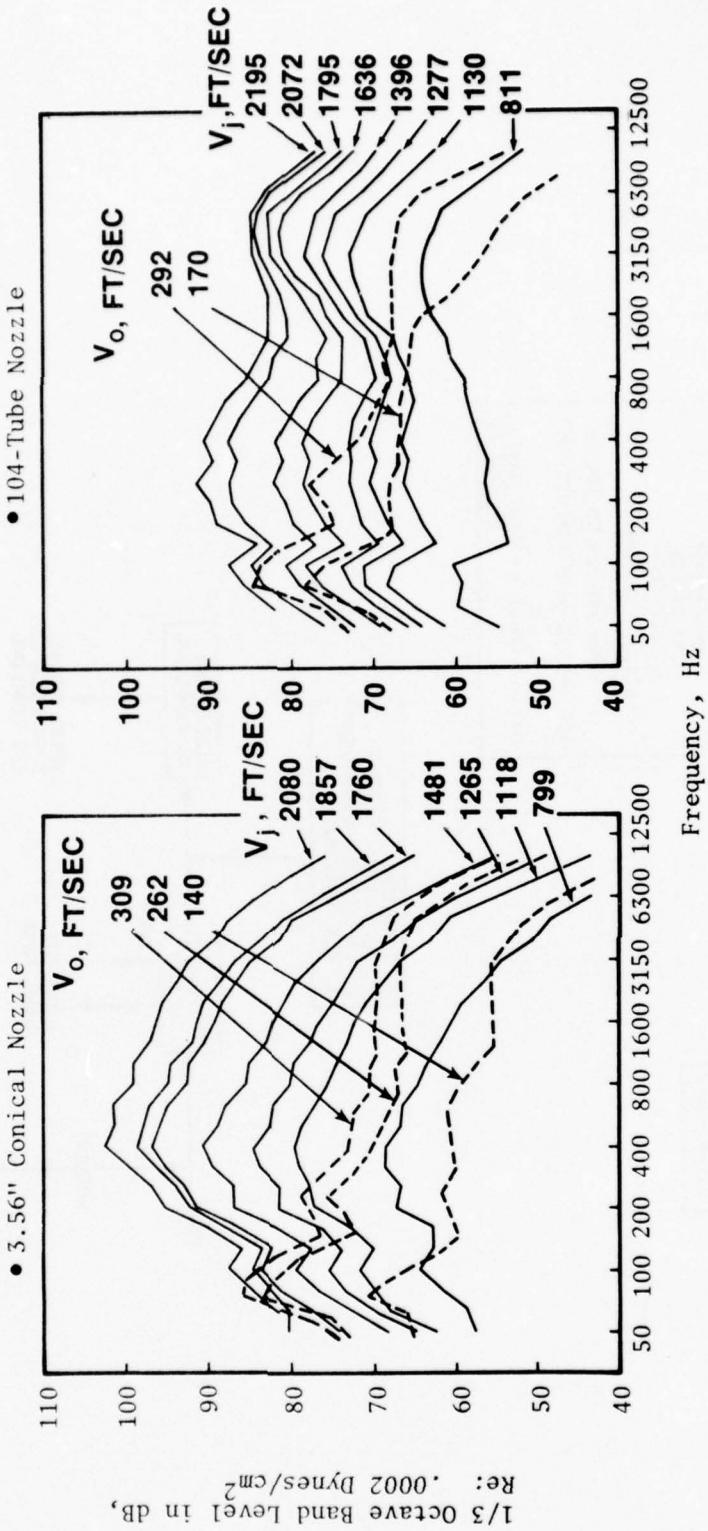


Figure 4-11. Typical Free Jet Background Noise Characteristics.

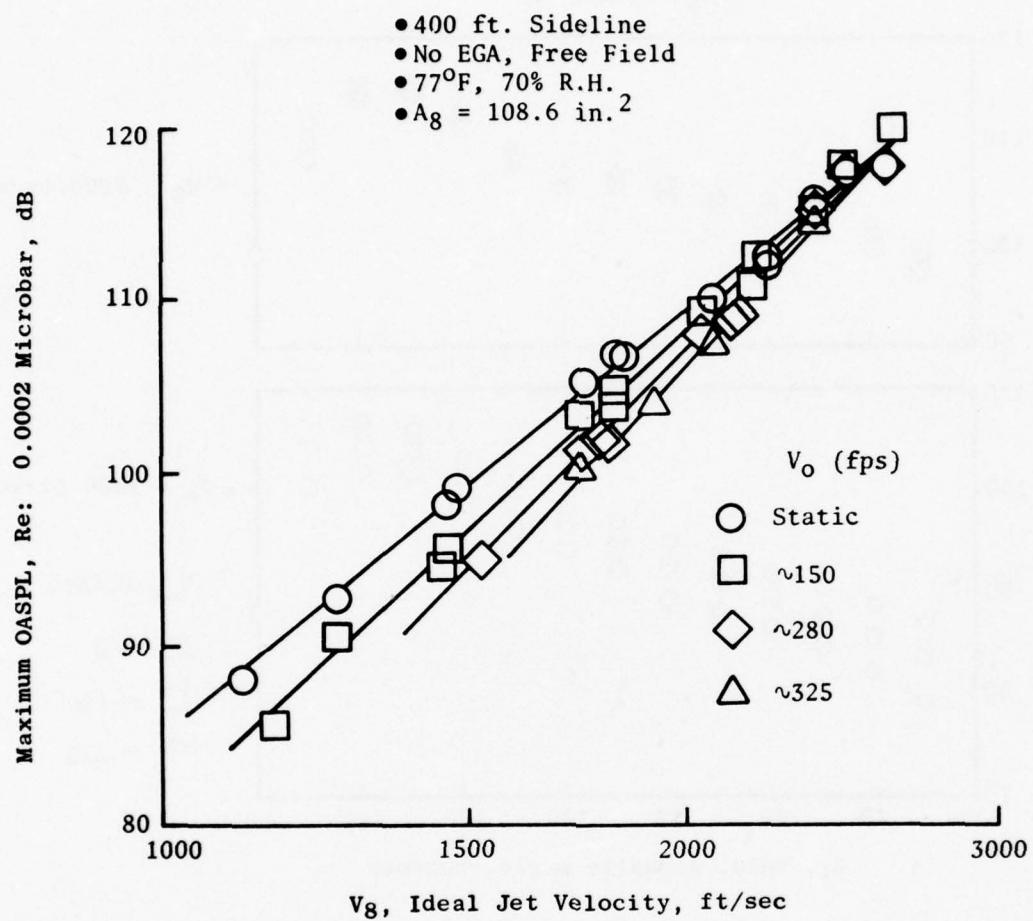


Figure 4-12. Fixed Frame Dmonstration Test - Conical Nozzle Peak OASPL Characteristics.

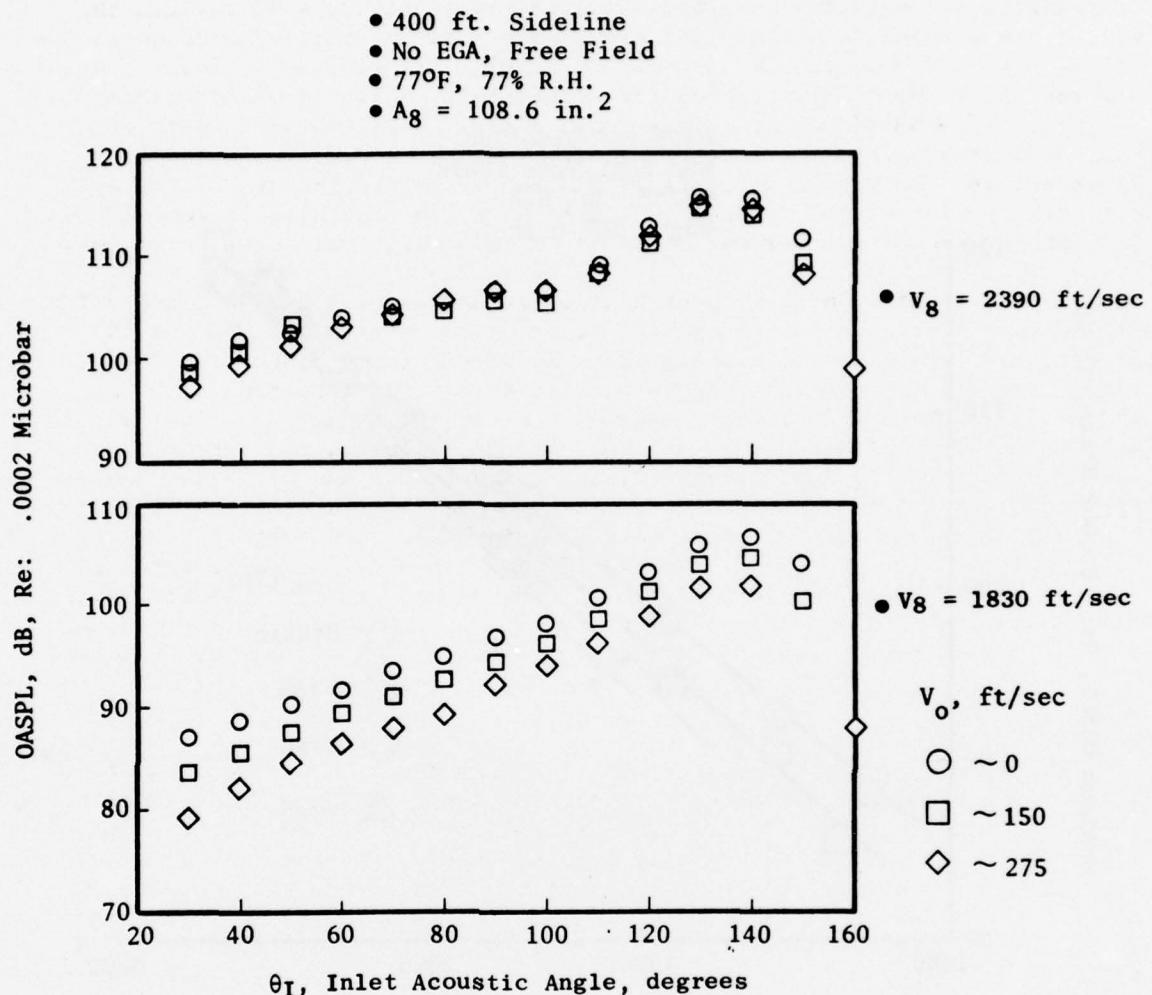


Figure 4-13. Fixed Frame Demonstration Test - Conical Nozzle OASPL Directivities.

signature decreases with increasing forward velocity and decreasing jet velocity, and OASPL reduction with increasing forward speed appears to be insensitive to angular location). Examination of Figure 4-12 reveals that static and wind-on data exhibited previously observed power-law dependencies (at $V_0 = 0$, $n \approx 7.8$, and at $V_0 \approx 325$, $n \approx 10$). As velocity (pressure ratio) was increased ($V_J \approx 2390$ ft/sec) the noise field became less directional (Figure 4-13), particularly in the forward arc. This characteristic of conical nozzles operating supercritically (underexpanded) was noted by Harper-Bourne and Fisher in their 1973 AGARD paper (Reference 24). The directivity plot at 1830 ft/sec in Figure 4-13, in contrast, is representative of convergent nozzles operating at or below critical pressure ratios.

Typical conical nozzle spectra at inlet angles of 140° , 90° , and 50° are included in Figures 4-14 through 4-16 for jet velocities of 2390 and 1830 ft/sec, respectively. As expected from the directivity plots, the 2390 ft/sec condition shows that little benefit is derived (spectrum wise) with increasing forward velocity. Spectrum shape at inlet angles of 140° and 90° show no apparent effect due to shocks. At 50° , however, the very peaked spectrum is characteristic shock-related noise (tonal and broadband) superimposed on pure turbulent mixing jet noise. The low-velocity spectra ($V_J = 1830$ ft/sec) exhibit universal reduction in noise level with increasing forward velocity at frequencies above 200 Hz. It should also be noted that, except for turbulent scattering at high frequencies, the 90° spectra suggest that some reduction in turbulence intensity was experienced by the conical nozzle. Major benefit due to forward flight appears to be in the frequency range of 250 and 3150 Hz, which corresponds to the peak noise region of the spectrum at 1830 ft/sec.

When the effect of free jet-to-nozzle area ratio on measured far-field jet noise was further assessed by conducting tests with the 2-inch diameter STA nozzle (which resulted in a free jet ratio of 163), the OASPL/jet velocity plots at three typical acoustic angles suggest that free jet area ratio does not appreciably affect the resultant measured jet noise. Comparison plots for the 2-inch ($AR_{FJ} \approx 163$) and 3.56-inch ($AR_{FJ} \approx 51$) conical nozzles at high simulated forward-velocity conditions ($\bar{V}_o \approx 280$ ft/sec) are summarized in Figures 4-17 and 4-18. The spectrum comparison at a jet velocity of 2410 ft/sec (Figure 4-18) for the same three inlet angles generally substantiates the OASPL trends. Spectrum shapes, including duplication of the apparent shock noise level and frequency (particularly at the 50° inlet angle), are very similar. Some variance is noted at the higher frequencies; however, it should be noted that these are scaled-up data and that the 8 kHz and 10 kHz correspond to test data of 31.5 to 40 kHz, respectively, at which frequencies variance in the true value of atmospheric absorption coefficient may account for the somewhat poor agreement. The series of free jet area ratio tests generally substantiate the conclusion reached in the "as-is" assessment phase of Task 4 (see Section 3.1.2.1) that a free jet area ratio of 40 would in all probability provide a technically acceptable compromise to attaining simulated flight noise signatures (assuming suitable corrections are made for refraction, turbulence scattering, and dynamic effects).

- $A_8 = 108.6 \text{ in.}^2$
- 400 ft. Sideline
- No EGA, Free Field
- 77°F, 70% R.H.
- $\theta_1 = 140^\circ$

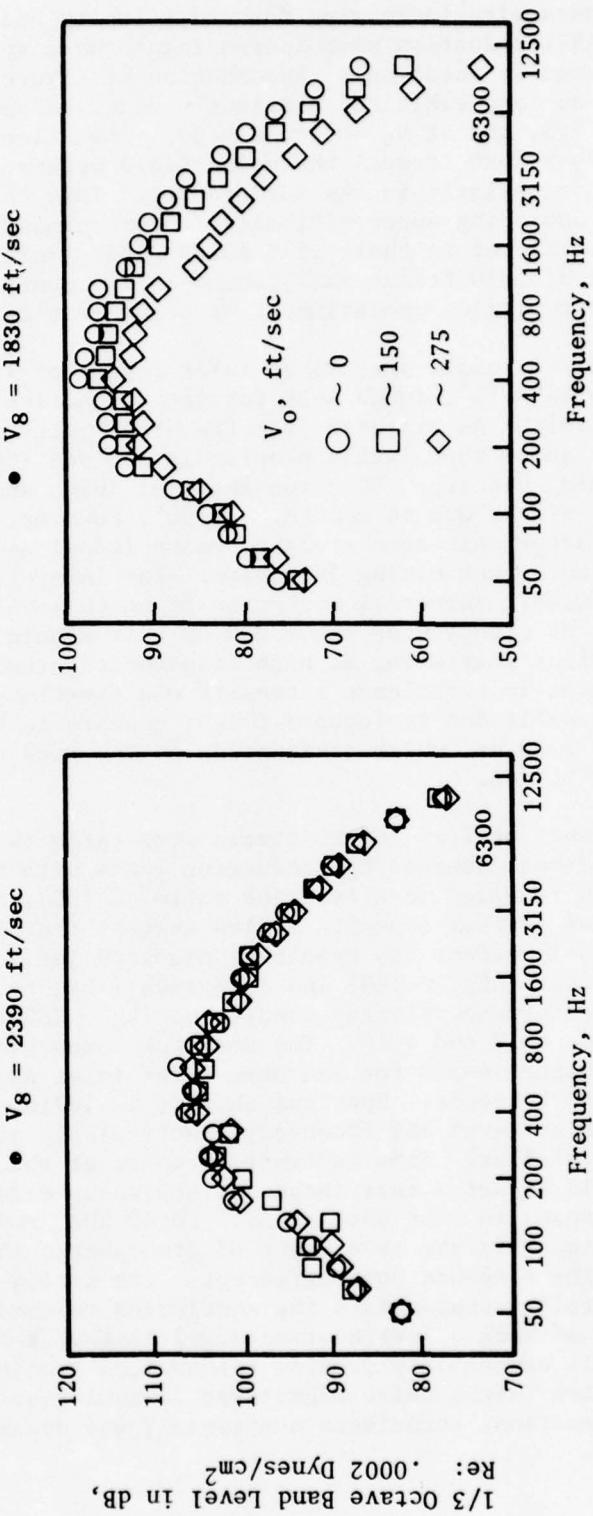


Figure 4-14. Fixed Frame Demonstration Test - Conical Nozzle SPL Spectra, $\theta_1 = 140^\circ$.

- $A_8 = 108.6 \text{ in.}^2$
- 400 ft. Sideline
- No EGA, Free Field
- 77°F, 70% R.H.
- $\theta_I = 90^\circ$
- $V_8 = 1830 \text{ ft/sec}$
- $V_8 = 2390 \text{ ft/sec}$

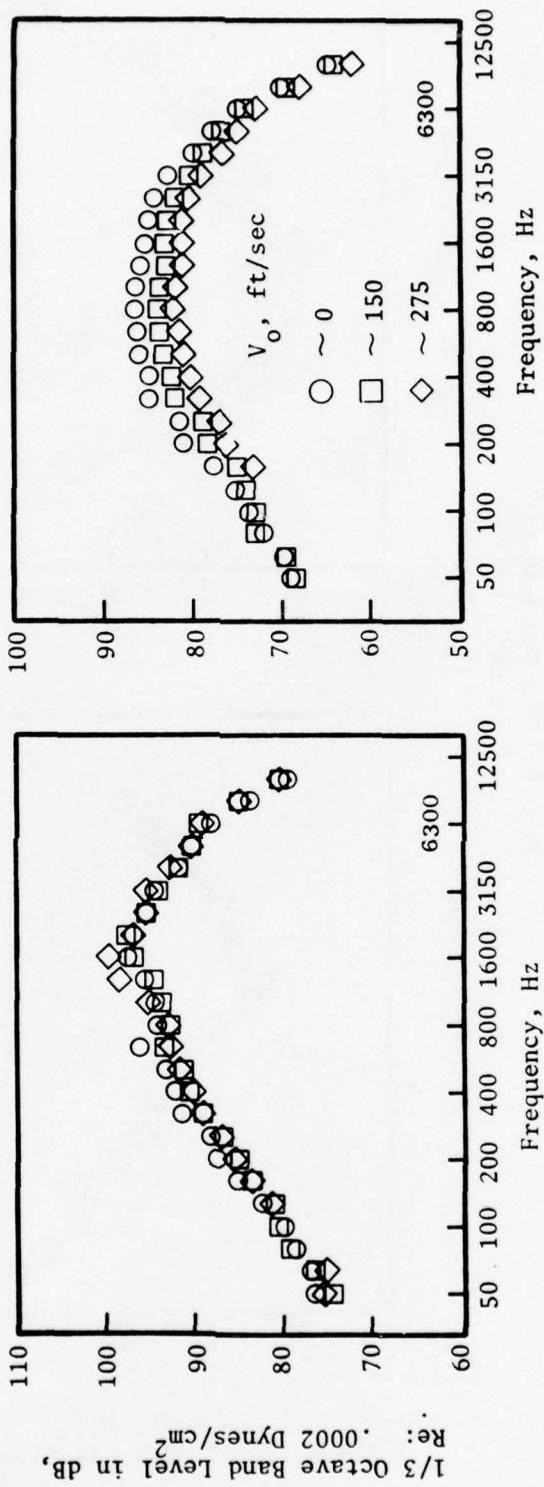


Figure 4-15. Fixed Frame Demonstration Test - Conical Nozzle SPL Spectra, $\theta_I = 90^\circ$.

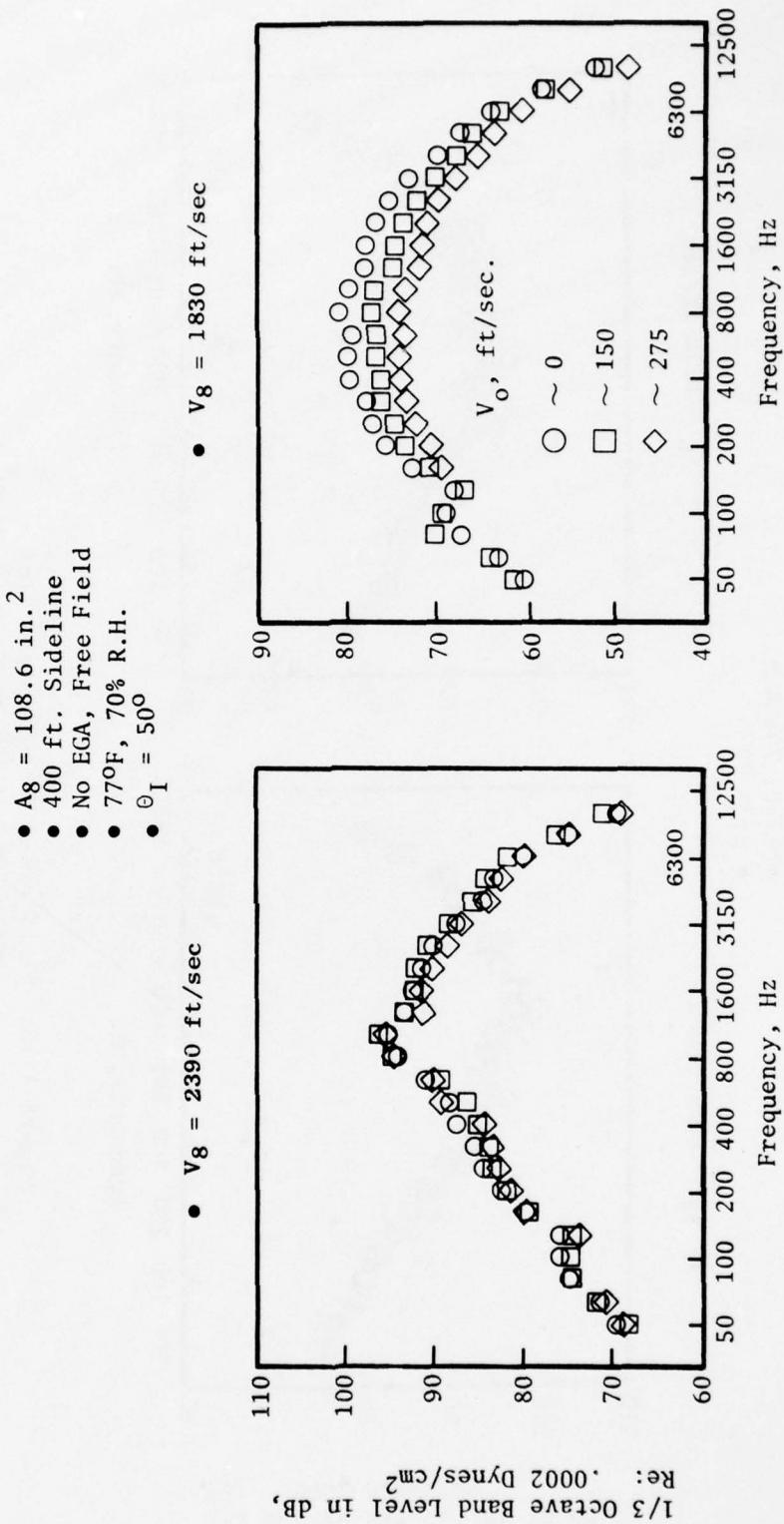


Figure 4-16. Fixed Frame Demonstration Test - Conical Nozzle SPL Spectra, $\theta_1 = 50^\circ$.

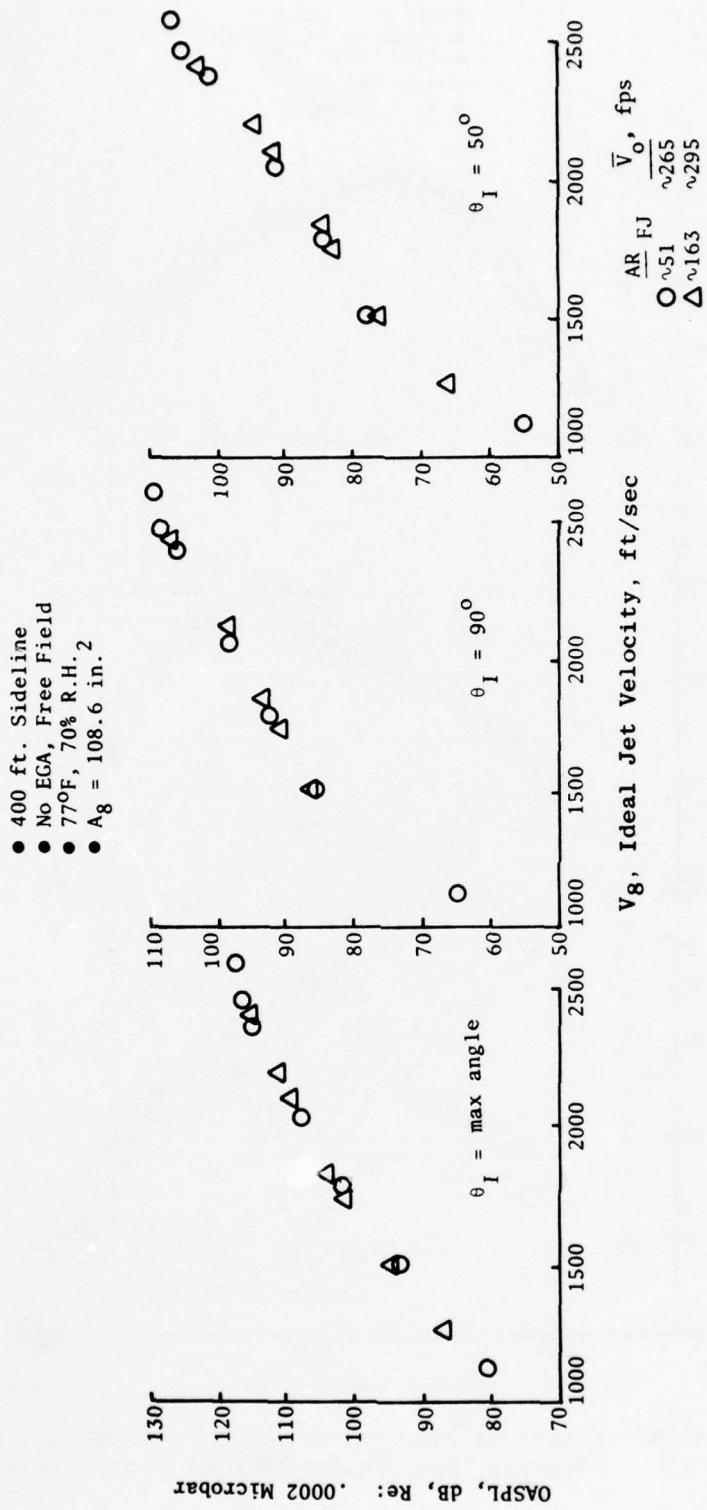


Figure 4-17. Effect of Free Jet Area Ratio on OASPL Forward Flight Characteristics.

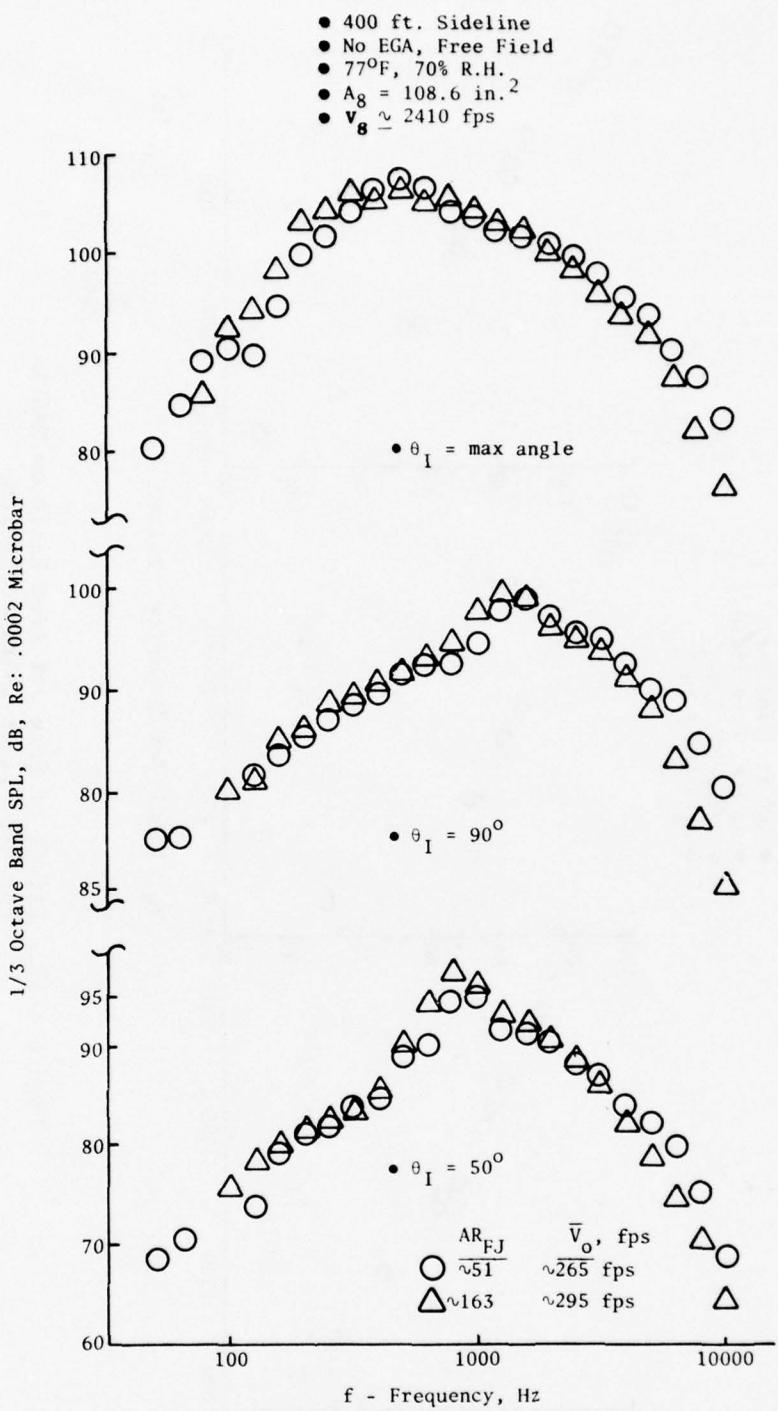


Figure 4-18. Effect of Free Jet Area Ratio on Sound Pressure Level Forward Flight Characteristics.

The maximum OASPL/jet velocity characteristics of the 8-lobe daisy are shown in Figure 4-19. The data exhibit the often-observed multielement suppressor trends, namely the relatively low slope of the noise level in the low velocity region (primarily attributed to the premerged portion of the jet) and the rather abrupt increase in slope at the higher velocities (usually associated with the coalesced region of the jet).

The 8-lobe daisy OASPL_{max} exhibits a noise reduction with increasing forward flight (as was the case for the conical nozzle); however, the reduction with primary velocity remains essentially invariant for velocities below 2200 ft/sec. At higher velocities, the reduction due to forward flight decreases with increasing jet velocity (same as conical). The directivity characteristics of the 8-lobe daisy nozzle are shown in Figure 4-20 for jet velocities of 1800 and 2400 ft/sec. The 1800 ft/sec jet velocity data tends to show the same insensitivity to angle from the inlet with increasing forward flight velocity that was exhibited by the conical nozzle. The directivity plot at $V_J = 2400$ ft/sec tends to be less directional. Shocks may be contaminating the forward arc (since the nozzle is operating supercritically). This speculation is reinforced by looking at the 50° spectra shown in Figure 4-21. Figures 4-21 and 4-22 are each typical of the spectra obtained for the above two jet velocities. The "just-choked" 1800 ft/sec data at 140° and 50° exhibit essentially a broadband reduction in SPL, with some biasing of the benefit in the high frequency portion of the double-humped spectrum. Data below 160 Hz are not presented because the free jet noise contaminated the jet noise.

The 2400 ft/sec spectra at 50° and 140° show a marked reduction in forward flight benefit compared to the 1800 ft/sec spectra. The 50° spectra at 2400 ft/sec (Figure 4-21) is definitely affected by the shock structure. The tone (which corresponds to the high frequency portion of the double-humped pure jet noise spectrum) remains insensitive to forward flight velocity. As in the aft-quadrant case, the benefit of forward speed is not fully realized until free-stream velocity is increased to 275 ft/sec. The effect on the spectrum, however, is contrary to that observed at 140°. The low frequency region corresponding to the coalesced region of the jet) benefits from the V_R effect rather than the high frequency region which appears to be infested with shocks and not affected by forward speed).

The 140° spectra for $V_g = 2400$ ft/sec (Figure 4-22), however, show that little benefit is derived at the 150 ft/sec simulated-flight condition. There is a substantial reduction between 250 and 2000 Hz, however, at 275 ft/sec flight speed. Increasing forward speed beyond 275 ft/sec had little impact on the spectrum.

The 104-tube noise characteristics are summarized in Figures 4-23 through 4-27. The peak OASPL/jet velocity trends shown in Figure 4-23 again exhibit noise level reduction with increasing forward flight velocity. Background noise at the high free jet velocities combined with the inherent low noise characteristics of the 104-tube nozzle limited the jet velocity range of interest over which acoustically clean data could be utilized. For most of

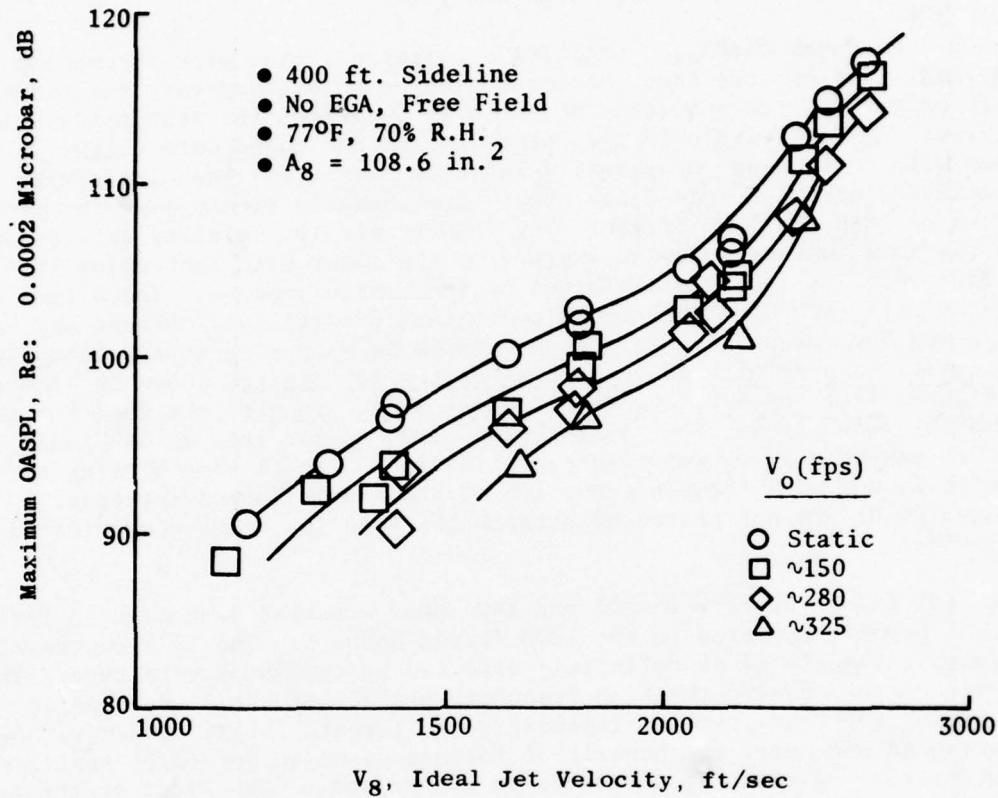


Figure 4-19. Fixed Frame Demonstration Test -
8-Lobe Daisy Nozzle Peak OASPL Characteristics.

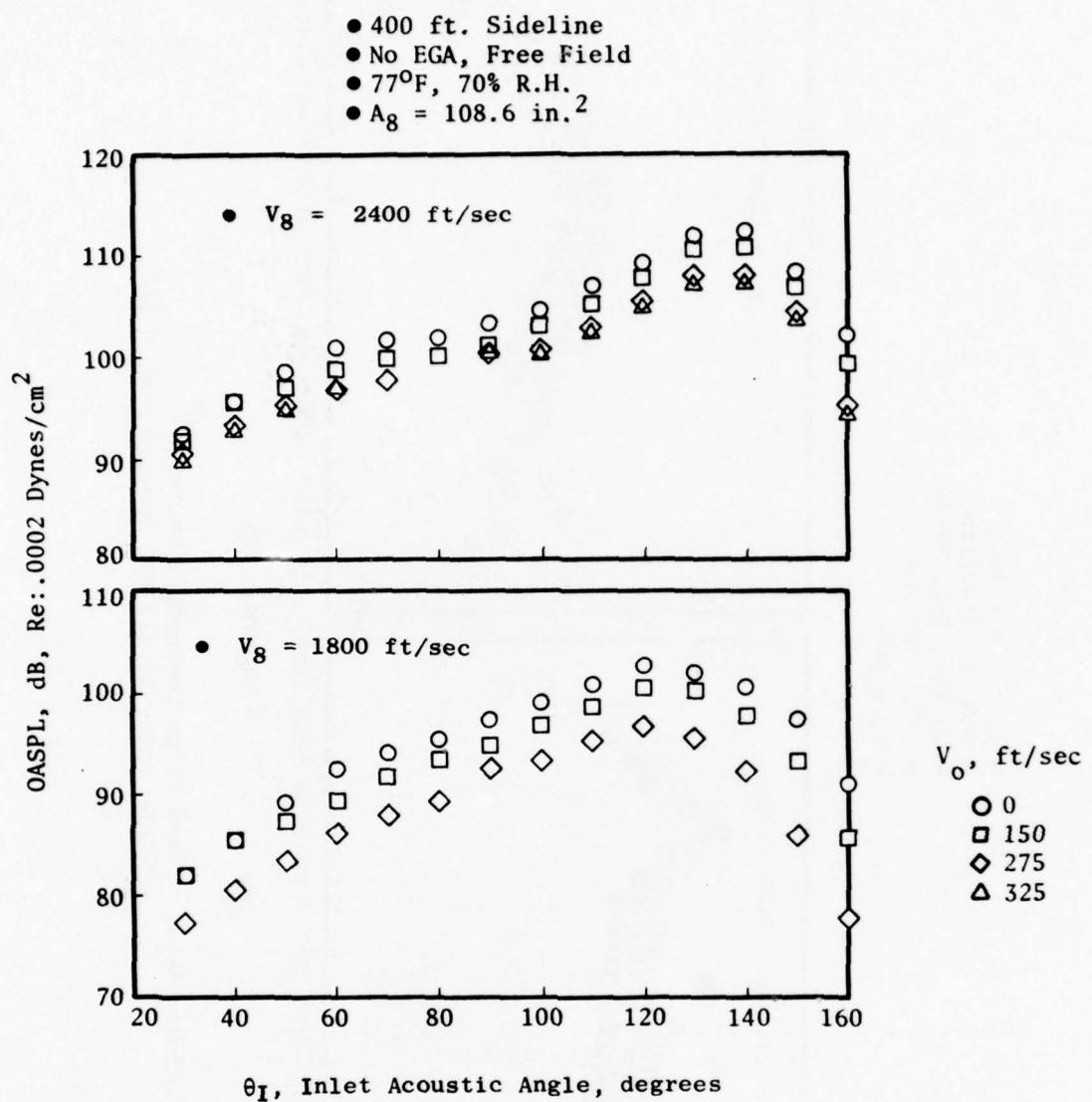


Figure 4-20. Fixed Frame Demonstration Test -
8-Lobe Daisy Nozzle OASPL Directivities.

- $A_8 = 108.6 \text{ in.}^2$
- 480 ft. Sideline
- No EGA, Free Field
- 77°F , 70% R.H.
- $\theta_1 = 50^\circ$

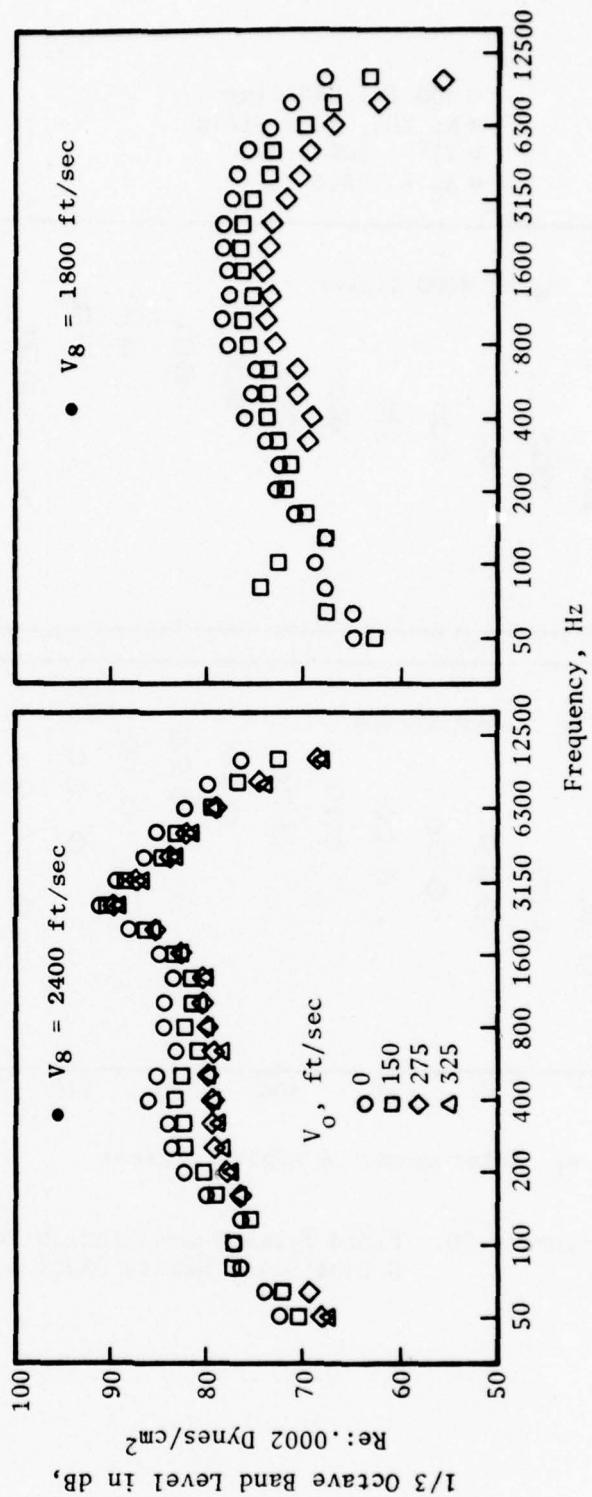


Figure 4-21. Fixed Frame Demonstration Test -
8-Lobe Daisy Nozzle SPL Spectra - $\theta_1 = 50^\circ$.

- $A_8 = 108.6 \text{ in.}^2$
- 400 ft. Sideline
- No EGA, Free Field
- 77°F , 70% R.H.
- $\theta_I = 140^\circ$

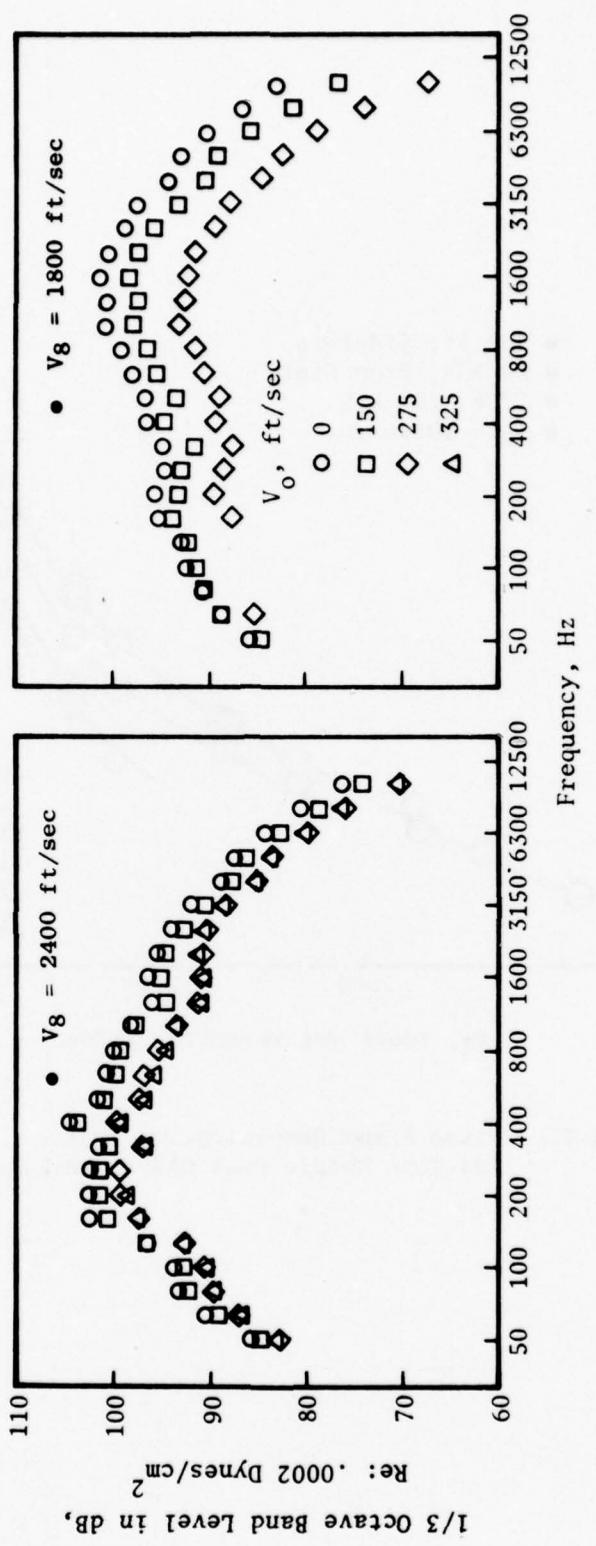


Figure 4-22. Fixed Frame Demonstration Test -
8-Lobe Nozzle SPL Spectra, $\theta_I = 140^\circ$.

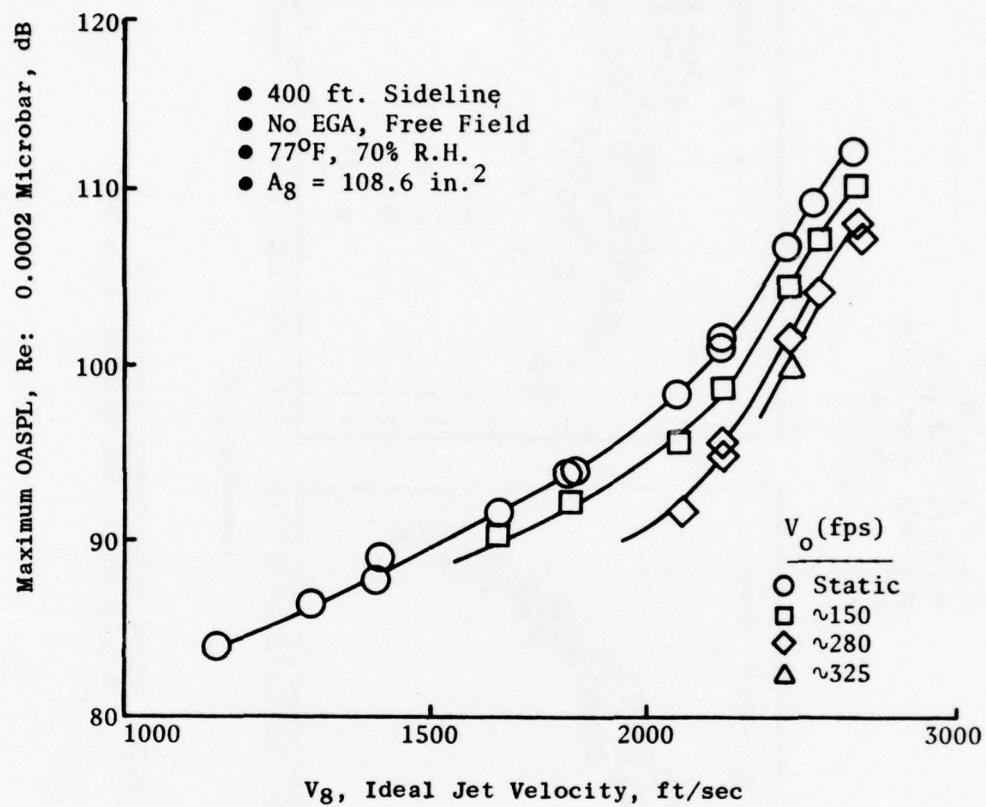


Figure 4-23. Fixed Frame Demonstration Test -
104-Tube Nozzle Peak OASPL Characteristics.

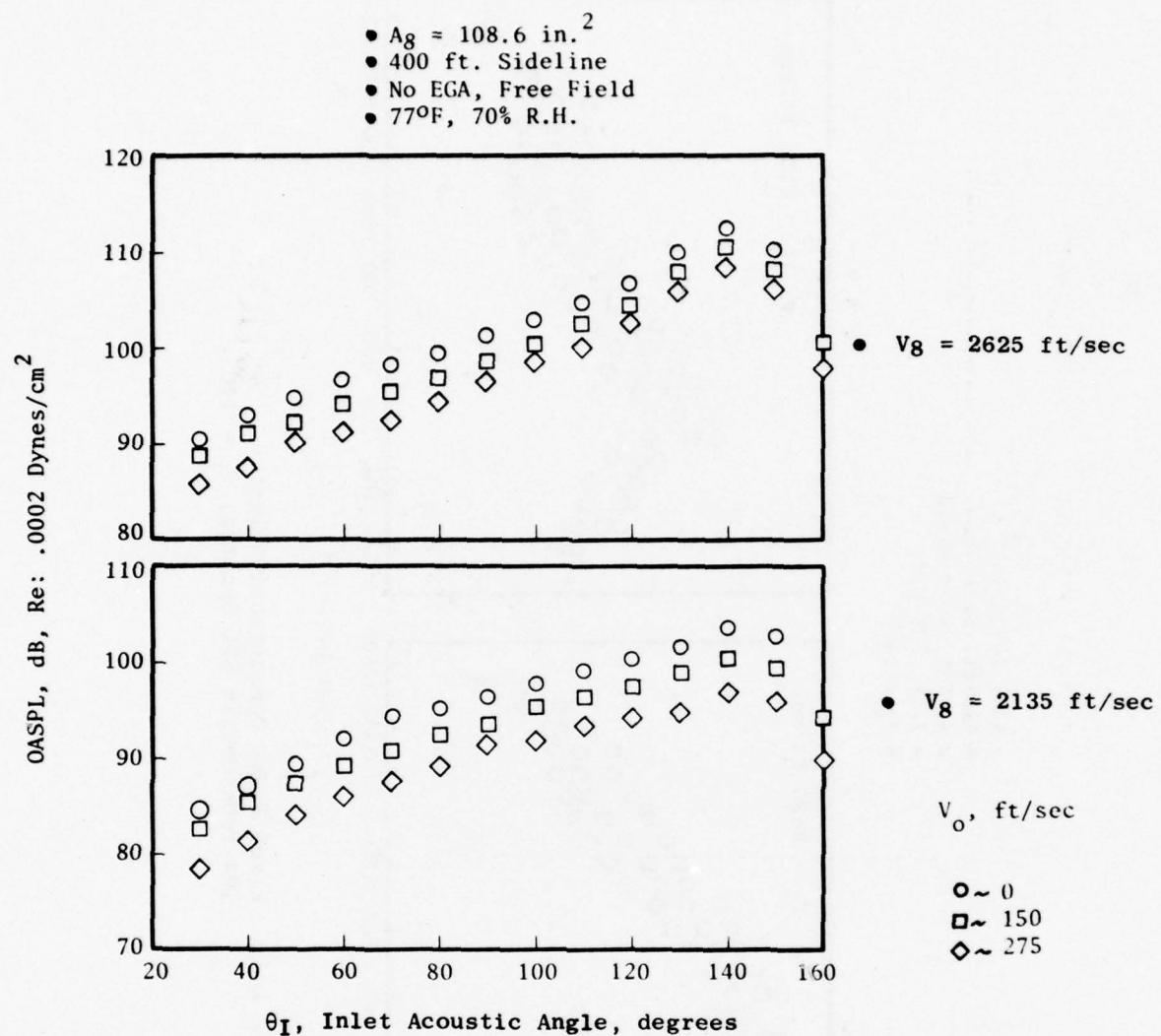


Figure 4-24. Fixed Frame Demonstration Test -
104-Tube Nozzle OASPL Directivities.

- $A_8 = 108.6 \text{ in.}^2$
- 400 ft. Sideline
- No EGA, Free Field
- 77°F , 70% R.H.
- $\theta_1 = 140^\circ$

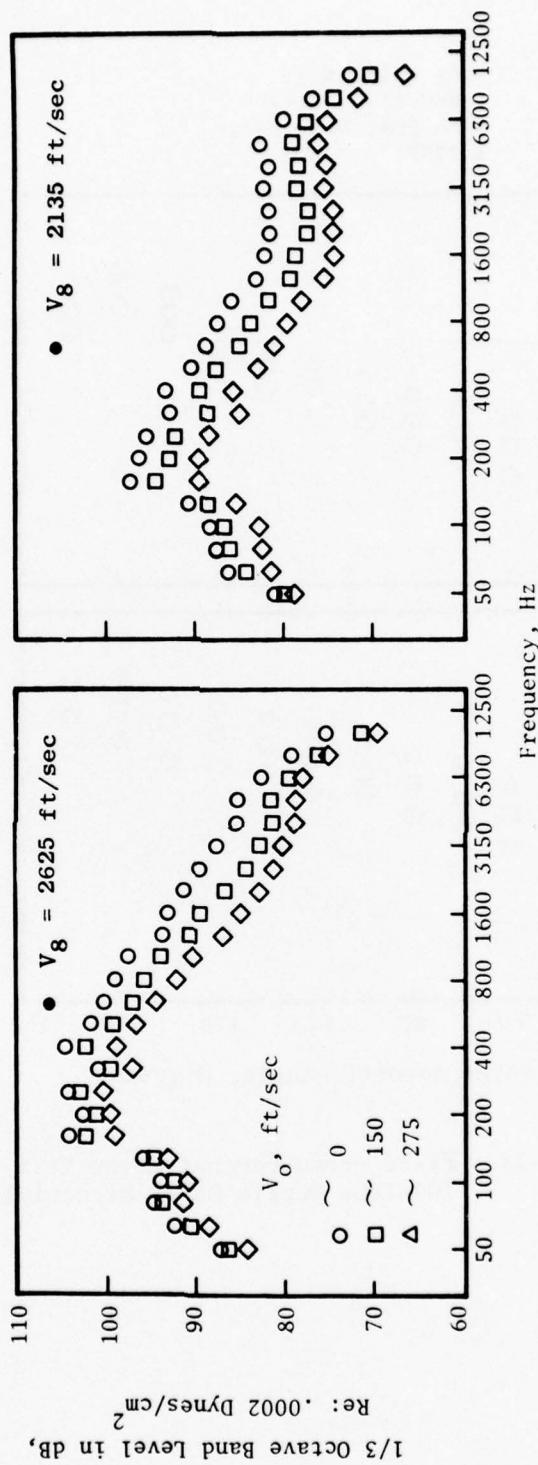


Figure 4-25. Fixed Frame Demonstration Test -
104-Tube Nozzle SPL Spectra, $\theta_1 = 140^\circ$.

- $A_8 = 108.6 \text{ in.}^2$
- 400 ft. Sideline
- No EGA, Free Field
- 77°F , 70% R.H.
- $\theta_1 = 140^\circ$

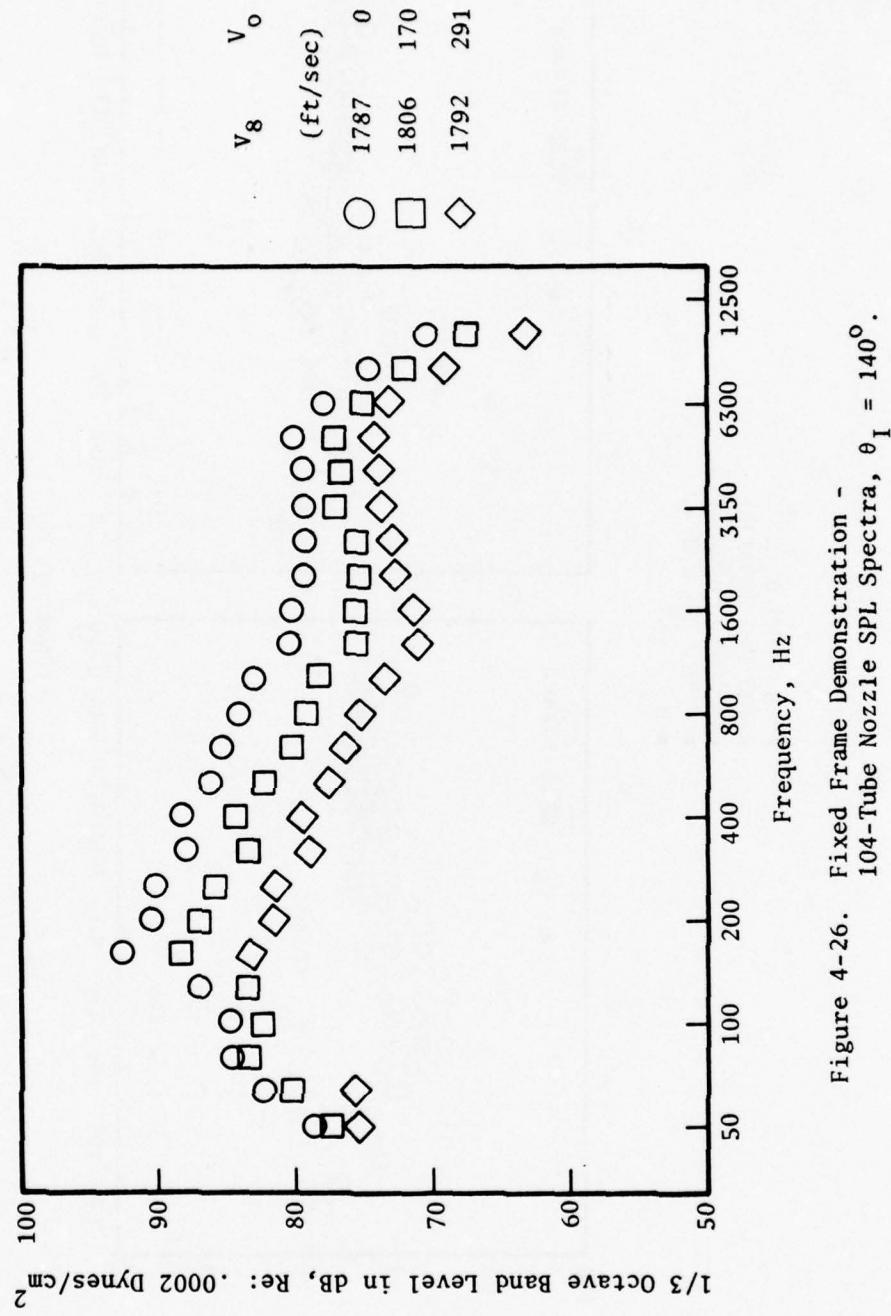


Figure 4-26. Fixed Frame Demonstration -
104-Tube Nozzle SPL Spectra, $\theta_1 = 140^\circ$.

- $A_8 = 108.6 \text{ in.}^2$
- 400 ft. Sideline
- No EGA, Free Field
- 77°F , 70% R.H.
- $\theta_1 = 50^\circ$

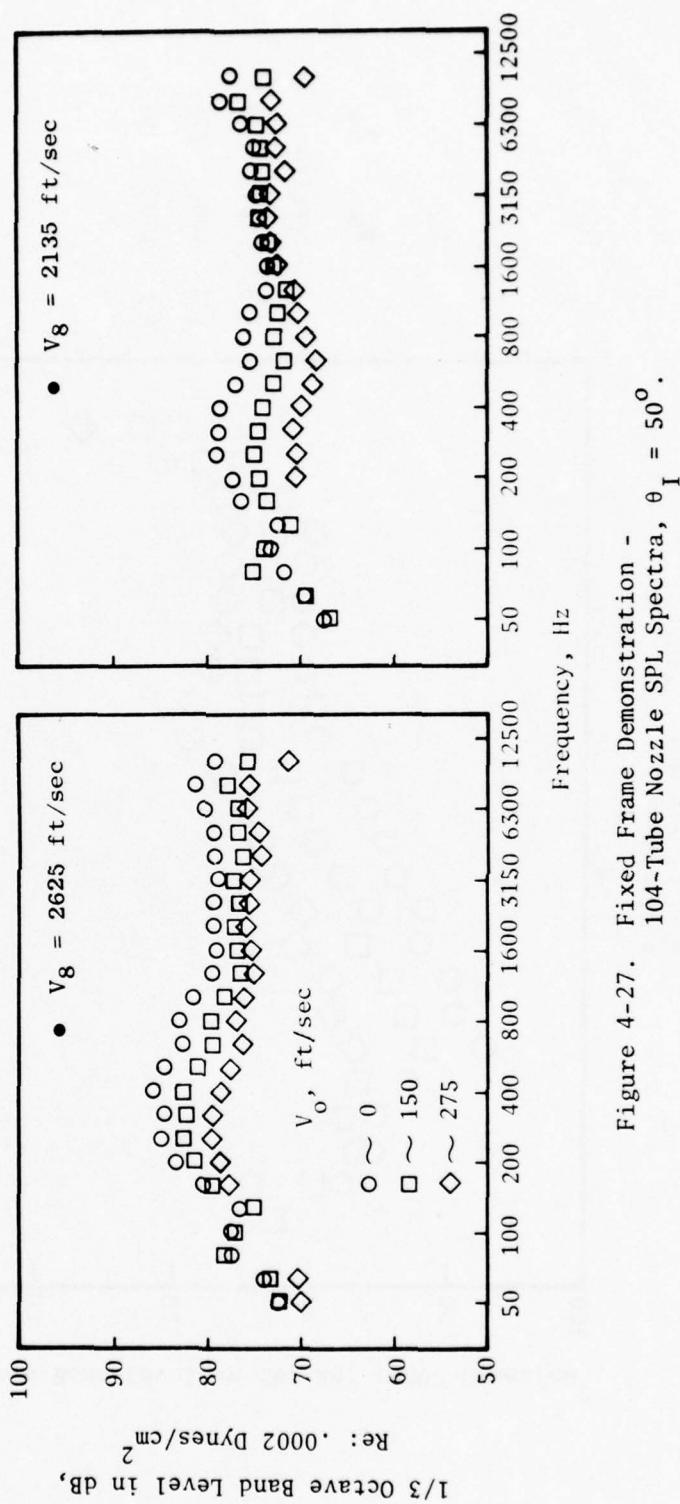


Figure 4-27. Fixed Frame Demonstration -
104-Tube Nozzle SPL Spectra, $\theta_1 = 50^\circ$.

the analysis, cutoff jet velocity was approximately 1600 ft/sec for free-stream velocities below 300 ft/sec. The $V_o = 150$ ft/sec peak-OASPL trends exhibit the typical multielement suppressor noise characteristic discussed previously for the daisy nozzle (a wide angle "V") and appear to be insensitive to jet velocity. The trend above $V_o = 150$ ft/sec is not as conclusive, however. The directivity plots of Figure 4-24 (for jet velocities of 2625 and 2135 ft/sec, respectively) exhibit much more directionality than their conical and daisy nozzle counterparts, especially at the higher jet velocity. This corresponds to the area of supercritical nozzle operation. The noise reduction with increasing free-stream velocity is also seen to be insensitive to angle. The high jet-velocity directivity plots suggest that shock-related noise may not be a factor.

Examination of the 140° spectra in Figures 4-25 and 4-26 illustrates the transition with increasing jet velocity, of a double-humped spectrum to one dominated by a merged or low velocity, low frequency coalesced jet. SPL reduction is observed with increasing free-stream velocity. The largest suppressions occur in the 200 to 5000 Hz frequency range. The 50° spectra in Figure 4-27 exhibit some interesting characteristics. The 2135 ft/sec jet velocity condition (also operating supercritically) exhibits little or no suppression with increasing forward flight speed, suggesting that shock noise may be present. Reexamination of the $V_j = 2135$ ft/sec noise field plot shows less directionality than the 2625 ft/sec jet velocity counterpart.

It appears that the pressure-ratio/temperature conditions at $V_j = 2135$ ft/sec are such that the shock noise in the forward arc is dominating the high frequency portion of the spectrum and is not affected by forward speed; whereas, the turbulent mixing noise associated with the merged jet region enjoys the benefit of increasing the free-stream velocity. The 2625 ft/sec jet velocity spectra at 50° (Figure 4-27) show a benefit (a reduction in noise level) with increasing forward velocity for all frequencies above 160 Hz. Some slight convergence (SPL's remaining essentially invariant with V_o) of the spectra is observed in the 1000 to 2500 Hz frequency region especially for the $V_o = 275$ ft/sec case (which might be indicative of the emergence of shock-related noise as turbulent mixing noise is reduced with increased forward speed).

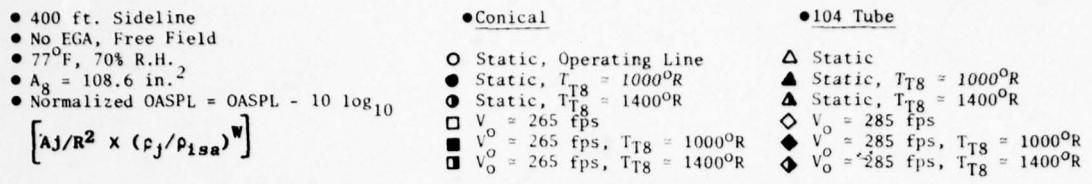
A number of pressure-ratio and temperature excursions were made from the standard operating-line test matrices in an attempt to assess how the far-field acoustic signature is influenced by nozzle underexpansion. Several tests were conducted on all three nozzles in an attempt to identify their noise-field characteristics, (particularly around the forward quadrant where, during simulated flight, the tone and broadband shock contribution could appreciably alter the noise levels). Fisher and Harper-Bourne found (1973 AGARD paper on Shock Cell Noise, Reference 24) that forward-arc noise is governed by the nozzle's degree of underexpansion (degree of supercritical pressure ratio) at a given temperature. Jet velocity and density remain the dominant factors in the aft quadrant, however.

A series of exploratory tests was conducted at JENOTS. These super-critical velocity temperature dependency noise studies were conducted for stagnation temperatures of 1000° and 1400° R, which resulted in pressure ratio excursions from 2.5 to 3.5 in two jet velocity regimes (1550 to 1900 and 1950 to 2250 ft/sec) at both static and simulated forward-flight ($V_o \approx 265 - 280$ ft/sec) speeds. (See Tables 4-I, 4-III, and 4-IV for details). Figure 4-28 summarizes the normalized OASPL at inlet angles corresponding to peak noise and at 50° for the conical and tube nozzles at jet velocities ranging from 1600 to 2300 ft/sec. The data were normalized (based on the NGTE/SNECMA jet density exponent technique, Reference 8) so that any variations from the operating line data could be truly attributed to nozzle under-expansion. In general, the data for the tube nozzle suggest that the shock contribution are minimal for static operation and at $V_o = 280$ ft/sec. This contributions are minimal for static operation and at $V_o = 280$ ft/sec. This constant-temperature data are identical for both the static and the simulated flight cases. This same conclusion is only valid for the conical nozzle, at the peak noise angle. Examination of the normalized OASPL results at the 50° inlet angle strongly suggests that nozzle shock structure is grossly influencing the noise level statically. At $V_o \approx 280$ ft/sec, the constant-temperature results show only a slight reduction (≈ 2 dB) when compared to the static results, and are well above the forward flight operating line data. The results of this exploratory study tend to support previous experimentalist's observations on shock noise. These data will be catalogued and included in the study of shock noise under Task 3 of this program.

4.1.5 Laser Velocimeter Measurements

The purpose of taking laser velocimeter (LV) measurements in this test program was to demonstrate the capabilities of the LV for determining changes in turbulent mixing characteristics of three basic exhaust systems due to the addition of free-stream velocity.

The laser velocimeter system was developed by General Electric during the AF/DOT Supersonic Jet Exhaust Noise Investigation (Reference 25) for measurement of mean and rms turbulent velocities in high-temperature, high-velocity jets. The LV is a noncontacting optical system in which the velocities of seed particles are measured (in a single direction) as they pass through the fringes of an interference pattern created by two intersecting beams of coherent radiation. The ellipsoidal control volume formed by the intersecting beams has a major axis of 0.25 inch and a minor axis of 0.02 inch. Figure 4-29 shows a schematic arrangement of the system. References 25, 26, and 27 contain detailed descriptions of the system and its validation, as well as results for measurements on scale-model nozzles under static conditions.



Note: $T_{T8} = 1000^\circ/1400^\circ R$ Excursions Are at Supercritical Pressure Ratios ($P_{T8}/P_0 = 2.5 \rightarrow 3.5$)

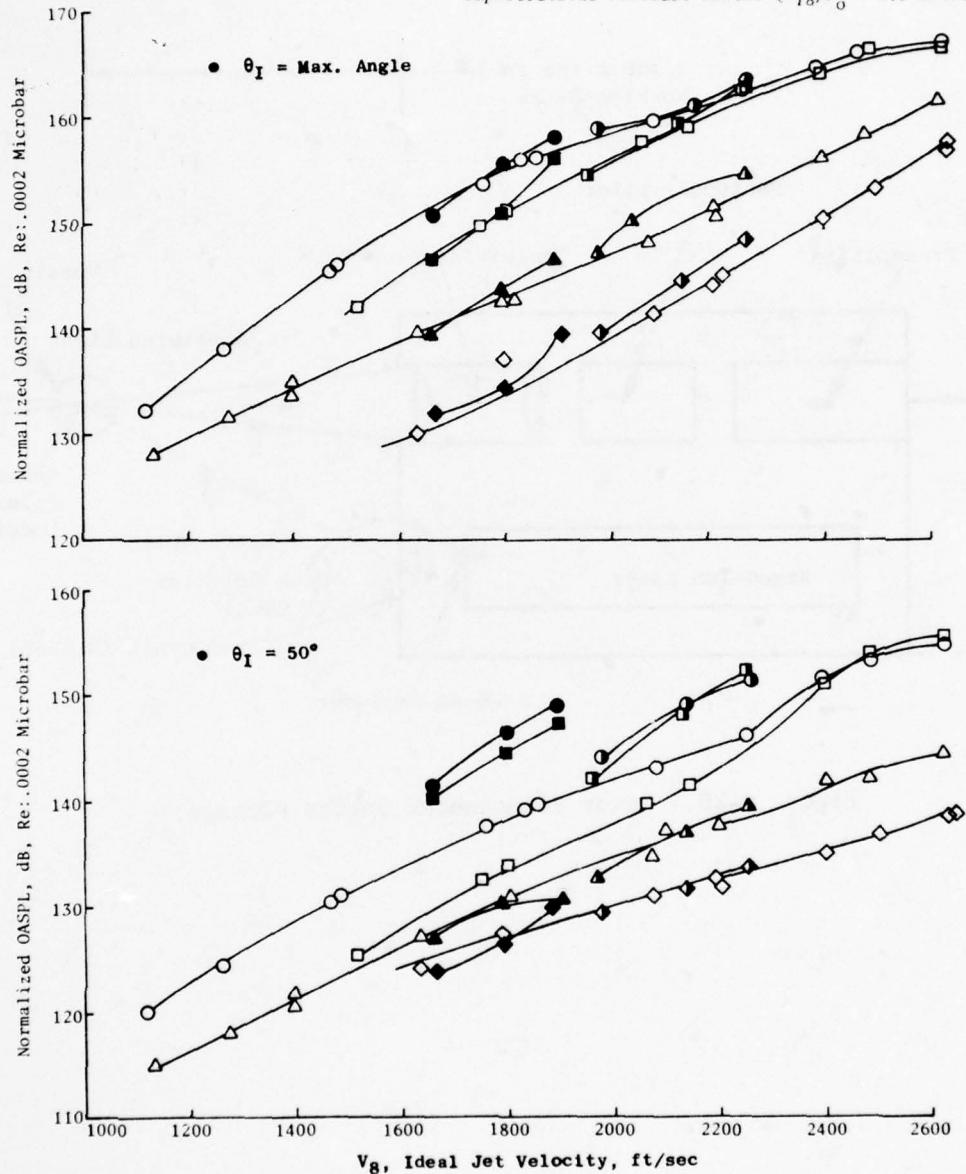


Figure 4-28. Supercritical Velocity - Temperature Dependency Noise Characteristics of Conical and 104-Tube Nozzles, Static and Flight.

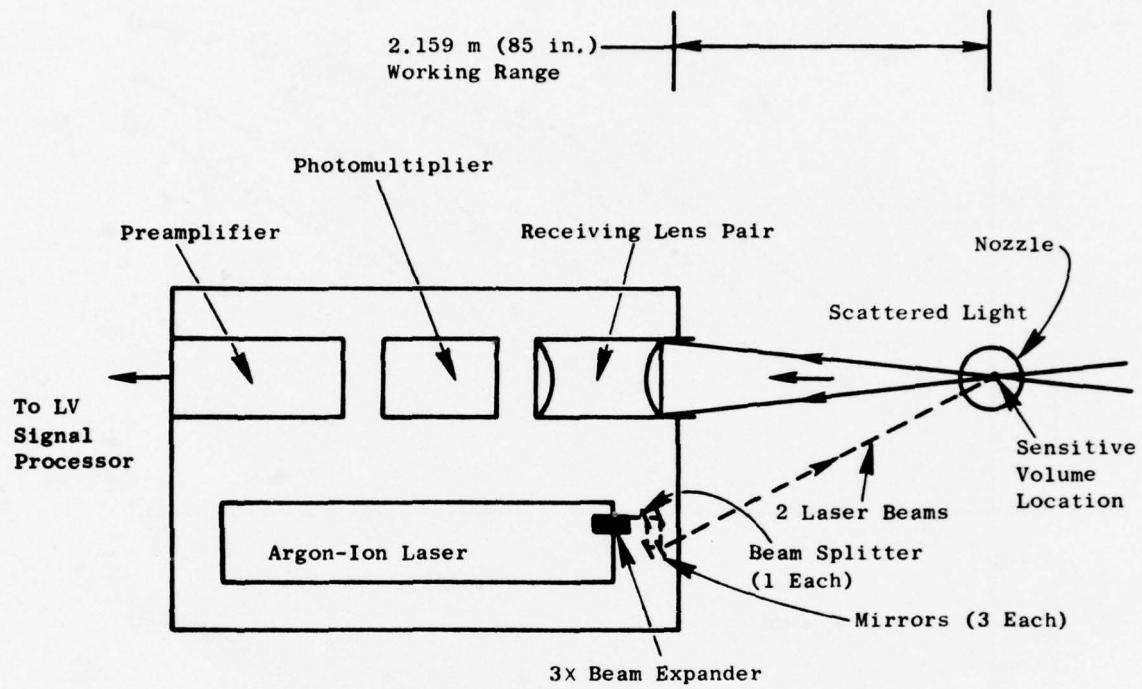


Figure 4-29. Laser Velocimeter Optics Package.

4.1.5.1 Test Setup and Conditions

The tests were conducted at the General Electric JENOTS free jet facility in Evendale. The setup of the laser velocimeter at JENOTS (for a static jet) is shown in Figure 4-30. The LV optics package is mounted on a remotely actuated platform on tracks parallel to the jet axis. Since the LV has a fixed working range of 85 inches, measurements at different points in the jet are accomplished by traversing the platform along three axes: horizontal, vertical, and axial (jet axis). Travel capabilities along the three axes are 32, 32, and 240 inches, respectively.

The laser velocimeter can be operated in a traversing mode to obtain continuous profiles of mean axial velocity, or it can be operated in a stationary mode to construct velocity histograms for determination of both mean and rms turbulent axial velocities at discrete points.

Traverses can be made along any of the three LV axes. In this mode of operation, the velocity levels and positions of incoming data are continuously recorded by an x-y plotter. Sampling rates on the order of at least 250 samples per inch of travel are typical for good definition. If data rates are low or details of a profile aren't clear, the traversing speed can be reduced or portions of the traverse can be repeated one or more times. Better definition can also be obtained by executing the traverse as a series of "stutter" steps, with short pauses interspersed to accumulate additional data.

Histograms are located at strategic points to verify details from the mean velocity traverses and to obtain rms turbulence levels. The histogram is formed from a large number of samples, typically 500 to 1000.

Tests using the previously described data acquisition methods were conducted on four different nozzle configurations representing two baseline nozzles and two types of multielement suppressors:

- 3.56-in. Conical (Figure 4-3)
- 2.0-in. STA (Figure 4-4)
- 8-Lobe Daisy (Figure 4-6)
- 104-Tube (Figure 4-8)

The LV test matrix for these configurations is presented in Table 4-VII.

A detailed plan of measurement locations in the jet was established for each test point on each configuration. Data was taken, in the form of traverses and histograms, up to 100 inches downstream of the nozzle exit. In the case of "wind-on" test points, limited data were also taken in the free jet.

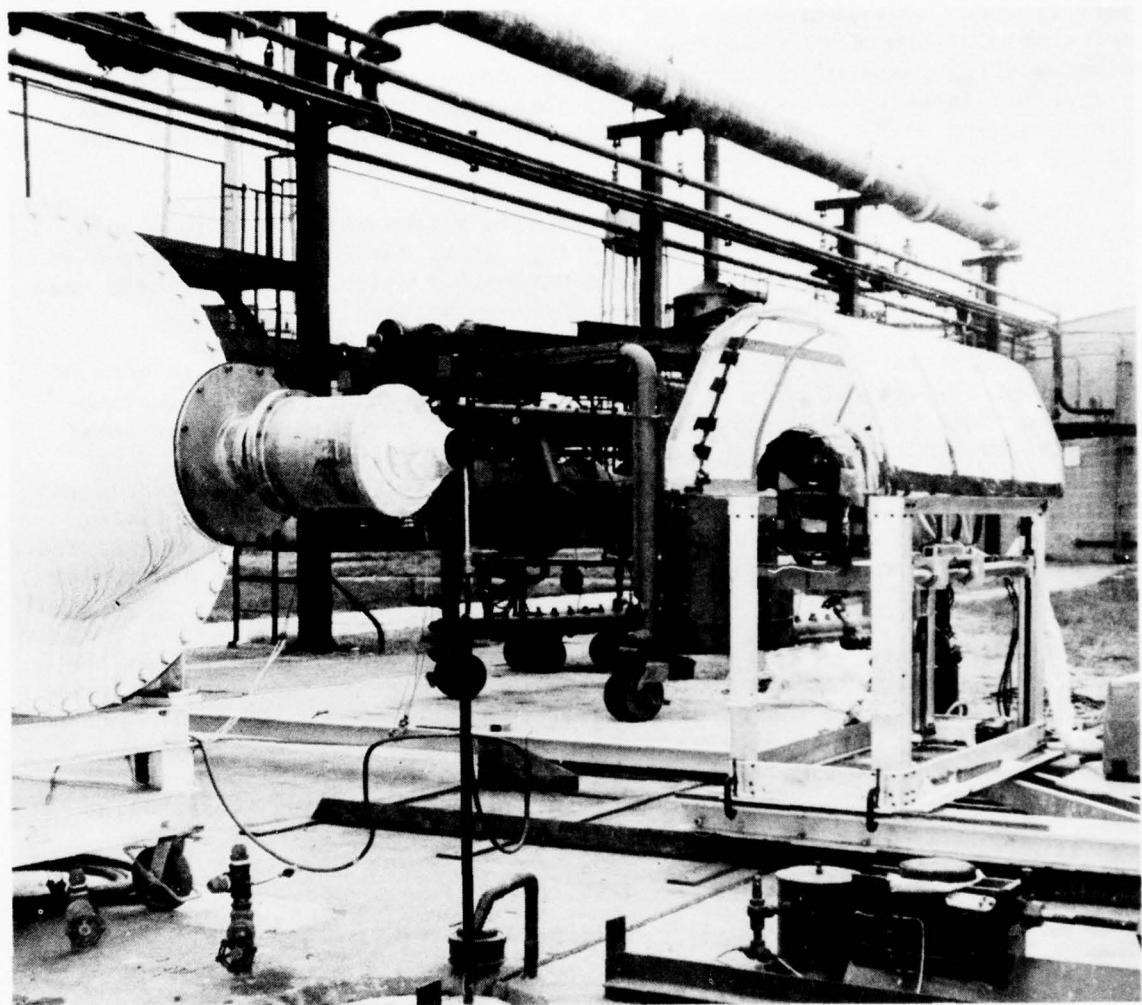


Figure 4-30. Laser Velocimeter Setup at JENOTS.

Table 4-VII. Test Matrix for Laser Velocimeter Measurements.

Data Point No.	Config.	V_8 (fps)	V_o (ips)	P_{T8}/P_o	T_{T8} (°R)
A	3.56" Conic	1130	0	1.363	1250
B		1130	150	1.363	1250
C		2200	0	2.550	1690
D		2200	150	2.550	1690
E		2200	275	2.550	1690
A	8 Lobe Daisy	1130	0	1.363	1250
B		1130	150	1.363	1250
C		2200	0	2.550	1690
A	104" Tube	1130	0	1.363	1250
B		1130	150	1.363	1250
A	2.0" STA	1130	0	1.363	1250
B		1130	150	1.363	1250
C		2200	0	2.550	1690
D		2200	150	2.550	1690

4.1.5.2 Data Analysis

The velocity data which were taken during this test have been analyzed to determine the capability of the LV to detect changes in mixing characteristics between static and "wind-on" operation for different basic types of scale-model exhaust nozzles. Basic comparisons were made using mean velocity traverses, with confirmation from histogram results.

Exact reproductions of several typical mean velocity traverses for the 3.56-inch conical nozzle and 104-tube nozzle are shown in Figures 4-31 thru 4-38. Locations where histogram measurements were made are also defined. Superimposed on each traverse is a hand-drawn line which was fitted through the data to represent the mean line of the distribution. The x and y scales for these plots are determined from the known calibration constants. The mean lines have been transferred to dimensioned plots in Figures 4-31 thru 4-38, with histogram results added for verification of velocity levels. Note the excellent agreement between the mean velocity traverses and the levels based on the histogram measurements. The results presented on Figure 4-34 are of particular note because this is a wind-on case at the nozzle exit plane. Figure 4-36 is also a wind-on case at six diameters downstream of the nozzle exit plane. Here, as before, the histograms and mean velocity traverses agree in absolute level, thus demonstrating the validity of the mean velocity traversing technique. The comparisons presented in the following section are based on mean velocity traverses similar to those described here. In all cases the mean-line is used to represent the velocity distribution. Some additional histograms are also presented for further verification of the mean velocity traverses.

In data reduction, the diameter, D_8 , was taken as the equivalent diameter for the total nozzle area:

- 3.56 in. $D_8 = 3.56$ in.
- 2.0 in. STA $D_8 = 2.00$ in.
- 8-Lobe Daisy $D_8 = 4.01$ in.
- 104-Tube $D_8 = 4.07$ in.

3.56 Inch Conical Nozzle - Previous experimental studies with circular nozzles (Reference 28) have demonstrated a pronounced effect of external velocity on jet mixing characteristics. The initial constant velocity region (potential core) is lengthened and centerline velocity decay is less rapid with increasing free-stream velocity. Laser velocimeter data for the 3.56-inch conical nozzle confirm these trends, as shown in Figure 4-39, for the subsonic jet (1130 ft/sec) with 0 and 150 ft/sec free jet velocities. Nozzle exit-plane turbulence levels of 3-1/2 to 5-1/2 percent were found for both points. The initial rise in centerline velocity is caused by the combined effects of vena contracta downstream of the exit plane and a defect in the center of the mean velocity profile due to the presence of an upstream center-body. This can be seen from the velocity profiles shown in Figures 4-40 and

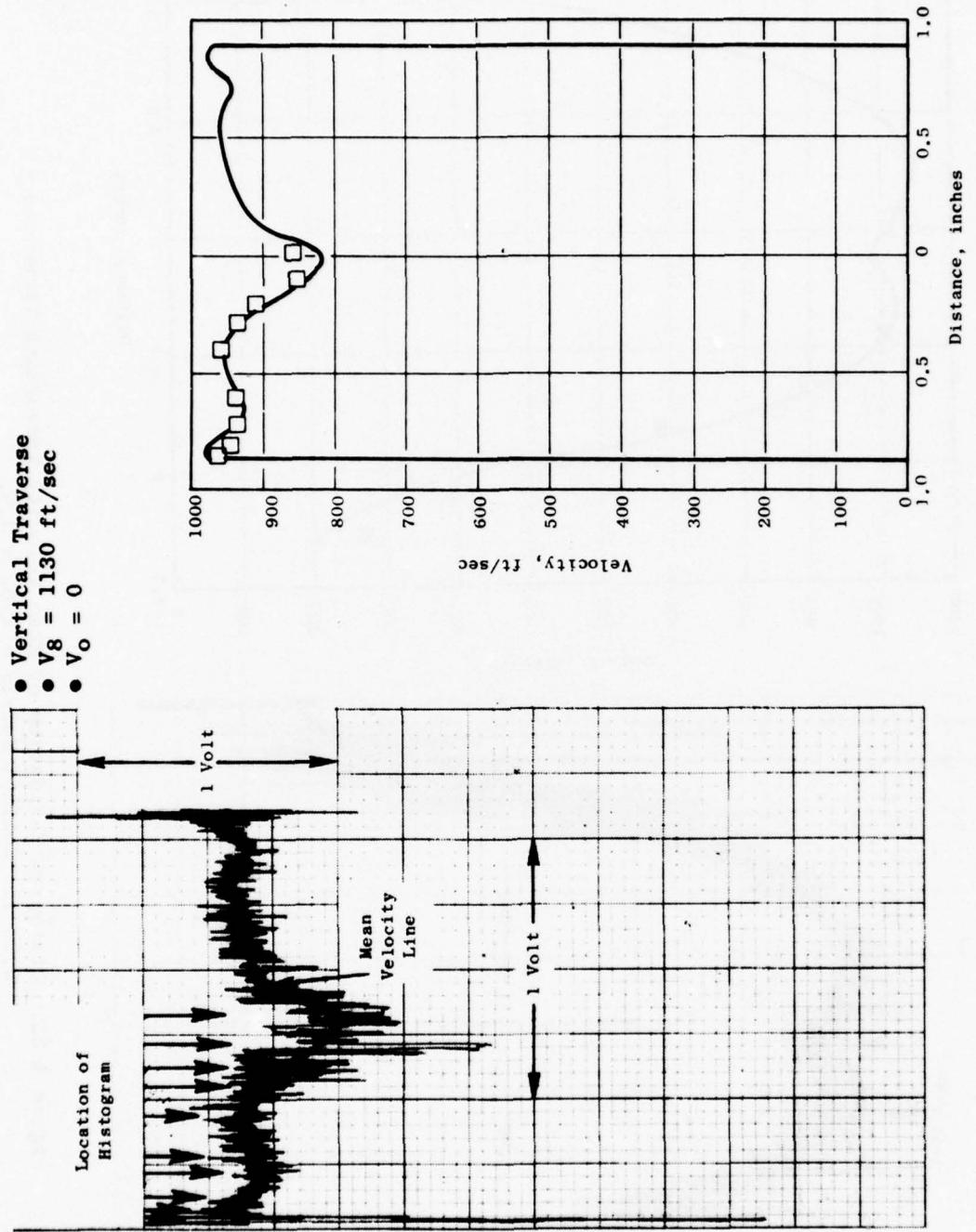


Figure 4-31. Histogram Validation of Mean Velocity Traversing Technique -
3.56-in. Conical Nozzle - $X/D_8 = 0.1$.

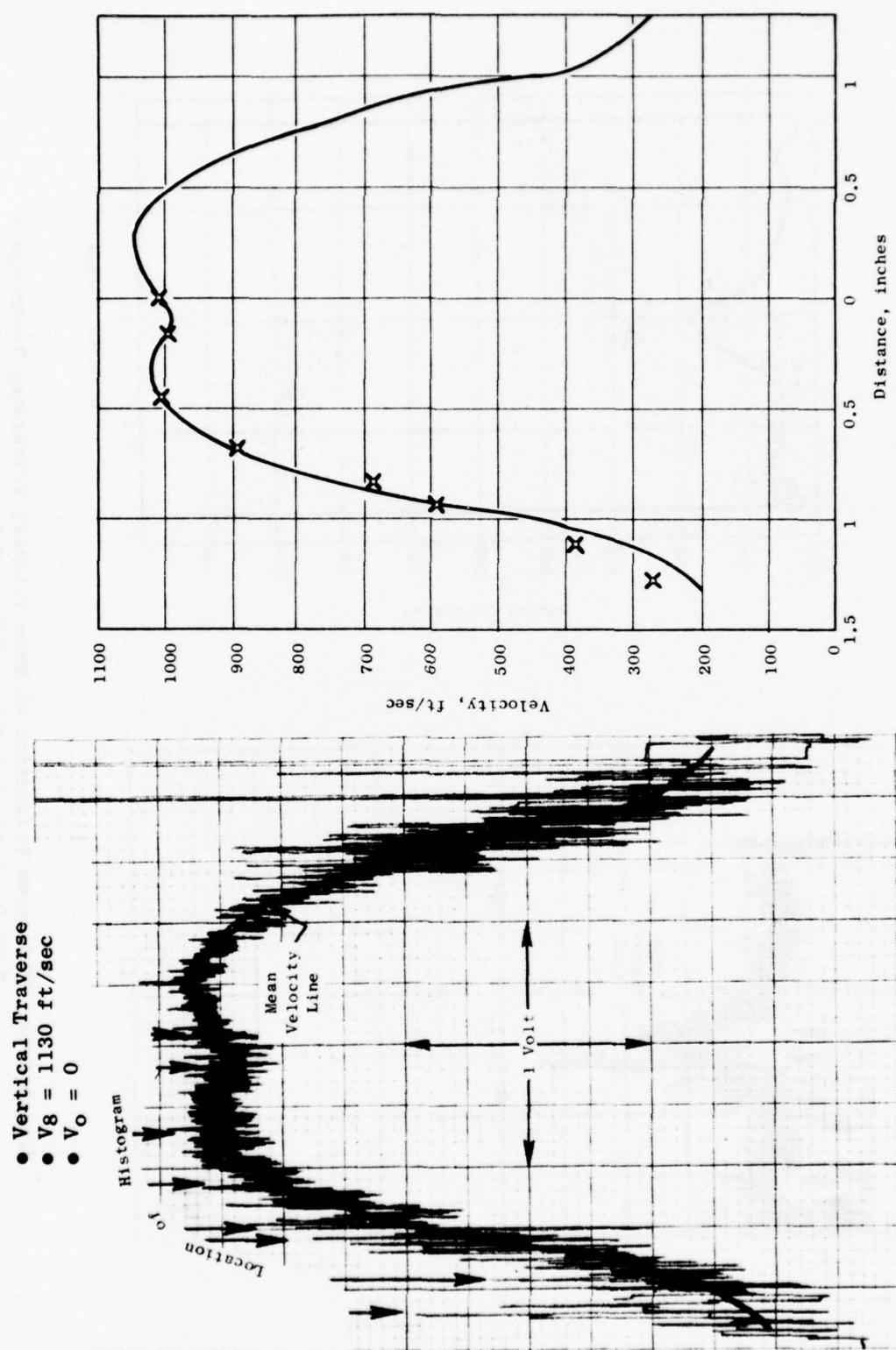


Figure 4-32. Histogram Validation of Mean Velocity Traversing Technique - 3.56-in. Conical Nozzle - $X/D_8 = 3.0$.

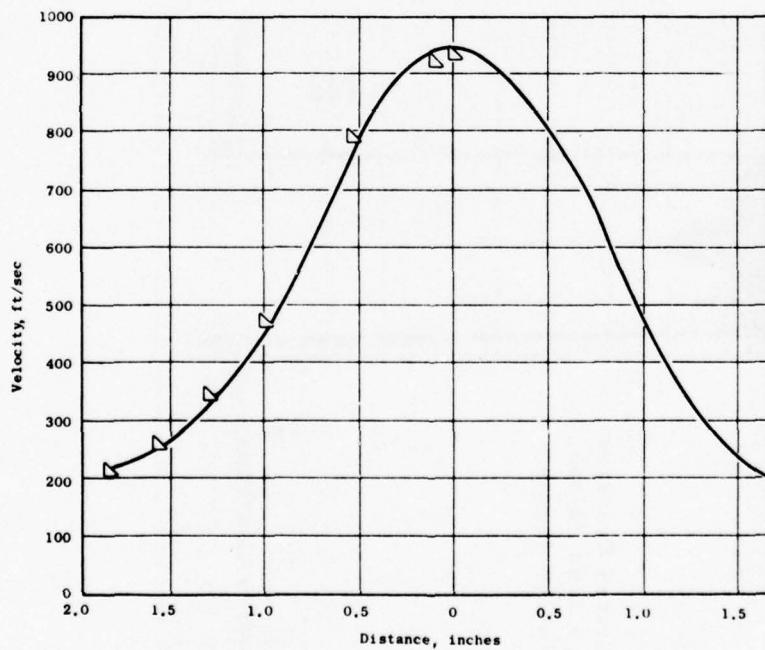
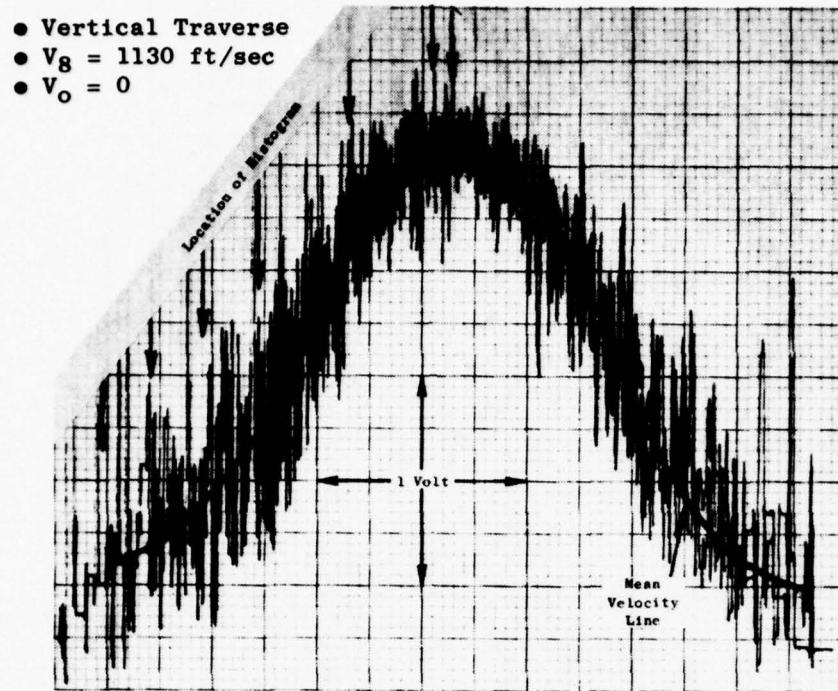


Figure 4-33. Histogram Validation of Mean Velocity Traversing Technique - 3.56-in. Conical Nozzle - $X/D_g = 6.0$.

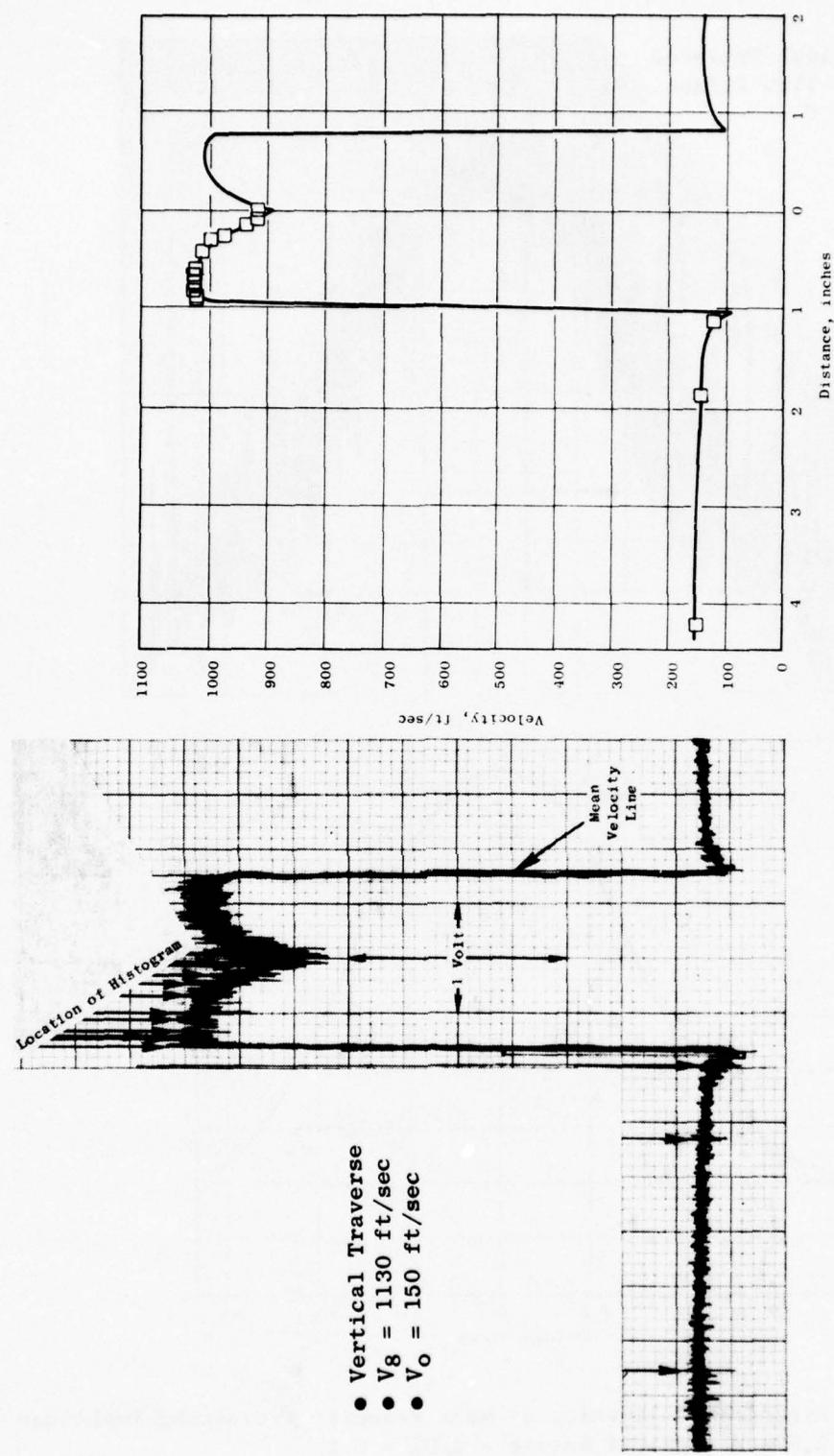


Figure 4-34. Histogram Validation of Mean Velocity Traversing Technique -
3.56-in. Conical Nozzle Wind-On - $X/D_8 = 0.1$.

- Vertical Traverse
- $V_8 = 1130 \text{ ft/sec}$
- $V_o = 150 \text{ ft/sec}$

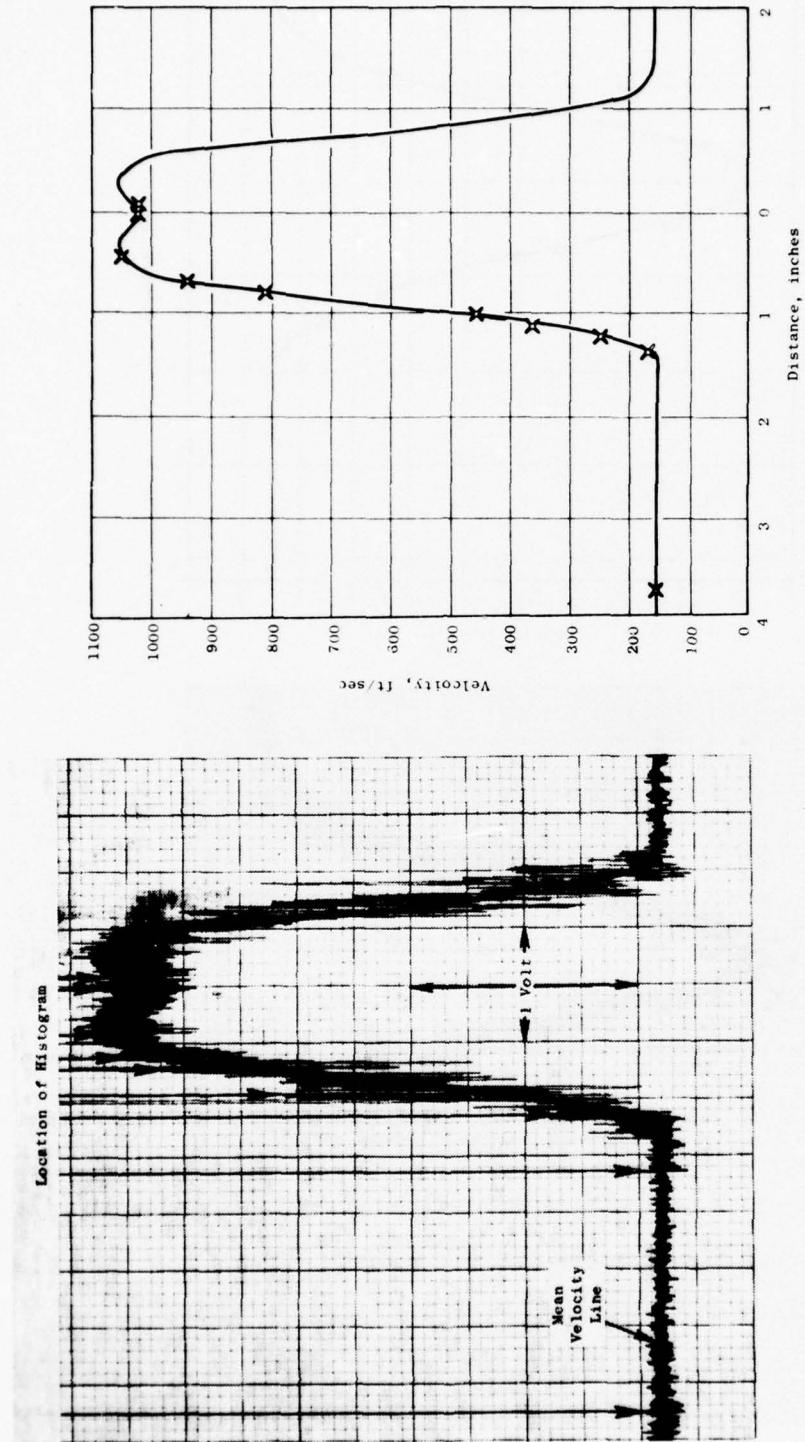


Figure 4-35. Histogram Validation of Mean Velocity Traversing Technique -
3.56-in. Conical Nozzle Wind-On - $X/D_8 = 3.0$.

- Vertical Traverse
- $V_8 = 1130 \text{ ft/sec}$
- $V_0 = 150 \text{ ft/sec}$

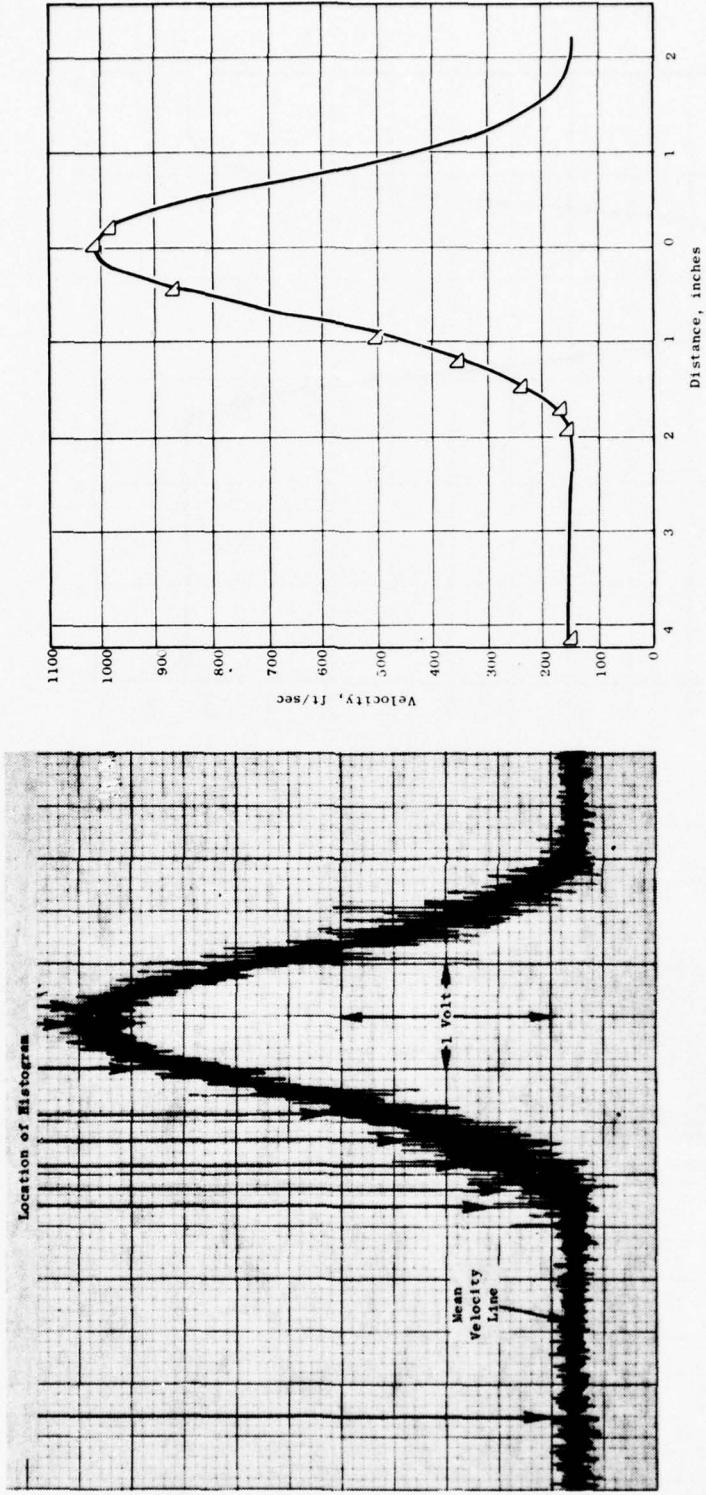


Figure 4-36. Histogram Validation of Mean Velocity Traversing Technique -
3.56-in. Conical Nozzle Wind-On - $X/D_8 = 6.0$.

- Horizontal Traverse
- $V_8 = 1130 \text{ ft/sec}$
- $V_0 = 0$

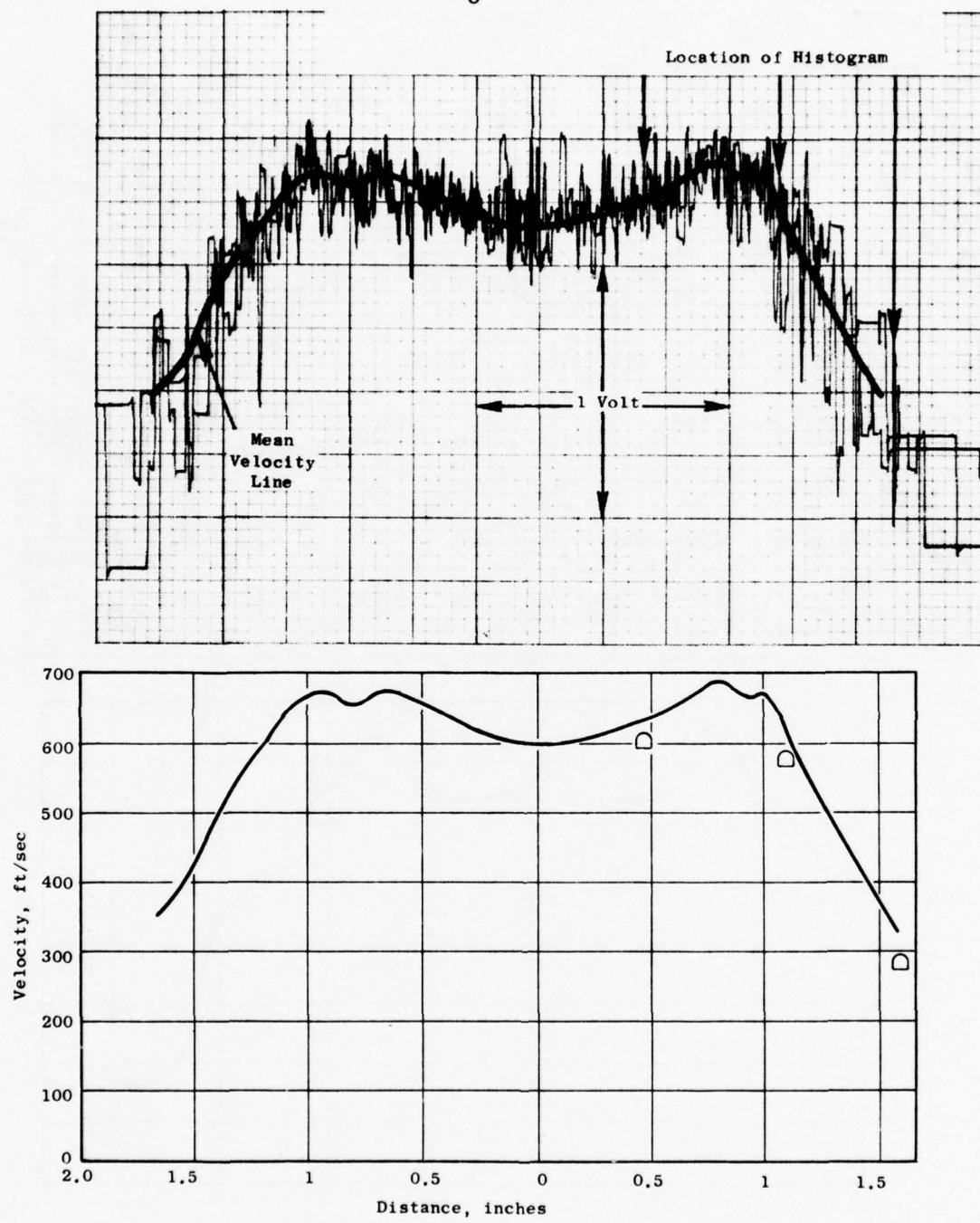


Figure 4-37. Histogram Validation of Mean Velocity Traversing Technique -
104-Tube Nozzle - $X/D_8 = 2.0$.

- Horizontal Traverse
- $V_g = 1130 \text{ ft/sec}$
- $V_o = 150 \text{ ft/sec}$

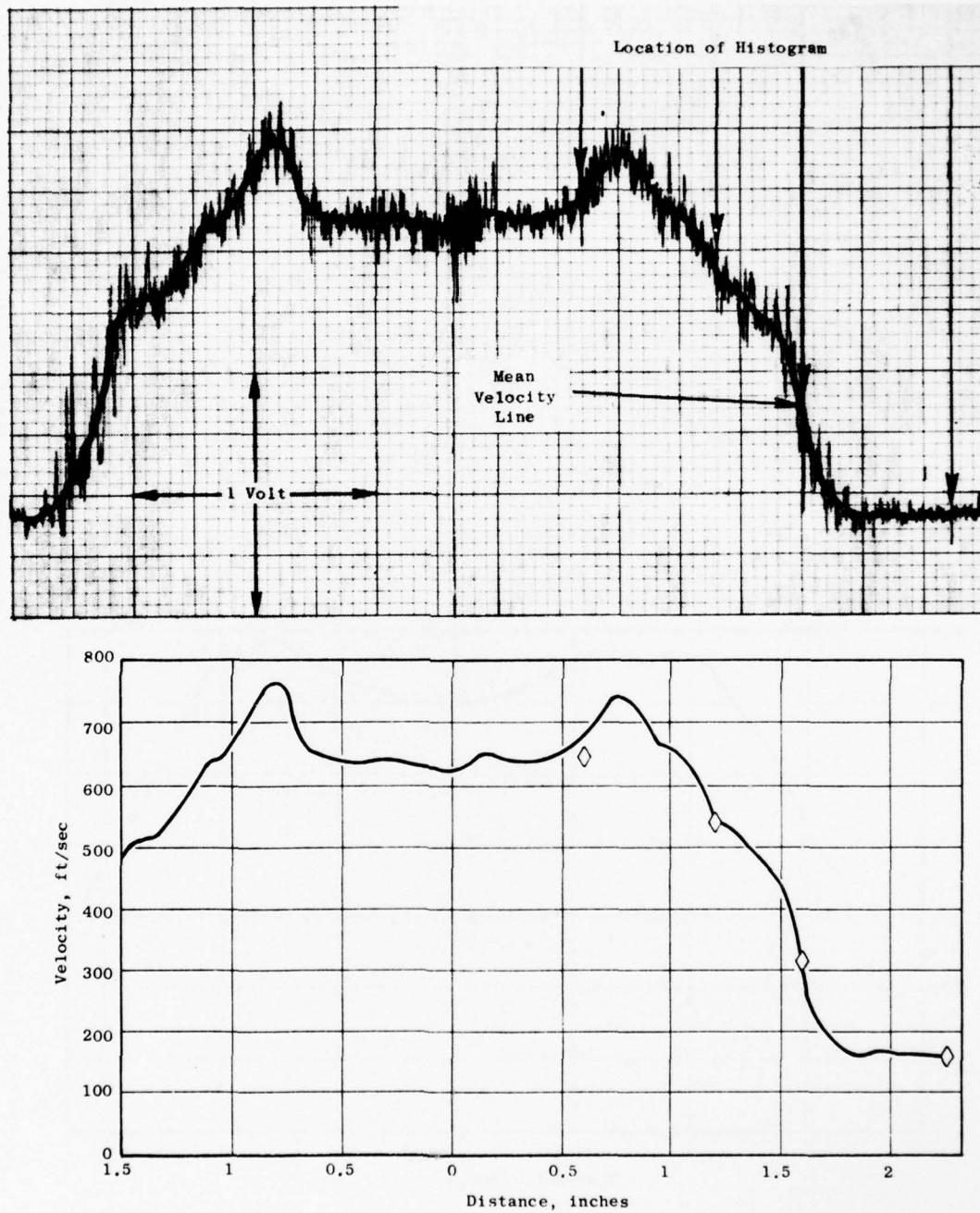


Figure 4-38. Histogram Validation of Mean Velocity Traversing Technique - 104-Tube Nozzle - $X/D_g = 1.0$.

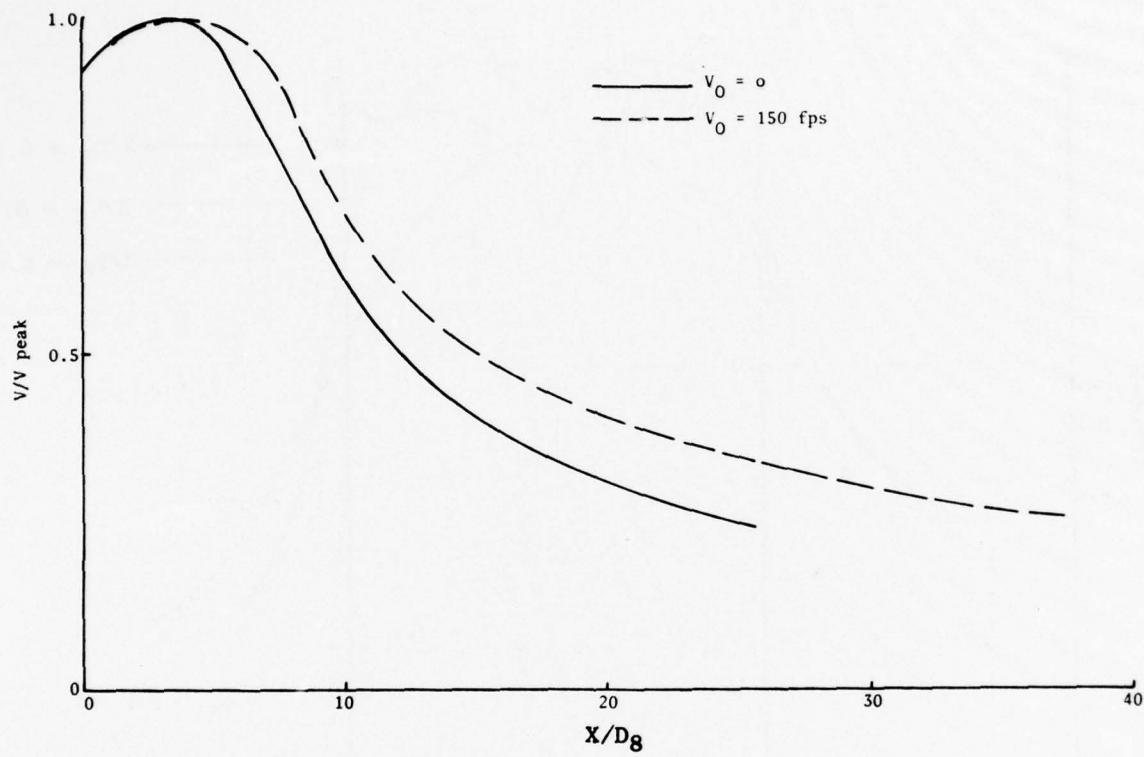


Figure 4-39. Centerline Velocity Decay for 3.56-Inch Conical Nozzle, $V_J = 1130 \text{ ft/sec.}$

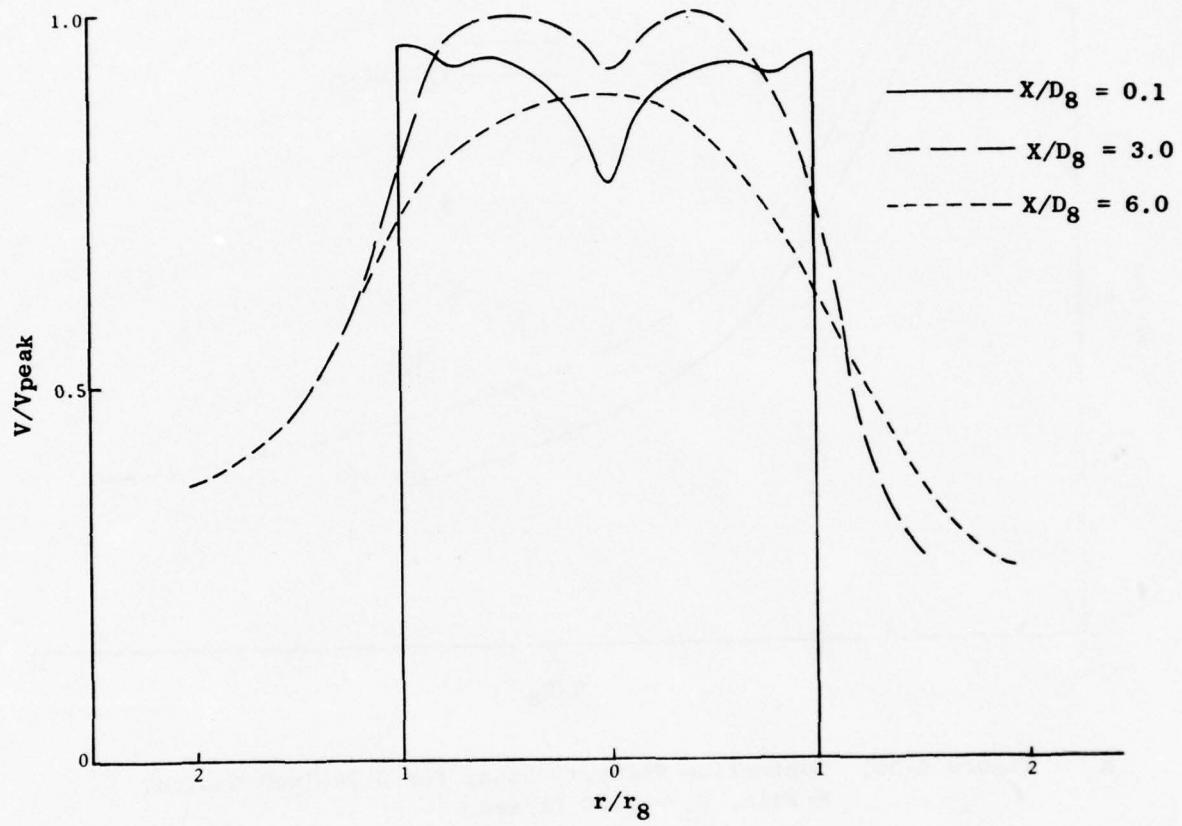


Figure 4-40. Velocity Profiles for 3.56-Inch Conical Nozzle, $V_J = 1130$ ft/sec, $V_0 = 0$.

4-41 for the static and wind-on conditions, respectively. This may be the cause of the differences between the noise signatures of the two conical nozzles. Inspection of the profiles at downstream locations indicates that the velocity defect has mixed out within six nozzle diameters. As an example of the detail which can be obtained from LV traverses, note that the nozzle exterior boundary layer profile is evident at the first axial station in Figure 4-41.

A comparison of centerline velocity decay for the supersonic jet (2200 ft/sec) with three different free jet velocities (0, 150, and 275 ft/sec), is shown in Figure 4-42, indicating the same trends noted previously. The measured exit plane turbulence intensities were the same as for the subsonic jet. The effect of external velocity on the characteristic shock pattern of an underexpanded jet is clearly seen in the centerline axial traverses shown in Figure 4-43. The shock cells appear to be "stretched" axially in the presence of external flow. The data for this figure were obtained by making traverses over a limited range with a precision drive system on the LV platform.

8-Lobe Daisy Nozzle - One of the major questions to be answered with regard to use of the laser velocimeter for multielement suppressor nozzles is whether or not the flow fields of individual elements can be discriminated and accurately measured near the nozzle exit plane. The capability of the LV in this regard was demonstrated with the 8-lobe nozzle by taking horizontal traverses in a plane 1.85 inches below the centerline, intersecting the three bottom lobes (see Figure 4-44). Data for the static subsonic jet are shown in Figure 4-44. At the first axial station ($x/D_8 = 0.1$), the velocity profiles across the individual lobes are quite apparent. The velocity between lobes was not detected at this station since there was no seeding of the ambient air. Moving downstream, the mixing between lobes can be seen as the individual flow fields merge. Data for the subsonic jet with 150 ft/sec external velocity is shown in Figure 4-45. Since the external (free jet) flow is seeded for LV operation, the velocity between lobes can be measured at the first axial station. This velocity is seen to be higher than the overall level of external velocity, indicating that the flow is accelerated slightly in the passage between lobes; otherwise, there are no significant differences apparent from comparing data for static and wind-on operation. A comparison of velocity decay behind an individual lobe for the two conditions is shown in Figure 4-46. This suggests that there is very little, if any, effect on mixing characteristics due to external velocity.

104-Tube Nozzle - The 104-tube nozzle (Figure 4-9) presents a formidable challenge to the capabilities of the LV for resolution of individual-element flow fields. In this case, horizontal traverses were made in a plane 0.22 inch below centerline, intersecting 10 individual tubes. Since the tubes are staggered, it was not possible to traverse through the centerline of each one. Data for the subsonic jet, run statically, and with 150 ft/sec external velocity are shown in Figures 4-47 and 4-48, respectively. In each case, the individual tube flows can be detected at the first axial station ($x/D_8 = 0.25$). Moving downstream, the flow fields merge so that the effects of

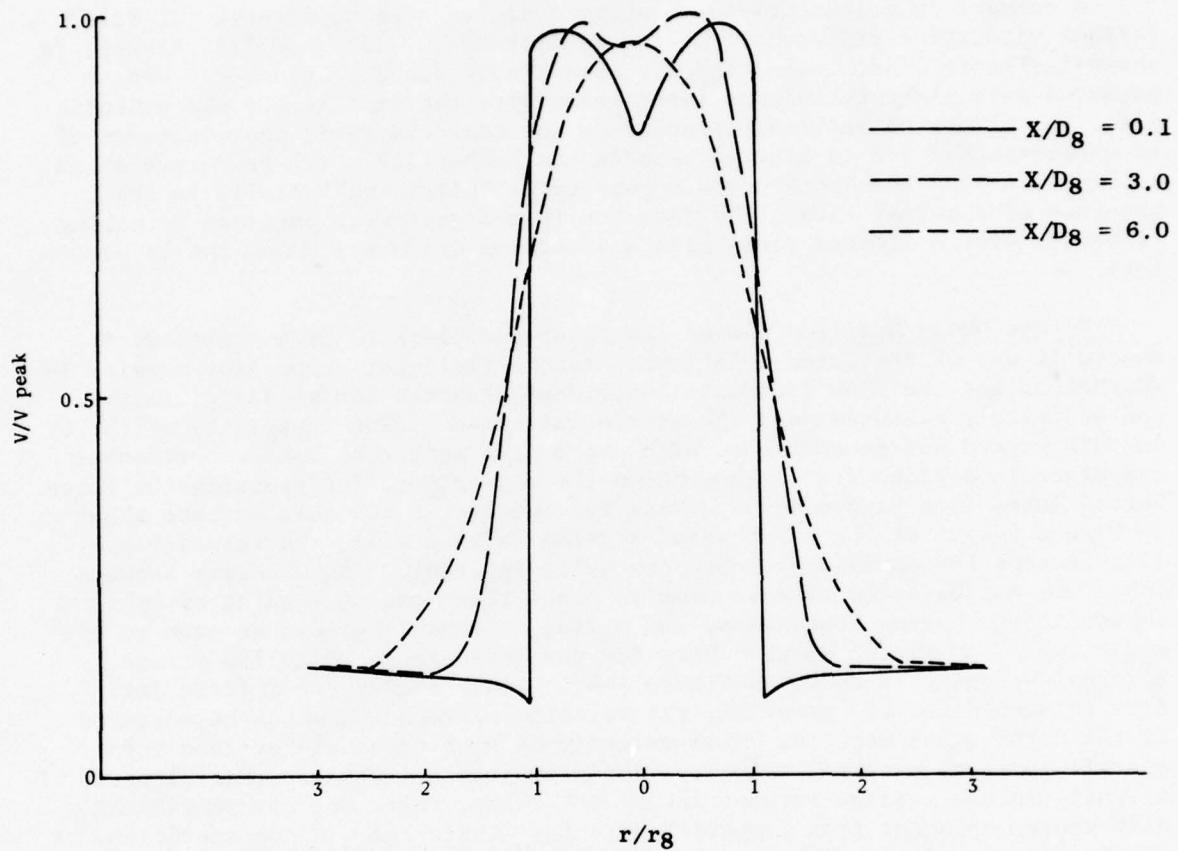


Figure 4-41. Velocity Profiles for 3.56-Inch Conical Nozzle,
 $V_J = 1130 \text{ ft/sec}$, $V_O = 150 \text{ ft/sec}$.

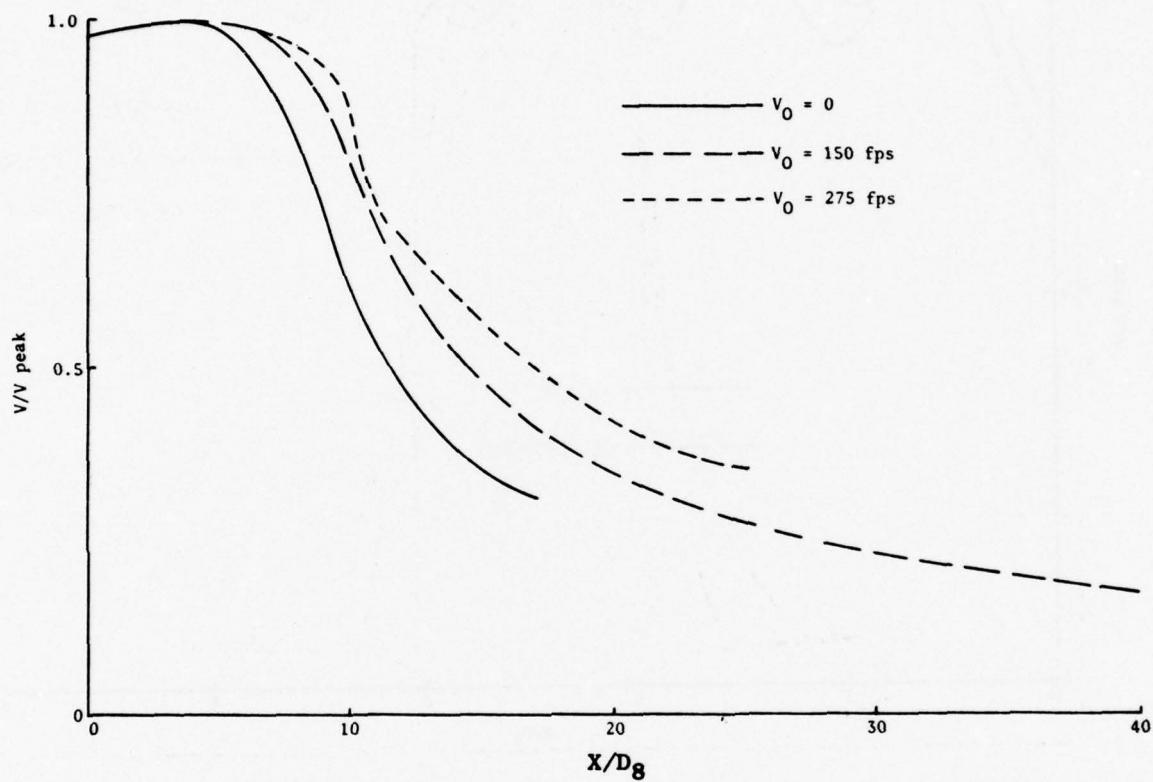


Figure 4-42. Centerline Velocity Decay for 3.56-Inch Conical Nozzle,
 $V_J = 2200 \text{ ft/sec.}$

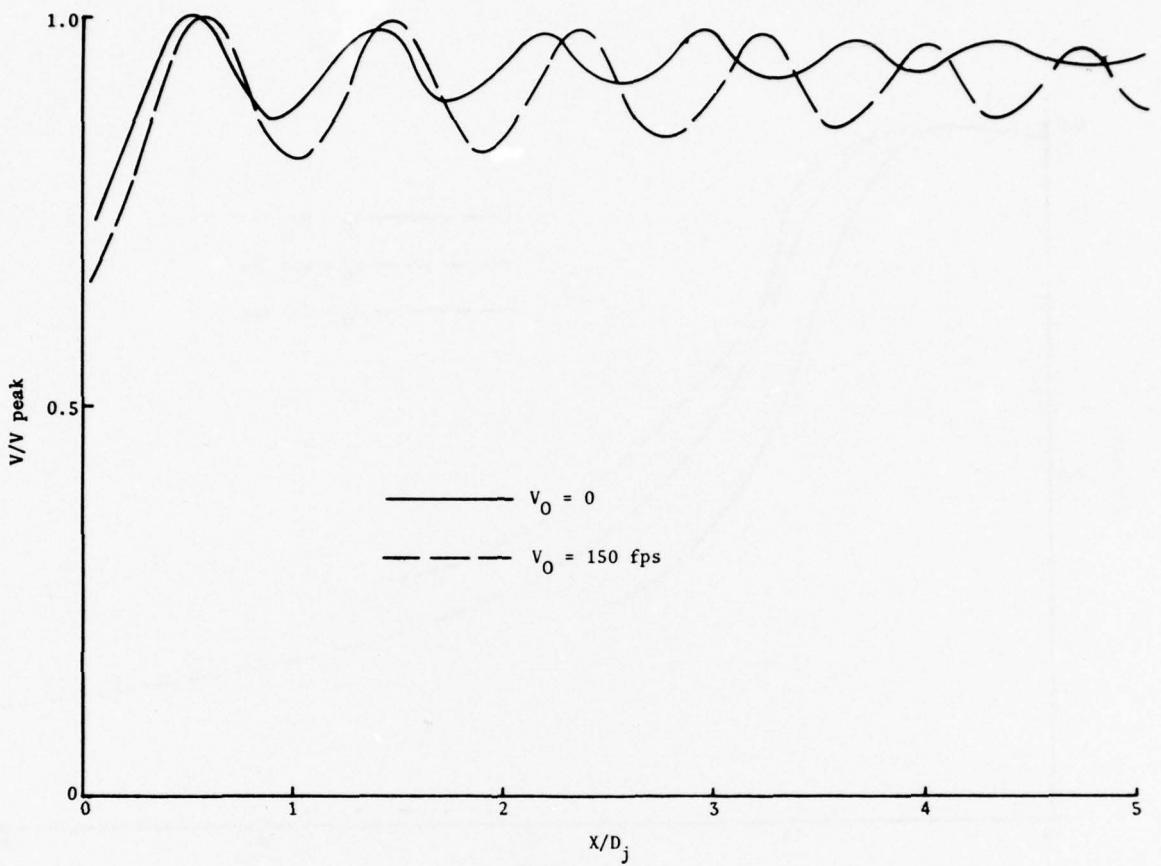


Figure 4-43. Centerline Velocity Near Nozzle Exit for 3.56-Inch Conical Nozzle, $V_J = 2200 \text{ ft/sec.}$

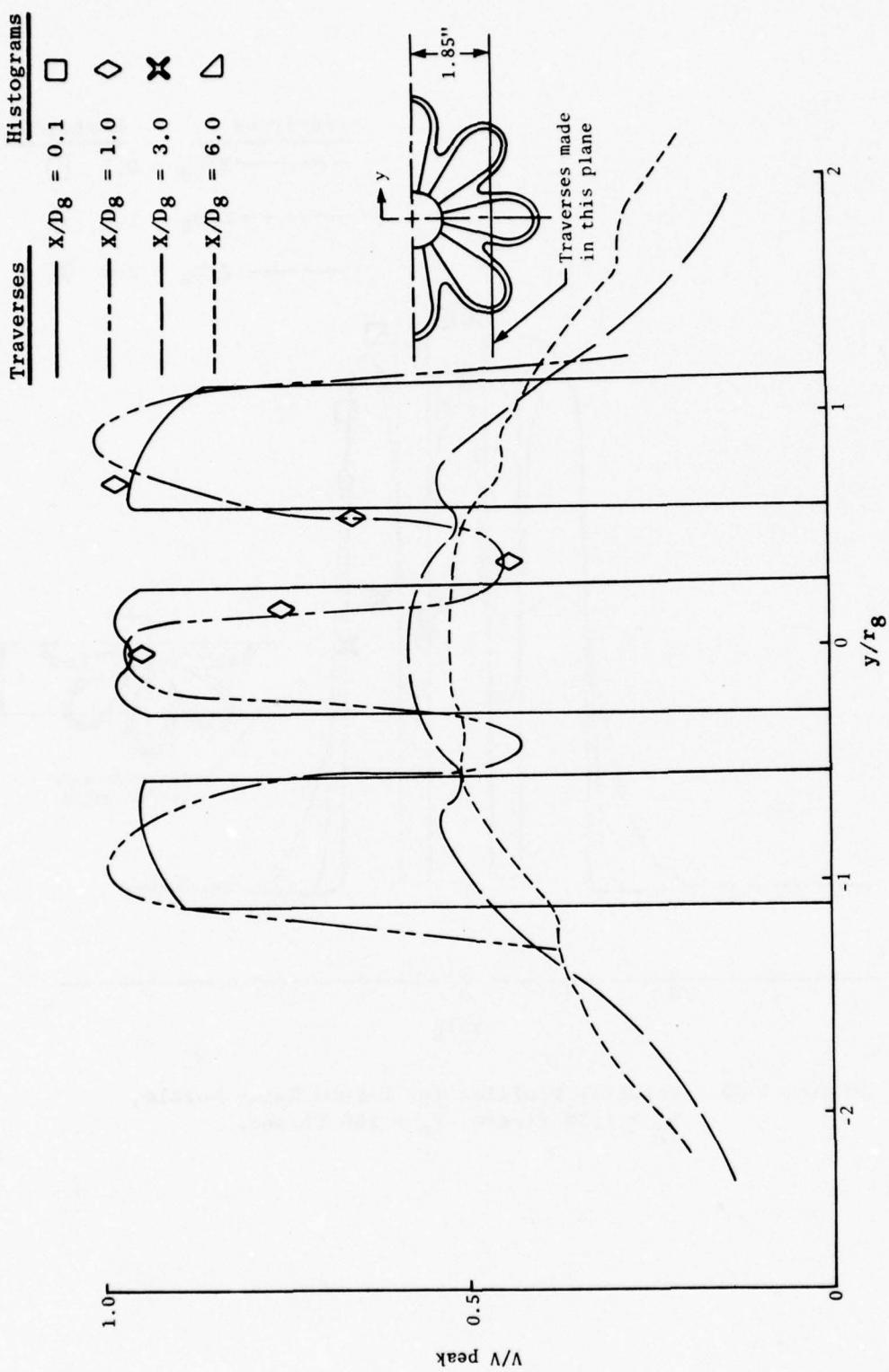


Figure 4-44. Velocity Profiles for 8-Lobe Daisy Nozzle,
 $V_J = 1130 \text{ ft/sec}$, $V_o = 0$.

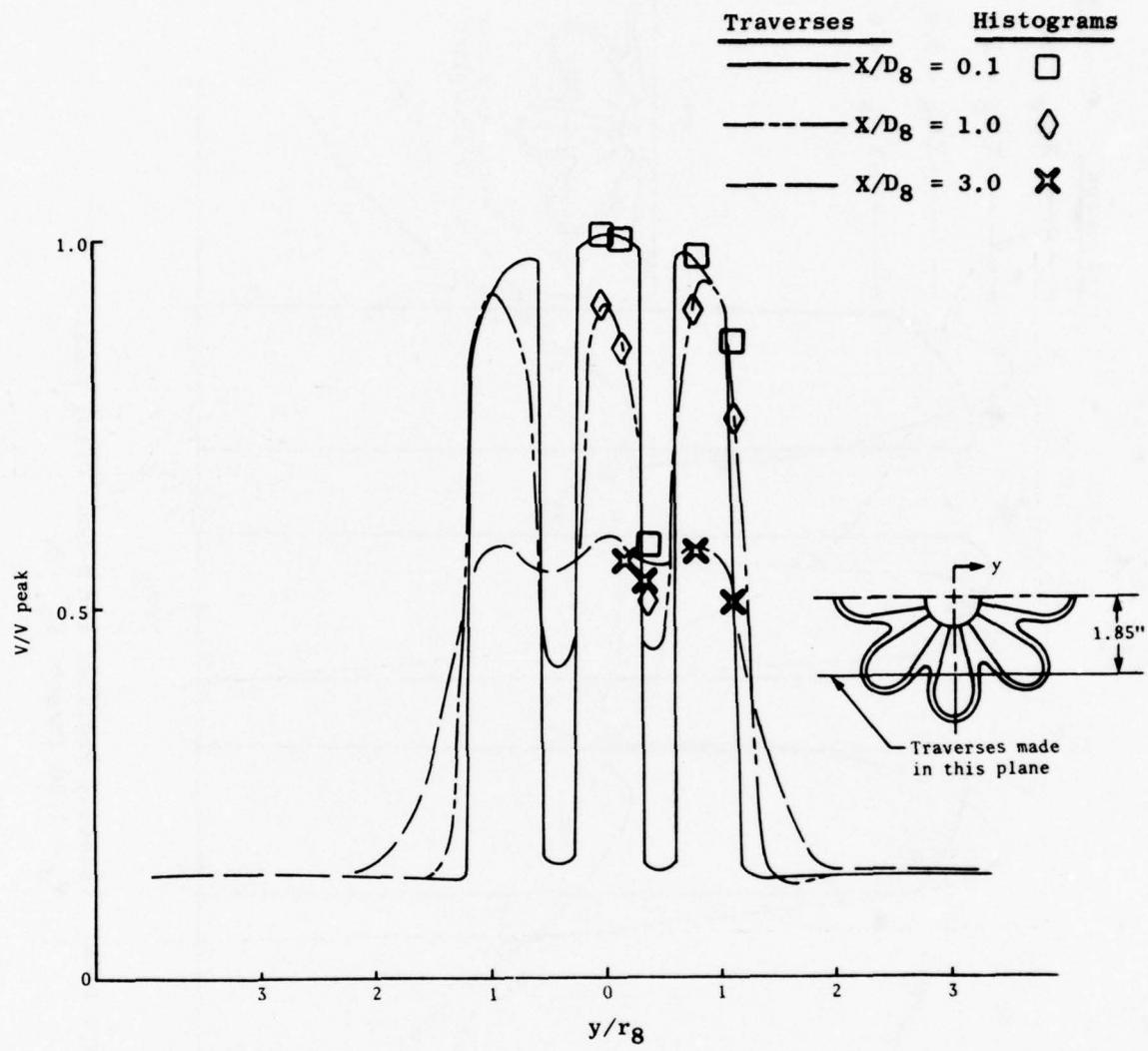


Figure 4-45. Velocity Profiles for 8-Lobe Daisy Nozzle,
 $V_J = 1130 \text{ ft/sec}$, $V_o = 150 \text{ ft/sec}$.

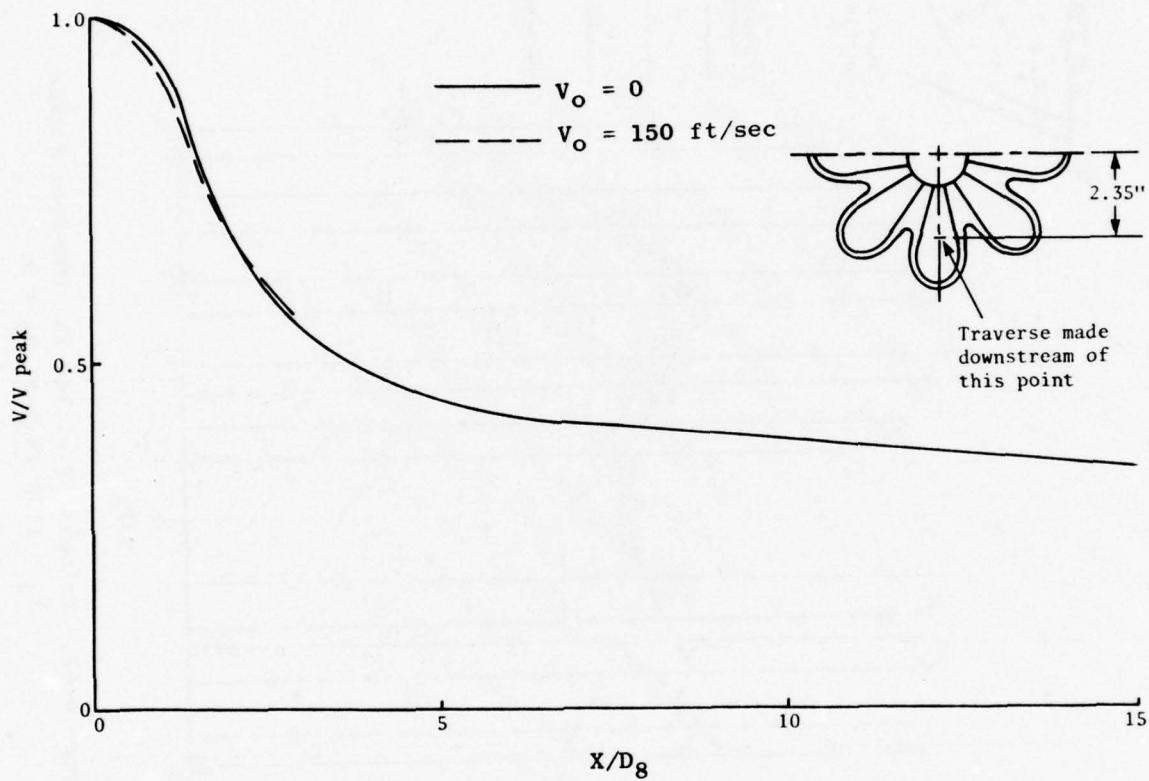


Figure 4-46. Axial Velocity Traverse Behind a Lobe -
8-Lobe Nozzle, $V_J = 1130 \text{ ft/sec.}$

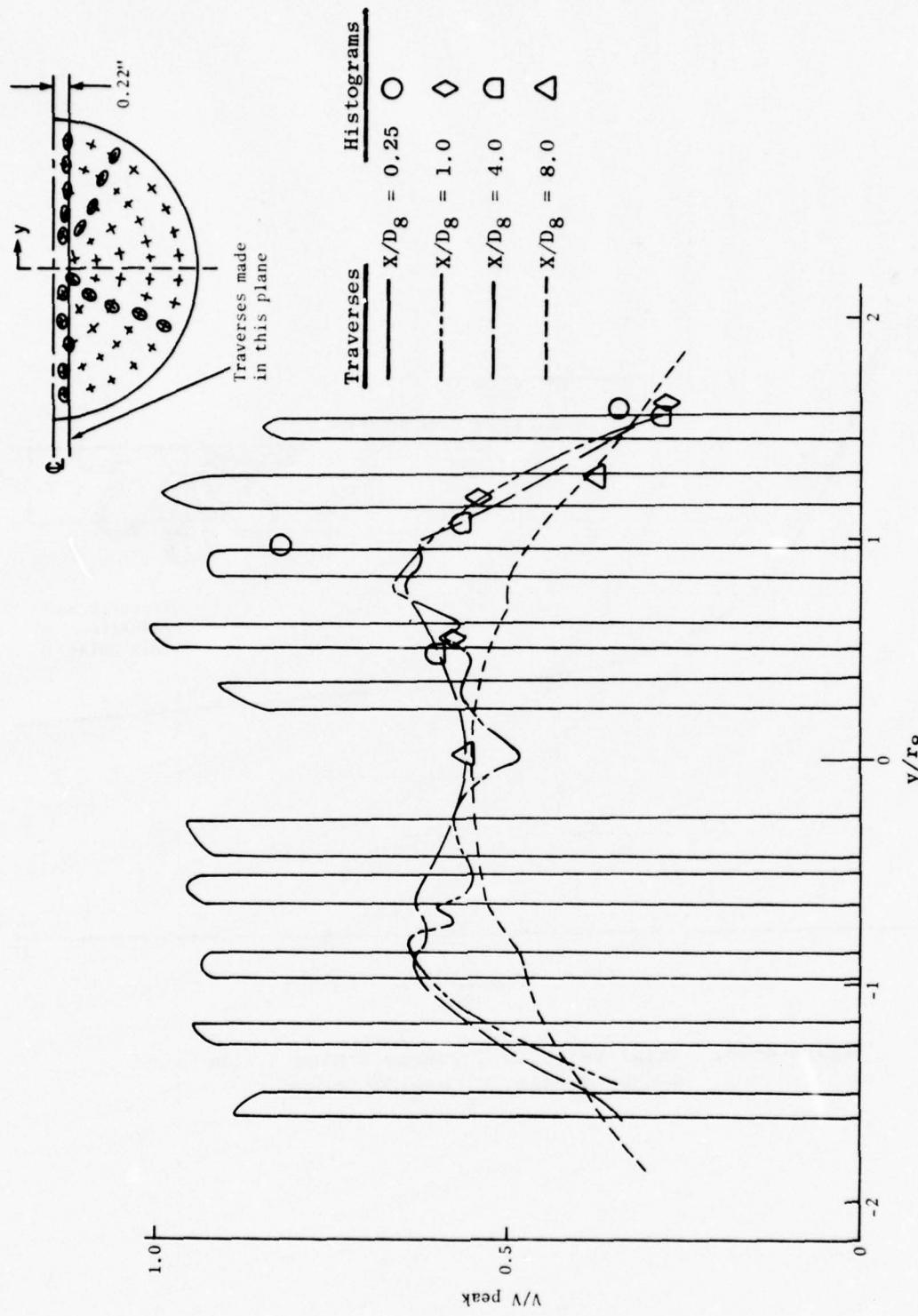


Figure 4-47. Velocity Profiles for 104-Tube Nozzle,
 $V_J = 1130 \text{ ft/sec}$, $V_O = 0$.

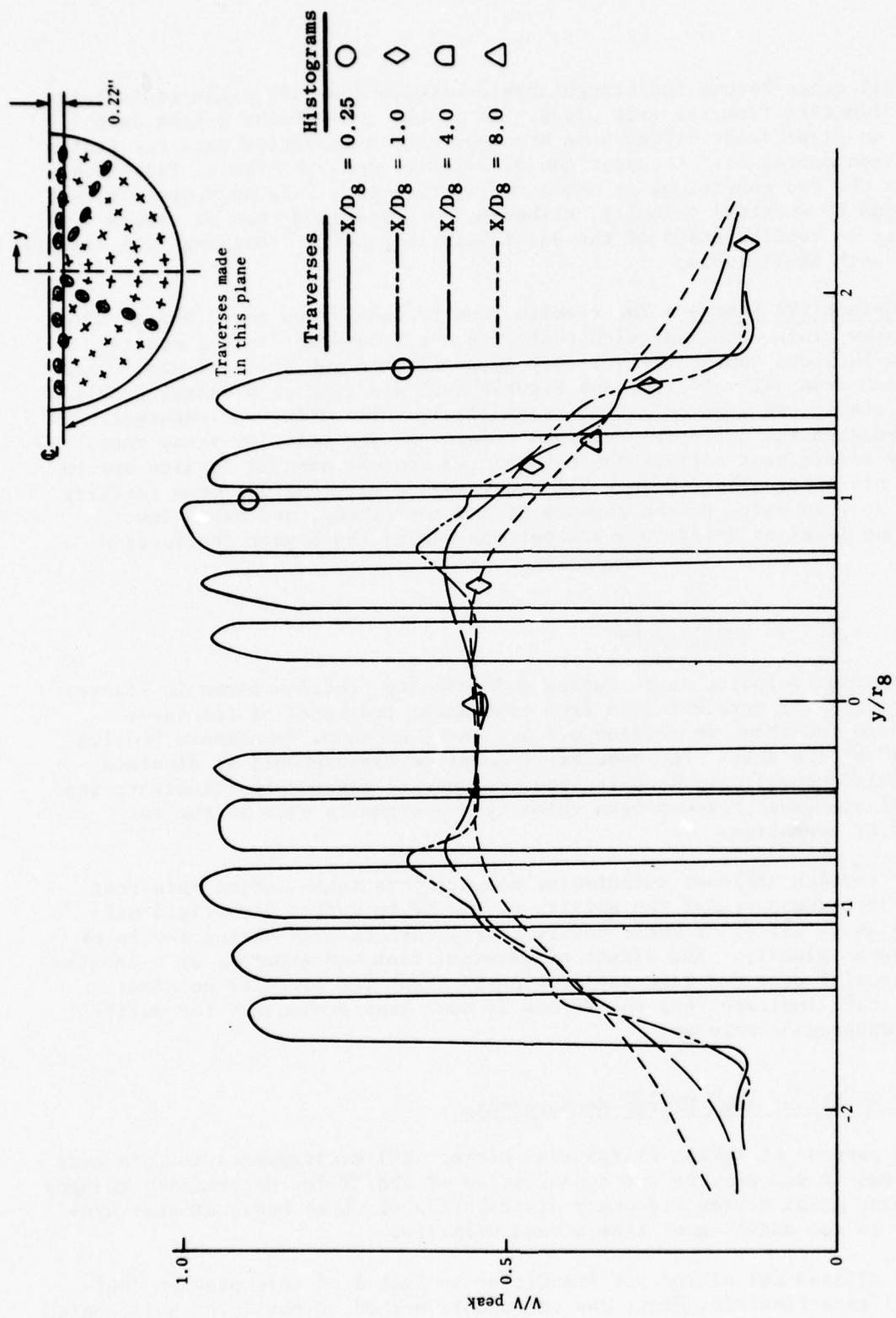


Figure 4-48. Velocity Profiles for 104-Tube Nozzle,
 $v_J = 1130$ ft/sec, $v_o = 150$ ft/sec.

individual tubes become indistinguishable between four and eight equivalent nozzle diameters from the exit plane. As in the case of the 8-lobe daisy nozzle, no significant differences are apparent in comparing data for static and wind-on operation. A comparison of velocity decay behind an individual tube for the two conditions is shown in Figure 4-49. This suggests a modest effect due to external velocity, although the comparison must be viewed carefully in consideration of the difficulty in exactly "tracking" the centerline of such small tubes.

2.0-Inch STA Nozzle - The results from LV testing on the 2.0-inch STA nozzle show close agreement with those for the 3.56-inch conical nozzle. Figure 4-50 shows centerline velocity decay for the subsonic jet with 0 and 150 ft/sec free jet velocity, and Figures 4-51 and 4-52 show radial profiles for the static and wind-on cases, respectively. The effect of external flow is to lengthen the potential core and reduce the jet velocity decay rate. The only significant differences between the conical and STA results are in initial profiles. The 2.0-inch STA nozzle has a very uniform mean velocity profile due, in part, to the absence of any centerbody, and has a lower turbulence level of 2-1/2 to 4-1/2 percent due to the higher contraction ratio.

4.1.5.3 Conclusions

The axial velocity decay curves and velocity profiles shown in Figures 4-31 through 4-52 were obtained from continuous traverses of the laser velocimeter (as shown in Section 4.1.5.2) and, as such, constitute "moving averages" of the data. The results of detailed measurements at discrete points (histograms) have been included on several figures to illustrate the excellent agreement between mean velocity measurements made in the two modes of LV operation.

The results of laser velocimeter measurements taken during this test program have demonstrated the ability of the LV to detect flow-field differences among different basic nozzle configurations with varied levels of free-stream velocity. The effect of external flow was apparent in a lengthened potential core and less rapid velocity decay for circular nozzles; however, data indicate that the effect is much less pronounced for multi-element suppressor nozzles.

4.1.6 Ellipsoidal Mirror Measurements

The purpose of taking ellipsoidal mirror (EM) measurements in this test program was to demonstrate the capabilities of the EM for determining changes in the peak axial source frequency distribution of three basic exhaust systems due to the addition of free-stream velocity.

The ellipsoidal mirror was identified in Task 1 of this program (Reference 7) as a flexible, fast, and acceptable method of obtaining axial noise

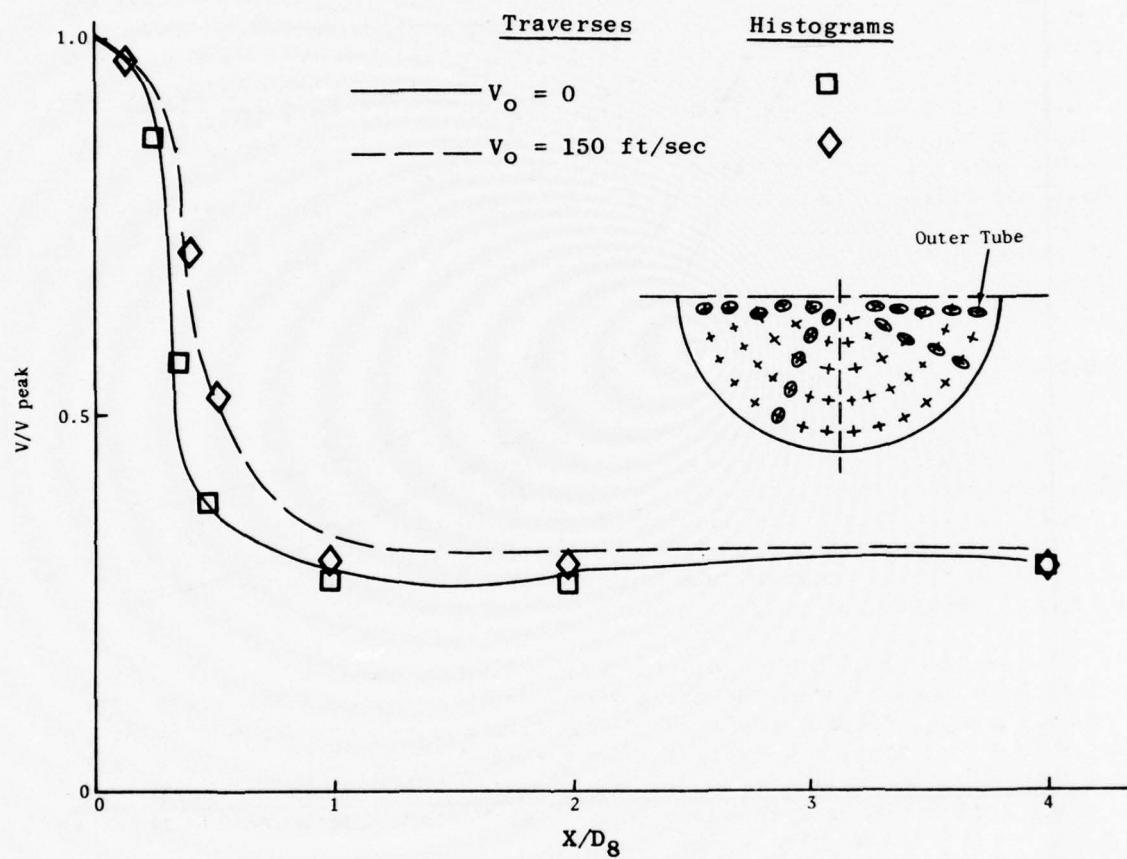


Figure 4-49. Axial Velocity Traverse Behind an Outer Tube,
104-Tube Nozzle, $V_J = 1130 \text{ ft/sec.}$

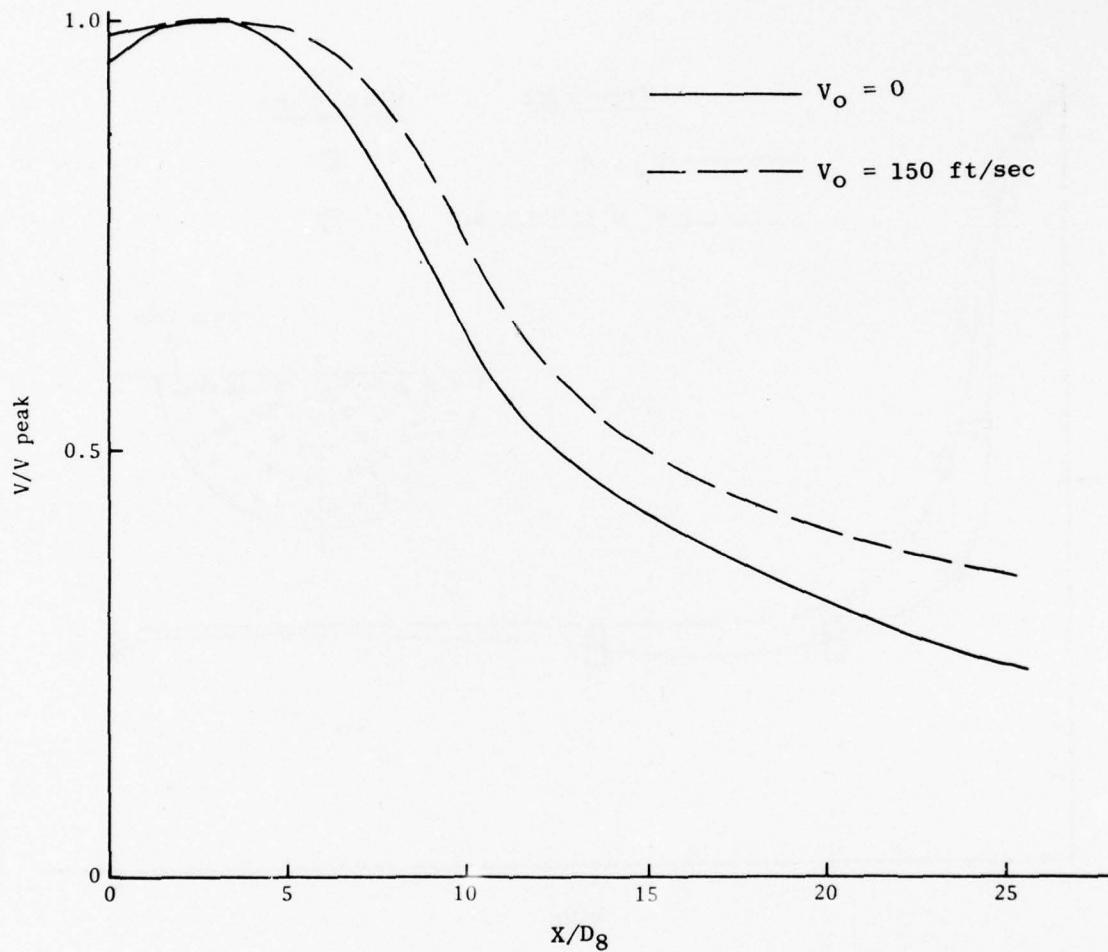


Figure 4-50. Centerline Velocity Decay for 2.0 Inch STA Nozzle, $V_J = 1130 \text{ ft/sec}$.

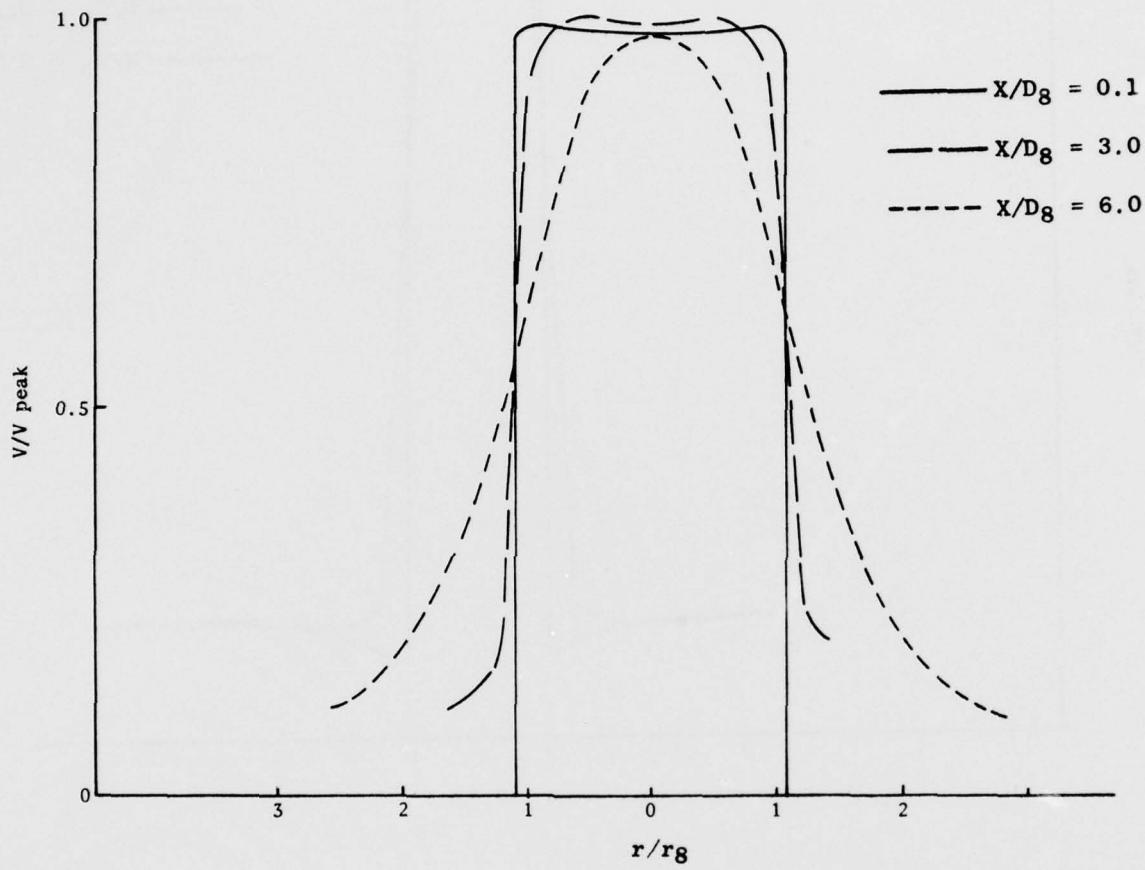


Figure 4-51. Velocity Profiles for 2.0 Inch STA Nozzle,
 $V_J = 1130 \text{ ft/sec}$, $V_O = 0$.

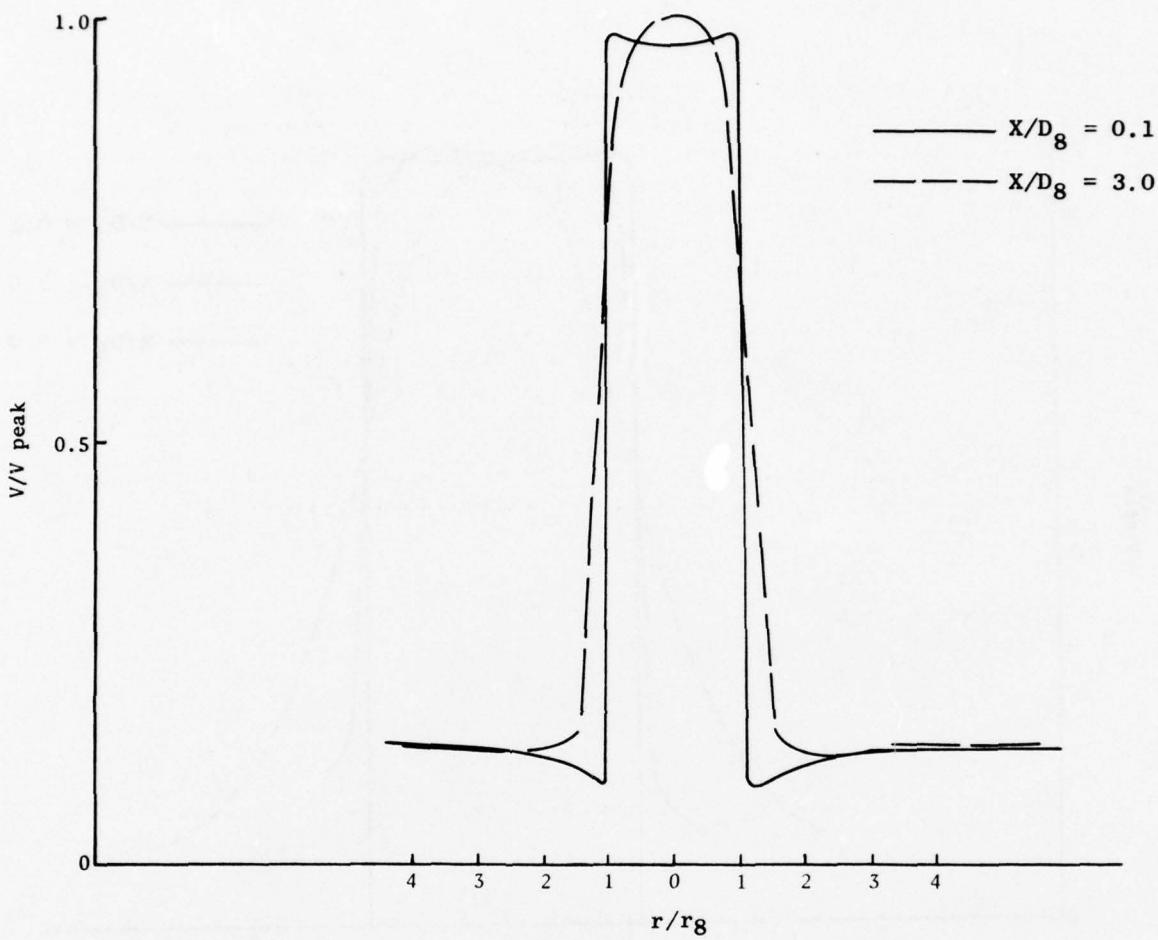


Figure 4-52. Velocity Profiles for 2.0 Inch STA Nozzle,
 $V_J = 1130$ ft/sec, $V_O = 150$ ft/sec.

source distributions in a jet. The EM is a directional microphone system in which an ellipsoidal dish (mirror) focuses acoustic radiation from a specific source region in the jet onto a microphone placed outside the flow. Figure 4-53 shows a schematic arrangement of the system.

4.1.6.1 Test Setup and Conditions

The tests were conducted at the General Electric JENOTS free jet facility in Evendale. Measurements were taken using the 18-inch diameter EM (Figures 4-54 and 4-55) that was designed, built, and demonstrated for static jets in Task 1. Referring to the figure, the microphone (1/4-in. B&K 4136) is inserted through the rear of the mirror and located at the primary focus. The 9-foot working distance represents the distance between the focii of the ellipse. The EM is mounted on the remotely driven laser velocimeter cart on tracks parallel to the jet axis. Surveys of the jet are accomplished by traversing the cart, with the mirror axis fixed normal to the jet axis and the secondary focus on the jet centerline. Travel capability of the cart is 20 inches (i.e., the equivalent of 60 nozzle diameters for a 4-in. conical nozzle).

Tests were conducted on four different nozzle configurations, representing two baseline nozzles and two types of multielement suppressors:

- 3.56-in. Conical (Figure 4-3)
- 2.0-in. STA (Figure 4-4)
- 8-Lobe Daisy (Figure 4-6)
- 104-Tube (Figure 4-8)

A set of nine basic data points was defined for EM testing by the combination of three jet velocities (1400, 1800, and 2200 ft/sec) with three free jet velocities (0, 150, and 275 ft/sec). The actual test matrix is defined in Table 4-VIII, where the point numbers also refer to corresponding far-field acoustic test points.

For each test point, data were taken on both "outbound" and "inbound" traverses of the cart over the full 20-foot length of travel. The microphone signal, a DC cart position signal, and a time code are recorded on magnetic tape using the standard JENOTS data acquisition system.

4.1.6.2 Data Reduction

Ellipsoidal mirror data reduction is accomplished as a two-step procedure. The first step utilizes procedures established for handling of flyover data (Section 5.1.3), with the EM data being processed through a General Radio Model 1921 Real Time Analyzer coupled with a GEPAC 30 computer and a Terminet 300 printer. The microphone signal is resolved into twenty-four 1/3-octave bands and averaged over each of 80 consecutive discrete time

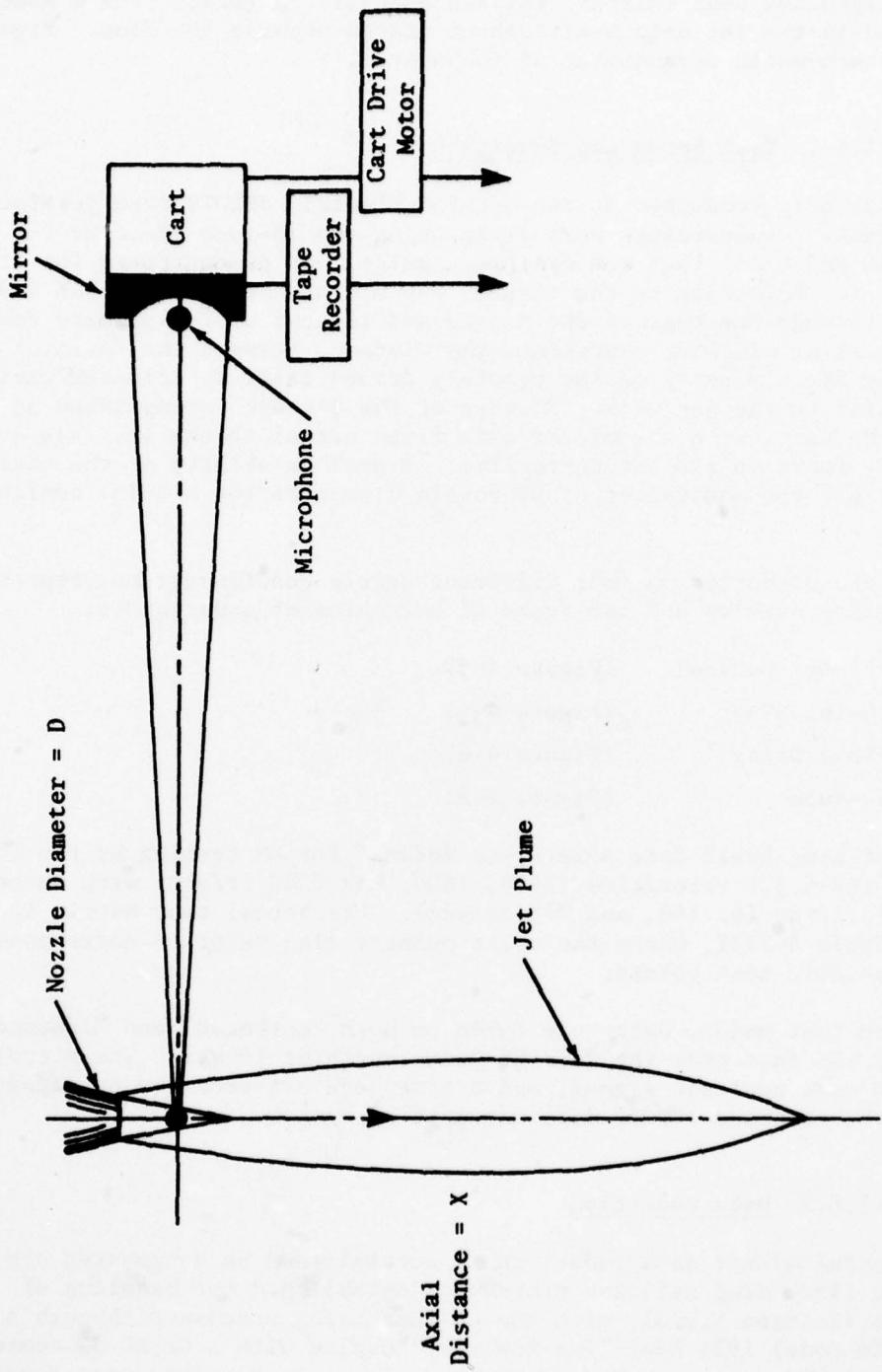


Figure 4-53. Test Set-up for Ellipsoidal Mirror Surveys.

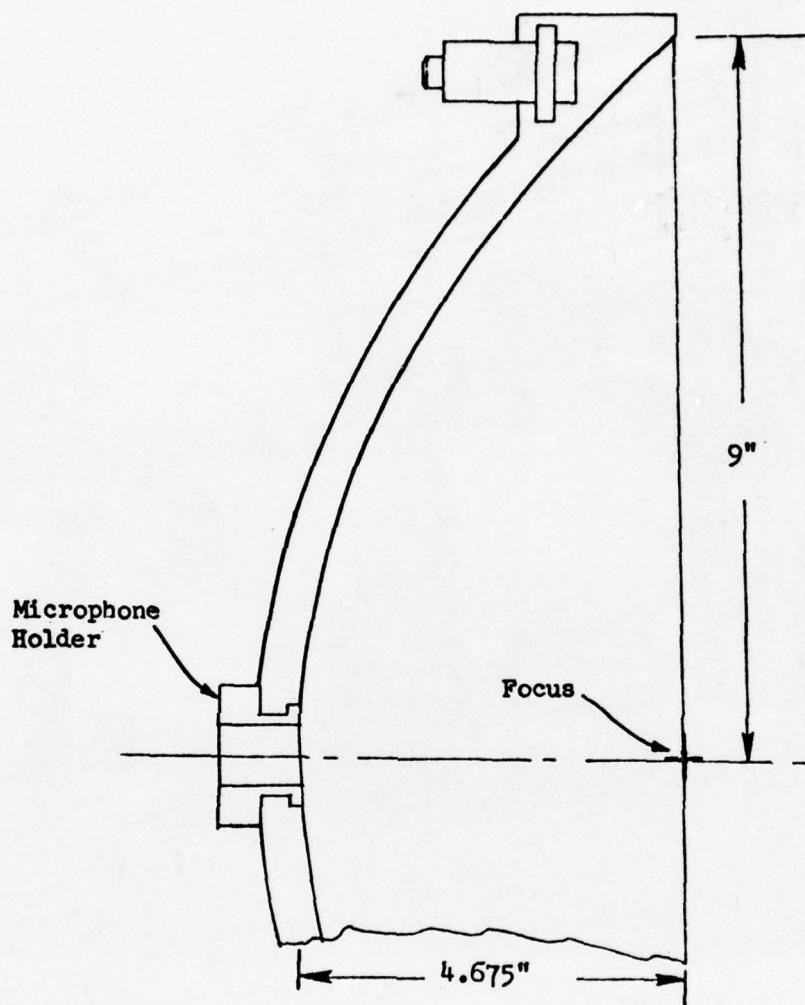


Figure 4-54. 18-Inch Diameter Shallow Dish EM with 9-Foot Working Distance.

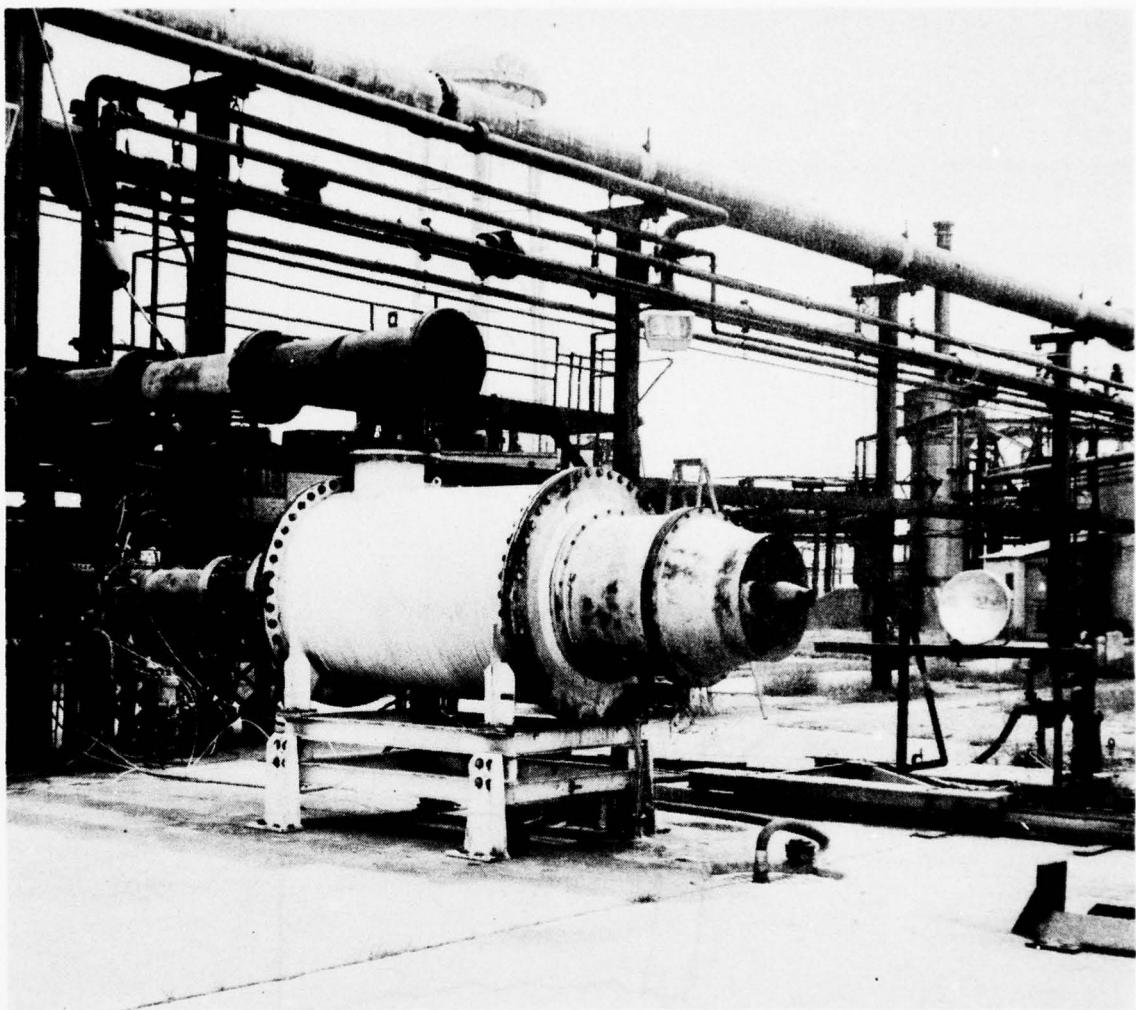


Figure 4-55. Ellipsoidal Mirror Setup at JENOTS.

Table 4-VIII. Test Matrix for Ellipsoidal Mirror Surveys.

Data Point No.	Config.	v_8 (fps)	v_o (fps)	P_{T8}/P_o	T_{T8} (°R)
4	3.56" Conic	1481	0	1.605	1435
6		1857	0	2.000	1582
8		2253	0	2.447	1844
18		1461	139	1.586	1429
20		1828	148	1.965	1570
22		2205	150	2.392	1809
73	8 Lobe Daisy	1800	0	1.990	1497
75		2200	0	2.559	1689
79		1376	0	1.575	1290
85		1405	161	1.606	1290
87		1815	169	2.012	1501
99		1421	281	1.569	1385
101		1788	280	1.903	1570
109		2154	278	2.312	1790
138	104 Tube	1396	0	1.589	1303
140		1795	0	1.985	1495
142		2195	0	2.551	1686
152		1401	168	1.597	1299
154		1801	168	1.990	1499
156		2204	170	2.556	1697
166		1387	289	1.581	1297
168		1793	297	1.979	1498
170		2203	295	2.558	1694
205	2.0" STA	1375	0	1.575	1286
207		1794	0	1.968	1509
209		2194	0	2.536	1694
214		1474	151	1.590	1448
216		1833	153	1.965	1578
218		2213	152	2.397	1818
227		2225	291	2.497	1767

steps, then digitized and corrected for nonlinear frequency response and gain of the data acquisition system. The cart position signal is also processed, resulting in a trace of position versus time. Cart position during the time step corresponding to each of the 80 spectra is readily determined through use of the time-code signal, and an average is calculated. Thus, the output of this step is a series of spectra and cart positions representing jet noise sources as functions of distance from the nozzle exit plane.

The length of time steps (integration time) and the frequency range to be covered can be specified, within certain limits, to suit the requirements of a particular test. The integration time, while remaining constant during processing of an individual point, can be set for 1/8, 1/4, 1/2, 1, 2, 4, 8, 16, 32, or 64 seconds. A short integration time is required to accurately define location and strength of the high frequency source regions near the nozzle exit; however, a longer time step is generally required to cover (within 80 steps) a sufficient length of the jet for defining low frequency source regions. An additional consideration is that the uncertainty in locating true axial source position increases with increasing integration time since data is averaged over this interval. The cart speed used in obtaining the data will determine the exact integration times necessary for obtaining the desired resolution. In this test, the cart speed was 3 inches/second. In order to accommodate both high and low frequency requirements, each data point was processed twice. Outbound traverses were reduced with both 1/8-second and 1-second integration times.

The frequency range for data reduction, while not as flexible as integration time, can be varied. Data can be resolved into twenty-four 1/3-octave bands over a range of 50 Hz - 10 kHz, 100 Hz - 20 kHz, or 200 Hz - 40 kHz. For this test, a range of 200 Hz - 40 kHz was chosen.

The second step of the EM data reduction process involves correction of data for the mirror gain and diffraction window function. These are both fixed, frequency-dependent characteristics of the mirror system which can be determined by calibration and "removed" from data by proper numerical processing.

The correction for mirror gain is relatively simple, requiring the subtraction (in dB) of a factor for each 1/3-octave band of the measured spectra. The experimentally determined gain characteristics of the 18-inch diameter mirror are shown in Figure 4-56.

The diffraction window function represents the finite directivity of the EM. In the limit of high frequencies with wavelengths very small relative to the mirror dimensions, an ellipsoidal mirror should theoretically resolve a point source at one focus onto a microphone at the other focus. This is based on the approximation of sound traveling as straight-line rays. However, at lower frequencies, the wave character of sound becomes apparent and the resolution of the EM is limited by diffraction. The "point" which is resolved onto the microphone is spread into a three-dimensional volume described by the diffraction pattern of the dish. A slice through the three-

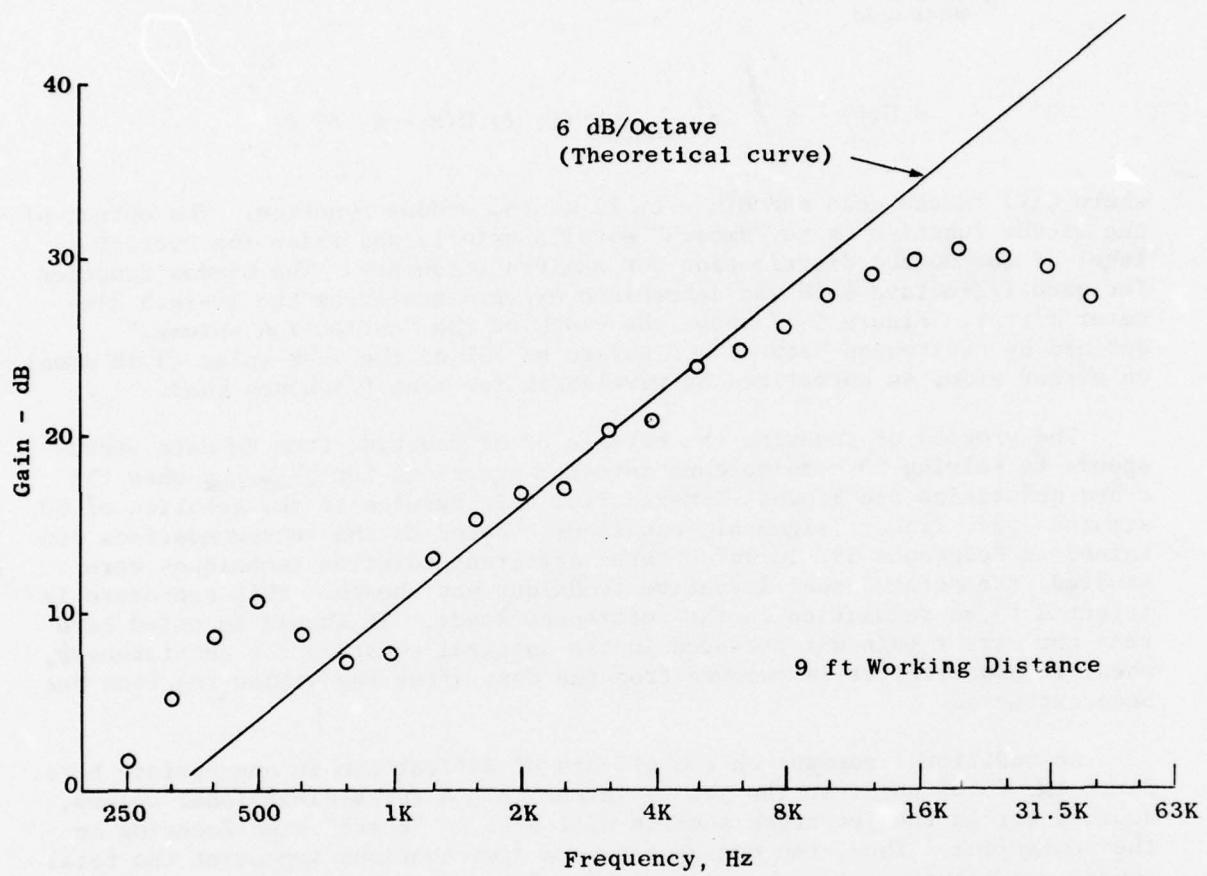


Figure 4-56. Gain of the 18 Inch Diameter Ellipsoidal Mirror.

dimensional diffraction pattern on a plane parallel to the jet axis and normal to the mirror axis yields the "window function." This function represents the weighting given adjacent sources along the jet axis in focusing on a given location. Analytically, the relation between actual and measured source distributions is represented by:

$$p_{\text{measured}}^2(x, f) = G(f) \int_0^{\infty} p_{\text{actual}}^2(\xi, f) H(x - \xi, f) d\xi$$

where $G(f)$ is the gain and $H(x - \xi, f)$ is the window function. The effect of the window function is to "smooth" details axially and raise the overall level of the source distribution for a given frequency. The window function for each 1/3-octave band was determined experimentally on the 18-inch diameter mirror. Figure 4-57 shows the width of the "collection volume," defined by the region between the points at 50% of the peak value (3 dB down) on either side, as normalized by wavelength for each frequency band.

The process of removing the effects of diffraction from EM data corresponds to solving 80 simultaneous integral equations for p_{actual}^2 when the other quantities are known. Numerically, this reduces to the solution of 80 simultaneous, linear, algebraic equations. Based on the recommendations contained in Reference 33, in which three different solution techniques were studied, the point Jacobi iterative technique was chosen. This procedure is referred to as relaxation in the referenced study. It should be noted here that the mirror gain was included in the integral equation for completeness, when, in practice, it is removed from the data after the window function has been extracted.

An additional comment on the effects of diffraction is appropriate here. Since the focal point in the jet is spread into a three-dimensional volume, sources across the jet cross section will also be "heard" when focusing on the centerline. Thus, the measured source distributions represent the total source contribution at each axial station (i.e., a slice of jet measurements).

A FORTRAN program has been written for the HIS 6000 computer to perform the second step of ellipsoidal mirror data reduction. This program matches each measured spectrum with its proper axial position, numerically removes the mirror window function and gain, identifies the peak source region for each 1/3-octave band, and prepares the data for machine plotting. It also performs required calculations for the integral closure check, which will be discussed under data analysis.

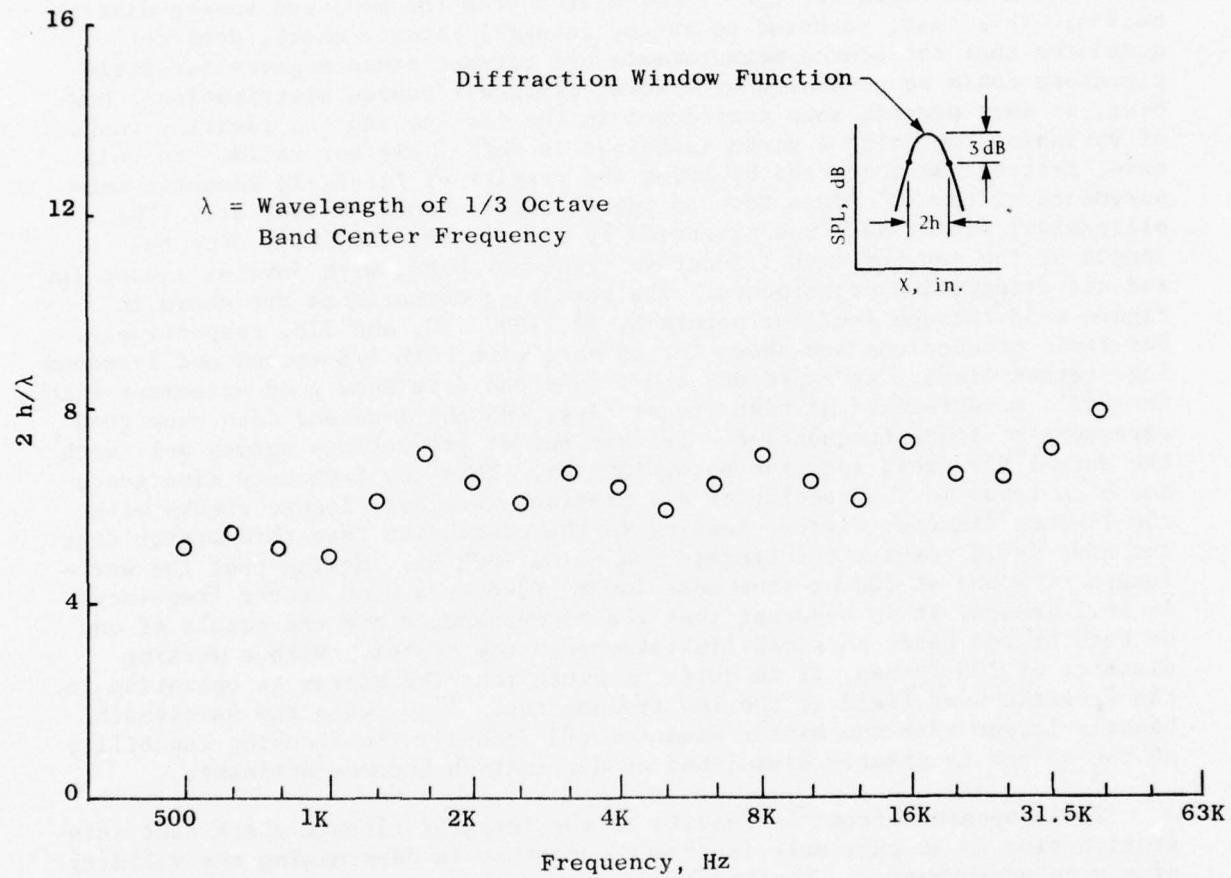


Figure 4-57. Width of "Collection Volume" for the 18-Inch Diameter Ellipsoidal Mirror.

4.1.6.3 Data Analysis

Ten of the data points in Table 4-VIII were chosen for detailed analysis as a demonstration of EM capabilities. The specific points represent all four configurations and include all three free jet velocities with the supersonic jet (2200 ft/sec).

An important test of a source location technique is to see if a measured far-field noise signature can be calculated from the measured source distribution. This test, referred to as the integral closure check, does not guarantee that the source measurements are correct since a given far-field signature could be generated by several different source distributions; however, it does provide some confidence in the results and can identify ranges of variables for which a given technique is definitely not valid. In this case, testing was conducted by using the results of far-field acoustic measurements at the 90° microphone on the standard JENOTS 40-foot arc. The ellipsoidal mirror data was processed by integrating the SPL's over the length of the jet for each 1/3-octave frequency band, with inverse square law and air attenuation adjustments. The resulting comparisons are shown in Figure 4-58 through 4-62 for points 8, 22, 109, 170, and 218, respectively. Far-field predictions are shown for EM data with both 1/8-second and 1-second integration times. As expected, the 1/8-second data show good agreement with far-field measurements at high frequencies, and the 1-second data show good agreement at lower frequencies. Neither set of predictions agrees well with the actual far-field spectrum below 1000 Hz. This low frequency divergence has been found in the results of all previous integral closure checks with the 18-inch diameter mirror, leading to the conclusion that this mirror does not give valid results for frequencies below 1000 Hz. Noting that the wavelength of sound at 800 Hz (the next lower 1/3-octave band center frequency) is 16.7 inches, it is apparent that the discrepancies are the result of one or both of two basic physical limitations on the system. With a working distance of 108 inches, it is quite probable that the mirror is operating in the acoustic near field at the low frequencies. Also, when the wavelength becomes larger than the mirror diameter (18 inches), the focusing capability of the mirror is greatly diminished as diffraction becomes dominant.

It is apparent from the results of the integral closure check that integration time is an extremely important parameter in determining the validity of source measurements. Further study is required to determine the optimum value or combination of values to be used.

The measured source distributions expressed as fD_8/V_8 versus x_{peak}/D_8 , are shown in Figures 4-63 through 4-69. The diameter, D_8 , was taken as the equivalent diameter for the total nozzle area:

- 3.56 in. Conical $D_8 = 3.56$ in.
- 2.0 in. STA $D_8 = 2.00$ in.
- 8-Lobe Daisy $D_8 = 4.01$ in.
- 104-Tube $D_8 = 4.07$ in.

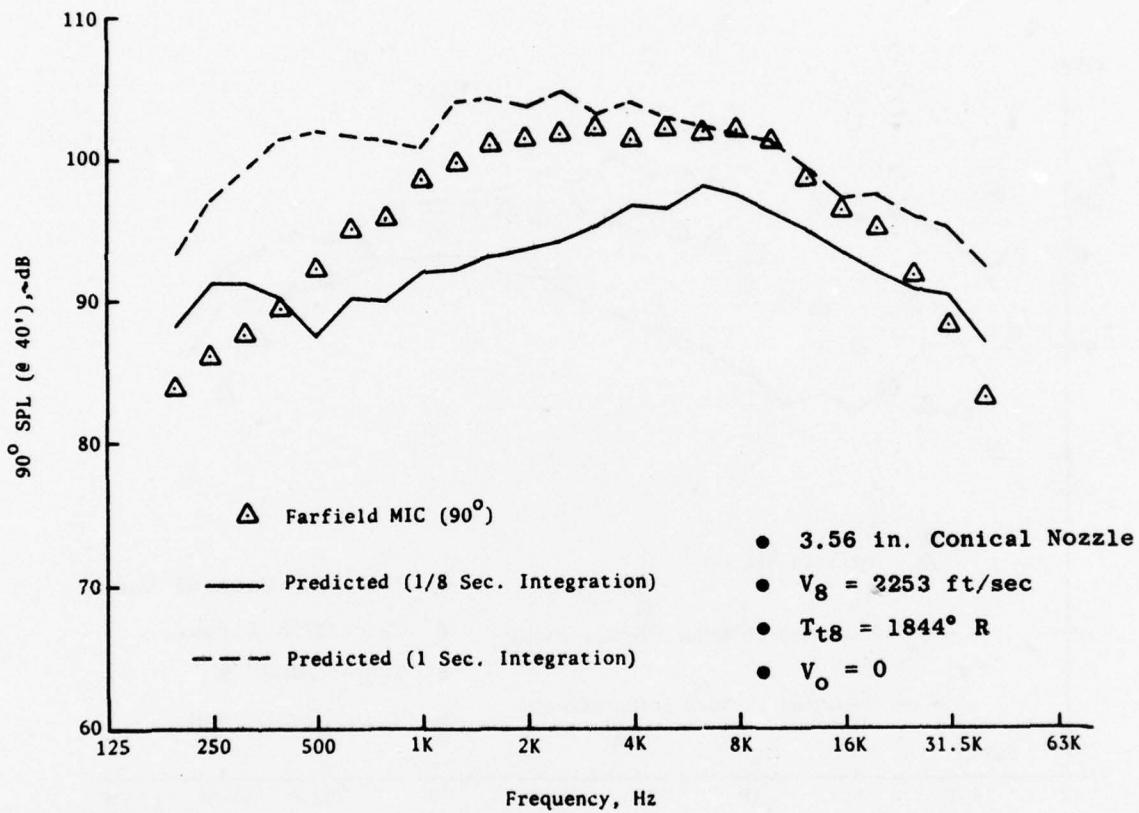


Figure 4-58. Integral Closure Check for 3.56-Inch Conical Nozzle, $V_g = 2253 \text{ ft/sec}$, $V_o = 0$.

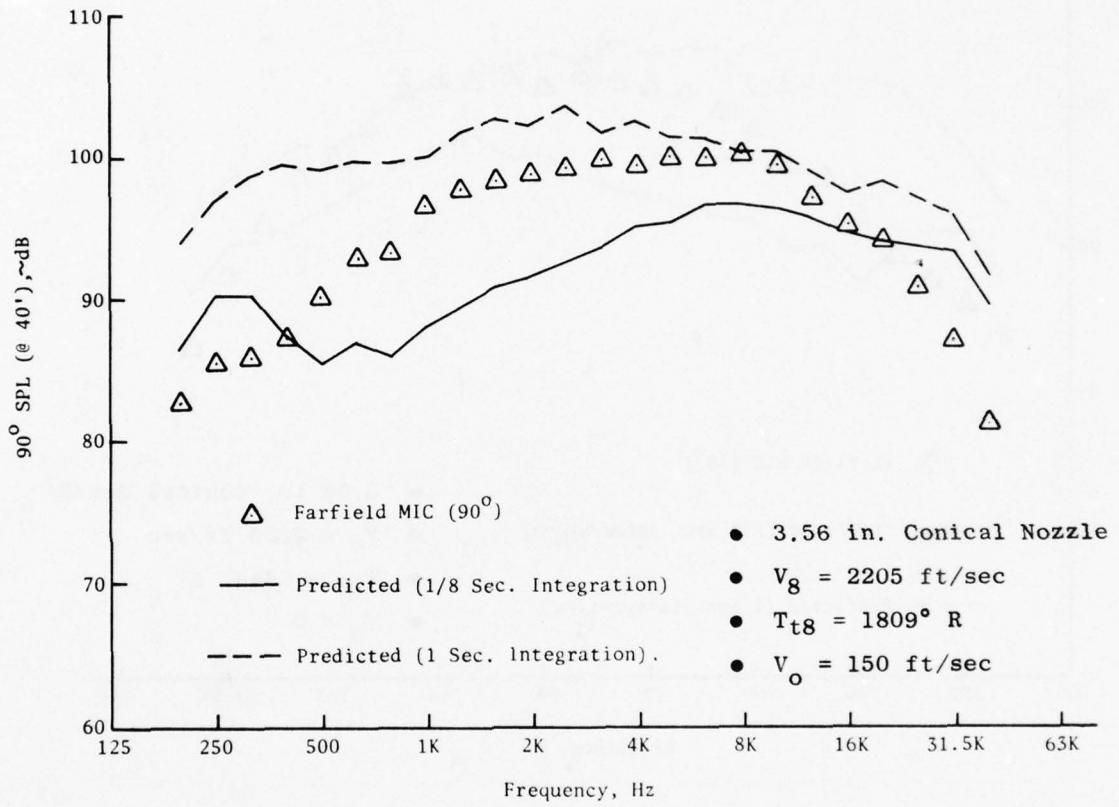


Figure 4-59. Integral Closure Check for 3.56-Inch Conical Nozzle, $V_8 = 2205$ ft/sec, $V_o = 150$ ft/sec.

AD-A041 849

GENERAL ELECTRIC CO CINCINNATI OHIO AIRCRAFT ENGINE GROUP F/G 20/1
HIGH VELOCITY JET NOISE SOURCE LOCATION AND REDUCTION. TASK 4. --ETC(U)
FEB 77 W S CLAPPER, E J STRINGAS DOT-05-30034

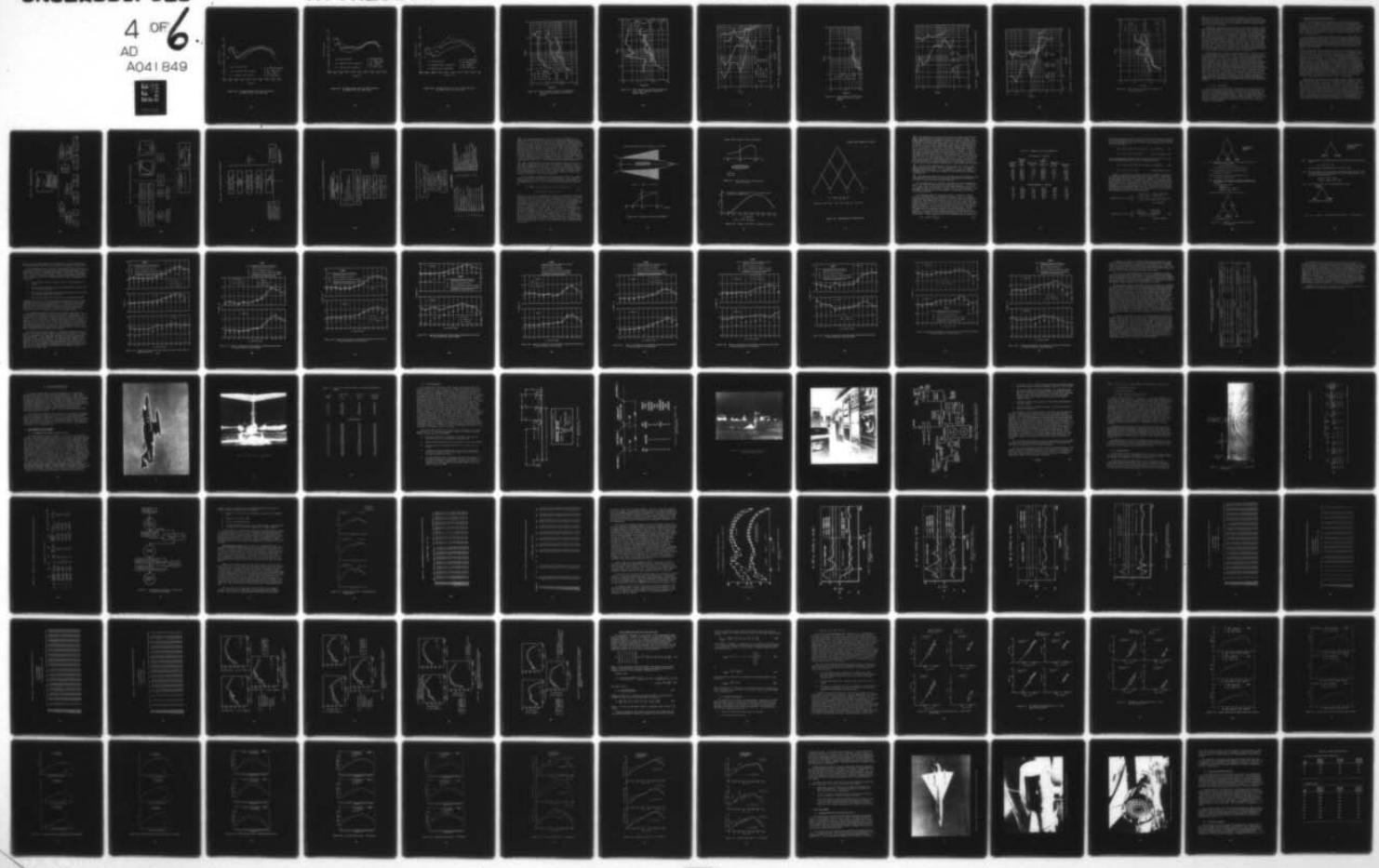
UNCLASSIFIED

4 OF 6
AD
A041 849

R77AEG189

FAA-RD-76-79-4

NL





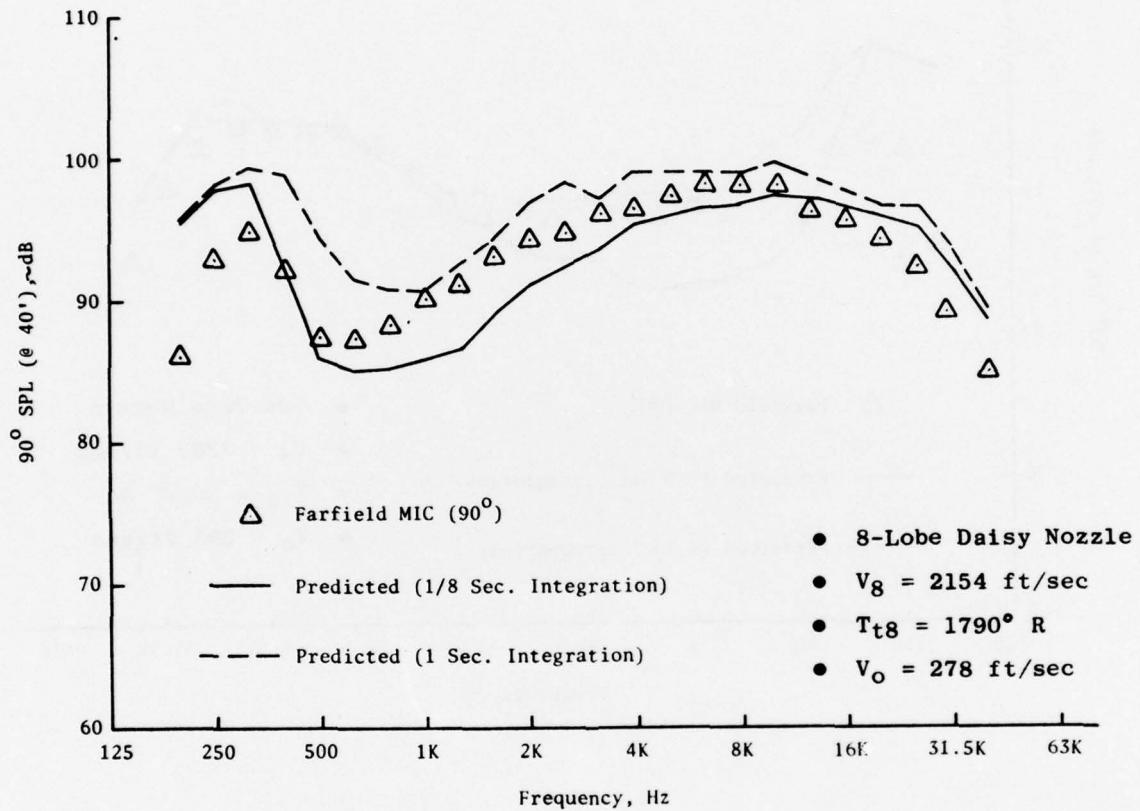


Figure 4-60. Integral Closure Check for 8-Lobe Nozzle,
 $V_8 = 2154 \text{ ft/sec}$, $V_o = 278 \text{ ft/sec}$.

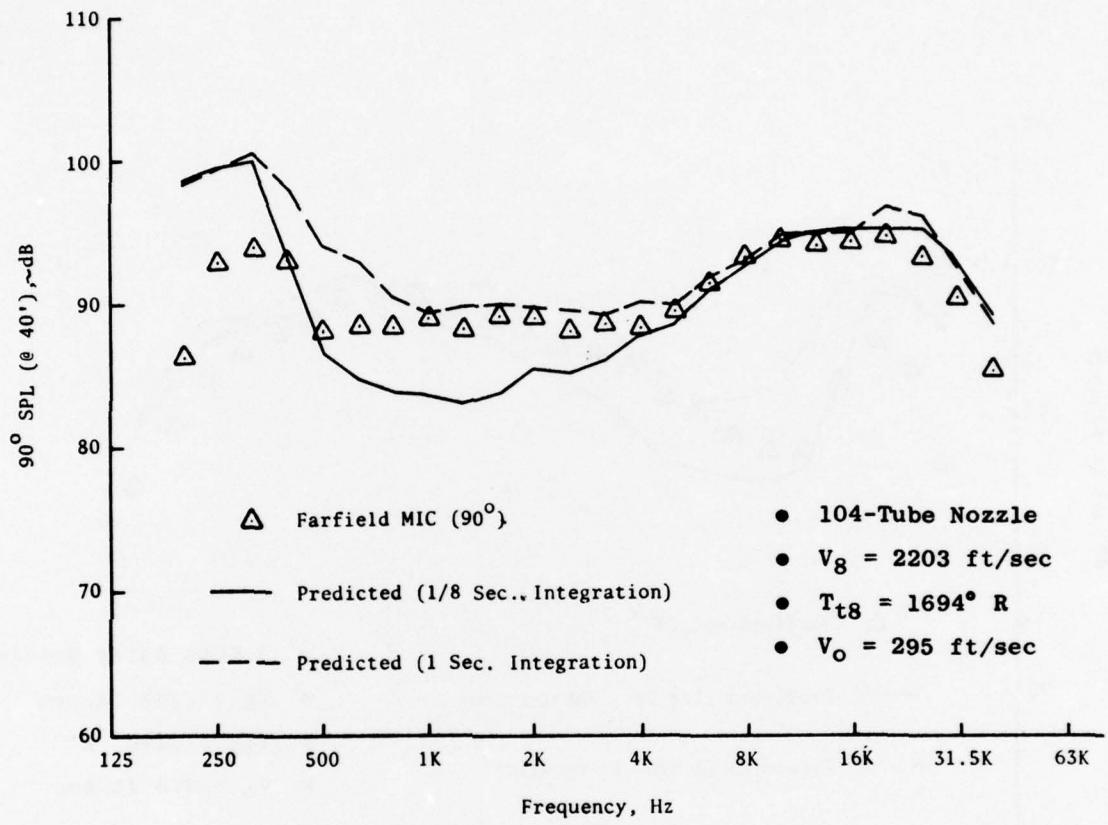


Figure 4-61. Integral Closure Check for 104-Tube Nozzle,
 $V_8 = 2203$ ft/sec, $V_o = 295$ ft/sec.

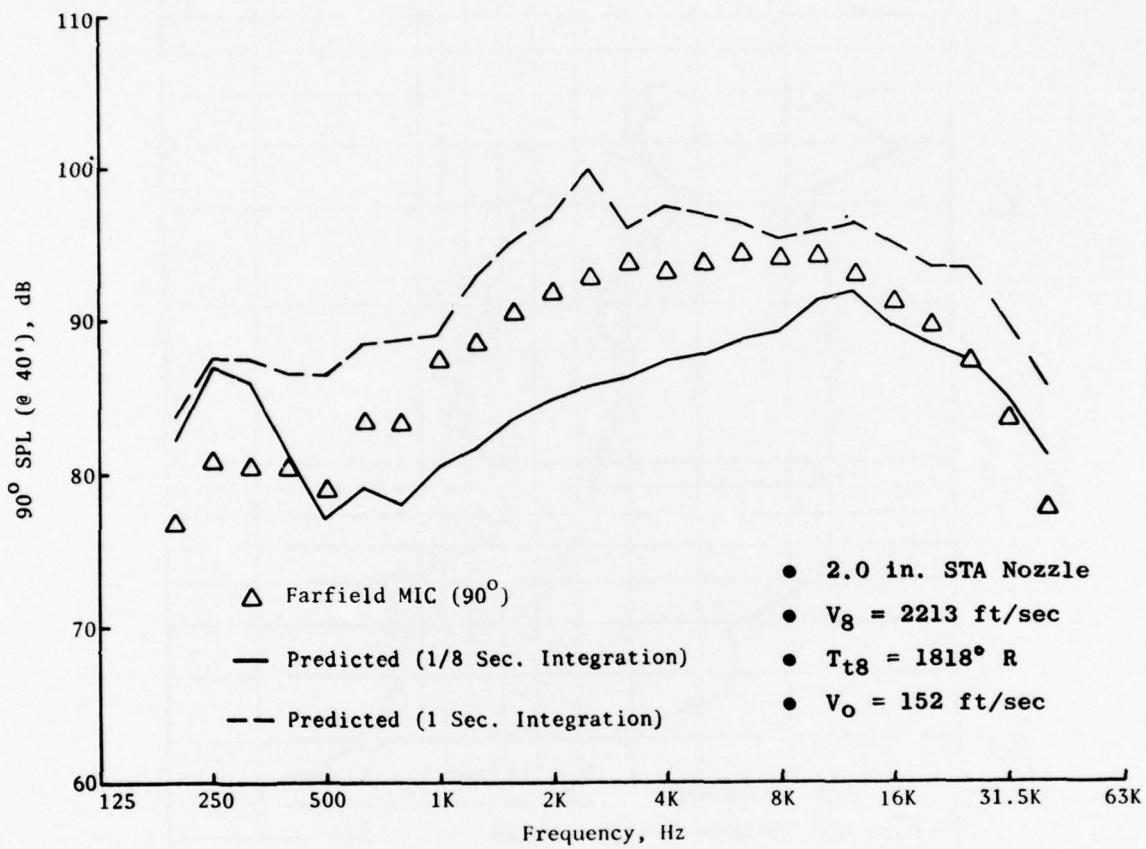


Figure 4-62. Integral Closure Check for 2.0-Inch STA Nozzle,
 $V_8 = 2213 \text{ ft/sec}$, $V_o = 152 \text{ ft/sec}$.

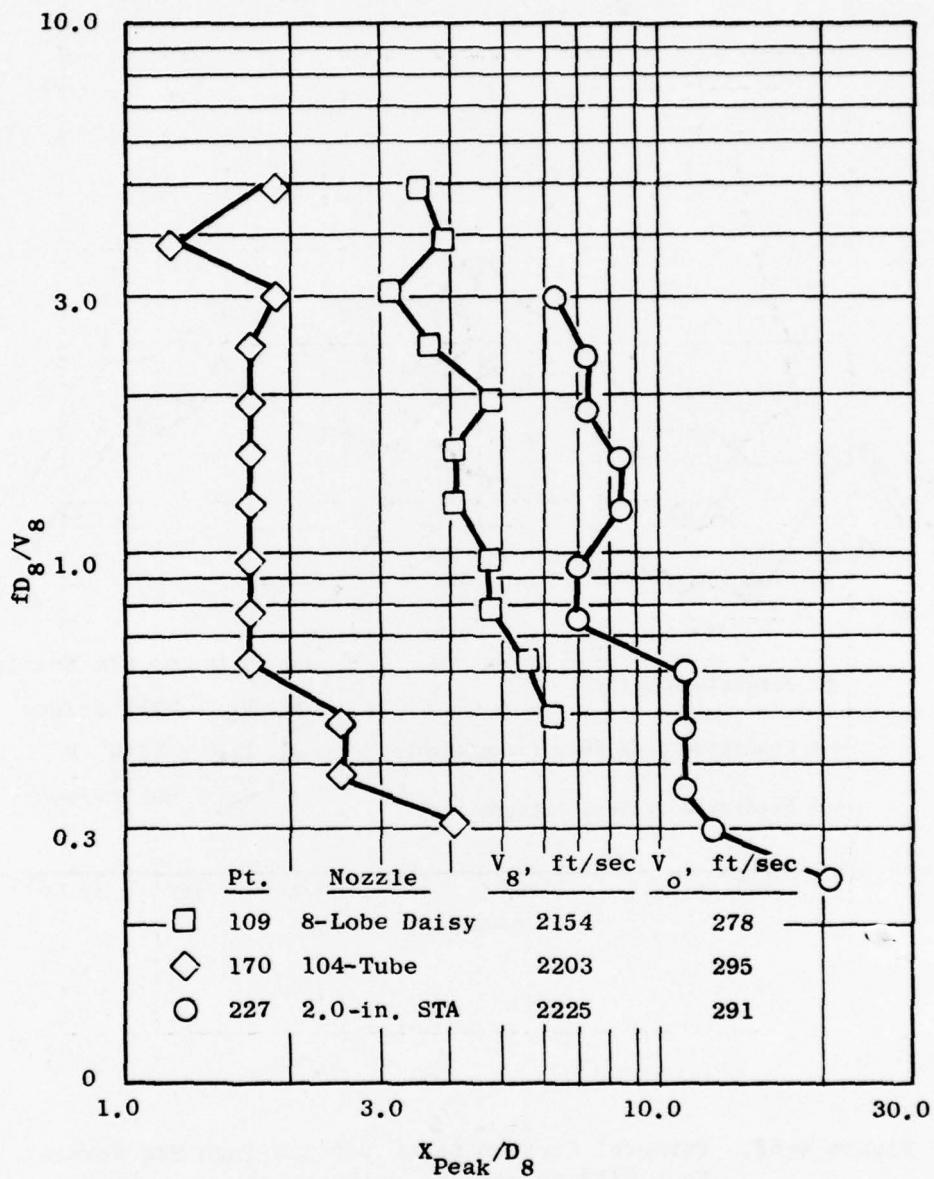


Figure 4-63. Axial Location of Peak Source Regions for 2.0-in. STA, 8-Lobe Daisy and 104-Tube Nozzles.

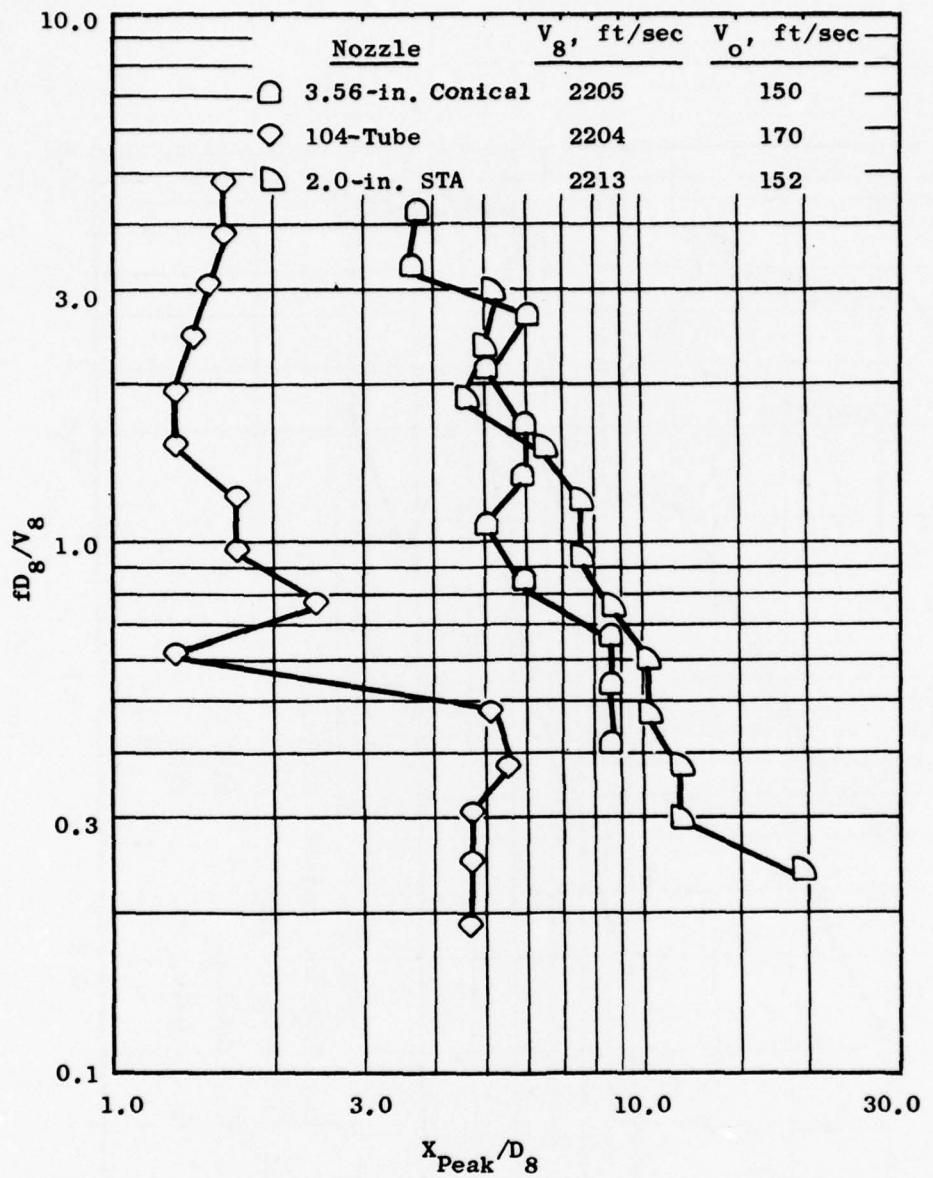


Figure 4-64. Axial Location of Peak Source Regions for 2.0-in. STA, 104-Tube, and 3.56-in. Conical Nozzles.

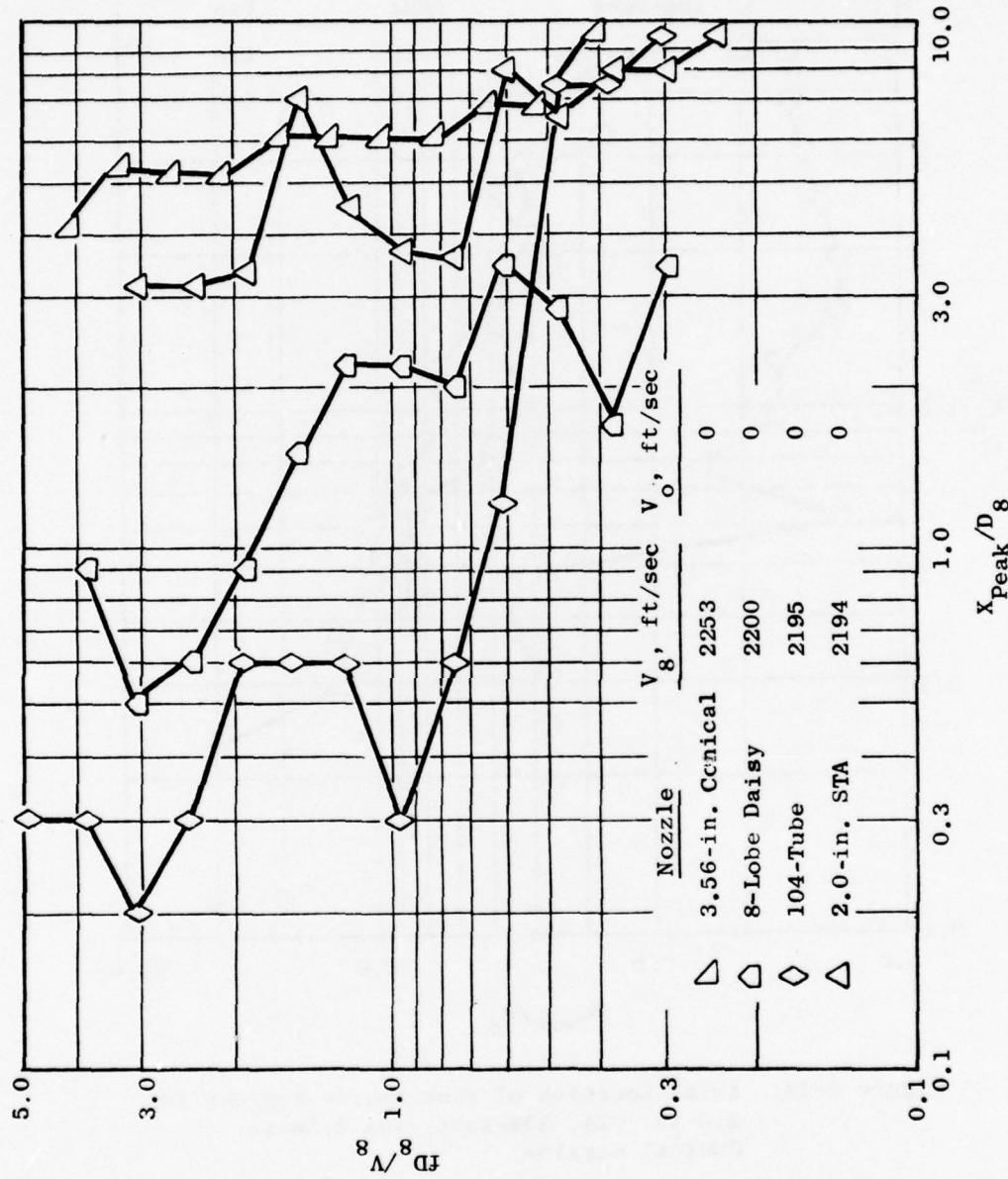


Figure 4-65. Axial Location of Peak Source Regions for 3.56-in. Conical, 8-Lobe Daisy, 104-Tube, and 2.0-in. STA Nozzles.

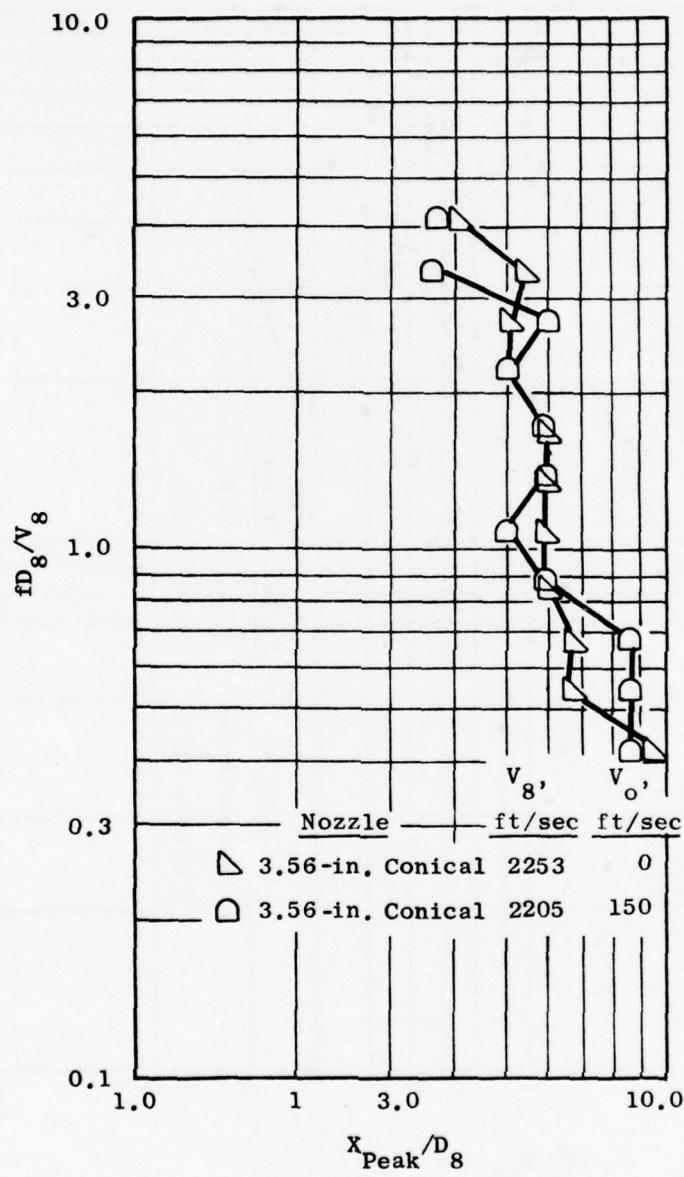


Figure 4-66. Axial Location of Peak Source Regions for 3.56-in. Conical Nozzle.

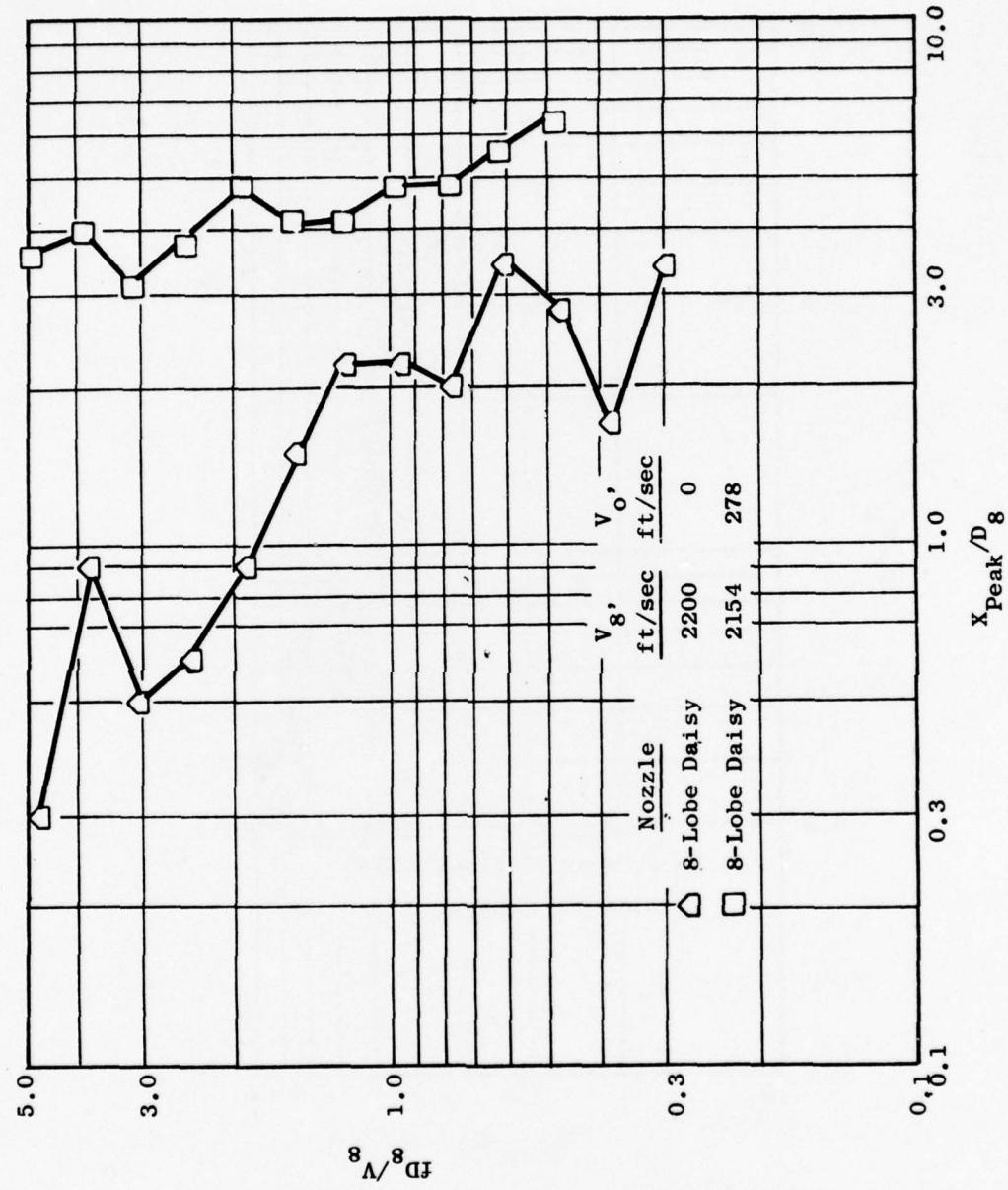


Figure 4-67. Axial Location of Peak Source Regions for 8-Lobe Daisy Nozzle.

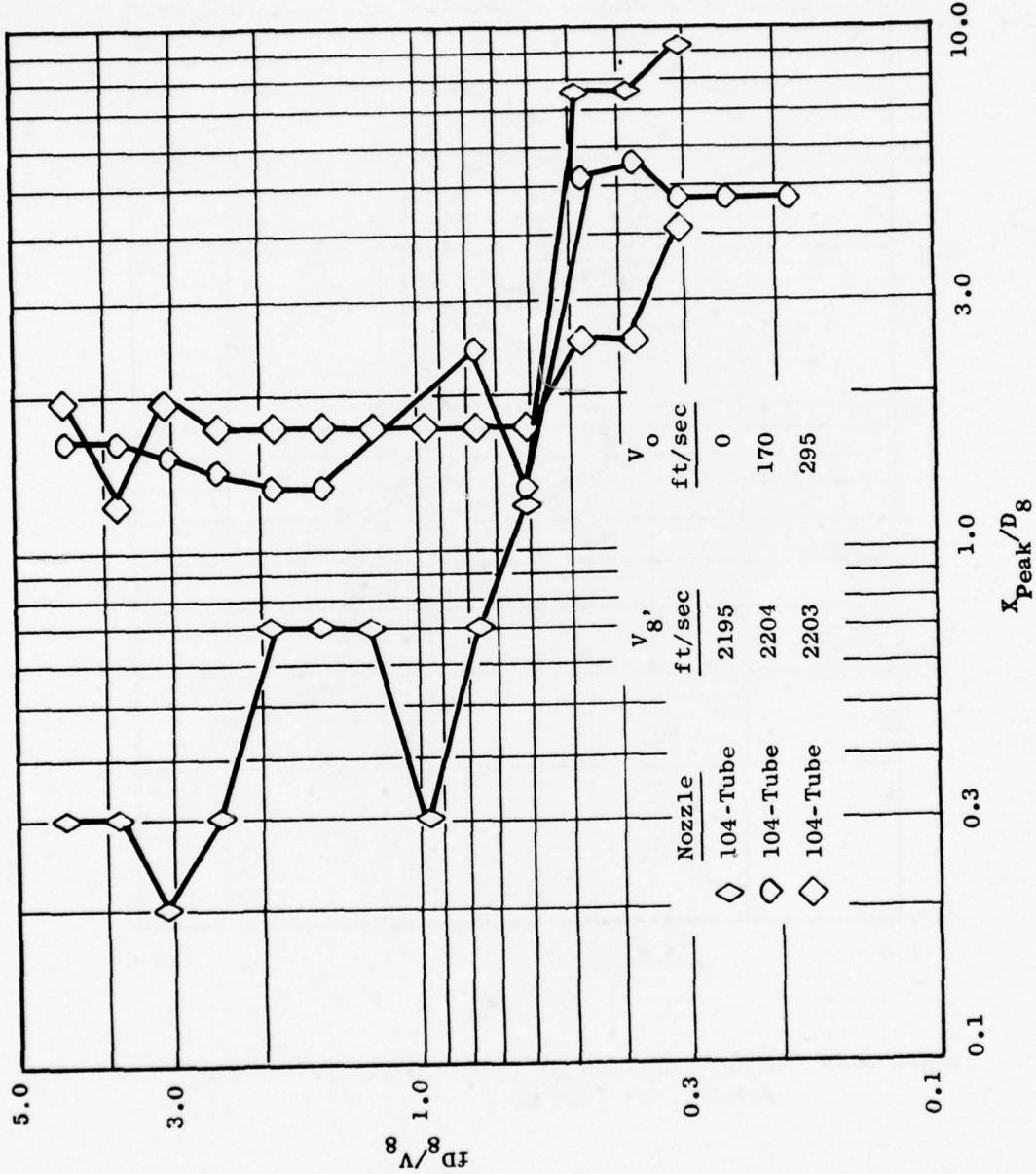


Figure 4-68. Axial Location of Peak Source Regions for 8-Lobe Daisy Nozzle.

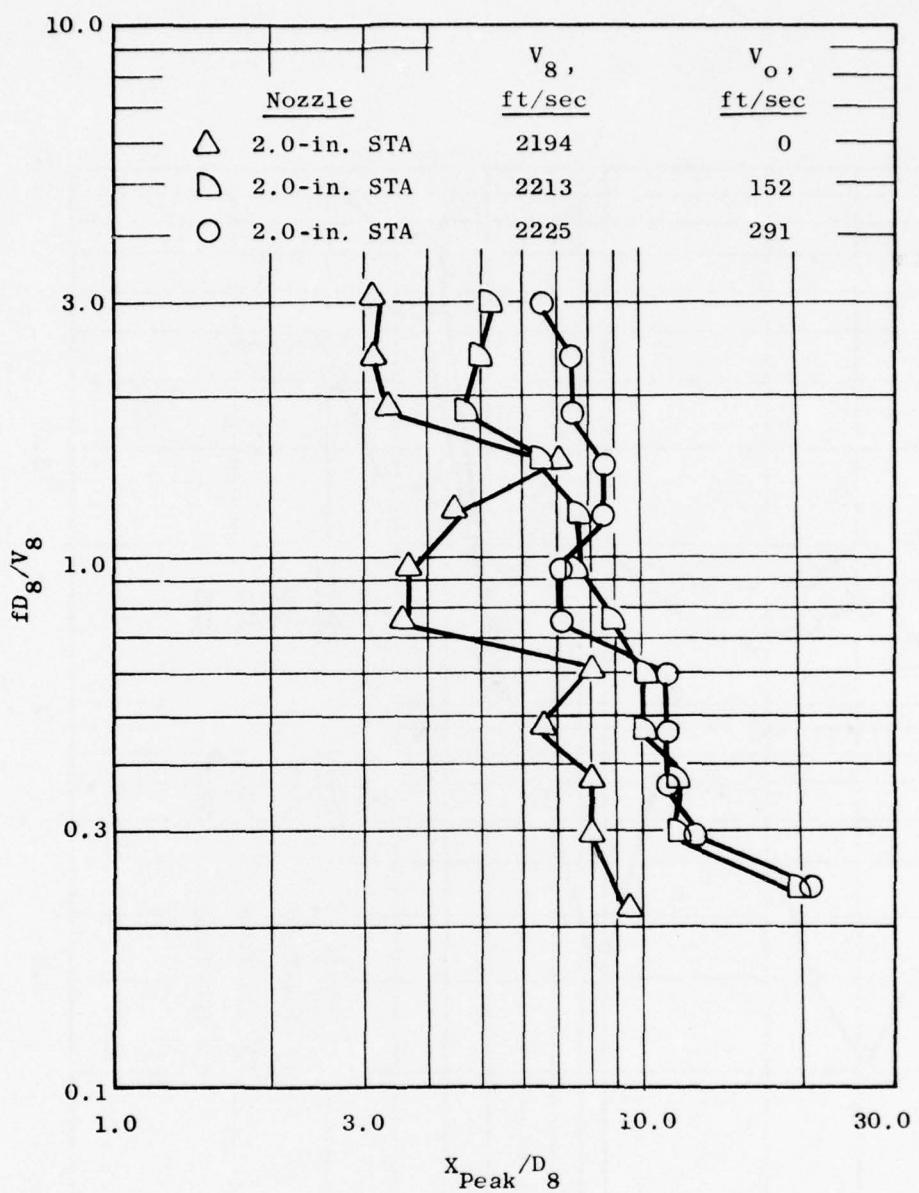


Figure 4-69. Axial Location of Peak Source Regions for 2.0-in. STA Nozzle.

The velocity, V_8 , was taken as the ideally expanded jet velocity for the particular data point. The peak source locations, X_{peak} , were obtained from the results of 1/8-second integrations for high frequencies and from 1-second or 1/2-second integrations for lower frequencies, with the integral closure check being used for guidance.

Comparisons of peak source locations for the different nozzles, as functions of Strouhal number, are shown in Figures 4-63, 4-64, and 4-65 at free jet velocities of 275, 150, and 0 ft/sec respectively. The observed strouhal number (fD_8/V_8) dependence of the source distributions is consistent with expectations and with previous measurements. The high frequency sources are found closer to the nozzle exit with the low frequency source regions appearing further downstream; also, as intuitively expected, the peak source region for a given strouhal number is found to occur closer to the exit (on a normalized basis) with increasing number of nozzle elements. Note the extreme difference between the STA Nozzle and the 104-tube nozzle results presented on Figure 4-63. Similar source distributions are found for the two Figures 4-64 and 4-65. Overall, these results clearly demonstrate the ability of the EM to differentiate between the characteristic source distributions of different nozzle types in both static and "wind-on" environments.

Figures 4-66, 4-67, 4-68, and 4-69 show comparisons of static and "wind-on" source distributions for the 3.56-inch conical, 8-lobe, 104-tube, and 2.0-inch STA nozzles, respectively. Figure 4-66 shows no apparent difference between 0 and 150 ft/sec free jet velocities with the 3.56-inch conical nozzle; however, this result is not entirely consistent with those of the three remaining figures. Figure 4-67 shows a significant downstream movement of the sources in going from 0 to 275 ft/sec, for the 8-lobe daisy nozzle, while Figures 4-68 and 4-69 show significant differences between 0 and 150 ft/sec, with very little additional change apparent from a further increase to 275 ft/sec, for the 104-tube and 2.0-inch STA nozzles. There appears to be a significant difference in supersonic jet noise source distributions between 0 and 275 ft/sec free jet velocities. The results are consistent with the idea of sources being "swept" downstream in flight; however, the results for a 150 ft/sec free jet velocity are apparently configuration dependent and suggest that the free-stream velocity must attain a minimum level before a significant axial displacement of the apparent peak noise source distribution occurs.

4.1.6.4 Conclusions

The results of ellipsoidal mirror measurements taken during this test program have demonstrated the ability of the EM to detect differences in jet-noise source distribution among different basic nozzle configurations and different levels of free-stream velocity. It has also been shown that the validity of results in different frequency ranges is strongly affected by the choice of integration time used in obtaining discrete spectra. This test program provides an experimental data base that will be extremely useful in optimizing this parameter.

4.2 RECOMMENDED ANALYTICAL TRANSFORMATION

This section presents the recommended procedure for transformation of free jet noise to flight noise. The procedure was evolved based on the results of the screening study presented in Section 3.4. The method utilizes the measured free jet data, extracting from it a "basic" directivity which is the directivity that the sources associated with the primary nozzle plume would create if they radiated into a static rather than the free jet environment. Next, this basic directivity pattern is used to estimate what the noise in flight would be.

A flow chart describing the methodology used in the transformation procedure is presented on Table 4-IX. A copy of the computer program of the method is included in the Appendix. A narrative describing the details of the procedure presented on the flow chart is presented as follows. Circled capitol letters (e.g. "(A)") preceding elements of the narrative will help guide the reader through the flow chart where the same circled letter correlates to the narrative.

(A) To retrieve the basic directivity, subtract out the refractive effect of the free jet flow. At low frequencies (for $k_0a < 3$), the plug flow model solution for a point pressure source is used to make this correction. For $k_0a > 3$, in the inlet arc, the asymptotic high-frequency solution for a pressure source, namely $p_{PJ} \approx (1 - M \cos \theta)^{-1}$ is employed to subtract out the refractive effect. For $k_0a > 3$ the exhaust arc was used to deduce the refractive effect at the suggestion of Schubert (Reference 29). Schubert has suggested that one first determine the refractive effect in dB along the jet exhaust axis as the refractive dip on jet axis proportional to free jet Mach number times the frequency parameter, k_0a , (Reference 24). He then suggests, based on extensive numerical calculations, that an essentially frequency- and Mach number-independent shape factor be employed to deduce the refraction at any other angle. This procedure was adopted for $3 < k_0a < 6$ using the experimental data taken by Ribner and his students with point sources in jets (Reference 25). The data are actually available only for $k_0a < 1.25$ and, hence, a linear extrapolation of it for $6 > k_0a > 1.25$ was used.

The test data from the free jet experiments showed a tendency for the refractive dip to saturate for $k_0a > 6$, presumably due to turbulent scattering. This was inferred by examining, for example, the difference between the SPL's at $\theta_J = 40^\circ$ and $\theta_J = 20^\circ$. Such a difference (at a given jet Mach number) does not increase indefinitely with k_0a , but levels off for $k_0a > 6$. The refractive correction for the exhaust arc was therefore taken independent of k_0a for $k_0a > 6$, though still linearly proportional to free jet Mach number. One of the very important conclusions that emerged from this study is that, for the range of k_0a of interest in a "Hybrid" facility (extends up to 150 for the GE facility) a calculation based only on wave propagation in a steady, variable-property flow will overestimate the refractive effects at high frequencies and shallow angles when compared to the experimental data.

Table 4-IX. Algorithm Description.

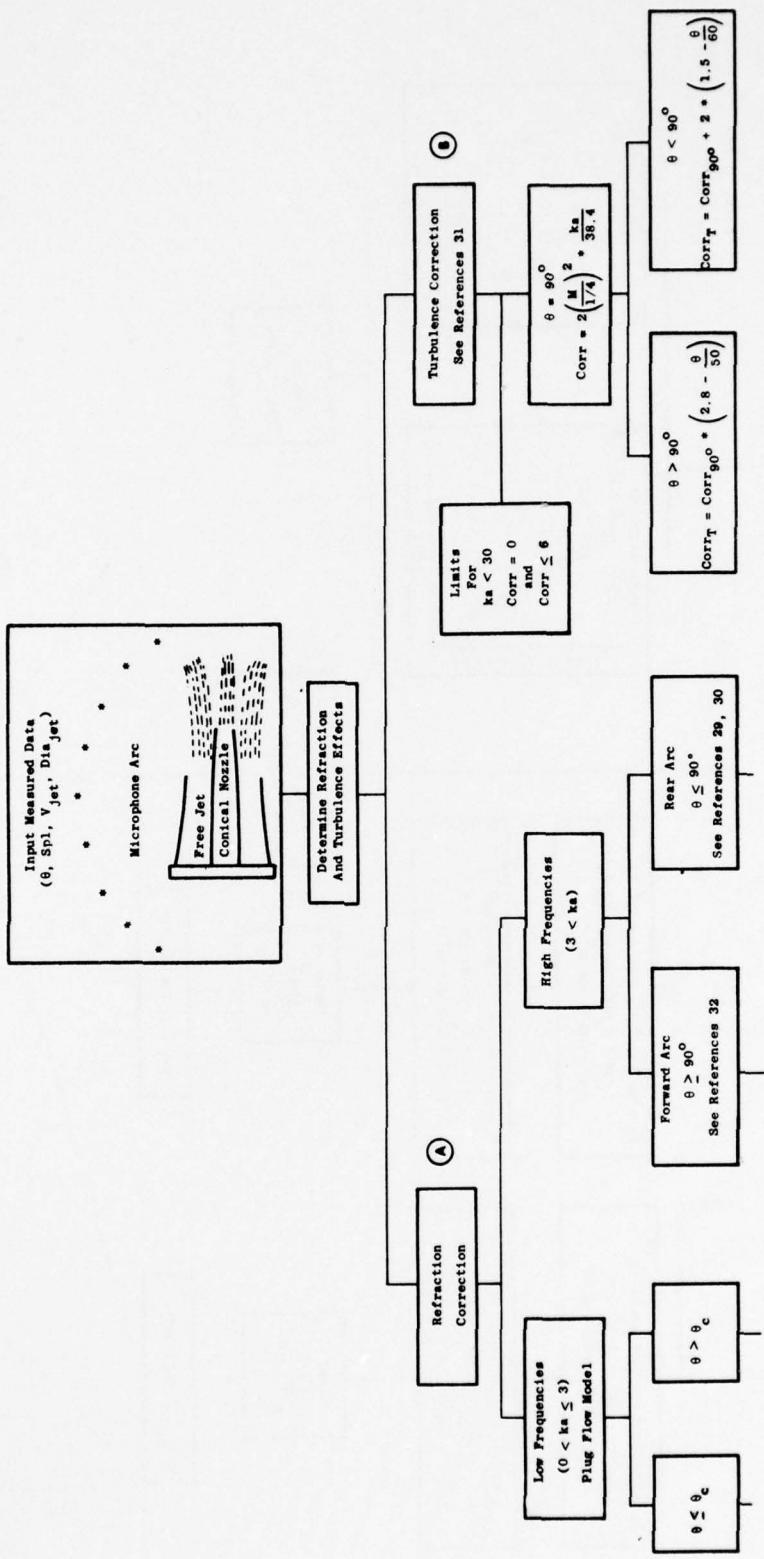


Table 4-IX. Algorithm Description (Continued).

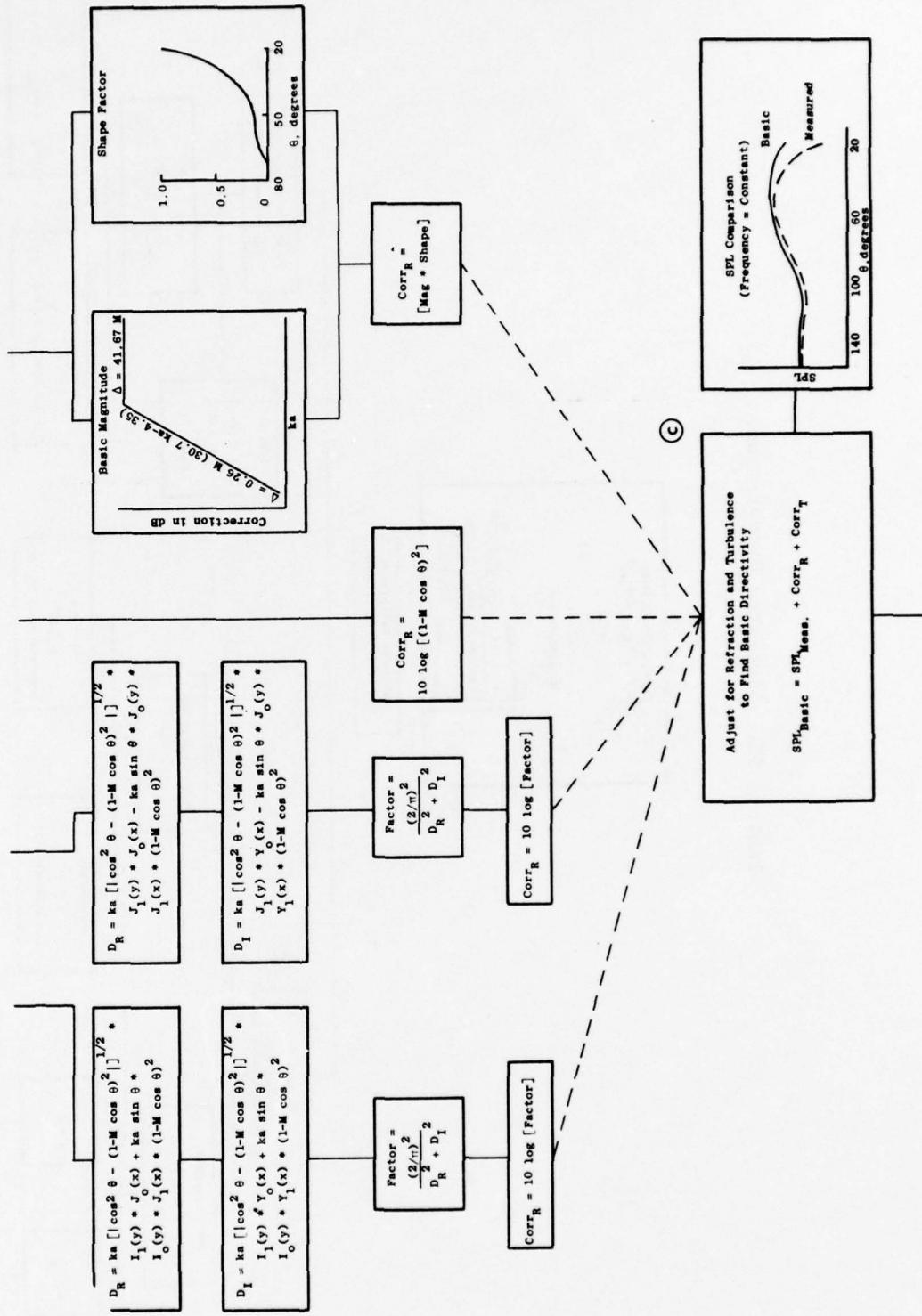


Table 4-IX. Algorithm Description (Continued).

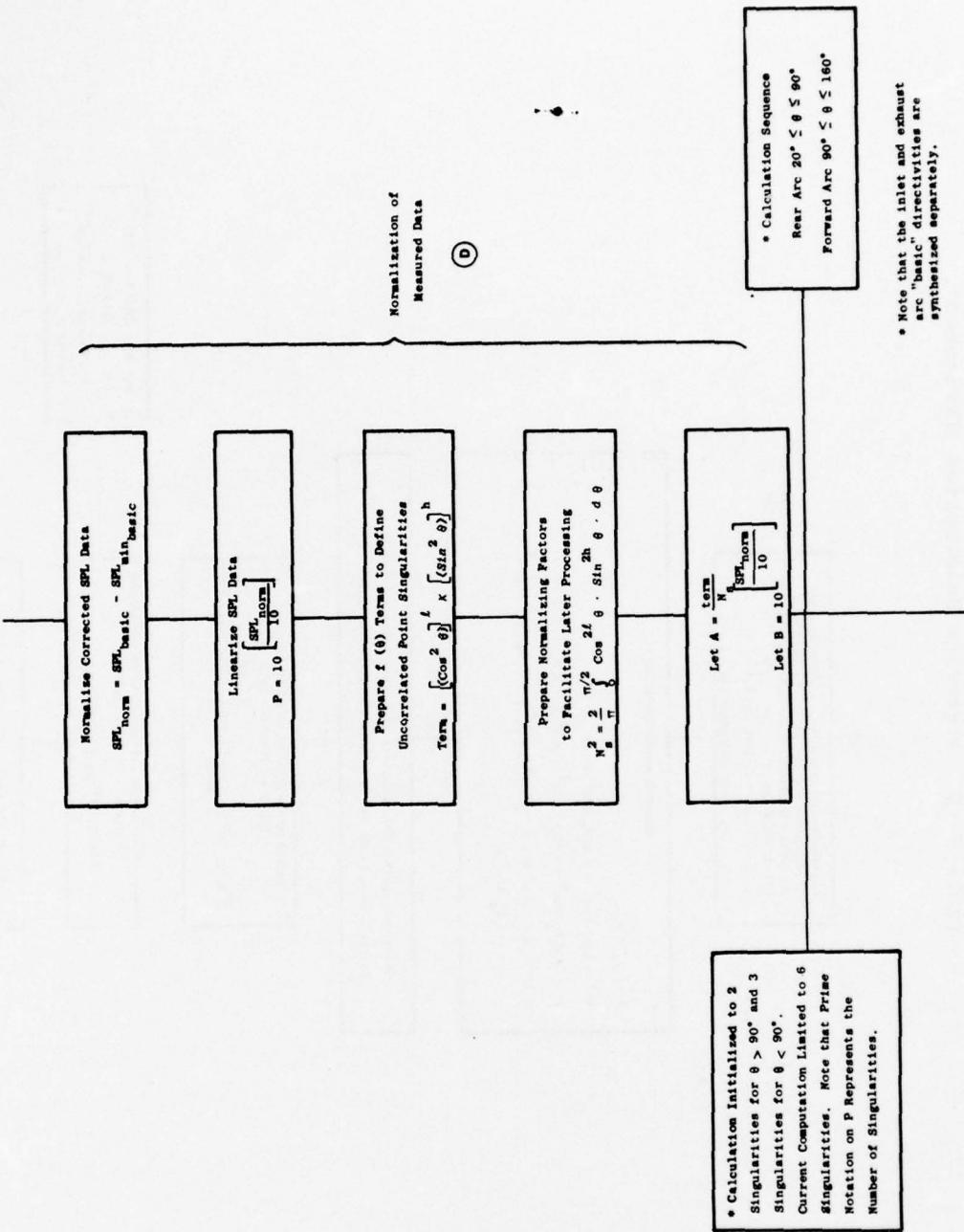


Table 4-IX. Algorithm Description (Continued).

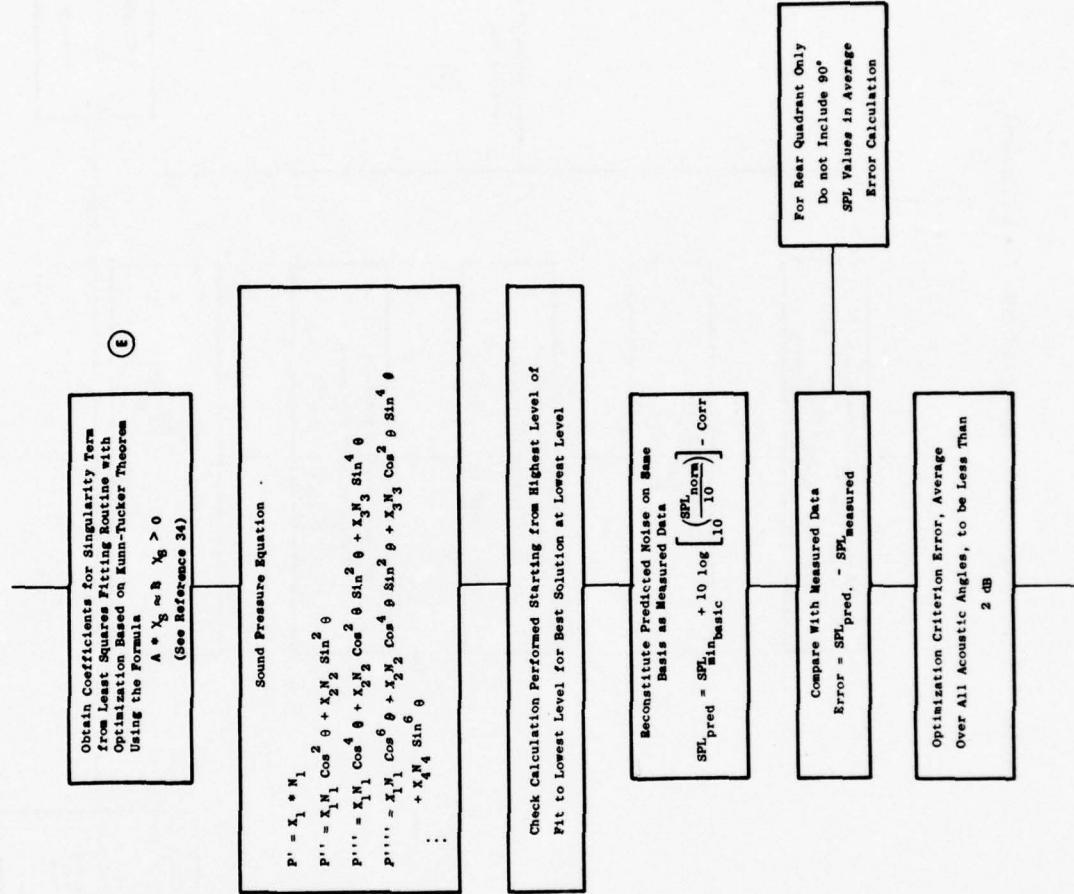
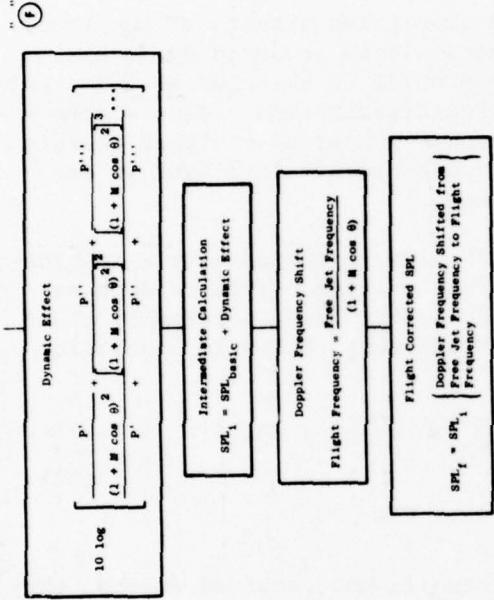


Table 4-IX. Algorithm Description (Concluded).



List of Symbols

A	An Input Quantity to the Least Squares Fitting Procedure
B	An Input Quantity to the Least Squares Fitting Procedure
Corr	An Acronym used to Identify the Refraction and/or Turbulence Correction
D _R	Real Root of Denominator Term in Solution of the Sound Pressure for the Plug Flow Model
D _I	Imaginary Root of Denominator Term in Solution of the Sound Pressure for the Plug Flow Model
F	Subscript for Flight Corrected SPL
h	Numerical Value Varies with Level of Singularity Considered
I	Subscript on SPL to Identify an Intermediate Calculation
I _n (x)	Modified Bessel Function of the First Kind of Order n, Argument in x
I _n (y)	Modified Bessel Function of the First Kind of Order n, Argument in y
J _n (x)	Bessel Function of the First Kind of Order n, Argument is x
J _n (y)	Bessel Function of the First Kind of Order n, Argument in y
ka	Frequency Parameter = (Free Jet Frequency Band of Interest in Radians per Second) x (Free Jet Radius in Feet) ÷ (Ambient Speed of Sound)
l	Numerical Value Varies with Level of Singularity Considered
M	Mach Number = (Free Jet Velocity) + (Ambient Speed of Sound)
N	Normalizing Factor, Function of Singularity
P	Sound Pressure in Microbars
P _{ref}	0.0002 Microbars
R	Subscript for Refraction Correction
S	Singularity Subscript
SPL	Sound Pressure Level = 10 log (P ² /P _{ref} ²)
T	Subscript for Turbulence Correction
Term	Acronym Used to Identify a Unique Algebraic Grouping
X	Bessel Function Argument, X = ka sin θ
X	A Constant Derived from Least Squares Fitting, Function of Singularity
y	Bessel Function Argument, y = ka [cos ² θ - (1 - M cos θ) ²] ^{1/2}
Y _n (x)	Bessel Function of the Second Kind of Order n, Argument x
θ	Angle from the Jet Axis Referred to the Exhaust
θ _c	Critical Angle that Defines the Jet Zone of Silence = Arc tan (M + M ²) ^{1/2}

(B) One additional propagation effect of the free jet needs to be accounted for. This relates to the fact that fine-grained turbulence in the shear layer of the free jet can absorb sound, especially at high frequencies. Crow has presented a theory for this effect (Reference 31) indicating that it results in an effective absorption coefficient proportional to frequency and free jet Mach number squared. This absorption is also confirmed by the experimental results presented in Reference 35. Based on the path lengths that the sound has to traverse through the free jet, it is assumed that the absorption varies with θ_I , as shown in Figure 4-70. An eddy viscosity about 70 times as effective as the molecular viscosity at a free jet Mach number of 0.25 and frequency of 50 kc was assumed to calculate the absorption. For $k_o a < 30$, this mechanism yields an insignificant amount of absorption. The exact expressions for calculation of this parameter are presented in Table 4-IX.

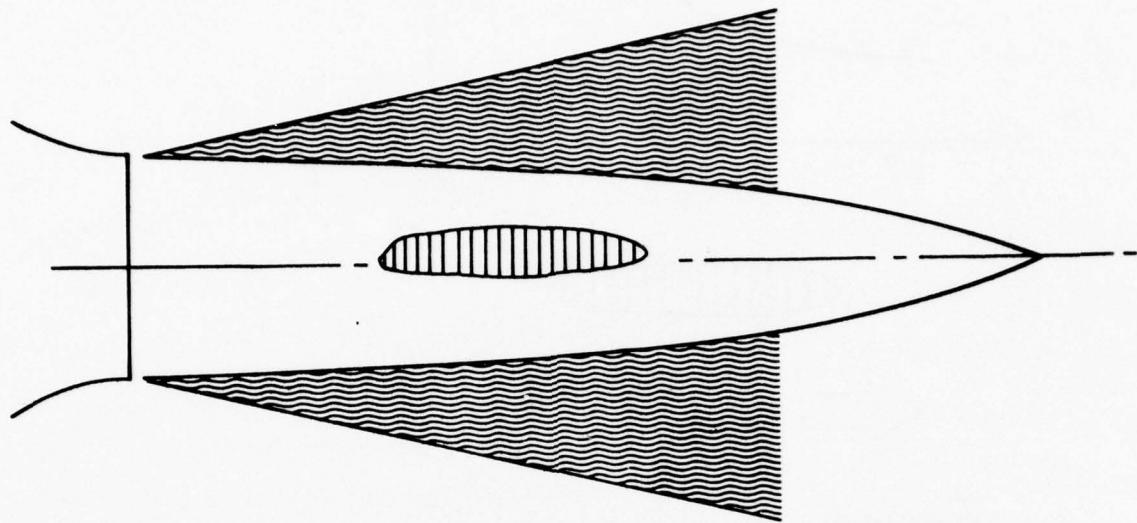
(C) After subtracting the refractive and absorptive effects of the free jet, (B), as described above, the noise that would be produced by such a source distribution must be predicted. The problem is sketched in a generalized sense on Figure 4-71. An extended source distribution yields a directivity pattern in the far field for each frequency band as sketched therein. The noise distribution that such a pattern would produce in flight is predicted as described in the following paragraph.

First, attempt to synthesize the "basic" directivity data by a combination of nozzle fixed, uncorrelated, point singularities. This is done by assuming the noise field in a given frequency band to be generated by a set of singularities F_o , F_x , F_y , etc., such that the sound field is a solution to:

$$\nabla^2 p + k_o^2 p = F_o \delta(x) \delta(y) \delta(z) + F_x \delta'(x) \delta(y) \delta(z) \\ + F_y \delta(x) \delta'(y) \delta(z) + \dots \text{etc} \quad (52)$$

where F_o , F_x , F_y , etc., are assumed to be mutually uncorrelated so that they contribute to the far-field mean square pressure only additively. An example is given in Figure 4-72 of how a certain combination of a radial dipole, axial dipole, and a fourth-order singularity (all mutually uncorrelated) can be employed to synthesize an exhaust arc radiation pattern characterized by a 15-dB convection fall off, a 10-dB refraction dip, and a peak at about $\theta_I = 150^\circ$. Because the mean square pressure of any such singularity is symmetric about both $\theta = 0^\circ$ and $\theta = 90^\circ$, it is necessary to synthesize both the inlet and exhaust arc noise separately. Also, as shown in Figure 4-73, an issue of uniqueness arises. Due to relations such as $(1 = \cos^2 \theta + \sin^2 \theta)$, the pressure pattern of a pressure source can be synthesized from that of a sum of equal transverse and radial dipoles, etc. As indicated on the right of Figure 4-73, the dynamic exponent required to derive the flight result associated with each level of the singularity "tree" varies with the level of the singularity. Hence, the following singularity fitting procedure was adopted.

Correction for Absorption by Turbulence (Fine Grained)



• Crow: $\gamma \sim (M_{FJ}^2) (f) \text{ (distance)}$

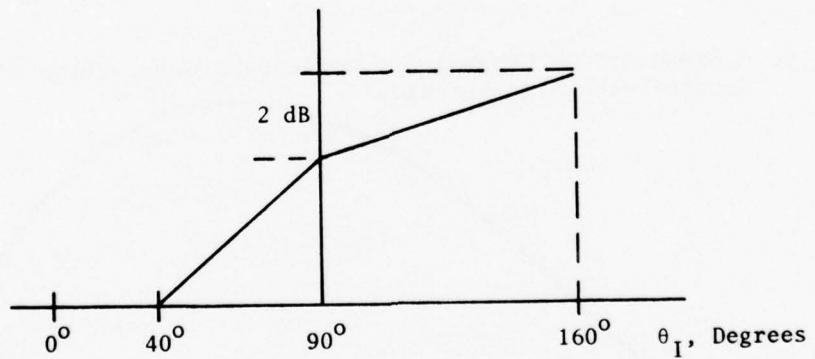


Figure 4-70. Absorption of Sound by Turbulence.

Dynamic Effect Applied to Basic Directivity

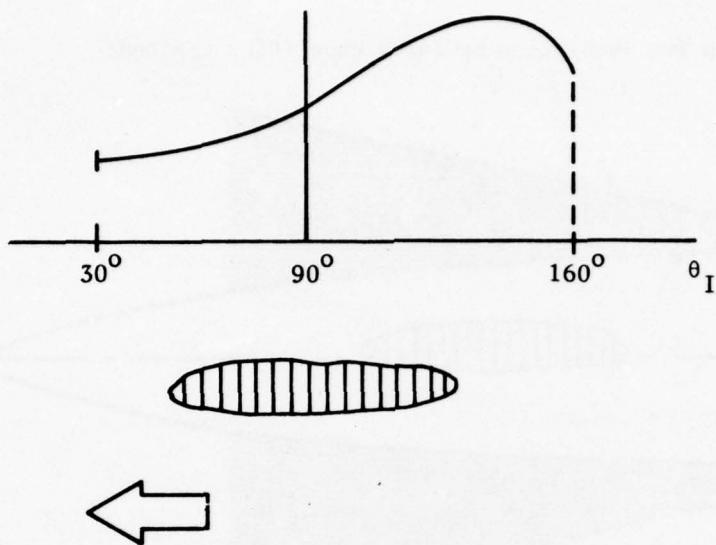


Figure 4-71. The Problems of Transforming from Static to Flight.

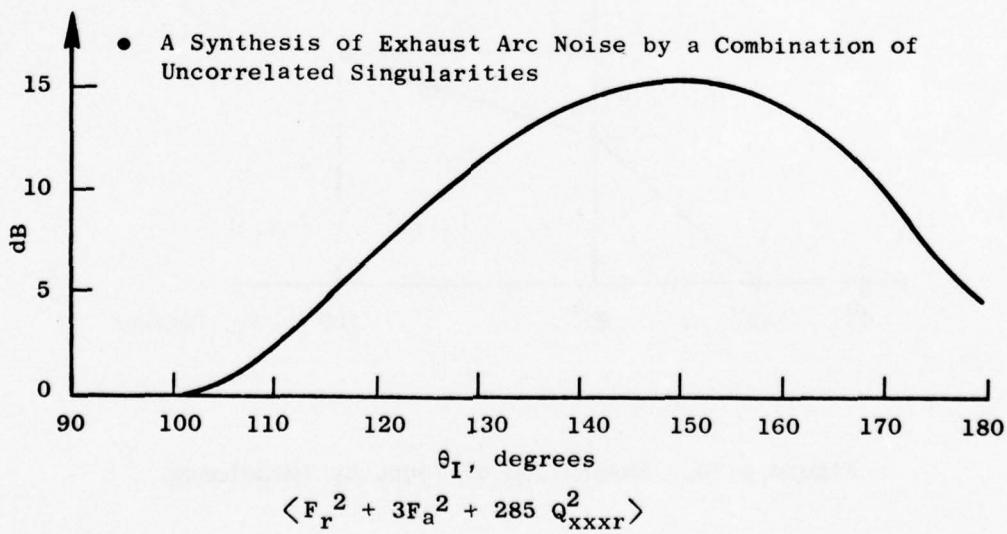
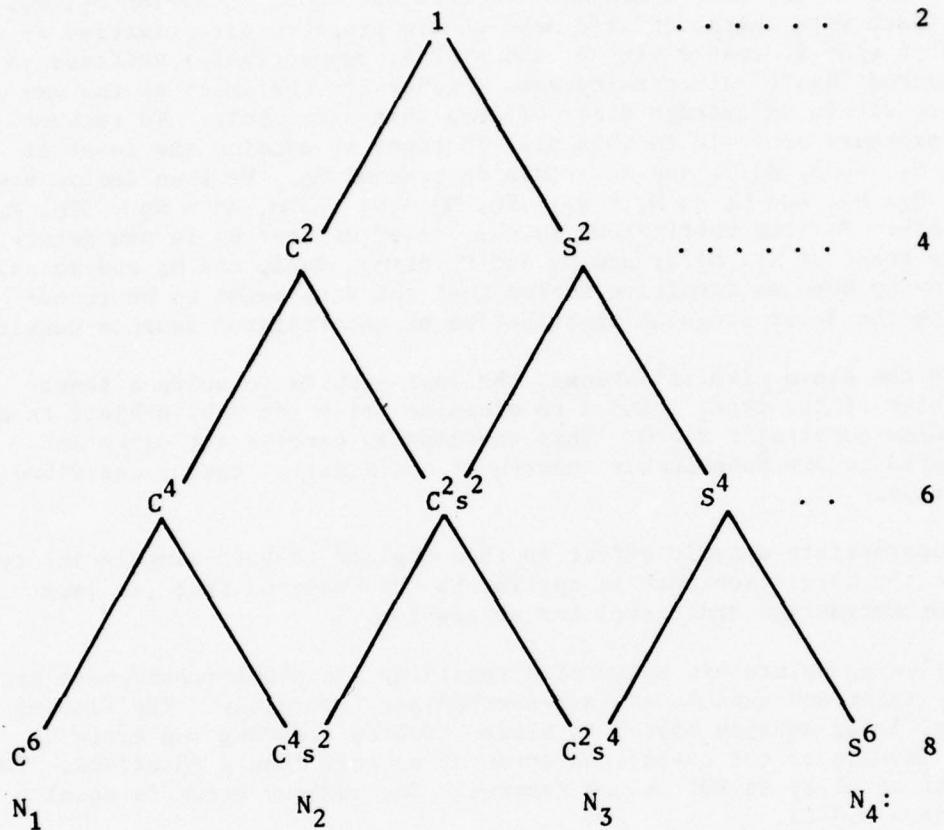


Figure 4-72. Example of Synthesis of Exhaust Arc Noise.

Dynamic Effect Exponent for $\langle p' \rangle^2$



$$F_o = \min(N_1, \frac{N_2}{3}, \frac{N_3}{3}, N_4)$$

Reset $(N_1 - F_o)$, $(N_2 - 3 F_o)$, $(N_3 - 3 F_o)$, $(N_4 - F_o)$, Etc.

Figure 4-73. Recombination of Singularities.

(D) First decide on a level of fitting using the criterion that the data ought to be reconstructed to within an error of 2 dB on the average. Any hidden symmetries in the singularity distribution, however, are detected by a recombination procedure indicated in Figure 4-73. What is meant by this is as follows. Let us say that a nonnegative combination of octopoles N_1 , N_2 , N_3 , and N_4 (each with characteristic mean square pressure directivities as $\cos^6 \theta$, $\cos^4 \theta \sin^2 \theta$, $\cos^2 \theta \sin^4 \theta$, and $\sin^6 \theta$, respectively) suffices to fit the measured "basic" directivity data (either for the inlet or the exhaust arc) to within an average error of less than 2 decibels. To recover the hidden pressure monopole in this distribution, we examine the least of the numbers N_1 , $N_2/3$, $N_3/3$, and N_4 . This determined F_0 . We then derive new numbers M_1 , M_2 , M_3 , and M_4 as $M_1 = N_1 - F_0$, $M_2 = N_2 - 3F_0$, $M_3 = N_3 - 3F_0$, $M_4 = N_4 - F_0$, etc. F_1 (the coefficient in the "tree" of $\cos^2 \theta$) is now determined as the least of M_1 , $M_2/2$, and M_3 and F_2 of M_2 , $M_3/2$, and M_4 and so on. We are employing here an intuitive notion that the data ought to be reconstructed with the least singular distribution of uncorrelated sources possible.

(E) After the above simplifications, the last step is to solve a least-squares problem of the type: find \bar{x} to minimize $|\bar{r}| = (\bar{A}\bar{x} - b)$ subject to a nonnegativeness constraint $\bar{x} \geq 0$. This exercise is carried out using an algorithm based on the Kuhn-Tucker theorem of optimization theory described in Reference 34.

(F) The appropriate dynamic effect is then applied to each singularity type to determine the correction that is applied to the measured free jet data corrected for refraction and turbulence absorption.

The following points are reiterated regarding the above-recommended procedure: The inlet and exhaust arc are synthesized separately. The fitting (on a linear, least squares basis) is biased towards reducing the error at the highest levels; on the average an error of no more than 2 dB exists. The constraint of equality at 90° is not imposed. The maximum error is equal to or less than 3.5 dB.

The following example for the 8-lobe nozzle is presented to further illustrate the details of the calculation procedure. Table 4-X presents typical measured sound pressure levels for the 8-lobe nozzle at a frequency of 1000 Hz. These data were obtained for a jet velocity of 2200 ft/sec and flight velocity of 270 ft/sec. As stated above, the first step in the transformation procedure is to correct the measured data for refraction and turbulence absorption. The corrections are shown in Table 4-X. The turbulence absorption correction is zero for the specific example chosen. Further illustrations will be provided, however, to show the importance of this parameter. The corrected sound pressure levels are then referenced to the lowest levels observed in the aft and forward quadrants (97.7 dB and 94.7 dB, respectively). These normalized levels are linearized using the expression:

$$p^{-2} = 10^{[\text{SPL} - \text{SPL}_{\min.}]} \quad (53)$$

Table 4-X. Example of Source Decomposition.

Aft Quadrant $f = 1000$ Hz

Acoustic Angle, Degrees	Measured Freejet SPL Levels, dB	Refraction Correction dB	Data Corrected for Refraction, dB	Normalized SPL's re: 90°	Linearized Levels
150	98.1	5.21	103.31	5.61	3.64
140	105.4	2.60	108.0	10.3	10.72
130	106.3	1.74	108.04	10.34	10.81
120	106.2	1.30	107.5	9.8	9.55
110	102.4	0	102.4	4.7	2.95
100	99.8	0	99.8	2.1	1.62
90	97.7	0	97.7	0	1.00

Forward Quadrant $f = 1000$ Hz

90	97.7	0	97.7	4.48	2.8
80	96.16	0.36	96.52	2.94	1.97
70	95.62	0.72	96.34	2.40	1.74
60	95.12	1.02	96.14	1.9	1.55
50	94.6	1.3	95.9	1.38	1.38
40	93.2	1.52	94.72	0	1.00
30	94.0	1.70	95.7	0.78	1.20

The linearized pressure levels are then fitted using the Kuhn-Tucker theorem to within an average error of two decibels. The results of this fitting procedure yielded the following "mix" of uncorrelated singularities for the aft and forward quadrants:

$$P_\theta'^2 = 38.95 \cos^2 \theta \sin^2 \theta + 0.789 \sin^4 \theta \quad (\text{aft quadrant}) \quad (54)$$

$$P_\theta'^2 = 0.451 \cos^2 \theta + 2.196 \sin^2 \theta \quad (\text{forward quadrant}) \quad (55)$$

Using the recombination procedure and noting that $\sin^2 \theta + \cos^2 \theta = 1$, the least singular decomposition for the two expressions become:

$$P_\theta'^2 = 38.161 \cos^2 \theta \sin^2 \theta + 0.789 \sin^2 \theta \quad (\text{aft quadrant}) \quad (56)$$

$$P_\theta'^2 = 0.451 + 1.745 \sin^2 \theta \quad (\text{forward quadrant}) \quad (57)$$

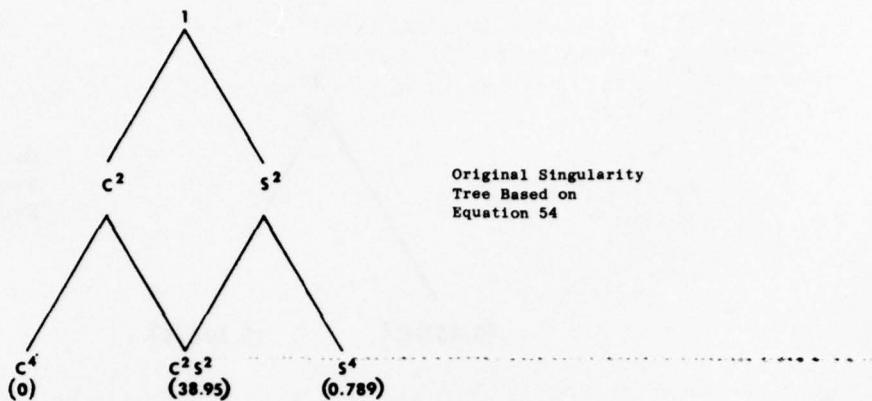
Using the recombination procedure described in step D, Equations 54 and 55 can be reduced to Equations 56 and 57, respectively. The procedure for performing this reduction is indicated on Figures 4-74 and 4-75. The linear levels in Equations 54 through 57 are relative to the minimum SPL for each individual arc. These expressions show that the mean squared pressure distribution in the aft quadrant can be synthesized from the sum of an "xy" quadrupole and a "y" dipole; however, in the forward quadrant the pressure distribution is synthesized by using the sum of a monopole and a "y" dipole. The calculation of the dynamic effect is accomplished for the aft and forward quadrants using the following expressions:

$$\text{Dynamic Effect} = 10 \log \frac{P_F'^2}{P_S'^2} = \frac{\frac{0.789 \sin^2 \theta}{(1+M \cos \theta)^4} + \frac{38.161 \cos^2 \theta \sin^2 \theta}{(1+M \cos \theta)^6}}{0.789 \sin^2 \theta + 38.161 \cos^2 \theta \sin^2 \theta} \quad (58)$$

(aft quadrant)

$$\text{Dynamic Effect} = 10 \log \frac{P_F'^2}{P_S'^2} = \frac{\frac{0.451}{(1+M \cos \theta)^2} + \frac{1.745 \sin^2 \theta}{(1+M \cos \theta)^4}}{0.451 + 1.745 \sin^2 \theta} \quad (59)$$

(forward quadrant)



Original Singularity
Tree Based on
Equation 54

Step 1 - For this level of fitting the coefficient of the omnidirectional term is the minimum value of N_1 , $N_2/2$, N_3 where

$$N_1 = 0, N_2/2 = 38.95/2, N_3 = 0.789$$

For this example the minimum value is N_1 , which is equal to 0.

Step 2 - The coefficient of the x-dipole is the minimum value of N_1 , N_2 .

For this case it is N_1 which is 0

Step 3 - The coefficient of the y-dipole is the minimum value of N_2 , N_3 .

For this case it is N_3 which is 0.789,

Step 4 - The coefficients of the xx-quadrupole, xy-quadrupole, yy-quadrupole are their initial values N_1 , N_2 , N_3 reduced by the values assigned to the lower order singularities.

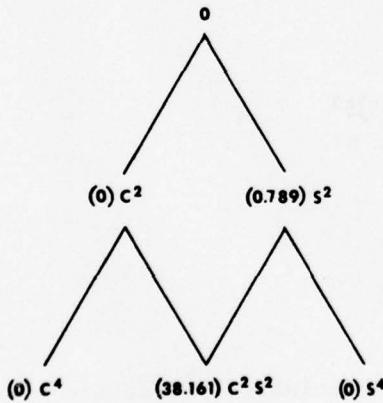
For this case the coefficients are:

$$\text{xx-quadrupole} = 0$$

$$\text{xy-quadrupole} = 38.95 - 0.789 = 38.161$$

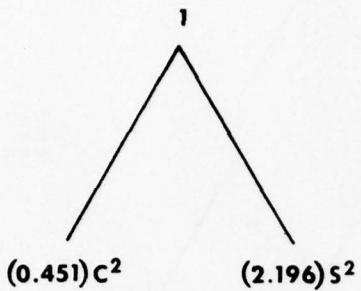
$$\text{yy-quadrupole} = 0.789 - 0.789 = 0$$

Step 5 - Thus the coefficients of the reconstituted tree will be



which correspond to Equation 56.

Figure 4-74. Example of the Recommended Procedure
- Aft Quadrant.



Original Singularity
Tree Based on
Equation 55

Step 1 - The coefficient of the omnidirectional term is the minimum value of N_1 , N_2 where

$$N_1 = 0.451, N_2 = 2.196$$

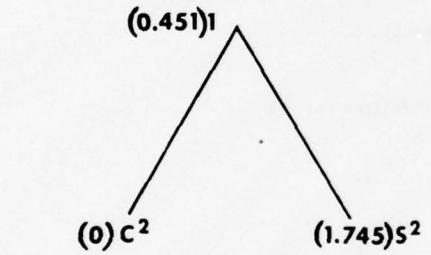
For this example, the minimum value is N_1 which is 0.451.

Step 2 - The coefficients of the x-dipole and the y-dipole are their initial values, N_1 , N_2 , reduced by the value assigned to the lower order singularity. For this case the coefficients are:

$$x\text{-dipole} = 0.451 - 0.451 = 0$$

$$y\text{-dipole} = 2.196 - 0.451 = 1.745$$

Step 3 - Thus the coefficients of the reconstituted tree will be



which correspond to Equation 57.

Figure 4-75. Example of the Recombination Procedure - Forward Quadrant.

These corrections, when added to the measured free jet data corrected for refraction and turbulence absorption, represent the predicted flight results.

The following cases for the conical, 8-lobe, and 104-tube nozzles further illustrate the effects of the refraction and turbulence absorption corrections on the results of the transformation procedure. Primary jet velocities of 2200 ft/sec and free-jet velocities of 270 ft/sec are common to the example cases. Figure 4-76 presents a summary of the predicted flight OASPL directivity patterns for each of the following levels of data transformation and correction:

- Free jet data as measured without using the transformation procedure.
- Free jet data transformed using the transformation procedure without refraction corrections.
- Free jet data transformed using the transformation procedure without turbulence absorption corrections.
- Free jet data transformed using the total recommended procedure.

Comparisons of the four levels of predictions resulting from these various assumptions indicate that the maximum effect of refraction in the forward quadrant is 1 dB (it is actually zero at 20°). A significant effect is observed in the aft quadrant angles close to the jet axis, as one would expect based on classical theory. The impact of the refraction effect is within 1.5 dB for all configurations even at the extreme angles.

The turbulence absorption corrections are between 0 and 3 dB in the forward quadrant and vary as a function of the nozzle configuration. At 90°, a 1.5-dB effect is observed for the conical nozzle, a 2-dB difference is observed for the 8-lobe, and a 4.0-dB difference is observed for the 104-tube nozzle. In the aft quadrant the turbulence absorption correction causes differences of 1 to 2 dB for the conical nozzle; however, for the 8-lobe and 104-tube nozzles the effect is 2 to 4 dB. This results because the turbulence absorption correction is applied to the high frequency portion of the spectra and suppressor noise spectra are strongly dominated by high frequency noise, whereas the conical nozzle spectra are not.

To further illustrate the impact of the turbulence absorption and refraction corrections, similar examples are presented on Figures 4-77 through 4-85 for the typical 1/3-octave band frequencies of 250, 500, 1000, 2000, 4000, and 8000 Hz. These comparisons show that turbulence absorption has no influence on the data below 2000 Hz. At frequencies above 2000 Hz, this parameter increases with increasing frequency, and at the extreme case of 8000 Hz, both the aft quadrant and forward quadrant corrections are on the order of 5 dB. The refraction corrections have no impact on the forward arc data and are extremely large (as expected based on classical theory) at angles close to the jet axis.

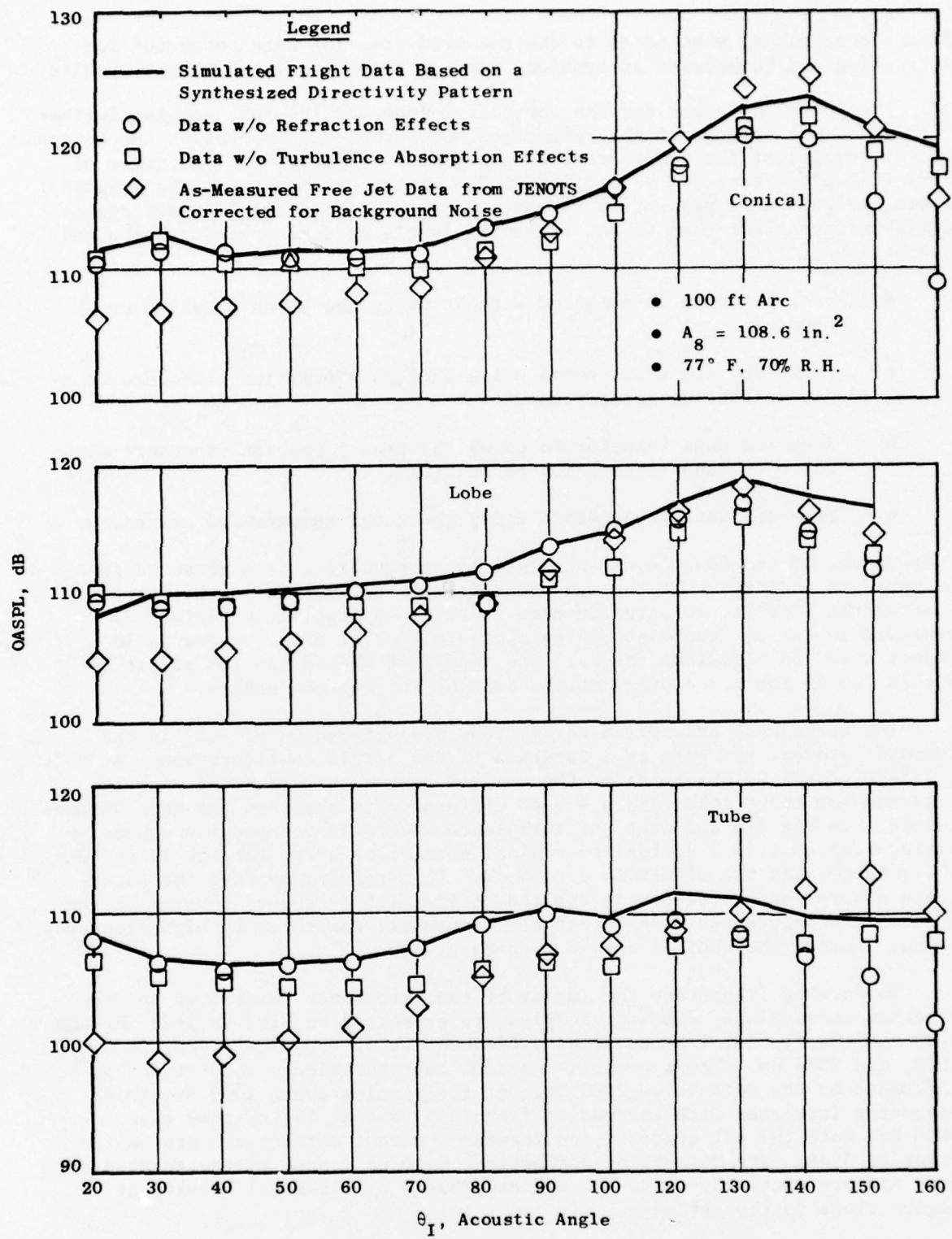


Figure 4-76. Impact of Refraction and Turbulence Absorption Corrections on OASPL Directivity.

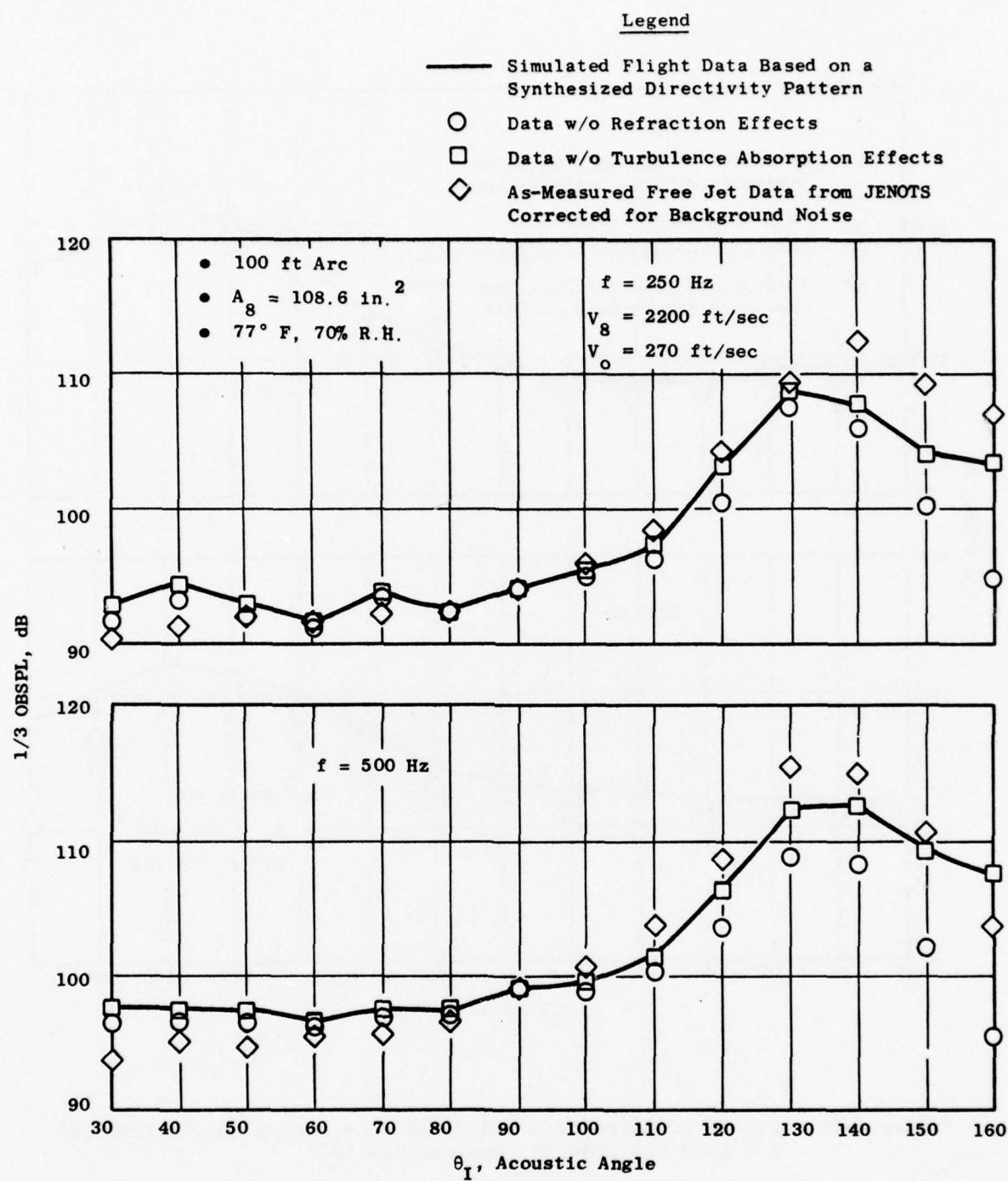


Figure 4-77. Impact of Refraction and Turbulence Absorption Corrections, $f = 250$ and 500 Hz , Conical Nozzle.

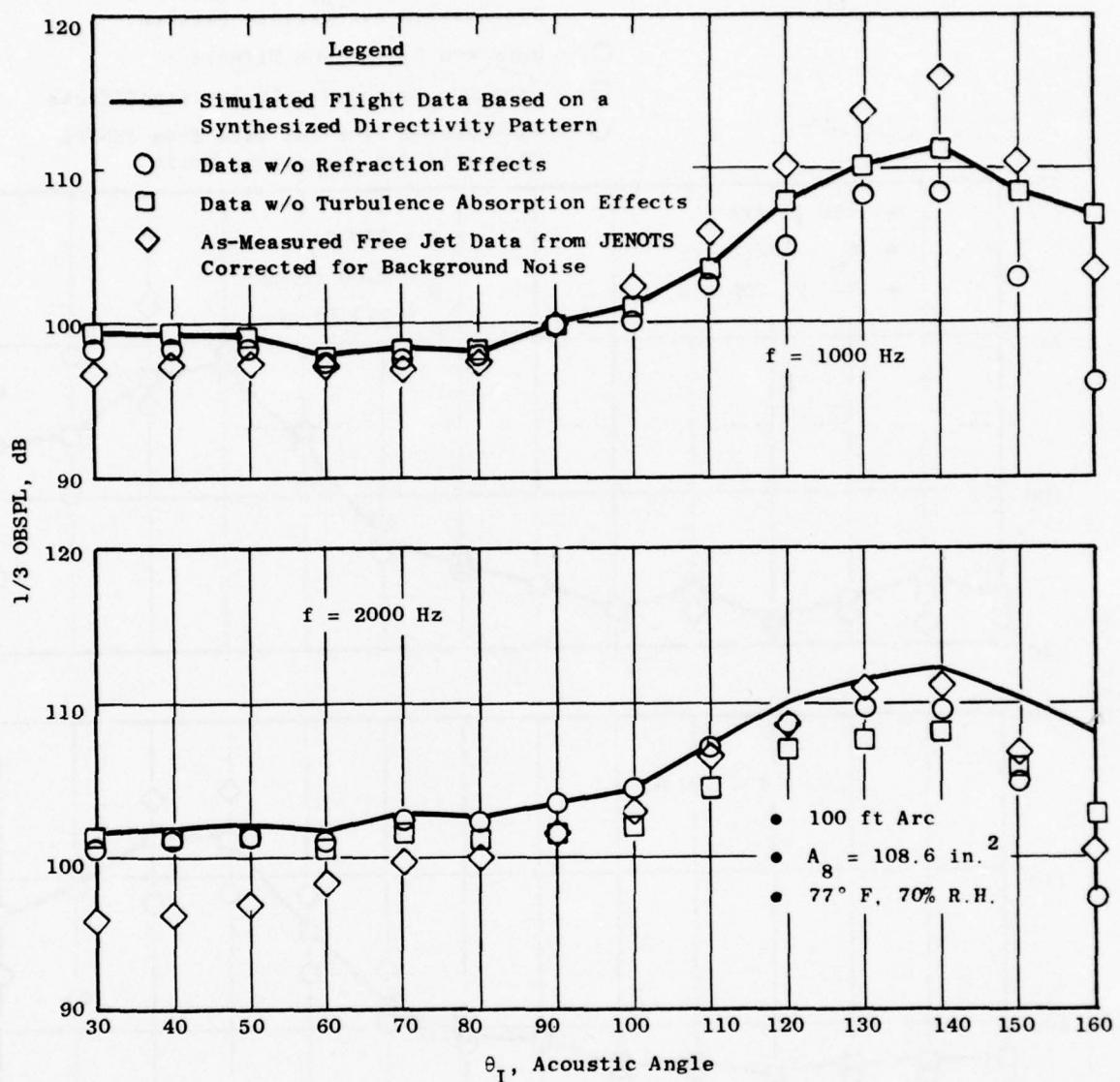


Figure 4-78. Impact of Refraction and Turbulence Absorption Corrections, $f = 1000$ and 2000 Hz, Conical Nozzle.

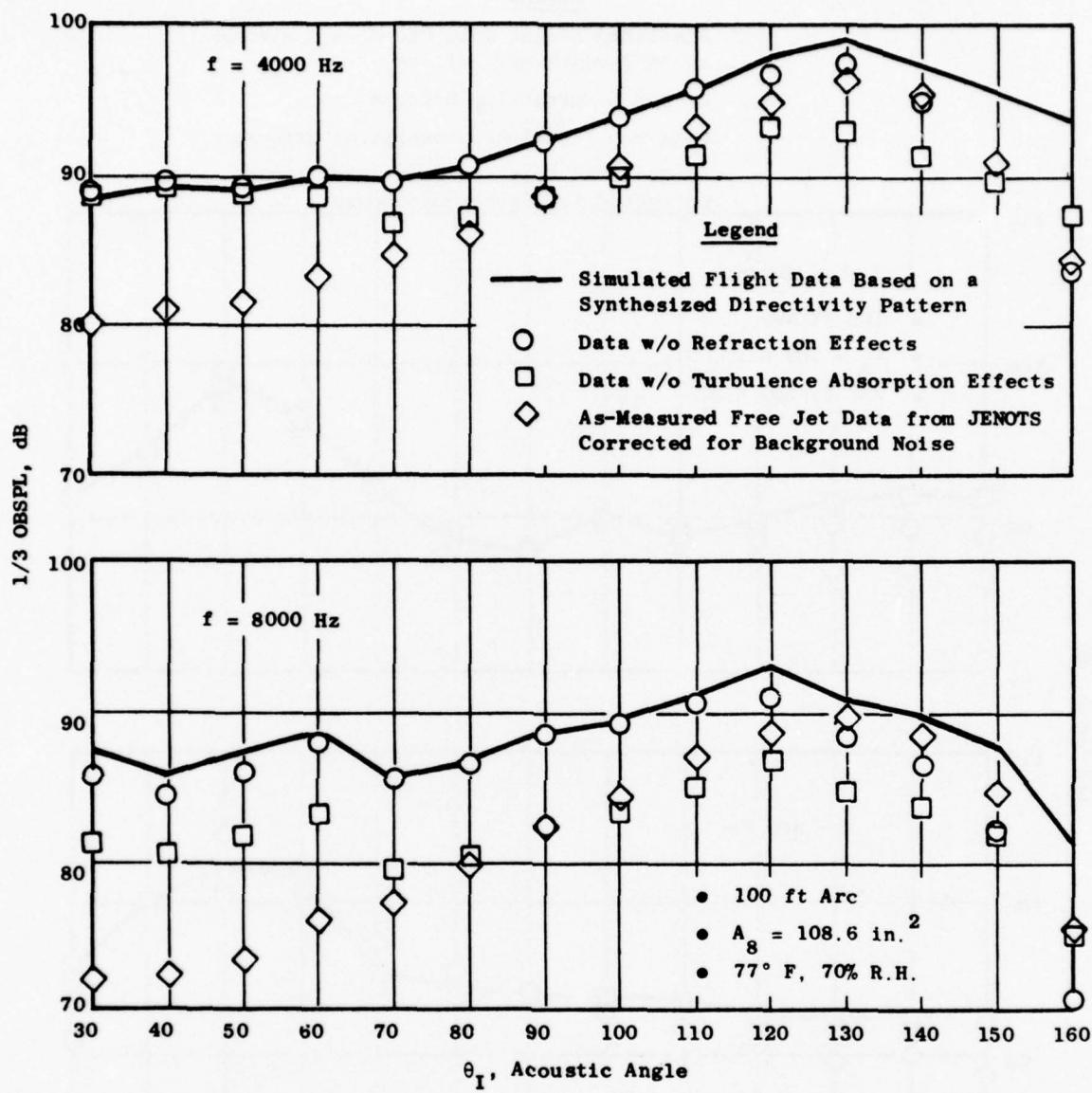


Figure 4-79. Impact of Refraction and Turbulence Absorption Corrections, $f = 4000$ and 8000 Hz, Conical Nozzle.

Legend

Simulated Flight Data Based on a Synthesized Directivity Pattern

Data w/o Refraction Effects

Data w/o Turbulence Absorption Effects

As-Measured Free Jet Data from JENOTS
Corrected for Background Noise

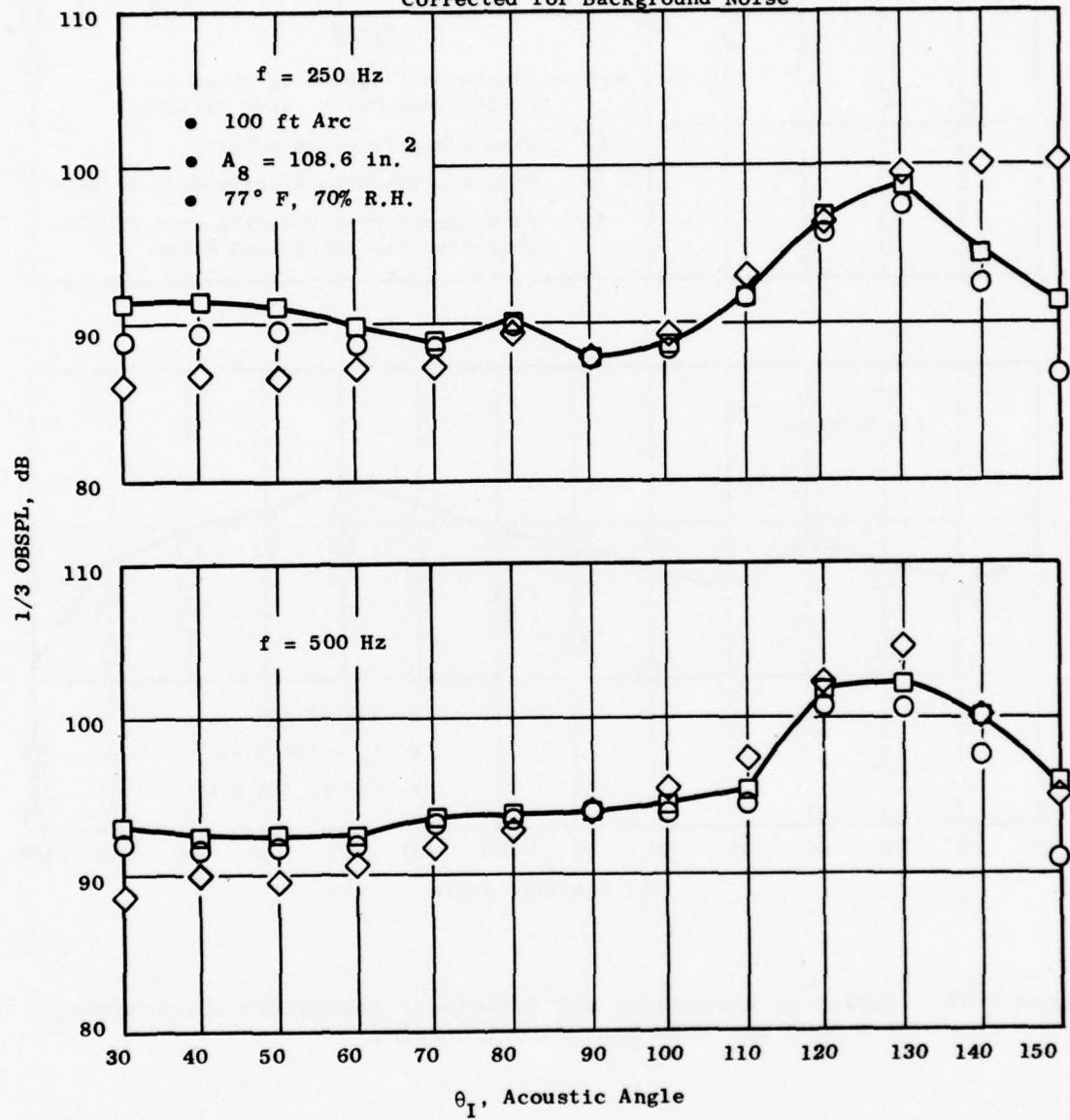


Figure 4-80. Impact of Refraction and Turbulence Absorption Corrections, $f = 250$ and 500 Hz, 8-Lobe Nozzle.

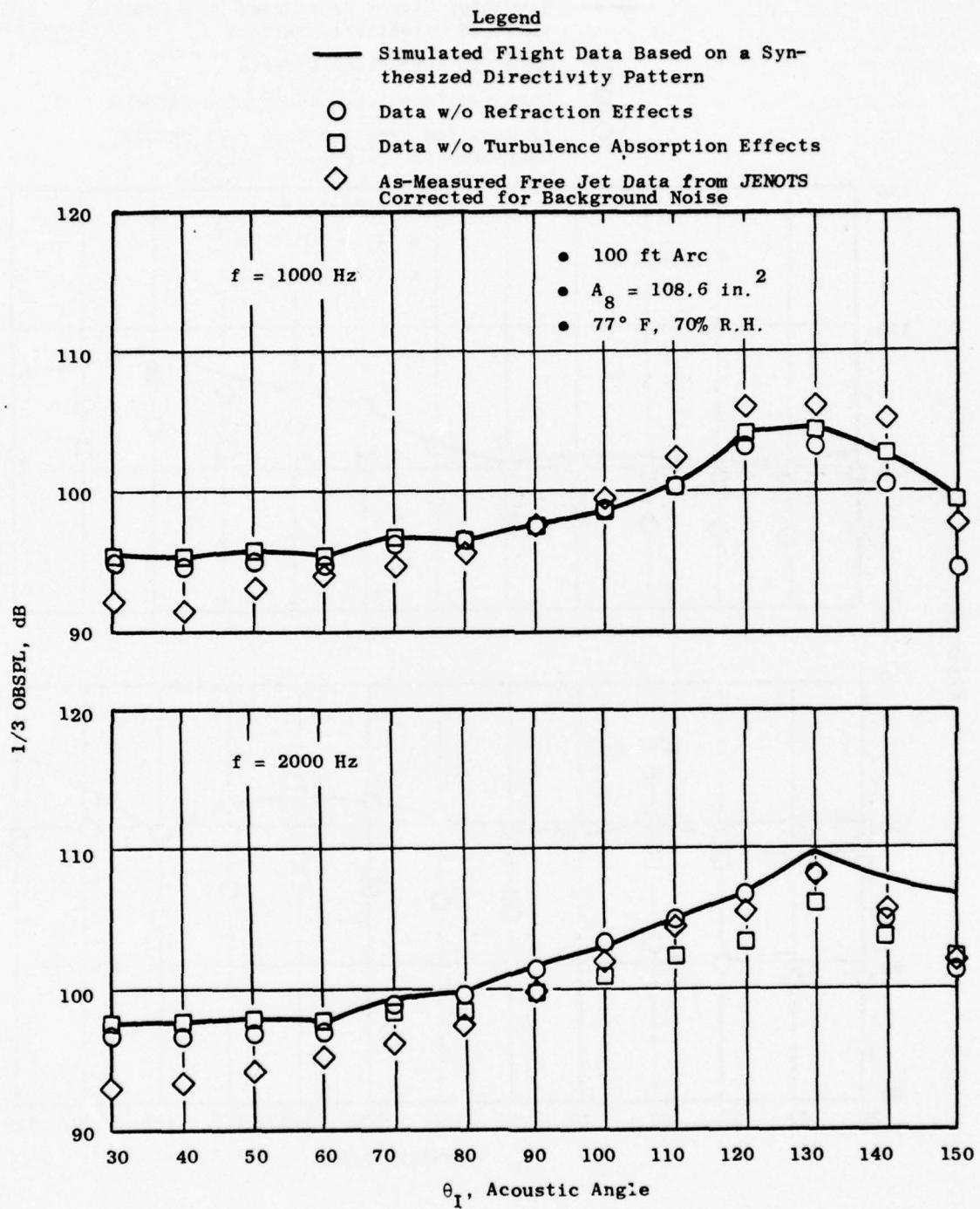


Figure 4-81. Impact of Refraction and Turbulence Absorption Corrections,
 $f = 1000$ and 2000 Hz , 8-Lobe Nozzle.

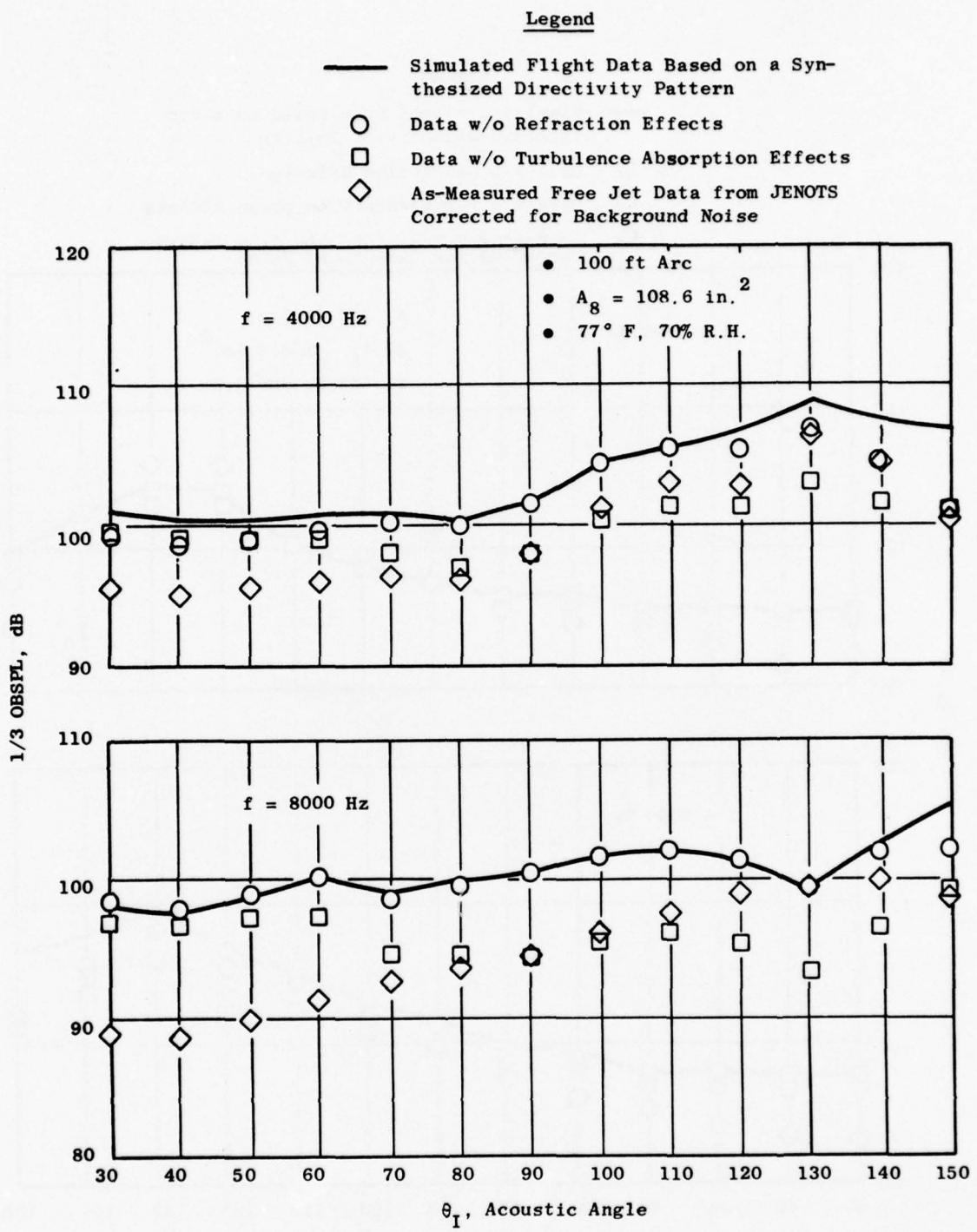


Figure 4-82. Impact of Refraction and Turbulence Absorption Corrections, $f = 4000$ and 8000 Hz, 8-Lobe Nozzle.

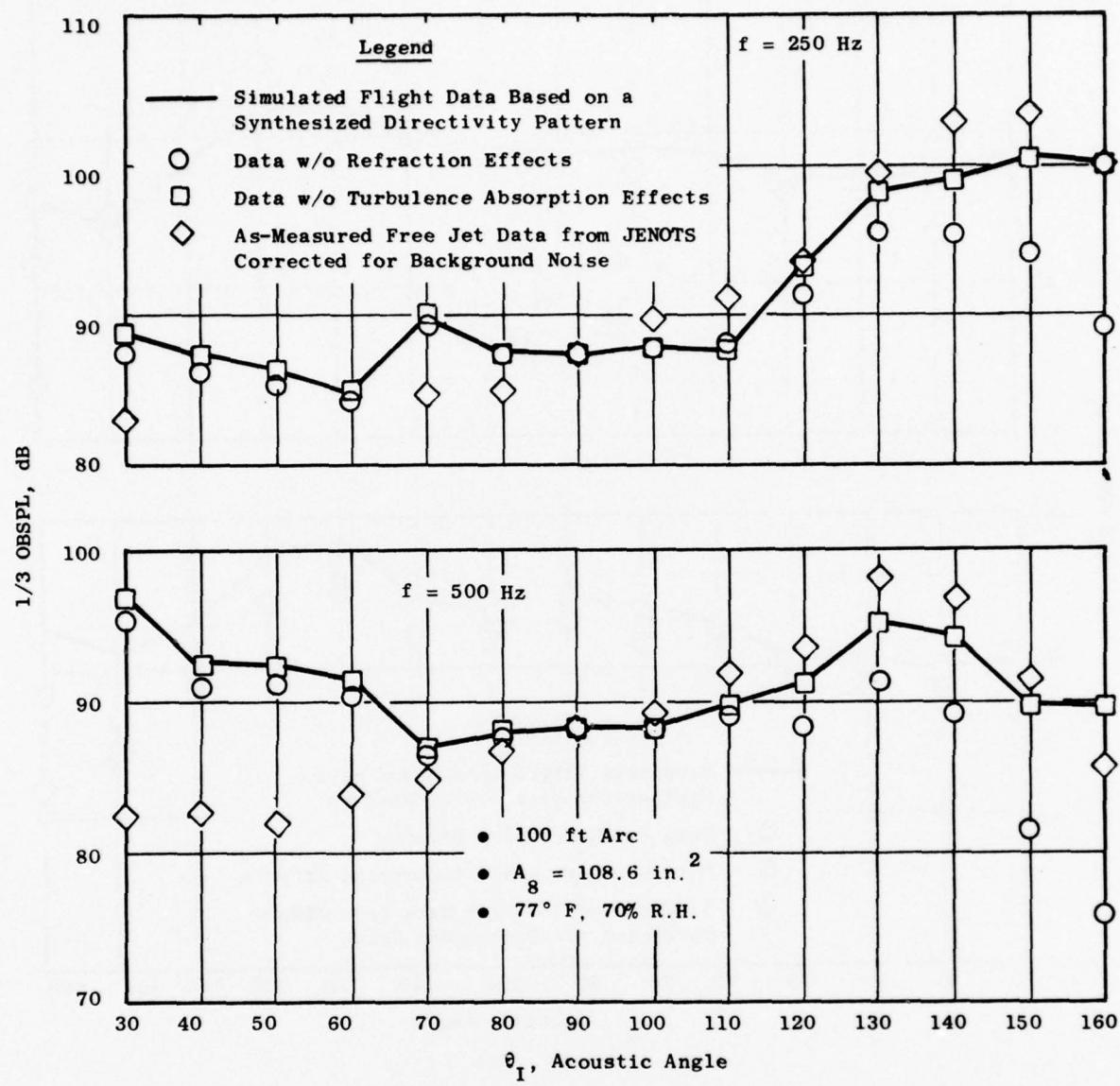


Figure 4-83. Impact of Refraction and Turbulence Absorption Corrections, f = 250 and 500 Hz, 104-Tube Nozzle.

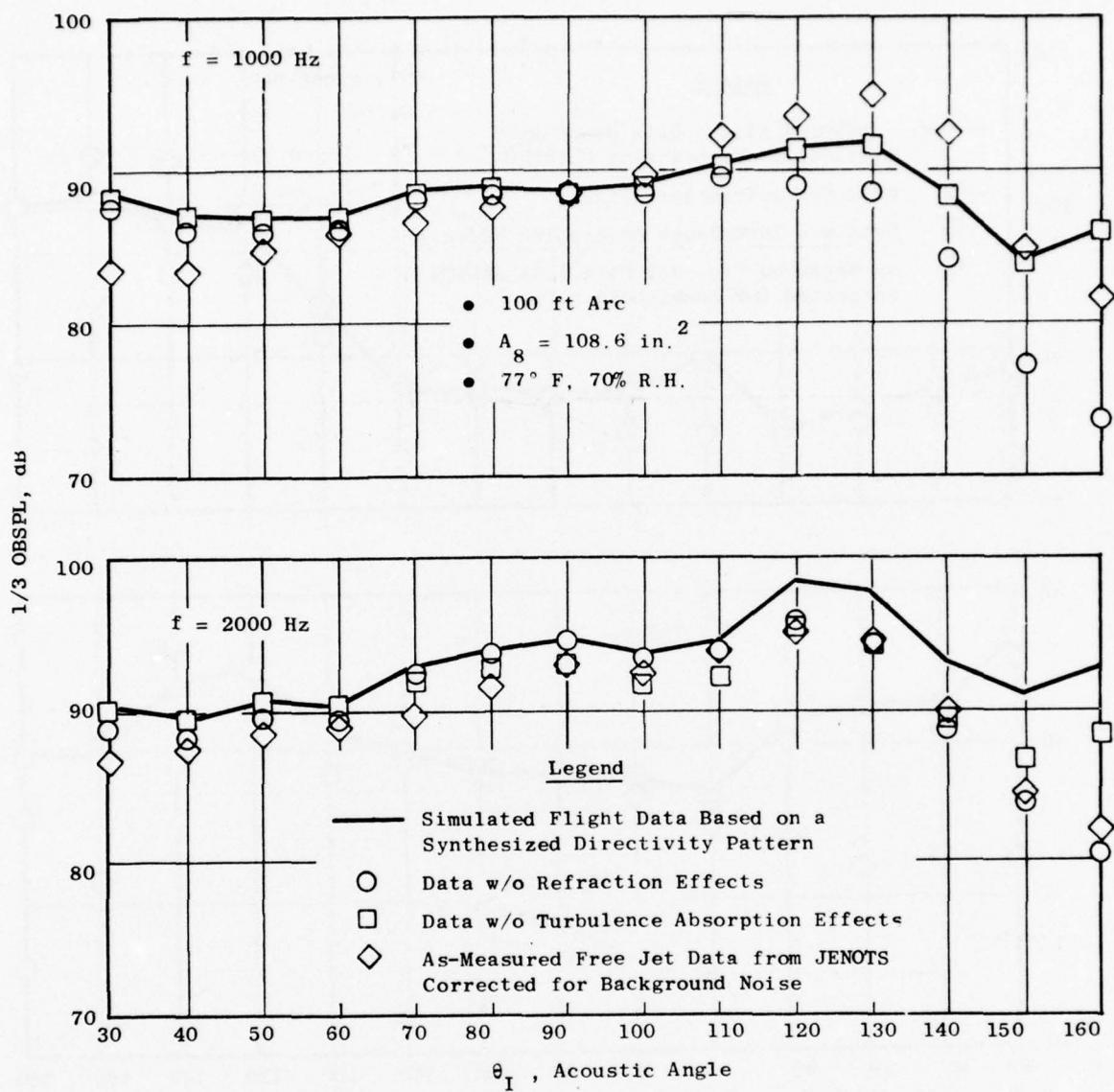


Figure 4-84. Impact of Refraction and Turbulence Absorption Corrections, $f = 1000$ and 2000 Hz , 104-Tube Nozzle.

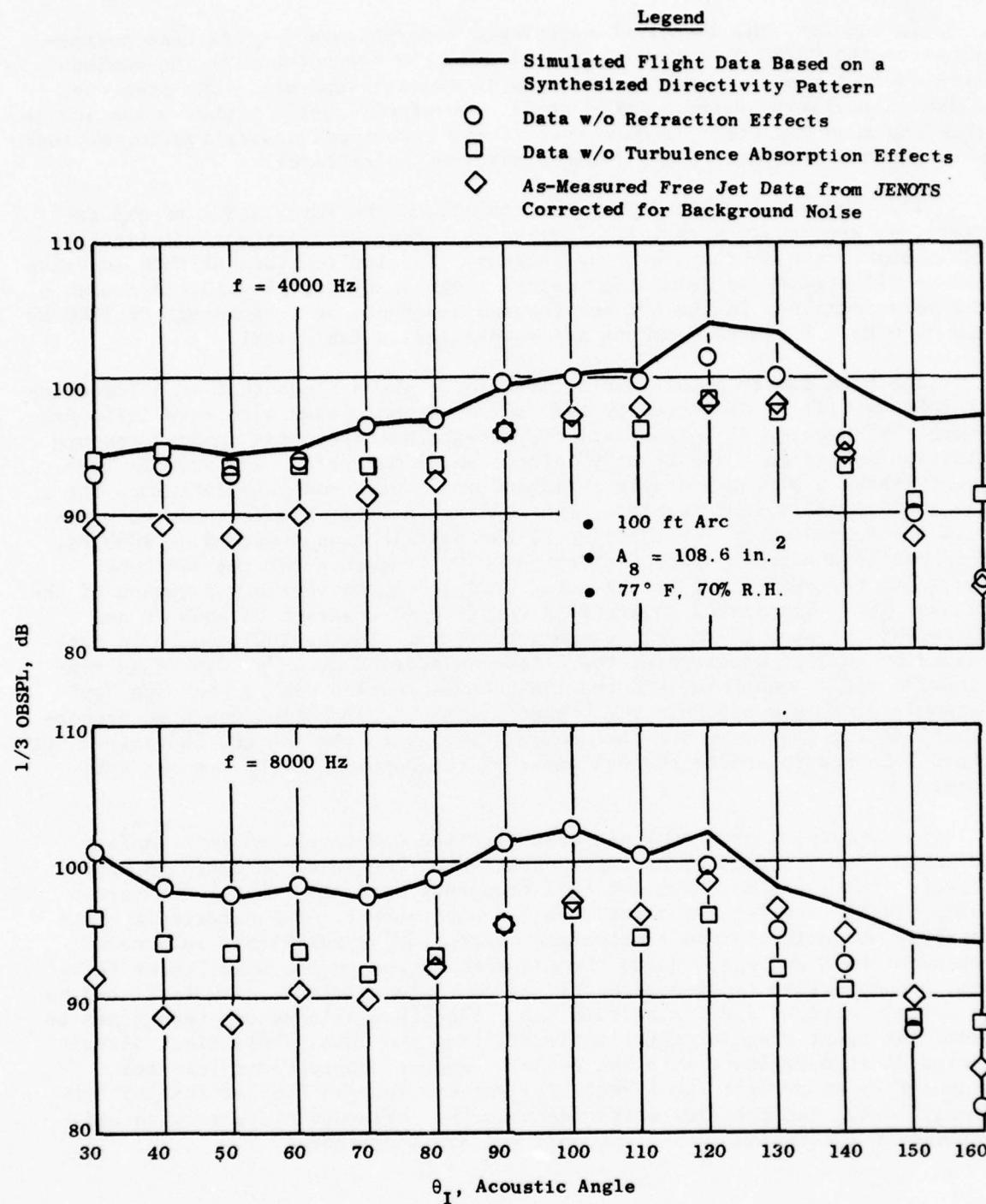


Figure 4-85. Impact of Refraction and Turbulence Absorption Corrections, $f = 4000$ and 8000 Hz, 104-Tube Nozzle.

In summary, the impact of turbulence absorption and refraction corrections on the OASPL directivity is configuration dependent with the maximum influence of the corrections occurring in the aft quadrant. The predicted flight directivity pattern would still have significantly higher noise levels than the measured free jet data even if the turbulence absorption corrections were not used to predict the forward quadrant noise level.

The concept of source decomposition allows the formulation of expressions, as previously shown, that define the type of uncorrelated singularities which make up the jet noise sources. The implications of this modeling can be illustrated by examining typical singularity distributions for each of the three nozzles, in the aft and forward quadrant, at frequencies of 1000 Hz and 4000 Hz. These expressions are summarized on Table 4-XI.

The mean square pressure distribution in the aft quadrant at a frequency of 1000 Hz will be dominated by the "xy" quadrupole term with some influence from a "y" dipole. In contrast, the forward quadrant mean square pressure distribution is governed by a "y" dipole and a monopole. The 4000 Hz frequency shows a stronger dipole influence and a weak monopole influence for the conical and 8-lobe nozzles. The 104-tube nozzle, however, has no monopole influence and is very similar to the distribution observed at 1000 Hz. This may be due to the fact that the 4000 Hz frequency for the 104-tube nozzle is representative of the noise produced in the premerged region of the exhaust jet. The trends observed in the forward quadrant at 4000 Hz are different for each of the three configurations. The conical nozzle is dominated by an "yy" quadrupole, the 8-lobe is modeled by a "y" dipole in combination with a monopole, and the 104-tube is modeled with a "xx" and "yy" octopoles. This means that the "dynamic effect" correction would be proportional to the 6th power for the conical nozzle, to the 4th and 2nd powers for the 8-lobe nozzle and to the 8th power of the Doppler factor for the tube nozzle.

In summary, a procedure has been selected and developed to transform measured free jet data to be representative of the noise produced in actual flight. The input data consist of a frequency parameter ($k_0 a$), SPL versus angle directivity data, and the free jet Mach number. The directivity data is first corrected for refraction and absorption by turbulence in a manner dependent on M and $k_0 a$. Using the algorithm based on the Kuhn-Tucker theorem, a nonnegative least-squares fit of the data until the data is fitted to an average error < 2 dB is carried out. The singularities are recombined to yield the least singular distribution fitting the data. This final distribution is then employed with the dynamic exponent appropriate for each singularity to predict the directivity pattern in each Doppler shifted frequency band. The examples presented show the influence of refraction and turbulence absorption to be frequency and angle dependent.

Table 4-XI. Typical Examples of Source Decompositon by Nozzle
Fixed Uncorrelated Point Singularities.

f = 1000 Hz		Forward Quadrant *	
Configuration	Aft Quadrant		
Conical	$P_\theta^{'2} = 148.671 \cos^2\theta \sin^2\theta + 5.176 \sin^2\theta$	$P_\theta^{'2} = 0.2438 \sin^2\theta + 1.2872$	
8-Lobe	$P_\theta^{'2} = 38.161 \cos^2\theta \sin^2\theta + 0.789 \sin^2\theta$	$P_\theta^{'2} = 1.745 \sin^2\theta + 0.451$	
104-Tube	$P_\theta^{'2} = 16.882 \cos^2\theta \sin^2\theta + 1.0161 \sin^2\theta$	$P_\theta^{'2} = 1.604 \sin^2\theta + 0.458$	
f = 4000 Hz			
Configuration	Aft Quadrant		
Conical	$P_\theta^{'2} = 39.242 \cos^2\theta \sin^2\theta + 2.528 \cos^2\theta + 0.1149$	$P_\theta^{'2} = 7.61 \sin^4\theta$	
8-Lobe	$P_\theta^{'2} = 38.147 \cos^2\theta \sin^2\theta + 3.62 \cos^2\theta + 0.355$	$P_\theta^{'2} = 2.339 \sin^2\theta + 0.1654$	
104-Tube	$P_\theta^{'2} = 8.558 \sin^2\theta \cos^2\theta + 1.368 \sin^2\theta$	$P_\theta^{'2} = 1.088 \cos^6\theta + 2.757 \sin^6\theta$	

*Note that each of the expressions for the aft and forward quadrants were normalized separately with respect to the minimum SPL on each of the quadrants.

The relationship of the apparent source reconstruction used in the present analysis to the physics of the processes producing flight jet noise is somewhat tenuous. The source decomposition, as used in the present study, is only an apparent reconstruction. It represents some amalgam of the way in which refraction and convection effects and the various mechanisms of jet noise such as mixing noise, shock noise, and lip noise collectively manifest themselves. The source decomposition for the conical nozzle noise does suggest that exhaust arc noise is primarily quadrupole in character, especially at low frequencies. At higher frequencies, the exhaust arc "static" directivity is often amenable to decomposition of only (uncorrelated) dipole singularities. Conversely, the low frequency inlet arc noise often requires only dipoles to adequately synthesize. The high frequency inlet arc noise often requires the use of quadrupole or octopole singularities.

Transformed free jet data is compared with aerotrain data in Section 7.0 for evaluation of the inflight simulation technique.

5.0 FLIGHT ASSURANCE TESTING

An important requirement of any given experiment is to accurately simulate those conditions under which actual events occur. While flight testing provides the best basis for examining the flight velocity effect on the jet noise signature under actual operating conditions, there are inherent disadvantages associated with flight testing. Operating line variation is inflexible and requirements for flight-worthy test hardware, and the testing requirements themselves, are more costly in terms of time and money than other techniques discussed in Section 3. Problems associated with aircraft positioning, atmospheric gradients, and background noise levels are encountered, and unless closely controlled, the resulting uncertainties may bias interpretation of results.

Nevertheless, high quality flight-test data, with appropriate confidence bands, are required to assess the validity of the results from any flight simulation techniques. Independent tests were conducted using a Gates Learjet-25C and F-106 aircraft, in conjunction with Gates, Learjet, and NASA-Lewis, respectively, to provide this flight assurance data. The details of these flight test series using both baseline and suppressor type nozzles are described in the following sections.

5.1 GATES LEARJET-25C TEST PROGRAM

5.1.1 Configuration Description and Test Matrix

The Gates Learjet tests were completed in 1973 under a joint General Electric - Gates Learjet program at Fresno, California. The aircraft used was powered by two CJ610-6 engines (basically nonafterburning commercial versions of the J85). Both a baseline conical nozzle and an 8-lobe suppressor nozzle were evaluated. Testing was performed with both engines operating at the same power setting and with identical nozzle configurations. Figures 5-1 and 5-2 show the aircraft with conical nozzles and 8-lobe nozzles used in this test series. Table 5-I shows the test matrix run. Five jet velocities from 1400 ft/sec to 2100 ft/sec were run at altitudes of 1000 ft and 400 ft with flight velocities of 180 to 220 KIAS (304 - 371 ft/sec). At least two points were obtained at each altitude and jet velocity condition. In addition, a set of flight velocities up to 300 KIAS (506 ft/sec) were run at a jet velocity of 2100 ft/sec for the purpose of obtaining a wider range of in-flight information. In all cases, the engines were carefully adjusted to equal power settings. Static data at jet exhaust velocities corresponding to those tested in flight were obtained on a 100-ft arc with only one engine running to eliminate possible fuselage shielding problems with the other engine. Cockpit indicators provided readout of engine pressure ratio (EPR), turbine exhaust total temperature (T_5), and engine speed to calculate jet velocity for both static and flight. Readings of aircraft velocity and altitude were recorded for use in aircraft positioning, as described in Section 5.1.2.

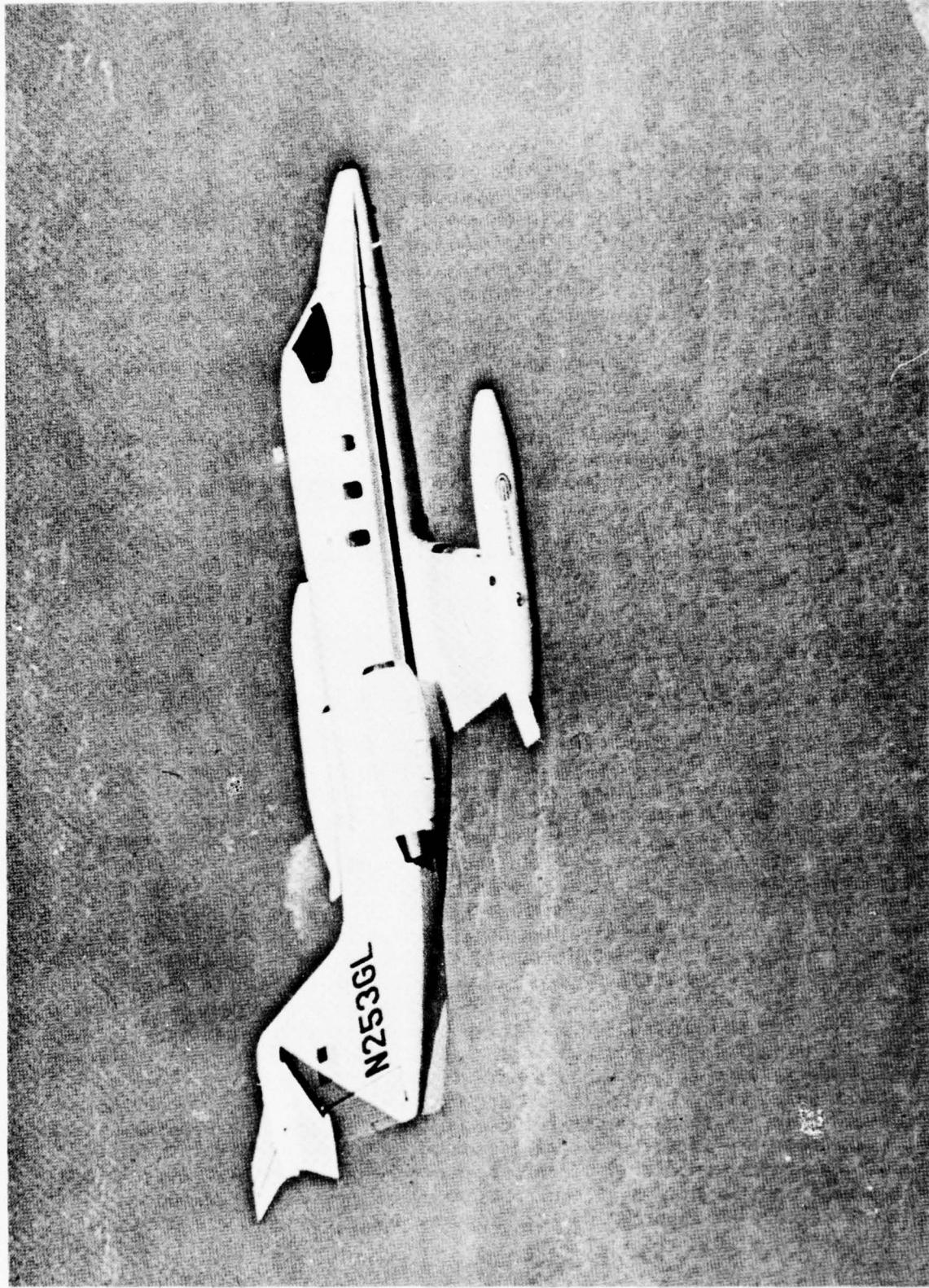


Figure 5-1. Gates Learjet - Conical Nozzle.

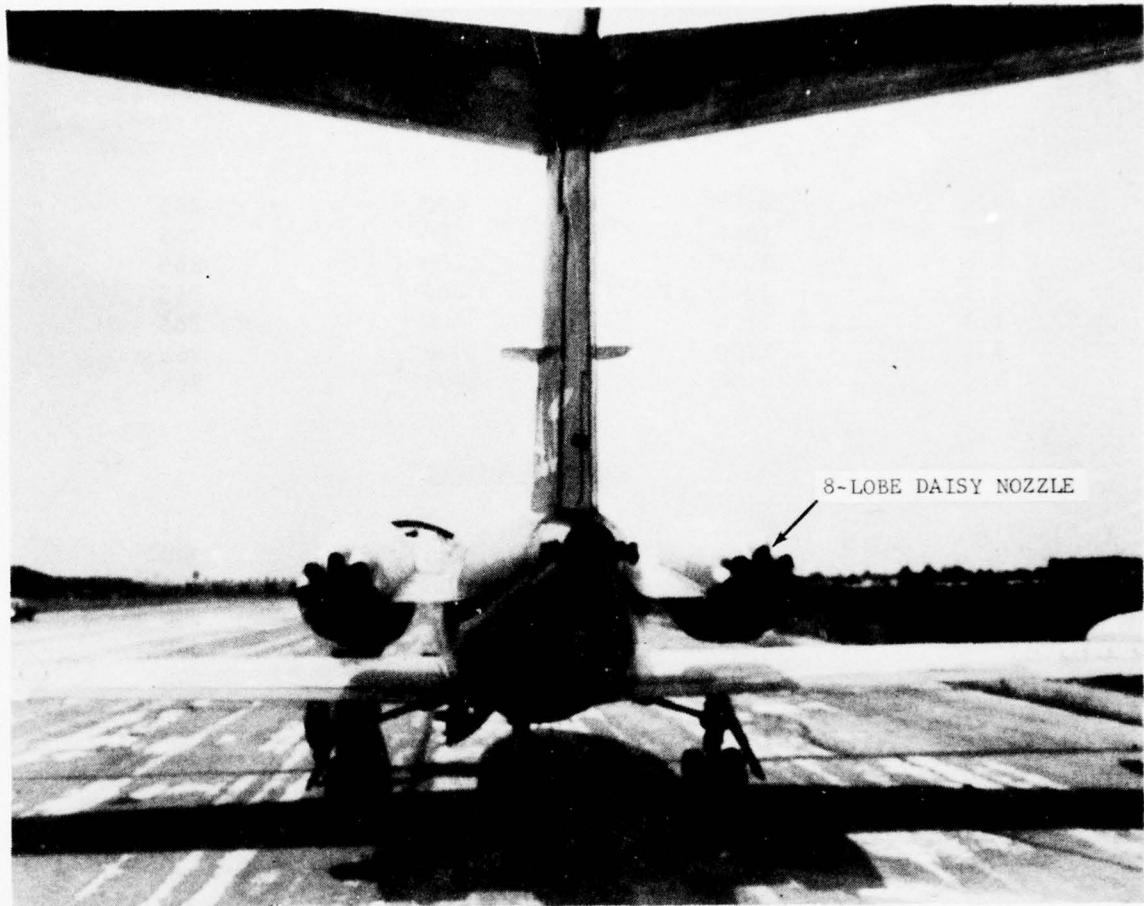


Figure 5-2. Gates Learjet - 8-Lobe Nozzle.

Table 5-I. Learjet Test Conditions Matrix, 8-Lobe Daisy Suppressor Nozzle.

Engine EPR	Conditions V ₈ (ft/sec)	Aircraft Alt. (ft.)	Aircraft Velocity (ft/sec)
2.4	2160	400	265
2.0	1800	400	265
1.8	1650	400	265
1.5	1320	400	265
1.3	1100	400	265
2.5	2180	2000	265
2.5	2180	2700	265

Conical Nozzle

2.3	2080	400	300
2.2	1960	400	300
2.0	1800	400	300
1.8	1650	400	300
1.6	1480	400	300
1.5	1320	400	300
1.4	1200	400	300
1.3	1100	400	300
2.3	2080	400	370
2.3	2080	400	440
2.3	2080	400	500
2.3	2080	1000	300
2.2	1960	1000	300
2.0	1800	1000	300
1.8	1650	1000	300
1.6	1480	1000	300
2.3	2080	1000	370
2.3	2080	1000	440
2.3	2080	1000	500

5.1.2 Data Acquisition

The acquisition of the Learjet level flyover acoustic data was accomplished for the conical and 8-lobe nozzles using the microphone arrays presented on Figures 5-3 and 5-4, respectively. The arrays were positioned to achieve statistically independent data samples as described in Section 3.3. The microphones were equipped with wind screens and were mounted over concrete or asphalt to provide uniform surface reflection characteristics to facilitate ground reflection corrections. The flush-mounted microphones did not have wind screens and were mounted in a metal-covered plywood surface. Different microphone arrays were chosen for the two test series because analysis of the 8-lobe nozzle test data revealed that the conical nozzle microphone array would be the best way to minimize the impact of ground reflections. Data were recorded using the General Electric Acoustic Van shown on Figures 5-5 and 5-6. The van is a self-contained, mobile, acoustic-data acquisition system that has been specifically developed for obtaining acoustic measurements on flight or static engine testing. The vehicle is capable of operating in remote areas without the need of additional support equipment. In addition to the data acquisition, the capability exists for performing both on- and off-line 1/3-octave analysis in the field by means of an on-board octave analyzer and minicomputer system. The details of this on-line data reduction capability are discussed fully in Section 5.1.3. This system has been successfully used in obtaining flight acoustic data both independently and in conjunction with other companies. Although the system was designed primarily for flight testing, it has also been used for obtaining ground static data in the absence of permanent acoustic facilities.

Some of the main features of the vehicle and the equipment it contains are described in the following paragraphs. Figure 5-7 presents a detailed diagram illustrating the van equipment.

- Recording capability is provided by a Honeywell 7600, 28-track recorder setup for IRIG intermediate band operation.
- Signal conditioning amplifiers are available for all tape channels.
- Data monitoring is provided by means of two, 2-channel oscilloscopes.
- A time code generator/reader system, which can be synchronized with WWV, is connected to the tape recorder for accurate event location during data retrieval.
- For both flight and static testing, quick-look 1/3-octave data is available by means of a General Radio 1921 Real Time Analyzer coupled with a GEPAC-30 computer and a Terminet 300 printer, with capability of providing 1/3-octave SPL, PNL, OASPL, and in the case of flight data, EPNL.

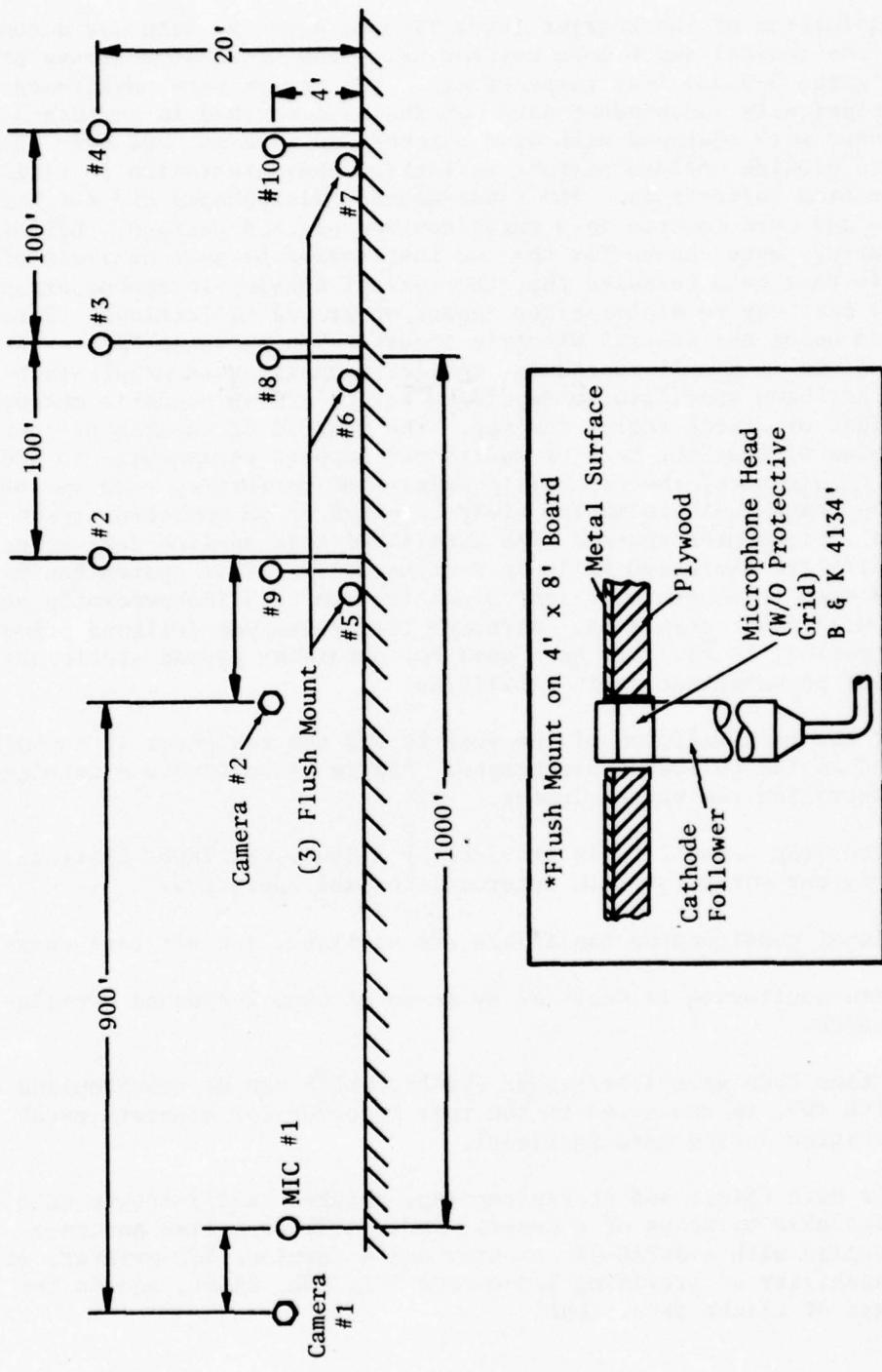
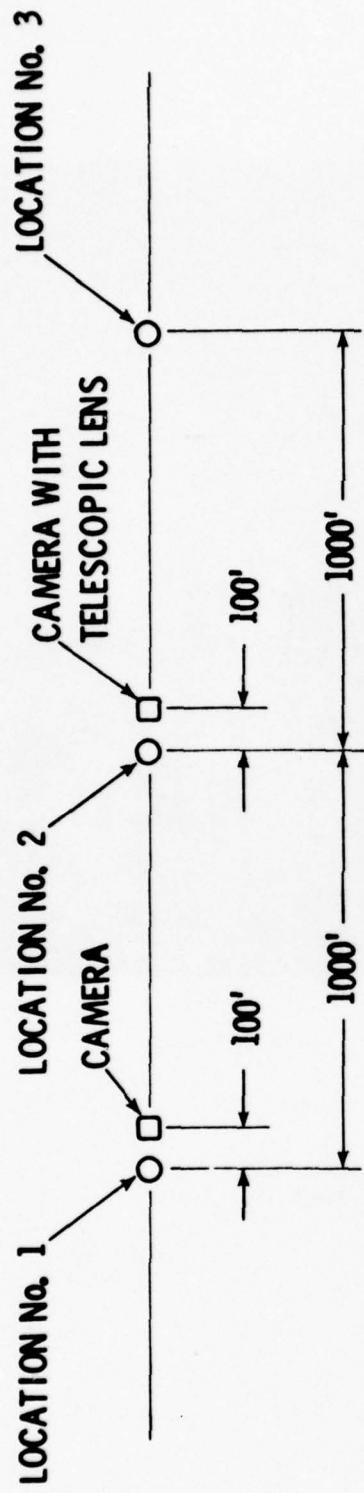


Figure 5-3. Microphone Array - Learjet Conical
Nozzle Flight Test.



<u>MIC No.</u>	<u>LOCATION</u>	<u>MIC HEIGHT</u>	<u>SURFACE TYPE</u>
1	1	4'	SCOTTFELT
2	1	4'	CONCRETE
3	2	4'	DIRT
4	2	2'	DIRT
5	2	FLUSH	HARDBOARD
6	2	4'	CONCRETE
7	3	4'	DIRT
8	3	4'	CONCRETE

Figure 5-4. Microphone Array - Learjet 8-Lobe
Nozzle Flight Test.

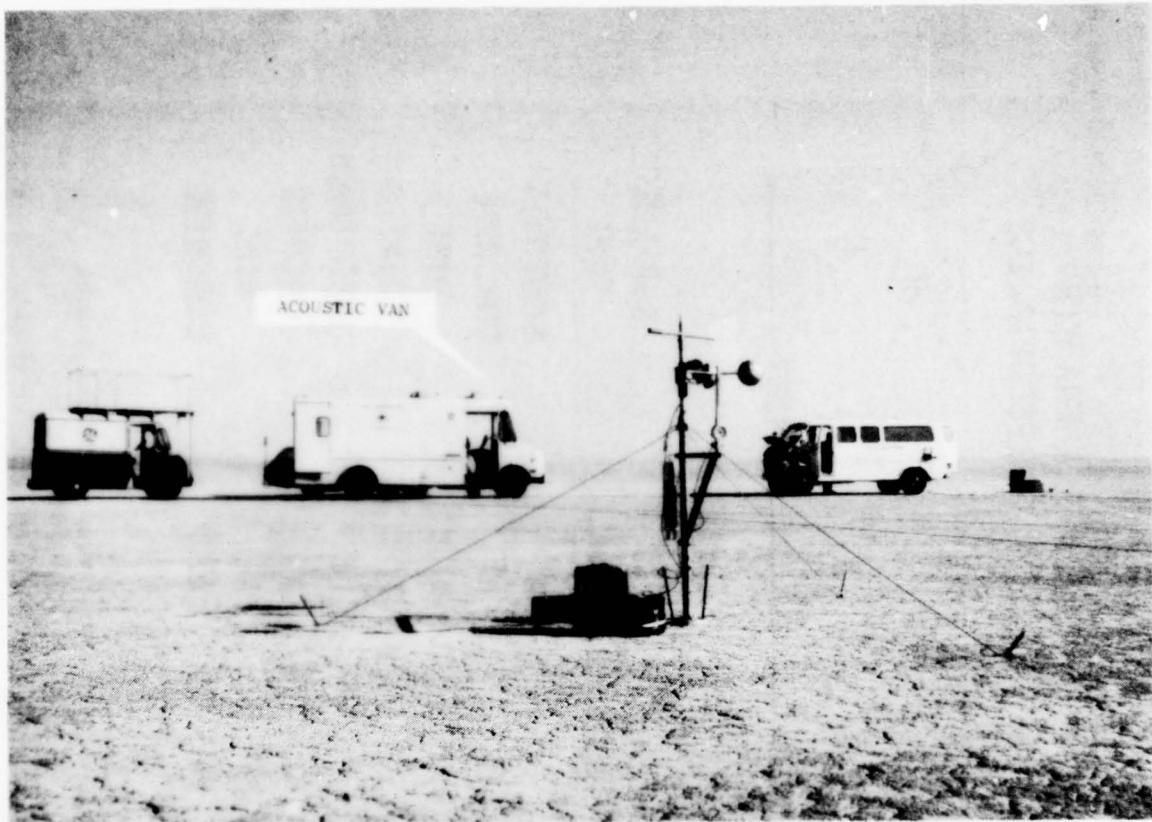


Figure 5-5. General Electric Acoustic Van -
Gates Learjet Flyover Test.

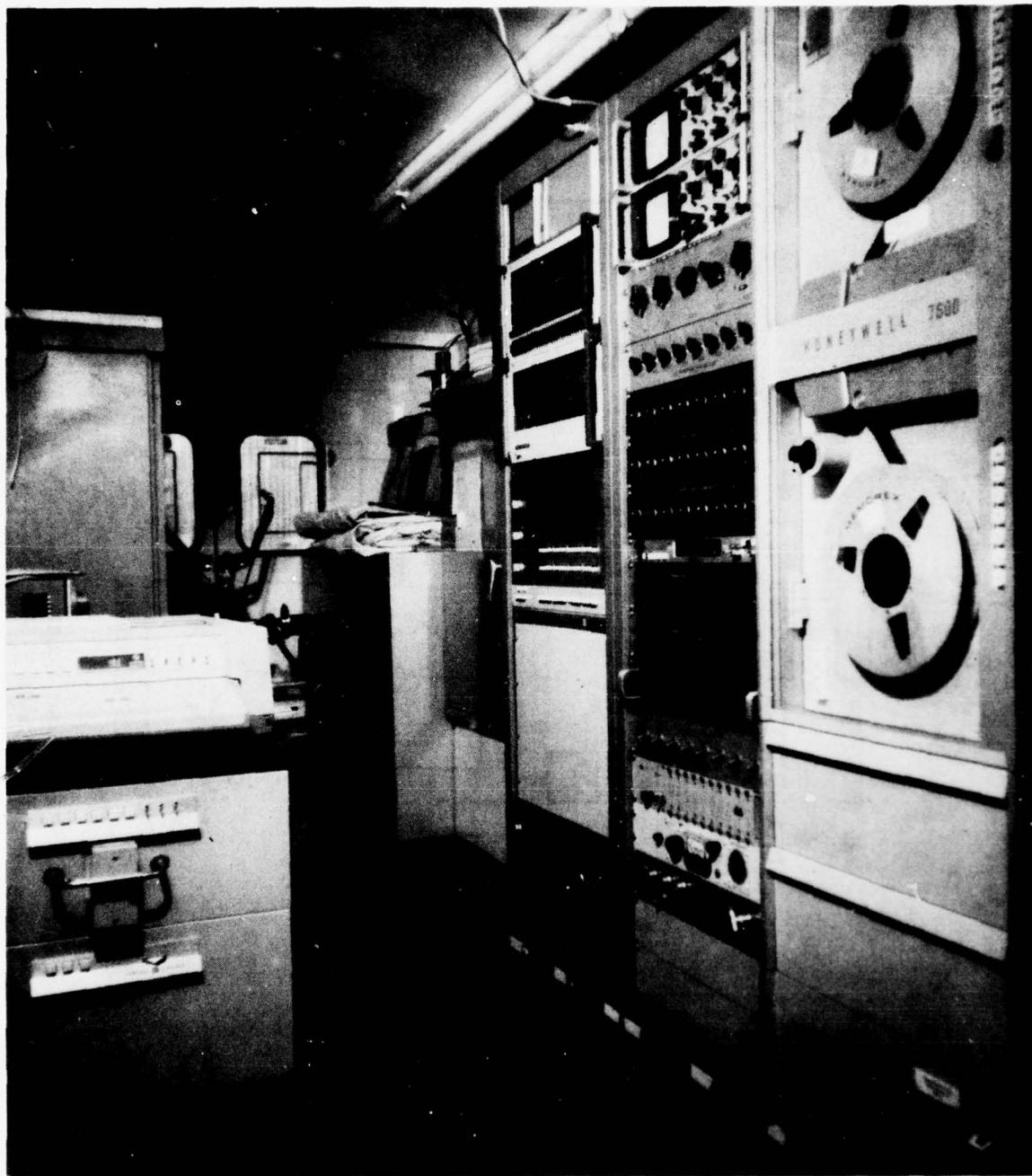


Figure 5-6. Interior of Acoustic Van.

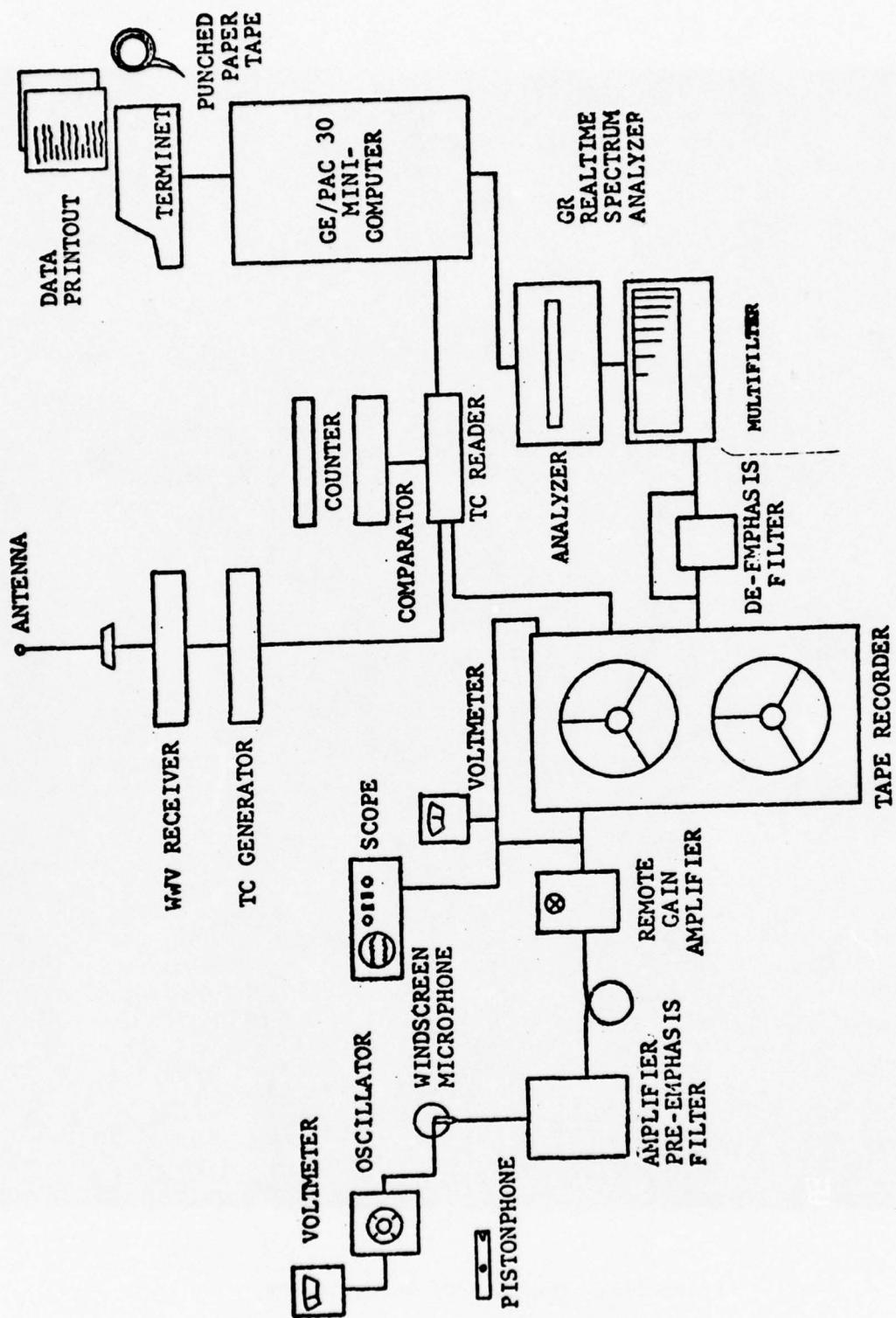


Figure 5-7. Equipment Schematic for Data Acquisition and Processing - General Electric Acoustic Van.

- For flight testing, 10 B&K 141A battery-operated microphone systems, having remote gain and signal preemphasis capability, are available.
- For static testing, the B&K 141A systems can be supplemented with B&K 2630 battery-driven cathode followers for normal arc measurements 10° to 160° in 10° increments. For testing over an extended period of time, 2801 B&K power supplies (120 VAC), with power supplied from the van, could be used in place of the battery-operated systems.
- Sufficient cable for most ground or flight testing applications is carried on-board.
- Electrical power for equipment operation is provided by means of an Onan 5-kW generator.

Three different systems were available to determine aircraft speed and position. Aircraft cockpit indicators were used to determine speed and altitude. A photographic method was used to determine speed, altitude, and overhead time. This method employed two cameras separated by approximately 1000 feet. For velocity determination, two exposures were made on the same film frame but differentiated by a short time interval. The displacement between the two images provides a measure of the instantaneous velocity. The photographic system was used as a backup for the determination of aircraft velocity and the cockpit indicator was considered as the primary system. To determine the altitude photographically, the focal length of the camera is calibrated and the aircraft is then photographed during passing. Using a known aircraft dimension such as wing span, the aircraft altitude may be calculated. Time reference for aircraft location is provided by electrical pulse inputs to the acoustic tape triggered during camera operation. The photographic method was considered as the primary altitude determination system.

The third system, employing the acoustic ground plane null/reinforcement principle, was the primary system to determine aircraft overhead location. This system is described in the following paragraphs.

As an aircraft approaches and passes a ground microphone mounted at some height (h) above the ground, ground-reflection, cancellation and reinforcement patterns are set up and recorded by the microphones. The frequency of these nulls (cancellations) will vary with aircraft position (assuming no phase shift between source and mike) according to:

$$f = \frac{nc}{4h \sin \theta} \quad (60)$$

where: n is 1, 2, 3, etc. (even numbers for reinforcement, odd for null)

c is local speed of sound

h is microphone height

θ is angle between ground and aircraft

At the overhead location $\theta = 90^\circ$, $\sin \theta = 1$ and f is a minimum value for fixed h for all values of n. Although the ground nulls (reinforcements) are recorded on magnetic tape along with the acoustic signal, a special type of data reduction is required to define the time that the minimum frequency occurs. This is an intensity-modulated spectrum which is generated by recording successive narrowbands at a high rate of speed, i.e., a narrowband (Bandwidth ≈ 10 Hz) every 1/20 sec on paper with time code identification. The visual effect on these closely spaced spectrums reveals the ground reinforcement and cancellation patterns with a typical example shown on Figure 5-8. These traces are produced using a Honeywell Viscorder with a fiber-tipped recording pen. Figure 5-8 also illustrates how the null effect is used to determine the acoustic overhead location with respect to time, and this information is used in conjunction with aircraft altitude and velocity for determination of acoustic angles. To check the validity of this procedure, comparisons were made with two independent methods of aircraft tracking.

Using data acquired during a joint General Electric/Douglas Aircraft Company (DAC) DC-10-30 flight test program (Yuma, 1972), where DAC provided laser-tracker aircraft positioning, comparisons were made with results as indicated on Table 5-II. Similarly, comparisons were made with some Boeing (TBC)/GE data acquired during 747 Noise Compliance testing (Moses Lake, 1973), using the TBC camera tracking system. Results of this comparison are shown on Table 5-III.

Assuming that both the laser system and the camera system give the true overhead time and that any error is associated with the fiber optics system, the resulting differences between these systems and the fiber optics system is seen to be on the order of an acceptable 0.1 second.

5.1.3 Data Reduction

The procedure to adjust the measured acoustic data to a form suitable for analysis and comparison is described in the following paragraphs. Figure 5-9 provides an information flow diagram of the process.

The measured signal recorded at the test site on magnetic tape is played back through a General Radio 1921 1/3-Octave Spectrum Analyzer and resolved into the 24 1/3-octave frequency bands. The signal is arranged in discrete 1/8-second groups of spectra and recorded on tape, along with time code information for correlating with aircraft position. These 1/8-second

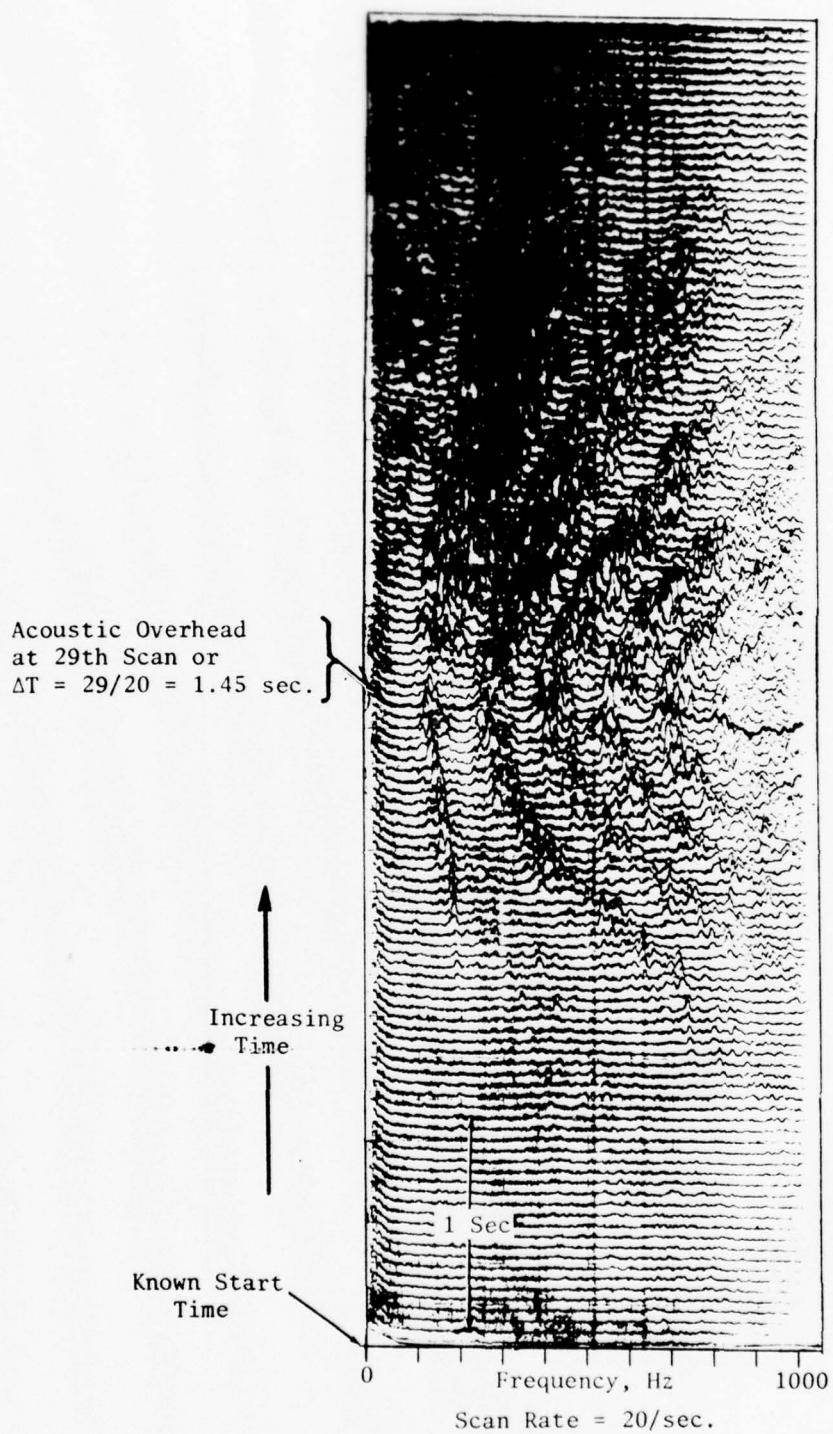


Figure 5-8. A Typical Fiber Optics Trace for Overhead Determination.

Table 5-II. Comparison of Fiber Optics and Laser-Tracker Overhead Determination.

UC10-30 Flight Test (Yuma, 1972)											
(1)	(2)	(3)	(4)	(5)	(6)	(7)	(8)	(9)	(10)	(11)	(12)
A/C O.H. Time From Fiber Optics Pass No	A/C O.H. Time From Laser Tracker	A/C Velocity Knots	A/C Alt Ft	T ⁰ _F	\sqrt{gRT}	DAC to GE Mike Sec.	Laser O.H. To Acoustic O.H. Sec.	Time DAC to GE Mike Sec.	Laser Tracker. GE Time Code Acoustic O.H. Corrected To GE Mike Pos.	Offset Between Fiber Optics And Laser Tracker-Sec.	Difference Between Fiber Optics And Laser Tracker-Sec.
DAC Pass No											
302	00:21:07.62	152.3	664	65.5	1126	+1.55	.59	00:21:7.14	00:21:7.64	-.02	
312	02:20:20.53	156.6	596	64	1124	-1.51	.53	02:20:19.92	02:20:20.43	+.10	
315	02:49:55.21	149.8	619	63.5	1123	-1.58	.55	02:49:54.67	02:49:55.07	+.14	

Table 5-III. Comparison of Fiber-Optics and Camera System Overhead Determination.

747 Compliance Test (Moses Lake, 1975)

	(1)	(2)	(3)	(4)	(5)	(6)	(7) = (1) - (5)	(8) = (7) - (6)
Flt No.	Nic No.	A/C Acoustic Overhead From Fiber Optics	A/C Alt (Ft) Re Boeing	T_0^g (R)	$\sqrt{\delta g RT}$ Ft/Sec.	Time For Sound + Mission A/C To Grd	A/C Visual Overhead Re Boeing Data (Camera)	A/C Overhead Re Fiber Optics
1	1	12:29:39.983	401.712	.512	1110	.363	12:29:39.552	12:29:39.620 .068
	2	12:29:42.083	389.134	.512	1110	.350	12:29:41.920	12:29:41.733 -.187
	3	12:29:44.533	377.384	.512	1110	.340	12:29:44.256	12:29:44.193 -.063
4	2	12:54:56.603	398.579	.512.5	1110	.359	12:54:56.208	12:54:56.244 .036
	3	12:54:58.853	381.855	.512.5	1110	.344	12:54:58.544	12:54:58.509 -.035
6.1	2	13:16:24.078	362.667	.513.5	1111	.326	13:16:23.80	13:16:23.752 -.048
	3	13:16:26.378	345.101	.513.5	1111	.310	13:16:26.144	13:16:26.068 -.076
14	2	15:39:08.120	815.380	.515	1112	.732	15:39:07.344	15:39:07.388 .044
	3	15:39:10.220	827.099	.515	1112	.743	15:39:09.280	15:39:09.477 .197

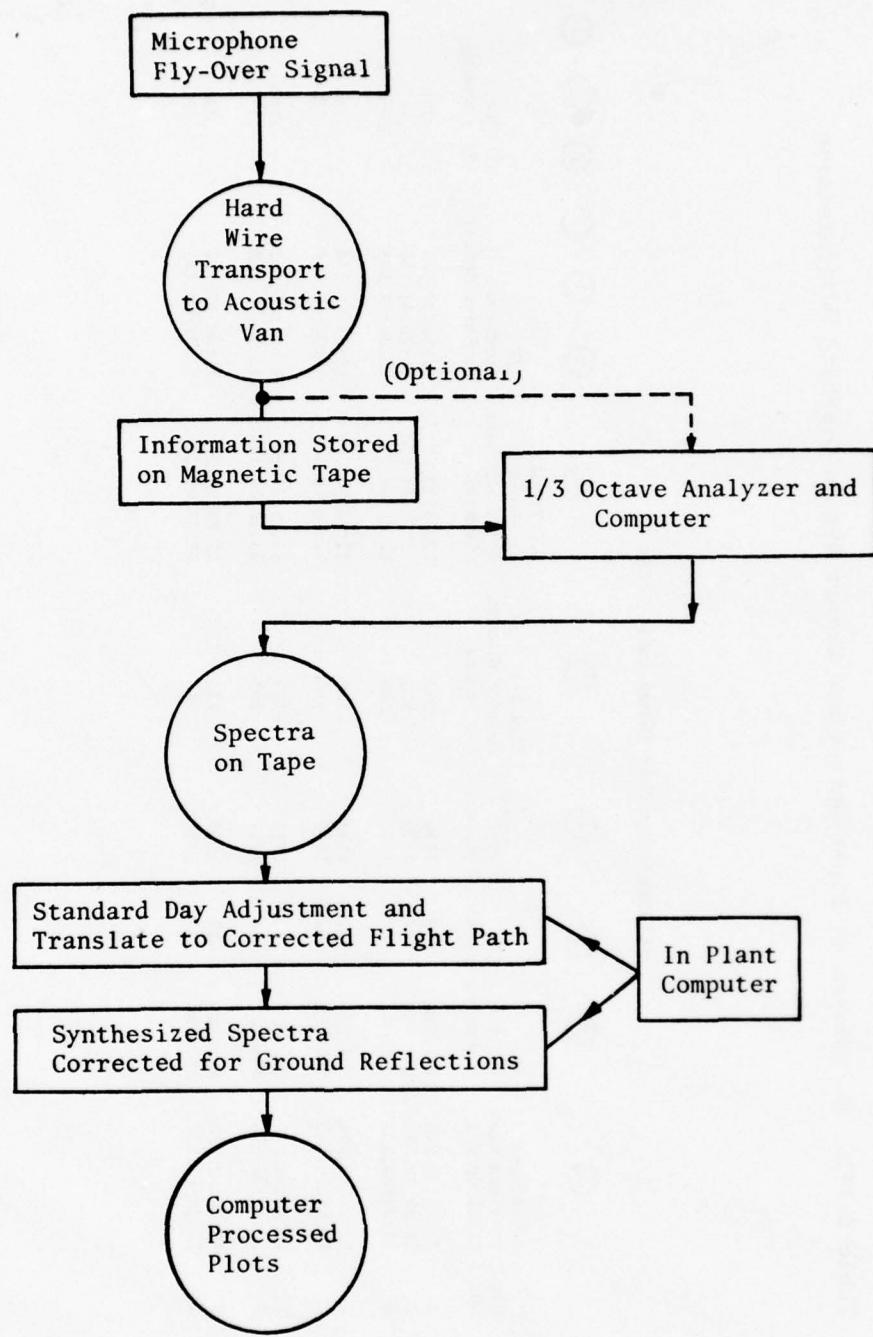


Figure 5-9. Information Flow Diagram - Flyover Data Processing and Adjustment.

groups, along with aircraft course and timing information, are input to a computer program. Calculations are performed to:

- Adjust from actual test day conditions to an ISA + 10° C standard day
- Determine the acoustic angle
- Correct for background noise
- Provide adjustments from the actual flight path to a corrected path in order that all data may be presented on a common sideline.

The next step is to translate the corrected 1/8-second spectra to a form that permits comparisons with static and simulated flight data recorded from microphones with fixed acoustic angles. Consequently, flight spectra are synthesized from the 1/8-second recorded flyover data at the specific acoustic angles obtained during free jet testing. This is accomplished by linearly interpolating between flyover angles that bracket the ground test angles. An adjustment is also made to account for background noise influence, if any, in the data.

Ground Reflection Corrections - Both static and flight data were corrected for ground reflections to ensure that true "flight effects" were being observed. The theoretical method presented in Section 4.3 of Reference 7 was used as a starting point. Corrections were calculated using this method for the various static and flight acoustic path geometries assuming that the phase factor (ϕ) and coefficient of reflection (Q) were both one. This initial assumption was justified, to some extent, by the fact that all data were obtained over an acoustically hard surface as stated in Section 5.1.2. The assumption did, however, lead to poor corrections in selected 1/3-octave bands.

Samples of the measured and corrected conical nozzle free-field static spectra for three acoustic angles are presented on Figure 5-10. Note that the "corrected" spectra, using the theoretical method, do not exhibit free-field characteristics. To minimize the impact of the error introduced in these 1/3-octave bands, an additional set of correction factors was determined based on engineering judgment. The resulting spectra using these correction factors are also presented on Figure 5-10. The major difference between the two sets of correction factors is at the 50° acoustic angle. The failure of the theoretical corrections in certain regions of the spectra is probably due to the reflection of sound by the fuselage and wing of the test aircraft. The correction matrix for the Learjet conical nozzle static data is presented on Table 5-IV. The similar matrix for the 8-lobe nozzle is presented on Table 5-V.

The correction of the flight data to free field is a more complex problem than correcting the static data because measurements were made on sideline. This change in propagation path length causes the free-field

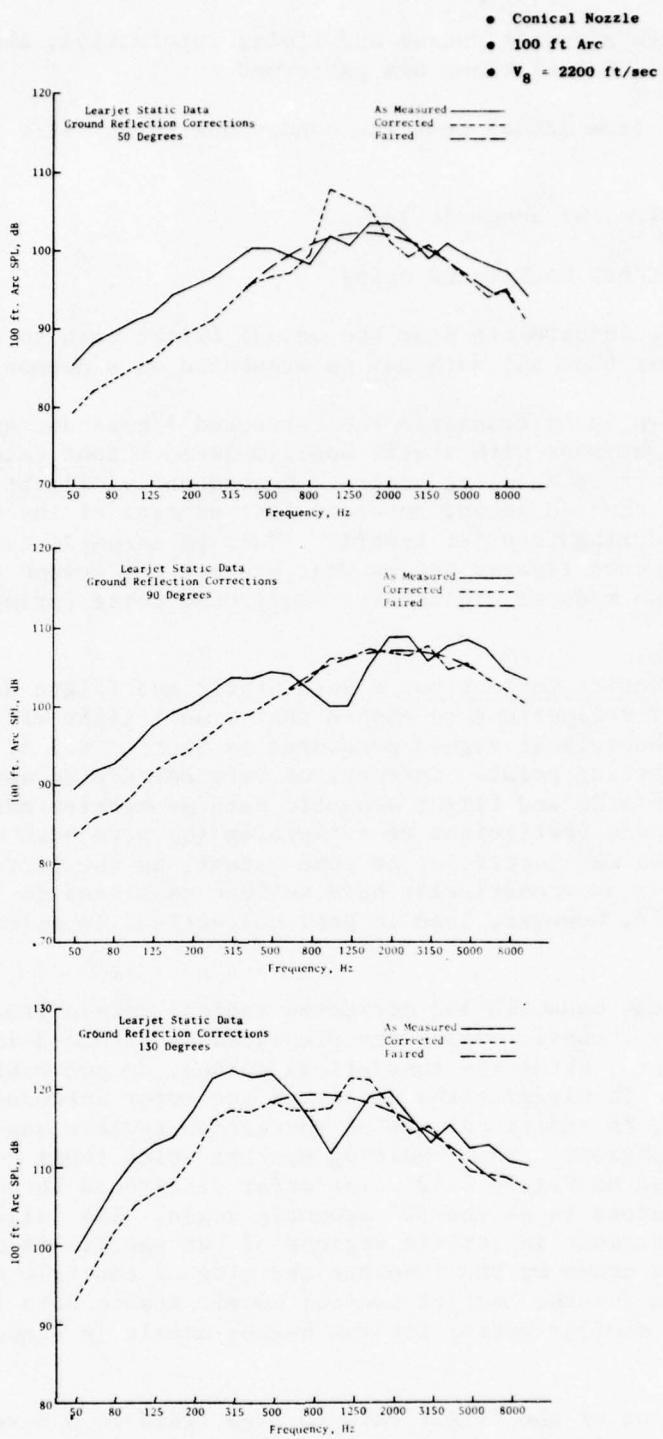


Figure 5-10. Learjet Static Data - Ground Reflection Corrections.

Table 5-IV. Learjet Conical-Nozzle Static Ground Reflection Corrections.

θ_I , Acoustic Angle, re: Inlet

Table 5-V. Learjet 8-Lobe Nozzle Static Ground Reflection Corrections.

Frequency	θ_I , Acoustic Angle, re: Inlet												
	40	50	60	70	80	90	100	110	120	130	140	150	160
50	-6.0	-6.0	-6.0	-6.0	-6.0	-6.0	-6.0	-6.0	-6.0	-6.0	-6.0	-6.0	-6.0
63	-6.0	-6.0	-6.0	-6.0	-6.0	-6.0	-6.0	-6.0	-6.0	-6.0	-6.0	-6.0	-6.0
80	-6.0	-6.0	-6.0	-6.0	-6.0	-6.0	-6.0	-6.0	-6.0	-6.0	-6.0	-6.0	-6.0
100	-5.9	-5.9	-5.9	-5.9	-5.9	-5.9	-5.9	-5.9	-5.9	-5.9	-5.9	-5.9	-5.9
125	-5.3	-5.3	-5.3	-5.3	-5.3	-5.3	-5.3	-5.3	-5.3	-5.3	-5.3	-5.3	-5.3
160	-5.3	-5.3	-5.3	-5.3	-5.3	-5.3	-5.3	-5.3	-5.3	-5.3	-5.3	-5.3	-5.3
200	-5.0	-5.0	-5.0	-5.0	-5.0	-5.0	-5.0	-5.0	-5.0	-5.0	-5.0	-5.0	-5.0
250	-4.8	-4.8	-4.8	-4.8	-4.8	-4.8	-4.8	-4.8	-4.8	-4.8	-4.8	-4.8	-4.8
315	-4.0	-4.0	-4.0	-4.0	-4.0	-4.0	-4.0	-4.0	-4.0	-4.0	-4.0	-4.0	-4.0
400	-2.8	-2.8	-2.8	-3.0	-3.0	-3.0	-3.0	-3.0	-3.0	-3.0	-3.0	-3.0	-3.0
500	-2.0	-1.0	-1.0	-1.8	-1.8	-1.8	-1.0	-0.5	-0.5	-3.0	-4.5	-8.0	-8.0
630	0.5	0.5	0.5	0.5	1.0	2.0	3.0	6.0	6.0	6.0	10.0	8.0	8.0
800	3.0	3.0	4.5	6.5	7.5	9.0	11.5	11.0	12.0	12.0	12.0	12.0	12.0
1000	-1.0	3.0	5.5	5.0	4.5	4.5	5.5	6.0	7.0	7.0	7.0	7.0	7.0
1250	-1.0	2.0	1.5	1.0	-1.0	-1.0	0.0	0.5	1.0	1.0	1.0	1.0	1.0
1600	-1.8	-1.3	-2.0	-2.5	-4.5	-4.0	-4.0	-3.0	-3.0	-3.0	-3.0	-3.0	-3.0
2000	-2.0	-1.5	-3.0	-3.5	-4.0	-3.5	-3.5	-3.0	-3.0	-3.0	-3.0	-3.0	-3.0
2500	1.5	2.2	1.5	1.3	1.5	1.5	1.5	1.5	1.5	1.5	1.0	0.5	0.5
3150	-2.5	-0.5	0.5	0.5	-1.5	-2.0	-2.5	-2.5	-2.5	-2.5	-1.5	-2.5	-2.5
4000	-4.0	-2.5	-1.5	-1.5	-2.0	-2.0	0	0.5	1.0	1.0	0.5	0.5	0.5
5000	-2.5	-2.5	-2.0	-2.5	-2.5	-2.5	-2.5	-2.5	-2.5	-2.5	-2.5	-2.5	-2.5
6300	-2.5	-2.5	-2.5	-2.5	-2.5	-2.5	-2.5	-2.5	-2.5	-2.5	-2.5	-2.5	-2.5
8000	-2.5	-2.5	-2.5	-2.5	-2.5	-2.5	-2.5	-2.5	-2.5	-2.5	-2.5	-2.5	-2.5
10000	-2.5	-2.5	-2.5	-2.5	-2.5	-2.5	-2.5	-2.5	-2.5	-2.5	-2.5	-2.5	-2.5

corrections not only to vary with frequency but also to vary as a function of acoustic angle. The microphone array for the 8-lobe nozzle was designed to study the optimum microphone height or combinations of microphone heights that would minimize the impact of ground reflections. The importance of correcting the flyover acoustic data to free field is illustrated on Figure 5-11. Note the data scatter before the data was corrected to free field compared to that observed after the free-field corrections have been applied (particularly at low frequencies).

The free-field corrections applied to the data presented on Figure 5-11 vary as a function of microphone height and frequency. Based on the theoretical method described in Reference 7, the corrections were calculated for each microphone height at acoustic angles of 100° and 140°. The corrections are presented as a function of frequency on Figures 5-12 and 5-13. These figures also illustrate increments, as a function of frequency, obtained when the data from the 20-ft microphone and flush-mounted microphones are subtracted from the 4-ft microphone data. If the theoretical corrections were valid, the increment at each 1/3-octave band frequency would be zero. The increments are observed to be 10 dB in the low frequencies and 3 dB in the high frequencies. Further study of the corrections shows that the corrections for the 4-ft microphone vary significantly with frequency, whereas the corrections for the 20-ft and flush-mounted microphones are relatively constant with frequency. The impact of 4-ft data was determined by comparing the 20-ft and flush-mounted data on an incremental basis. These comparisons are presented on Figures 5-14 and 5-15. They show some improvement in the frequency range from 125 Hz thru 10 kHz relative to 4-ft microphone increments. Below 125 Hz, the free-field corrections do not make the data collapse, however. The results of this study show that the 20-ft and flush-mounted microphone data when corrected are, for most instances, representative of free-field flight data between 200 Hz and 10 kHz.

Based on this study, the microphone arrays for the Learjet conical nozzle test series and F-106 baseline nozzle test series were chosen to be three microphones flush mounted in conjunction with three microphones 20 ft off the ground. Three microphones were also placed at 4-ft height to provide comparable data with the previous test. Multiple microphones were chosen to increase the data accuracy in the low frequency portion of the spectra.

The data for the Learjet conical nozzle flight test series were corrected using the corrections presented on Tables 5-VI through 5-IX. These ground reflection corrections also include some engineering judgement, particularly for the 4-ft microphone data. Figures 5-16 through 5-19 are typical examples of where the calculated and the judgement correction factors differ. Note that the differences are in the region where the primary null patterns occur.

In summary, ground reflection corrections have been determined for the three microphone heights. These corrections are applied to the data. The data from the multiple microphone heights and passes are averaged to further minimize the impact of ground reflections. This averaging procedure is described in the next section.

• GE/Lear Jet, 8-Lobe Daisy, Flight Data

$\theta_1 = 140^\circ$ Microphone, $V_8 = 2170 \text{ ft/sec}$, $V_0 = 325 \text{ ft/sec}$

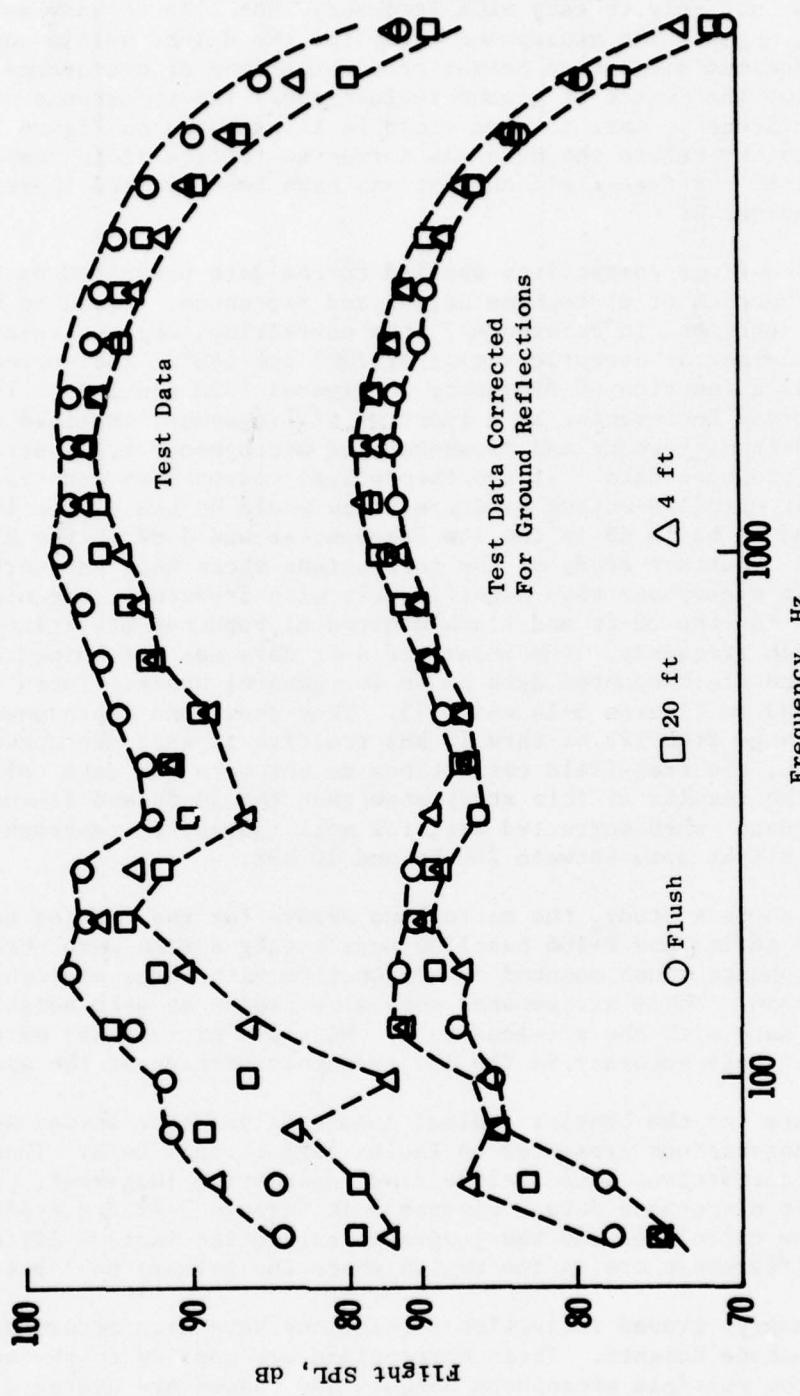


Figure 5-11. Comparison of Measured and Free Field Flight Data.

$$\theta_1 = 100^\circ, V_8 = 2170 \text{ ft/sec}, V_0 = 325 \text{ ft/sec}$$

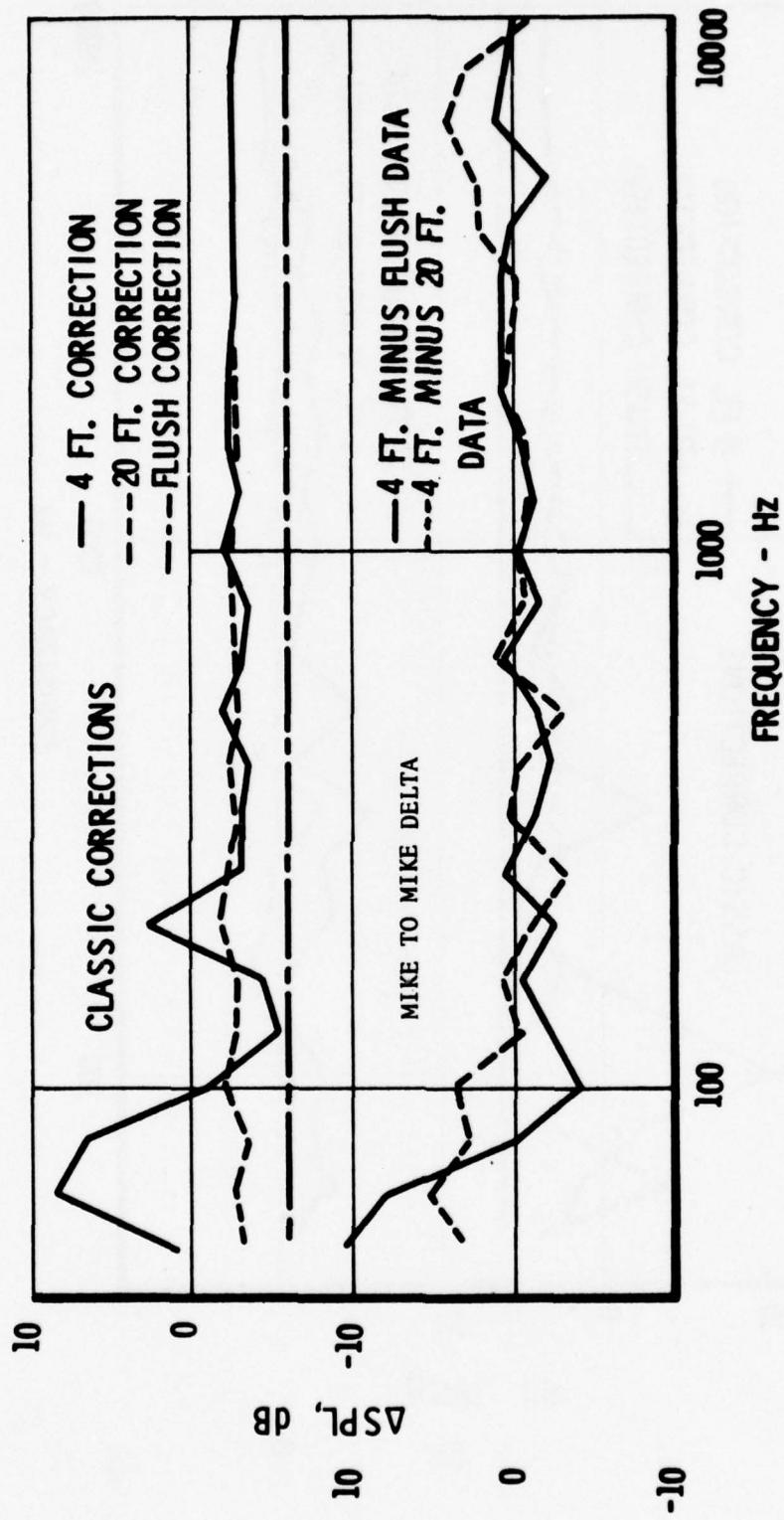


Figure 5-12. Comparison of Classical Free Field Corrections for 8-Lobe Nozzle Flight Data - $\theta_1 = 100^\circ$.

$\theta_1 = 140^\circ$, $V_8 = 2170$ ft/sec, $V_0 = 325$ ft/sec

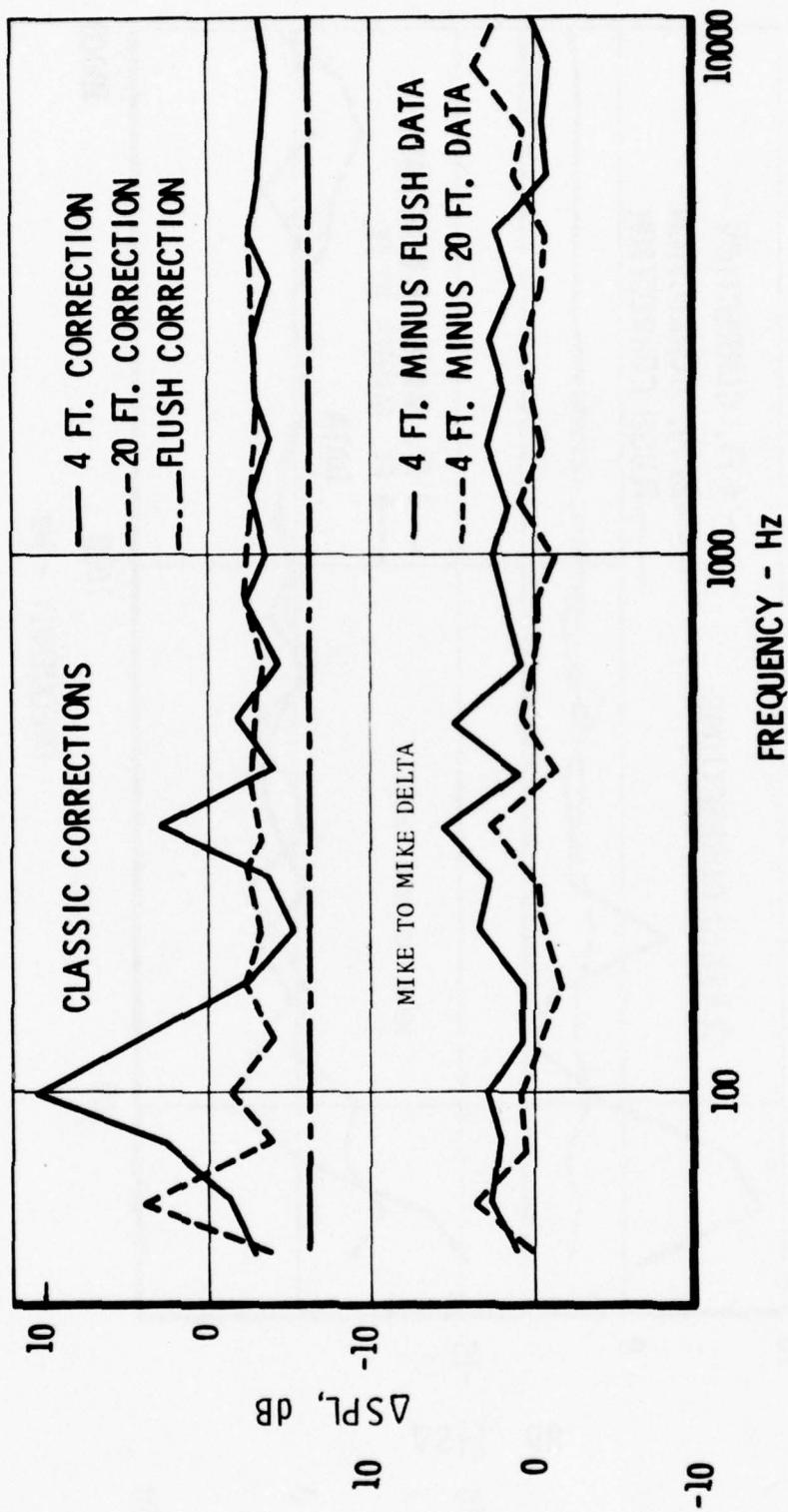


Figure 5-13. Comparison of Classical Free Field Corrections for 8-Lobe Nozzle Flight Data - $\theta_1 = 140^\circ$.

$\theta_1 = 100^\circ$, $V_8 = 2170 \text{ ft/sec}$, $V_0 = 325 \text{ ft/sec}$

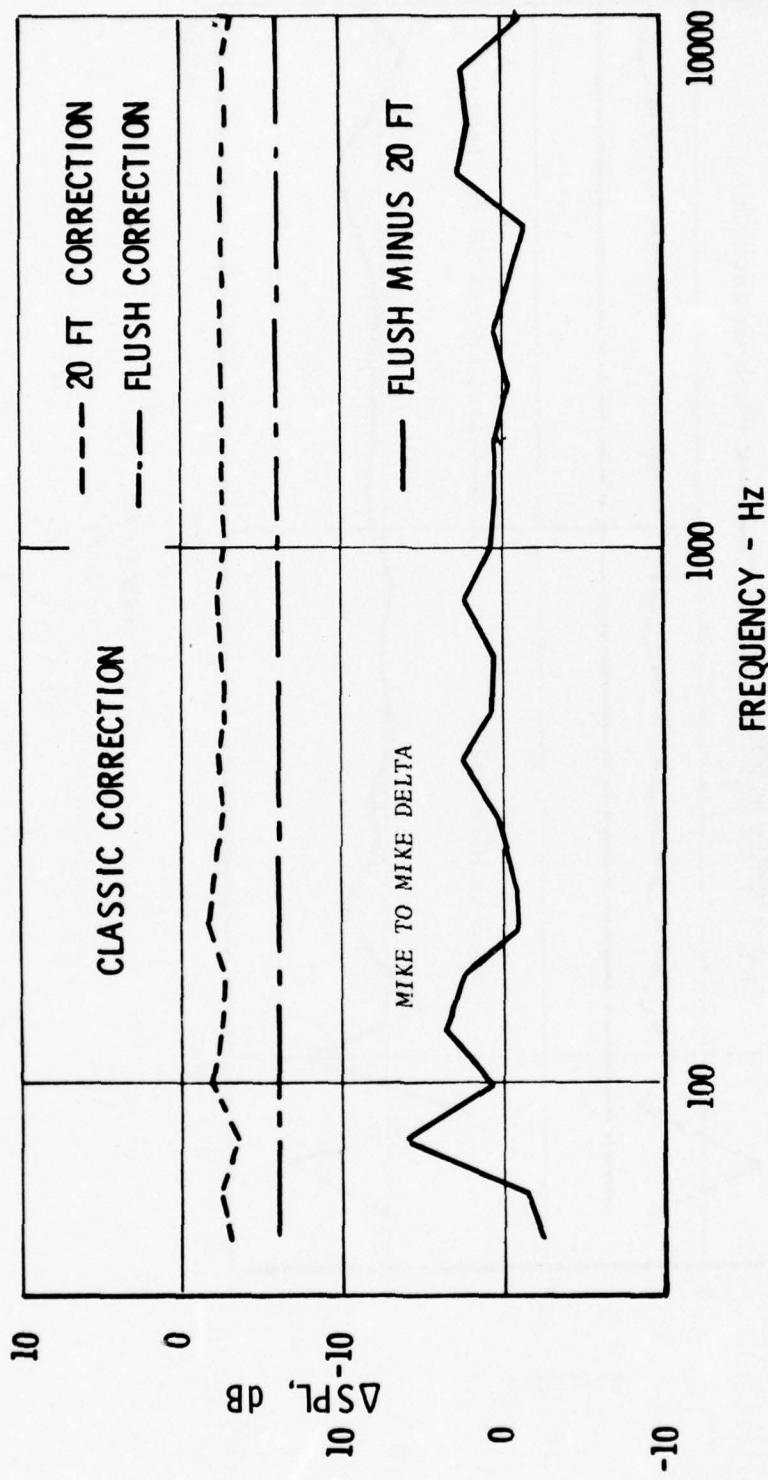


Figure 5-14. Comparison of Flush-Mounted and 20-Foot Microphone 8-Lobe Nozzle Free Field Flight Data - $\theta_1 = 100^\circ$.

$\theta_1 = 100^\circ$, $v_8 = 2170 \text{ ft/sec}$, $v_o = 325 \text{ ft/sec}$

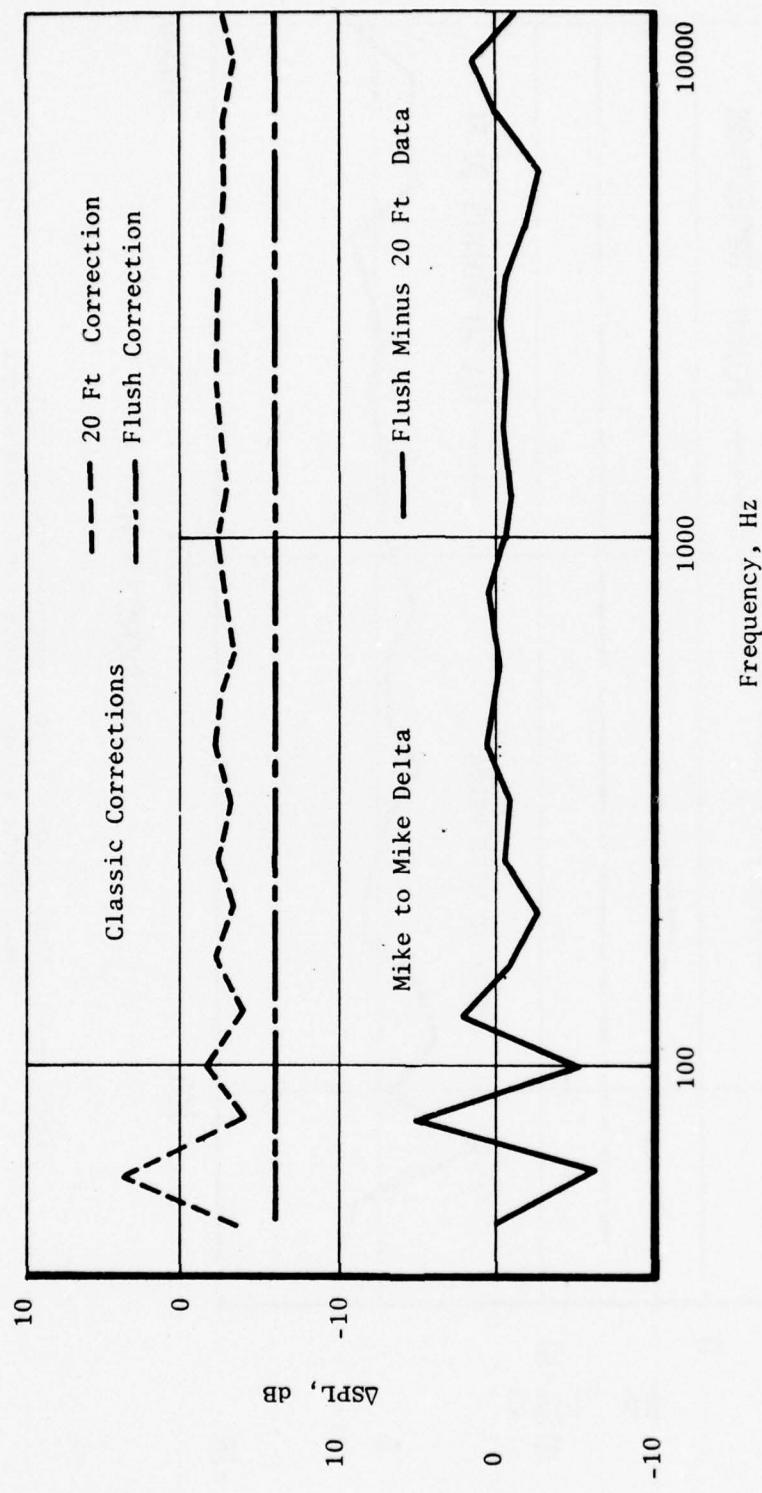


Figure 5-15. Comparison of Flush-Mounted and 20-Foot Microphone 8-Lobe Nozzle Free Field Flight Data - $\theta_1 = 140^\circ$.

Table 5-VI. Learjet Flight Ground Reflection Correction.

	• 4 Ft Microphone		• 400 Ft Altitude		θ_I , Acoustic Angle, re: Inlet										
FREQ	20.0	30.0	40.0	50.0	60.0	70.0	80.0	90.0	100.0	110.0	120.0	130.0	140.0	150.0	160.0
50.	0.	-6.0	-4.5	-2.5	-1.5	3.0	-2.5	-2.0	-1.5	-7.0	0.	2.0	-1.5	-5.0	-5.0
63.	0.	-5.0	-3.5	-2.0	-3.5	4.0	4.5	5.0	6.0	5.0	4.5	0.	-2.0	-3.5	-5.5
80.	0.	-4.0	-1.0	4.0	6.0	7.0	10.0	4.5	8.0	8.5	12.5	9.0	-0.5	2.0	-4.5
100.	0.	-3.0	1.0	4.0	1.0	-8.5	-6.5	0.	-1.5	1.0	6.5	6.5	1.5	-2.5	-3.0
125.	0.	-4.5	-5.5	-3.0	-4.5	-4.0	-3.0	-5.5	-4.0	-0.5	-5.5	2.5	3.0	1.5	-2.5
160.	0.	-2.0	-1.0	-6.0	-5.0	-6.0	-4.0	-6.5	-5.0	-7.0	-8.0	-5.5	0.5	8.5	-1.5
200.	0.	4.0	-6.0	-2.0	-5.5	-0.5	1.5	3.0	1.5	-1.0	-2.5	-2.0	-7.5	-5.5	2.5
250.	0.	5.0	-4.0	-0.5	6.0	-0.5	-2.5	-2.0	-2.5	0.	3.5	2.5	-1.0	-3.0	1.5
315.	0.	-6.5	-3.5	-5.5	-5.0	-3.0	-5.0	-3.0	-3.0	-7.0	-7.5	-3.5	1.0	-5.0	8.0
400.	0.	-6.0	-4.5	-4.5	-4.5	0.	-5.0	-5.0	-4.0	-4.0	-4.0	-4.5	0.	-4.0	-4.0
500.	0.	-2.0	-2.0	-1.5	-2.5	-1.5	0.	-2.0	-2.5	-2.5	-2.5	-2.5	-2.5	-1.0	-5.0
630.	0.	2.0	2.0	-2.0	-1.5	-2.0	-2.0	-1.0	-2.5	-2.5	-3.0	-4.5	-1.5	-2.5	-2.5
800.	0.	-1.0	-1.5	-2.0	-3.0	-2.5	-2.5	-3.0	-2.5	-4.5	-2.5	-1.5	-3.0	-4.0	0.5
1000.	0.	0.5	-2.5	-2.5	-3.5	-2.5	-2.5	-4.0	-2.5	-2.5	-4.5	-4.5	-4.0	-2.5	-4.0
1250.	0.	-3.0	-2.5	-2.5	-2.5	-2.5	-2.5	-2.5	-2.5	-2.5	-2.5	-2.5	-1.5	-2.5	-1.5
1600.	0.	-3.0	-2.5	-2.5	-2.5	-2.5	-2.5	-2.5	-2.5	-2.5	-2.5	-2.5	-2.5	-2.5	-3.0
2000.	0.	-2.5	-2.5	-2.5	-2.5	-2.5	-2.5	-2.5	-2.5	-2.5	-2.5	-2.5	-2.5	-2.5	-2.5
2500.	0.	-2.5	-2.5	-2.5	-2.5	-2.5	-2.5	-2.5	-2.5	-2.5	-2.5	-2.5	-2.5	-2.5	-2.5
3150.	0.	-2.5	-2.5	-2.5	-2.5	-2.5	-2.5	-2.5	-2.5	-2.5	-2.5	-2.5	-2.5	-2.5	-2.5
4000.	0.	-2.5	-2.5	-2.5	-2.5	-2.5	-2.5	-2.5	-2.5	-2.5	-2.5	-2.5	-2.5	-2.5	-2.5
5000.	0.	-2.5	-2.5	-2.5	-2.5	-2.5	-2.5	-2.5	-2.5	-2.5	-2.5	-2.5	-2.5	-2.5	-2.5
6300.	0.	-2.5	-2.5	-2.5	-2.5	-2.5	-2.5	-2.5	-2.5	-2.5	-2.5	-2.5	-2.5	-2.5	-2.5
8000.	0.	-2.5	-2.5	-2.5	-2.5	-2.5	-2.5	-2.5	-2.5	-2.5	-2.5	-2.5	-2.5	-2.5	-2.5
10000.	0.	-2.5	-2.5	-2.5	-2.5	-2.5	-2.5	-2.5	-2.5	-2.5	-2.5	-2.5	-2.5	-2.5	-2.5

Table 5-VII. Learjet Flight Ground Reflection Corrections.

Frequency	● 4 Ft Microphone										● 1000 Ft Altitude										θ_I , Acoustic Angle, re: Inlet										
10.0	20.0	30.0	40.0	50.0	60.0	70.0	80.0	90.0	100.0	110.0	120.0	130.0	140.0	150.0	160.0	10.0	20.0	30.0	40.0	50.0	60.0	70.0	80.0	90.0	100.0	110.0	120.0	130.0	140.0	150.0	160.0
50	0.	0.	0.	0.	-2.0	0.	2.0	0	2.0	2.0	-4.0	-1.0	-2.0	-4.0	0.	63	0.	0.	0.	-0.5	4.5	3.0	-3.0	5.5	4.0	0.5	-1.0	-1.0	-2.5	0.	
80	0.	0.	0.	0.	0.	0.	13.5	7.5	4.0	3.5	2.5	8.5	5.5	1.5	-2.0	100	0.	0.	0.	-4.0	-3.0	-7.5	-6.0	-7.5	-1.0	0.5	2.5	10.0	6.5	-1.0	0.
100	0.	0.	0.	0.	0.	0.	4.5	-3.0	0.	-6.0	-7.5	-1.0	-0.5	2.5	10.0	125	0.	0.	0.	-6.0	-4.0	-2.5	-1.5	-4.0	-3.0	-3.0	-5.5	6.0	7.0	0.	0.
125	0.	0.	0.	0.	0.	0.	-4.0	-3.0	-3.0	-6.0	-2	-3.5	-3.5	-3.0	-2.5	160	0.	0.	0.	-3.5	-3.0	-2.0	-1.5	-2.5	-2.5	-2.5	-5.5	2.0	5.0	0.	0.
160	0.	0.	0.	0.	0.	0.	-3.5	-3.0	-3.0	-6.0	-2	-3.5	-3.5	-3.0	-2.5	200	0.	0.	0.	-3.5	-3.0	-2.5	-2.0	-2.5	0.	0.5	-5.5	-4.5	-4.0	0.	0.
200	0.	0.	0.	0.	0.	0.	-3.0	-2.0	-2.0	-1.0	-0.5	-4.5	-1.5	8.0	1.5	250	0.	0.	0.	0.	0.	0.	0.	0.	-1.0	-1.5	-1.5	-3.5	0.	0.	0.
250	0.	0.	0.	0.	0.	0.	-2.5	-5.0	1.0	-3.0	-3.0	-4.5	-4.5	-6.0	-3.0	315	0.	0.	0.	0.	0.	0.	0.	0.	-3.0	-6.0	-6.0	-3.0	1.0	-6.5	0.
315	0.	0.	0.	0.	0.	0.	-3.0	0.5	0.	-4.0	-6.0	-3.0	-1.5	1.0	-5.5	400	0.	0.	0.	0.	0.	0.	0.	0.	-2.0	-3.0	-1.0	-2.0	0.	-2.5	0.
400	0.	0.	0.	0.	0.	0.	-3.0	-3.0	-2.0	-2.0	-2.5	-2.5	-1.0	-3.0	500	0.	0.	0.	0.	0.	0.	0.	0.	-3.0	-3.0	-3.0	-3.0	0.	3.0	0.	
500	0.	0.	0.	0.	0.	0.	-2.5	-3.0	-2.0	-2.0	-2.5	-2.5	-1.5	-3.0	630	0.	0.	0.	0.	0.	0.	0.	0.	-2.0	-2.0	-2.0	-2.0	0.	-6.0	0.	
630	0.	0.	0.	0.	0.	0.	-2.5	-2.5	-2.0	-2.0	-2.5	-2.5	-1.5	-3.5	800	0.	0.	0.	0.	0.	0.	0.	0.	-1.5	-1.5	-1.5	-1.5	0.	-1.0	0.	
800	0.	0.	0.	0.	0.	0.	-2.5	-4.0	-4.0	-2.5	-2.5	-2.5	-1.5	-3.5	1000	0.	0.	0.	0.	0.	0.	0.	0.	-2.5	-2.5	-2.5	-2.5	0.	-3.5	0.	
1000	0.	0.	0.	0.	0.	0.	-1.5	-3.5	-1.5	-1.5	-2.5	-2.5	-2.5	-3.0	1250	0.	0.	0.	0.	0.	0.	0.	0.	-2.5	-2.5	-2.5	-2.5	0.	-3.5	0.	
1250	0.	0.	0.	0.	0.	0.	-2.5	-2.0	-2.0	-2.0	-2.5	-2.5	-2.5	-3.0	1600	0.	0.	0.	0.	0.	0.	0.	0.	-2.5	-2.5	-2.5	-2.5	0.	-2.5	0.	
1600	0.	0.	0.	0.	0.	0.	-6.0	-3.0	-4.0	-4.0	-2.5	-2.5	-2.5	-3.0	2000	0.	0.	0.	0.	0.	0.	0.	0.	-2.5	-2.5	-2.5	-2.5	0.	-2.5	0.	
2000	0.	0.	0.	0.	0.	0.	-3.5	-4.0	-3.0	-2.5	-2.5	-2.5	-2.5	-3.0	2500	0.	0.	0.	0.	0.	0.	0.	0.	-2.5	-2.5	-2.5	-2.5	0.	-2.5	0.	
2500	0.	0.	0.	0.	0.	0.	-3.0	-3.5	-2.5	-2.5	-2.5	-2.5	-2.5	-2.5	3150	0.	0.	0.	0.	0.	0.	0.	0.	-2.5	-2.5	-2.5	-2.5	0.	-2.5	0.	
3150	0.	0.	0.	0.	0.	0.	-2.5	-2.0	-1.5	-1.5	-2.5	-2.5	-2.5	-3.0	4000	0.	0.	0.	0.	0.	0.	0.	0.	-2.5	-2.5	-2.5	-2.5	0.	-2.5	0.	
4000	0.	0.	0.	0.	0.	0.	-2.5	-2.5	-2.0	-2.0	-2.5	-2.5	-2.5	-2.5	5000	0.	0.	0.	0.	0.	0.	0.	0.	-2.5	-2.5	-2.5	-2.5	0.	-2.5	0.	
5000	0.	0.	0.	0.	0.	0.	-2.5	-2.5	-2.5	-2.5	-2.5	-2.5	-2.5	-2.5	6300	0.	0.	0.	0.	0.	0.	0.	0.	-2.5	-2.5	-2.5	-2.5	0.	-2.5	0.	
6300	0.	0.	0.	0.	0.	0.	-2.5	-2.5	-2.5	-2.5	-2.5	-2.5	-2.5	-2.5	8000	0.	0.	0.	0.	0.	0.	0.	0.	-2.5	-2.5	-2.5	-2.5	0.	-2.5	0.	
8000	0.	0.	0.	0.	0.	0.	-2.5	-2.5	-2.5	-2.5	-2.5	-2.5	-2.5	-2.5	10000	0.	0.	0.	0.	0.	0.	0.	0.	-2.5	-2.5	-2.5	-2.5	0.	-2.5	0.	

Table 5-VIII. Learjet Flight Ground Reflection Corrections.

	• 20 Ft Microphone		• 400 Ft Altitude		θ_1 , Acoustic Angle, re: Inlet											
FREQ	20.0	30.0	40.0	50.0	60.0	70.0	80.0	90.0	100.0	110.0	120.0	130.0	140.0	150.0	160.0	
50.	0.	-2.5	-5.0	-4.0	-1.0	3.0	0.	-5.0	2.0	-3.0	0.5	2.5	-4.0	-3.0	-6.5	
63.	0.	-1.0	-2.0	1.5	-1.5	-5.0	-3.0	1.0	0.	-3.0	-7.0	-5.0	4.0	-1.5	3.0	
80.	0.	0.5	1.5	-1.0	-3.5	2.5	-4.0	-5.5	-2.0	-3.0	-2.0	0.	-4.5	-2.0	-5.5	
100.	0.	0.	1.0	1.5	2.0	-7.0	-5.5	-6.0	-6.0	-2.0	-5.0	-2.0	-3.0	-1.5	-0.5	
125.	0.	-3.5	-4.0	-10.0	-3.5	-4.0	0.	-1.0	-2.0	-2.5	-2.5	-2.5	-4.5	0.5	-7.0	-0.5
160.	0.	-4.5	-3.0	-1.5	-4.0	0.	-3.0	-0.5	-0.5	-1.5	-3.5	-1.0	-5.0	-2.5	-2.5	
200.	0.	1.5	-4.0	-2.0	-2.0	-3.0	-2.5	-2.5	-2.5	-2.0	-2.0	-2.0	-3.0	-7.5	-7.5	
250.	0.	-1.5	0.	-1.5	-0.5	-3.0	-3.0	0.	-3.0	-2.5	-2.5	-2.5	-5.5	-2.0	-4.0	
315.	0.	-4.5	-5.5	-5.5	-4.0	-3.0	-4.5	-2.5	-2.0	-2.5	-3.0	-3.0	-1.5	-2.5	-3.0	
400.	0.	-3.5	2.5	1.5	-2.0	-0.5	-2.0	-2.5	-3.5	-2.5	-2.5	-2.5	-3.5	-2.0	-2.5	
500.	0.	-1.5	-1.0	-2.0	-1.0	-1.0	-2.5	-2.5	-2.5	-2.5	-2.5	-2.5	-2.5	-1.0	-2.5	
630.	0.	-2.0	-1.5	0.	-1.5	-2.5	-2.5	-2.5	-2.5	-2.5	-2.5	-2.5	-2.5	-4.0	-2.5	
800.	0.	-2.0	-3.0	-2.0	-2.5	-2.5	-2.5	-2.5	-2.5	-2.5	-2.5	-2.5	-2.5	-3.5	-2.5	
1000.	0.	-2.5	-2.5	-2.5	-2.5	-2.5	-2.5	-2.5	-2.5	-2.5	-2.5	-2.5	-2.5	-3.0	-2.5	
1250.	0.	-2.5	-2.5	-2.5	-2.5	-2.5	-2.5	-2.5	-2.5	-2.5	-2.5	-2.5	-2.5	-2.5	-2.5	
1600.	0.	-2.5	-2.5	-2.5	-2.5	-2.5	-2.5	-2.5	-2.5	-2.5	-2.5	-2.5	-2.5	-2.5	-2.5	
2000.	0.	-2.5	-2.5	-2.5	-2.5	-2.5	-2.5	-2.5	-2.5	-2.5	-2.5	-2.5	-2.5	-2.5	-2.5	
2500.	0.	-2.5	-2.5	-2.5	-2.5	-2.5	-2.5	-2.5	-2.5	-2.5	-2.5	-2.5	-2.5	-2.5	-2.5	
3150.	0.	-2.5	-2.5	-2.5	-2.5	-2.5	-2.5	-2.5	-2.5	-2.5	-2.5	-2.5	-2.5	-2.5	-2.5	
4000.	0.	-2.5	-2.5	-2.5	-2.5	-2.5	-2.5	-2.5	-2.5	-2.5	-2.5	-2.5	-2.5	-2.5	-2.5	
5000.	0.	-2.5	-2.5	-2.5	-2.5	-2.5	-2.5	-2.5	-2.5	-2.5	-2.5	-2.5	-2.5	-2.5	-2.5	
6300.	0.	-2.5	-2.5	-2.5	-2.5	-2.5	-2.5	-2.5	-2.5	-2.5	-2.5	-2.5	-2.5	-2.5	-2.5	
8000.	0.	-2.5	-2.5	-2.5	-2.5	-2.5	-2.5	-2.5	-2.5	-2.5	-2.5	-2.5	-2.5	-2.5	-2.5	
10000.	0.	-2.5	-2.5	-2.5	-2.5	-2.5	-2.5	-2.5	-2.5	-2.5	-2.5	-2.5	-2.5	-2.5	-2.5	

Table 5-IX. Learjet Flight Ground Reflection Corrections.

FREQ	θ _I , Acoustic Angle, re: Inlet	20 Ft Microphone										1000 Ft Altitude									
		10.0	20.0	30.0	40.0	50.0	60.0	70.0	80.0	90.0	100.0	110.0	120.0	130.0	140.0	150.0	160.0	10.0	20.0	30.0	40.0
50.	0.	0.	0.	-5.0	-6.0	-5.5	-4.5	-3.5	-2.5	-2.0	-1.5	-1.0	-1.5	-2.0	-3.0	-4.0	-5.0	-6.5	-7.0	-7.5	0.
63.	0.	0.	0.	2.5	1.0	-5.5	0.	-1.0	-8.5	-5.0	-2.5	-4.0	-2.0	-2.5	-3.0	-4.0	-5.0	0.	0.	0.	0.
80.	0.	0.	0.	0.	-0.5	2.5	-8.5	-3.0	-2.0	-3.0	-5.0	-7.0	-7.5	-8.0	-8.5	-9.0	-9.5	0.	0.	0.	0.
100.	0.	0.	0.	-0.5	-1.5	-1.5	-4.0	-6.0	-1.5	-1.5	-2.5	-6.0	-7.0	-7.5	-8.0	-8.5	-9.0	-9.5	0.	0.	0.
125.	0.	0.	0.	-9.5	-1.5	-3.0	0.	-2.0	-2.0	-2.0	-2.0	-2.0	-2.0	-2.0	-2.0	-2.0	-2.0	-2.0	-2.0	-2.0	0.
160.	0.	0.	0.	-5.5	-4.5	-2.5	-4.5	-1.0	-4.5	-0.5	-1.0	-3.0	-7.5	-2.0	-2.0	-2.0	-2.0	-2.0	-2.0	-2.0	0.
200.	0.	0.	0.	-1.5	-4.0	-2.5	-2.5	-2.5	-1.0	0.5	-3.0	-1.5	-1.5	-1.5	-1.5	-1.5	-1.5	-1.5	-1.5	-1.5	0.
250.	0.	0.	0.	-4.0	-1.5	-2.5	-3.0	-2.5	-4.0	-3.0	-2.5	-2.5	-2.5	-2.5	-2.5	-2.5	-2.5	-2.5	-2.5	-2.5	0.
315.	0.	0.	0.	-3.0	-4.0	-3.0	-2.5	-2.5	-3.0	-3.0	-2.5	-3.0	-3.0	-3.0	-3.0	-3.0	-3.0	-3.0	-3.0	-3.0	0.
400.	0.	0.	0.	-1.5	-1.5	-2.5	-3.0	-2.5	-2.5	-2.5	-2.5	-4.0	-3.5	-3.5	-3.5	-3.5	-3.5	-3.5	-3.5	-3.5	0.
500.	0.	0.	0.	-1.0	-0.5	-2.5	0.	-2.5	-2.5	-2.5	-2.5	-2.5	-2.5	-2.5	-2.5	-2.5	-2.5	-2.5	-2.5	-2.5	0.
630.	0.	0.	0.	-5.0	-2.0	-2.5	-2.5	-2.5	-2.5	-2.5	-2.5	-2.5	-2.5	-2.5	-2.5	-2.5	-2.5	-2.5	-2.5	-2.5	0.
800.	0.	0.	0.	-2.0	-2.5	-2.5	-2.5	-2.5	-2.5	-2.5	-2.5	-2.5	-2.5	-2.5	-2.5	-2.5	-2.5	-2.5	-2.5	-2.5	0.
1000.	0.	0.	0.	-3.0	-2.5	-2.5	-2.5	-2.5	-2.5	-2.5	-2.5	-2.5	-2.5	-2.5	-2.5	-2.5	-2.5	-2.5	-2.5	-2.5	0.
1250.	0.	0.	0.	-2.5	-2.5	-2.5	-2.5	-2.5	-2.5	-2.5	-2.5	-2.5	-2.5	-2.5	-2.5	-2.5	-2.5	-2.5	-2.5	-2.5	0.
1600.	0.	0.	0.	-2.5	-2.5	-2.5	-2.5	-2.5	-2.5	-2.5	-2.5	-2.5	-2.5	-2.5	-2.5	-2.5	-2.5	-2.5	-2.5	-2.5	0.
2000.	0.	0.	0.	-2.5	-2.5	-2.5	-2.5	-2.5	-2.5	-2.5	-2.5	-2.5	-2.5	-2.5	-2.5	-2.5	-2.5	-2.5	-2.5	-2.5	0.
2500.	0.	0.	0.	-2.5	-2.5	-2.5	-2.5	-2.5	-2.5	-2.5	-2.5	-2.5	-2.5	-2.5	-2.5	-2.5	-2.5	-2.5	-2.5	-2.5	0.
3150.	0.	0.	0.	-2.5	-2.5	-2.5	-2.5	-2.5	-2.5	-2.5	-2.5	-2.5	-2.5	-2.5	-2.5	-2.5	-2.5	-2.5	-2.5	-2.5	0.
4000.	0.	0.	0.	-2.5	-2.5	-2.5	-2.5	-2.5	-2.5	-2.5	-2.5	-2.5	-2.5	-2.5	-2.5	-2.5	-2.5	-2.5	-2.5	-2.5	0.
5000.	0.	0.	0.	-2.5	-2.5	-2.5	-2.5	-2.5	-2.5	-2.5	-2.5	-2.5	-2.5	-2.5	-2.5	-2.5	-2.5	-2.5	-2.5	-2.5	0.
6300.	0.	0.	0.	-2.5	-2.5	-2.5	-2.5	-2.5	-2.5	-2.5	-2.5	-2.5	-2.5	-2.5	-2.5	-2.5	-2.5	-2.5	-2.5	-2.5	0.
8000.	0.	0.	0.	-2.5	-2.5	-2.5	-2.5	-2.5	-2.5	-2.5	-2.5	-2.5	-2.5	-2.5	-2.5	-2.5	-2.5	-2.5	-2.5	-2.5	0.
10000.	0.	0.	0.	-2.5	-2.5	-2.5	-2.5	-2.5	-2.5	-2.5	-2.5	-2.5	-2.5	-2.5	-2.5	-2.5	-2.5	-2.5	-2.5	-2.5	0.

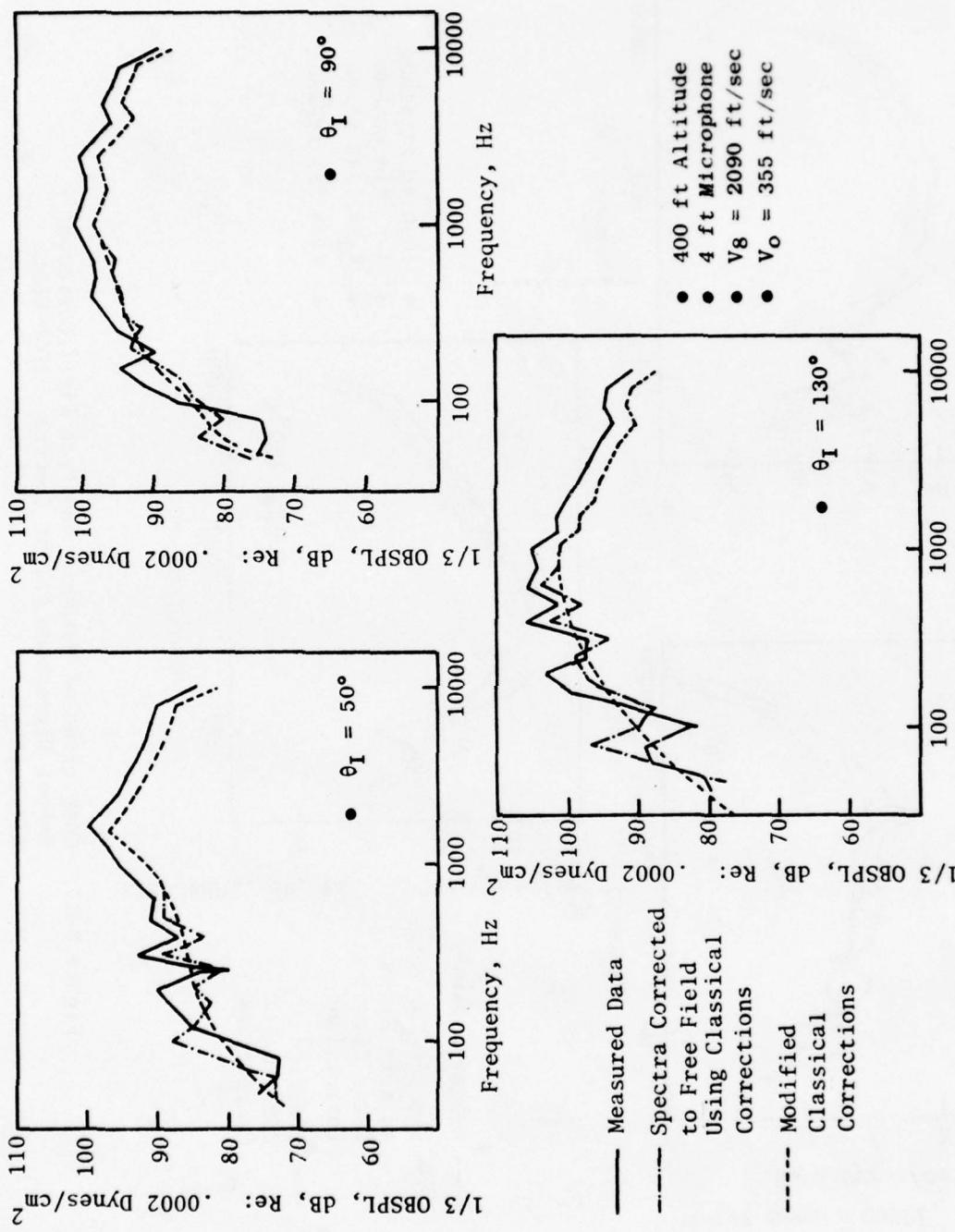


Figure 5-16. Comparison of Measured and Free Field Corrected - 4-Foot Microphone Flight Spectra - 400-Foot Altitude.

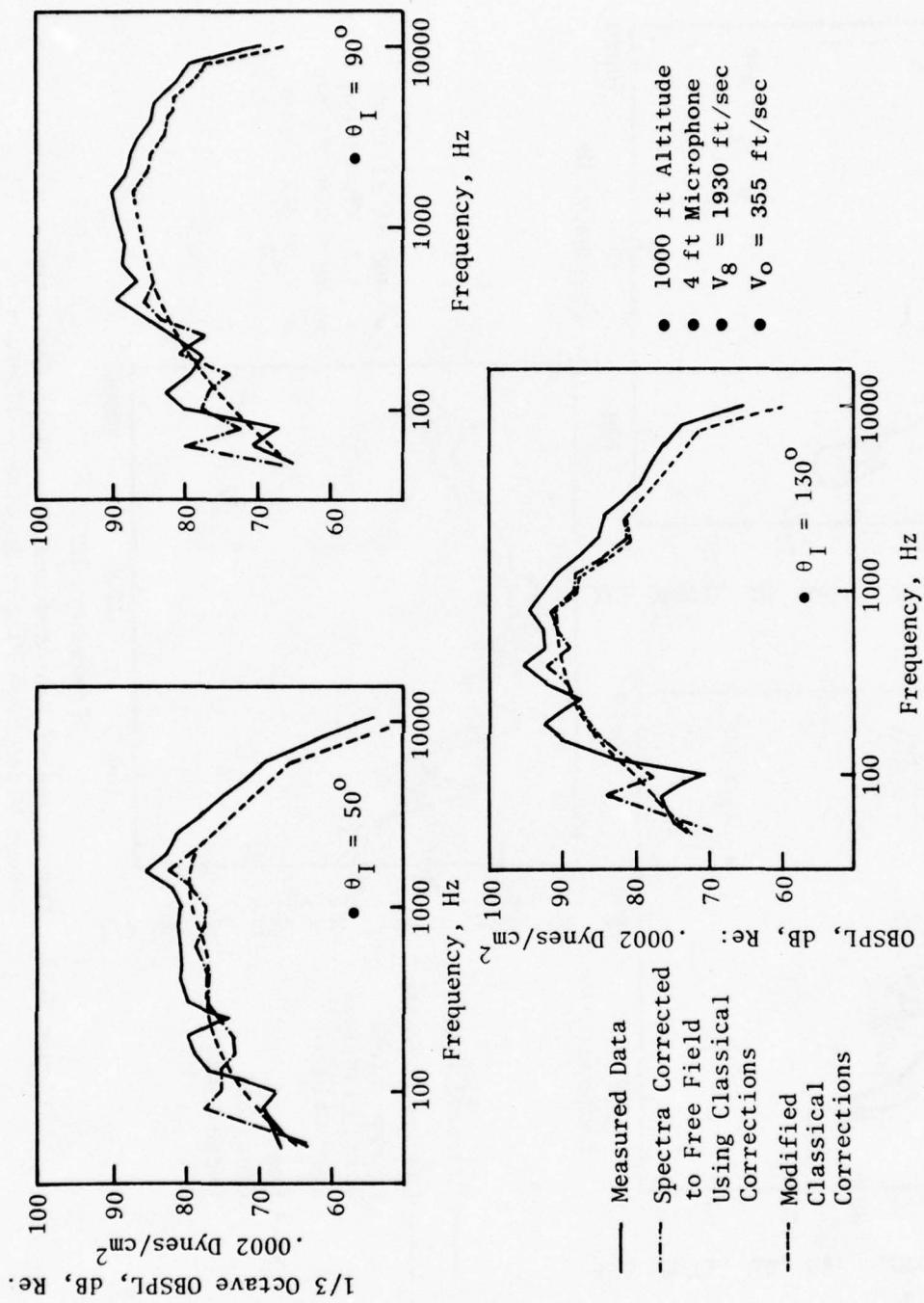


Figure 5-17. Comparison of Measured and Free Field Corrected - 4-Foot Microphone Flight Spectra - 1000-Foot Altitude.

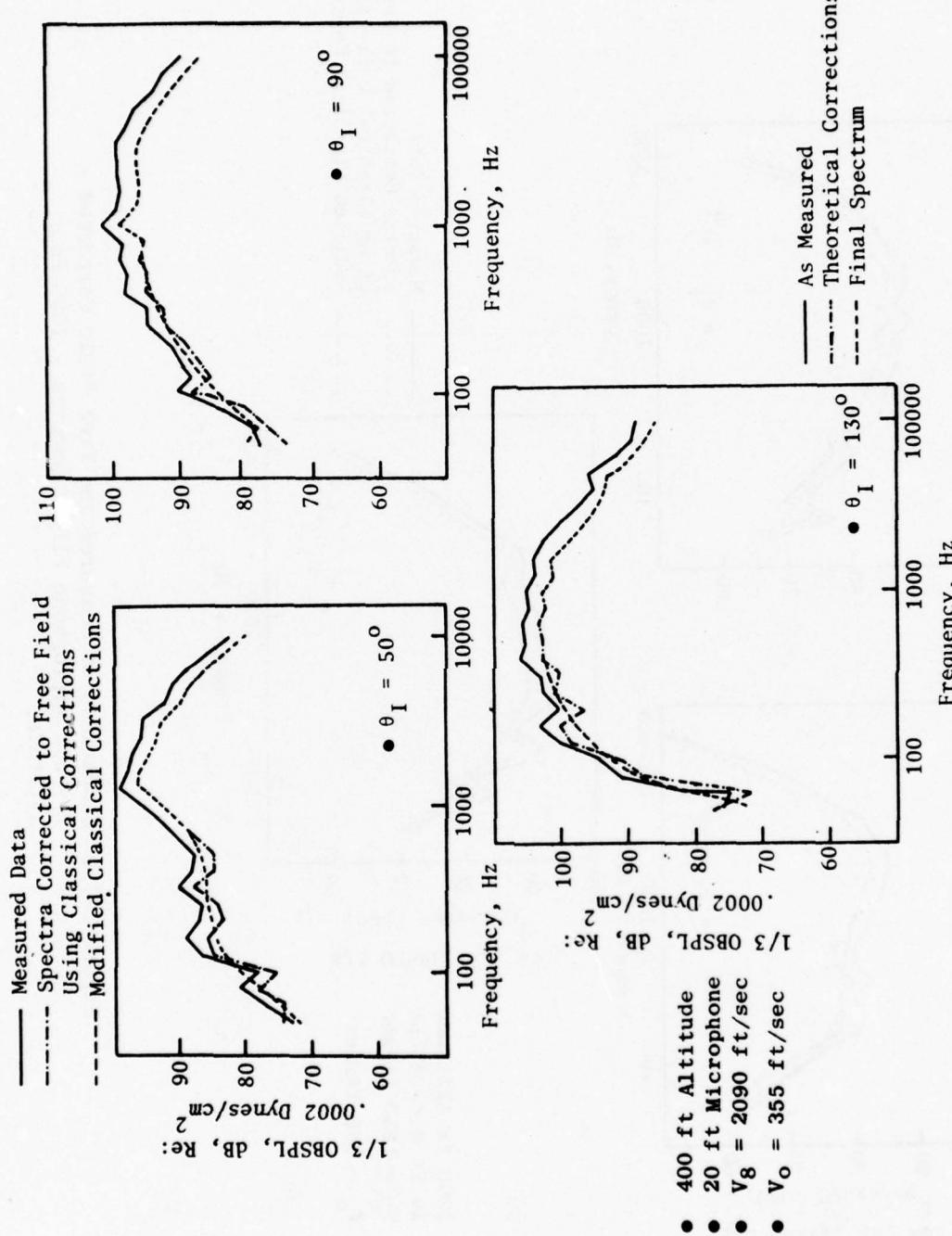


Figure 5-18. Comparison of Measured and Free Field Corrected -
20-Foot Microphone Flight Spectra - 400-Foot
Altitude.

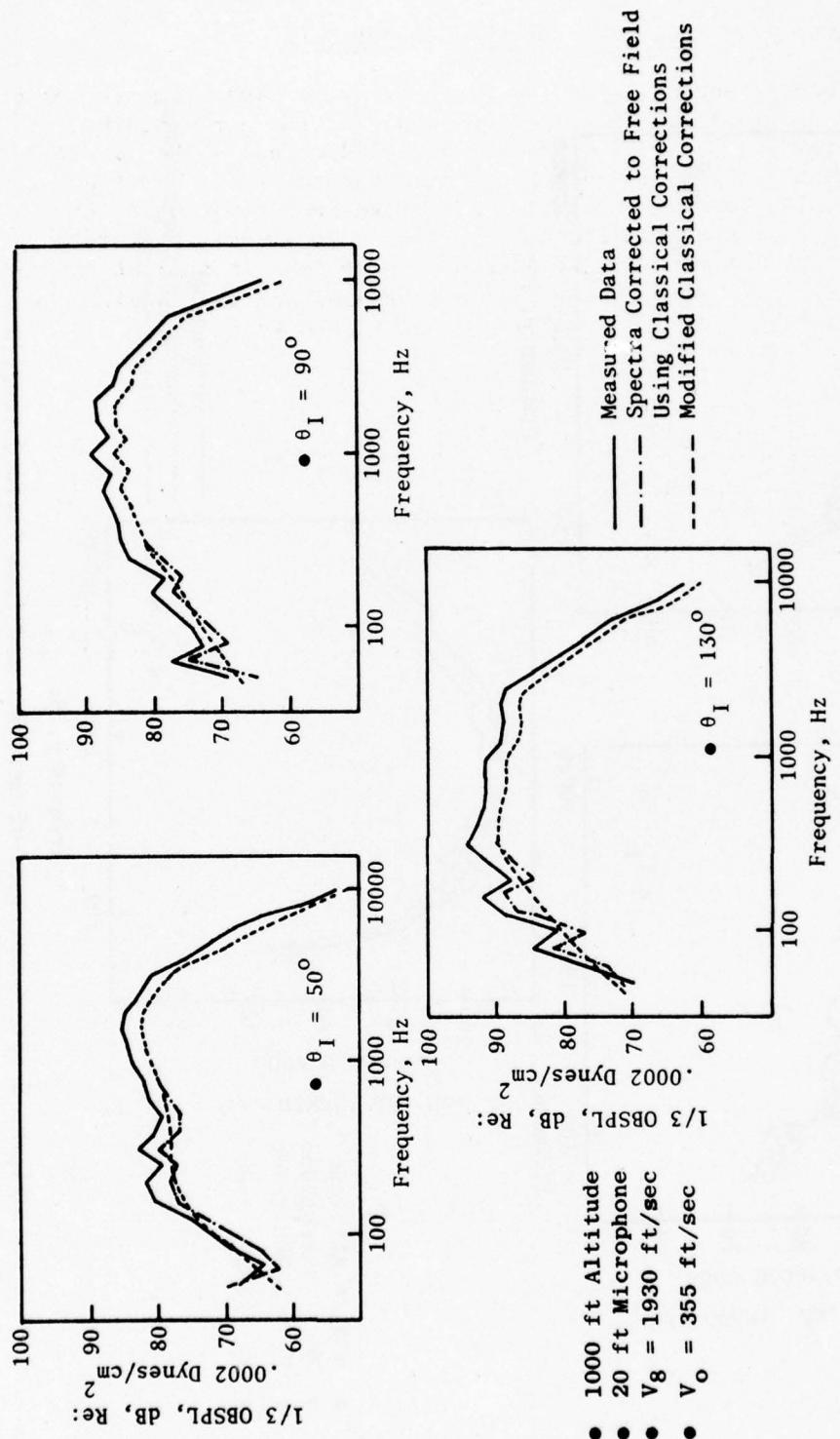


Figure 5-19. Comparison of Measured and Free Field Corrected -
20-Foot Microphone Flight Spectra - 1000-Foot
Altitude.

Data Averaging Procedure for the Learjet Data

The microphone arrangement for the Learjet flyover measurements was presented in Figure 5-3. In most of the data runs, records were obtained from microphone positions 2, 3, 4, 5, 6, 7, and 8 as indicated in the figure. The analysis in Section 3.3.2 shows that the data obtained from the different measurement poles is independent at all 1/3-octave band frequencies of interest, while data taken from the same pole will be almost completely correlated. With P_i^2 as the mean square pressure value (not in dB!) at the i -th measurement location for a particular 1/3-octave band and test angle, the estimation equation (eqs 29, 30 and 33) may be written as:

$$\phi = \begin{bmatrix} 1 & \rho & 0 & 0 & 0 & 0 & 0 \\ \rho & 1 & 0 & 0 & 0 & 0 & 0 \\ 0 & 0 & 1 & \rho & \rho & 0 & 0 \\ 0 & 0 & \rho & 1 & \rho & 0 & 0 \\ 0 & 0 & \rho & \rho & 1 & 0 & 0 \\ 0 & 0 & 0 & 0 & 0 & 1 & \rho \\ 0 & 0 & 0 & 0 & 0 & \rho & 1 \end{bmatrix} \text{ with } \underline{P}^2 = [P_2^2, P_5^2, P_4^2, P_7^2, P_3^2, P_6^2, P_8^2] \quad (61)$$

where ρ is the correlation coefficient between data taken at the same pole. Using ρ in the analysis at this point avoids a singularity problem with ϕ , although later on it will be allowed to approach 1.0 ($\rho \rightarrow 1$).

Using eq (12):

$$\hat{\sigma}^2 = \frac{(1 + \rho)(1 + \rho - 2\rho^2)}{7 + \rho - 11\rho^2} \left[\frac{1}{(1 + \rho)} (P_2^2 + P_5^2) + \frac{(1-\rho)}{(1 + \rho - 2\rho^2)} (P_4^2 + P_7^2 + P_3^2) + \frac{1}{(1 + \rho)} (P_6^2 + P_8^2) \right] \quad (62)$$

and using eq (33):

$$k = \frac{7 + 4\rho - 11\rho^2}{(1 + \rho)(1 + \rho - 2\rho^2)} \quad (63)$$

Taking the limit as $\rho \rightarrow 1$ defines the optimal estimate of the mean square pressure for each 1/3-octave band and angle the result is:

$$\hat{\sigma} = \frac{1}{3} \left[\frac{1}{2} (P_2^2 + P_5^2) + \frac{1}{3} (P_4^2 + P_7^2 + P_3^2) + \frac{1}{2} (P_6^2 + P_8^2) \right] \quad (64)$$

where $k = 3$ and is the equivalent number of independent data records in the average.

Standard programs for the analysis of multiple data records from the same experiment generally compute the arithmetic mean of the data records.

If such a program were used to reduce the Learjet flyover data, the sub-optimal estimate of the mean square pressure at each 1/3-octave band and angle would be:

$$\hat{\sigma}_{\text{SUBOPT}}^2 = \frac{1}{7} [P_2^2 + P_3^2 + P_4^2 + P_5^2 + P_6^2 + P_7^2 + P_8^2] \quad (65)$$

This estimate is unbiased. Standard statistical techniques, (see Reference 17 for example) are employed to determine the variance and equivalent number of independent data records for this estimate. Using the results of the previous derivation:

$$\Sigma_{\text{SUBOPT}} = \frac{1}{49} [1, 1, 1, 1, 1, 1, 1] \phi \begin{bmatrix} 1 \\ 1 \\ 1 \\ 1 \\ 1 \\ 1 \\ 1 \\ 1 \end{bmatrix} \frac{2\sigma^4}{n} \quad (66)$$

or

$$\Sigma_{\text{SUBOPT}} = \frac{2\sigma^4}{n} \frac{(7 + 10\rho)}{49} \quad (67)$$

As in the previous derivation, we determine the equivalent number of data records as

$$k_{\text{SUBOPT}} = \frac{49}{17} = 2.8824 \quad (68)$$

Thus, when the data are averaged in the suboptimal manner, to minimize the impact of ground reflections, there is less than the equivalent of an eighth of an independent data.

5.1.4 Learjet Data Analysis

The objective of the Learjet test program was to provide a set of high quality flight data for a concial and 8-lobe nozzle. The details of how these data were acquired and reduced have been presented in the preceding sections. The purpose of this section is to extract the salient static and flight noise characteristics from this data base. The presentation of results may be summarized as follows:

- Static and flight PNL, OASPL versus jet velocity
- Directivity characteristics

- Spectra at 50°, 90°, and 130°

The static and flight maximum PNL and OASPL levels are summarized as a function of jet velocity on Figure 5-20. The peak noise level reduction in flight is observed to be of the same magnitude on both OASPL and PNL basis for the conical nozzle. The 8-lobe nozzle, in contrast, shows significantly more reduction on the basis of OASPL than PNL and is most effective at a jet velocity of 1800 ft/sec. The changes from static to flight at the 90° acoustic angle (Figure 5-21) are substantially different than those observed at the maximum noise acoustic angle. The conical nozzle noise levels generally increase in flight relative to the static noise. The magnitude of the increase is on the order of one decibel. The 8-lobe nozzle is different in this regard, in that the static and flight noise levels are equivalent on the basis of PNL, while OASPL levels are reduced slightly. The forward quadrant trends (Figure 5-22) most aptly accentuate the difference between the two configuration noise levels. The conical increases by approximately 4 dB in flight, whereas the 8-lobe nozzle shows little change (even a slight decrease). The conical nozzle trends are relatively insensitive to jet velocity, but the 8-lobe nozzle trends are very sensitive.

The static and flight PNL and OASPL directivity patterns at three jet velocities for the two configurations are presented on Figures 5-23 through 5-26. The analysis of the directivity patterns for the conical nozzle indicate the following:

- At the two high velocity conditions, the flight noise levels are less than the static noise levels for acoustic angles greater than 110° and greater than the static noise levels for angles less than 110°.
- The peak noise angle shifts towards the 90° angle from static to flight.
- The amount of suppression in the aft quadrant is a strong function of jet velocity; whereas, the amount of increase in the forward quadrant is a weak function of jet velocity.

In general, the acoustic angle where the static and flight noise are equivalent is a function of jet velocity. Spectra comparisons at the maximum noise angle, 90°, and 50° are presented on Figures 5-27 through 5-32 for three jet velocities. Comparisons at the maximum noise angle show a reduction that is relatively constant with frequency except in regions where ground reflection corrections have a dominant influence. The most substantial difference between the 8-lobe nozzle and the conical nozzle is observed at the nominal jet velocity of 1800 ft/sec. At this particular condition, the 8-lobe nozzle realizes substantially more noise reduction from static to flight than the conical nozzle. This is due to the fact that the 8-lobe nozzle is representative of a conical nozzle operating at a low jet velocity because of the increase in mixing effectiveness of the 8-lobe nozzle. Examination of the 90° spectra reveals markedly different trends than those observed at the

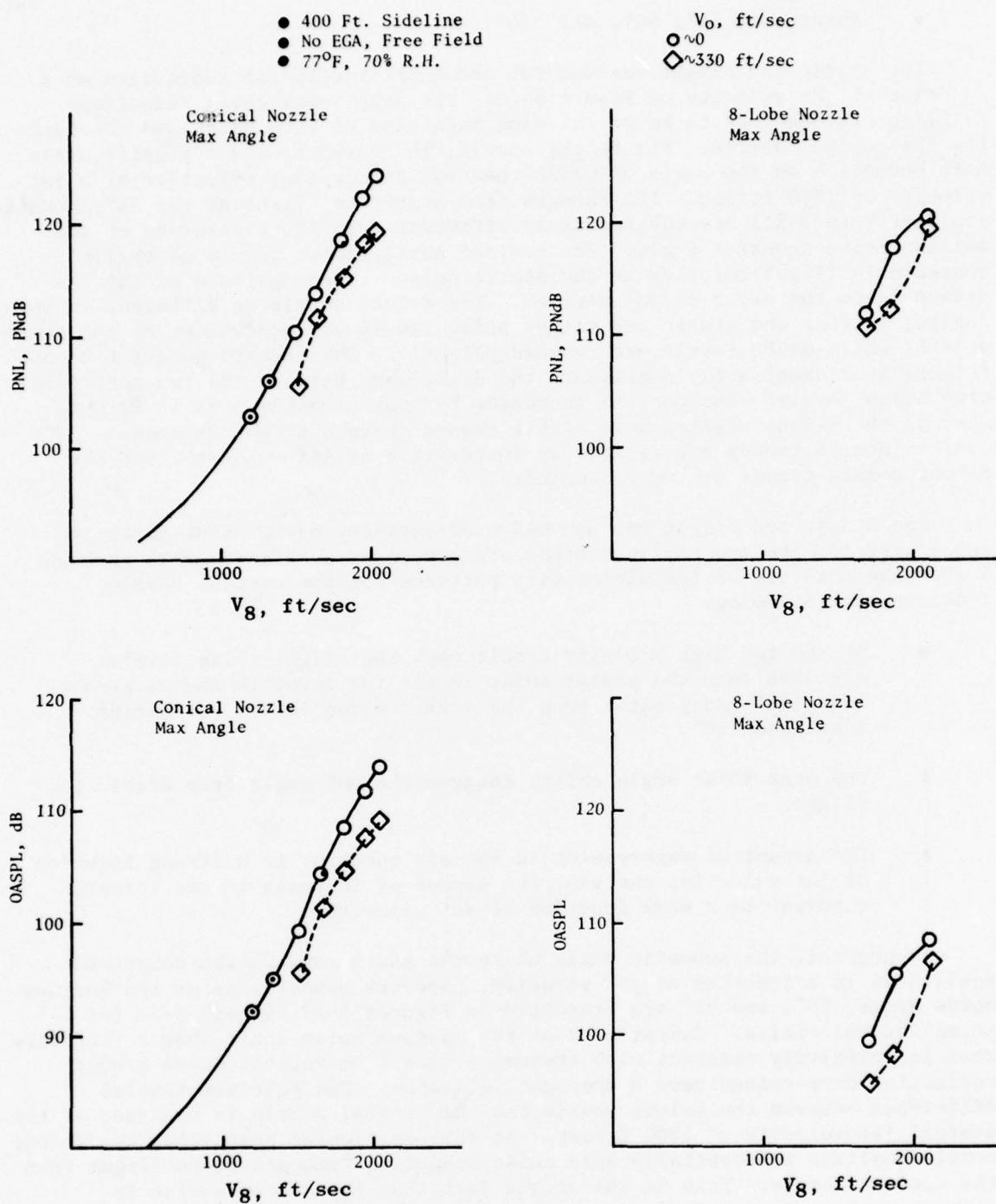


Figure 5-20. Peak OASPL and PNL Characteristics - Gates Learjet Flyover Test.

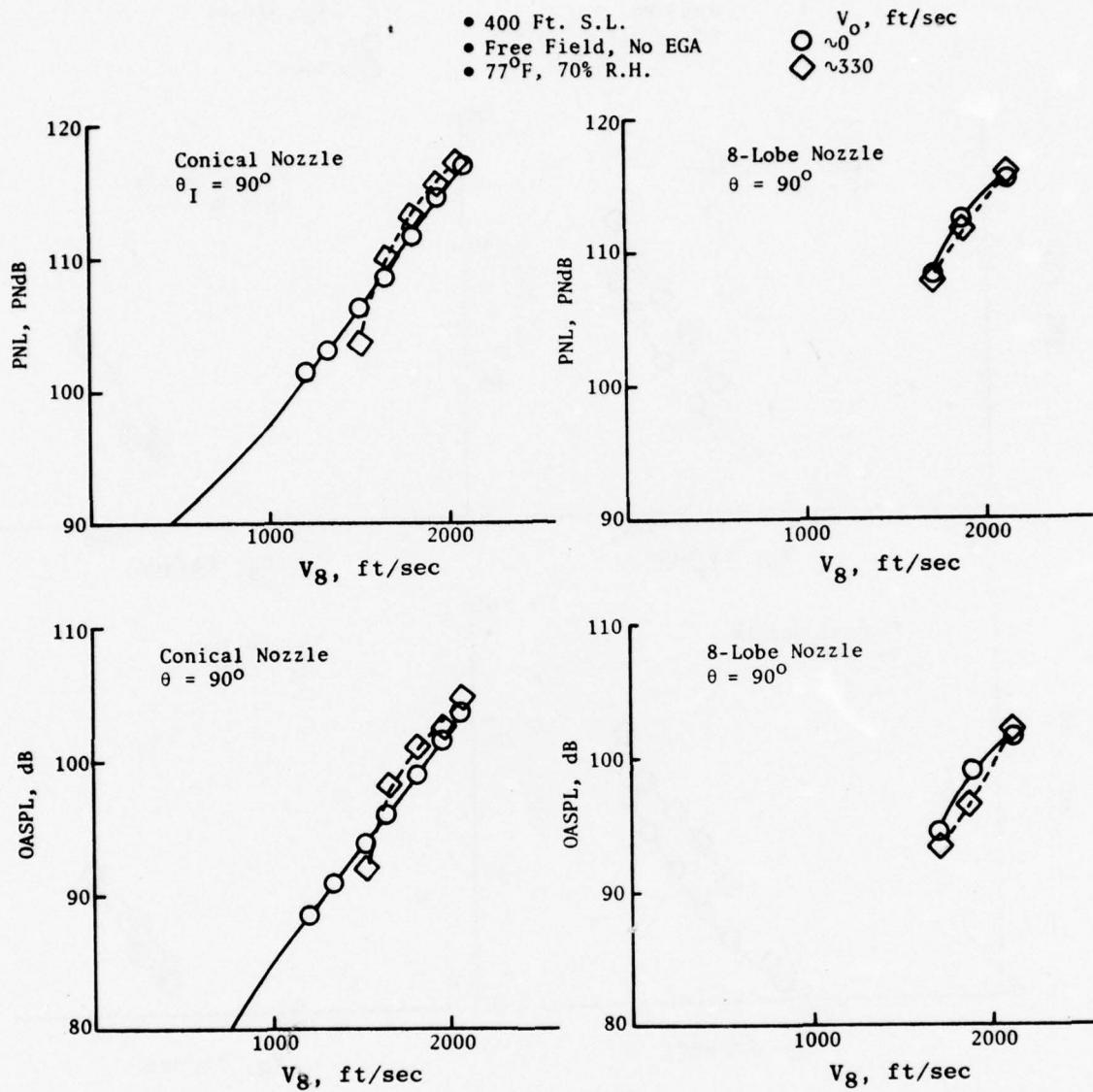


Figure 5-21. 90° OASPL and PNL Characteristics - Gates Learjet Flyover Test.

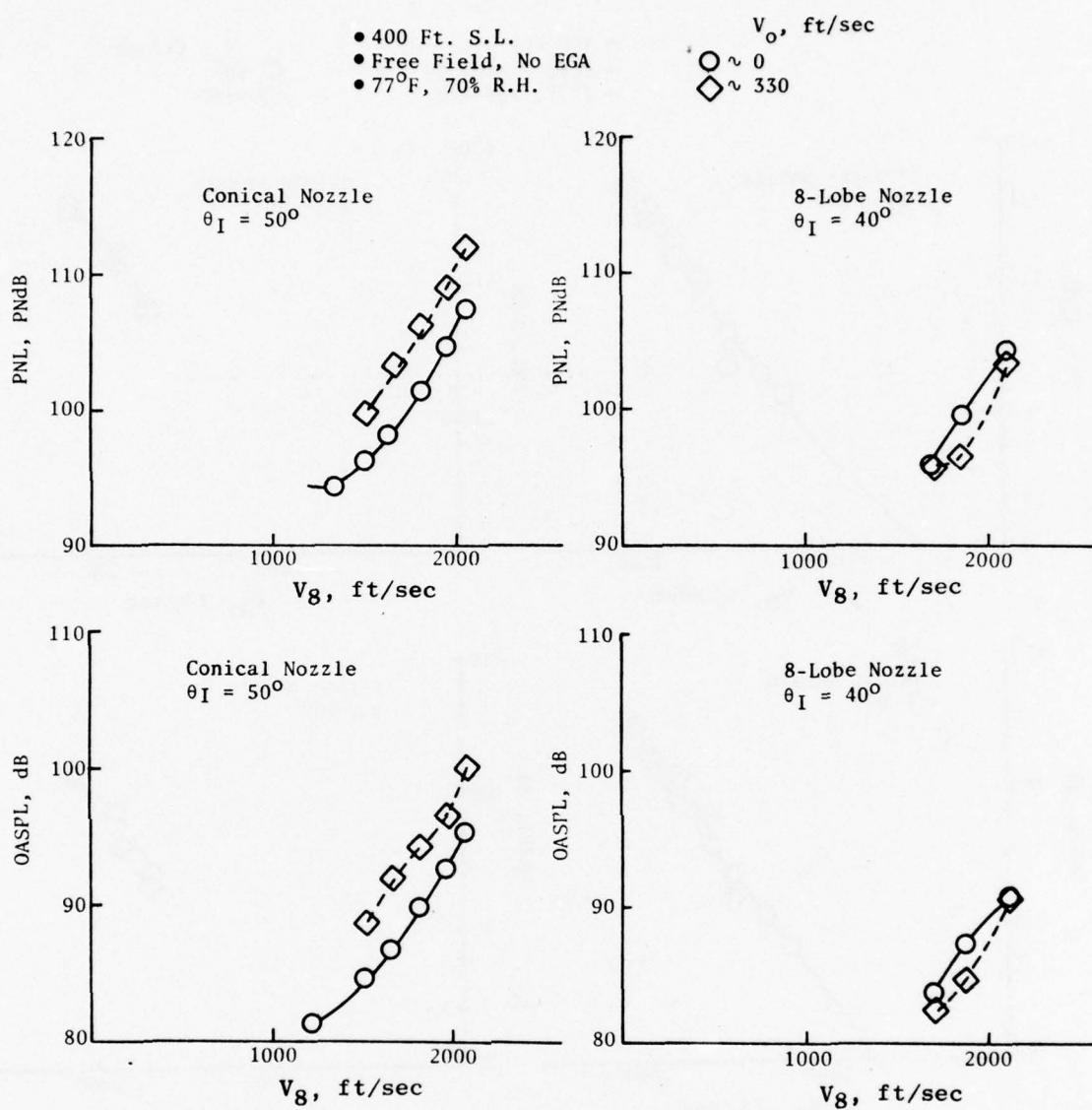


Figure 5-22. 50° OASPL and PNL Characteristics - Gates Learjet Flyover Test.

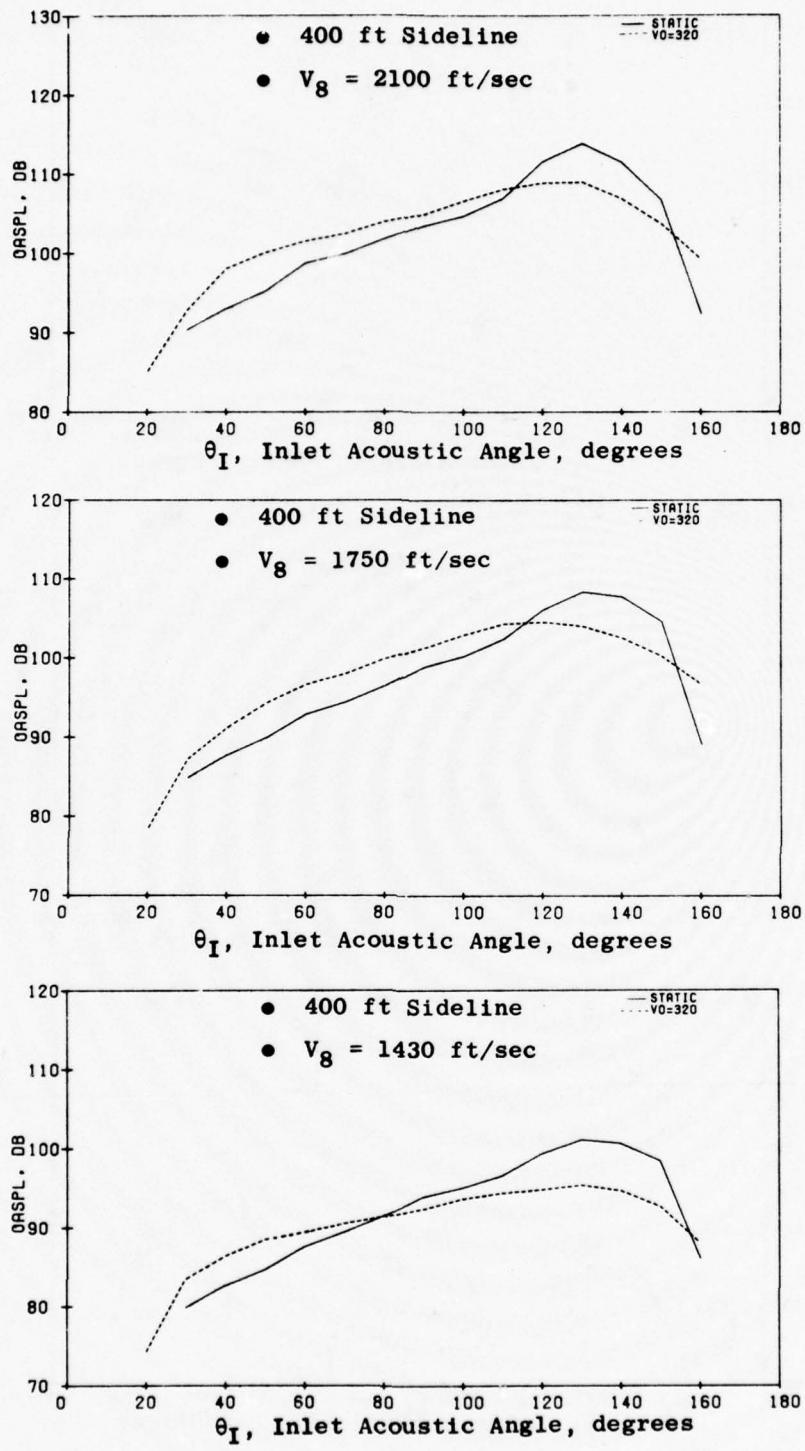


Figure 5-23. Learjet Conical Nozzle OASPL Directivity Patterns.

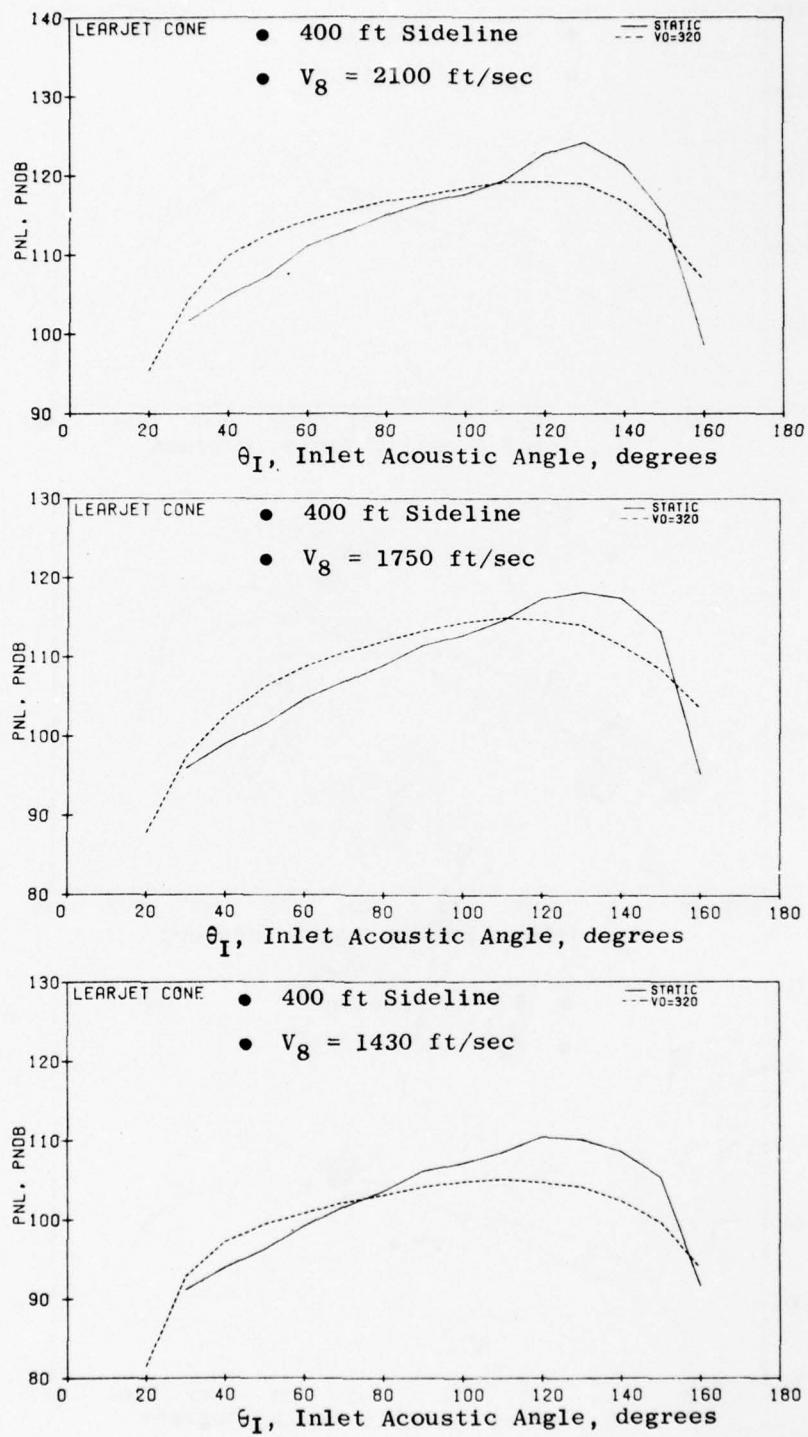


Figure 5-24. Learjet Conical Nozzle PNL Directivity Patterns.

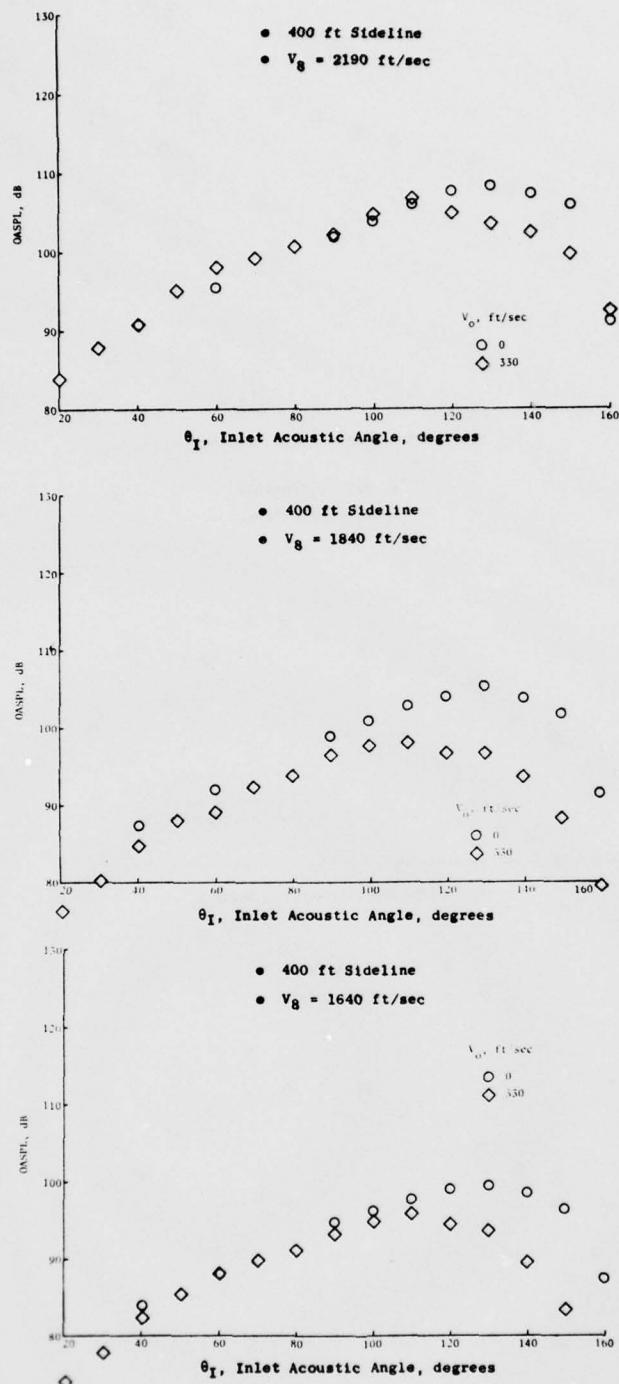


Figure 5-25. Learjet 8-Lobe Nozzle OASPL Directivity Patterns.

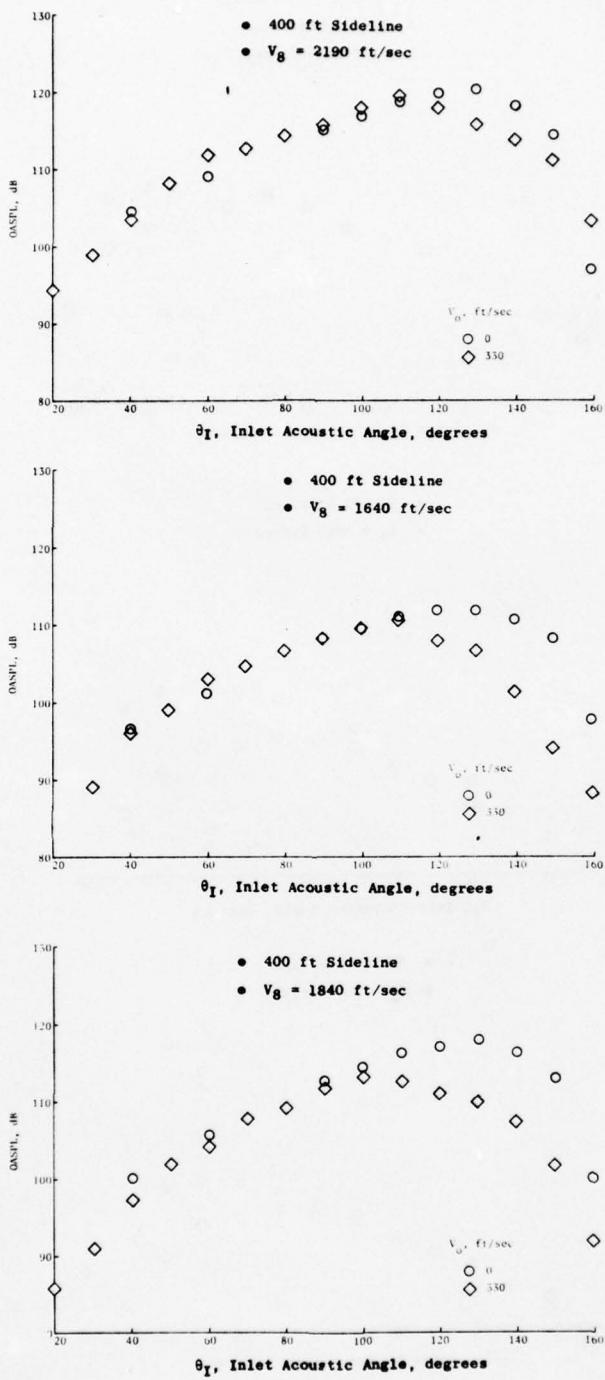


Figure 5-26. Learjet 8-Lobe Nozzle PNL Directivity Patterns.

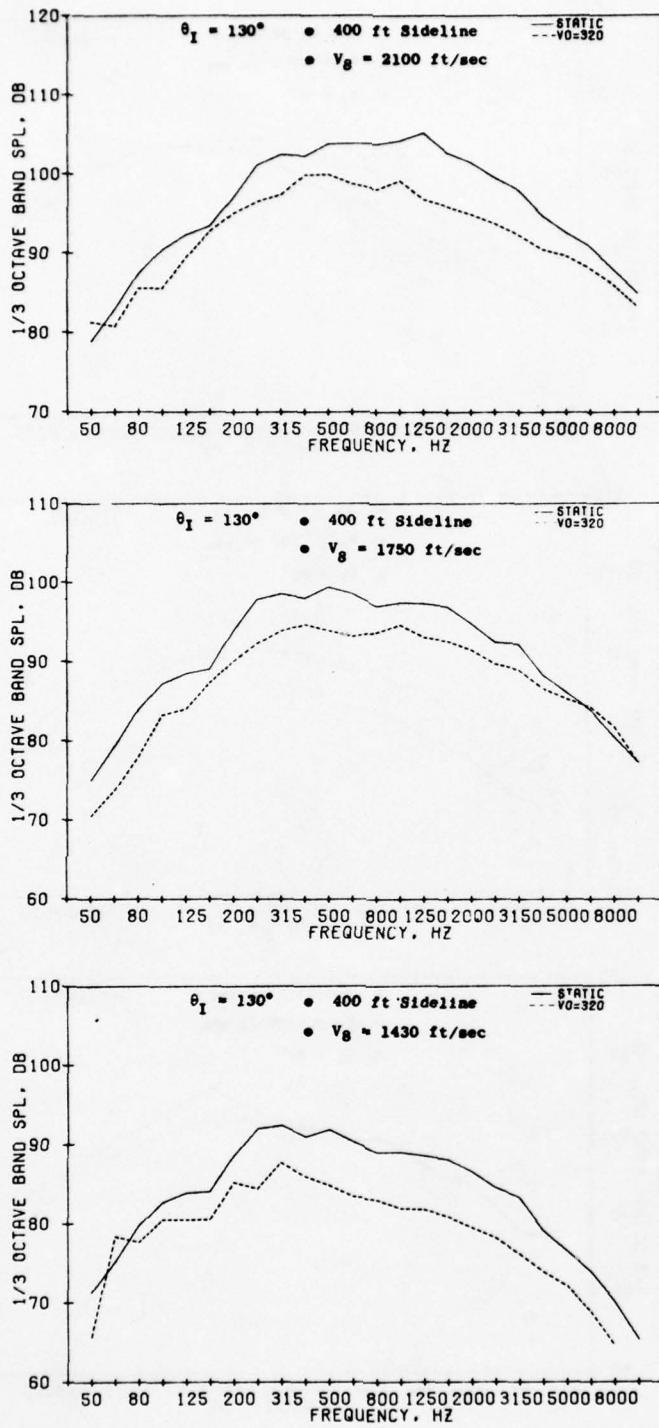


Figure 5-27. Learjet Conical Nozzle - Maximum Angle Spectra.

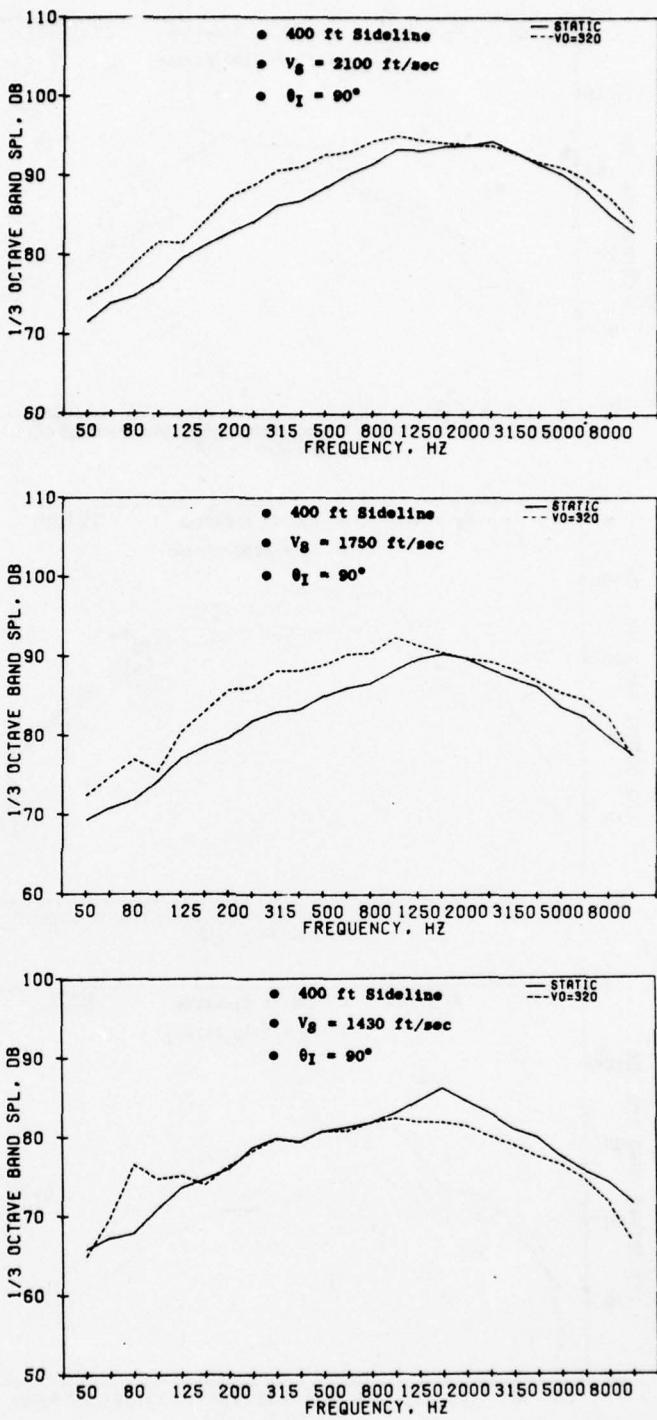


Figure 5-28. Learjet Conical Nozzle - 90° Spectra.

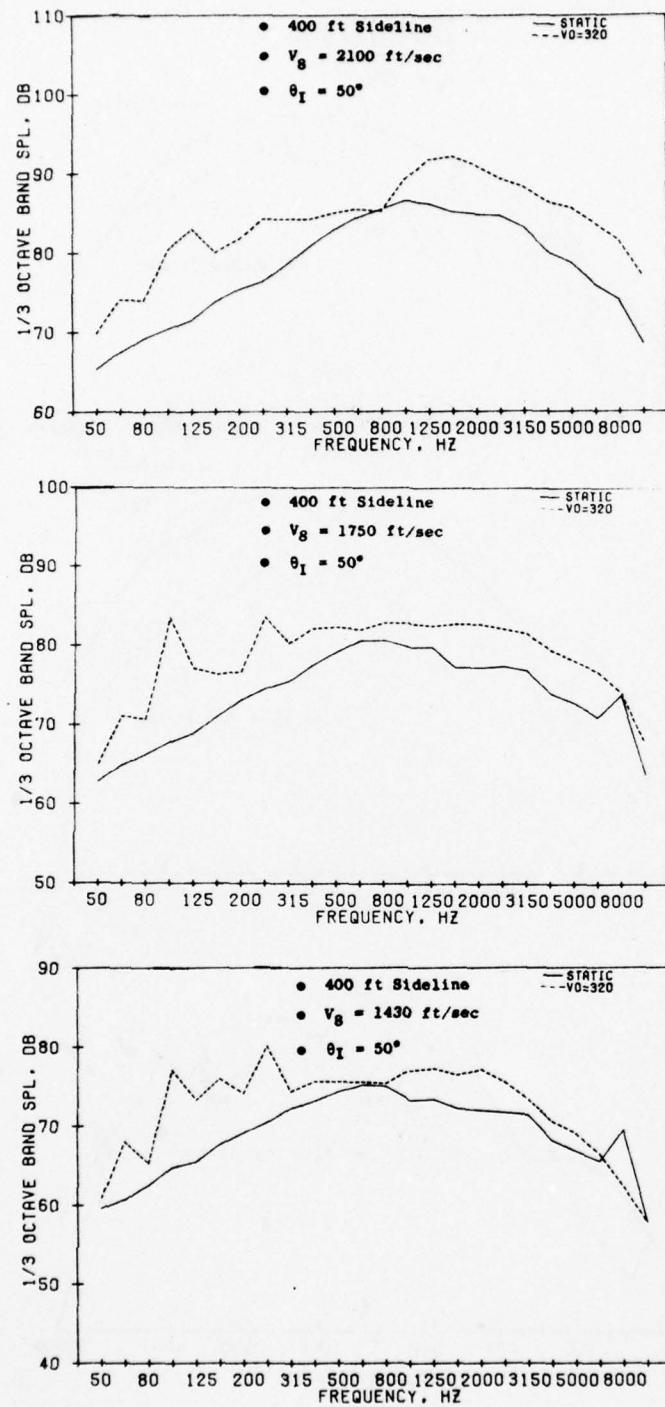


Figure 5-29. Learjet Conical Nozzle - 50° Spectra.

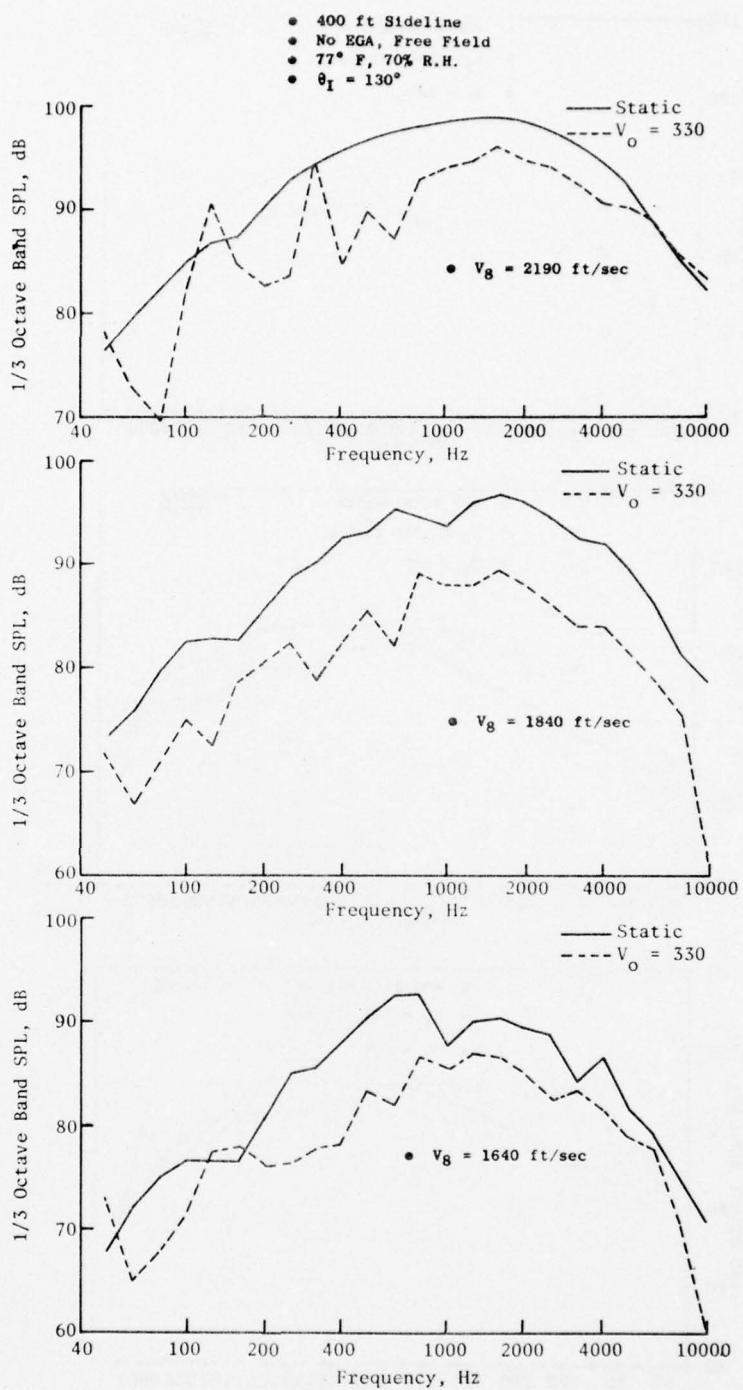


Figure 5-30. Learjet 8-Lobe Nozzle - 130° Spectra.

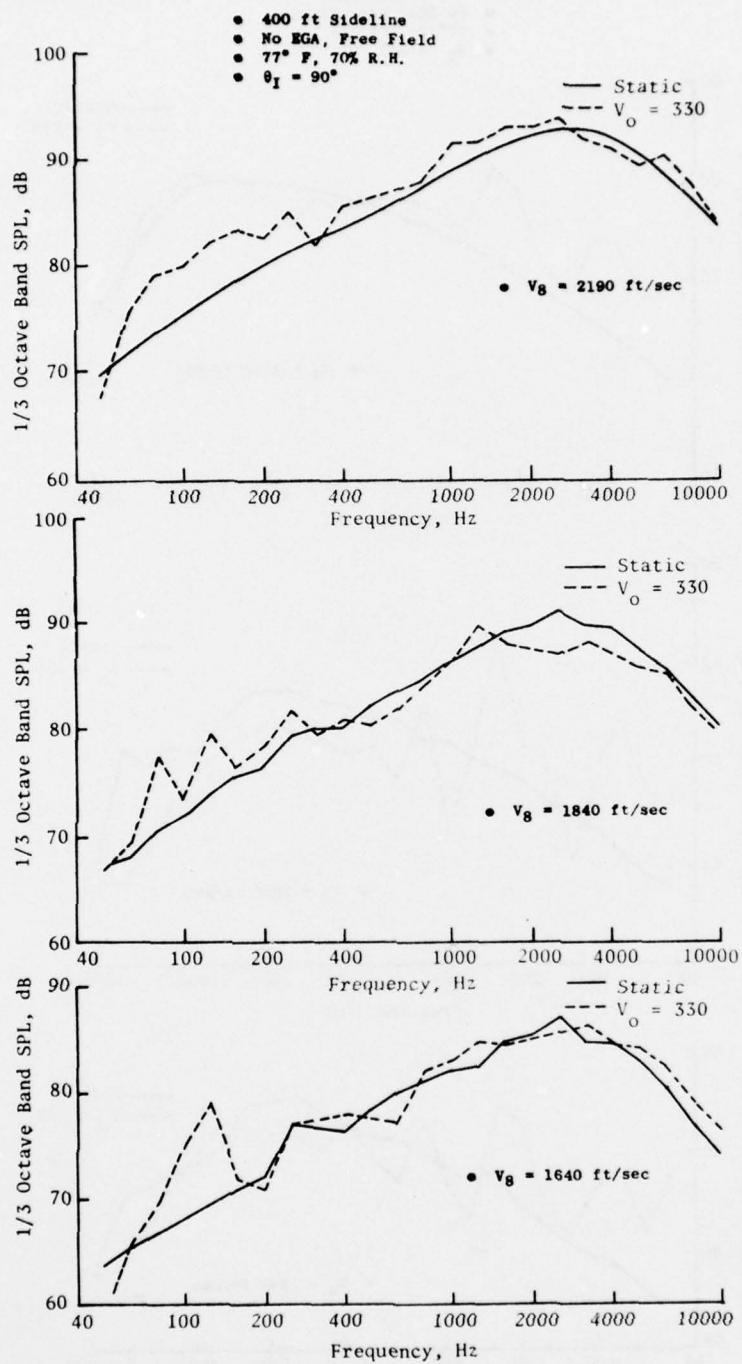


Figure 5-31. Learjet 8-Lobe Nozzle - 90° Spectra.

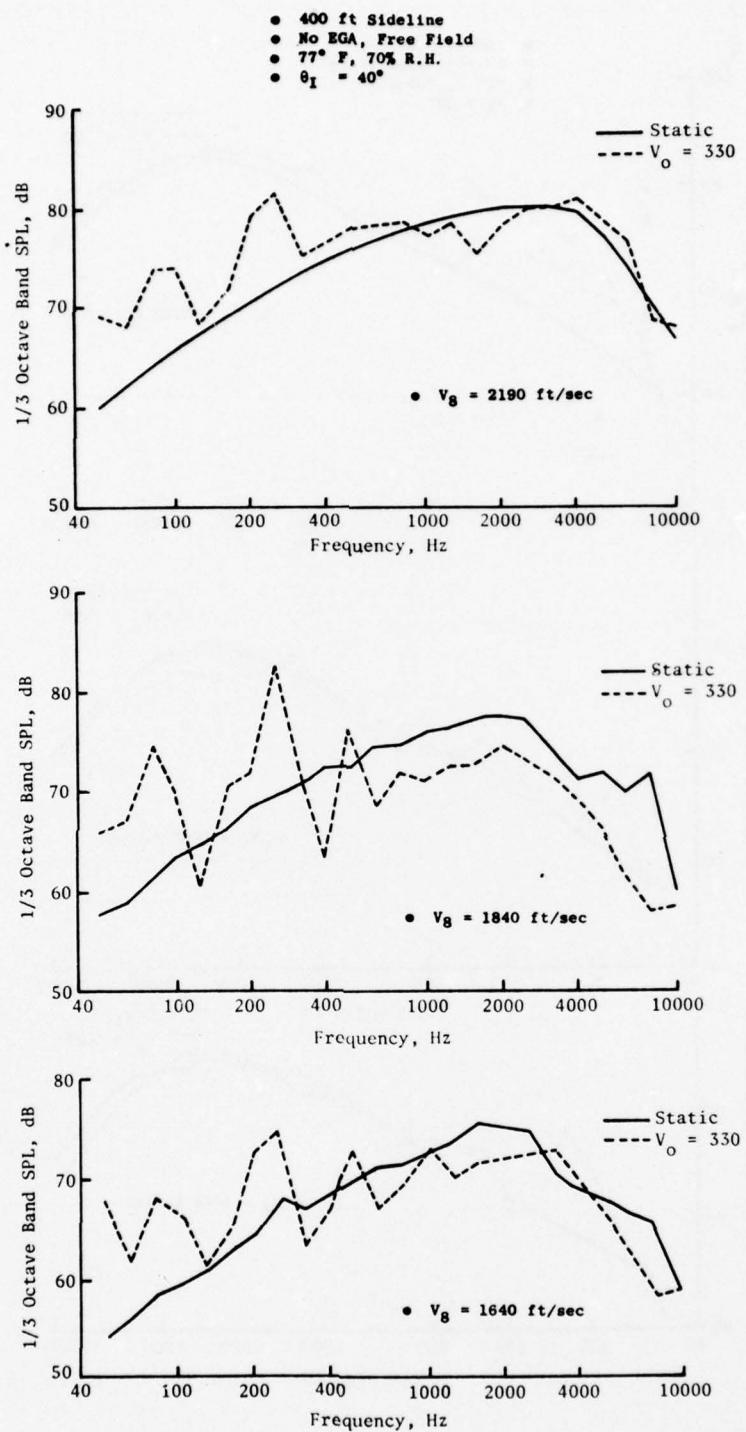


Figure 5-32. Learjet 8-Lobe Nozzle - 40° Spectra.

maximum noise angle. The conical nozzle spectra show a slight increase (or no change) from static to flight in the low frequency portion; whereas, the 8-lobe nozzle has static and flight spectra that are essentially equivalent. This point is emphasized, because of the classical theory which considers the 90° spectra to be indicative of pure source reduction. Based on these comparisons, over the range of conditions examined, there is a definite lack of agreement with the classical theory. This apparent paradox is examined further in Sections 5.2.4, 6.3, and 6.6.

Forward quadrant 50° and 40° acoustic angles were chosen for study for the conical and 8-lobe nozzle, respectively. In general, a substantial noise increase from static to flight is observed for the conical nozzle. The 8-lobe nozzle spectra show some reduction in the high frequencies, with some increase observed in the low frequency region. The exact amount of increase in the low frequency portion of the spectra is difficult to determine due to the significant impact of ground reflections on the 8-lobe nozzle data in this region.

In summary, PNL, OSAPL, directivity and spectra comparisons support the following conclusions for both the conical and 8-lobe nozzles:

- Significant reduction from static to flight is observed at the angle of maximum noise. This reduction varies as a function of jet velocity and nozzle configuration.
- At the 90° acoustic angle (indicative of pure source noise reduction), no change (or a slight increase) is observed.
- The forward quadrant trends are observed to be a function of nozzle type. The conical nozzle exhibits a substantial increase from static to flight, whereas the 8-lobe nozzle exhibits a slight reduction, or no change, depending on the condition being examined.

5.2 F-106 TEST PROGRAM

5.2.1 Configuration Description and Test Matrix

The F-106 acoustic testing was accomplished using NASA-Lewis Research Center's F-106 aircraft. This aircraft is used as a flying test bed for acoustic and aerodynamic research. The aircraft is equipped with two J85 engines, pod mounted one under each wing, as shown on Figure 5-33. Flyover testing was performed by setting the desired J85 operating condition on one of the engines only, and establishing the desired flight condition with the installed J75 powerplant. The J75 was throttled to flight idle while passing over the acoustic measuring arena.

Data from two types of nozzles were obtained using the NASA/F-106 aircraft. The baseline nozzle, shown on Figure 5-34, was tested during a joint NASA/General Electric flight test program performed at Selfridge AFB in November 1974. The 104-tube nozzle, Figure 5-35, was tested at Selfridge in

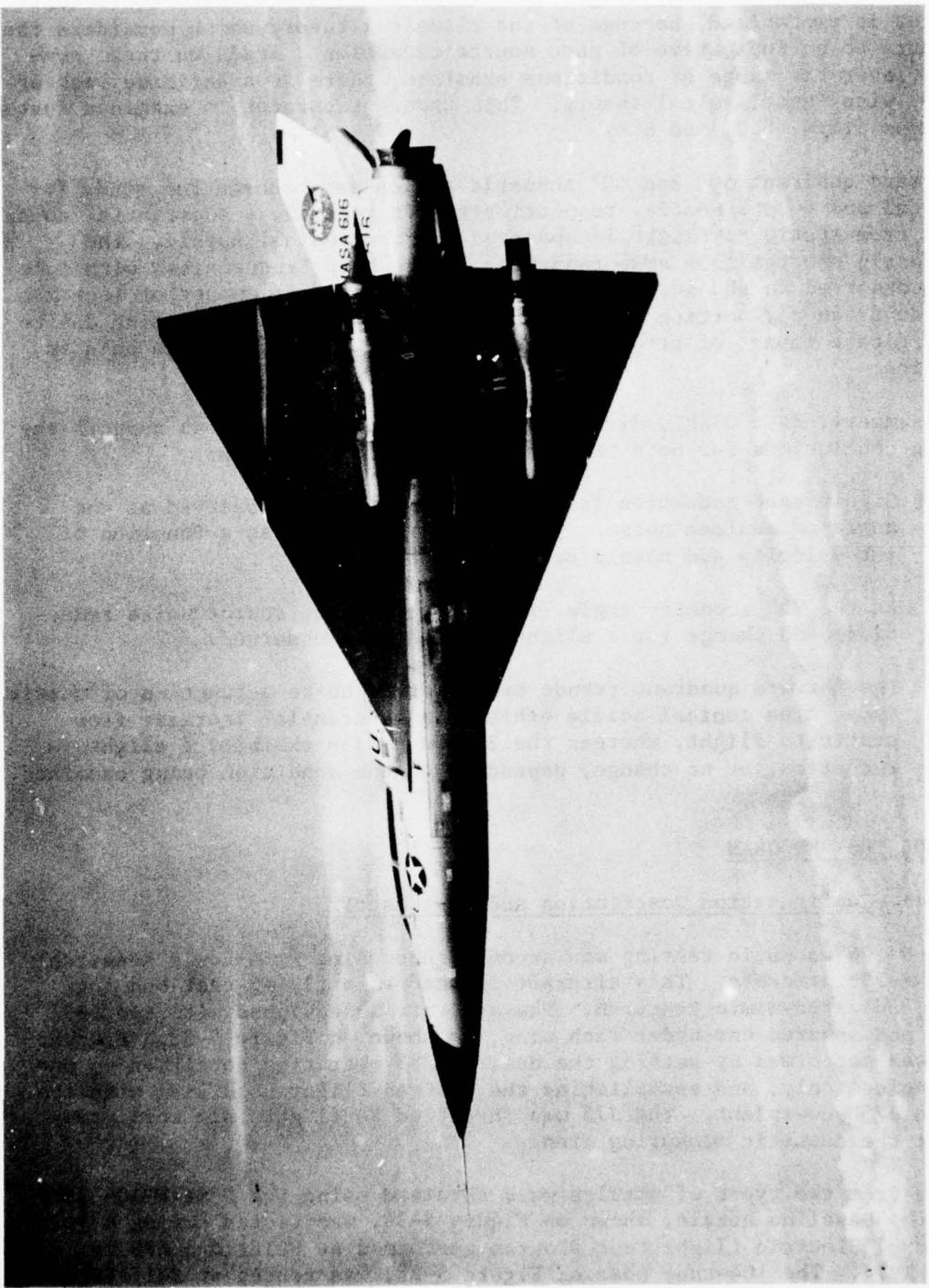


Figure 5-33. F-106 Test Vehicle; J75 Main Powerplant; J85's Under Wings.

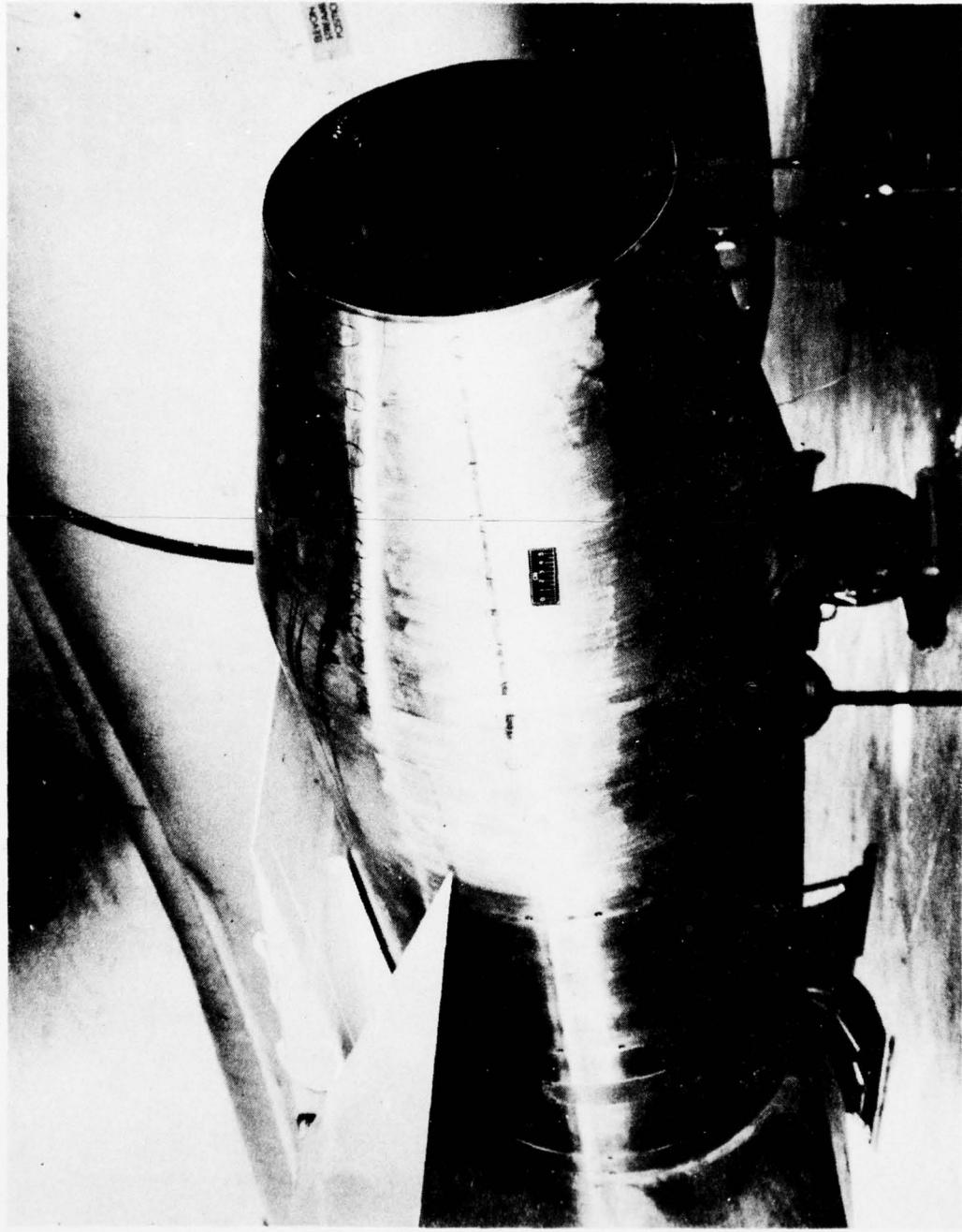


Figure 5-34. F-106 Flyover Test - Baseline Nozzle.

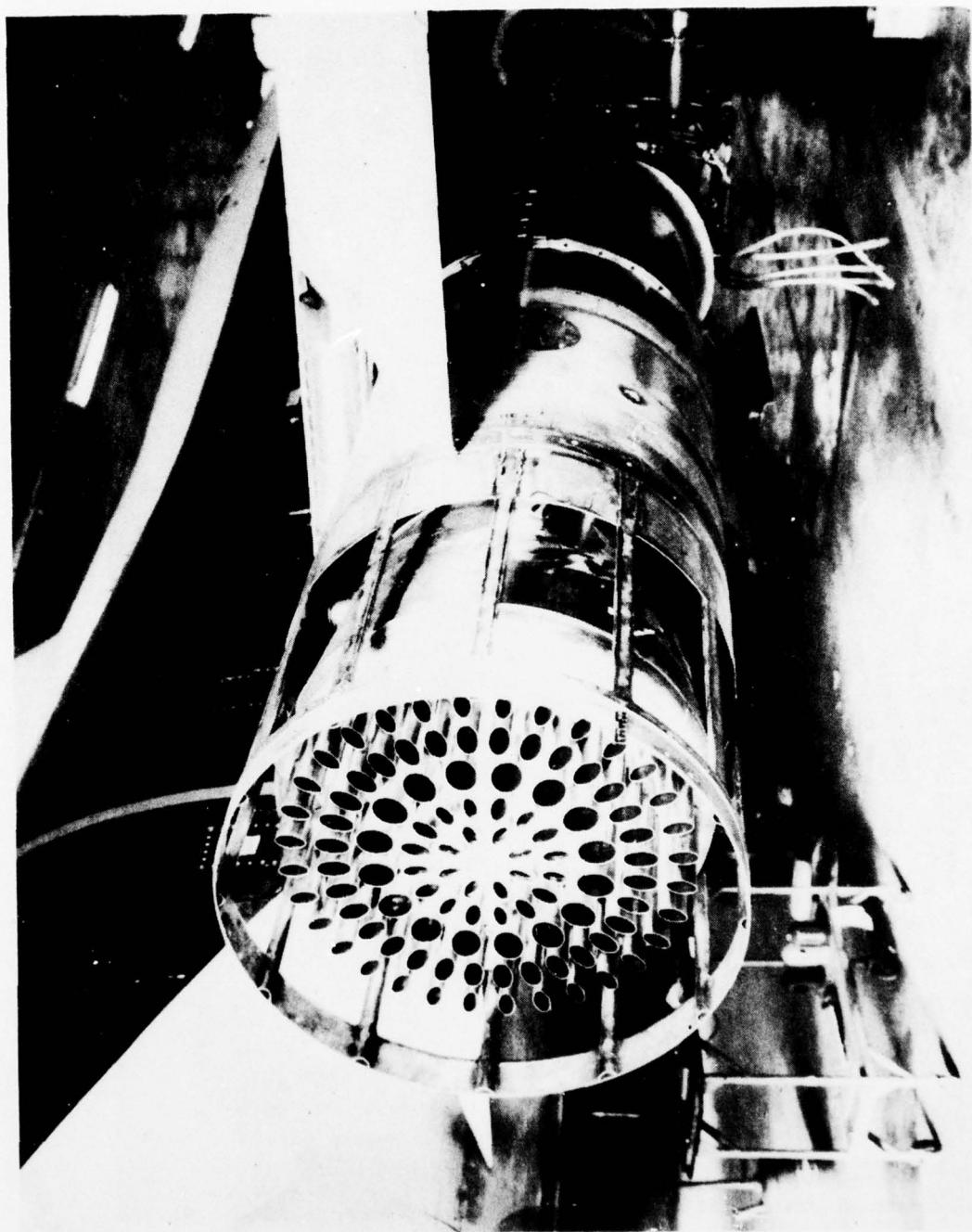


Figure 5-35. F-106 Flyover Test - 104-Tube Suppressor Nozzle.

early 1973 and the resulting data were provided to General Electric by NASA-Lewis for inclusion in this study. It should be noted that the baseline nozzle was not a true conical nozzle but a low-area-ratio, no-flow ejector system.

The test matrix for both the baseline and 104-tube nozzle tests are shown on Table 5-X. A minimum of two passes were conducted at each condition. In addition to the flight data, static ground run-up acoustic data were obtained at equivalent J85 operating conditions as a basis of assessing the static to flight effects.

5.2.2 Test Setup and Data Reduction

The microphone layout used by General Electric for the F-106/baseline nozzle testing was similar to that used for the Learjet conical nozzle discussed in Section 5.1.2, and is shown on Figure 5-36. Aircraft positioning information derived by photographic means, as well as aircraft instrumentation, were provided by NASA-Lewis; the procedures are described in Reference 36. Aircraft overhead time was determined by the fiber optics technique as applied to the Learjet test series discussed in Section 5.1.3. Data reduction procedures were performed duplicating those used for Learjet processing.

The ground reflective corrections were determined using the same procedure that was used for the Learjet Data. The baseline nozzle and 104-tube nozzle static corrections are presented on Tables 5-XI and 5-XII. The flight corrections for the baseline nozzle were the same as those used for the Learjet conical nozzle 400-ft test series, because the microphone array was duplicated. These corrections for the 4-ft and 20-ft microphones are presented on Tables 5-VI and 5-VII, respectively. The flight corrections for the 104-tube nozzle, for the 3.17-ft mike height, were determined using an analysis similar to the Learjet data. The corrections are presented on Table 5-XIII.

Data on the 104-tube nozzle were obtained by NASA-Lewis using the microphone setup shown on Figure 5-37. Aircraft location was determined by visual means and an electronic signal placed on tape for reference during data processing. Acoustic data processing used in this report was performed by General Electric from the data tape provided by NASA-Lewis, using methods described in Section 5.1.3.

5.2.3 F-106 Data Analysis

The objective of the F-106 flight test program was to provide a set of high quality flight data for a baseline and 104-tube nozzle. The details of how these data were acquired have been presented in the preceding sections. The F-106 program was chosen to complement the Learjet program because it was desirable to demonstrate the applicability of the inflight simulation technique for a complex geometry suppressor configuration such as the 104-tube

Table 5-X. NASA/F-106 Test Matrix.

• 104-Tube Suppressor Nozzle (Flight 224)

J85 %RPM	EXHAUST VELOCITY (FT/SEC)	AIRCRAFT ALTITUDE (FT)	AIRCRAFT VELOCITY (FT/SEC)
100	2170	300	420
96	1930	300	420
91	1670	300	420

• Baseline Nozzle

J85 %RPM	EXHAUST VELOCITY (FT/SEC)	AIRCRAFT ALTITUDE (FT)	AIRCRAFT VELOCITY (FT/SEC)
100	2170	300	420
96	1980	300	420
92	1750	300	420
88	1480	300	420
100	2170	500	420
96	1980	500	420
92	1750	500	420
88	1480	500	420

AD-A041 849

GENERAL ELECTRIC CO CINCINNATI OHIO AIRCRAFT ENGINE GROUP F/G 20/1
HIGH VELOCITY JET NOISE SOURCE LOCATION AND REDUCTION. TASK 4. --ETC(U)
FEB 77 W S CLAPPER, E J STRINGAS DOT-OS-30034

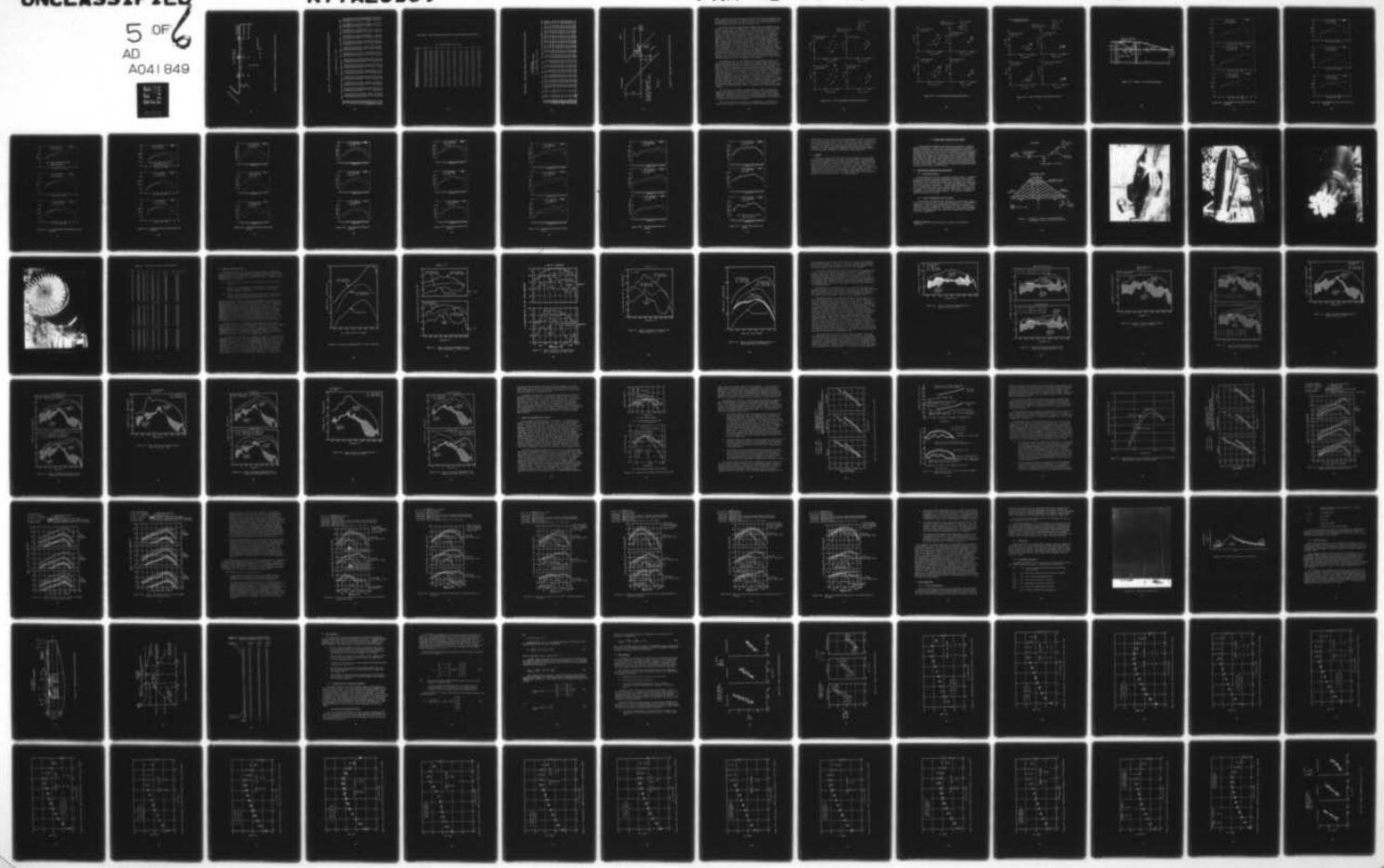
UNCLASSIFIED

5 OF 6
AD
A041 849

R77AEG189

FAA-RD-76-79-4

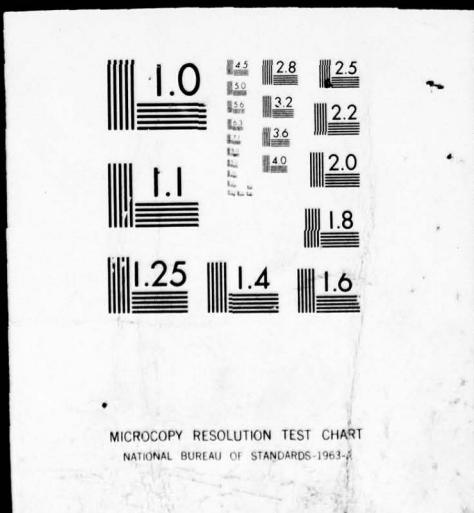
NL



SERIALIZED
5 OF

AD

A041 849



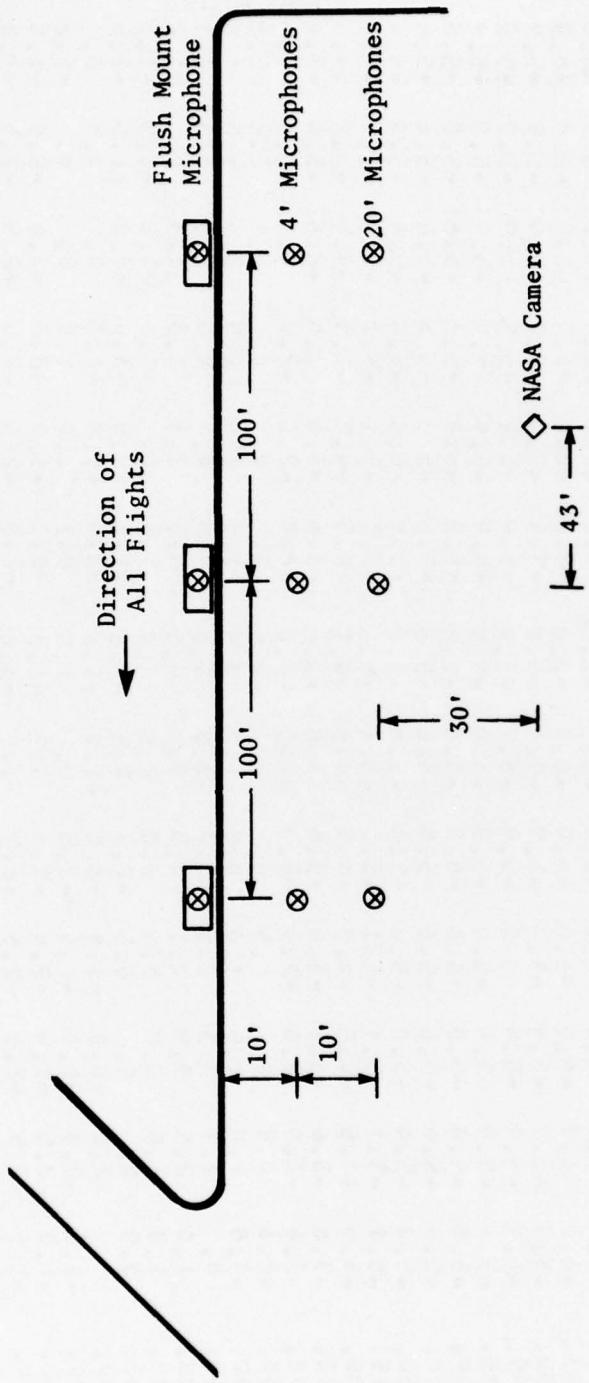


Figure 5-36. Microphone Setup - F-106 Baseline Nozzle Flyover Test.

Table 5-XI. F-106 Baseline Nozzle Static Ground Reflection Corrections.

 θ_1 , Acoustic Angle, re: Inlet

FREQ	160.0	150.0	140.0	130.0	120.0	110.0	100.0	90.0	80.0	70.0	60.0	50.0	40.0	30.0
50.	-6.0	-6.0	-6.0	-6.0	-6.0	-6.0	-6.0	-6.0	-6.0	-6.0	-6.0	-6.0	-6.0	-6.0
63.	-6.0	-6.0	-6.0	-6.0	-6.0	-6.0	-6.0	-6.0	-6.0	-6.0	-6.0	-6.0	-6.0	-6.0
80.	-5.9	-5.9	-5.9	-5.9	-5.9	-5.9	-5.9	-5.9	-5.9	-5.9	-5.9	-5.9	-5.9	-5.9
100.	-5.9	-5.9	-5.9	-5.9	-5.9	-5.9	-5.9	-5.9	-5.9	-5.9	-5.9	-5.9	-5.9	-5.9
125.	-5.9	-5.9	-5.9	-5.9	-5.9	-5.9	-5.9	-5.9	-5.9	-5.9	-5.9	-5.9	-5.9	-5.9
160.	-5.8	-5.8	-5.8	-5.8	-5.8	-5.8	-5.8	-5.8	-5.8	-5.8	-5.8	-5.8	-5.8	-5.8
200.	-5.6	-5.6	-5.6	-5.6	-5.6	-5.6	-5.6	-5.6	-5.6	-5.6	-5.6	-5.6	-5.6	-5.6
250.	-5.4	-5.4	-5.4	-5.4	-5.4	-5.4	-5.4	-5.4	-5.4	-5.4	-5.4	-5.4	-5.4	-5.4
315.	-5.1	-5.1	-5.1	-5.1	-5.1	-5.1	-5.1	-5.1	-5.1	-5.1	-5.1	-5.1	-5.1	-5.1
400.	-4.5	-4.5	-4.5	-4.5	-4.5	-4.5	-4.5	-4.5	-4.5	-4.5	-4.5	-4.5	-4.5	-4.5
500.	-3.6	-3.6	-3.6	-3.6	-3.6	-3.6	-3.6	-3.6	-3.6	-3.6	-3.6	-3.6	-3.6	-3.6
630.	-2.0	-2.0	-2.0	-2.0	-2.0	-2.0	-2.0	-2.0	-2.0	-2.0	-2.0	-2.0	-2.0	-2.0
800.	-0.5	0.	0.5	0.	0.	0.	0.	0.	0.	0.	0.	0.	0.	0.
1000.	-0.8	1.0	1.5	1.0	0.8	1.2	0.8	1.5	2.0	2.5	3.0	3.5	1.8	2.5
1250.	0.	1.7	3.3	2.5	3.2	3.0	3.3	4.5	4.5	4.0	4.3	3.3	1.1	1.0
1600.	1.0	2.5	3.9	4.1	4.5	5.0	4.5	4.5	2.5	1.3	0.	-1.2	-1.3	-1.3
2000.	1.0	1.5	3.0	3.5	2.8	2.5	2.8	1.5	0.	-1.5	-1.5	-1.5	-0.8	-0.8
2500.	0.5	0.	0.	0.5	0.5	0.5	0.5	-1.5	-2.5	-3.0	-2.0	-1.5	-1.5	-0.5
3150.	0.	-2.0	-0.8	-1.8	-2.8	-1.0	-1.8	-2.0	-1.0	-1.3	0.	0.5	0.	0.7
4000.	-0.5	-2.0	-1.0	-2.0	-2.5	0.	-1.6	0.7	1.0	1.0	0.	-1.2	-1.7	-1.7
5000.	-1.0	-2.5	-1.5	-2.0	-1.5	0.5	-1.0	-0.7	-1.0	-2.2	-3.0	-2.0	-1.5	-1.8
6300.	-1.5	-2.5	-2.5	-2.5	-2.5	-1.5	-3.0	-2.8	-2.5	-2.5	-2.5	-2.5	-2.5	-2.5
8000.	-2.5	-2.5	-2.5	-2.5	-2.5	-2.5	-2.5	-2.5	-2.5	-2.5	-2.5	-2.5	-2.5	-2.5
10000.	-2.5	-2.5	-2.5	-2.5	-2.5	-2.5	-2.5	-2.5	-2.5	-2.5	-2.5	-2.5	-2.5	-2.5

Table 5-XII. F-106 104-Tube Nozzle Static Ground Reflection Corrections.

Frequency	θ_I , Acoustic Angle, re: Inlet									
	80.0	90.0	100.0	110.0	120.0	130.0	140.0	150.0	160.0	170.0
50	-6.0	-6.0	-6.0	-6.0	-6.0	-6.0	-6.0	-6.0	-6.0	-6.0
63	-6.0	-6.0	-6.0	-6.0	-6.0	-6.0	-6.0	-6.0	-6.0	-6.0
80	-5.9	-5.9	-5.9	-5.9	-5.9	-5.9	-5.9	-5.9	-5.9	-5.9
100	-5.9	-5.9	-5.9	-5.9	-5.9	-5.9	-5.9	-5.9	-5.9	-5.9
125	-5.9	-5.9	-5.9	-5.9	-5.9	-5.9	-5.9	-5.9	-5.9	-5.9
160	-5.8	-5.8	-5.8	-5.8	-5.8	-5.8	-5.8	-5.8	-5.8	-5.8
200	-5.6	-5.6	-5.6	-5.6	-5.6	-5.6	-5.6	-5.6	-5.6	-5.6
250	-5.4	-5.4	-5.4	-5.4	-5.4	-5.4	-5.4	-5.4	-5.4	-5.4
315	-5.1	-5.1	-5.1	-5.1	-5.1	-5.1	-5.1	-5.1	-5.1	-5.1
400	-4.5	-4.5	-4.5	-4.5	-4.5	-4.5	-4.5	-4.5	-4.5	-4.5
500	-3.6	-3.6	-3.6	-3.6	-3.6	-3.6	-3.6	-3.6	-3.6	-3.6
630	-1.5	-2.5	-1.5	-2.0	-2.0	0.	0.	-2.0	-2.0	-3.6
800	-2.0	-1.0	-1.0	0.	0.	0.	0.5	1.0	1.0	0.
1000	0.	0.	1.5	2.0	0.5	2.0	4.0	3.5	3.0	0.
1250	3.0	0.5	2.5	6.0	3.0	5.0	3.0	3.5	3.0	1.5
1600	3.5	3.5	4.5	5.0	5.0	4.0	1.0	2.0	0.	3.5
2000	3.5	4.0	0.	0.5	0.	-2.0	-4.0	-1.5	-5.0	-0.5
2500	2.0	0.	-2.5	-4.0	-2.5	-3.0	-6.5	-4.5	-6.5	-1.6
3150	-2.0	-2.0	-5.0	-4.5	-4.5	-5.0	-5.0	-3.5	-5.0	-3.0
4000	-1.5	-2.5	-2.0	0.	-2.5	-0.5	-1.0	0.	-2.0	-1.0
5000	2.5	1.0	1.5	1.0	1.5	1.5	-1.5	-2.5	-2.5	-1.0
6300	0.	0.	0.	-1.5	-1.0	-2.5	-2.5	-2.5	-2.5	-1.5
8000	-1.0	-1.0	-1.0	-1.5	-1.5	-2.5	-2.5	-2.5	-2.5	-2.5
10000	-1.0	-1.0	-1.0	-1.5	-1.5	-2.5	-2.5	-2.5	-2.5	-2.5

Table 5-XIII. F-106 104-Tube Nozzle Flight Ground Reflection Corrections.

- 300 Altitude
- 3.17 Microphone Reight
- θ_1 , Acoustic Angle, re: Inlet

FRFG	100.0	200.0	300.0	400.0	500.0	600.0	700.0	800.0	900.0	1000.0	1100.0	1200.0	1300.0	1400.0	1500.0	1600.0
50.	0.	0.	-25.2	-31.5	-3.0	-2.7	-0.4	0.	-0.	-1.0	-2.0	-2.8	-1.8	-0.5	-2.2	-5.2
63.	0.	0.	-4.5	-5.2	-1.8	0.	1.0	1.6	2.0	1.0	-2.2	-6.0	-4.4	-4.4	-5.2	
80.	0.	0.	-3.3	0.	-0.4	4.2	4.5	4.6	6.4	8.5	8.0	3.0	0.8	-4.8	-5.2	
100.	0.	0.	-2.5	-1.5	1.6	1.6	0.5	1.4	0.5	3.0	4.0	5.6	4.2	2.5	-0.7	-1.7
125.	0.	0.	-6.0	-7.2	-6.8	-8.2	-9.2	-6.5	-8.0	-6.0	-6.8	-2.8	-1.2	-1.6	-2.4	-6.5
160.	0.	0.	-4.7	-3.0	-8.0	-9.2	-7.2	-4.5	-4.0	-4.6	-3.6	-0.5	5.2	8.0	0.	
200.	0.	0.	-4.6	-5.0	-5.2	-5.2	-4.8	-6.4	-6.0	-4.5	-6.6	-3.0	-6.2	6.0		
250.	0.	0.	-0.8	-3.0	-2.8	-2.8	-2.2	-1.0	1.2	1.0	-1.8	-3.5	-4.3	-5.2	1.0	4.0
315.	0.	0.	-1.6	-2.8	-1.8	-1.6	-1.0	-2.6	-4.0	-2.0	-1.0	3.3	1.2	-4.0	-3.2	5.0
400.	0.	0.	-2.7	-2.0	-2.2	-1.9	-1.2	-1.0	-0.5	-3.2	-3.3	-3.0	-3.0	-2.5	-4.0	1.0
500.	0.	0.	-1.0	-2.5	-1.2	-1.6	-1.5	-7.0	-5.0	-4.0	-3.2	-2.0	0.	-4.0	-2.2	-1.5
630.	0.	0.	-3.0	-1.8	-2.0	-1.8	-2.0	-3.0	-2.5	-2.5	-2.6	-3.3	-3.0	-2.7	-1.3	0.
800.	0.	0.	-2.0	-4.5	-2.0	-1.4	-3.0	-2.5	-3.0	-3.0	-3.0	-3.4	-2.0	-3.0	-1.8	-1.5
1000.	0.	0.	-2.5	-2.5	-2.2	-2.2	-2.2	-3.5	-2.5	-3.0	-3.0	-2.5	-2.5	-2.0	-2.5	-2.2
1250.	0.	0.	-2.5	-2.5	-2.5	-2.5	-2.5	-2.5	-2.5	-2.5	-2.5	-2.5	-2.5	-2.5	-2.5	-2.5
1600.	0.	0.	-2.5	-2.5	-2.5	-2.5	-2.5	-2.5	-2.5	-2.5	-2.5	-2.5	-2.5	-2.5	-2.5	-2.5
2000.	0.	0.	-2.5	-2.5	-2.5	-2.5	-2.5	-2.5	-2.5	-2.5	-2.5	-2.5	-2.5	-2.5	-2.5	-2.5
2500.	0.	0.	-2.5	-2.5	-2.5	-2.5	-2.5	-2.5	-2.5	-2.5	-2.5	-2.5	-2.5	-2.5	-2.5	-2.5
3150.	0.	0.	-2.5	-2.5	-2.5	-2.5	-2.5	-2.5	-2.5	-2.5	-2.5	-2.5	-2.5	-2.5	-2.5	-2.5
4000.	0.	0.	-2.5	-2.5	-2.5	-2.5	-2.5	-2.5	-2.5	-2.5	-2.5	-2.5	-2.5	-2.5	-2.5	-2.5
5000.	0.	0.	-2.5	-2.5	-2.5	-2.5	-2.5	-2.5	-2.5	-2.5	-2.5	-2.5	-2.5	-2.5	-2.5	-2.5
6300.	0.	0.	-2.5	-2.5	-2.5	-2.5	-2.5	-2.5	-2.5	-2.5	-2.5	-2.5	-2.5	-2.5	-2.5	-2.5
8000.	0.	0.	-2.5	-2.5	-2.5	-2.5	-2.5	-2.5	-2.5	-2.5	-2.5	-2.5	-2.5	-2.5	-2.5	-2.5
10000.	0.	0.	-2.5	-2.5	-2.5	-2.5	-2.5	-2.5	-2.5	-2.5	-2.5	-2.5	-2.5	-2.5	-2.5	-2.5

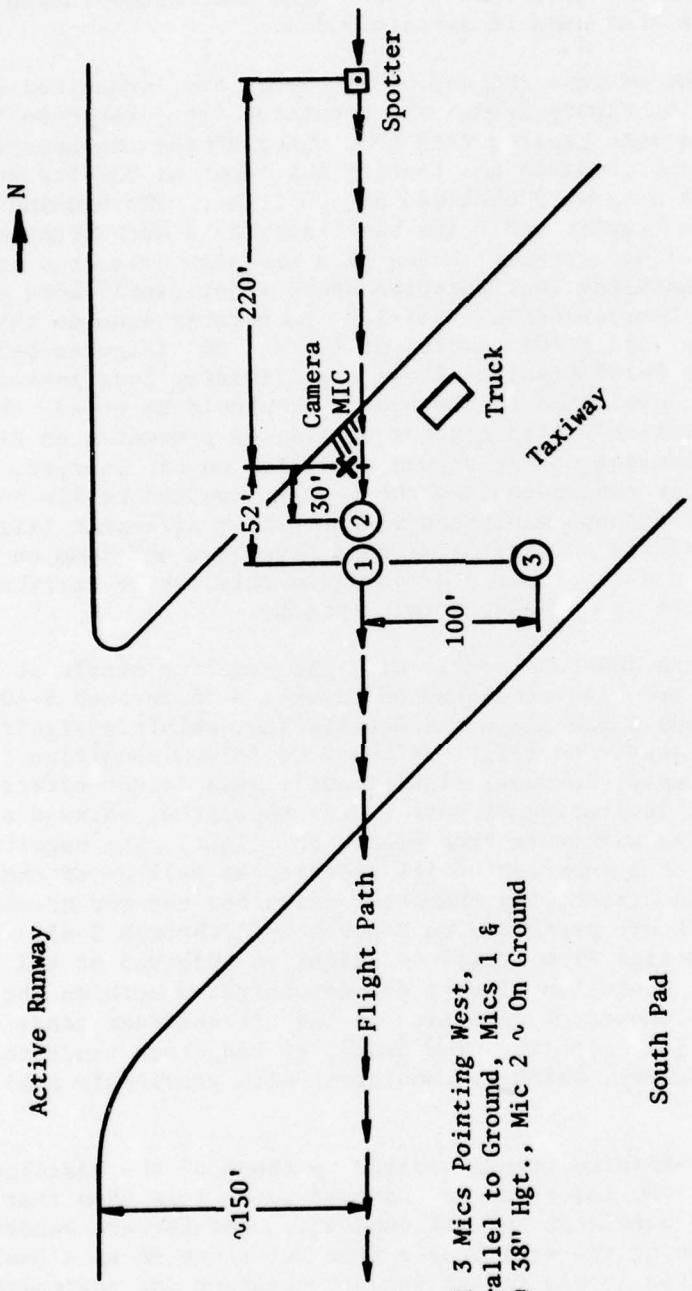


Figure 5-37. NASA Sound Field for F-106/104-Tube Nozzle Test.

nozzle. The test data presented in this section will show that changes in the noise signature from static to flight conditions for the baseline and 104-tube configurations have distinctly different trends. The data presentation will follow the same format as that used in Section 5.1.4.

The static and flight maximum PNL and OASPL levels are summarized as a function of jet velocity on Figure 5-38. The reduction from static to flight for the conical nozzle is much greater than that observed for the Learjet. This is somewhat consistent, because the Learjet was flown at 330 ft/sec; whereas, the F-106 flight data were obtained at 420 ft/sec. To examine the variance (if any) between Learjet and F-106 baselines, data were obtained flying the Learjet at $V_0 = 450$ ft/sec. These data are also presented on Figure 5-38. The F-106 baseline configuration shows significantly more peak angle reduction than the Learjet conical nozzle. To further examine this point, compare the Learjet and F-106 results at 90° and 50° (Figures 5-39 and 5-40, respectively). The F-106 baseline shows significantly less increase relative to static noise level than the Learjet. It should be noted that this configuration is a variable-flap ejector nozzle, as presented on Figure 5-41, and is not a true conical nozzle as was evaluated on the Learjet. Based on these comparisons, it is concluded that the Learjet conical nozzle and F-106 baseline configuration have exhibited significantly different flight effects at the cycle condition where similar data have been obtained on both systems. No conclusions can be properly drawn since this may be attributed to the differences between the two exhaust nozzle systems.

The comparisons of the 104-tube nozzle with the baseline nozzle at the three angles of interest are also presented on Figures 5-38 through 5-40. The 104-tube nozzle maximum noise angle characteristics exhibit a significant amount of reduction from static to flight at the 2100 ft/sec condition. As the jet velocity is decreased, however, significantly less flight effect is observed. The 90° angle, indicative of pure source reduction, shows a significant reduction in the noise signature from static to flight. The magnitude of reduction is observed to be a function of jet velocity as well as of exhaust nozzle configuration. The directivity characteristics for the two nozzles on the basis of PNL and OASPL are presented on Figures 5-42 through 5-45. In general, significant reduction from static to flight is observed at all angles for the baseline nozzle. Equivalent levels are demonstrated both on the basis of PNL and of OASPL. The amount of reduction in the aft quadrant tends to decrease with decreasing jet velocity. The amount of reduction tends to decrease in the forward quadrant, which is consistent with previously published results.

The 104-tube nozzle exhibits trends similar to those of the baseline nozzle. The magnitude of the reduction is observed to be less than that exhibited by the baseline nozzle in the aft quadrant. The forward quadrant trends were assessed by using the static data from Reference 36 as a basis. In general, the flight noise levels in the forward quadrant are equivalent to or greater than the static noise levels.

The spectra comparisons for the two configurations are presented on Figure 5-46 through 5-51. The maximum noise angle flight spectra show a

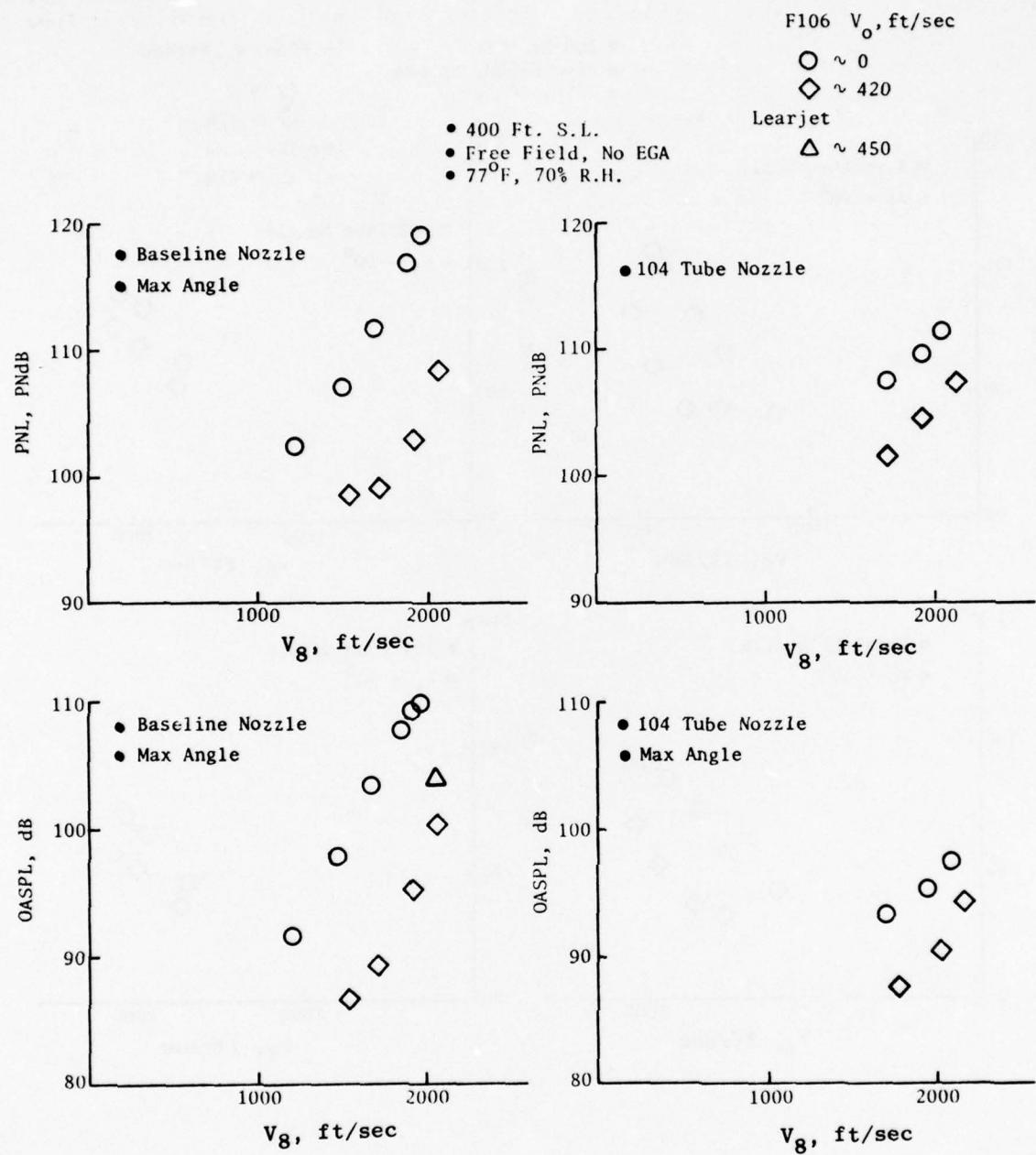


Figure 5-38. F-106 Peak OASPL and PNL Characteristics.

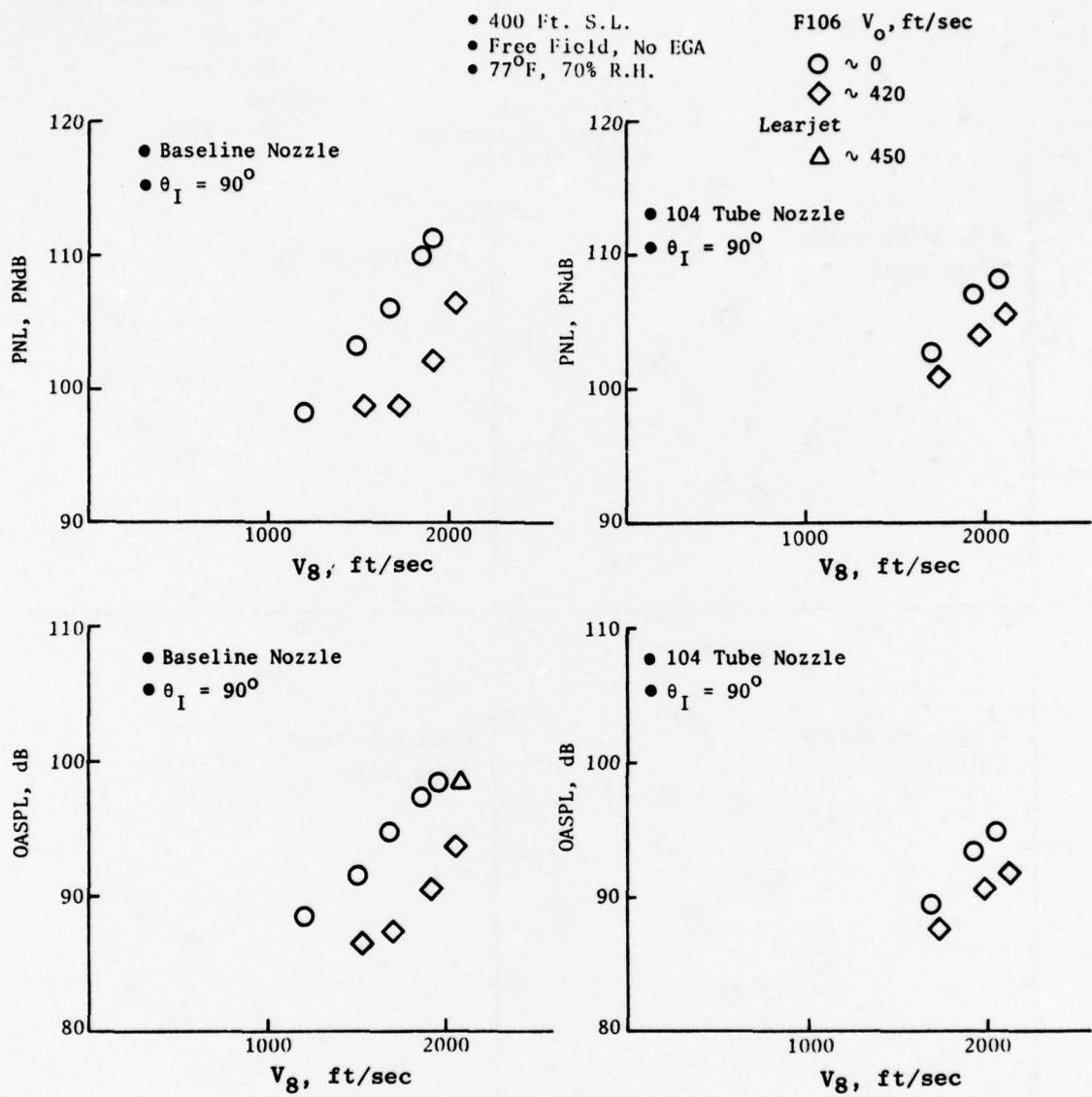


Figure 5-39. F-106 90° OASPL and PNL Characteristics.

Note: 104-Tube Static Data
Based on Reference 37

- 400 Ft. S.L.
- Free Field, No EGA
- 77°F, 70% R.H.

F106 V_o , ft/sec

$\circ \sim 0$

$\diamond \sim 420$

Learjet

$\Delta \sim 450$

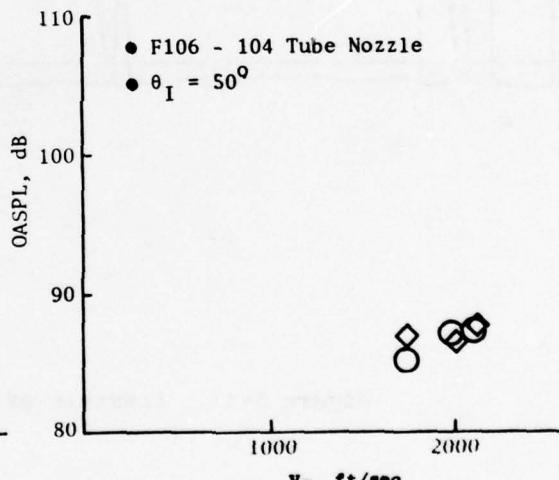
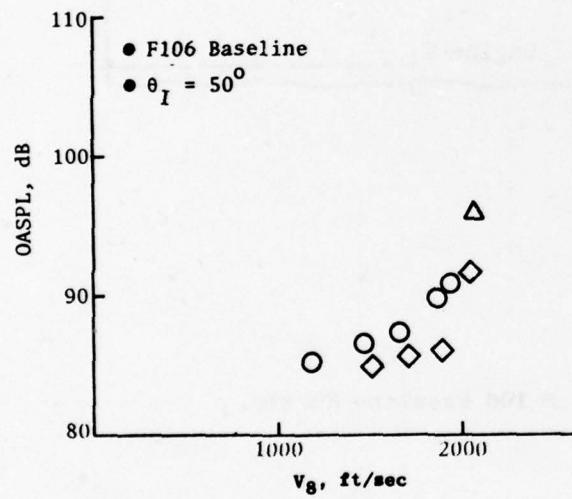
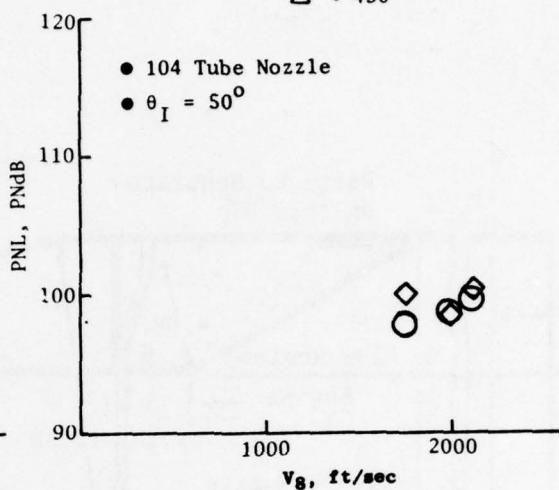
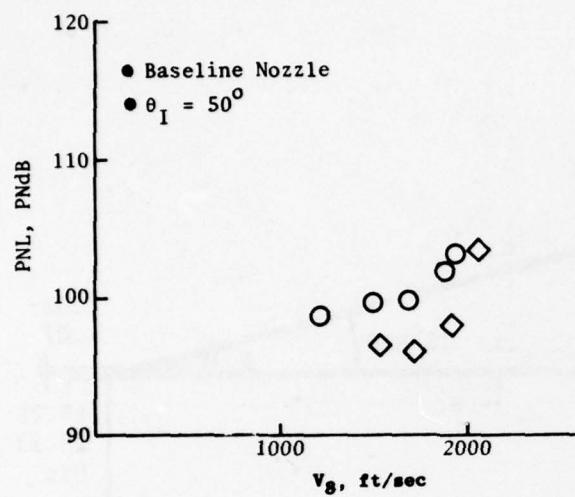


Figure 5-40. F-106 50° OASPL and PNL Characteristics.

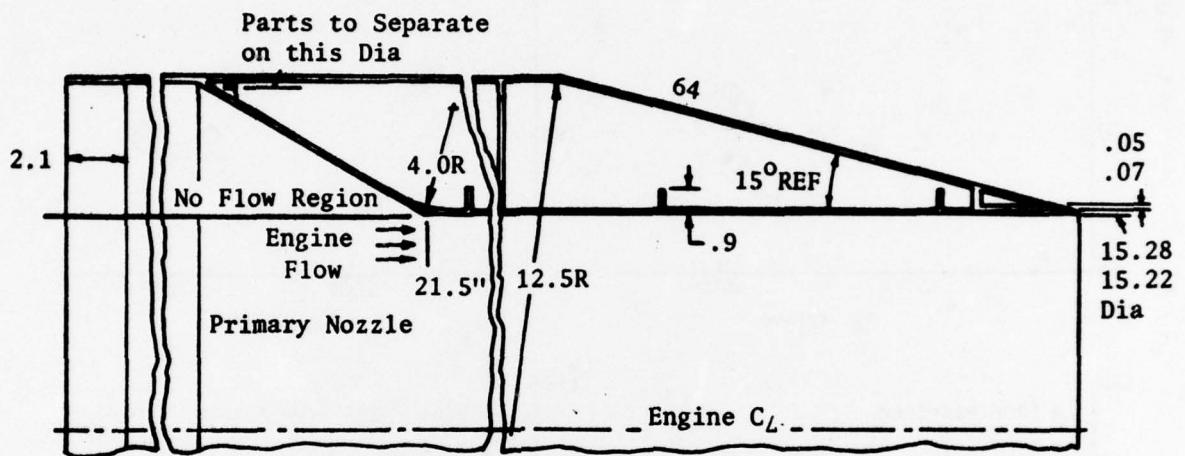


Figure 5-41. Scematic of F-106 Baseline Nozzle.

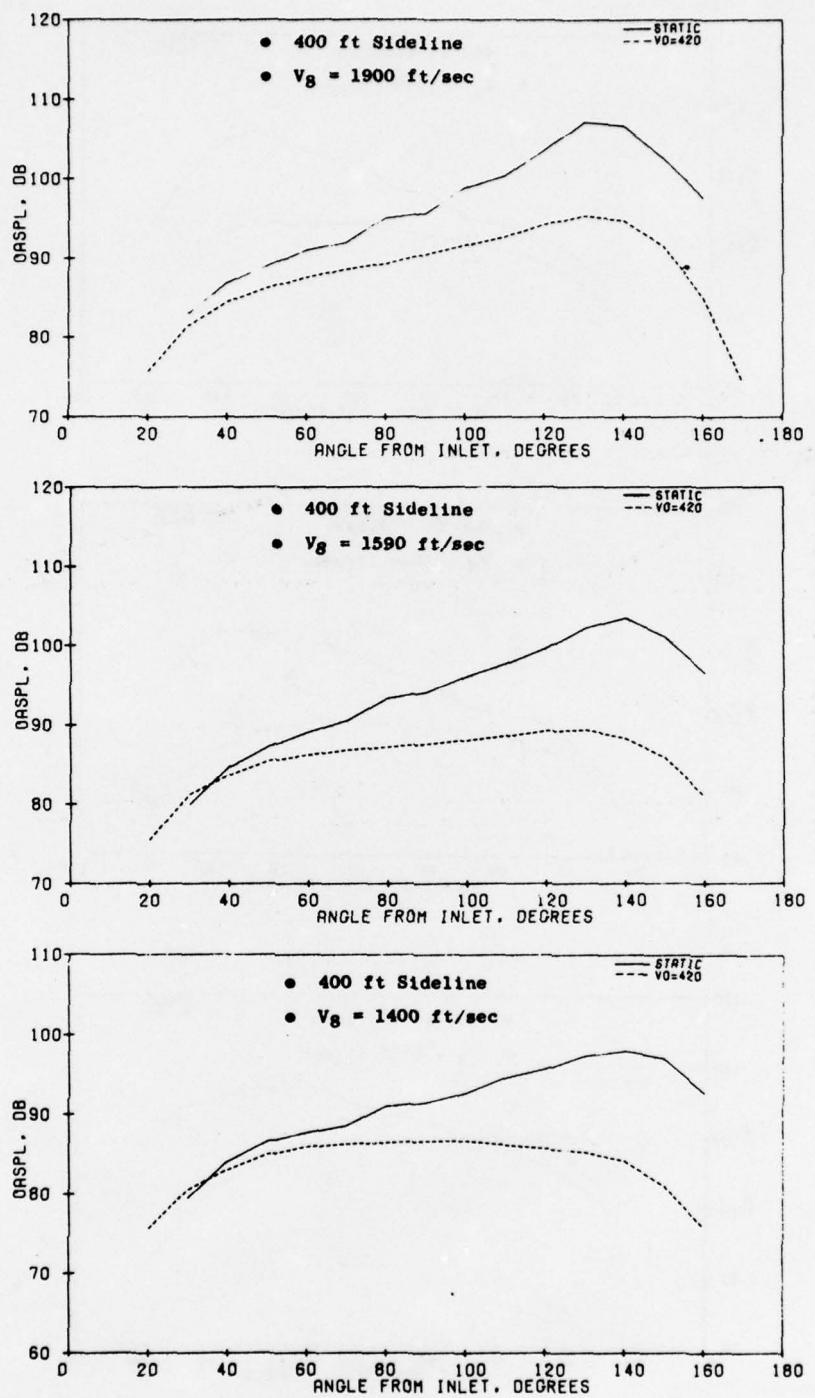


Figure 5-42. F-106 Baseline Nozzle OASPL Directivity Patterns.

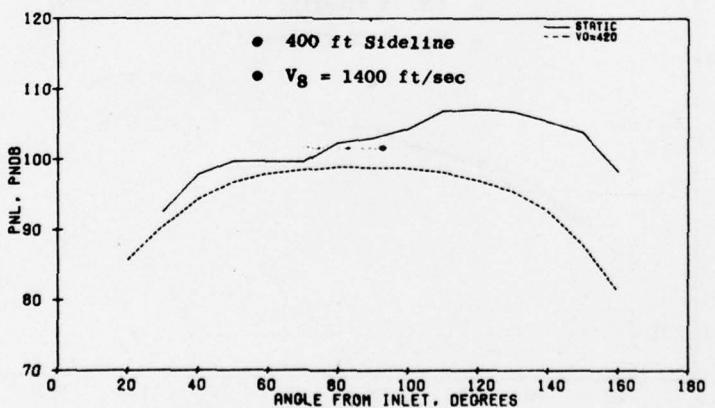
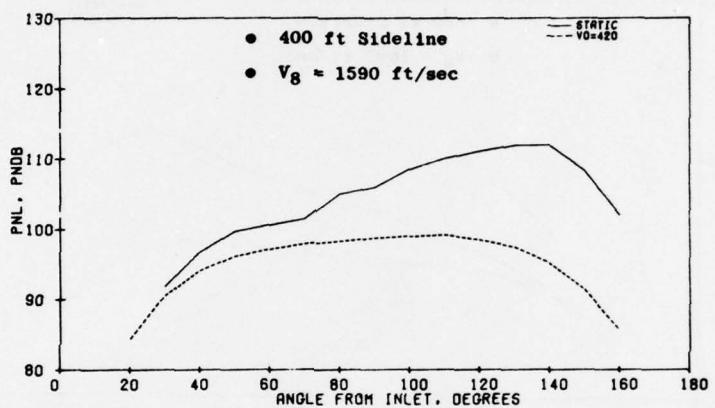
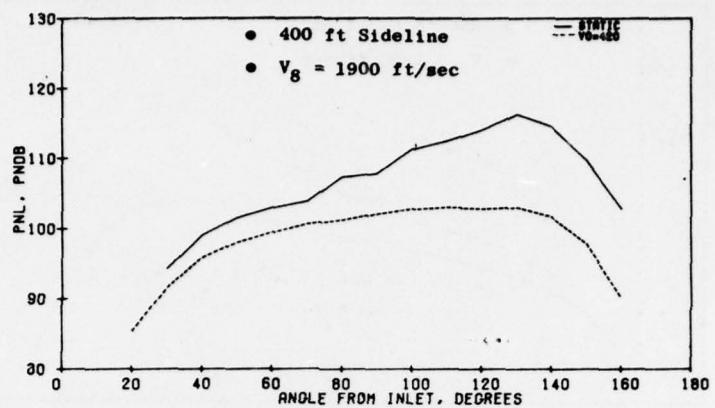


Figure 5-43. F-106 Baseline Nozzle PNL Directivity Patterns.

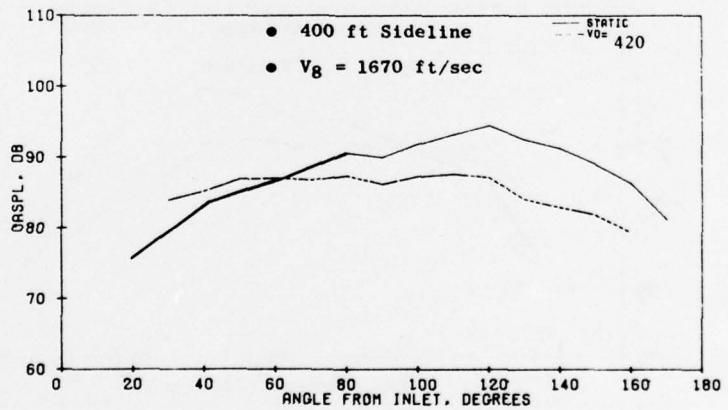
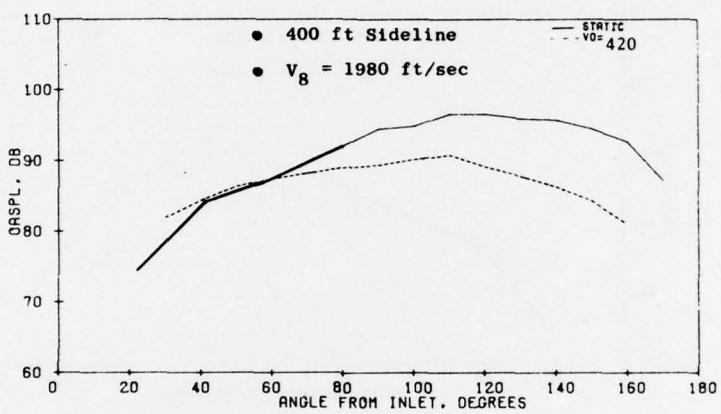
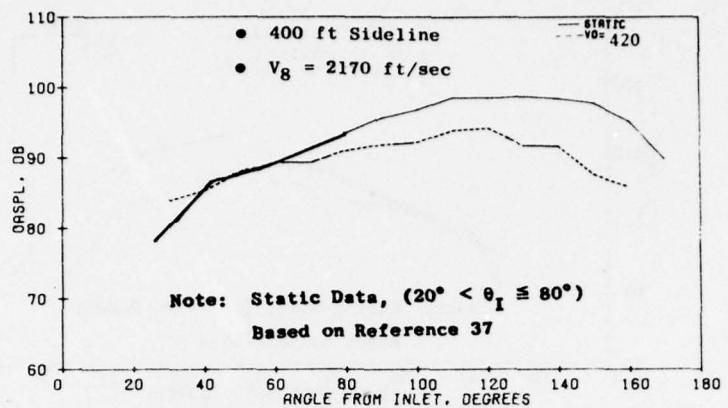


Figure 5-44. F-106/104-Tube Nozzle OASPL Directivity Patterns.

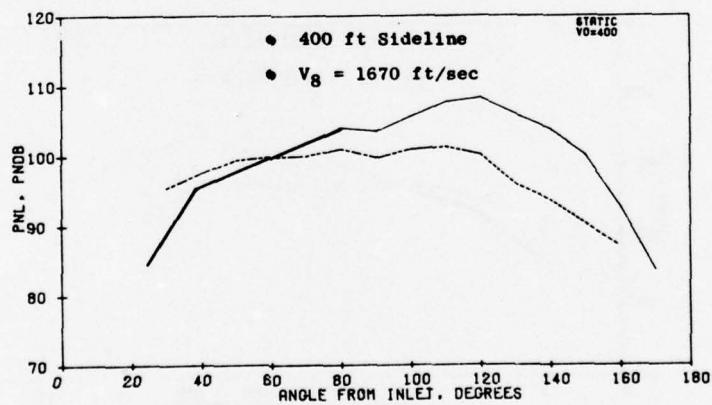
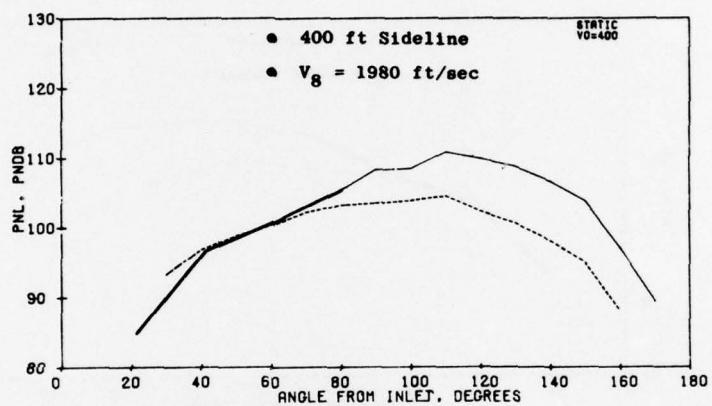
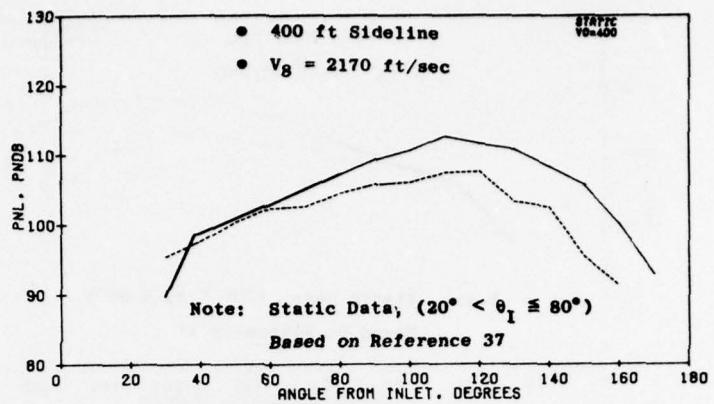


Figure 5-45. F-106/104-Tube Nozzle PNL Directivity Patterns.

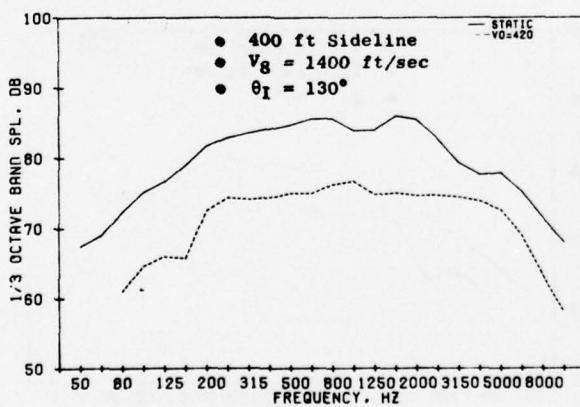
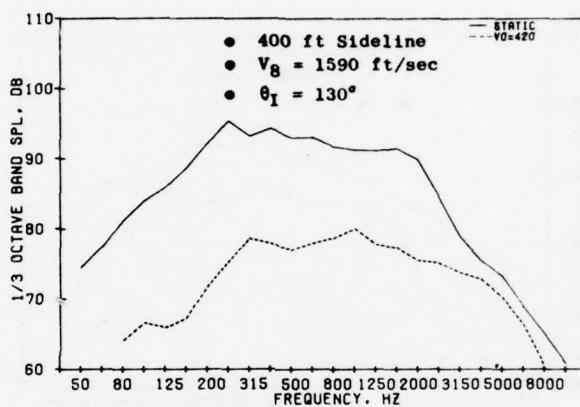
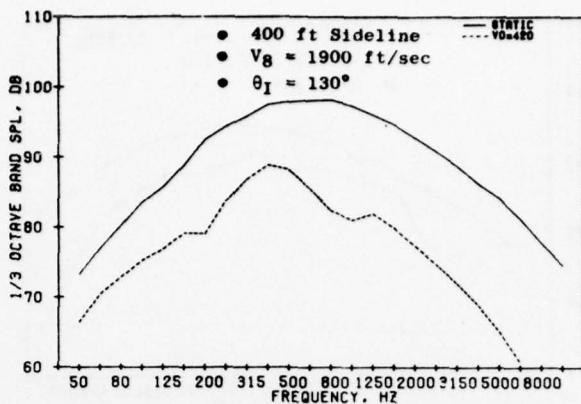


Figure 5-46. F-106 Baseline Nozzle Max Angle Spectra.

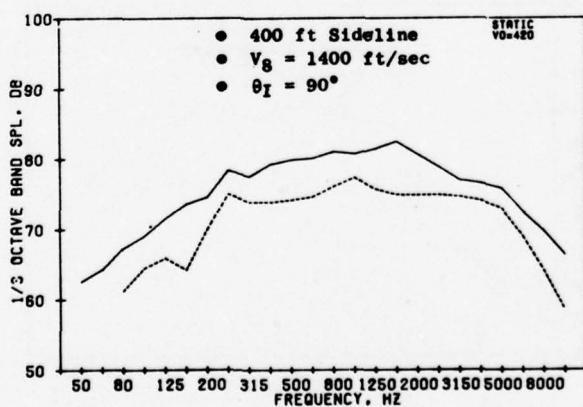
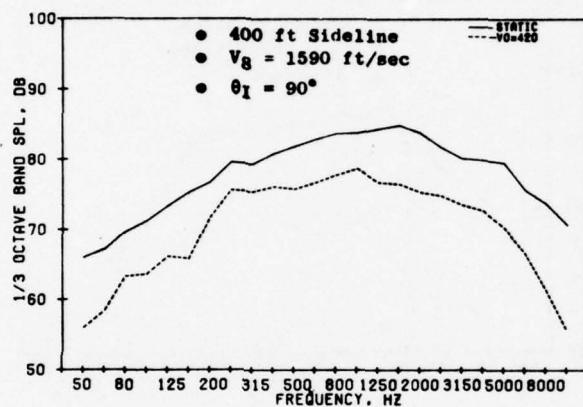
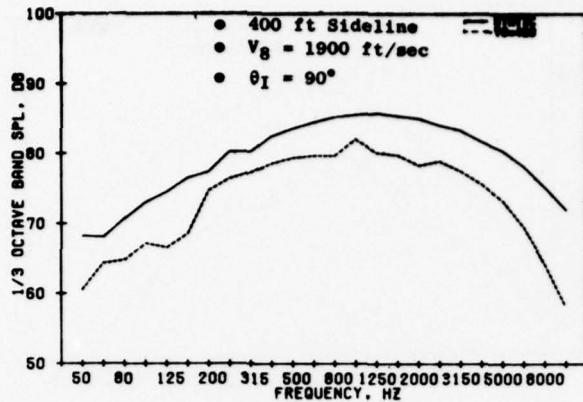


Figure 5-47. F-106 Baseline Nozzle 90° Spectra.

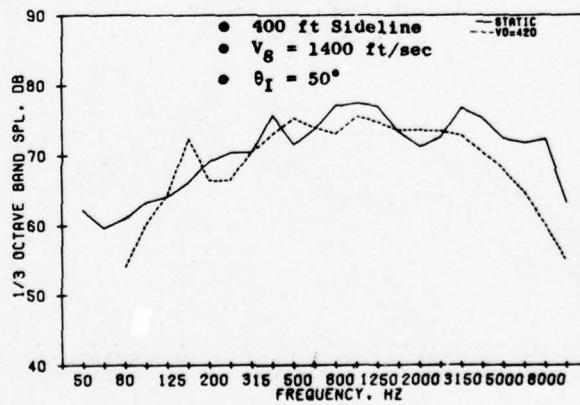
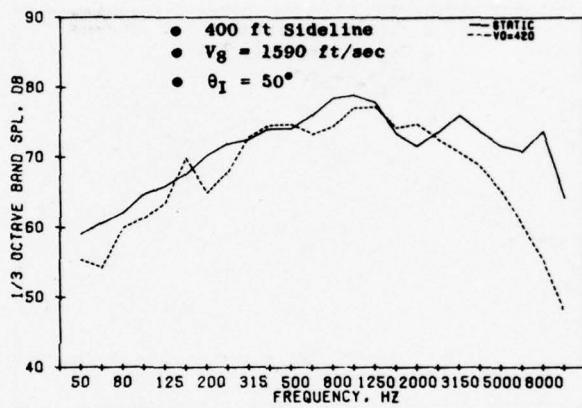
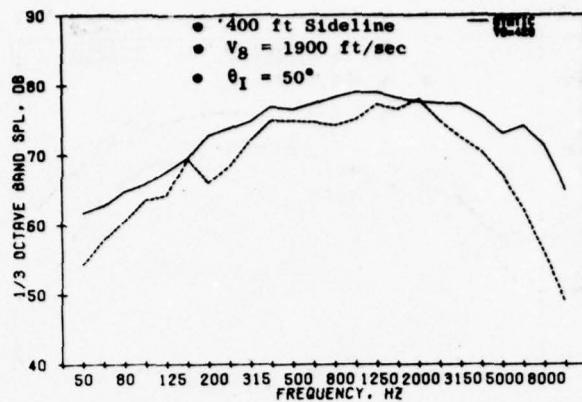


Figure 5-48. F-106 Baseline Nozzle 50° Spectra.

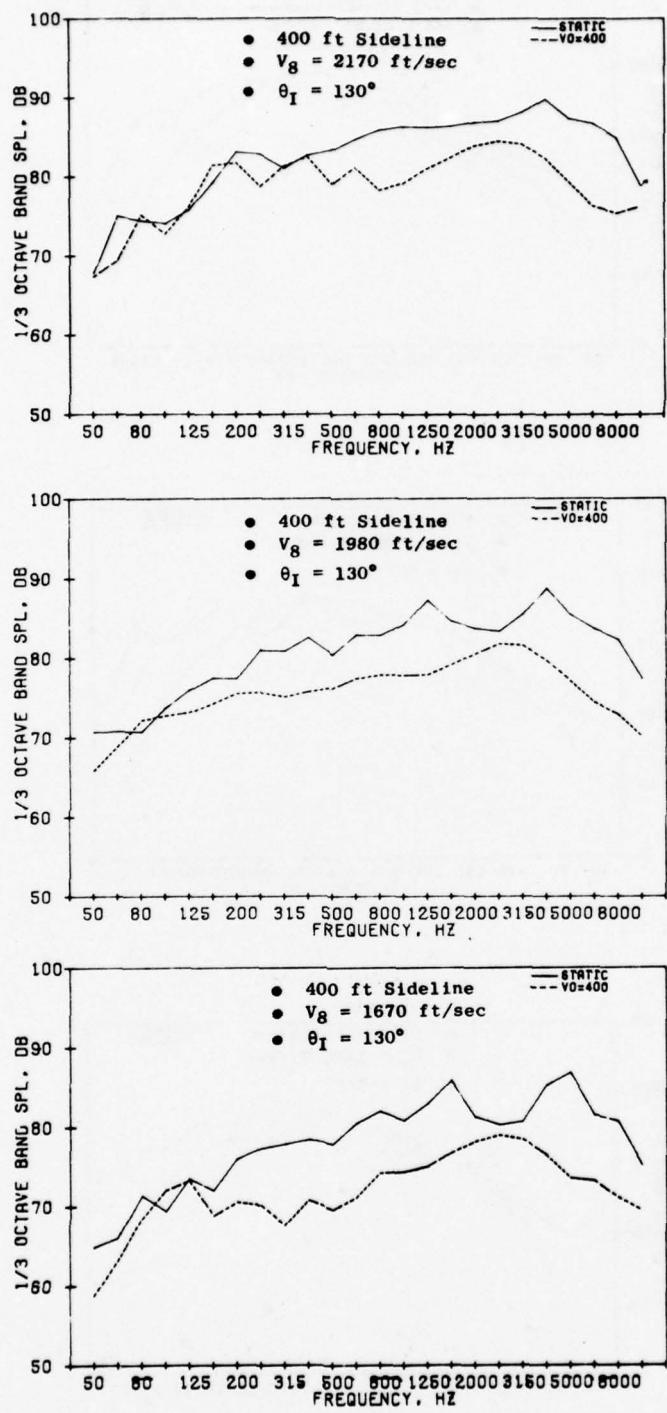


Figure 5-49. F-106/104-Tube Nozzle Max Angle Spectra.

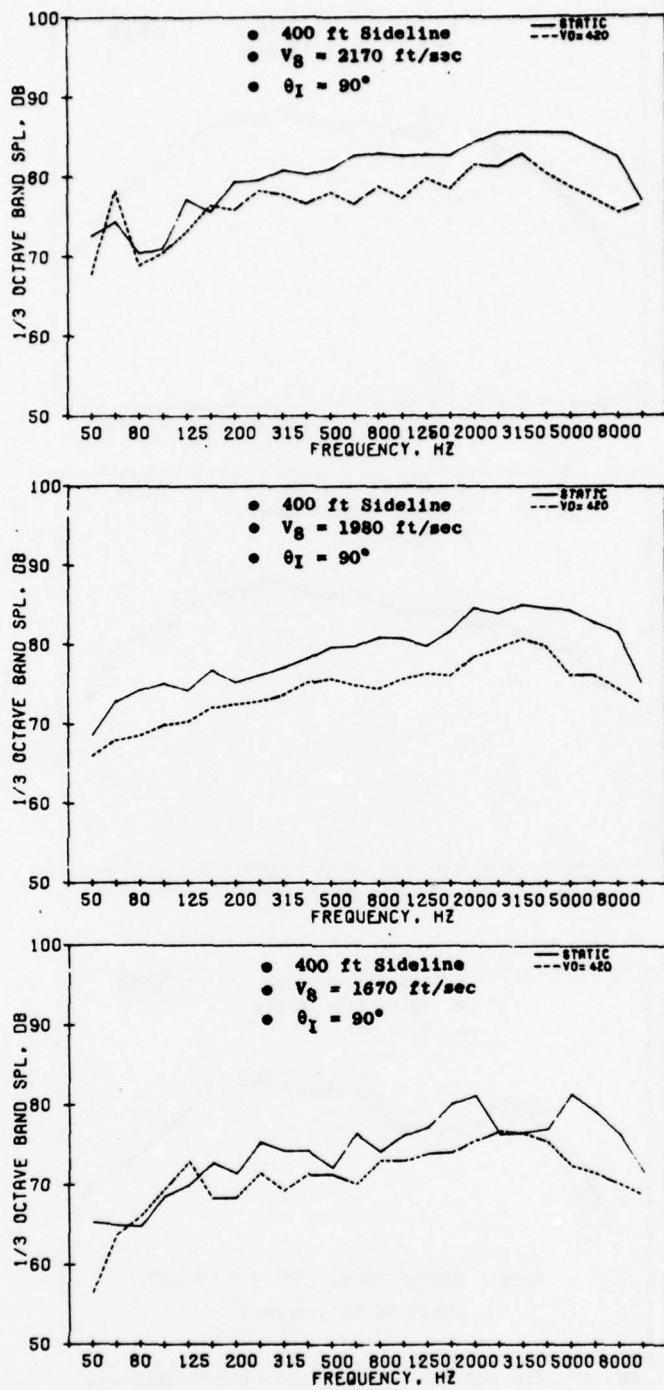


Figure 5-50. F-106/104-Tube Nozzle 90° Spectra.

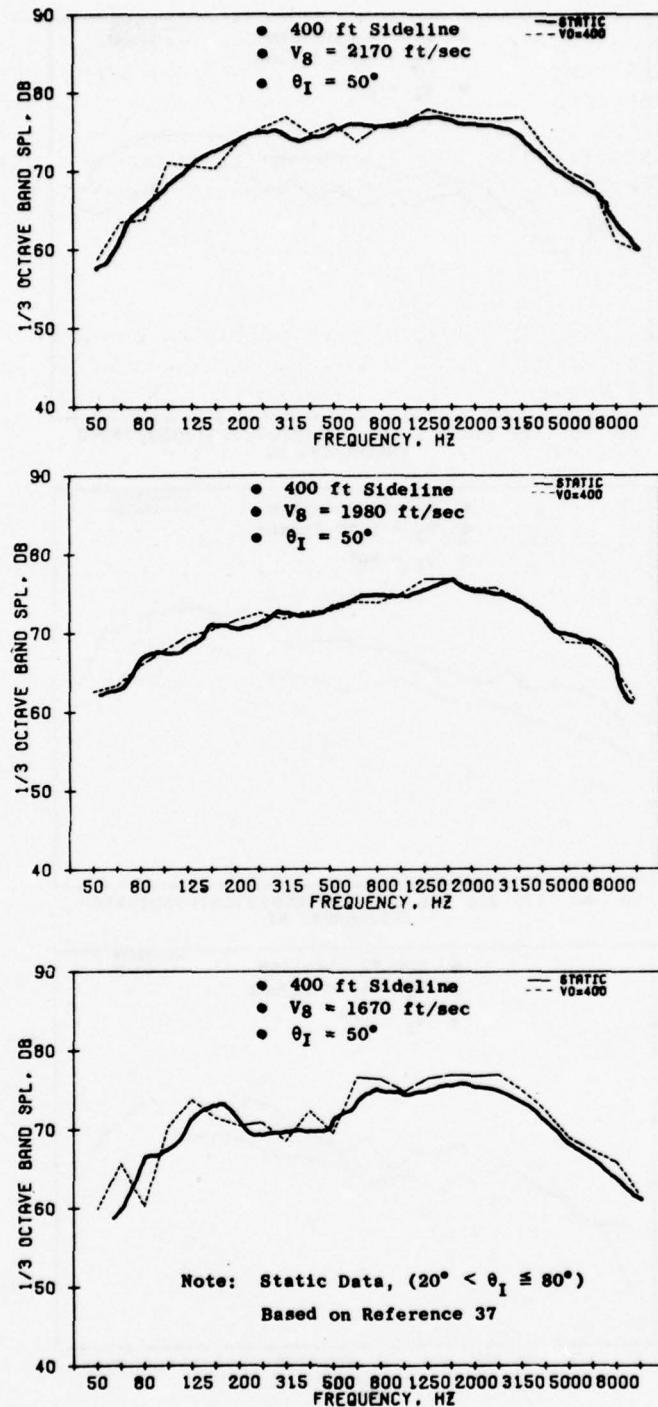


Figure 5-51. F-106/104-Tube Nozzle 50° Spectra.

marked reduction in the low-frequency and midfrequency portion of the spectra at all power settings; however, in the high frequency region, the reduction varies from essentially zero to 10 dB. The 90° spectra show a reduction that is relatively constant with frequency, and significantly more reduction is observed at the high jet velocity condition than at the low jet velocity condition. The 50° spectra show reductions on the order of 5 dB; whereas, for the lower power settings, no consistent trend is observable.

5.3 SUMMARY

The Gates Learjet and F-106 flight test series have static and flight free-field noise signatures of the four nozzles evaluated. Averaging data from several microphones has been shown to minimize the influence of ground reflections. Significant reduction from static to flight is observed at the angle of maximum noise. The level of reduction varies as a function of jet velocity and nozzle configuration. At the 90° acoustic angle, no change or a slight increase from static to flight noise levels is observed for the conical, F-106 baseline, and 8-lobe nozzles; whereas, a substantial reduction is observed for the 104-tube nozzle. The flight noise levels tend to approach or exceed the static noise levels in the forward quadrant.

6.0 MOVING-FRAME VALIDATION TEST PROGRAM

The moving-frame validation test program was conceived to provide a highly controlled set of "flight data" for verification of the inflight simulation technique. Based on the evaluation described in Section 3.2.2.2, the Aerotrain was found to have the unique capability to provide this complimentary data base for the J85 cycle. A joint General Electric/SNECMA* test program was formulated utilizing this vehicle to determine the static and flight noise signature of three exhaust nozzle systems for a range of engine power settings. The exhaust nozzles were a conical nozzle, 8-lobe nozzle, and 104-tube nozzle. The 8-lobe nozzle and 104-tube nozzle were the exact same nozzles that were tested on the Gates Learjet-25C and F-106 aircraft, respectively. All phases of this unique test program and resulting data are the subject of this section.

6.1 CONFIGURATION DESCRIPTION AND TEST MATRIX

6.1.1 Aerotrain Facility

The Aerotrain test facility is located at Gometz, France. A schematic of this six-kilometer track and corresponding locations of the acoustic measurement arena are presented on Figure 6-1. The Aerotrain vehicle is supported by an air cushion provided by a Palouste engine and is propelled by a General Electric J85 engine. A schematic and photograph of the Aerotrain are presented on Figure 6-2. The J85 engine was modified to have a 1.97-ft treated inlet and a 3.28-ft treated exhaust duct. The inlet and fan exhaust of the Palouste engine have also been treated to minimize the contamination of the J85 acoustic signature. The vehicle is capable of obtaining a speed of 270 ft/sec.

6.1.2 Nozzle Configuration and Test Matrix

Three nozzle configurations were evaluated on the Aerotrain. These were a conical nozzle, 8-lobe nozzle, and 104-tube nozzle. Photographs and schematics of these nozzles are presented on Figures 6-3 through 6-5, respectively. The corresponding test matrices for each of the configurations are presented on Table 6-I. The range of jet velocities and flight velocities investigated were from 1400 ft/sec through 2200 ft/sec and 0 - 270 ft/sec, respectively.

*SNECMA - Société Nationale D'Etude et De Construction De Moteurs D'Aviation

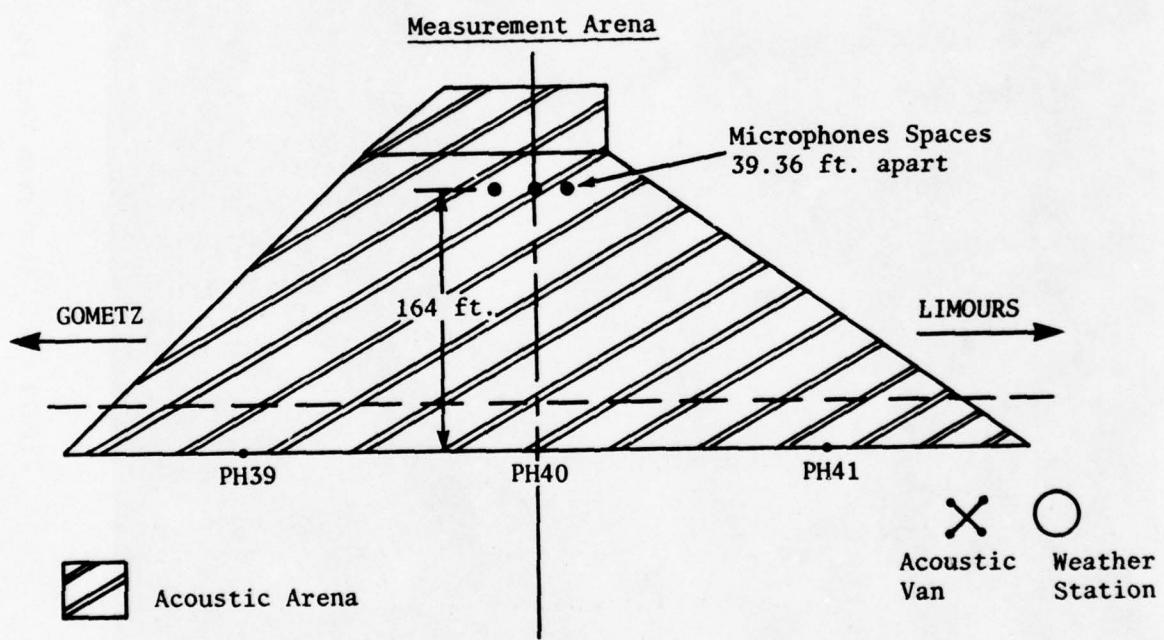
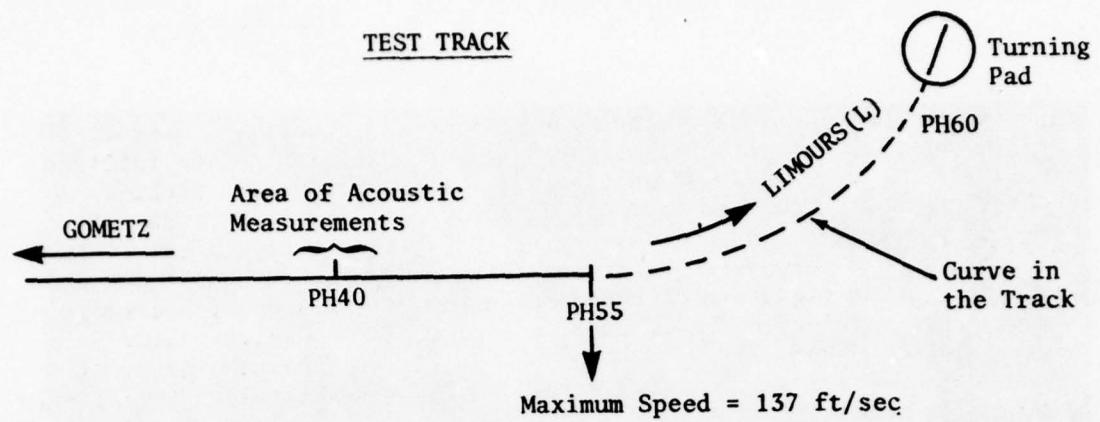
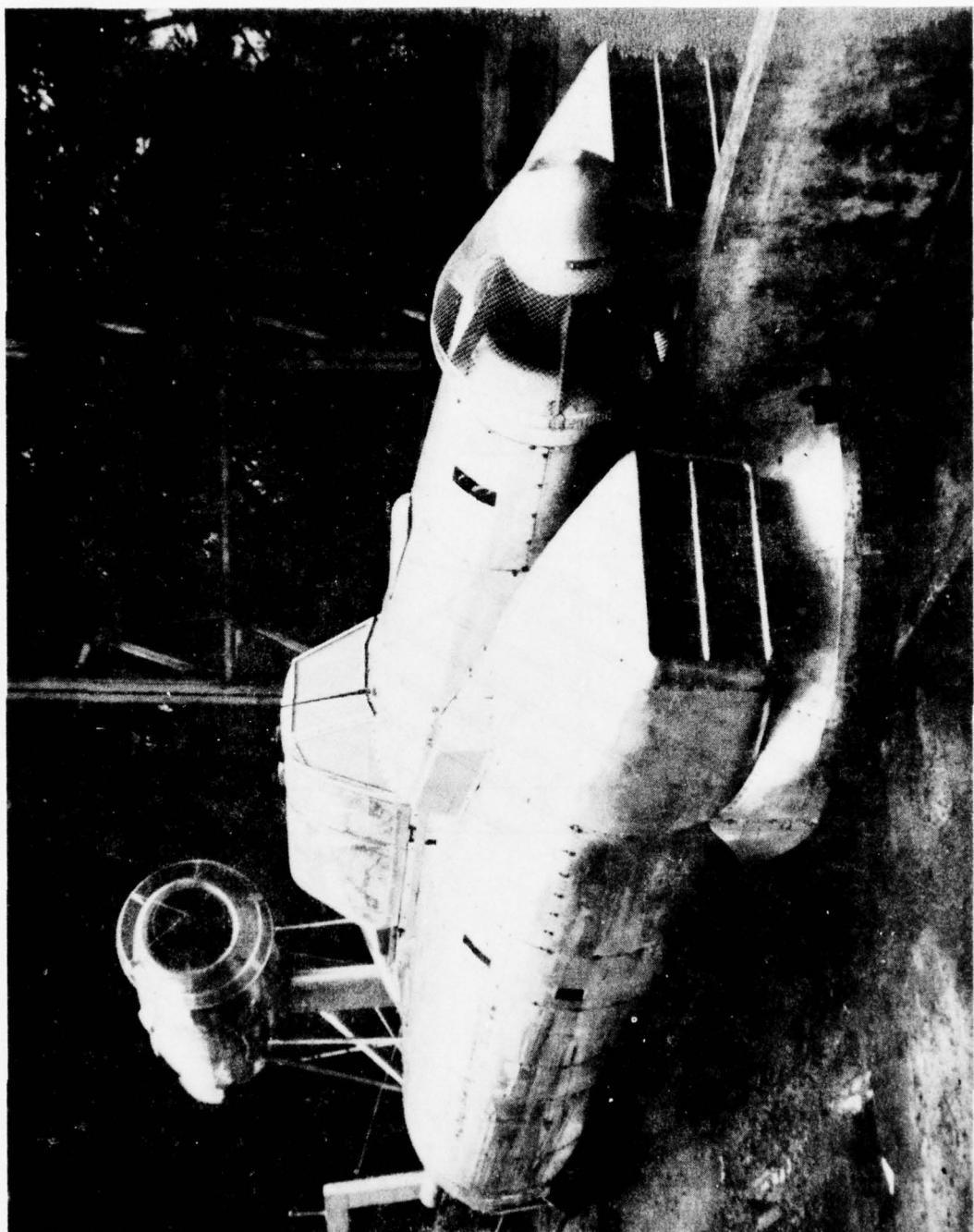


Figure 6-1. Schematic of the Test Track and Acoustic Measurement Arenas for the Bertin Aerotrain.

Figure 6-2. Aerotrain Test Facility.



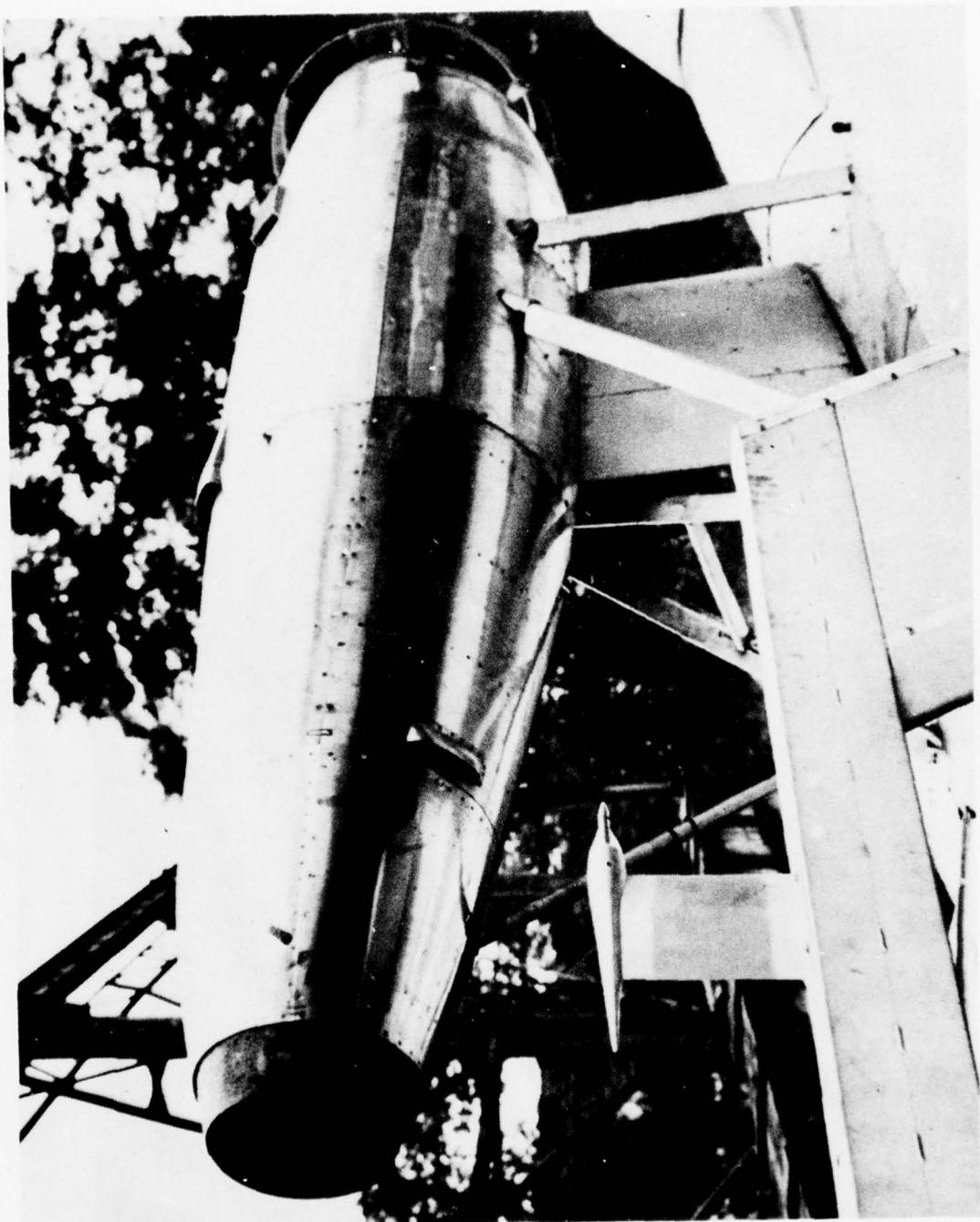


Figure 6-3. Bertin Aerotrain Conical Nozzle.



Figure 6-4. Bertin Aerotrain 8-Lobe Daisy Nozzle.



Figure 6-5. Bertin Aerotrain 104-Tube Nozzle.

Table 6-I. Aerotrain Test Matrix Conical Nozzle.

DATA PT. NO.	P_{T8}/P_0	T_{T8} OR	A_8 IN ²	V_8 FT/SEC	V_0 FT/SEC	$\log_{10}(V_j/A_0)$	$10 \log_{10}(\rho_j/\rho_{ISA})^w A_j/R^2$
43	1.604	1452	108.6	1489	0	.1174	-47.39
44	1.606	1425		1477		.1138	-47.17
45	1.600	1436		1477		.1138	-47.23
46	2.010	1584		1866		.2151	-49.43
47	1.995	1578		1853		.2121	-49.39
48	1.975	1573		1838		.2084	-49.34
49	2.433	1850		2254		.2966	-50.46
50	2.456	1828		2251		.2960	-50.33
51	2.453	1834		2253		.2964	-50.36
52	1.615	1438		1492	139	.1182	-47.33
53	1.595	1415		1462	132	.1093	-47.03
54	1.594	1448		1478	129	.1141	-47.30
55	1.988	1594		1859	132	.2133	-49.49
56	1.987	1574		1846	134	.2103	-49.35
57	1.954	1553		1813	130	.2024	-49.19
58	2.364	1815		2199	139	.2860	-50.35
59	2.422	1811		2244	137	.2909	-50.28
60	2.418	1812		2223	138	.2907	-50.28
61	1.631	1430		1503	257	.1211	-47.34
62	1.649	1431		1519	261	.1258	-47.44
63	1.698	1482		1588	265	.1450	-48.08
64	1.890	1536		1849	274	.1899	-48.99
65	1.965	1554		1820	276	.2043	-49.20
66	2.036	1588		1884	284	.2192	-49.45
67	2.361	1747		2155	278	.2773	-50.01
68	2.325	1734		2130	268	.2721	-49.98
69	2.361	1752		2158	266	.2779	-50.03
8-LOBE NOZZLE							
1	1.611	139	108.6	1463	0	.1099	-46.92
2	1.589	139		1443		.1039	-46.80
3	1.967	1595		1843		.2103	-49.49
4	1.941	1586		1820		.2051	-49.41
5	2.318	1781		2155		.2773	-50.22
6	2.295	1781		2142		.2751	-50.25
7	1.549	1375		1397	125	.0898	-46.43
8	1.543	1375		1391	146	.0880	-46.39
9	1.930	1574		1807	134	.2017	-49.32
10	1.964	1596		1843	148	.2100	-49.50
11	2.293	1783		2142	153	.2751	-50.26
12	2.279	1821		2158	150	.2783	-50.47
13	1.643	1403		1499	254	.1200	-47.17
14	1.584	1389		1437	257	.1022	-46.75
15	1.530	1398		1387	254	.0876	-46.49
16	1.940	1567		1807	266	.2023	-49.27
17	1.901	1556		1774	259	.1946	-49.16
18	1.891	1586		1788	268	.1971	-49.37
19	2.354	1785		2175	265	.2814	-50.21
20	2.295	1765		2132	266	.2730	-50.17
21	2.346	1797		2178	266	.2821	-50.28
104 TUBE NOZZLE							
22	1.571	1367	108.6	1415	18	.0950	-46.49
23	1.545	1386		1400	19	.0904	-46.49
24	1.957	1541		1808	17	.2012	-49.10
25	1.940	1536		1793	18	.1979	-49.05
26	2.328	1784		2162	18	.2787	-50.23
27	2.315	1787		2158	21	.2778	-50.26
28	1.543	1394		1402	148	.0910	-46.54
29	1.545	1395		1405	145	.0917	-46.56
30	1.946	1577		1822	129	.2046	-49.36
31	1.920	1563		1797	142	.1986	-49.23
32	2.315	1771		2148	136	.1691	-50.10
33	2.315	1771		2148	135	.1691	-50.10
34	1.549	1396		1408	252	.0931	-46.60
35	1.555	1398		1415	251	.0952	-46.65
36	1.556	1399		1417	250	.0957	-46.67
37	1.953	1532		1800	261	.1993	-49.03
38	1.939	1523		1785	263	.1959	-48.94
39	1.958	1529		1801	266	.1996	-49.01
40	2.350	1772		2166	260	.2794	-50.14
41	2.371	1787		2185	267	.2832	-50.20
42	2.351	1772		2167	269	.2794	-50.14

6.2 IMPACT OF BACKGROUND NOISE

The results presented in Section 3.2.1.1 describing the background noise measurements made at Holloman AFB show that background noise may have a major impact on moving-frame data. The background noise signature of the Aerotrain was determined, both for static and for flight conditions, using the following test procedure:

- Measure the noise signature of the Palouste only during static operation
- Measure the noise signature of the Palouste in conjunction with the J85 engine operating idle at static and at the maximum vehicle speed of 270 ft/sec
- Measure the noise signature of the conical, 8-lobe, and 104-tube nozzles operating at the lowest jet velocity ($V_J = 1400$ ft/sec) for both static and maximum vehicle speed (270 ft/sec).

The results of these static measurements are summarized on the basis of OASPL on Figure 6-6. Note that on the basis of OASPL, the only angles that show contamination for the 104-tube nozzle are 40° through 20° . The supporting 1/3-octave band spectra are presented on Figures 6-7 through 6-9. These comparisons indicate that the tube-nozzle noise signature, when compared to the Palouste only, has contamination in the 500-Hz to 1000-Hz frequency range; however, contamination at other frequencies is minimal except for the extreme inlet angles as illustrated by comparing a 10-dB down line for the 104-tube nozzle with that of the Palouste only spectra. Therefore, it is concluded that the static data for the conical and 8-lobe nozzles show no significant contamination, but the 104-tube nozzle is influenced in selective 1/3-octave bands and at the extreme inlet angles.

The second phase of the background noise study was to assess the impact of the aerodynamic and Palouste noise as the Aerotrain passed through the acoustic arena at a speed of 270 ft/sec. This was not possible in as direct a manner as was the determination of the Palouste static noise contamination. The limiting item was that the J85 engine could only be reduced to idle while the vehicle was translating at 270 ft/sec and, therefore, some judgement is necessary in interpreting the results.

To clarify the above point and to assess the impact of aerodynamically generated noise, the OASPL directivity patterns for several conditions are presented on Figure 6-10. Note that comparing the noise of the J85 at idle, plus the Palouste for static and simulated flight conditions, indicates that the noise decreased in the aft quadrant and increased in the forward quadrant; this is due to dynamic effects. If the aerodynamic noise signature had been significant in the aft quadrant, this reduction would not have occurred. No conclusion can be drawn relative to the aerodynamic noise contribution in the forward quadrant, however, except that whatever its contribution is, it is included in the measurement. The most conser-

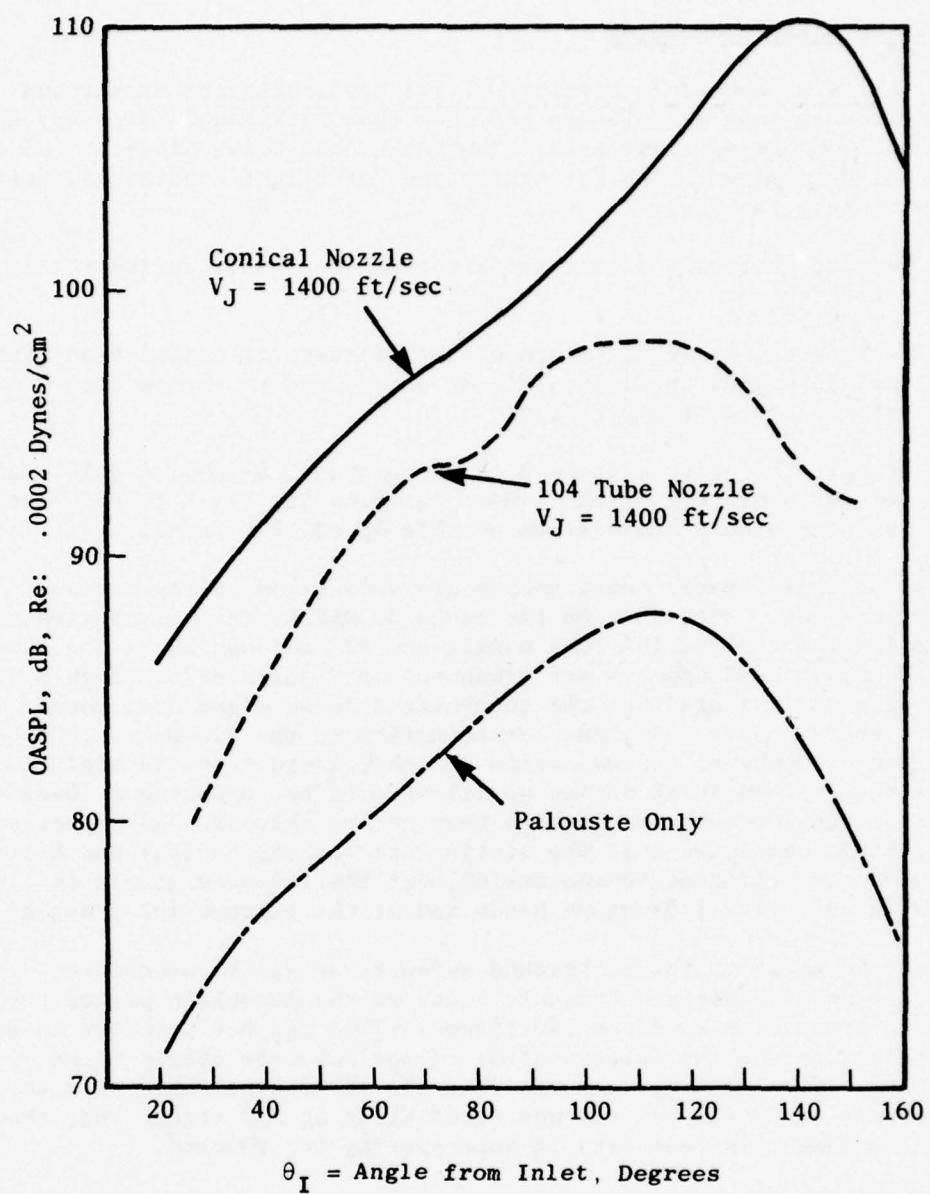


Figure 6-6. Aerotrain Background Noise - Static Conditions.

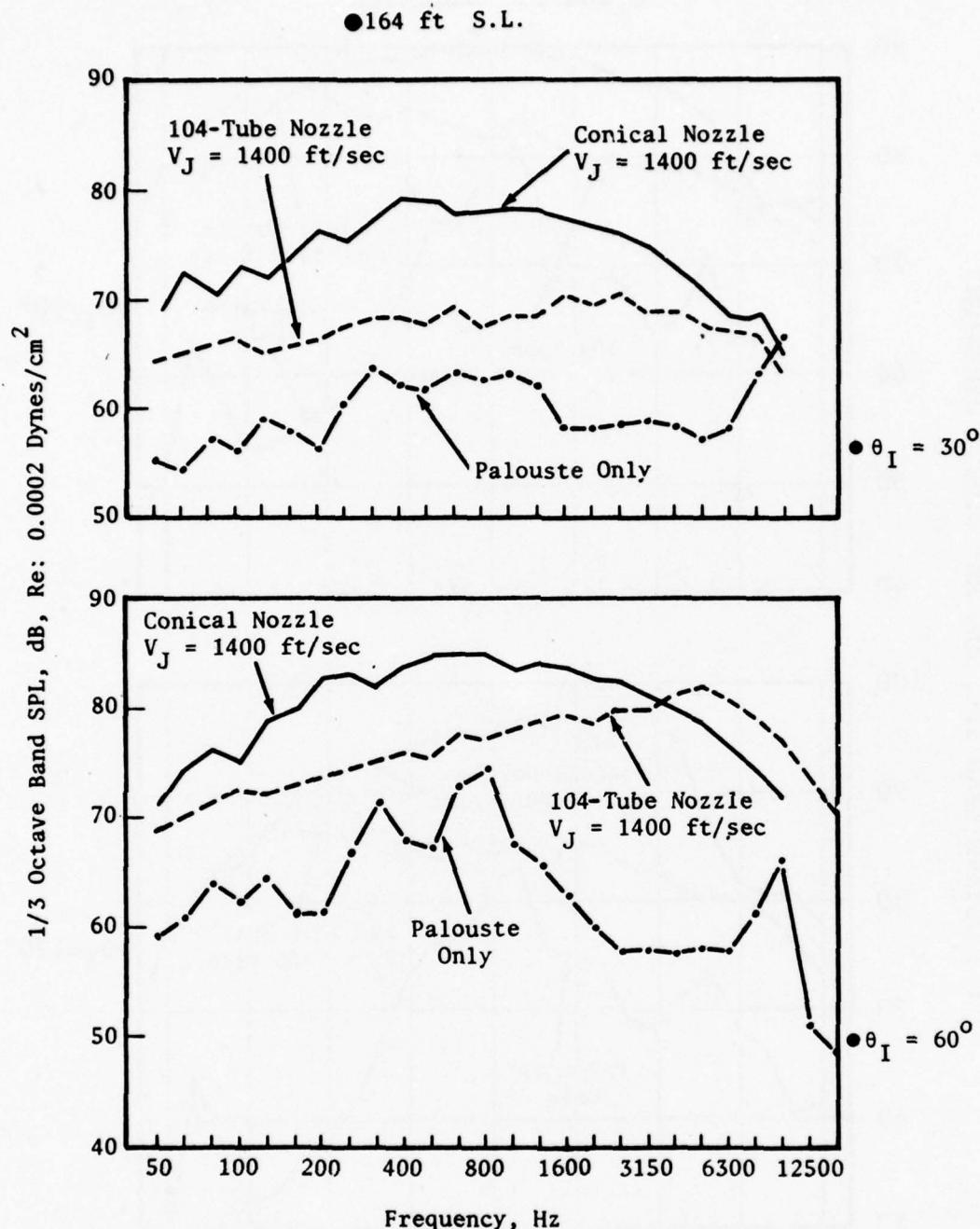


Figure 6-7. Impact of Aerotrain Background Noise - Static Conditions, $\theta_I = 30^\circ$, $\theta_I = 60^\circ$.

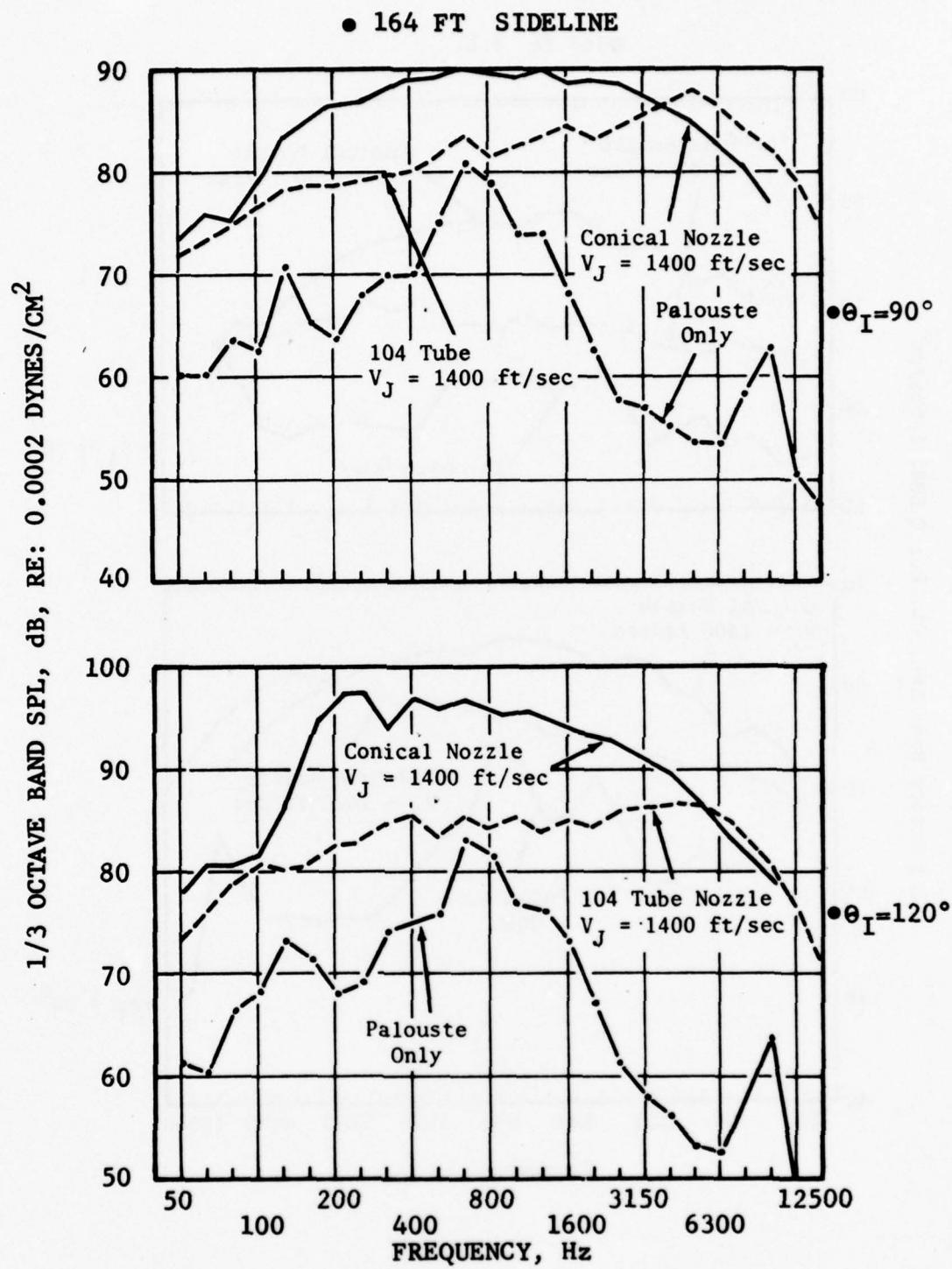


Figure 6-8. Impact of Aerotrain Background Noise - Static Conditions, $\theta_I = 90^\circ, 120^\circ$.

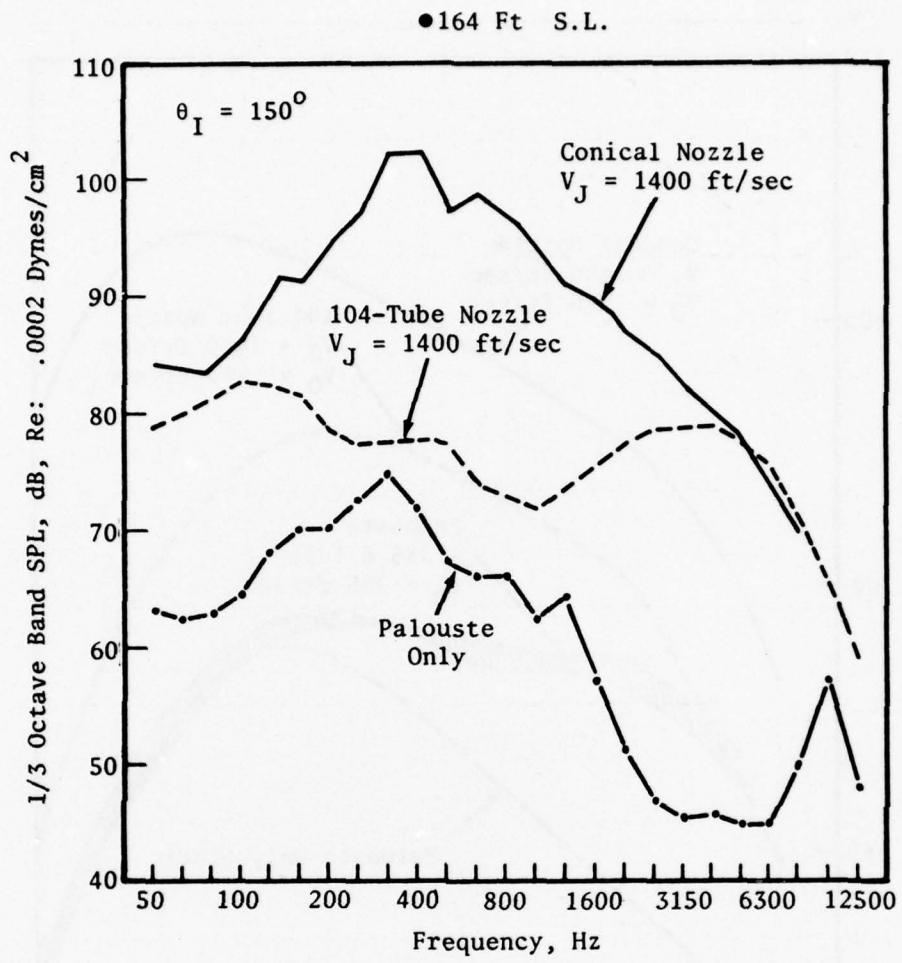


Figure 6-9. Impact of Aerotrain Background Noise - Static Conditions, $\theta_I = 150^\circ$.

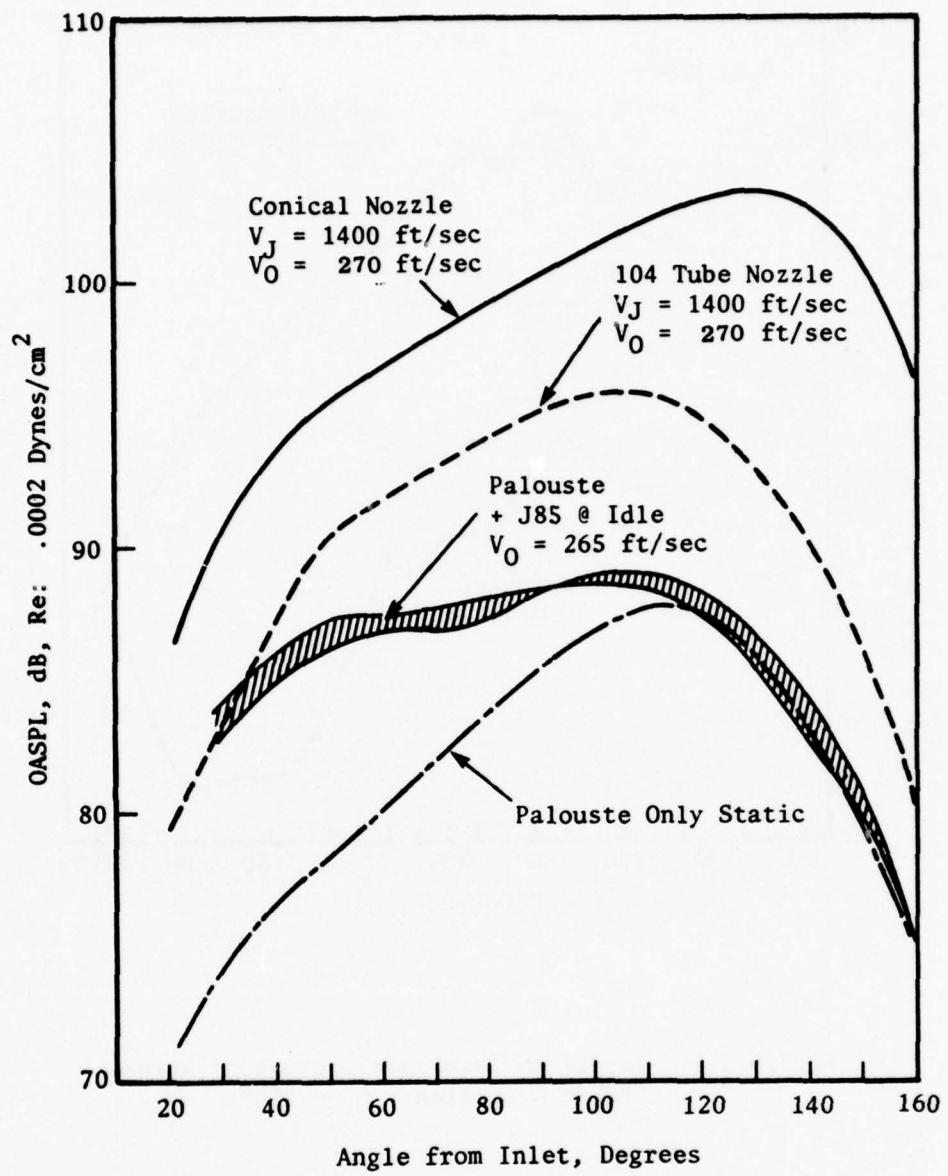


Figure 6-10. Impact of Aerotrain Background Noise on Flight OASPL Directivity Patterns.

vative approach is to use the J85 at idle, plus Palouste noise signature with the vehicle speed of 270 ft/sec. The most optimistic approach would be to use the static noise signature of the Palouste and assume that the aerodynamic vehicle noise was well below that of the Palouste.

If the J85 at idle plus the Palouste is chosen as the background noise floor, the 104-tube nozzle data would have significant contamination for acoustic angles less than 50° and greater than 130°. However, if the Palouste static noise signature constitutes the background noise floor, significant contamination of OASPL directivity pattern occurs only in the aft quadrant. The conservative approach is the only logical assumption for the validation data; thus, it must be concluded that the OASPL levels for the 104-tube nozzle at acoustic angles greater than 120° are contaminated by background noise.

The impact of the background noise on the 1/3-octave band spectra is presented on Figures 6-11 through 6-20. The reason for performing a detailed spectrum analysis is that the analytical transformation of the free jet data is done for each 1/3-octave band, and the noncontaminated region of the spectra must be determined to provide useful validation data.

The spectrum analysis was conducted separately for the conical, 8-lobe, and 104-tube nozzles. The results at the 30° acoustic angle for the three configurations are presented on Figures 6-11 and 6-12. The high frequency portion of the spectra (6300 Hz to 10,000 Hz) is contaminated for all three of the configurations. The degree of contamination for the rest of the spectra depends on which background noise level is assumed. If the minimum noise line is assumed to be correct, no contamination occurs; however, if the maximum noise line is assumed, the low frequency portion of the spectra (50 Hz to 400 Hz) is invalid. Similar trends are observed for the 8-lobe and 104-tube nozzle, with one important difference. The 104-tube nozzle data is actually below the maximum background noise line, providing evidence that the real background noise level is nearer the minimum noise line. The validity of the 104-tube data at this acoustic angle is certainly questionable for all the power settings. The 60° acoustic angle shows a much less confusing picture for the conical nozzle. The only portion of the spectra that may have some contamination is the low frequency portion from 50 Hz to 200 Hz. The suppressors, in contrast, have low frequency levels considerably below the conical nozzle and show insignificantly more low frequency contamination. The higher frequency portion of the spectra are well above the background noise.

The conical nozzle at the 90° acoustic angle is significantly above the background noise, except at the extreme low frequencies. The suppressors still have some low frequency contamination if the conservative line is utilized. The 120° acoustic angle, representative of the maximum noise angle, shows no contamination of the conical nozzle data. However, for the suppressors, some low frequency contamination may occur (particularly for the 104-tube nozzle). The peak noise of the Palouste at 630 Hz, for example, would contaminate the 104-tube nozzle. At the 120° acoustic angle, both

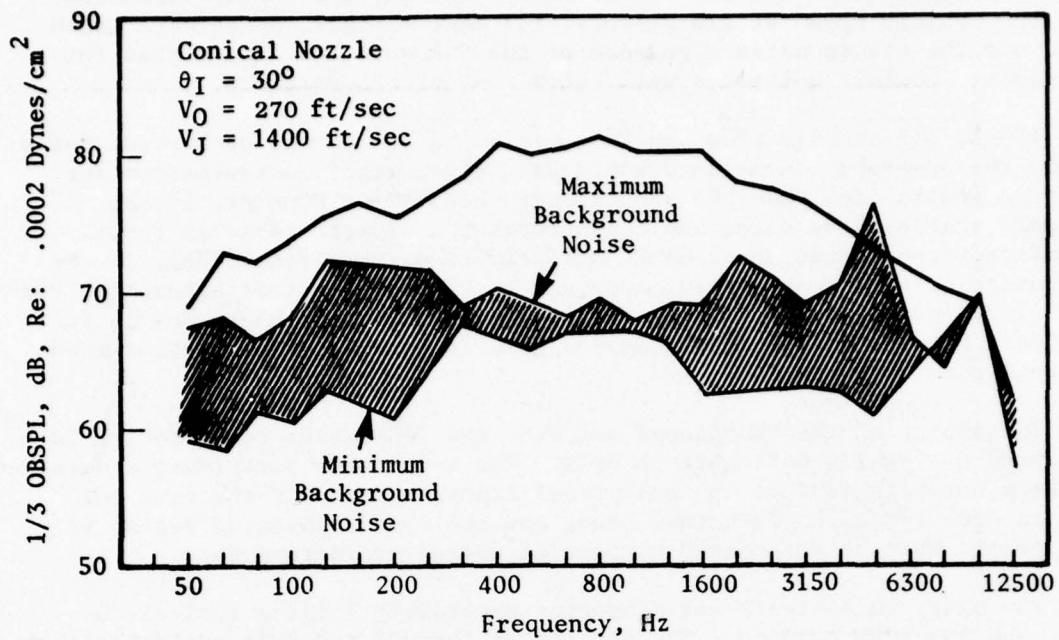


Figure 6-11. Impact of Aerotrain Background Noise - Conical Nozzle, $\theta_I = 30^\circ$.

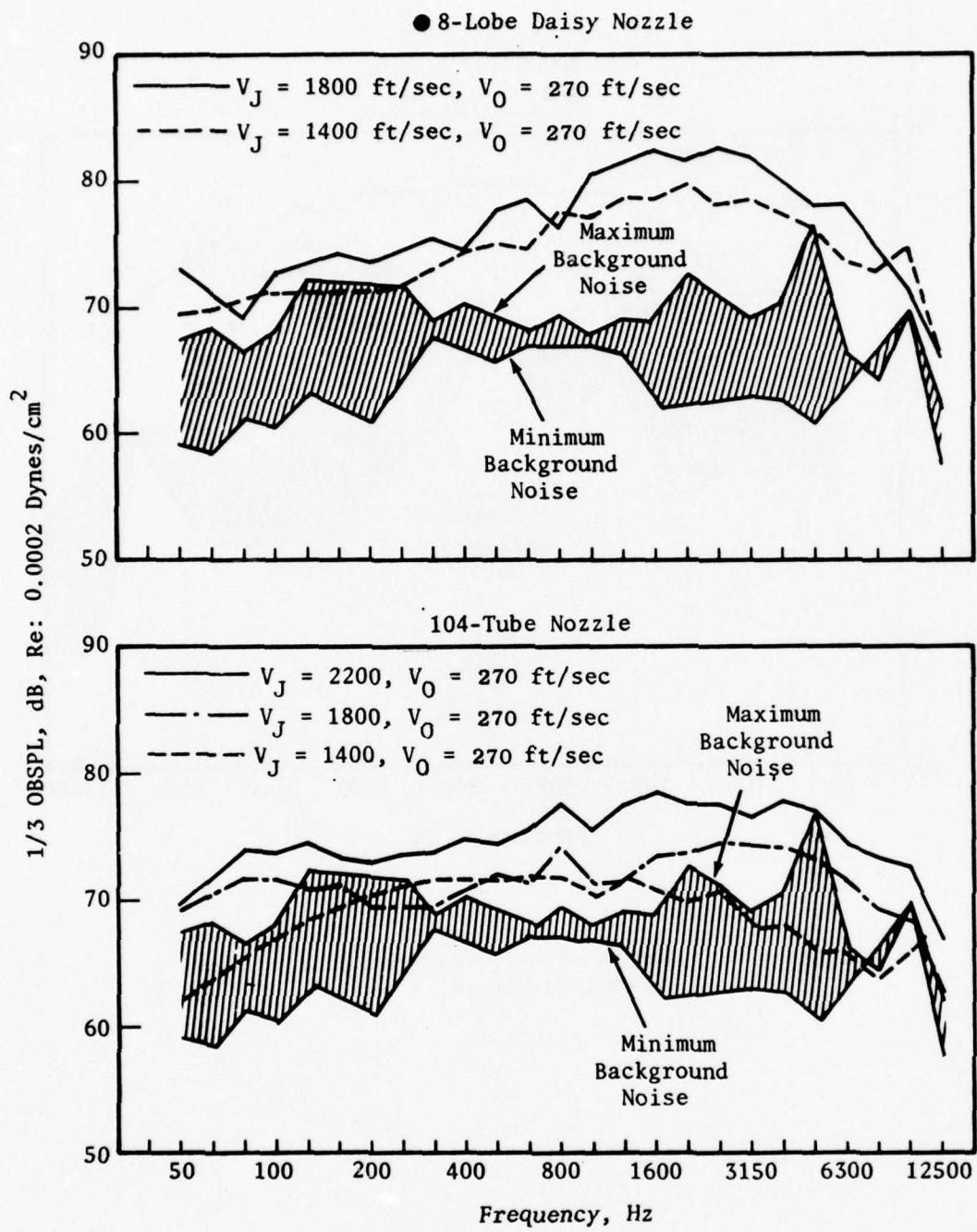


Figure 6-12. Impact of Aerotrain Background Noise - 8-Lobe and 104-Tube Nozzles, $\theta_I = 30^\circ$.

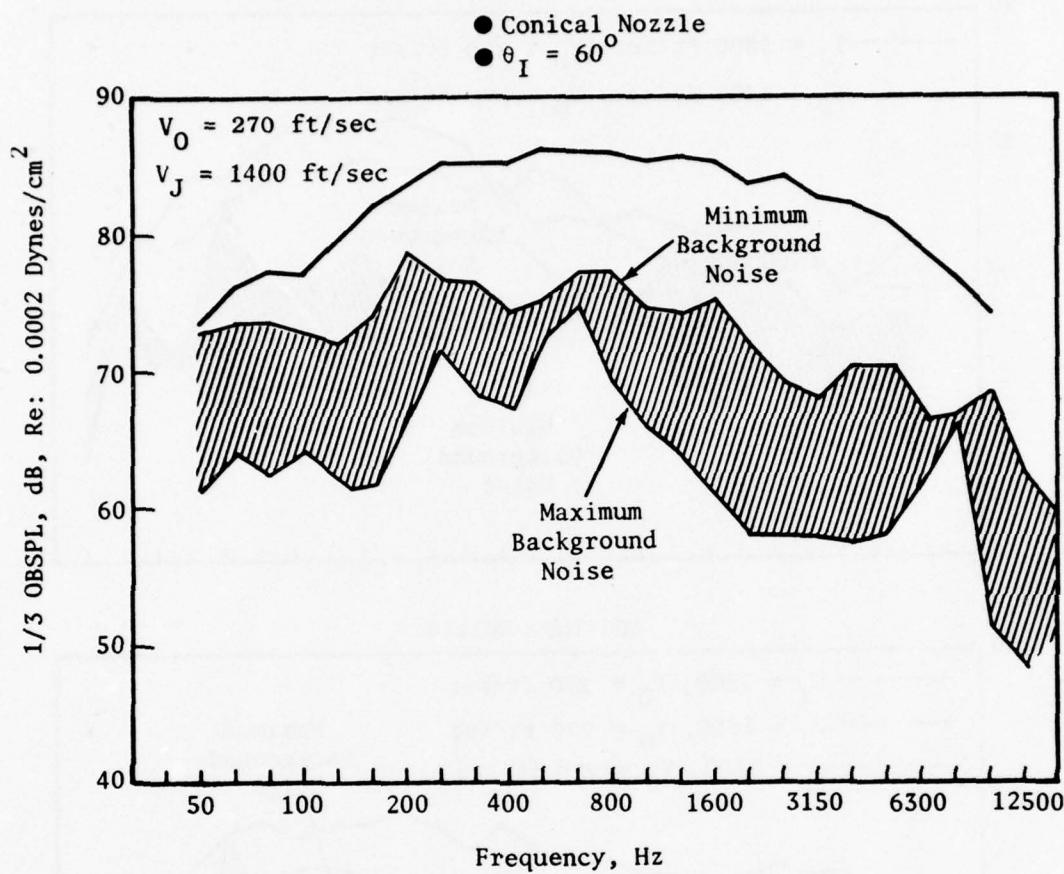


Figure 6-13. Impact of Aerotrain Background Noise - Conical Nozzle, $\theta_I = 60^\circ$.

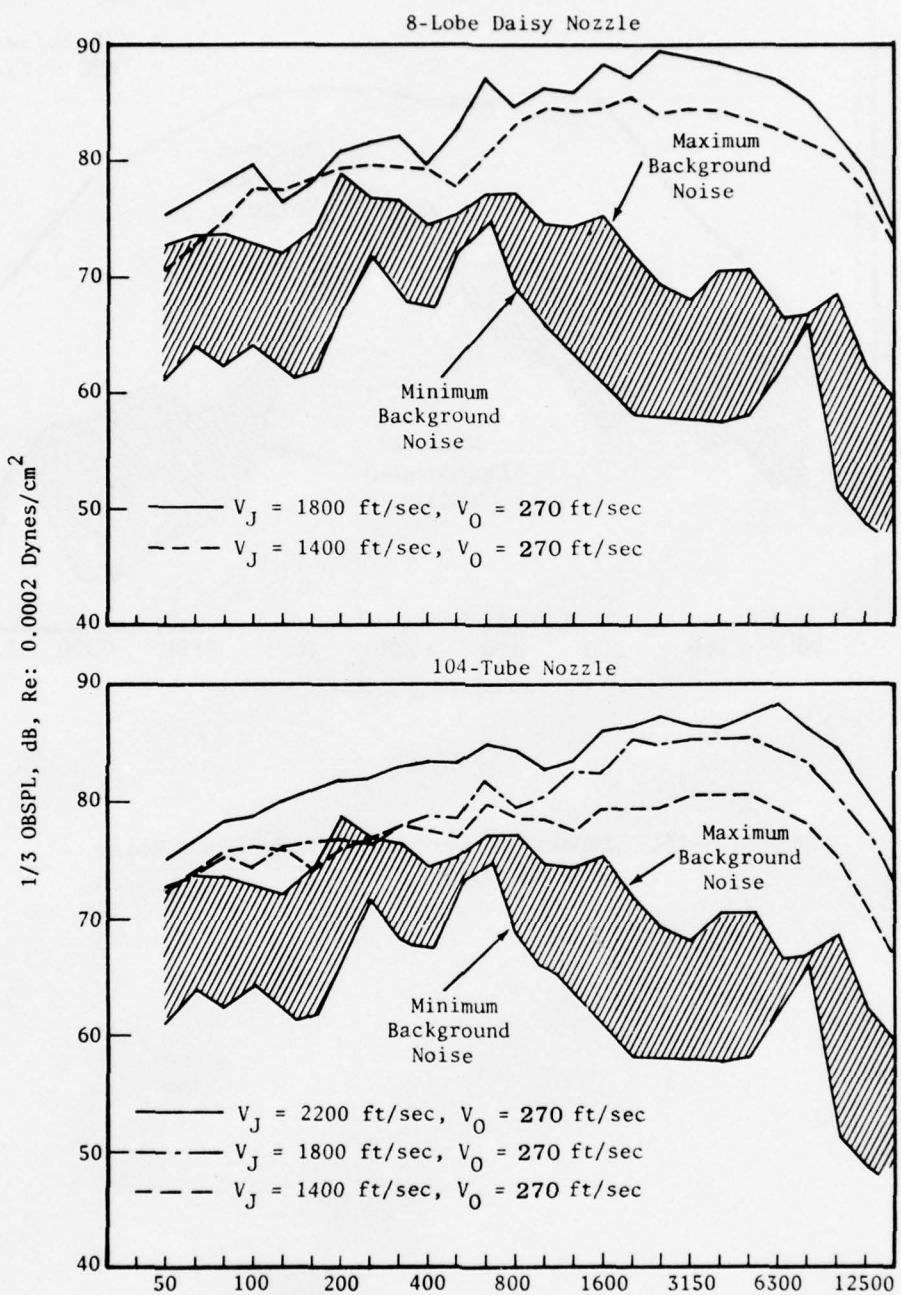


Figure 6-14. Impact of Aerotrain Background Noise -
8-Lobe and 104-Tube Nozzles, $\theta_I = 60^\circ$.

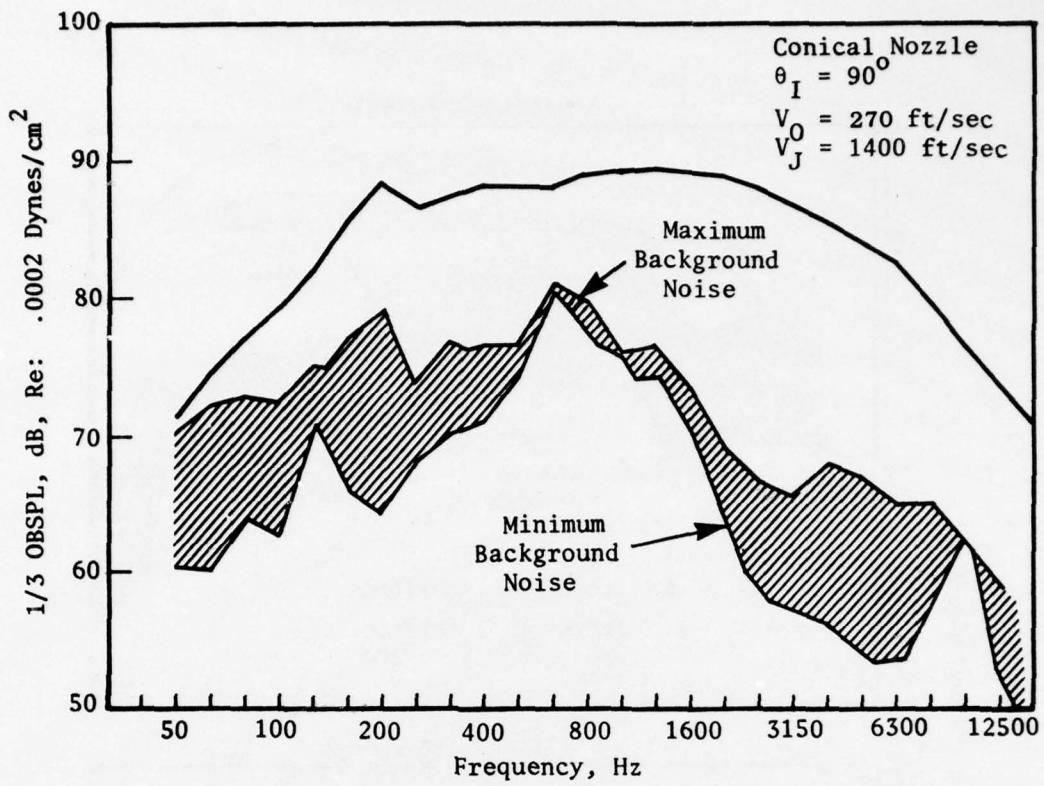


Figure 6-15. Impact of Aerotrain Background Noise - Conical Nozzle, $\theta_I = 90^\circ$.

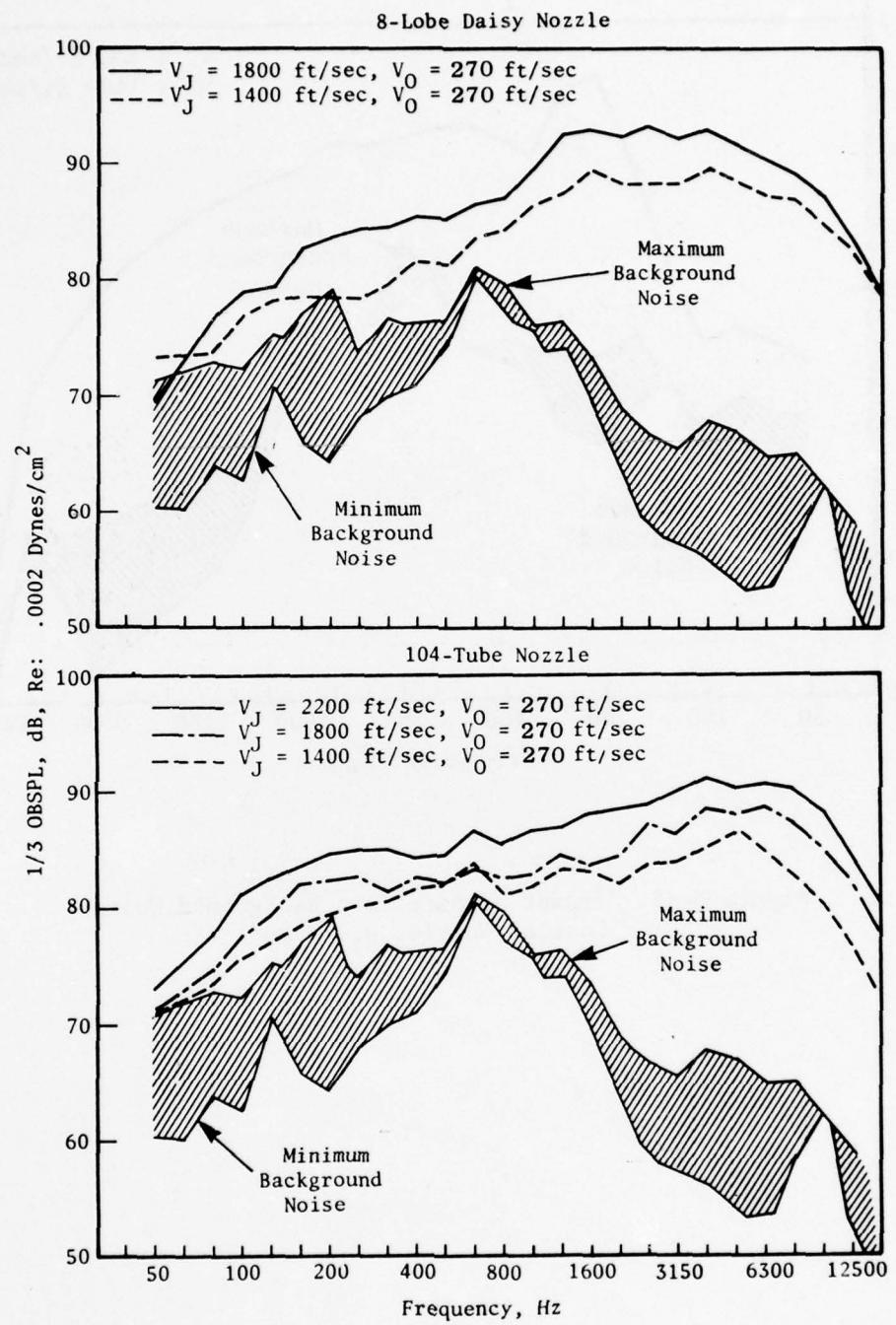


Figure 6-16. Impact of Aerotrain Background Noise -
8-Lobe and 104-Tube Nozzles, $\theta_I = 90^\circ$.

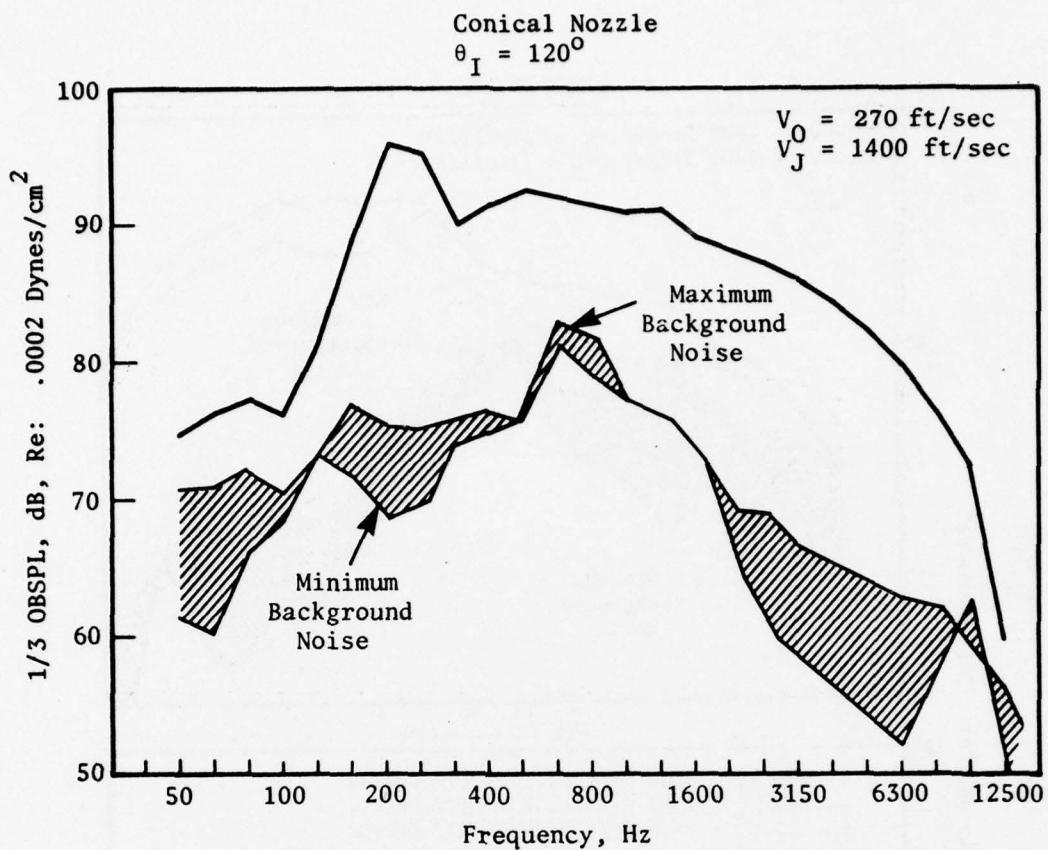


Figure 6-17. Impact of Aerotrain Background Noise - Conical Nozzle, $\theta_I = 120^\circ$.

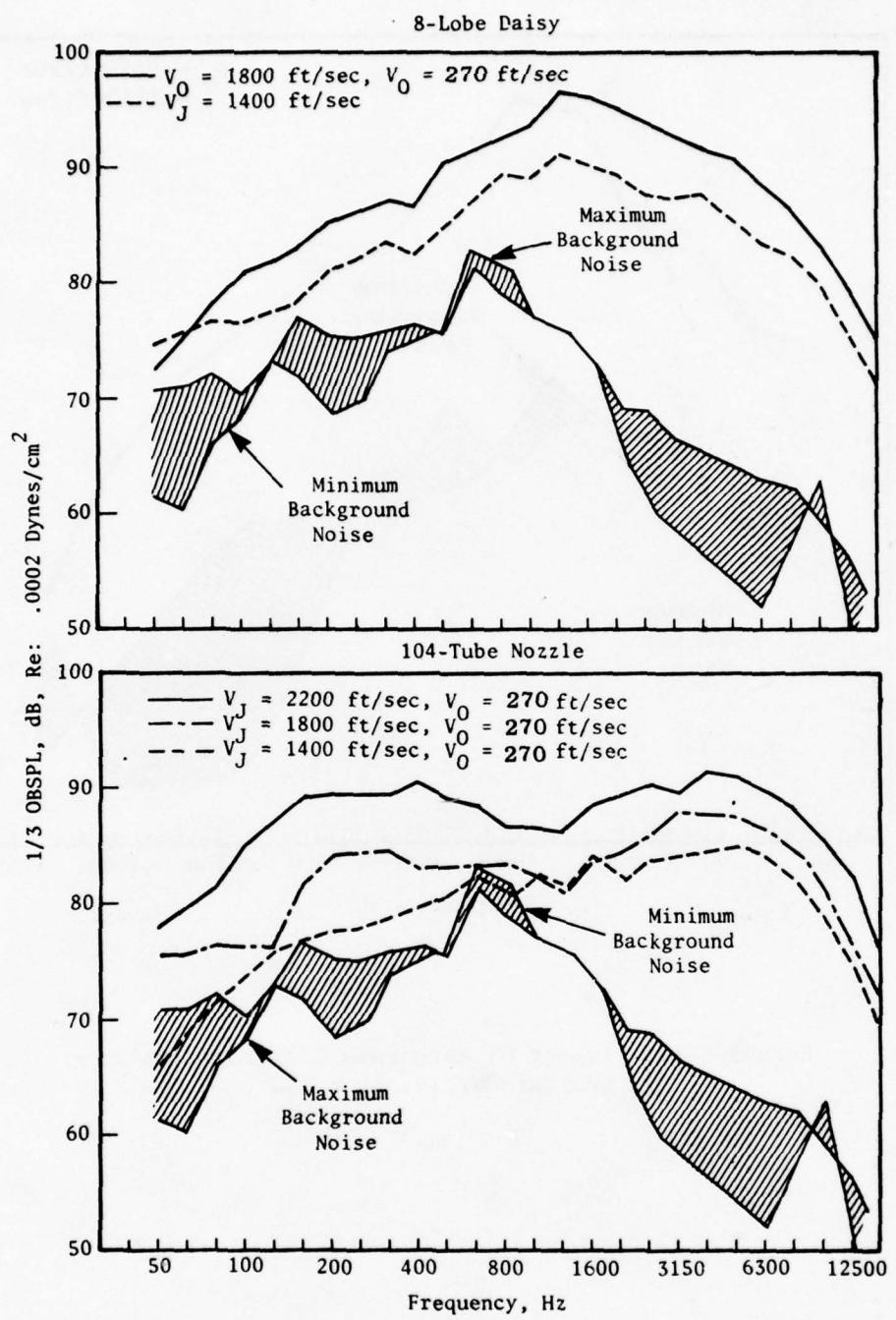


Figure 6-18. Impact of Aerotrain Background Noise - 8-Lobe and 104-Tube Nozzles, $\theta_I = 120^\circ$.

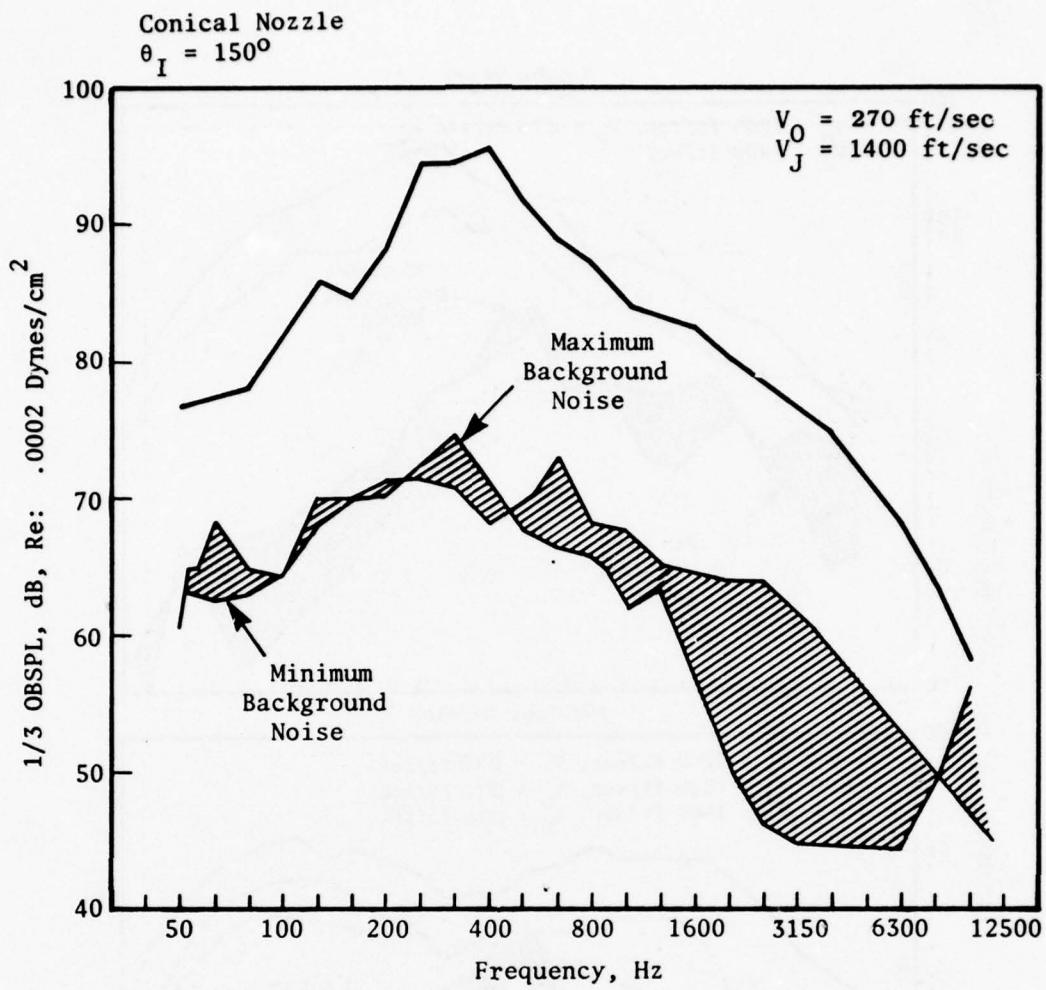


Figure 6-19. Impact of Aerotrain Background Noise - Conical Nozzle, $\theta_I = 150^\circ$.

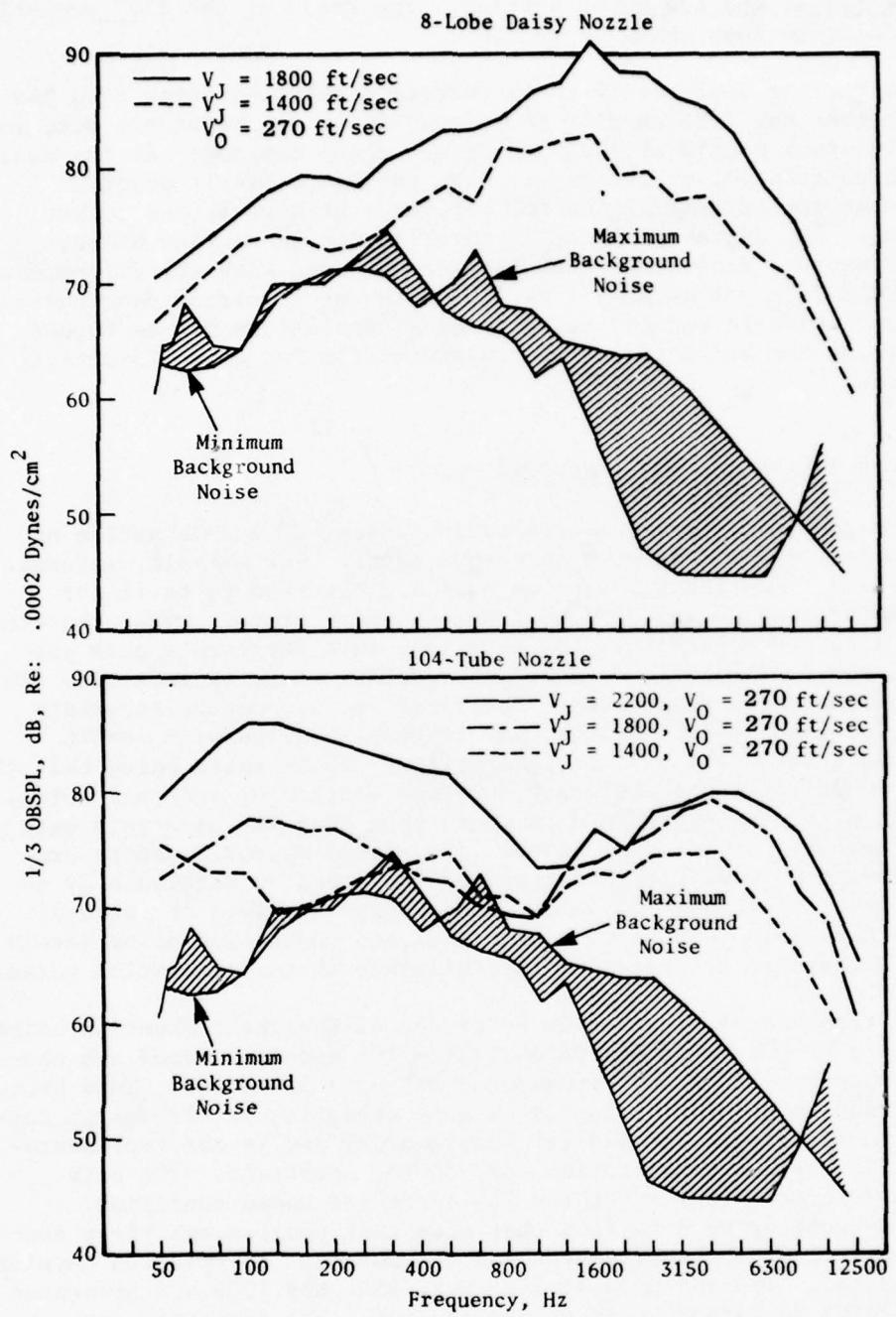


Figure 6-20. Impact of Aerotrain Background Noise -
8-Lobe and 104-Tube Nozzles, $\theta_I \approx 150^\circ$.

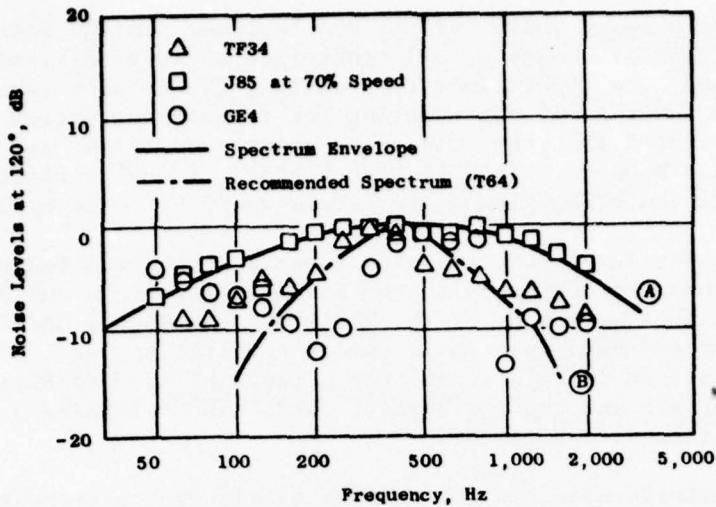
the daisy and tube nozzles would have minimum contamination at the two higher power setting points, with some contamination observed for select 1/3-octave bands at the low power setting. The trend at the 150° acoustic angle is similar to that observed at 120°.

In summary, the analysis of the Aerotrain background noise data has demonstrated that the influence of background noise on the static data is limited to 104-tube nozzle at the 1400 ft/sec power setting. At the maximum flight condition ($V_0 = 270$ ft/sec), PNL and OASPL levels would be contaminated at the extreme angles for all three nozzles at the lowest power setting. The degree of spectra contamination is configuration, angle, and frequency dependent; therefore, comparison with the flight data and transformed free jet data will be made with the Aerotrain data corrected for background noise to assure that erroneous conclusions not be formed when determining the validity of the transformation for each 1/3-octave band frequency.

6.3 IMPACT OF EXTRANEous NOISE SOURCES

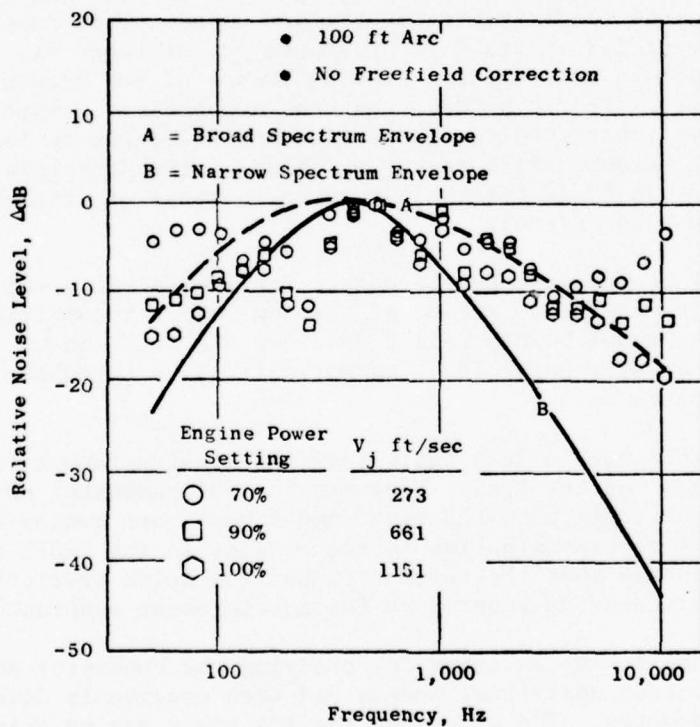
Actual engine noise measurements could consist of a combination of signals from many noise sources within the engine. For example, internal noise may have a significant impact on what are observed to be flight effects. (References 38 and 39). Extraneous noise sources were, therefore, assessed in order to verify that the Aerotrain data represents pure jet noise and is not contaminated for the jet velocity range of interest. This assessment utilized two approaches. The first was to compare Aerotrain static data for the conical, 8-lobe, and 104-tube nozzles with JENOTS scale-model data for these same configurations. The premise being that the JENOTS scale-model data are obviously not contaminated by internal noise, and agreement with the Aerotrain data would show that the Aerotrain data are not contaminated by internal noise. The second approach was to use existing combustion noise prediction procedures based on Reference 39 to predict the level of combustion noise at the power settings of interest. The measured Aerotrain noise levels and predicted combustion noise levels would then be compared to determine the influence of the combustion noise.

The spectrum shapes proposed in Reference 40 for the combustion noise predictions are presented in Figure 6-21(a). Two spectra shapes are shown. The broader spectrum "A" fits the measured J85 data presented. This broader spectrum was due to the particular J85 engine operating at off-design conditions (because of increased exhaust nozzle area) and is not representative of the J85 engine configuration used on the Aerotrain. The data presented in Reference 39 were at the 70% corrected speed condition. Eighty-five percent speed data from that same test program exhibit a spectrum shape typical of the more narrow and recommended "B" spectrum envelope of Figure 6-21(a). The J85 data at 85%, 90%, 95%, and 100% are presented on Figure 6-21(b) to support this recommendation. The Aerotrain test points were nominally at 87%, 93%, and 100%. This recommended narrow spectrum envelope is more representative for the higher power setting data



(a) Gas Turbine Engines

Note: Data above 200 Hz is contaminated by turbomachinery noise.



(b) J85 at Typical Engine Power Settings

Figure 6-21. Combustor Noise Spectra (From Reference 40).

and is used as the primary basis for all conclusions. In the interest of completeness and clarity, however, all combustion noise predictions are presented as a band; the upper limit representing the broader spectrum envelope, and the lower limit representing the recommended narrow envelope. It should also be noted that the combustion noise predictions are based on data which have not been corrected to free field. If such corrections were applied, the predicted combustion noise levels would be lower by 2.5 dB.

Jet mixing noise levels for a conical nozzle were predicted using the SAE and ANOPP methods to compare with the measured Aerotrain and JENOTS data. The comparisons were made on the basis of peak OASPL, OASPL directivity, and 1/3-octave band spectra at select acoustic angles. Figure 6-22 presents the normalized OASPL's at 90° for a range of jet velocities applicable to the Aerotrain and the scale-model data. The following observations and conclusions are pertinent.

- The Aerotrain data for the conical nozzle are consistently 1 dB above the scale-model data. The ANOPP and SAE jet mixing noise predictions agree well with the scale-model data for $\log V_J/a_0$ ratios less than 0.15. The higher jet velocity predictions are 1 to 3 dB below the scale-model data. The combustor noise prediction for the range of interest ($\log V_J/a_0 = 0.1$ through $\log V_J/a_0 = 0.3$) shows no contamination of the jet noise. This conclusion is further verified by the data presented in Reference 41. OASPL's and 1/3-octave band spectra from Reference 41 are presented on Figure 6-23. It can be seen that the Aerotrain J85 internal noise level corrected for convective amplification is lower than the total measured flight exhaust noise of the Aerotrain J85 by not less than 10 dB for the jet velocity range of interest (1400 ft/sec to 2200 ft/sec).
- Agreement between the 8-lobe nozzle scale-model data and Aerotrain results is excellent, except at the low velocity condition where two of the model points fall 2 dB above the mean line. The predicted combustor noise level is not sufficient to contaminate the 8-lobe nozzle data.
- The 104-tube nozzle data again show excellent agreement between scale model and Aerotrain; however, the J85 combustor noise prediction indicates that the data should have been contaminated. The fact that contamination is not evident in the OASPL comparisons indicates that the current combustion noise prediction procedure should be reassessed for multielement suppressor nozzles.

The 104-tube nozzle was selected for studying the combustor noise prediction validity because analytical models had been previously developed for this type of geometry. The effect of the 104 tubes may be calculated using the procedure described in Reference 42. The method is based on no-flow; however, the premises used to determine the no-flow case are equally valid in the flow case, in that the characteristic dimension of the

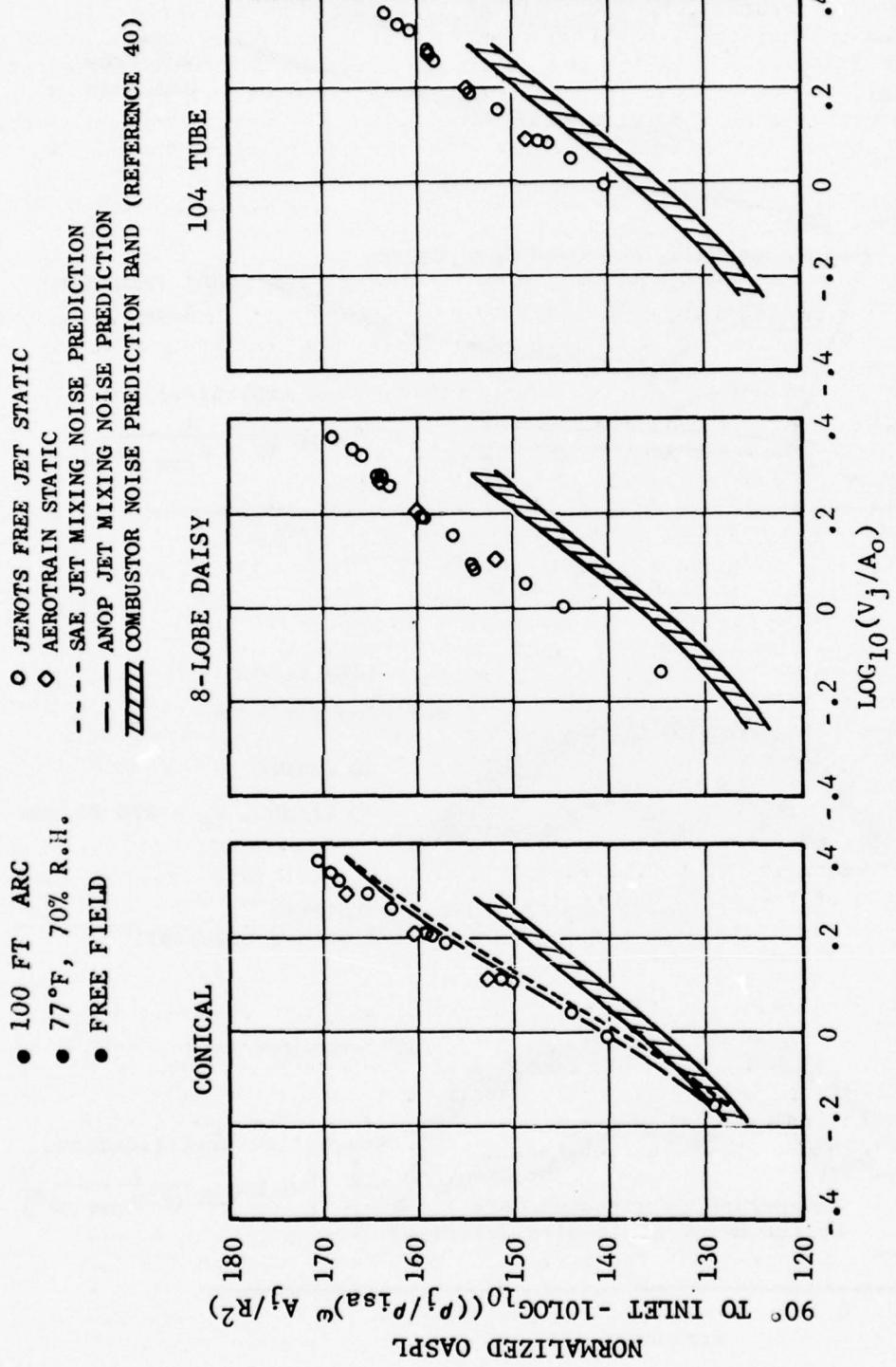


Figure 6-22. Impact of Extraneous Noise Sources on Aerotrain Data at 90°.

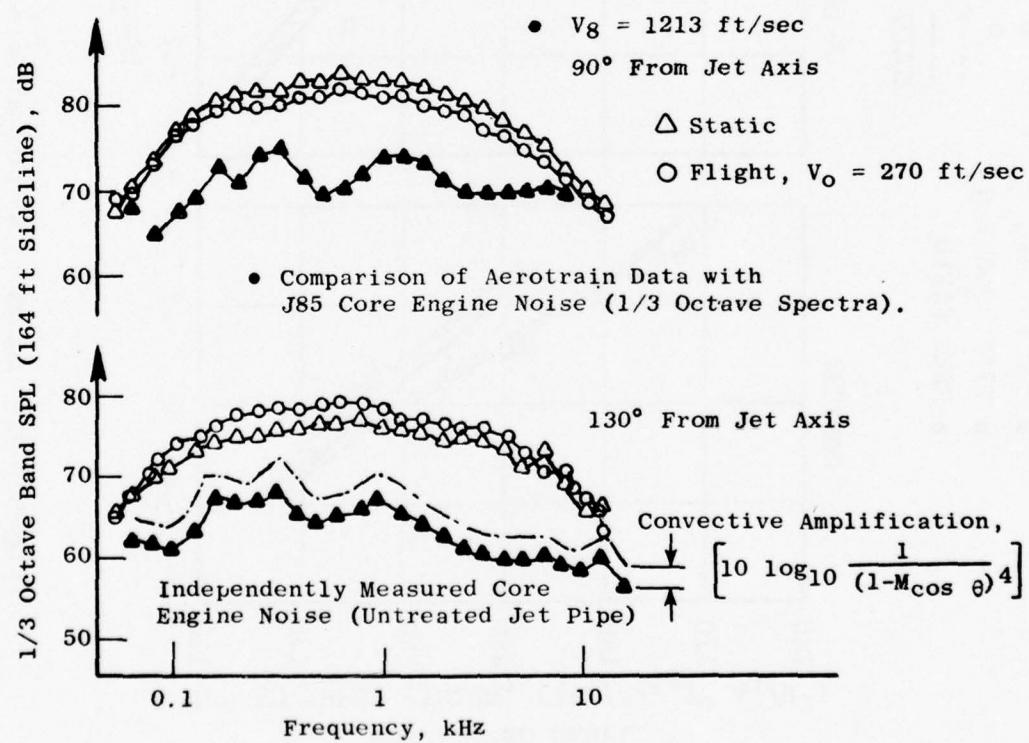
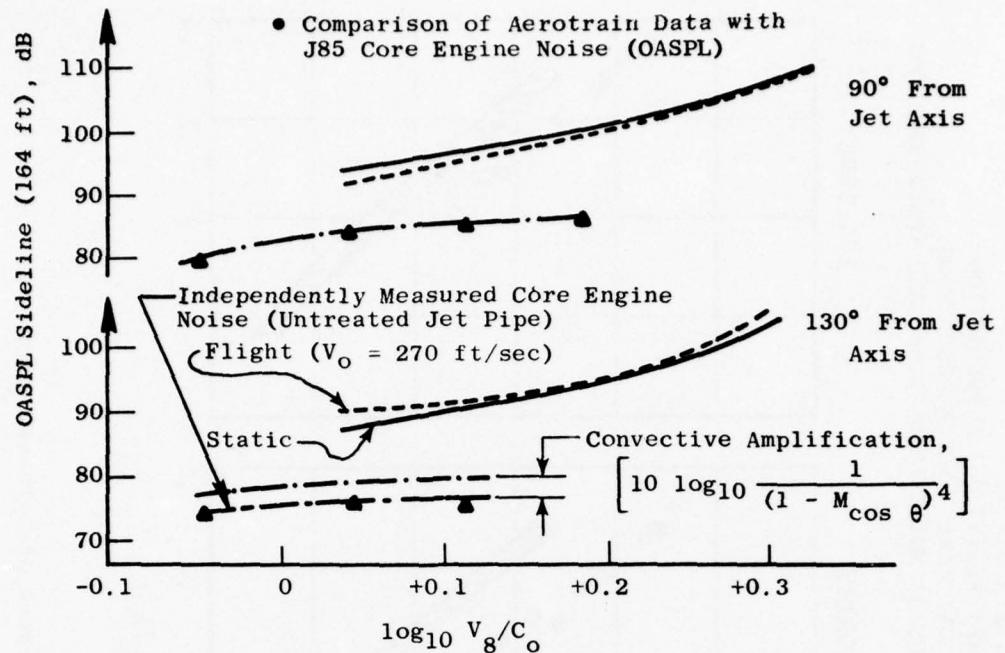


Figure 6-23. Comparison of Aerotrain Data with J85 Core Engine Noise (Reference 41).

radiation elements is much smaller than the wavelength of the sound. There is reason to assume that flow does not alter the basic mechanism involved, and noise reduction is still anticipated. Using this procedure, a 15-dB attenuation of combustor noise would occur in the 400 to 500-Hz region where it is generally accepted that the combustion noise peaks. The spectra shapes predicted by this method are presented on Figure 6-24 for both the 8-lobe and 104-tube nozzles.

It is logical to apply this 15-dB reduction to the combustor noise prediction for the 104-tube nozzle because the prediction was developed using conical nozzle test data. Based on this analysis, the combustion noise would have no influence on the noise signature of the 104-tube nozzle at the 90° acoustic angle. This conclusion is further supported by the spectra comparisons.

Similar comparisons were conducted at the maximum noise angles for all three configurations to substantiate trends observed at the 90° angle. These comparisons are presented on Figure 6-25. The same conclusions apply at this angle as were stated in the preceding paragraphs for the 90° angle comparisons of Figure 6-22.

The Aerotrain static OASPL directivity patterns for the conical, 8-lobe, and 104-tube nozzles are presented on Figures 6-26, 6-27, and 6-28, respectively. In addition to the conical scale-model data, the SAE and ANOPP jet mixing noise predictions are presented for comparisons with the static Aerotrain data. The Aerotrain background noise level at 270 ft/sec is also presented on these three figures to indicate the separation between the static J85 data and this contaminant. This separation gives an indication of the level of noise reduction that can occur due to flight without resulting in the data being influenced by background noise. The comparisons were conducted at three jet velocities: 2250 ft/sec, 1850 ft/sec, and 1475 ft/sec. Trends illustrated by the comparisons are as follows:

- In general, the Aerotrain conical nozzle data are 1 to 2 dB above the scale-model data. The ANOPP predicted levels are equivalent at the peak noise angles, but at acoustic angles greater than 140° the directivity patterns are different. The combustion noise prediction is approximately 10 dB below the Aerotrain levels at all three jet velocities, indicating no contamination of the static conical data. The background noise level of the Aerotrain is 15 to 40 dB below the measured static noise at 2250 ft/sec and 1850 ft/sec. The forward quadrant background noise for the 1475 ft/sec comparison approaches the level of the predicted combustion noise.
- The scale-model, 8-lobe data are within 1 dB of the Aerotrain static data at 2200 ft/sec and 1800 ft/sec. A 3-dB delta is observed for selected angles of the 1400 ft/sec comparison; however, it is important to note that the Aerotrain levels are below the scale-model data, and if the engine data were contami-

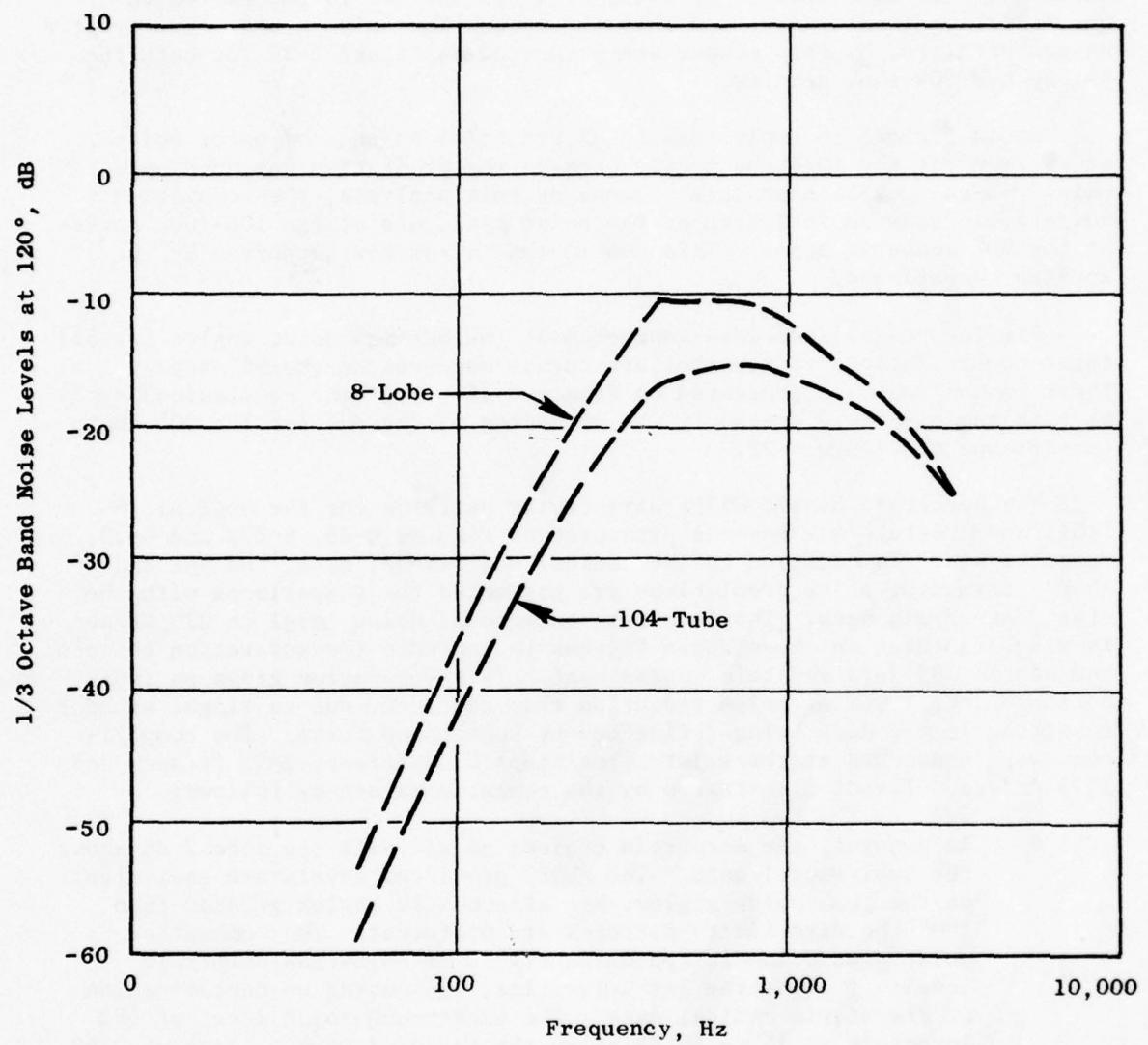


Figure 6-24. Modified Predictions of Combustion Noise Spectra for 8-Lobe and 104-Tube Nozzles (Based on Reference 42).

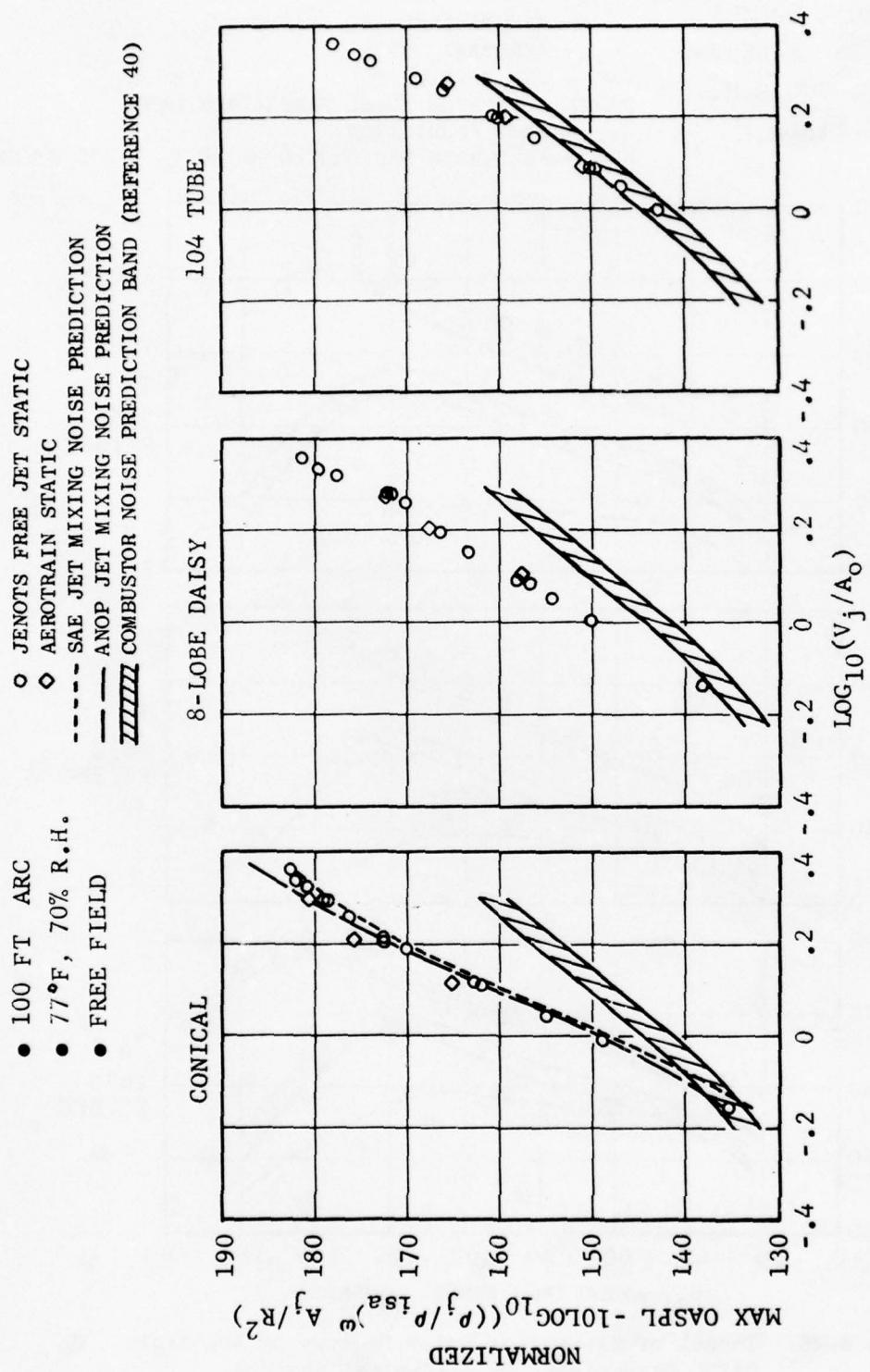


Figure 6-25. Impact of Extraneous Noise Sources on Aerotrain Data at Maximum Noise Angles.

● CONICAL NOZZLE
 ● 400 FT SIDELINE
 ● 77°F, 70% R.H.
 ● FREE FIELD

○ JENOTS FREE JET STATIC
 ◇ AEROTRAIN STATIC
 — SAE PREDICTION
 // COMBUSTOR NOISE PREDICTION BAND
 - - ANOP PREDICTION
 - - - AEROTRAIN BACKGROUND NOISE $V_0 = 270$ FT/SEC

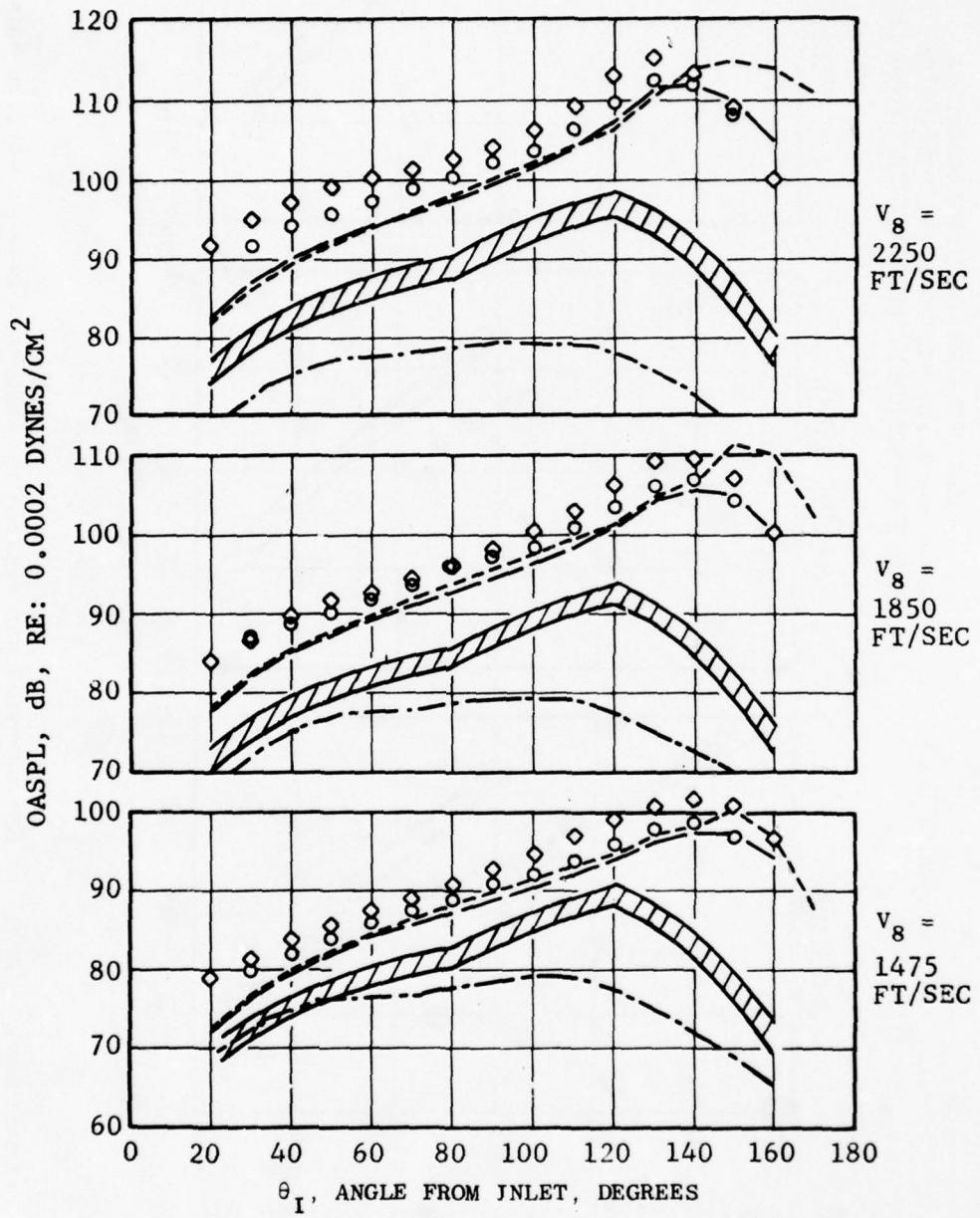


Figure 6-26. Impact of Extraneous Noise Sources on Aerotrain OASPL Directivity Data (Conical Nozzle).

• 8-LOBE DAISY
 • 400 FT SIDELINE
 • 77°F, 70% R.H.
 • FREE FIELD ○ JENOTS FREE JET STATIC
 ◊ AEROTRAIN STATIC
 // COMBUSTOR NOISE PREDICTION BAND
 // MODIFIED COMBUSTION NOISE PREDICTION BAND
 - - AEROTRAIN BACKGROUND NOISE, $V_0 = 270$ FT/SEC

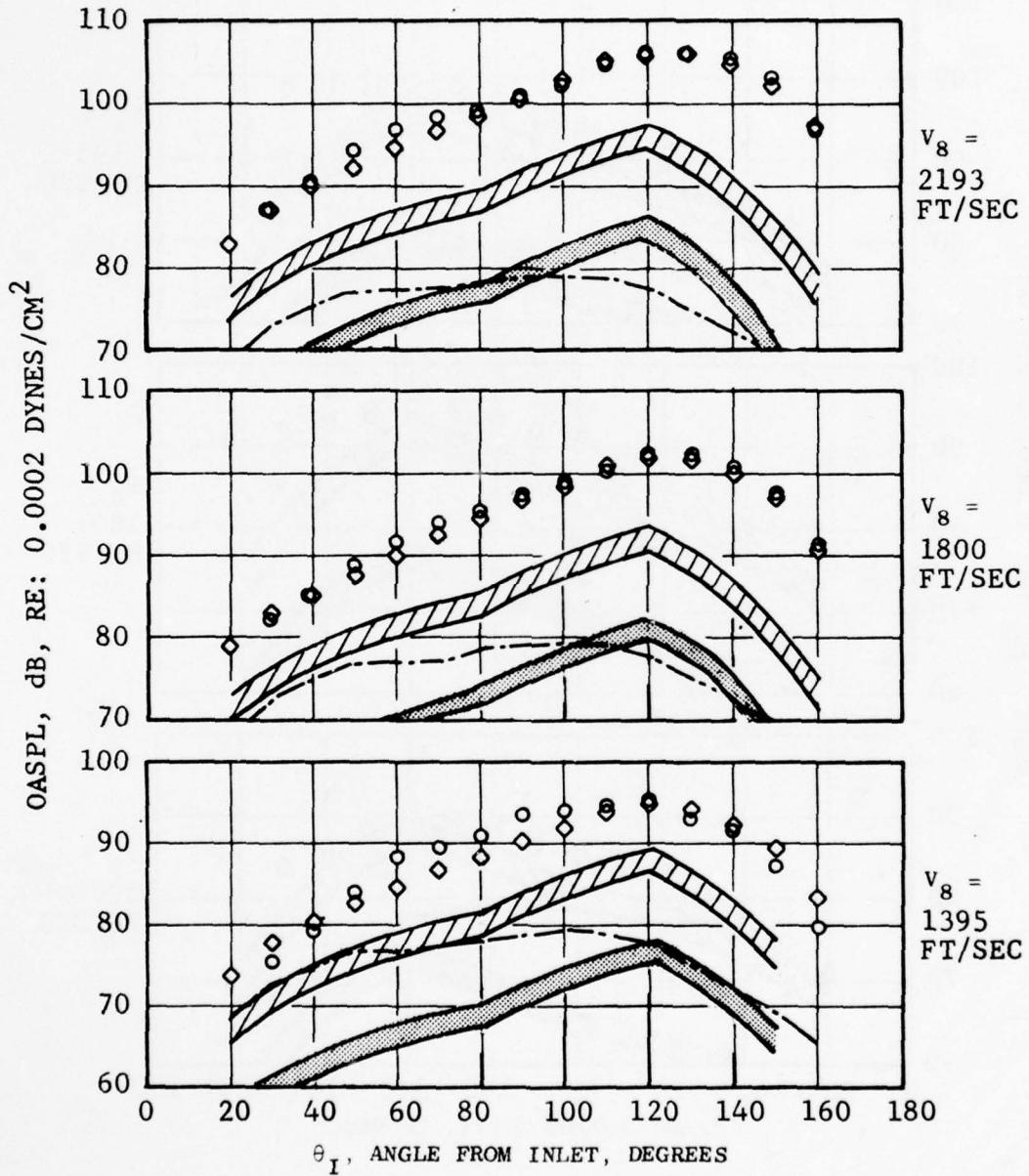


Figure 6-27. Impact of Extraneous Noise on Aerotrain OASPL Directivity Data (8-Lobe Nozzle).

- 104-TUBE NOZZLE
- 400 FT SIDELINE
- 77°F, 70% R.H.
- FREE FIELD
- JENOTS FREE JET STATIC
- ◇ AEROTRAIN STATIC
- ▨ COMBUSTOR NOISE PREDICTION BAND
- ▨ MODIFIED COMBUSTION NOISE PREDICTION BAND
- AEROTRAIN BACKGROUND NOISE, $V_0 = 270$ FT/SEC

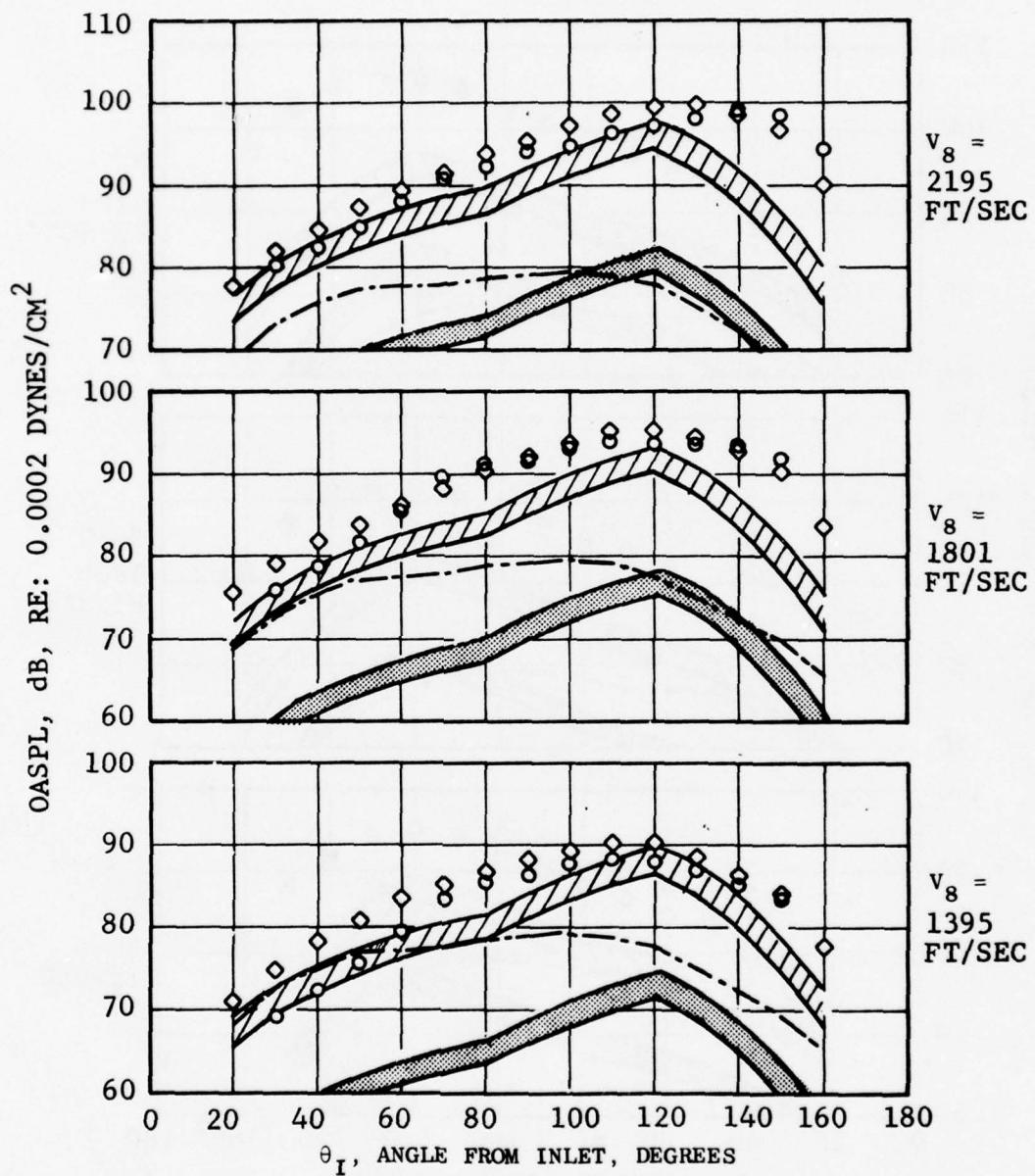


Figure 6-28. Impact of Extraneous Noise on Aerotrain OASPL Directivity (104-Tube Nozzle).

nated the opposite trend would be exhibited. The predicted combustor noise levels at selected angles for 1400 ft/sec and 1800 ft/sec are of sufficient level to cause some slight contamination, but, as stated previously, these predictions are based on conical nozzle exit-plane geometry. They are considered too high for the 8-lobe nozzle. Directivity characteristics of this nozzle compared with combustion noise predictions, based on the assumptions of the preceding analysis, indicate that the Aerotrain data are not contaminated by low frequency combustor noise. Comparisons with the background noise of the Aerotrain indicate that the measured static levels are sufficiently above the background noise for the 2193 ft/sec and 1800 ft/sec cases to avoid contamination. However, the 1395-ft/sec, forward-quadrant data would be contaminated and will be corrected for final comparisons with transformed free jet data in Section 7.0.

- The directivity comparisons for the 104-tube nozzle static data exhibited trends similar to those observed for the 8-lobe configuration except for the 1400 ft/sec case where a 6-dB difference is observed in the forward quadrant (30° through 60°). This difference is due to the noise signature of the Palouste, as illustrated previously on Figures 6-12 and 6-14. Also, the background noise directivity pattern for the Aerotrain at 270 ft/sec shows that the forward quadrant 104-tube flight data will be contaminated by background noise. Where possible, the 104-tube nozzle data at this condition were corrected for background noise.

The final phase of this extraneous noise investigation was accomplished by making select comparisons using 1/3-octave band spectra. The results are presented on Figures 6-29 through 6-34. The investigation again encompassed all three nozzles and was conducted for the extreme jet velocities (1400 ft/sec and 2200 ft/sec). Three typical acoustic angles were chosen for presentation (50° , 90° , and the angle of maximum noise).

These figures reveal the following points:

- At the angle of maximum noise, the SAE and ANOPP prediction methods have extremely different spectrum shapes than those exhibited by the Aerotrain and scale-model conical data.
- The conical nozzle scale-model data are 2 to 3 dB below the Aerotrain for the 2200-ft/sec case in the low- and midfrequencies. These differences increase to 5 to 7 dB at high frequencies. The combustion noise is predicted to contaminate in the 400-Hz to 500-Hz frequency bands; however, no contamination is observed based on comparisons with the scale-model data. The cause of the difference between the scale-model data and the Aerotrain is due to this high-frequency difference. The background noise is not of sufficient level to contaminate any part of the jet noise spectra.

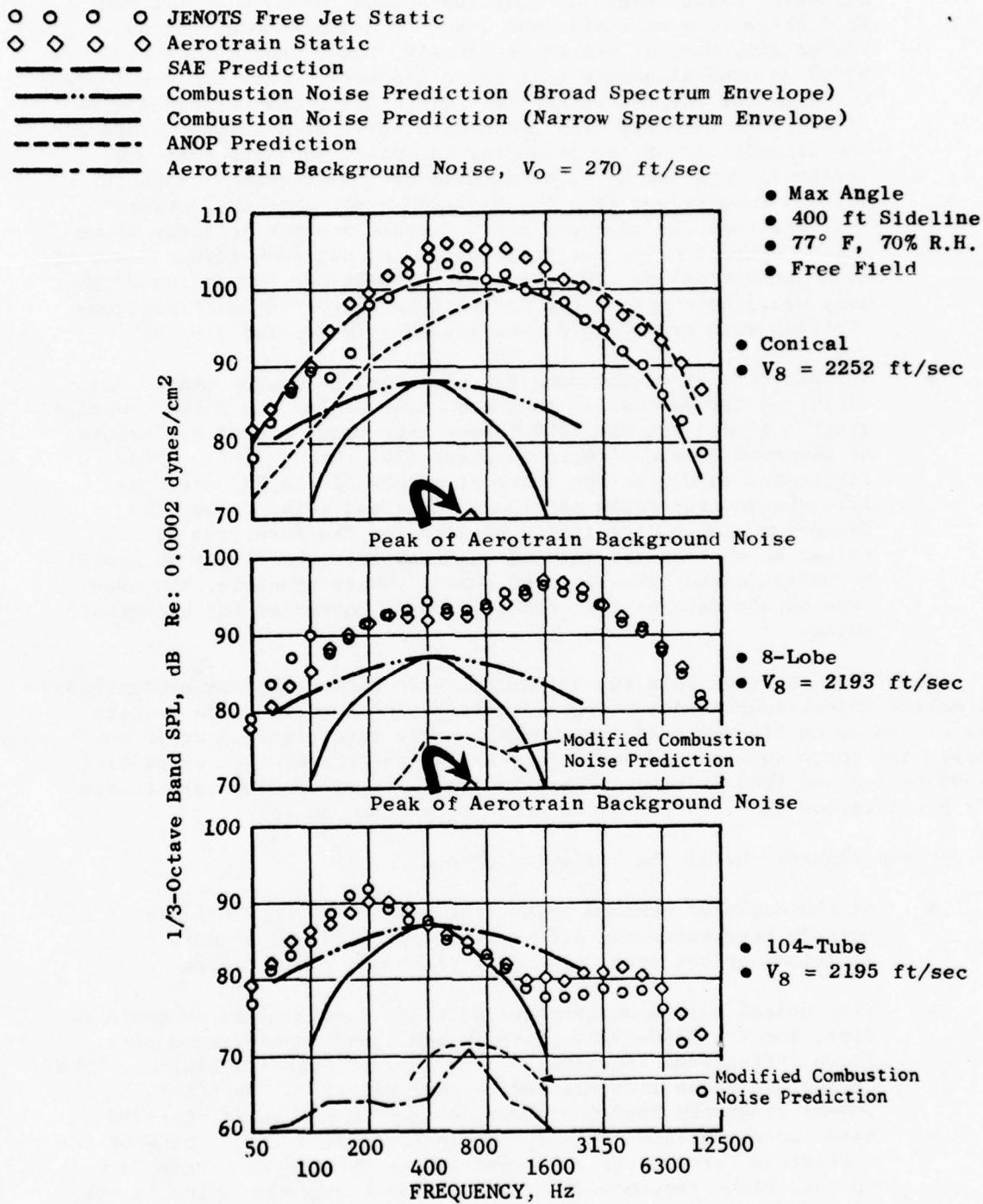


Figure 6-29. Impact of Extraneous Noise Sources on Aerotrain Spectra at Maximum Noise Angle.

○ ○ ○ ○ JENOTS Free Jet Static
 ◇ ◇ ◇ ◇ Aerotrain Static
 ——— SAE Prediction
 —·— Combustion Noise Prediction (Broad Spectrum Envelope)
 —— Combustion Noise Prediction (Narrow Spectrum Envelope)
 - - - ANOP Prediction
 —- Aerotrain Background Noise, $V_0 = 270$ ft/sec

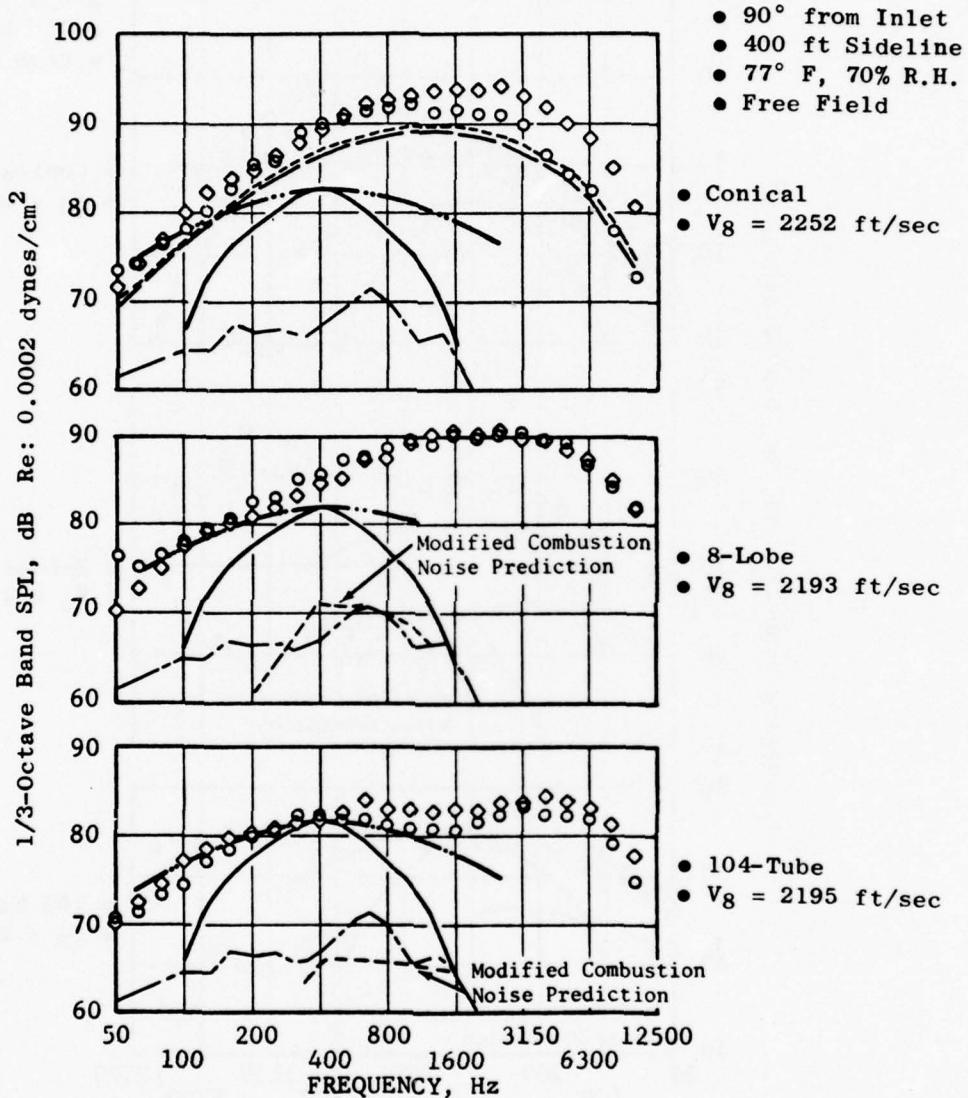


Figure 6-30. Impact of Extraneous Noise Sources on Aerotrain Spectra at 90° Angle.

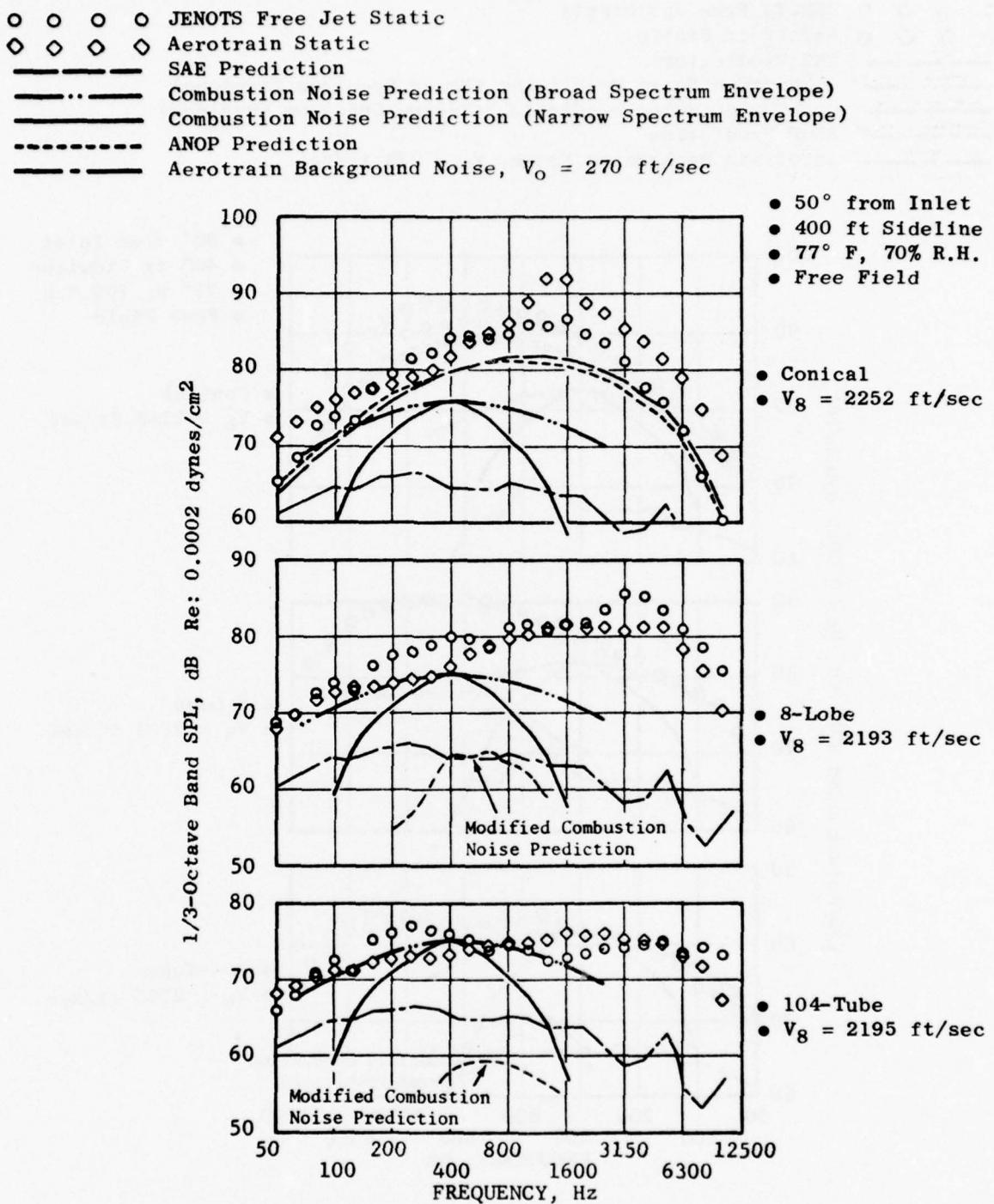


Figure 6-31. Impact of Extraneous Noise Sources on Aerotrain Spectra at 50° Angle.

○ ○ ○ ○ JENOTS Static
 ◇ ◇ ◇ ◇ Aerotrain Static
 - - - SAE Prediction
 - - - - Combustion Noise Prediction (Broad Spectrum Envelope)
 - - - - Combustion Noise Prediction (Narrow Spectrum Envelope)
 - - - - ANOP Prediction
 - - - - Aerotrain Background Noise, $V_O = 270$ ft/sec

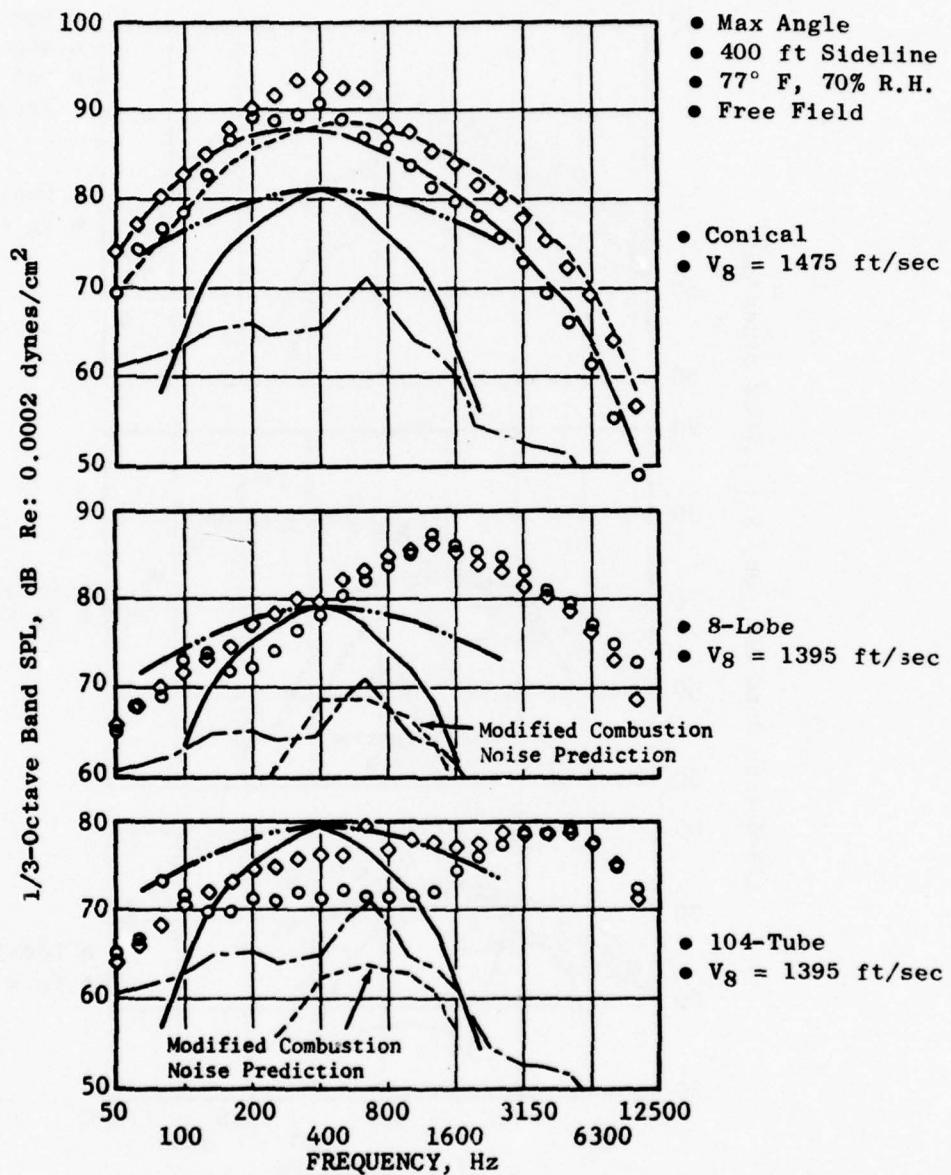


Figure 6-32. Impact of Extraneous Noise Sources on Aerotrain Spectra at Maximum Noise Angle.

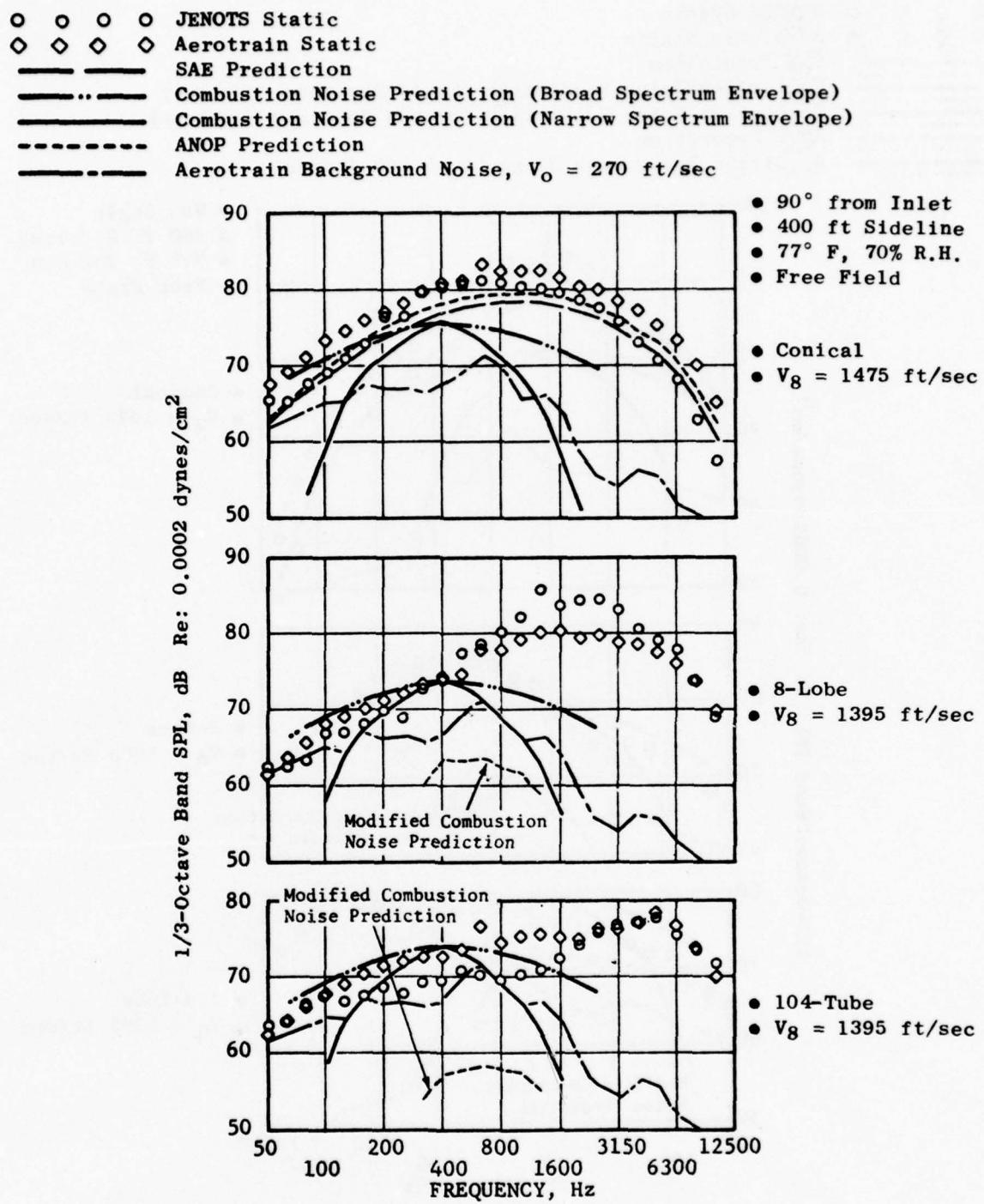


Figure 6-33. Impact of Extraneous Noise Sources on Aerotrain Spectra at 90° Angle.

○ ○ ○ ○ JENOTS Static
 ◇ ◇ ◇ ◇ Aerotrain Static
 ——— SAE Prediction
 —— Combustion Noise Prediction (Broad Spectrum Envelope)
 —— Combustion Noise Prediction (Narrow Spectrum Envelope)
 - - - ANOP Prediction
 - - - Aerotrain Background Noise, $V_o = 270$ ft/sec

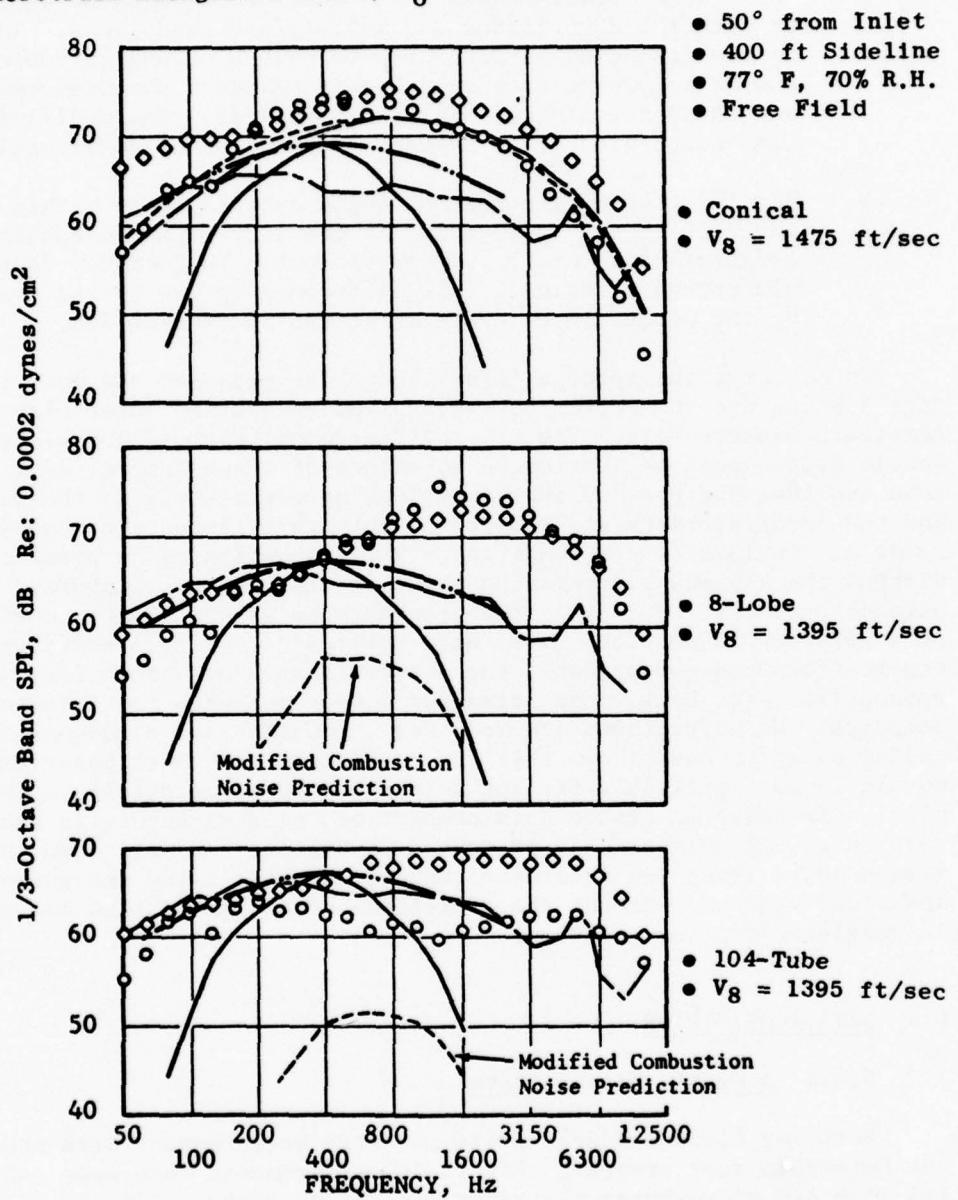


Figure 6-34. Impact of Extraneous Noise Sources on Aerotrain Spectra at 50° Angle.

- The conical nozzle scale-model data for the 1400 ft/sec case are consistently 3 to 5 dB below the Aerotrain data. The difference increases to 7 to 9 dB at high frequencies. Combustion noise and background noise are of sufficient level to contaminate the low frequency portion of the 90° and 50° spectra inflight but are not of sufficient level to cause the differences at high frequencies.
- The 8-lobe Aerotrain and scale-model spectra agree within ± 2 dB at both the 2200-ft/sec and 1400-ft/sec conditions. In general, combustion noise is predicted to have a strong influence in the 400-Hz to 500-Hz frequency bands; however, the scale-model data and the Aerotrain data agree within 1 dB. The modified combustion noise prediction procedure predicts no contamination.
- The 104-tube nozzle maximum angle spectra agree within ± 2 dB at the 2200-ft/sec condition. At the 1400-ft/sec condition, the Aerotrain data are 5 to 7 dB above the scale-model data in the midfrequency region. This difference is due to the contamination by the Aerotrain Palouste as stated in Section 6.2.

In summary, the spectra comparisons have provided the most insight in establishing the roles that background and combustion noise play in the Aerotrain measurements. The major differences observed between the conical nozzle data cannot be attributed to either of these contaminants. The 8-lobe and 104-tube nozzles show excellent agreement between the scale-model and the Aerotrain data at 2200 ft/sec but are influenced by background noise at the 1395-ft/sec condition. The combustion noise predictions, without the assumed transmission loss effects, are not supported by the data comparisons. Modifying the procedure to account for this effect, even on a first approximation, gives more realistic results. Based on these observations and comparisons, the Aerotrain data are corrected, where appropriate, for background noise for comparison with the transformed free jet data. No corrections are made for combustion noise because the preceding examples have shown that the prediction procedure based on conical nozzle is not applicable for the 8-lobe and 104-tube nozzles. This conclusion is based on static data comparisons between Aerotrain and JENOTS test data. All comparisons presented in Section 7.0 will show the background noise level and predicted combustion noise using the narrow spectrum shape and with and without the additional transmission loss due to a change in nozzle exit plane geometry.

6.4 DATA ACQUISITION

6.4.1 Acoustic Measurements

Both far field and near field acoustic measurements were made during the Aerotrain test program. Far field measurements were made using four 1/4-inch B&K microphones placed at a sideline distance of 164 ft from the test track. Three of the microphones were placed at a height of 51 ft and

spaced 39.4 ft apart, while the fourth microphone was at a height of 24.6 ft on the center pole. The spacing between the three microphones was chosen to provide statistically independent data samples. The two microphone heights were chosen to provide information on the impact of ground reflection. A photograph of the microphone array is presented on Figure 6-35.

The acoustic data were recorded using a one-track Nagra-III tape recorder operated by remote control.

Accurate determination of the noise signature as a function of acoustic angle requires synchronization of the location of the Aerotrain with the acoustic and aerodynamic parameters being recorded. This synchronization is obtained by recording telemetered signals simultaneously on the Nagra and Ampex recorders used for recording the acoustic and aerodynamic parameters. The synchronization signal superimposed on the transient acoustic signal is illustrated on Figure 6-36. This procedure relates the acoustic and aerodynamic parameters to a common reference time base.

6.4.2 Trajectory

Synchronization of the carrier vehicle position with the acoustic and aerodynamic data is of critical importance in any moving-frame test program. The Aerotrain guidance rail is provided with high frequency transmitters spaced 1.96 ft apart. This signal is recorded on tape in conjunction with the synchronization signals and allows the location of the Aerotrain position to be related to the acoustic and aerodynamic data as a function of time.

6.4.3 Aerodynamic Parameters

Aerodynamic parameters were recorded on board the Aerotrain for each pass using an Ampex tape recorder. The parameters recorded were:

P_{T2} - P_r , inlet total pressure measured with three Prandtl tubes averaged

P_{T2} - P_{s2} , Inlet total pressure minus inlet static pressure

P_{T5} - P_r , Total turbine discharge pressure

P_{s61} - P_r , Rake Static pressures at station 6

P_{s62} - P_r , Rake Static Pressures at station 6

P_{s63} - P_r , Rake Static Pressures at station 6

T_{T5} , Turbine discharge total temperature

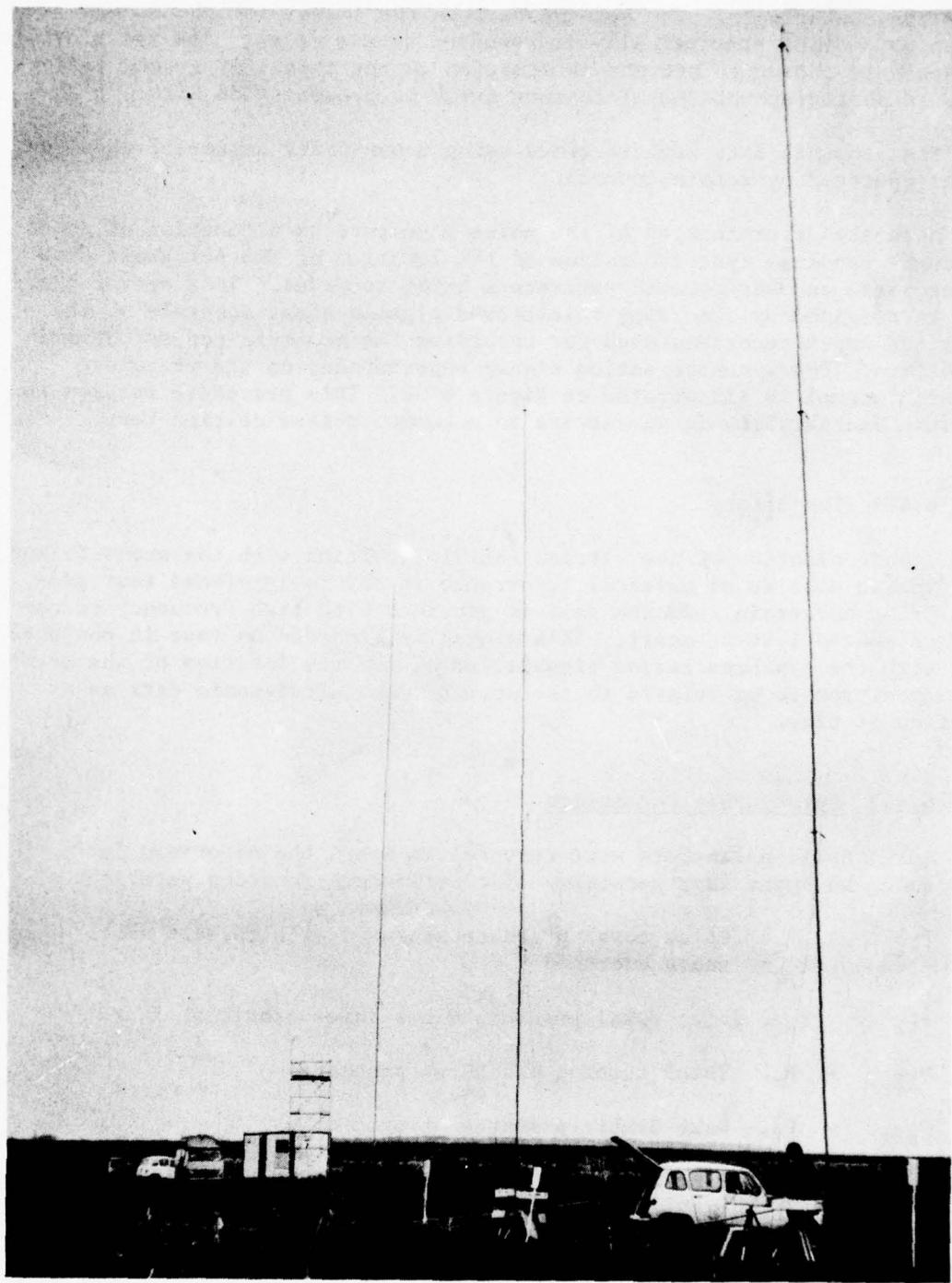


Figure 6-35. Aerotrain Microphone Array.

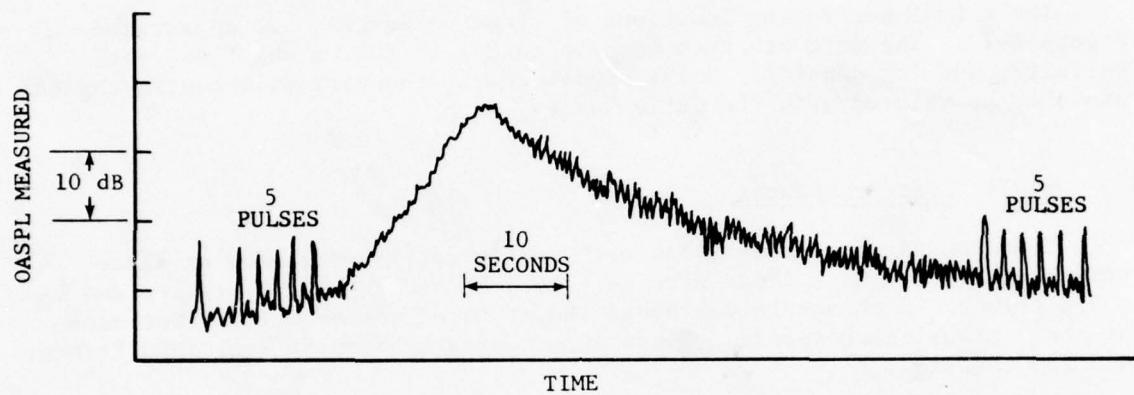


Figure 6-36. Aerotrain Synchronization Procedure.

P_r ,	Reference Pressure that is usually set to ambient before each pass
T_{carb} ,	Fuel temperature
N ,	Speed (rpm)
C_m ,	Fuel flow
	Gauge Time Signal
	Synchronized Acoustic Time Signal

The actual monitoring locations of these parameters are summarized on Figure 6-37. The data are then used to calculate the weight flow, jet velocity, and jet density. Noise signatures at the various acoustic angles can then be related with the jet velocity.

6.4.4 Test Procedures

The acoustic measurements on each configuration were made at three nominal train speeds. These were $V_0 = 16.4$ ft/sec, $V_0 = 130$ ft/sec, and $V_0 = 270$ ft/sec. Each nozzle was evaluated at three jet velocities for each of these translation speeds. These were nominally 1400 ft/sec, 1800 ft/sec, and 2200 ft/sec.

The translation speed of less than 16 ft/sec corresponds to static measurement conditions and will be referred to as such throughout the rest of the text. The advantage of using this type of procedure for static measurements is that it allowed the same data reduction procedure to be used for both the static and simulated-flight conditions. To acquire static data, the vehicle was placed 164 ft from the beginning of the acoustic arena, and the engine speed was stabilized. After stabilization, the Aerotrain proceeded through the acoustic arena using the wooden brakes for speed control.

For the forward speed operations, the vehicle was positioned at location X_i , as defined on Figure 6-38, which was determined based on the predicted nozzle thrust. The pilot then stabilized the engine conditions for a period of two minutes before brake release. After brake release and upon entering the acoustic arena, the pilot used the braking system to maintain constant speed. Two typical examples of how the Aerotrain velocity varied through the acoustic arena are presented on Table 6-II. The average variations about the mean velocity are ± 7 ft/sec.

- J85 ENGINE
- ON-BOARD TAPE RECORDING

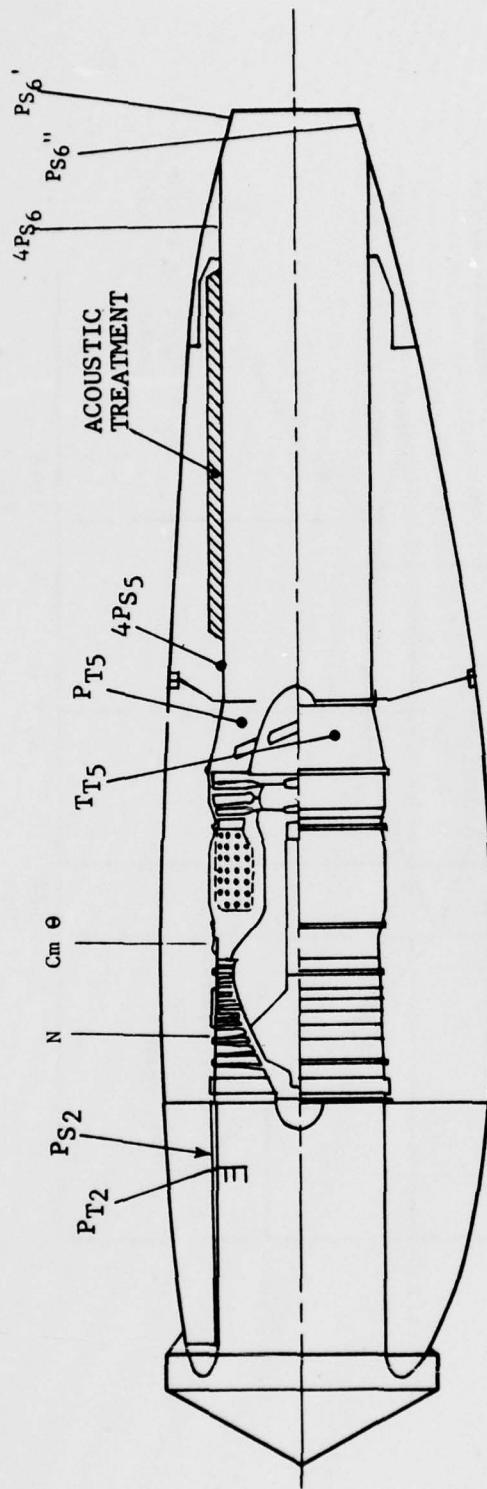


Figure 6-37. Monitoring Locations of Cycle Parameters.

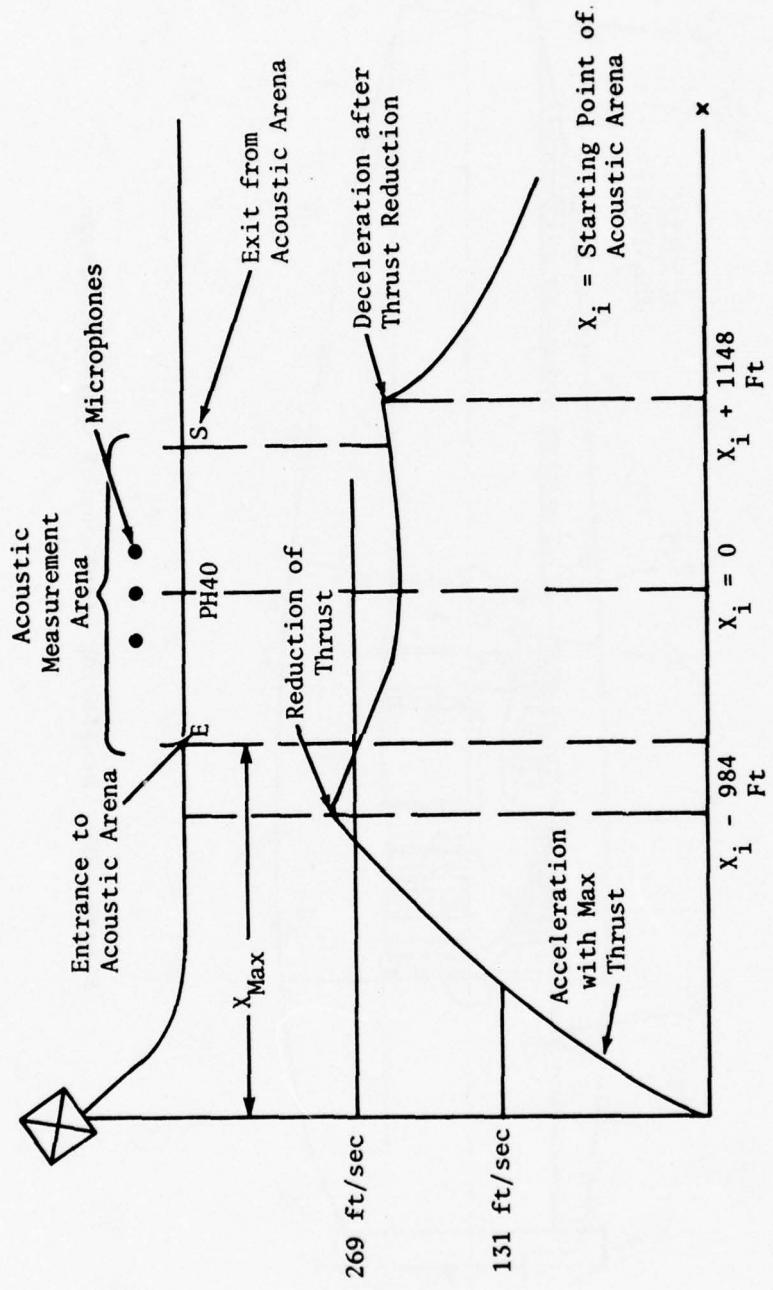


Figure 6-38. Schematic of Aerotrain Operating Procedure.

TABLE 6-II Examples of Aerotrain Flight Velocity Variation Through the Acoustic Arena.

Entrance to Acoustic Arena	x_i	Conical	8-Lobe	104-Tube
		Nozzle	Nozzle	Nozzle
	Ft.	Ft/Sec	Ft/Sec	Ft/Sec
-535	270	262	259	
-515	273	262	262	
-495	277	270	266	
-476	270	259	256	
-456	273	262	262	
-436	273	266	262	
-417	273	266	262	
-397	277	266	262	
-377	273	266	259	
-358	273	262	262	
-338	273	266	262	
-318	281	273	266	
-298	273	262	262	
-279	273	266	259	
-259	273	262	262	
-239	277	266	262	
-220	281	273	270	
-190	273	262	259	
-161	273	266	262	
-141	277	266	262	
-121	277	266	262	
-102	277	266	262	
-82	273	266	262	
-62	277	266	262	
-43	277	266	262	
-23	281	270	270	
-3	273	262	259	
16	277	266	262	
36	277	262	259	
56	277	266	266	
75	277	266	262	
95	277	270	266	
115	277	266	262	
134	281	270	266	
154	273	262	262	
184	275	264	262	
213	277	266	266	
233	277	262	262	
253	277	266	262	
272	277	266	266	
292	285	270	270	
312	270	262	259	
331	277	262	262	
351	277	266	262	
371	277	266	266	
390	277	266	266	
410	277	262	262	
430	281	270	270	
449	273	259	259	
469	277	266	266	
489	277	262	-	
499	-	-	264	
508	277	262	-	
528	277	263	266	
548	277	-	-	
Average Velocity		276	265	263

6.5 DATA REDUCTION

The reduction of the Aerotrain acoustic data followed the same procedure as used on the flight data described in Section 5. One-eighth-second integration was found to give the angular resolution of ± 6 degrees at the maximum forward speed condition for the 90° acoustic angle (which is the worst condition). The data reduction consisted of the following steps:

- For each simulated flight data point the 1/3-octave spectra, in dB, was presented based on 1/8-second integration. One-second integration was used for the static data. The measurements were corrected only for the frequency response of the system.
- These results were corrected to standard hot day conditions (ISA + 10° C, relative humidity 70%) and corrected for ambient and electronic background noise.
- Test data was corrected to free field using the procedure described in detail in Section 6.5.1.
- The 1/3-octave band spectra and corresponding OASPL, PNL, and PNLT were determined at 10° increments for acoustic angles from 20° through 160° .
- These arrays for each individual microphone and each pass were then averaged to determine the simulated inflight noise signature for each cycle condition.

6.5.1 Ground Reflection Correction Procedure

The ground reflection correction procedure used to correct the Aerotrain far field acoustic data to free field was developed by SNECMA for the Aerotrain acoustic arena. The method consisted of identifying the regions in the spectra where the primary and secondary null patterns occur, using a computer searching technique. After this was accomplished, corrections were applied using a correction curve based on classical theory and described in Reference 43. This computer searching technique for null determination eliminates phase shift problems which are the primary cause of poor ground reflection corrections (essentially accomplishes the same goal as the engineering judgment corrections applied to the Learjet and F-106 data). All Aerotrain data were corrected to free field conditions using this procedure.

Aerotrain Data Averaging Procedure

The next step in the data reduction was to correctly average the Aerotrain data to determine the statistically representative noise signature. This was accomplished using the procedure described in Section 3.3.2. The details describing the application of this procedure to the Aerotrain data are presented as follows.

The microphone arrangement for the Aerotrain tests was presented in Figure 6-1. The spacing between the microphone poles was 12 meters (39.4 feet) and the maximum Aerotrain velocity used for this example was 88 meters/second (289 feet/second). Evaluation of equation (15) with $T = 0.125$ establishes that the measurements obtained from different poles will be independent for all 1/3-octave band frequencies above 160 Hz. On the center pole, two microphones were spaced 2.6 ft apart. The discussion preceding equation (18) Section 3.3.2 shows that this data will be almost totally correlated (i.e.: $\rho_{27} = 1$).

For 1/3-octave band frequencies above 160 Hz, the estimation equations from Section 3.3.2 become:

$$\Phi = \begin{bmatrix} 1 & 0 & 0 & 0 \\ 0 & 1 & 0 & 0 \\ 0 & 0 & 1 & \rho \\ 0 & 0 & \rho & 1 \end{bmatrix} \text{ with } \underline{P^2} = \begin{bmatrix} P_1^2 \\ P_3^2 \\ P_2^2 \\ P_7^2 \end{bmatrix} \quad (69)$$

with: P_i^2 is 1/3-octave mean square pressure value (not in dB!) from location i in Figure 3-100.

P is the correlation coefficient between microphones on the second pole (later in the analysis $\rho \rightarrow 1$, however, making variable at this point avoids a singularity problem with ϕ).

The true values of the mean square pressure with minimum variance in the 1/3-octave band is

$$\hat{\sigma}^2 = \frac{(1 + \rho)}{2(2 + \rho)} \left[1, 1, \frac{1}{1 + \rho}, \frac{1}{1 + \rho} \right] \begin{bmatrix} P_1^2 \\ P_3^2 \\ P_2^2 \\ P_7^2 \end{bmatrix} \quad (70)$$

and

$$k = 2(2 + \rho)/(1 + \rho)$$

Taking the limit as $\rho \rightarrow 1$, the optimal procedure is obtained for combining the Aerotrain data from a single pass:

$$\hat{\sigma}^2 = \frac{1}{3} \left[P_1^2 + P_3^2 + \frac{1}{2} (P_2^2 + P_7^2) \right] \quad (71)$$

and the confidence curve is chosen with $K = 3$.

Standard computer programs available for the analysis of multiple data sets generally compute the mean of all the data records. If such a program were used to reduce the data from each pass of the Aerotrain, the suboptimal estimate would be given by:

$$\hat{\sigma}_{\text{SUBOPT}}^2 = \frac{1}{4} \left[P_1^2 + P_3^2 + P_2^2 + P_7^2 \right] \quad (72)$$

This estimate will be unbiased. Statistical theory may be applied to determine the variance of this estimate and the equivalent number of independent data records in it. The calculation of the suboptimal estimate is as follows:

$$\Sigma_{\text{SUBOPT}} = \frac{1}{16} [1, 1, 1, 1] \begin{bmatrix} 1 & 0 & 0 & 0 \\ 0 & 1 & 0 & 0 \\ 0 & 0 & 1 & \rho \\ 0 & 0 & \rho & 1 \end{bmatrix} \begin{bmatrix} 1 \\ 1 \\ 1 \\ 1 \end{bmatrix} \frac{2\sigma^4}{n} \quad (73)$$

or

$$\Sigma_{\text{SUBOPT}} = \frac{1}{16} (4 - 2\rho) \frac{\sigma^4}{n} \quad (74)$$

As before, the equivalent number of independent data records in this estimate is determined as:

$$k_{\text{SUBOPT}} = \lim_{\rho \rightarrow 1} \frac{16}{(4 + 2\rho)} = 2.667 \quad (75)$$

Thus, only the equivalent of one-third of an independent data record is lost if all the data from different microphone heights are averaged to minimize the impact of ground reflection corrections.

6.6 DATA ANALYSIS

As stated in the introduction to Section 6.0, the purpose of the Aerotrain test program was to provide a highly controlled set of "flight data" for verification of the inflight simulation technique. The results presented in this section show that the "flight effects" observed for each configuration tested on the Aerotrain are substantially different, providing a wide range of phenomena for the simulation technique to duplicate.

The results of the Aerotrain test program corrected for background noise are presented using the same format as the Learjet and F-106 data and are summarized as follows:

- Maximum PNL and OASPL as a function of jet velocity
- PNL and OASPL directivity patterns
- Selected 1/3-octave band spectra at acoustic angles of max noise, 90° and 50° respectively, relative to the nozzle inlet

Figures 6-39 and 6-40 present the maximum PNL and OASPL levels for each of the nozzles as a function of jet velocity and flight velocity. The conical nozzle peak noise level reduction is observed to increase with increasing flight velocity and increases with decreasing jet velocity. In contrast, for the two suppressor nozzles, the peak noise reduction is only a function of forward velocity.

The PNL and OASPL directivity patterns are presented on Figures 6-41 through 6-58 for the three configurations at each of three jet velocities. The trends on the basis of these two parameters are similar in some respects but different in others with salient points as follows:

- The angle of maximum noise is observed to stay constant, or to shift towards the forward quadrant from static to flight conditions.

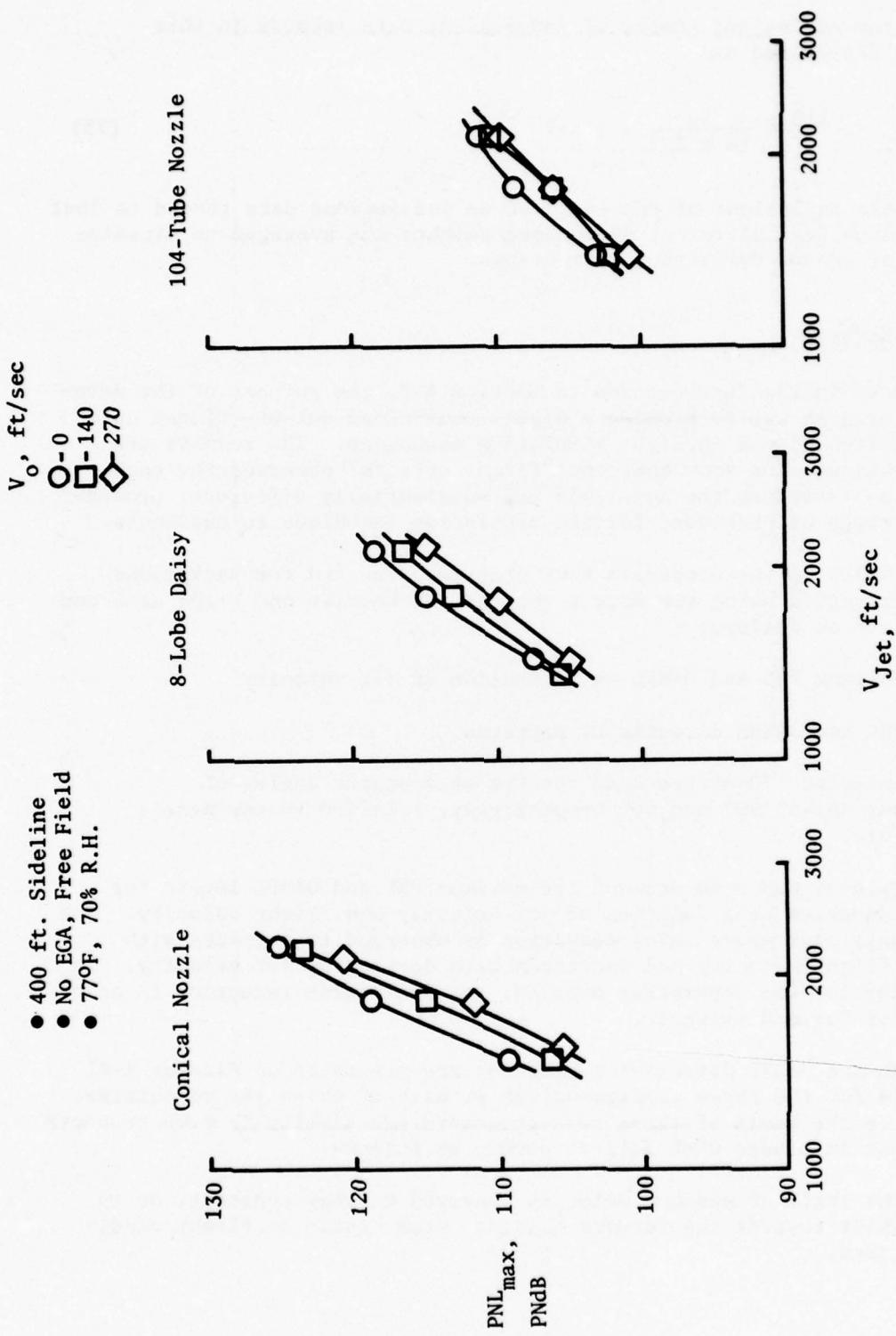


Figure 6-39. Summary of Peak PNL Characteristics.

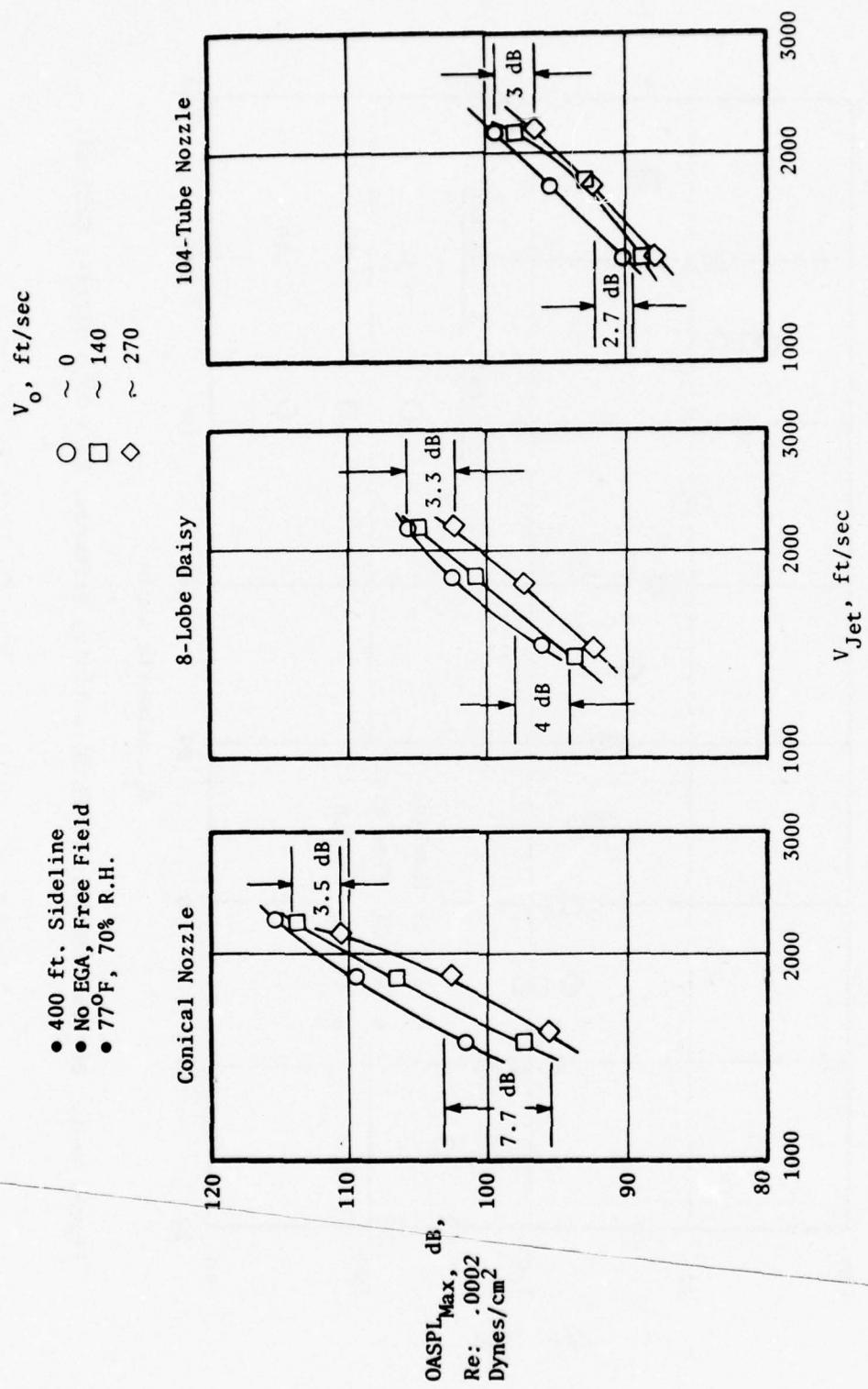


Figure 6-40. Summary of Peak OASPL Characteristics.

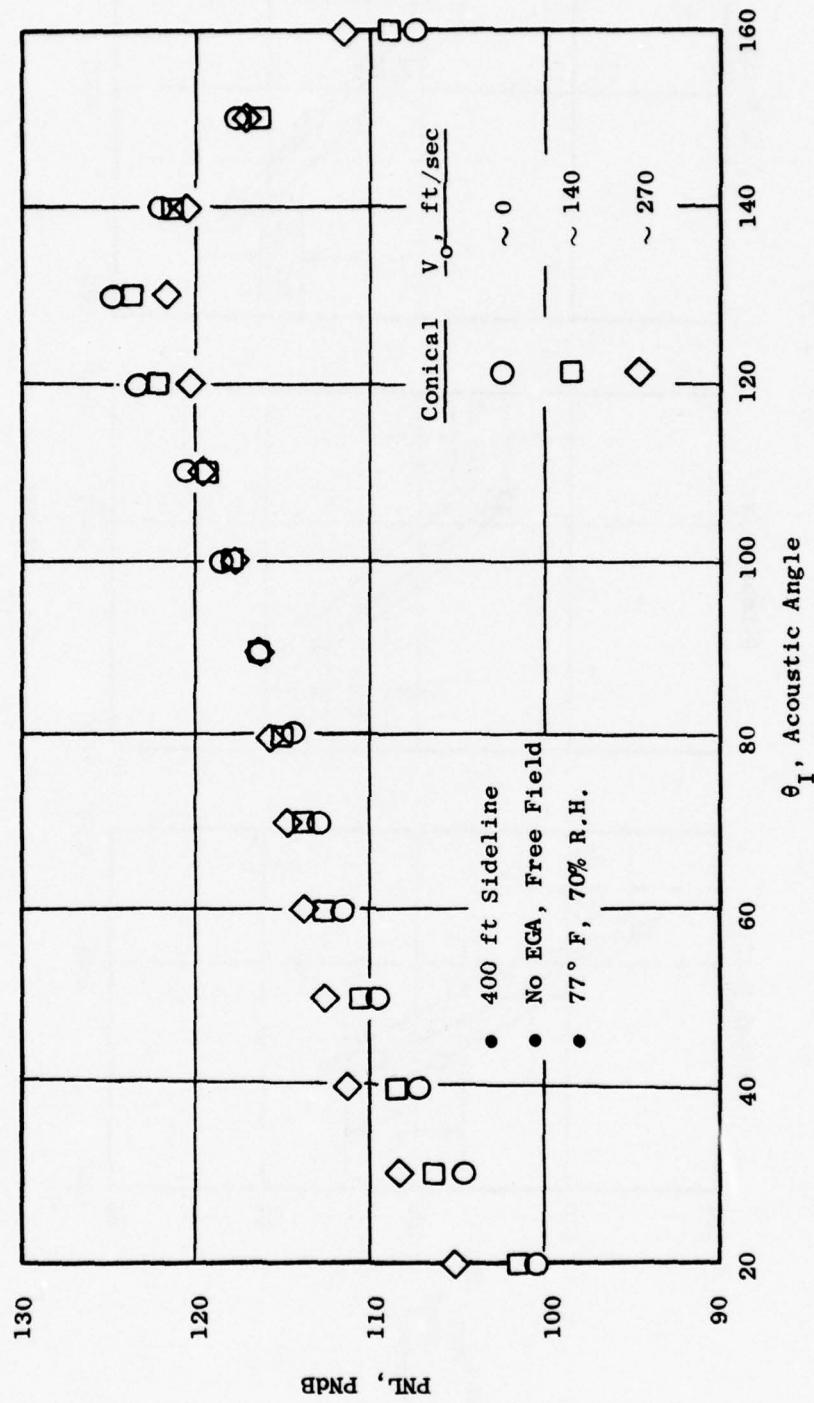


Figure 6-41. Bertin Aerotrain - PNL Directivity Patterns, $V_J = 2200$ ft/sec, Conical.

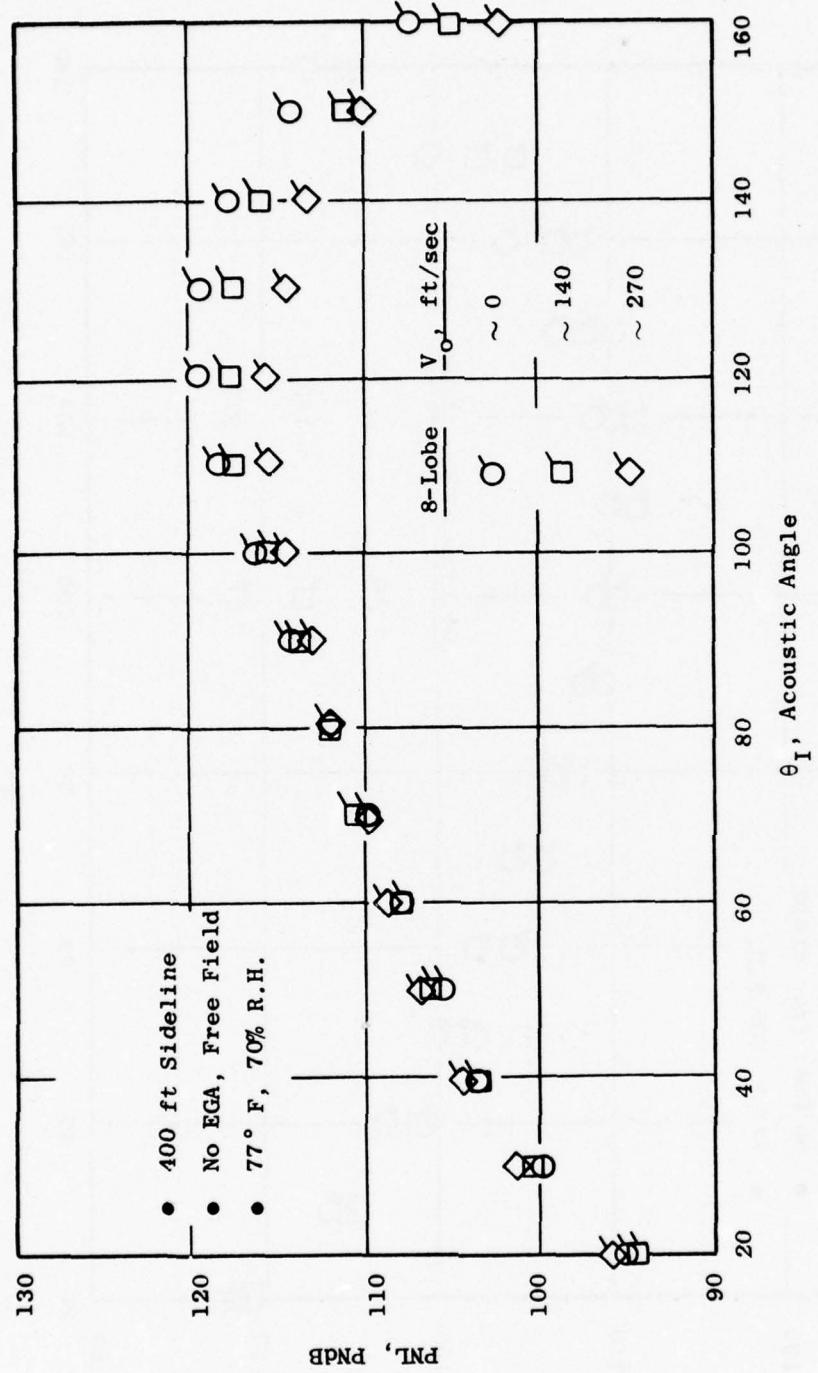


Figure 6-42. Bertin Aerotrain - PNL Directivity Patterns, $V_J = 2200$ ft/sec, 8-Lobe.

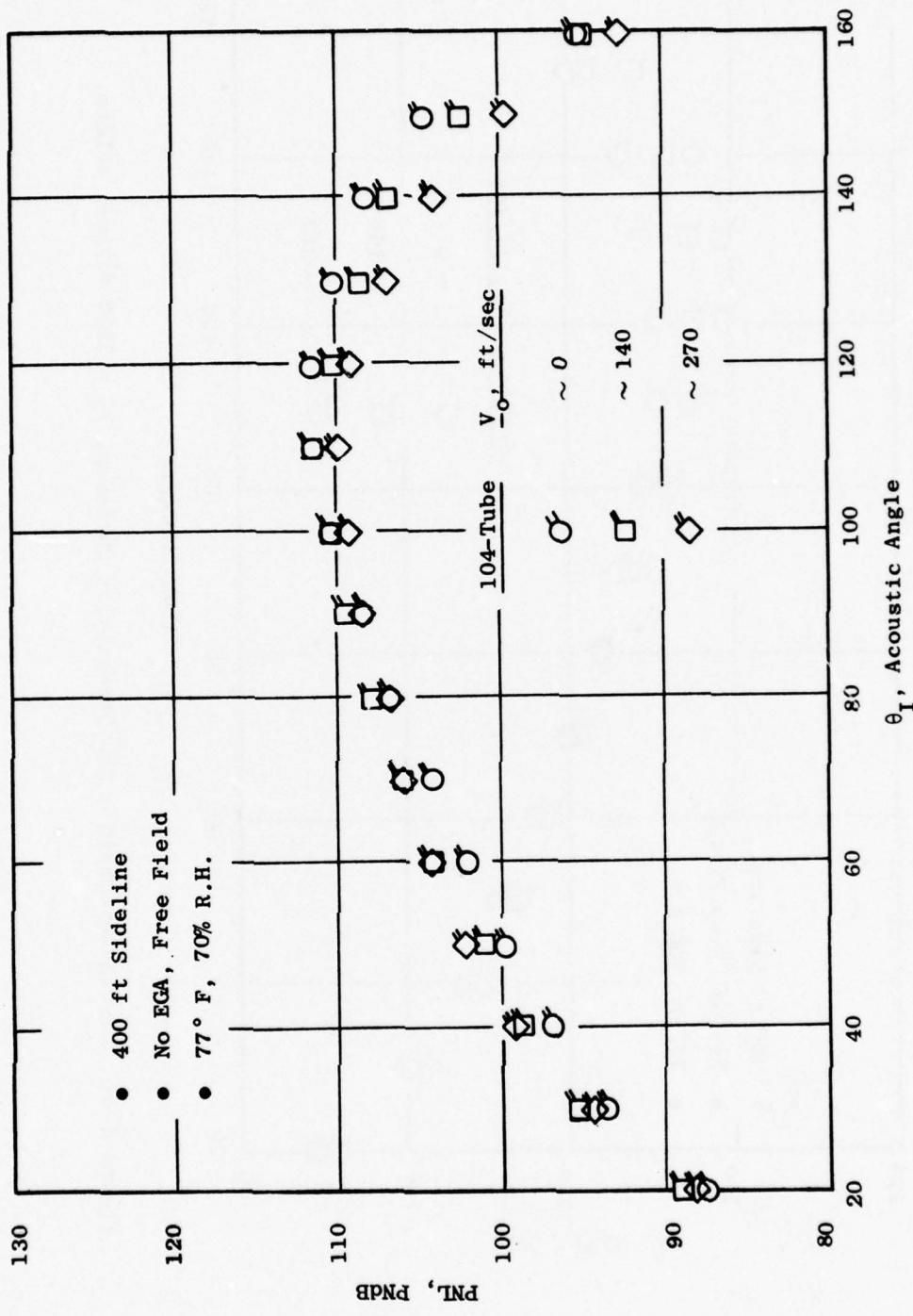


Figure 6-43. Bertin Aerotrain - PNL Directivity Patterns, $V_J = 2200 \text{ ft/sec}$, 104-Tube.

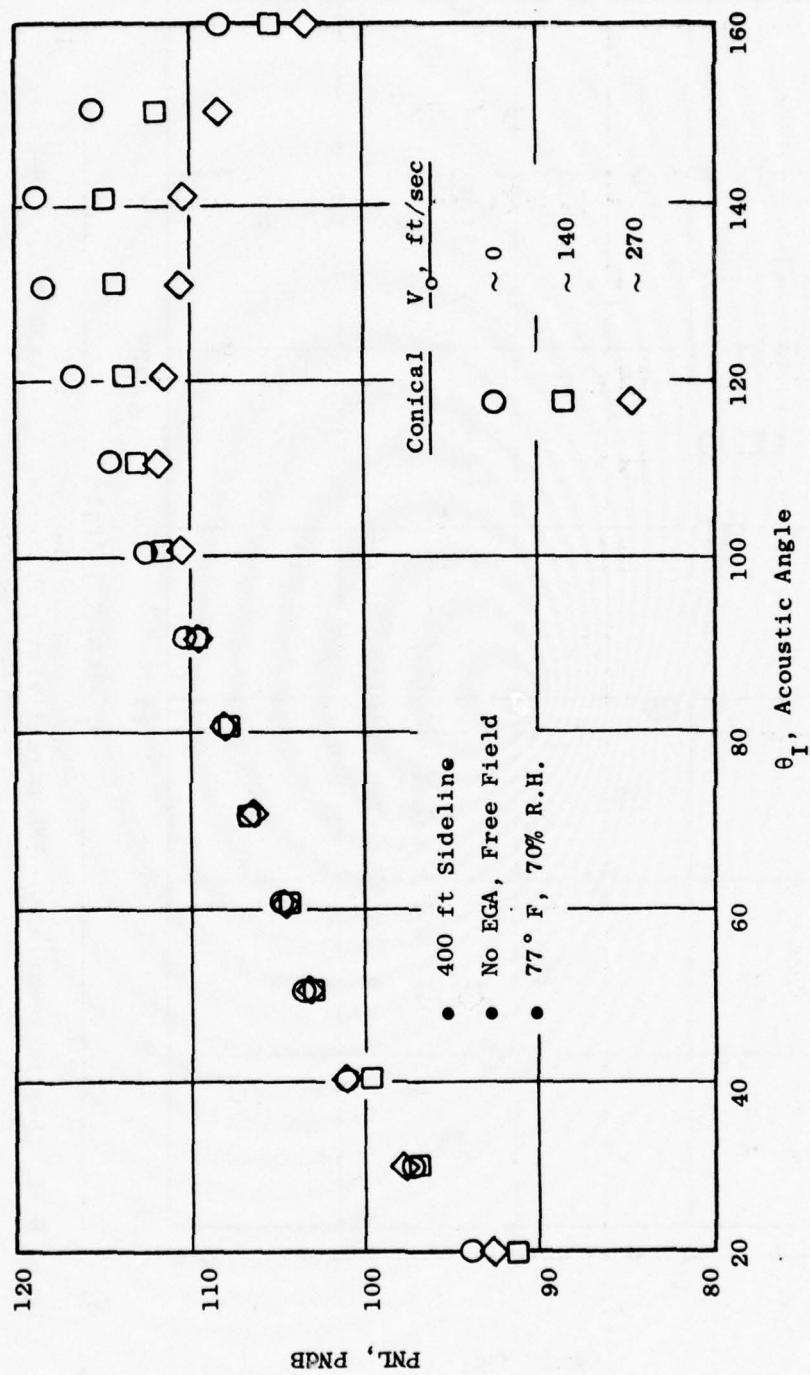


Figure 6-44. Bertin Aerotrain - PNL Directivity Patterns, $V_J = 1830$ ft/sec, Conical.

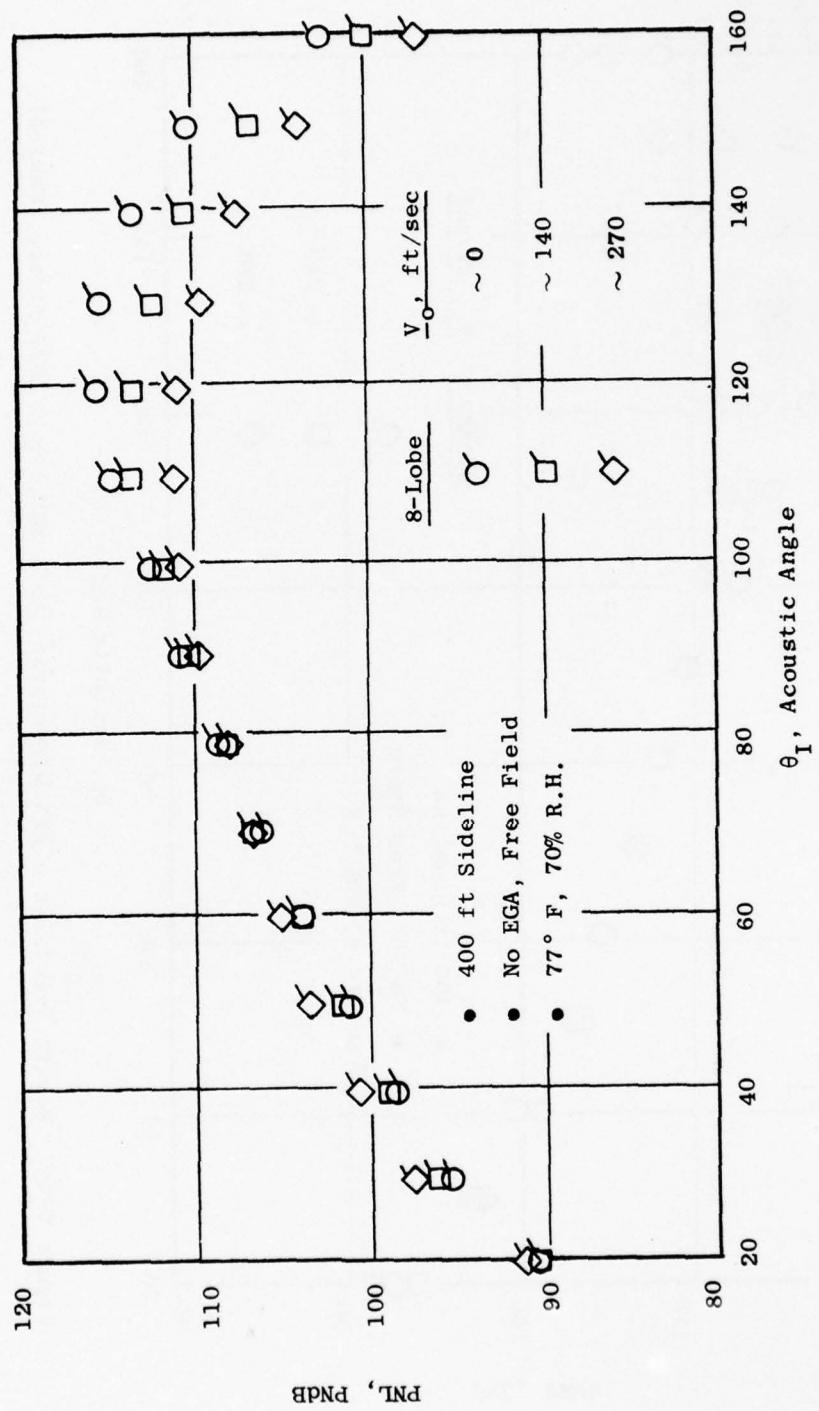


Figure 6-45. Bertin Aerotrain - PNL Directivity Patterns, $V_J = 1830$ ft/sec, 8-Lobe.

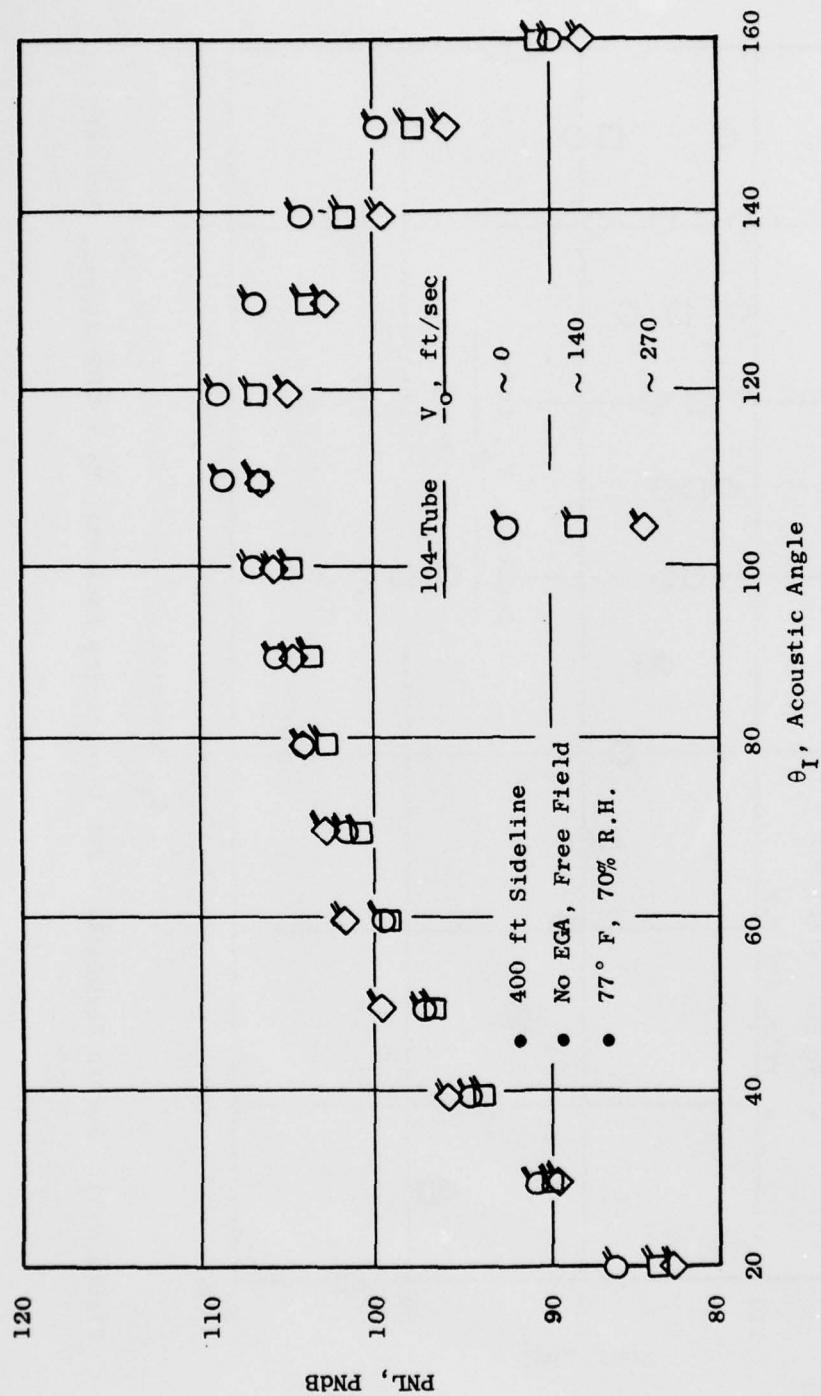


Figure 6-46. Bertin Aerotrain - PNL Directivity Patterns, $V_J = 1830$ ft/sec, 104-Tube.

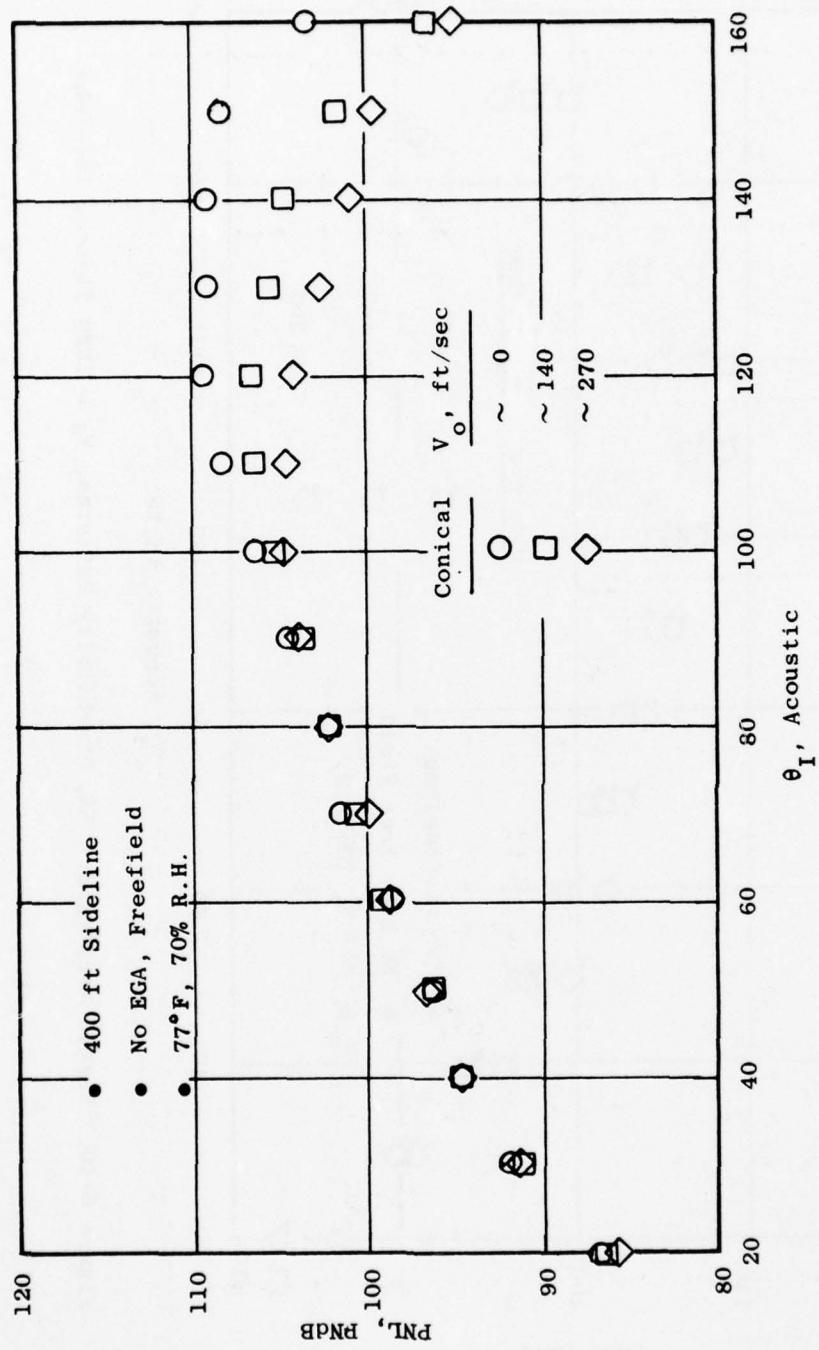


Figure 6-47. Bertin Aerotrain - PNL Directivity Patterns, $V_J = 1440$ ft/sec, Conical.

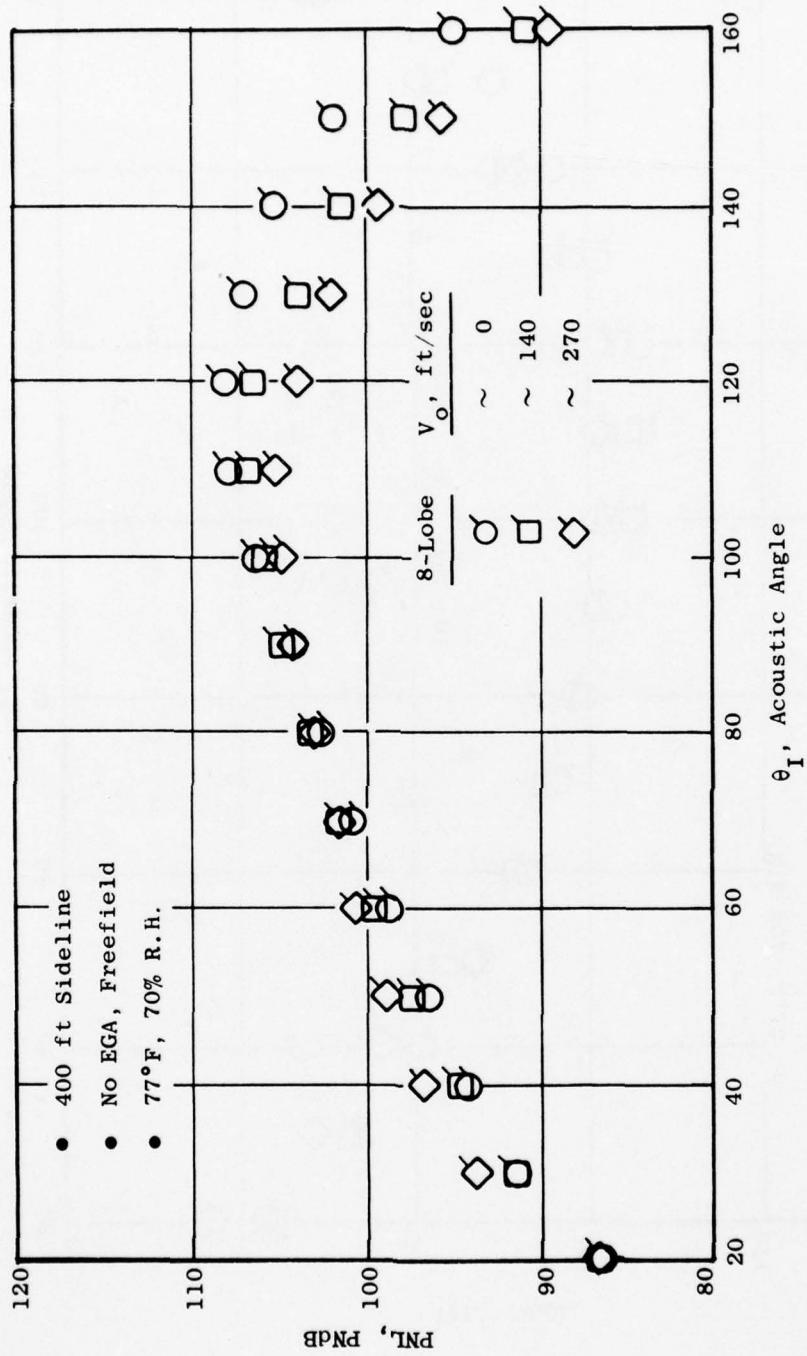


Figure 6-48. Bertin Aerotrain - PNL Directivity Patterns, $V_J = 1440$ ft/sec, 8-Lobe.

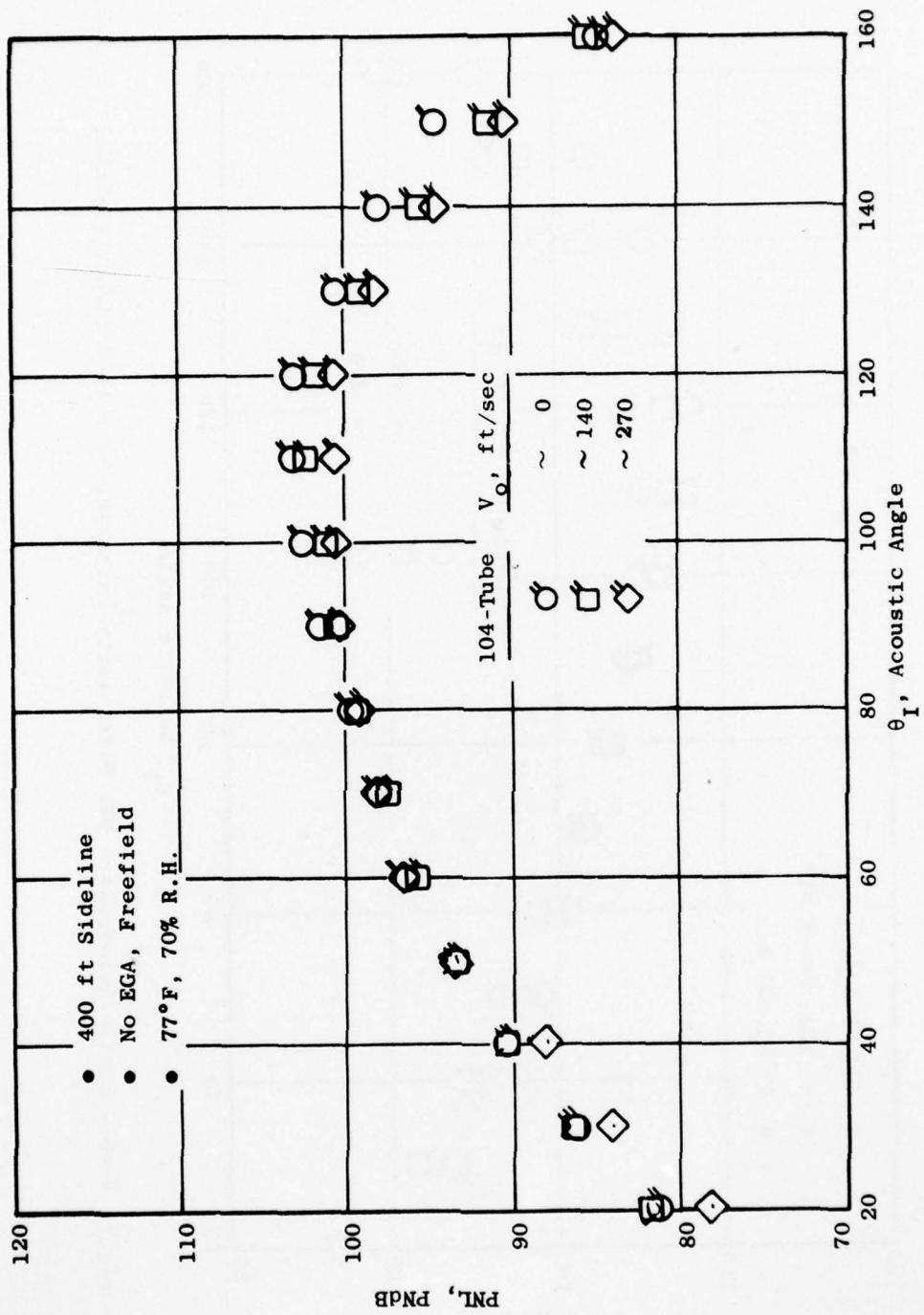


Figure 6-49. Bertin Aerotrain - PNL Directivity Patterns, $V_J = 1440$ ft/sec, 104-Tube.

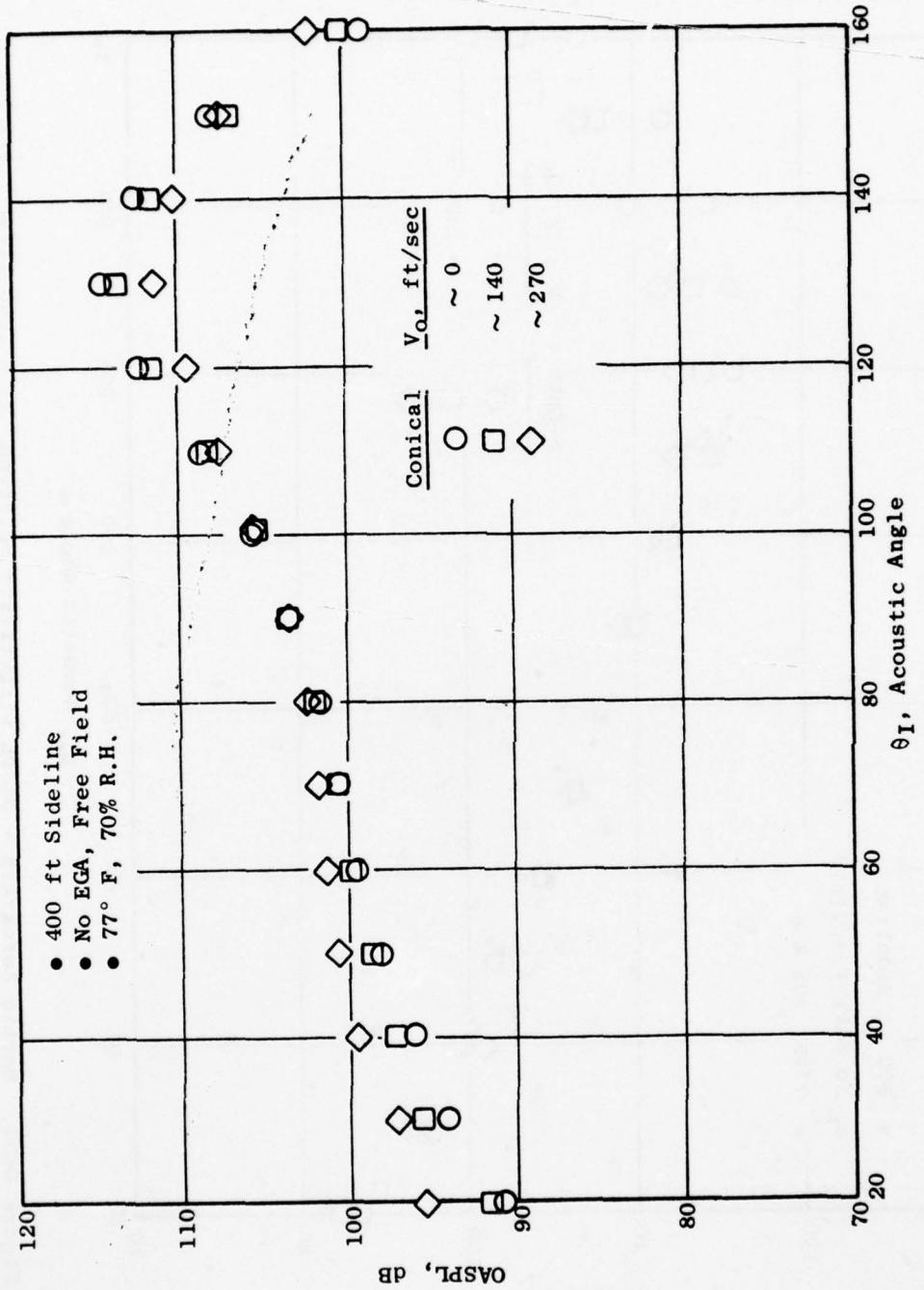


Figure 6-50. Bertin Aerotrain - OASPL Directivity Patterns, $V_J = 2200$ ft/sec, Conical.

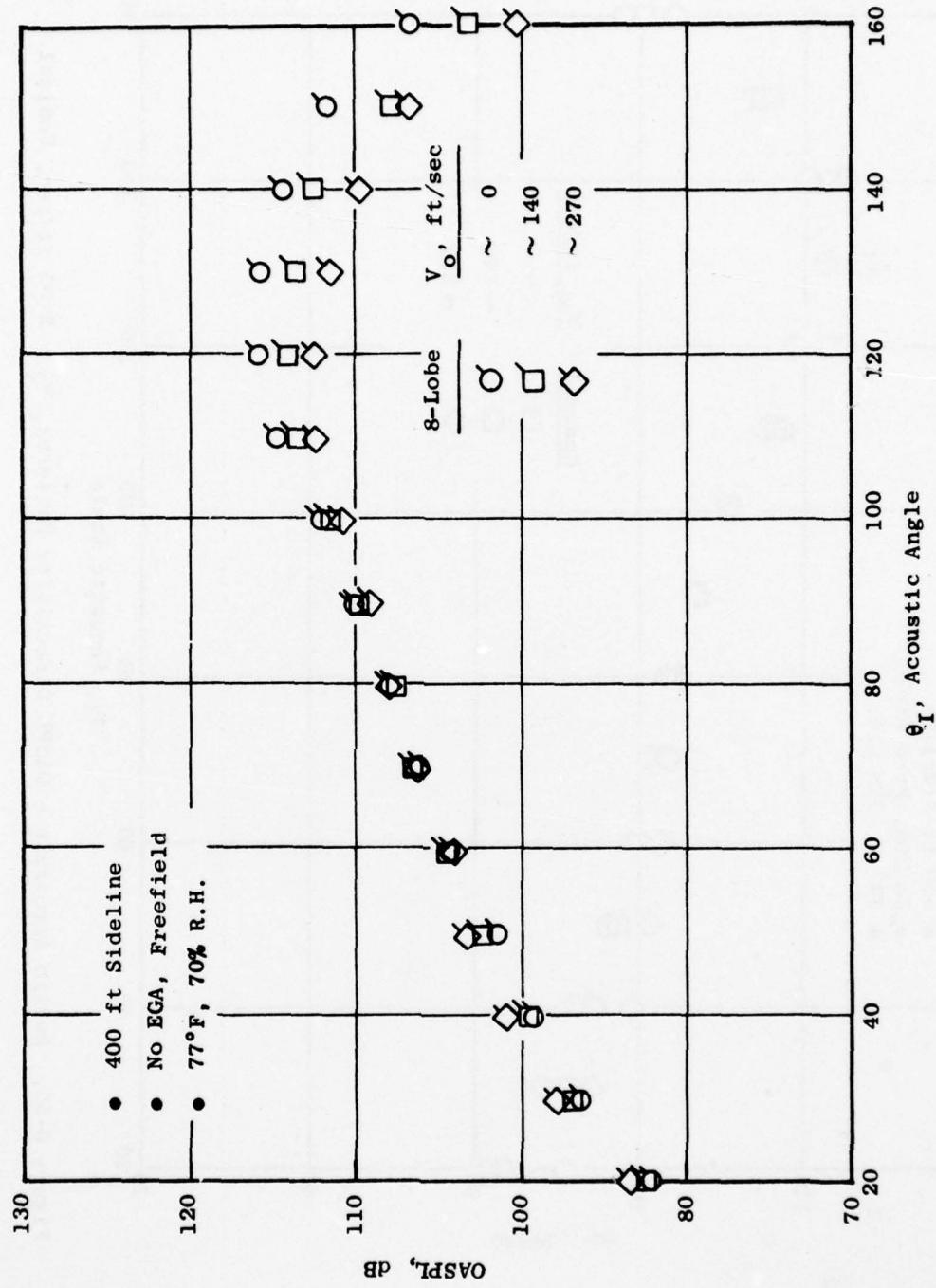


Figure 6-51. Bertin Aerostrain - OASPL Directivity Patterns, $V_J = 2200$ ft/sec, 8-Lobe.

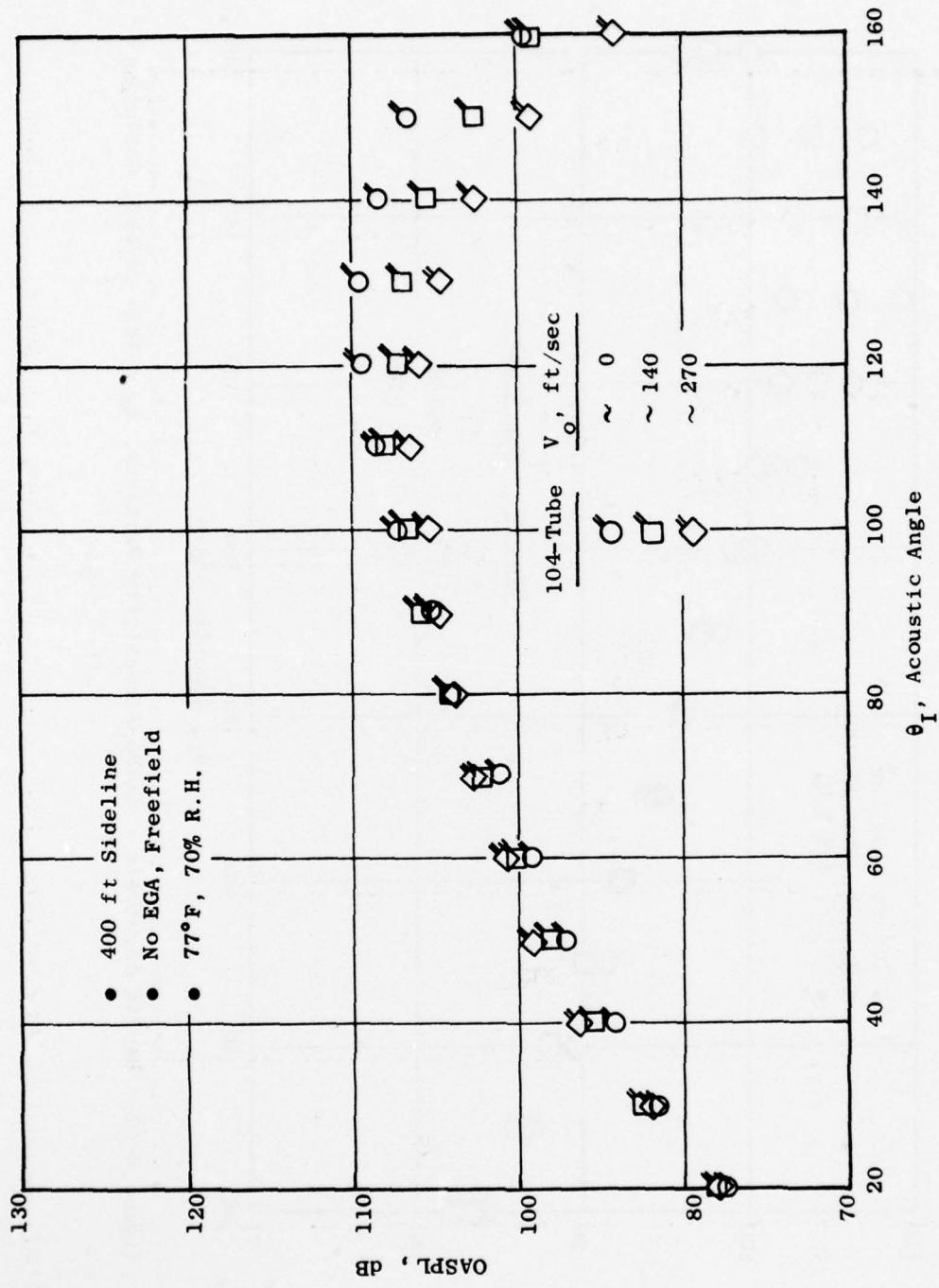


Figure 6-52. Bertin Aerotrain - OASPL Directivity Patterns, $V_J = 2200$ ft/sec, 104-Tube.

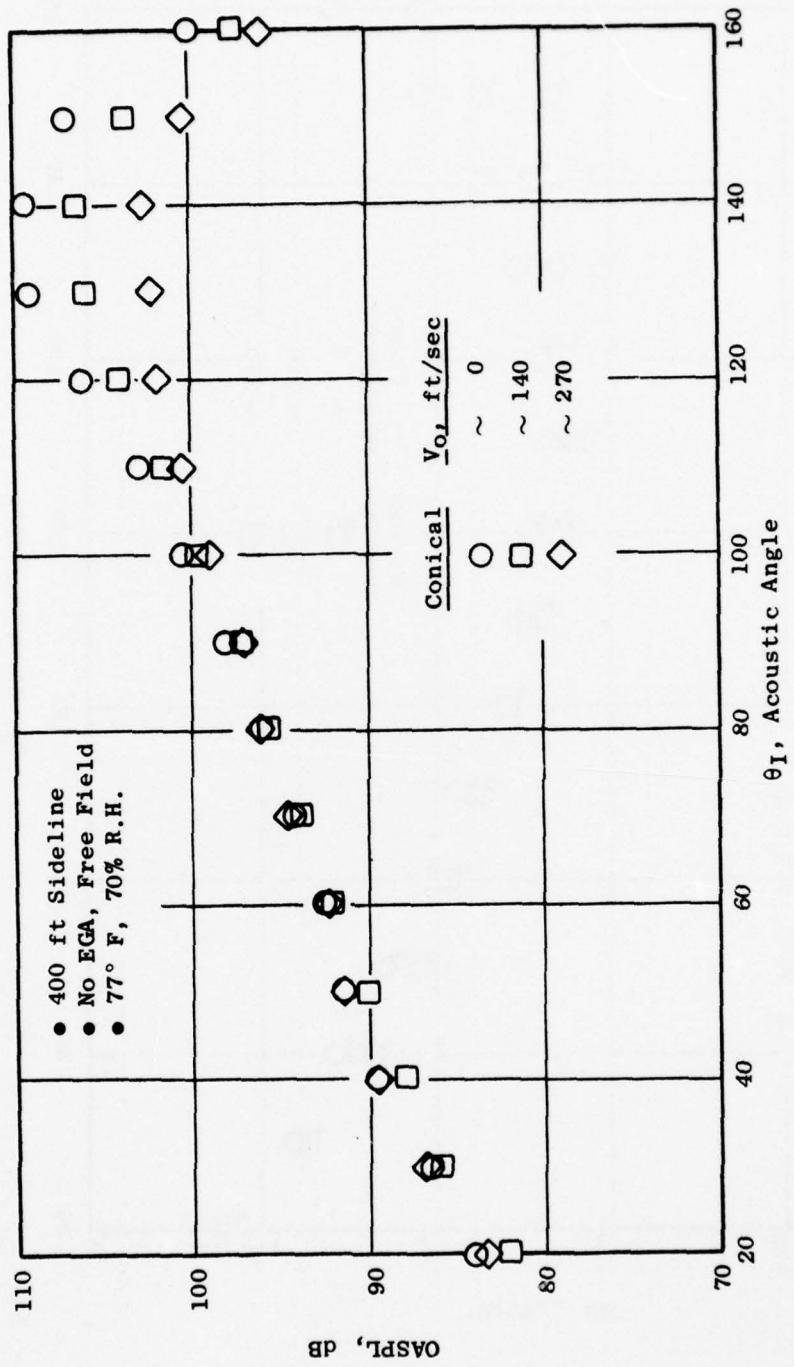


Figure 6-53. Bertin Aerotrain - OASPL Directivity Patterns, $V_J = 1830$ ft/sec, Conical.

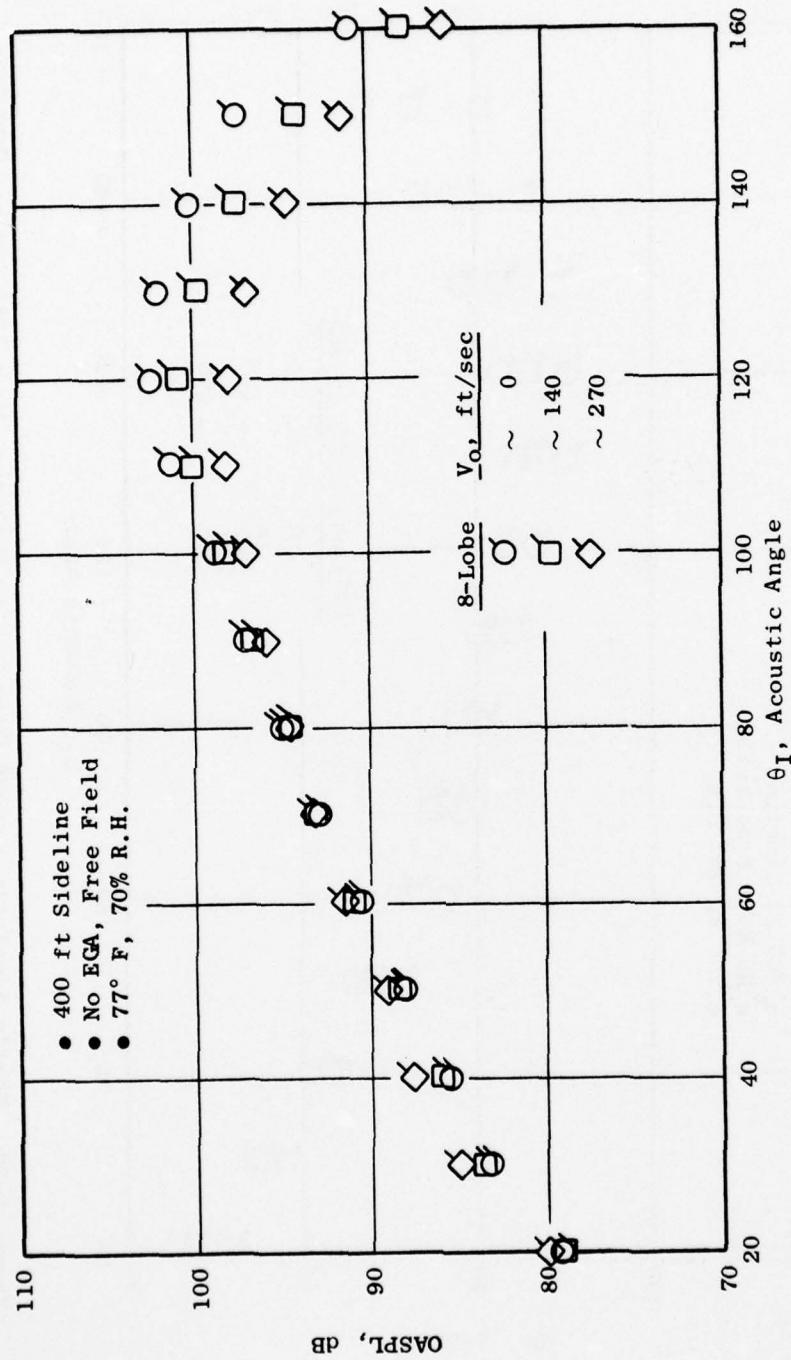


Figure 6-54. Bertin Aerotrain - OASPL Directivity Patterns, $V_J = 1830$ ft/sec, 8-Lobe.

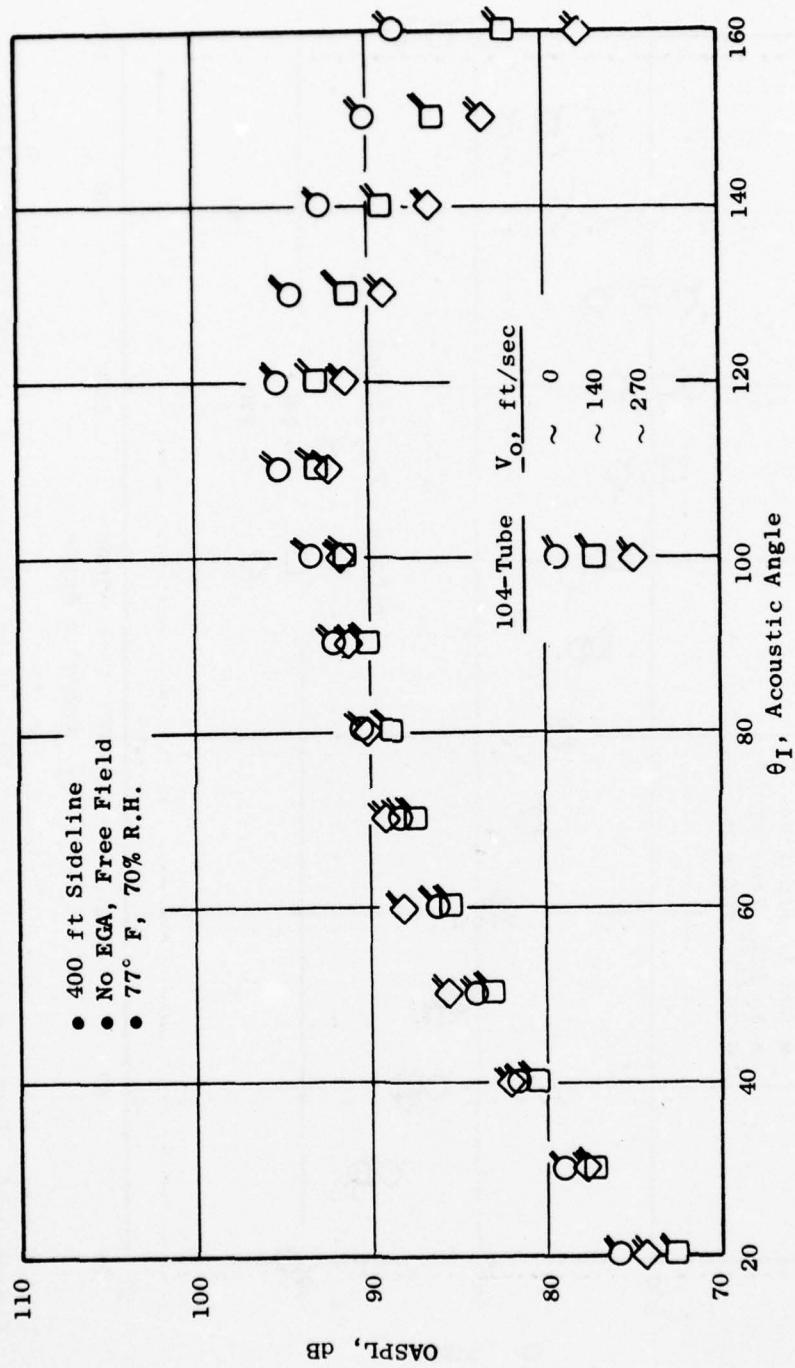


Figure 6-55. Bertin Aerotrain - OASPL Directivity Patterns, $V_J = 1830$ ft/sec, 104-Tube.

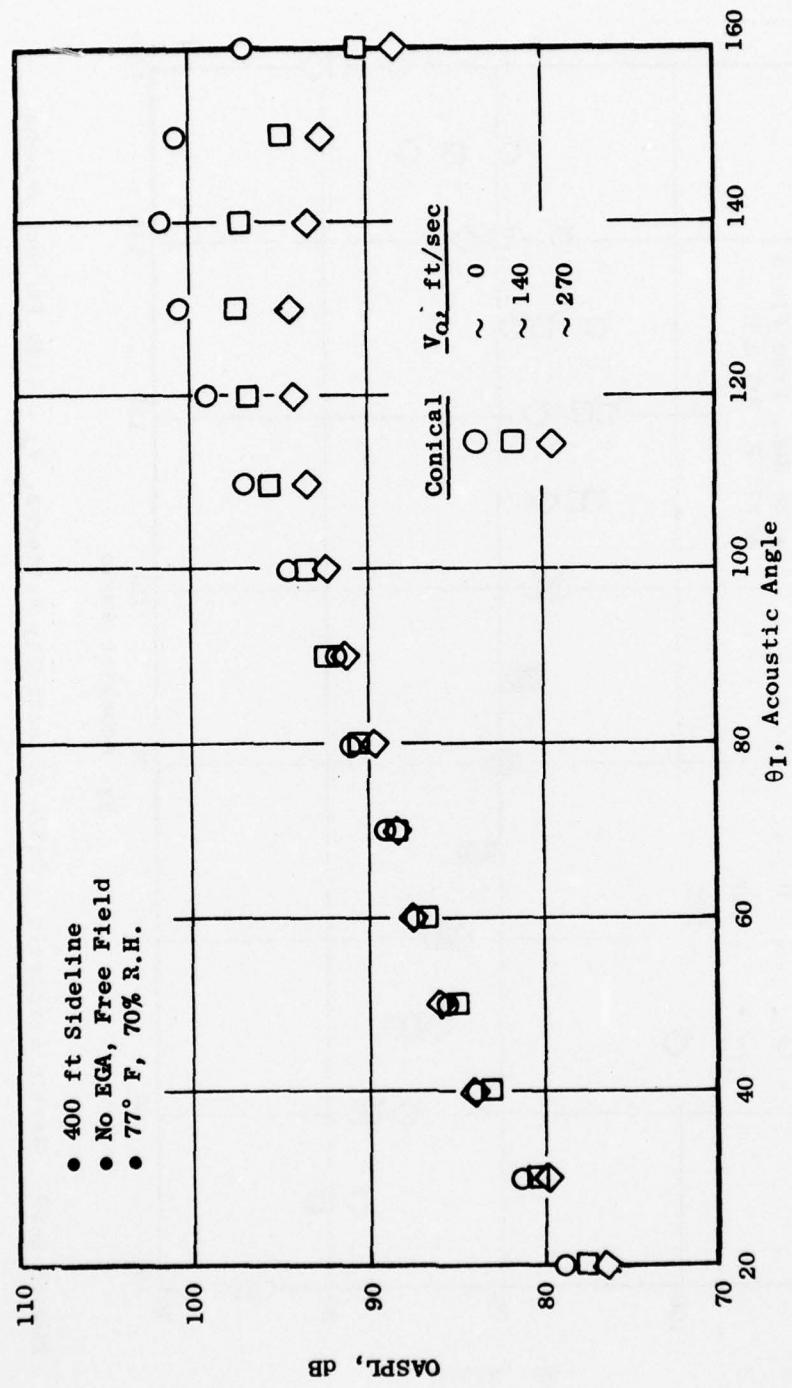


Figure 6-56. Bertin Aerotrain - OASPL Directivity Patterns, $V_J = 1440$ ft/sec, Conical.

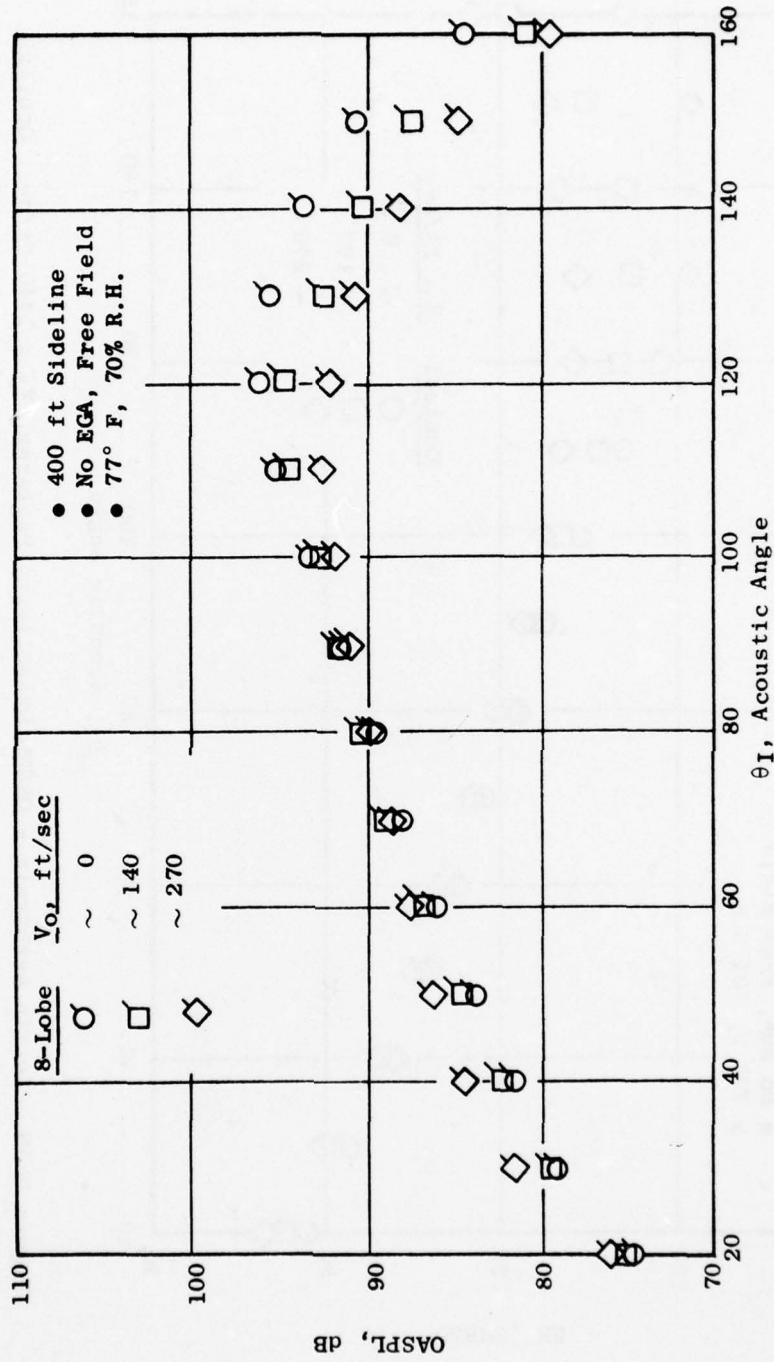


Figure 6-57. Bertin Aerotrain - OASPL Directivity Patterns, $V_J = 1440$ ft/sec, 8-Lobe.

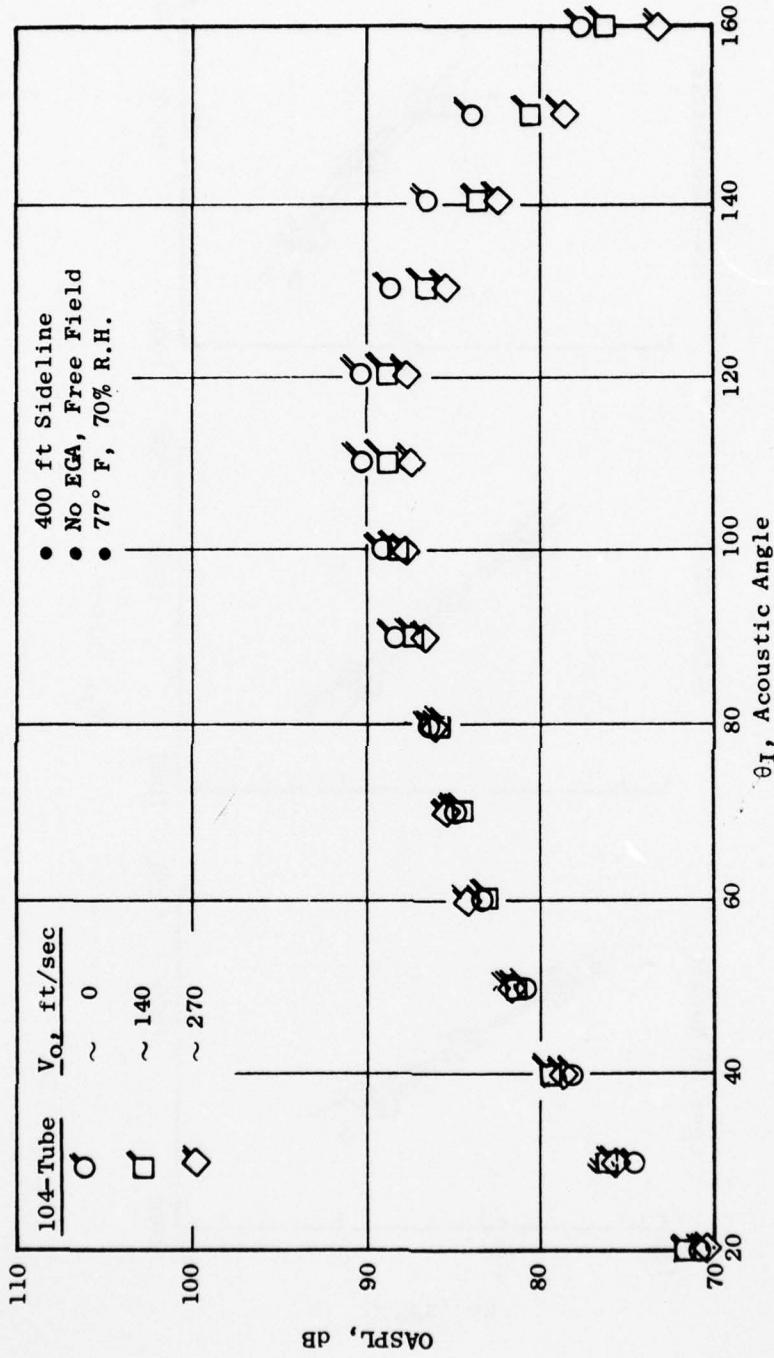


Figure 6-58. Bertin Aerotrain - OASPL Directivity Patterns, $V_J = 1440$ ft/sec, 104-Tube.

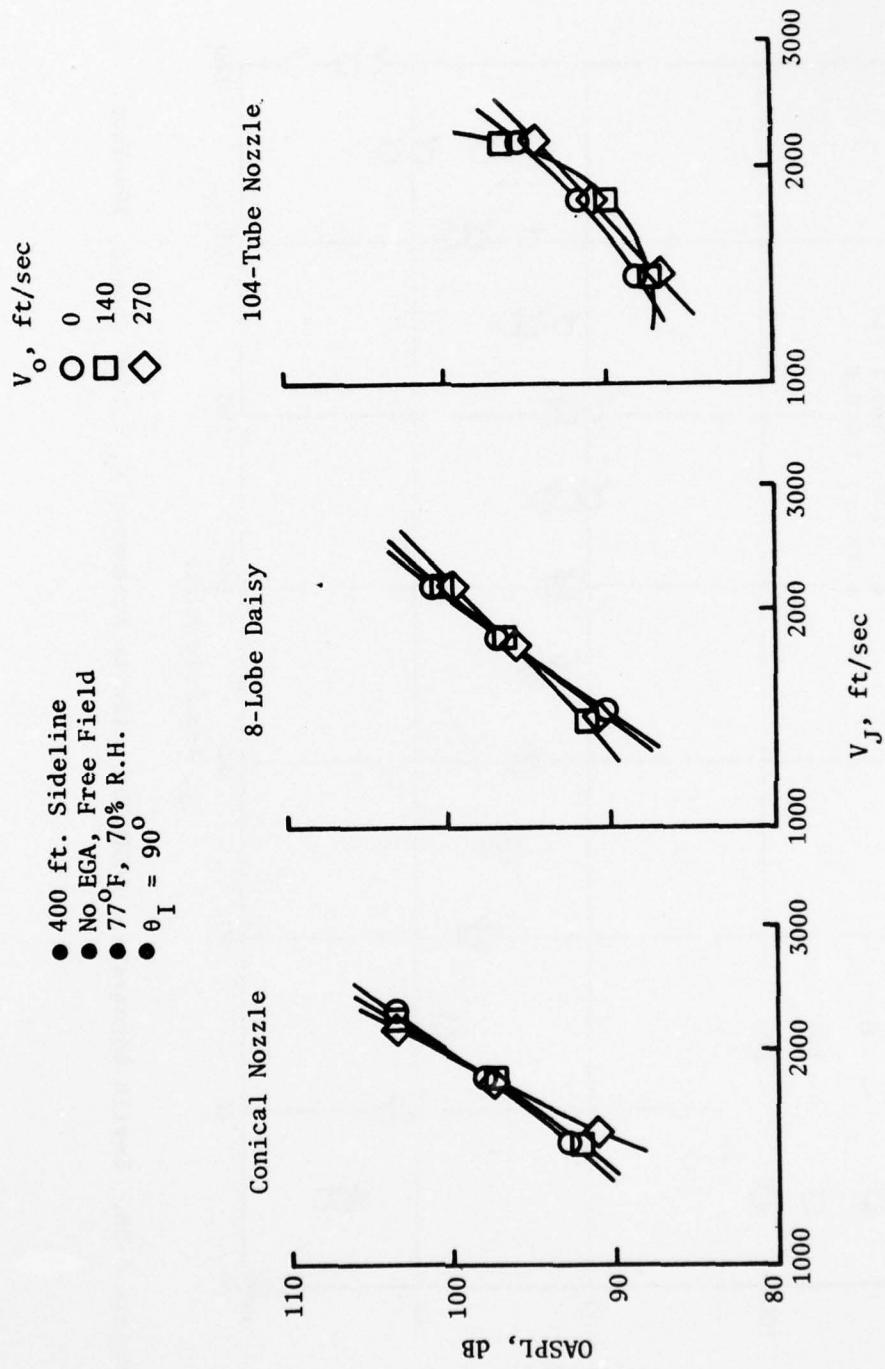


Figure 6-59. Summary of OASPL Characteristics, $\theta_1 = 90^\circ$.

AD-A041 849

GENERAL ELECTRIC CO CINCINNATI OHIO AIRCRAFT ENGINE GROUP F/G 20/1
HIGH VELOCITY JET NOISE SOURCE LOCATION AND REDUCTION. TASK 4. --ETC(U)
FEB 77 W S CLAPPER, E J STRINGAS DOT-05-30034

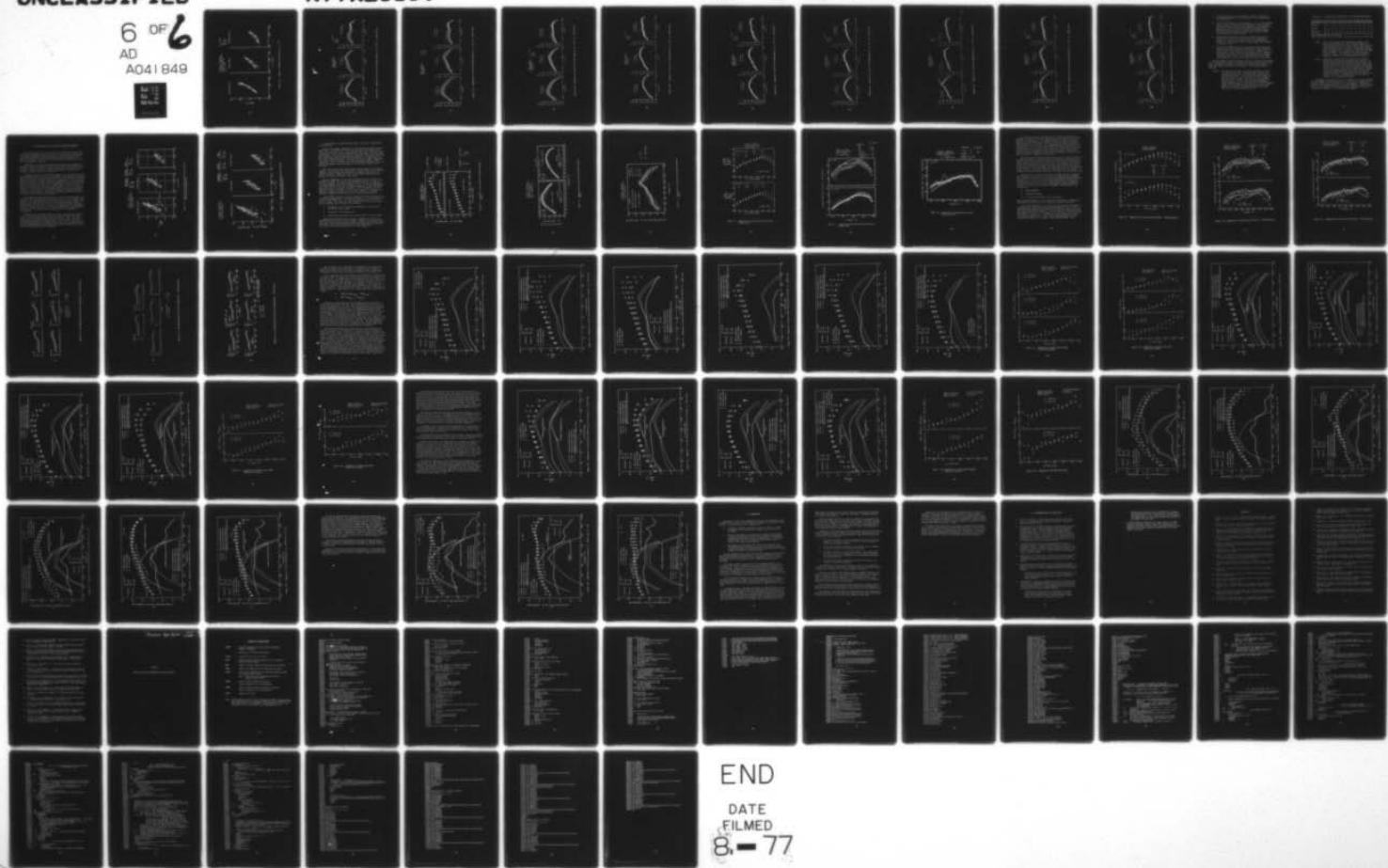
UNCLASSIFIED

6 OF 6
AD
A041 849

R77AEG189

FAA-RD-76-79-4

NL



END

DATE
FILMED
8-77

REF ID:
6 OF 6
AD
A04 | 849



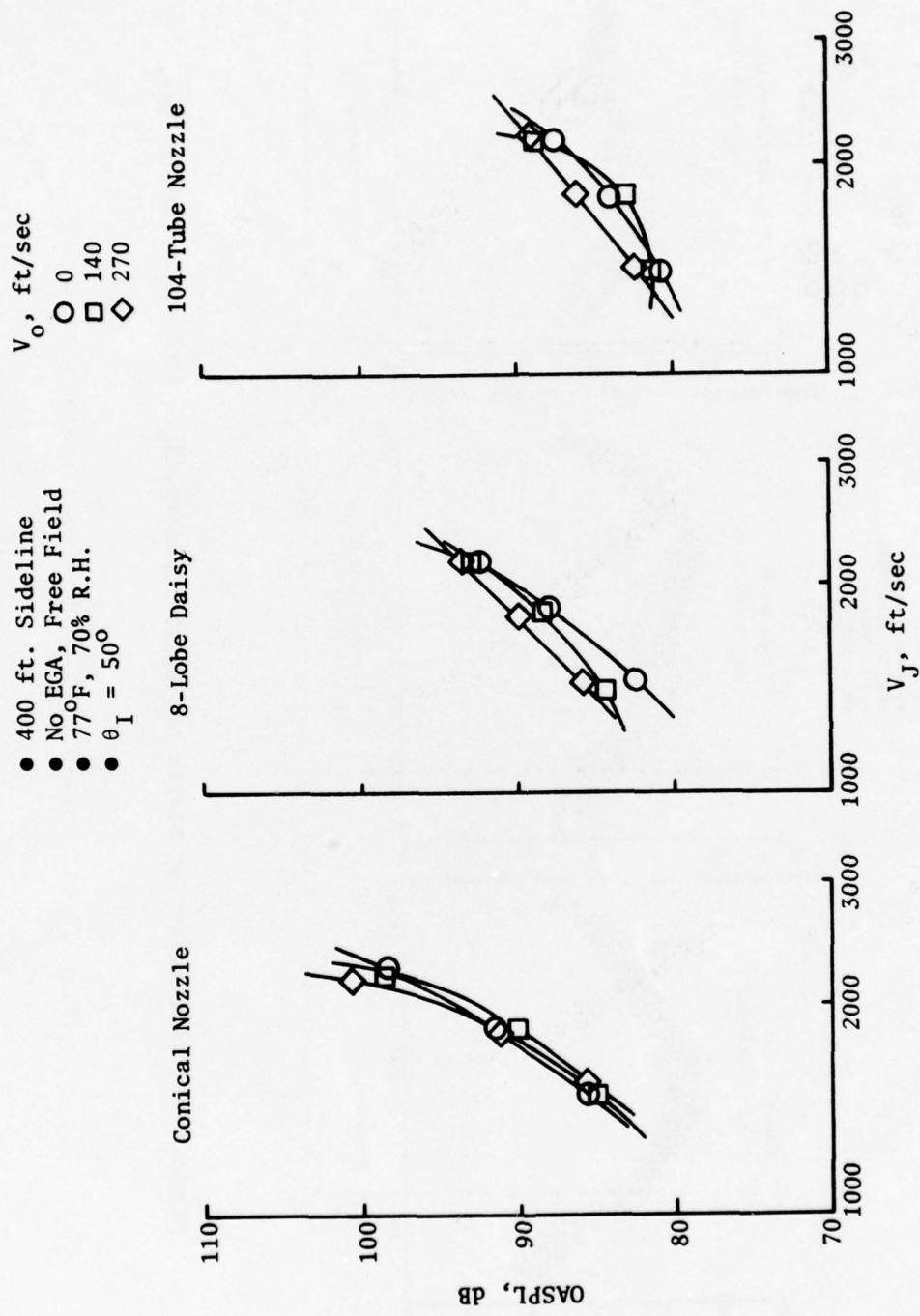


Figure 6-60. Summary of OASPL Characteristics, $\theta_1 = 50^\circ$.

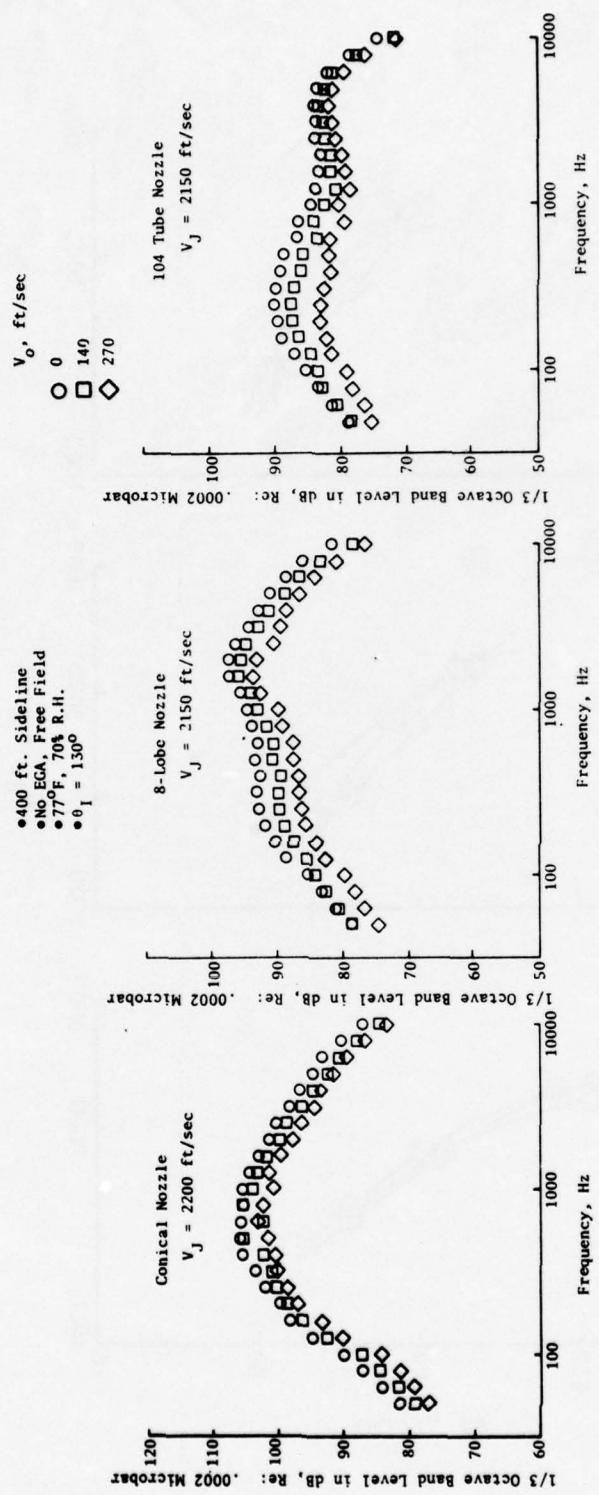


Figure 6-61. Comparison of Static and Flight Spectra, $\theta_1 = 130^\circ$, $v_J = 2200$ ft/sec.

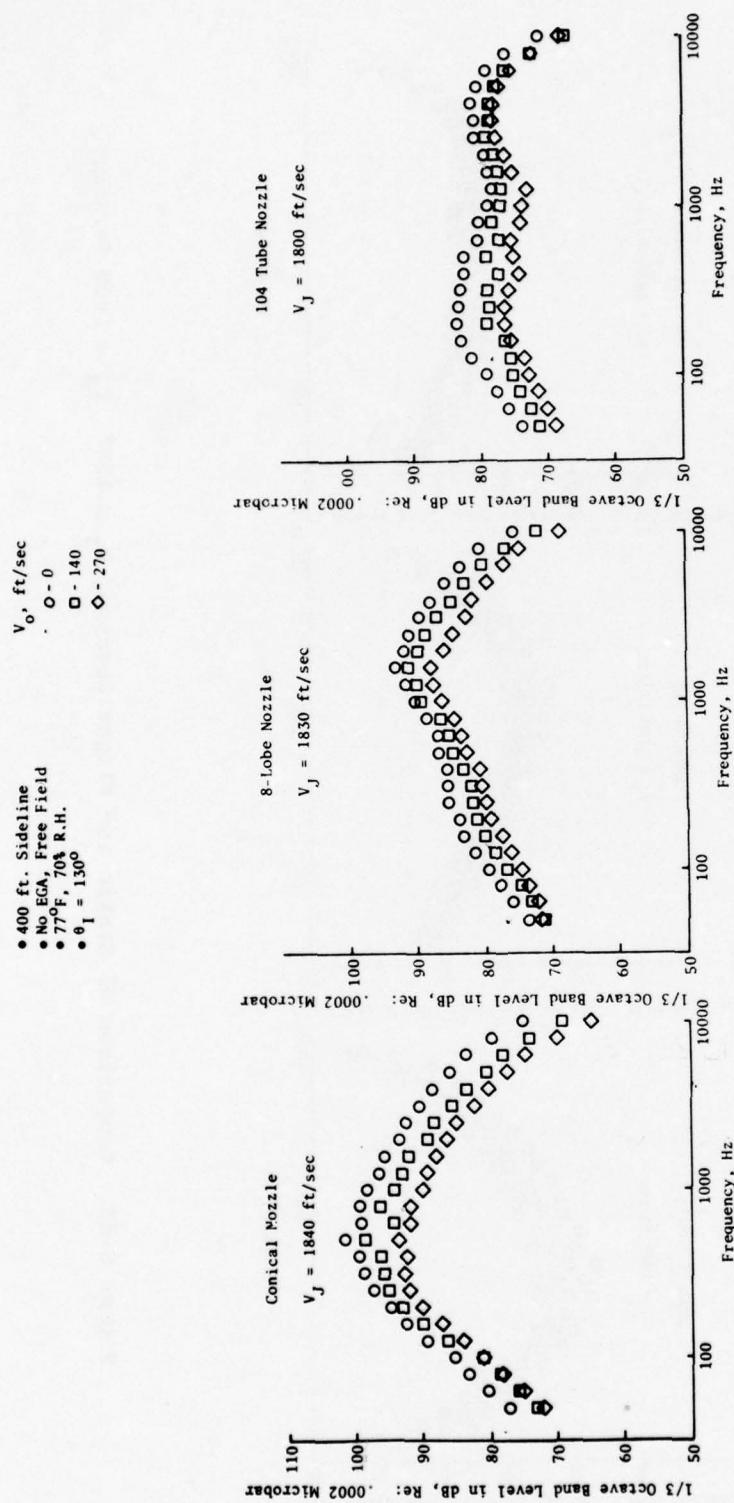


Figure 6-62. Comparison of Static and Flight Spectra, $\theta_1 = 130^\circ$, $V_J = 1800$ ft/sec.

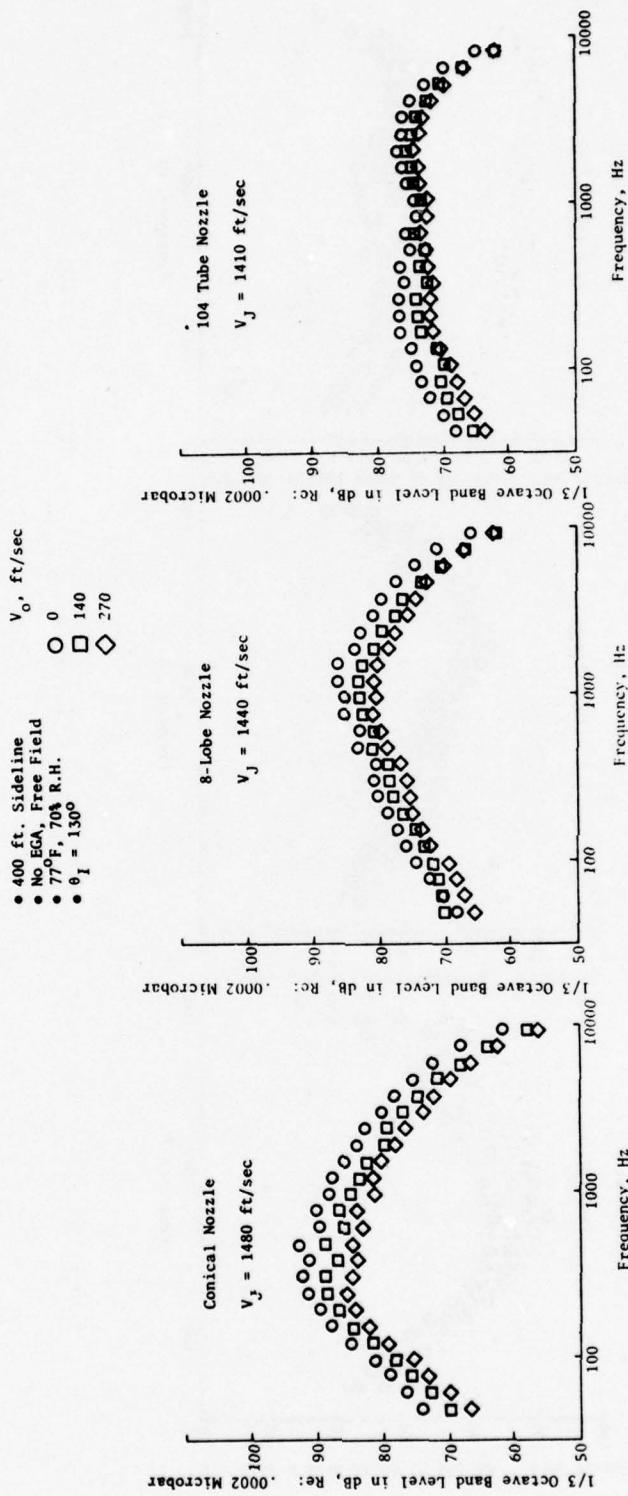


Figure 6-63. Comparison of Static and Flight Spectra, $\theta_1 = 130^\circ$, $V_J = 1400$ ft/sec.

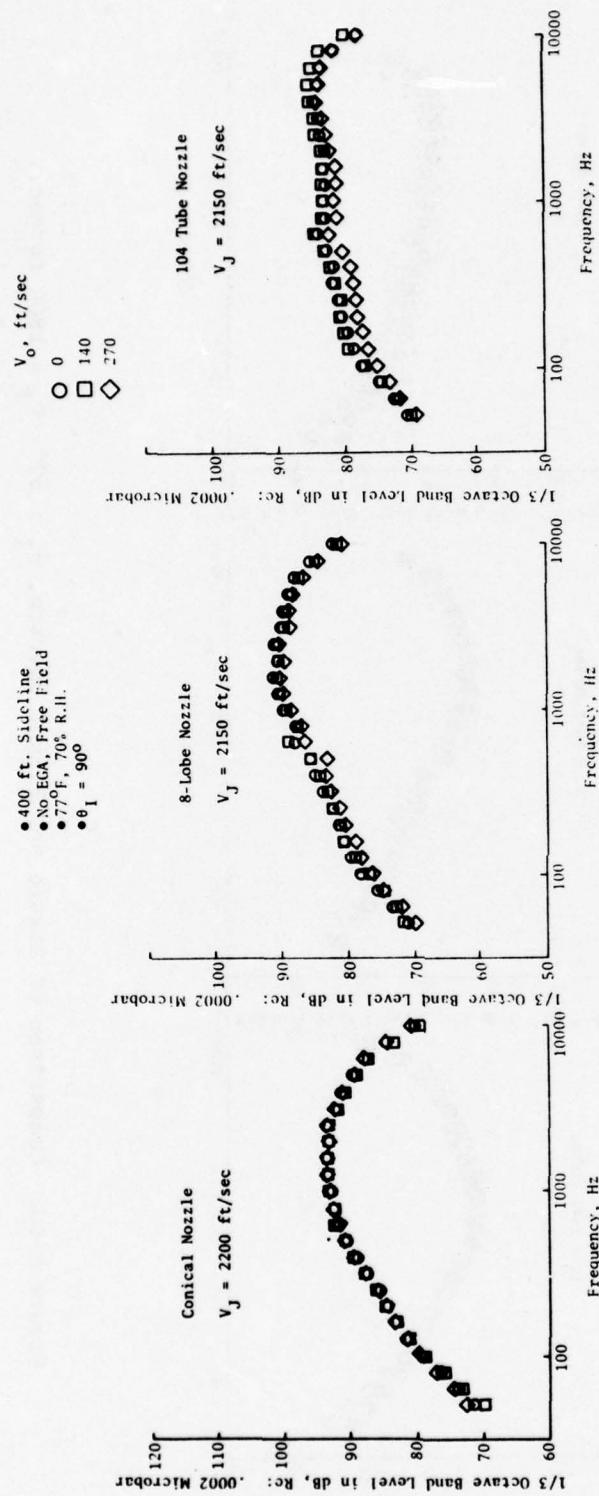


Figure 6-64. Comparison of Static and Flight Spectra, $\theta_1 = 90^\circ$, $V_J = 2200 \text{ ft/sec}$.

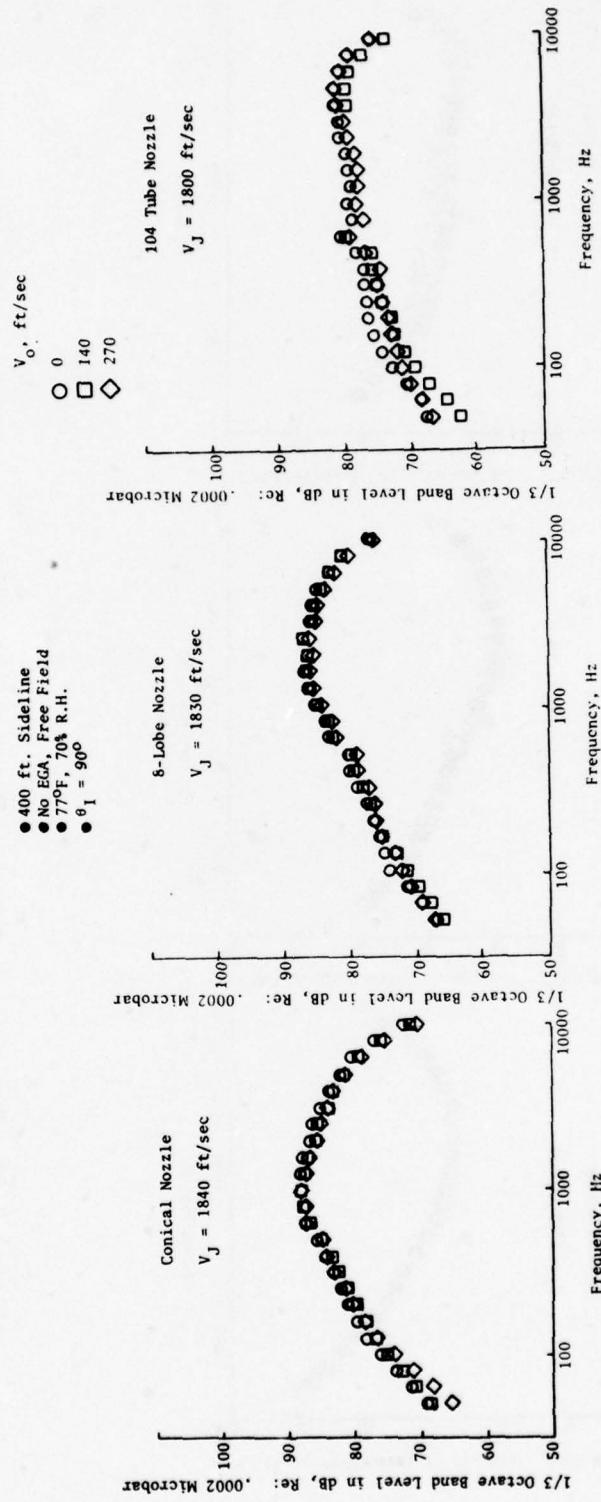


Figure 6-65. Comparison of Static and Flight Spectra, $\theta_1 = 90^\circ$, $V_J = 1800$ ft/sec.

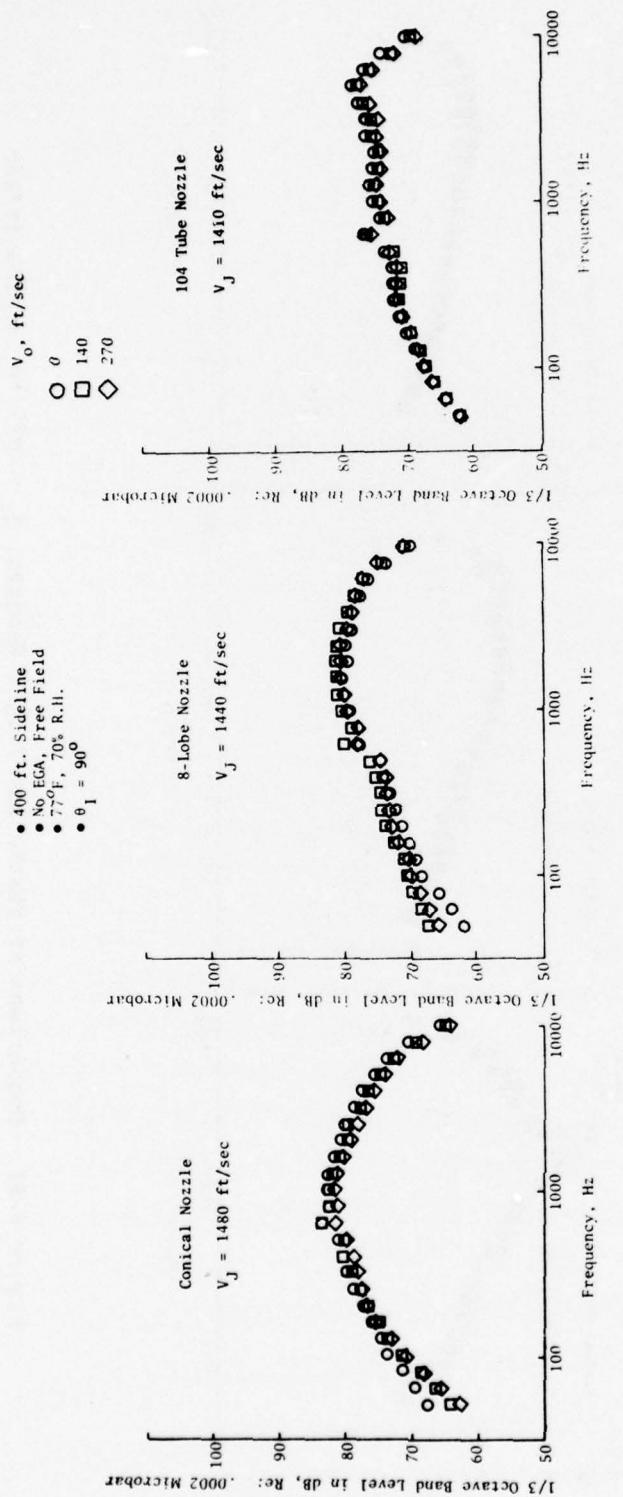


Figure 6-66. Comparison of Static and Flight Spectra, $\theta_I = 90^\circ$, $V_J = 1400 \text{ ft/sec.}$

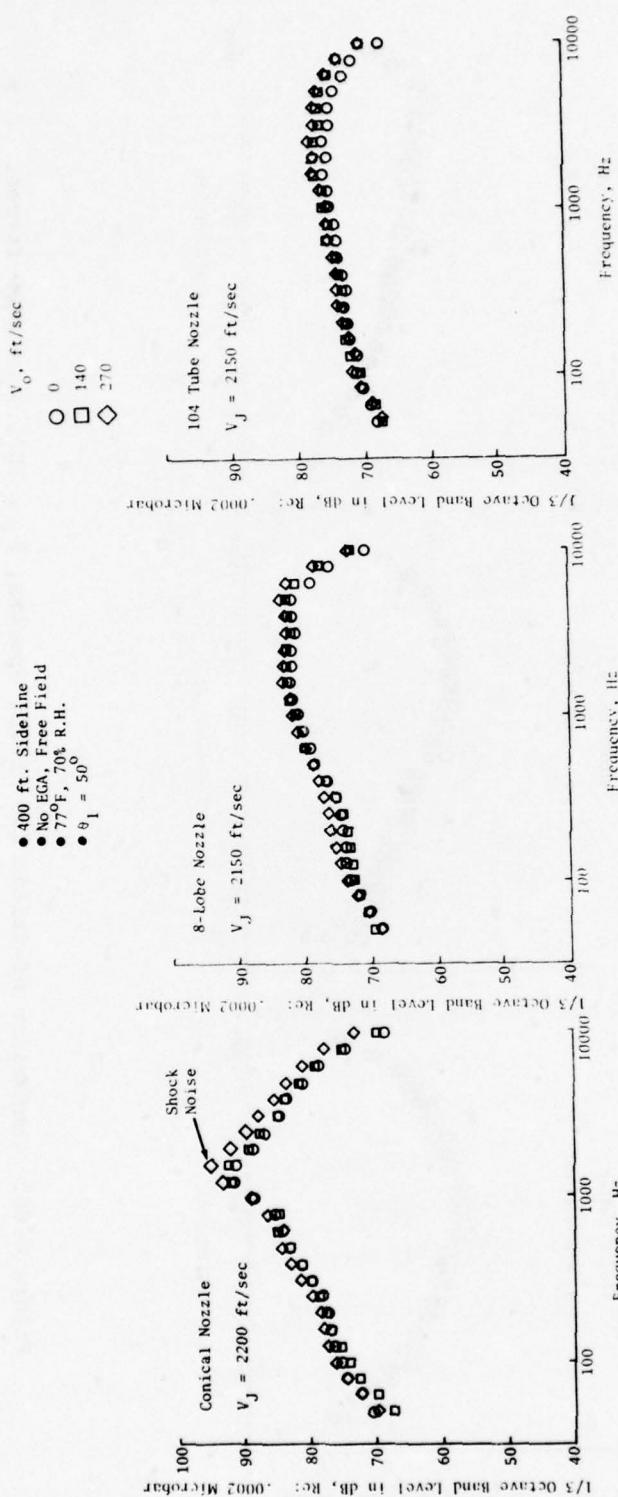


Figure 6-67. Comparison of Static and Flight Spectra, $\theta_1 = 50^{\circ}$, $V_J = 2200$ ft/sec.

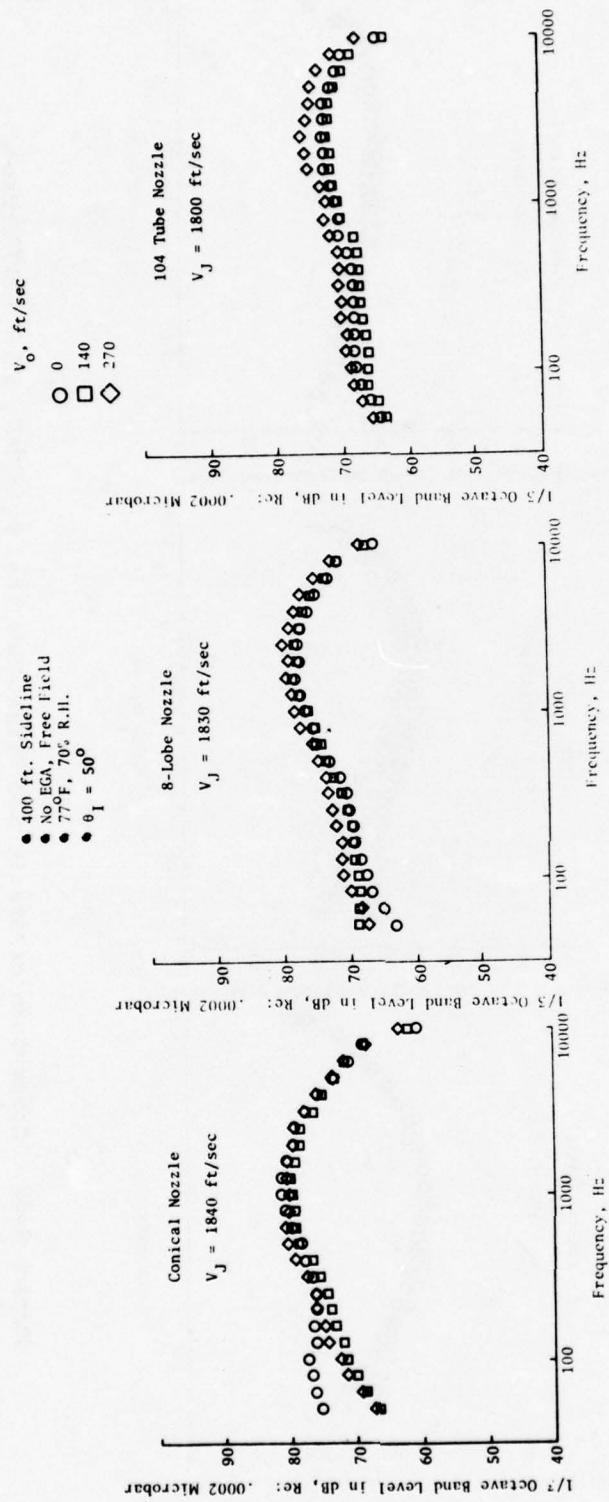


Figure 6-68. Comparison of Static and Flight Spectra, $\theta_1 = 50^\circ$, $V_J = 1800$ ft/sec.

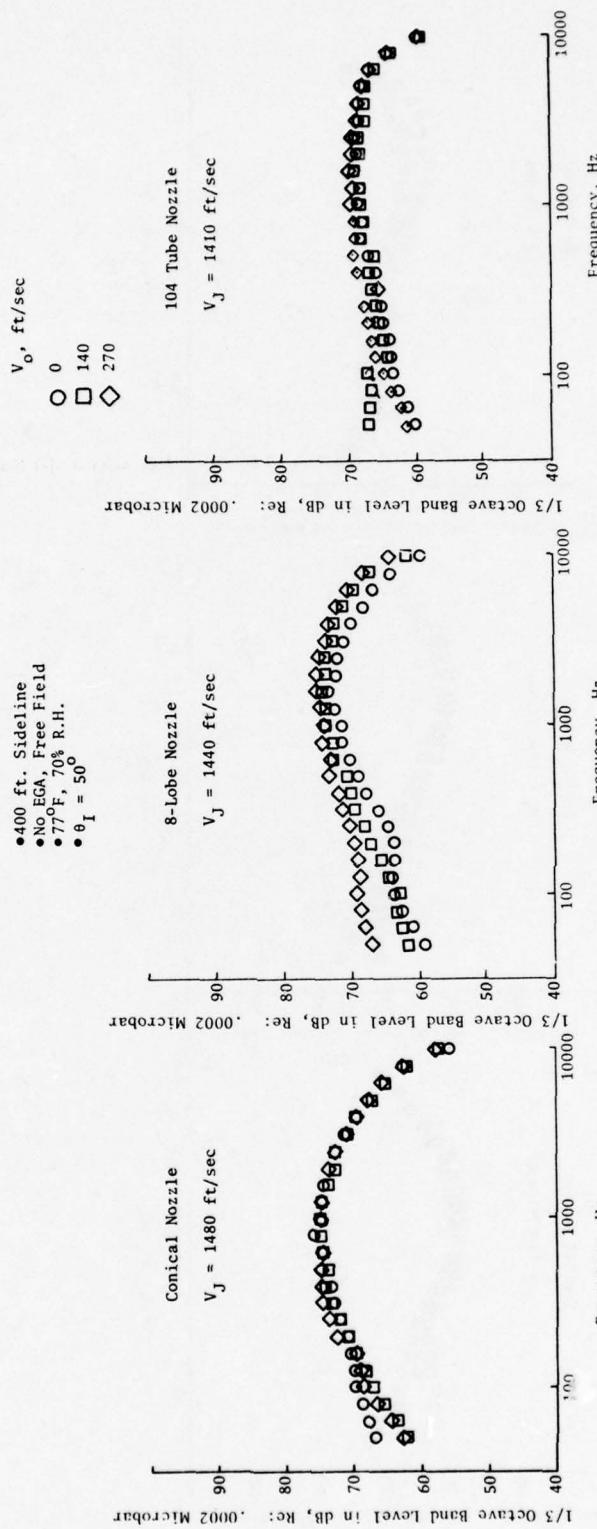


Figure 6-69. Comparison of Static and Flight Spectra, $\theta_I = 50^{\circ}$, $V_J = 1400$ ft/sec.

- The peak noise angle for the suppressor nozzles is observed to occur generally at 110° to 120° , whereas, for the conical nozzle, it is 130° to 140° .
- At the extreme angles in the aft quadrant, i.e., $\phi_I = 140^\circ$ through 160° , a decrease in OASPL and PNL is observed at forward speed relative to static operations. The magnitude of this decrease is significantly greater than the peak noise reduction observed. This observation is valid for the suppressor configurations at all three jet velocities; however, the conical nozzle at 2200 ft/sec indicates the opposite trend.
- The 90° OASPL and PNL show little or no change from static to flight for all three nozzle configurations, as illustrated on Figure 6-59. Based on the analysis of the data presented in Section 6.3, this apparent lack of reduction cannot be attributed to combustion noise.
- The forward quadrant directivity trends with forward motion are observed to be different than those exhibited in the aft quadrant. There is little or no reduction from static to flight on the basis of PNL or OASPL, and for acoustic angles of 20° through 70° the flight noise levels are 1 to 3 dB higher than the corresponding static noise levels. This observation holds for all three nozzle geometries as shown by the data presented on Figure 6-60.

The most dramatic differences between the three nozzles are illustrated by the 1/3-octave band spectra comparisons presented on Figures 6-61 through 6-69. The spectra comparisons are presented at three acoustic angles (130° , 90° , and 50°) at three jet velocities. The following trends are observed:

- 130° - The conical nozzle spectra show that reduction from static to flight increases with increasing flight velocity and decreasing jet velocity. The reduction is relatively constant with frequency. The 8-lobe spectra show a reduction that increases with flight velocity but is not a strong function of jet velocity. The reduction is somewhat frequency dependent. The 104-tube nozzle shows different trends than the conical or 8-lobe nozzles. The low frequency portion of the 104-tube spectra shows significantly more reduction from static to flight than the conical nozzle. This trend is illustrated by Table 6-III.

Table 6-III. One-Third-Octave Comparisons - Δ dB* Static Minus Flight.

Configuration	125 Hz	250 Hz	500 Hz	1000 Hz	2000 Hz	4000 Hz
Conical	4.5	3.1	4.0	4.2	3.8	3.0
8-Lobe	6.5	6.5	6.0	4.8	4.5	4.5
104-Tube	6.0	7.0	7.0	4.0	3.0	2.0
$*V_J = 2200 \text{ ft/sec}, V_o = 275 \text{ ft/sec}$						

- 90° - Figures 6-64 through 6-66, show similar trends for the conical and 8-lobe nozzles at 90° over the range of jet velocities and flight velocities evaluated. There is little or no change from static to flight. The 104-tube nozzle shows low frequency reduction for the 2200-ft/sec and 1800-ft/sec conditions, but no reduction is observed at the 1400-ft/sec condition. This apparent lack of low frequency reduction is due to the influence of background noise, as presented on Figure 6-16 and discussed in Section 6.2.
- 50° - Figures 6-67 through 6-69 show substantially different characteristics than those observed at 130° and 90°. The conical nozzle at 2200 ft/sec shows a strong influence of shock noise; whereas, the 8-lobe and 104-tube nozzles indicate no influence of shock noise. In general, an increase on the order of 1 to 2 dB is observed from static to flight for all the configurations at this condition. The 1800-ft/sec and 1400-ft/sec conditions are not influenced by shock noise and show increases from static to flight on the order of 3 to 5 dB. The magnitude of this increase is frequency and configuration dependent.

In summary, the changes from static to flight for the three configurations evaluated on the Aerotrain vary as a function of configuration, jet velocity, flight velocity, acoustic angle, and frequency. These data, because of the interrelationship of all these parameters, provide a strong test for the validation of the hybrid inflight simulation technique and accomplish the objective of the Aerotrain test program.

7.0 VERIFICATION OF THE INFLIGHT SIMULATION TECHNIQUE

The previous sections of this report have described the elements that provide the experimental and analytical results required for the assessment of the hybrid in-flight simulation technique. The presentation in this section will concentrate on comparisons to determine the ability of the "Hybrid" technique to duplicate the in-flight noise characteristics of the three configurations evaluated.

Comparison of the flight data and Aerotrain data, where possible, is the first step in establishing a basis for the validation of the simulation technique. Figures 7-1 and 7-2 present the peak noise characteristics on the basis of PNL and OASPL for the three configurations evaluated on the Aerotrain, Learjet, and F-106 test vehicles.

The baseline nozzles show excellent agreement when compared statically; the in-flight trends are significantly different. The Aerotrain and Learjet (both with conical nozzles) show the same trend at the 2200-ft/sec condition when the differences in flight velocity are accounted for. The lower power-setting Learjet data does not demonstrate the amount of peak noise reduction shown by the Aerotrain results. The F-106 baseline nozzle (a no-flow, low area ratio ejector) was evaluated at a higher flight velocity, $V_0 = 420$ ft/sec, and demonstrated peak angle noise reduction of 12 dB. As stated in Section 5.0, this nozzle is in a different family than the conical nozzles and should not be expected to demonstrate the same in-flight noise characteristics. Further baseline comparisons in this section will be limited to the Aerotrain and Learjet conical nozzles.

The 8-lobe nozzle was evaluated on the Learjet and the Aerotrain. The peak noise trends are summarized on Figures 7-1 and 7-2. The Learjet 8-lobe static data is 2 dB higher than the Aerotrain data at the two highest power settings. The reduction from static to flight demonstrated by Learjet is significantly less than that shown by the Aerotrain for highest and lowest power settings, but the level of reduction is comparable at the intermediate condition. Directivity and spectra comparisons made later demonstrate the cohesiveness of the Aerotrain and Learjet data for this suppressor configuration.

Comparison of the 104-tube nozzle peak noise characteristics observed in the F-106 and Aerotrain data is more straightforward than the 8-lobe nozzle. The static PNL and OASPL data agree within ± 1 dB. The F-106 flight results are lower than the Aerotrain (which is expected because the F-106 data was obtained at a flight velocity of 420 ft/sec). Both static and in-flight peak noise characteristics have been well established from the two test programs and show reasonable agreement when differences in flight velocity and installations are considered.

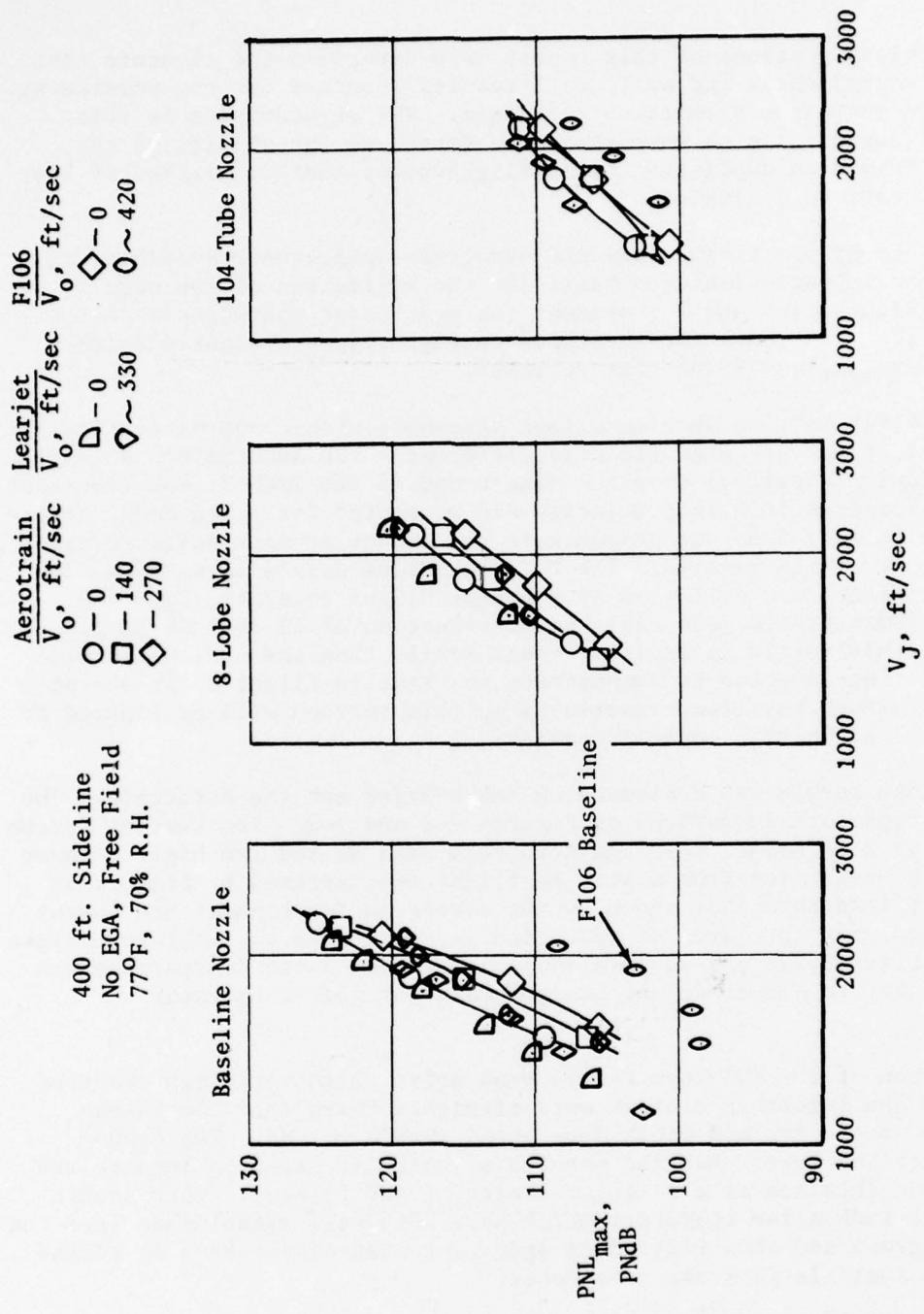


Figure 7-1. Comparison of Flight Assurance and Aerotrain Peak Noise Characteristics.

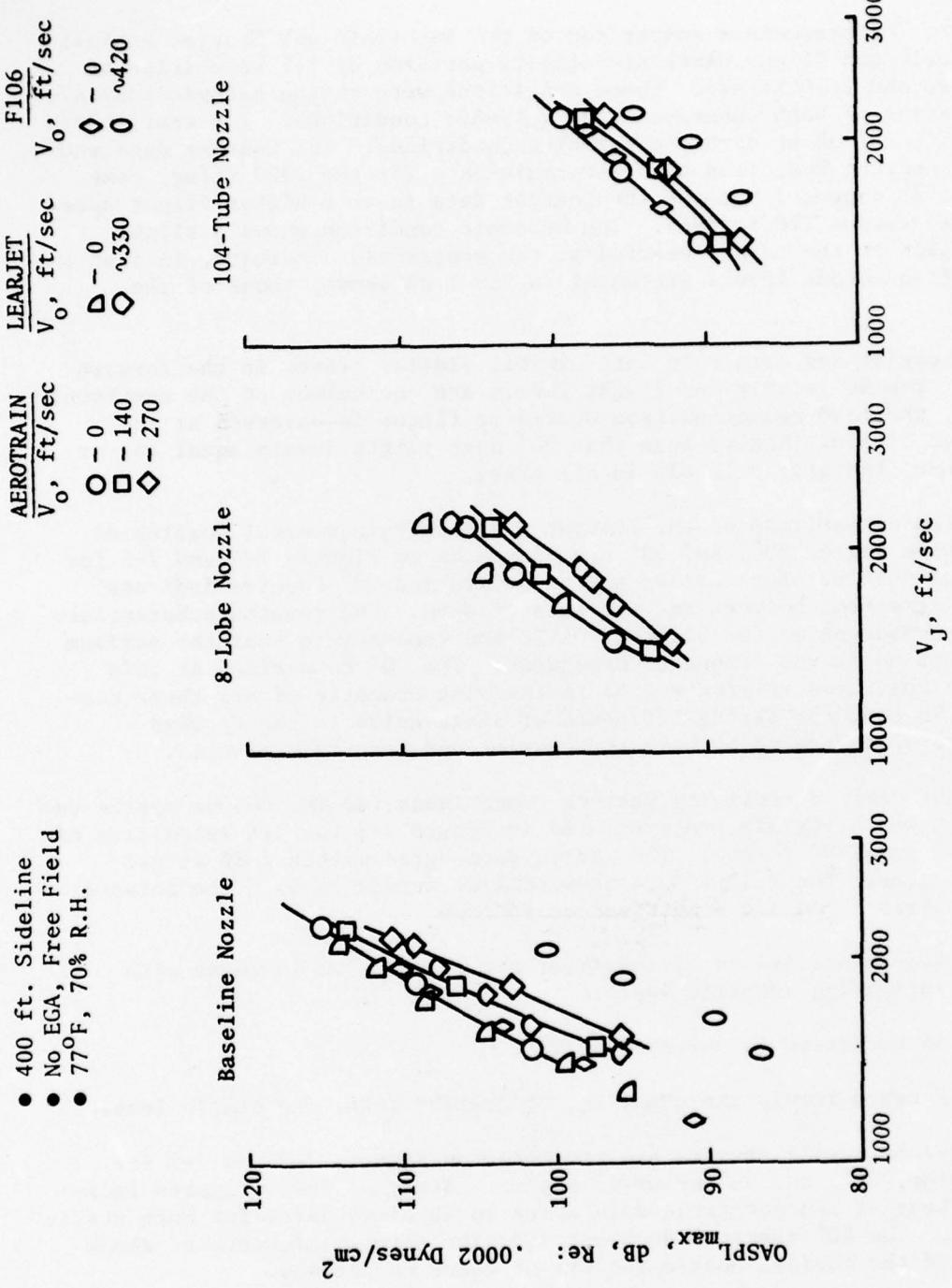


Figure 7-2. Comparison of Flight Assurance and Aerotrain Peak Noise Characteristics.

A second series of comparisons were made on the basis of OASPL directivity patterns.

Figure 7-3 presents a comparison of the Aerotrain and Learjet conical nozzle static and flight OASPL directivity patterns at jet velocities of 2200 ft/sec and 1440 ft/sec. These conditions were chosen because they are representative of both supersonic and subsonic conditions. The static data agree within ± 1 dB at both jet velocity conditions. The Learjet data shows more aft-quadrant reduction than Aerotrain data for the 2200 ft/sec case. This trend is expected because the Learjet data is at a higher flight speed (340 ft/sec versus 270 ft/sec). The subsonic condition shows a slight contradiction to the trend observed at the supersonic condition, in that the Learjet aft-quadrant levels are equal to, or 1 dB above, those of the Aerotrain.

The Learjet and Aerotrain data exhibit similar trends in the forward quadrant. The 90° static and flight levels are equivalent at the supersonic condition, and 1-dB reduction from static to flight is observed at the subsonic condition. Angles less than 90° have flight levels equal to, or greater than, the static levels in all cases.

Spectra comparisons of the Learjet and Aerotrain conical nozzles at maximum noise angle, 90°, and 50° are presented on Figures 7-4 and 7-5 for the conical nozzle. The maximum angle spectra and 90° spectra indicate excellent agreement between the two sets of data. The results substantiate the trends observed on the basis of OASPL and demonstrate that the maximum angle reduction is not frequency dependent. The 50° comparison at this supersonic condition ($P_{T8}/P_0 = 2.4$) is the most dramatic of all these comparisons, in that the strong influence of shock noise in the forward quadrant is demonstrated by both the Learjet and Aerotrain results.

Similar OASPL directivity pattern comparisons for the 8-lobe nozzle on the Learjet and Aerotrain are presented in Figure 7-6 for jet velocities of 2200 ft/sec and 1800 ft/sec. The static data agree within 2 dB at all acoustic angles. The flight data show similar trends in both the forward and aft quadrants and are summarized as follows:

- Reductions in the aft quadrant are observed to increase with increasing acoustic angle.
- No reduction is observed at 90°.
- Forward levels are equal to, or greater than, the static levels.

Eight-lobe nozzle spectra are presented on Figures 7-7 and 7-8 for maximum noise, 90°, and 40° acoustic angles. Study of these figures indicates the Learjet and Aerotrain data agree on absolute level for both static and flight. The 40° spectrum does not show the strong influence of shock noise as did the conical nozzle spectra at these conditions.

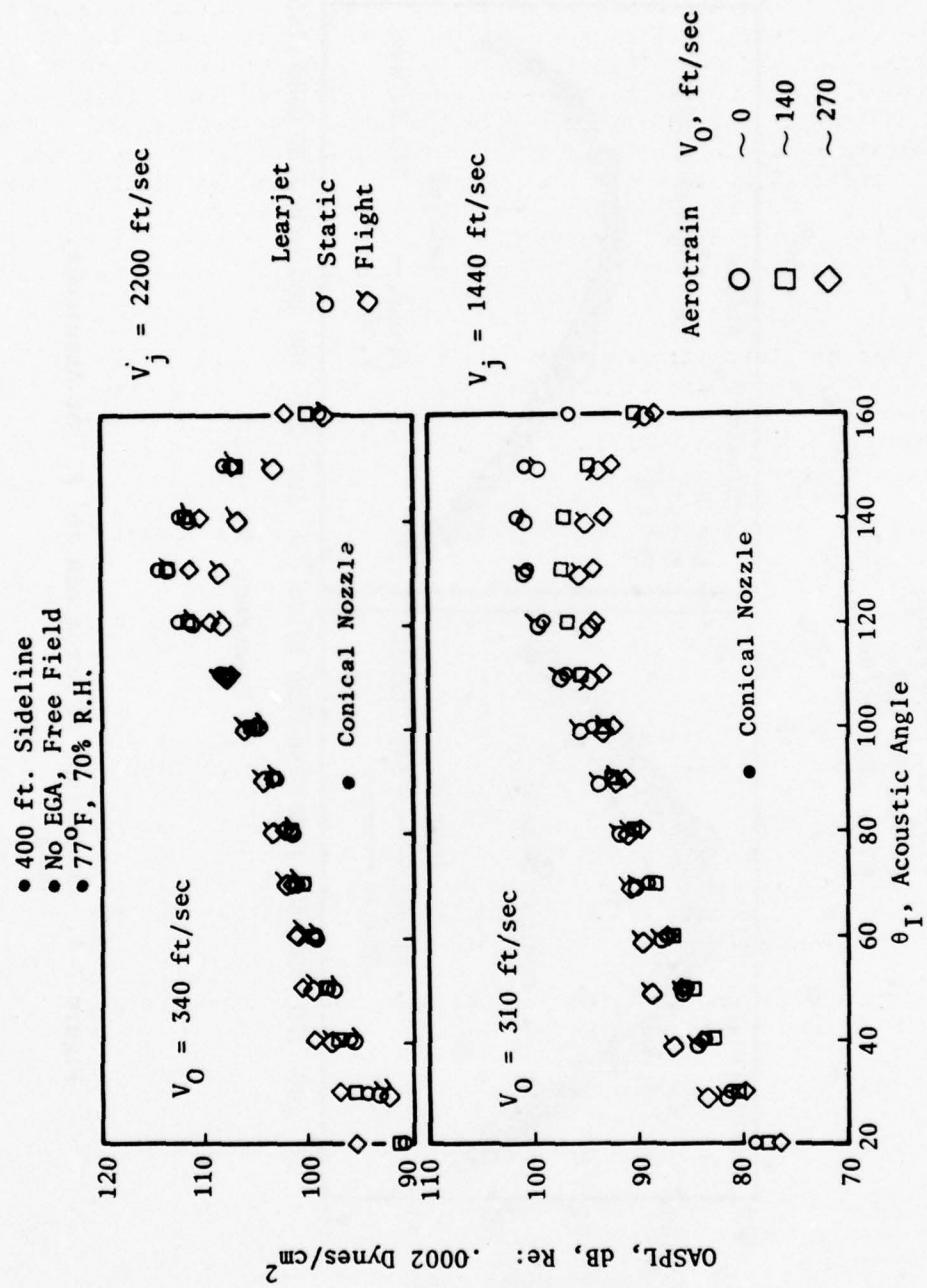


Figure 7-3. Comparison of Aerotrain and Flight Assurance Data.

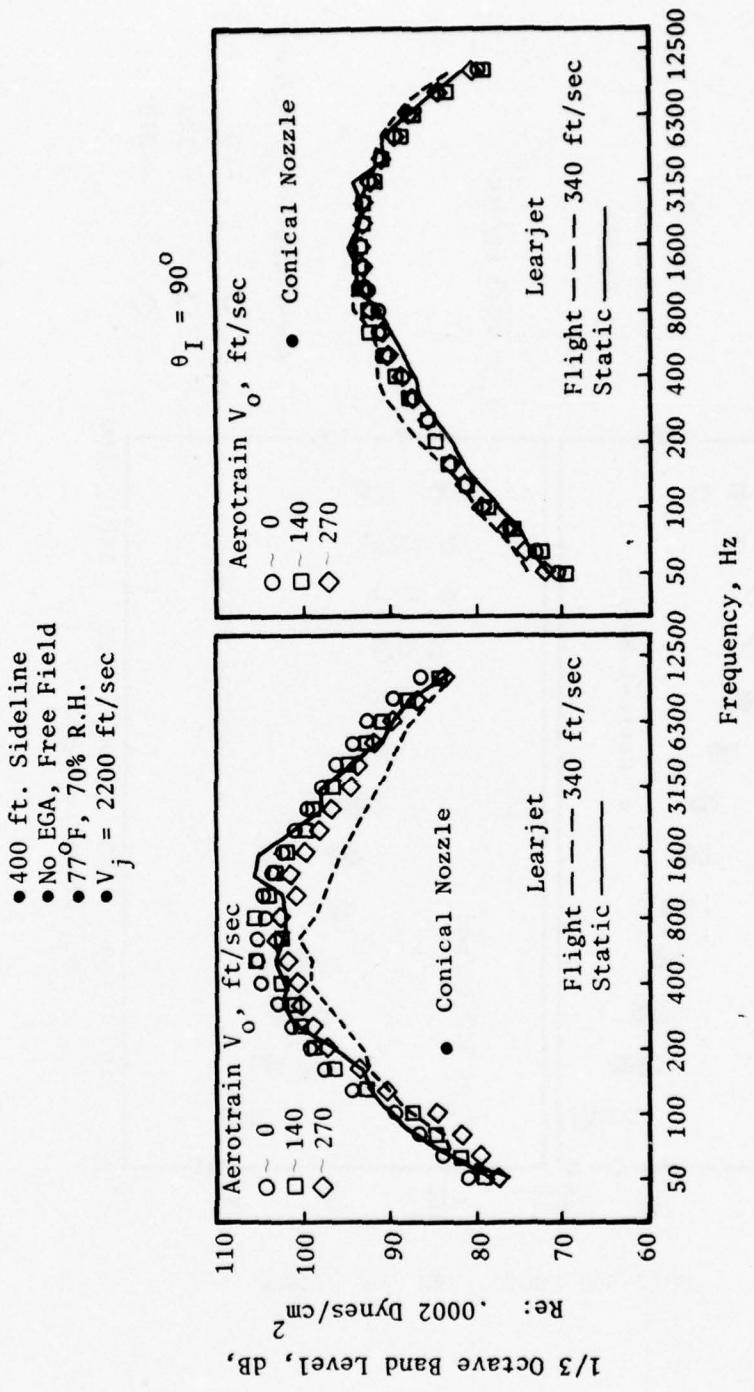


Figure 7-4. Comparison of Aerotrain and Flight Assurance Data.

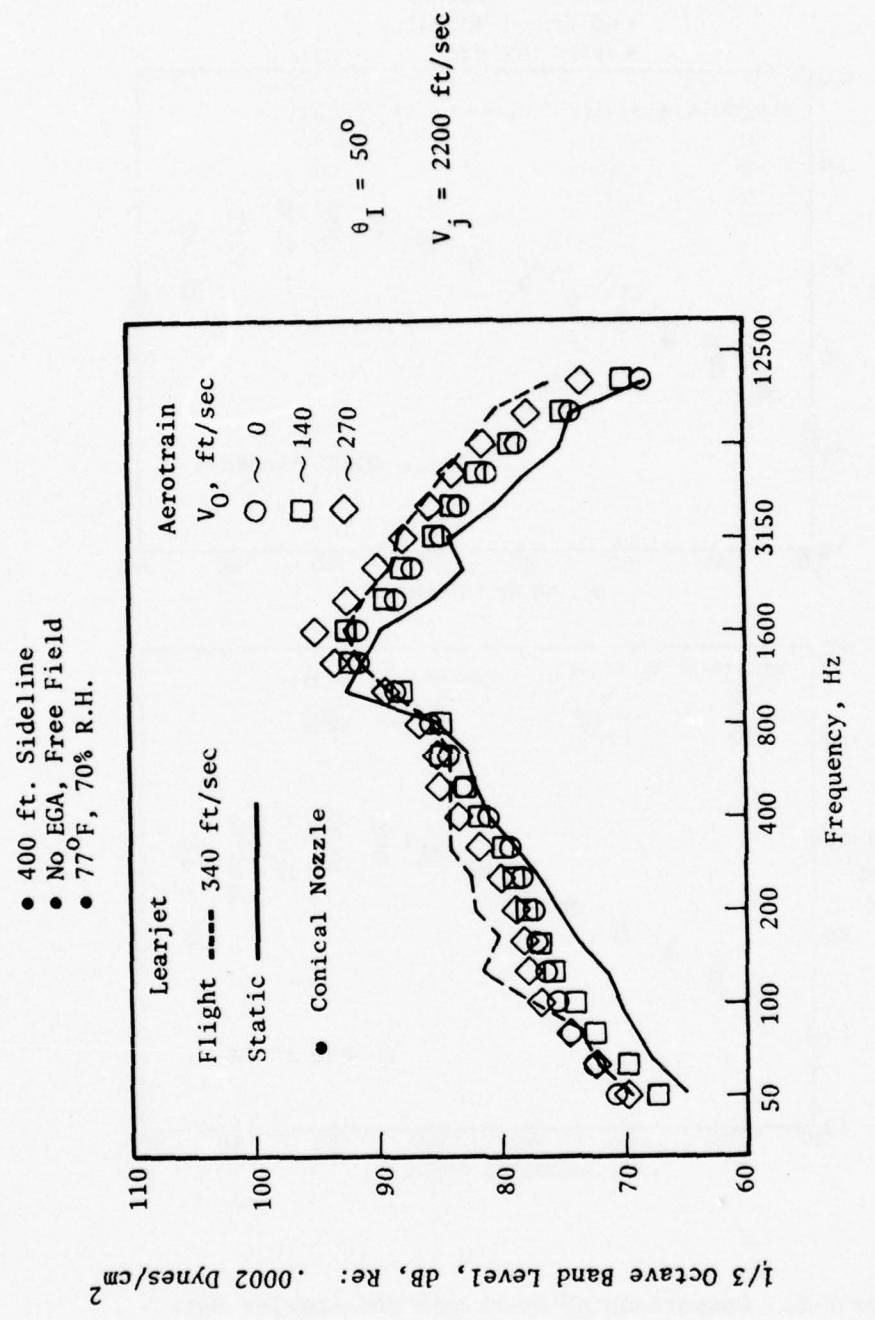


Figure 7-5. Comparison of Aerotrain and Flight Assurance Data.

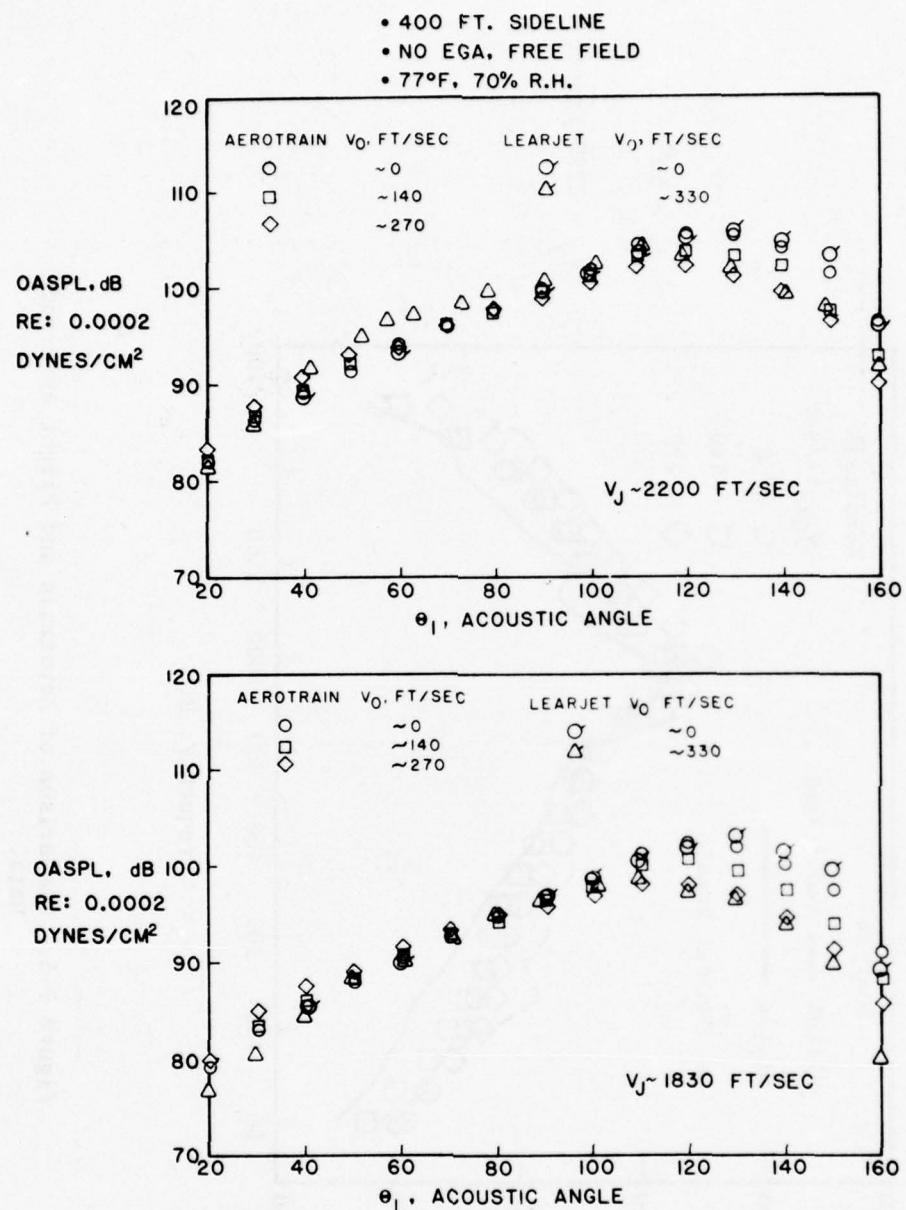


Figure 7-6. Comparison of Aerotrain and Learjet Data - 8-Lobe Nozzle.

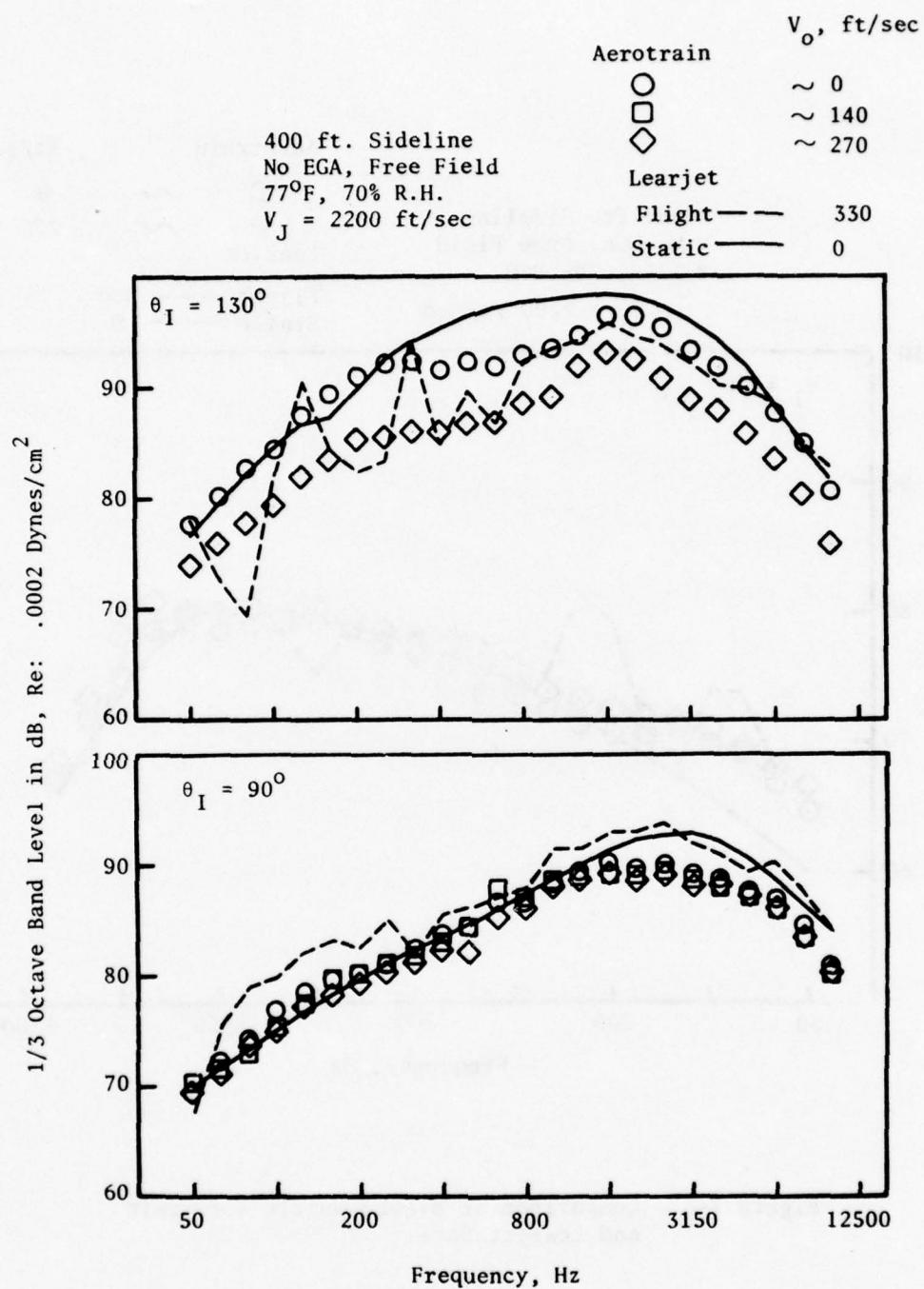


Figure 7-7. Comparison of 8-Lobe Nozzle Aerotrain and Learjet Data.

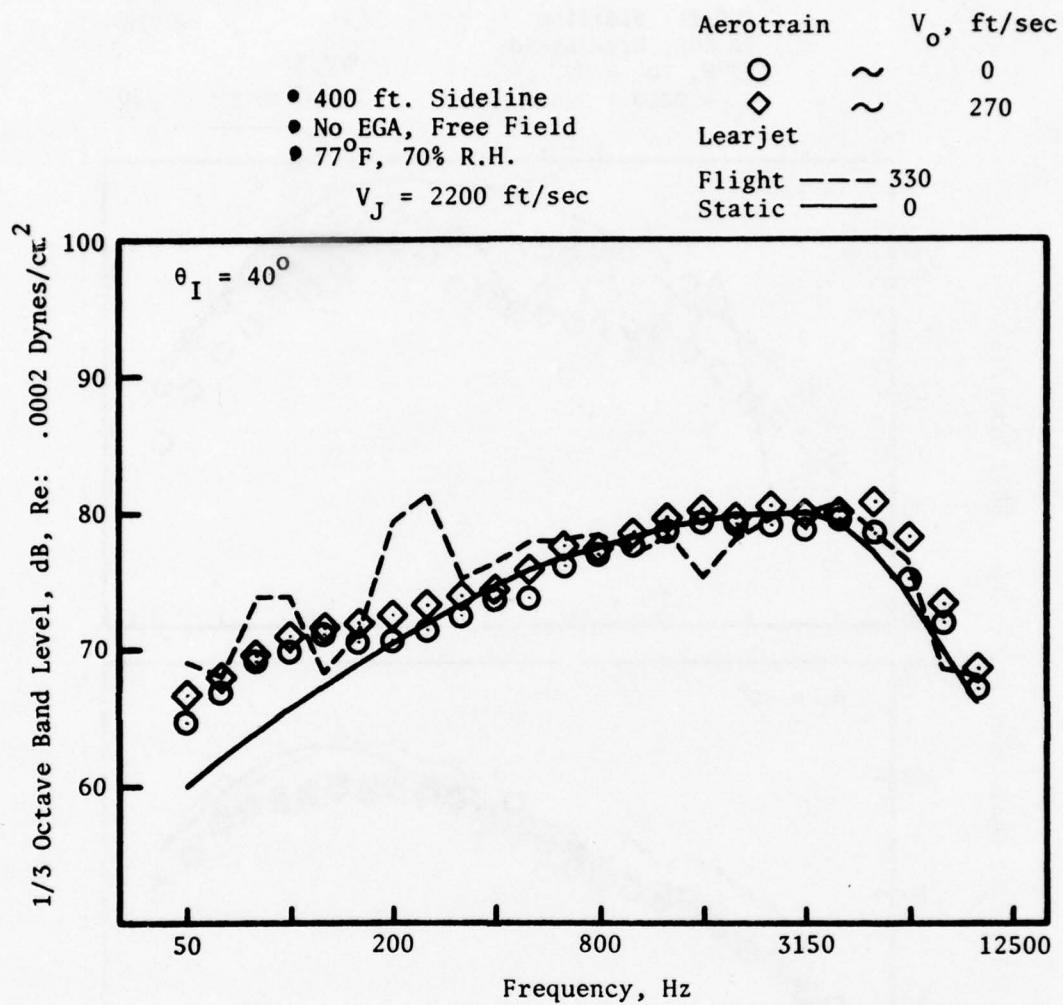


Figure 7-8. Comparison of 8-Lobe Nozzle Aerotrain and Learjet Data.

The 104-tube nozzle data measured on the F-106 and the Aerotrain are presented on Figure 7-9. Static comparisons are only available for acoustic angles of 80° through 160°. The agreement between the static F-106 and Aerotrain 104-tube nozzle data is within 2 dB for the range of conditions where comparisons are possible. The trends observed in the flight data are complementary (the F-106 results were obtained at higher flight speed than the Aerotrain; i.e., 420 ft/sec versus 270 ft/sec, respectively). More aft-quadrant reduction is observed for the F-106 than for the Aerotrain, which is exactly what is expected as flight speed is increased. The forward-quadrant trends are similar for both F-106 and Aerotrain in that the flight data is observed to approach the static data.

The 120° spectra comparisons presented on Figure 7-10 indicate that the aft-quadrant reduction is primarily due to low-frequency suppression; essentially no change is observed in the high-frequency portion of the spectra. The 90° spectra are presented on Figure 7-11. The Aerotrain data show some low-frequency reduction from static to flight at 90°; whereas, the F-106 results (at the much higher flight speed) show significantly more reduction, as was expected. These comparisons have demonstrated that the Aerotrain and flight test data, in general, exhibit the same directivity and spectra characteristics when the impact of different flight velocities are considered.

Comparisons for validating the hybrid in-flight-simulation technique will be made with the Aerotrain data because the free jet test conditions were designed to duplicate the cycle conditions obtained using the Aerotrain test vehicle. In all cases, the Aerotrain flight data is corrected for background noise, and the predicted combustion noise level is presented. It is important to note that the changes from static to flight have been a function of the following parameters, the degree of which depend on the configuration:

- Angle dependent
- Frequency dependent
- Jet velocity and flight velocity dependent

These interrelationships of the variables have established a comprehensive data base for the evaluation of the in-flight simulation technique.

The initial assessment of the hybrid in-flight-simulation technique is accomplished by comparing Aerotrain and transformed free jet, 1/3-octave band directivity patterns at the select 1/3-octave band frequencies of 250, 500, 1000, 2000, 4000, and 8000 Hz. Typical examples of these comparisons are presented on Figures 7-12 through 7-14 for the conical, 8-lobe, and 104-tube nozzles, respectively. The Aerotrain data is presented as a band to show the data repeatability. These initial comparisons show that the simulation procedure was, in general, duplicating the proper trends.

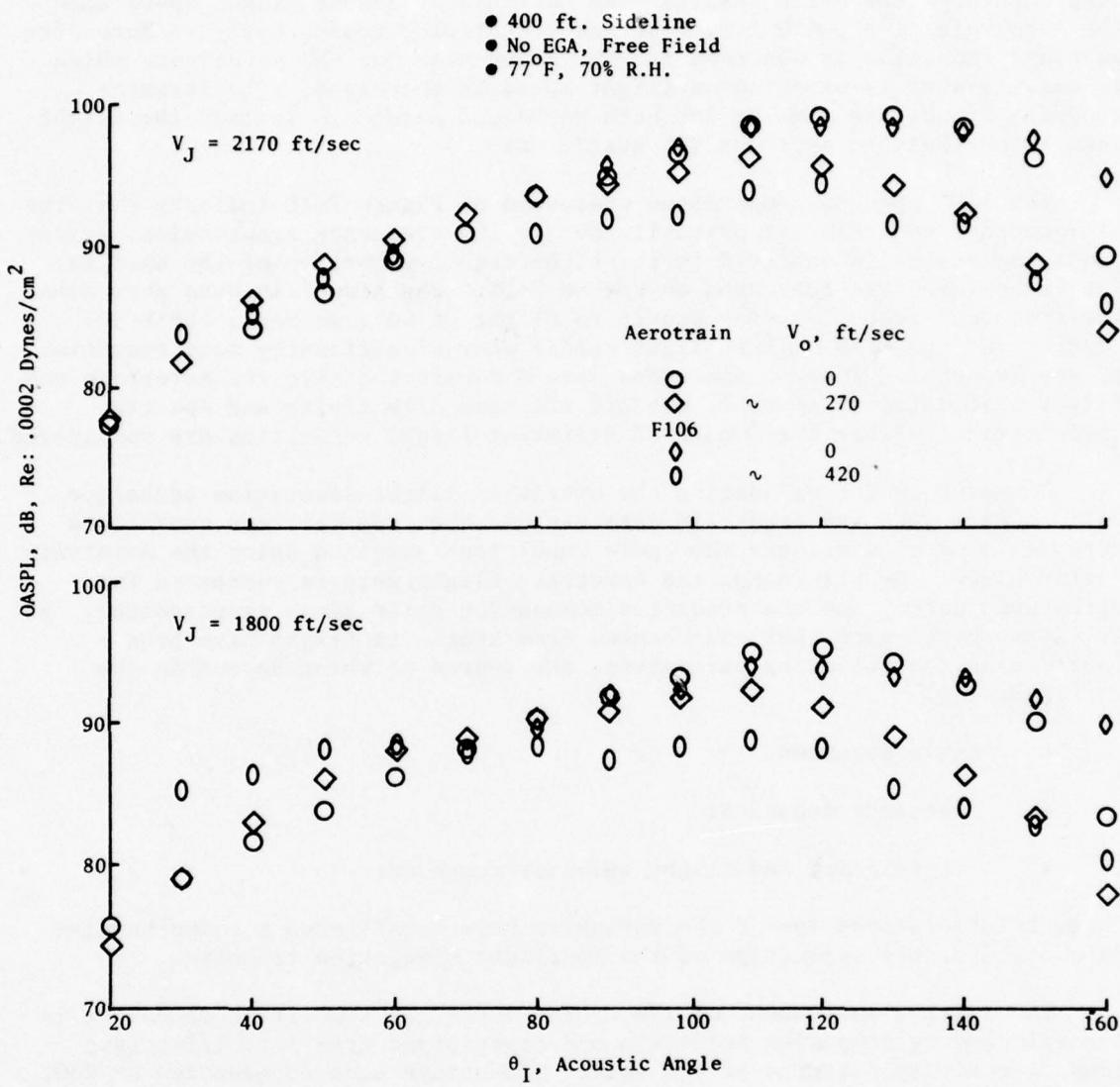


Figure 7-9. Comparison of Aerotrain and F-106 Data - 104-Tube Nozzle.

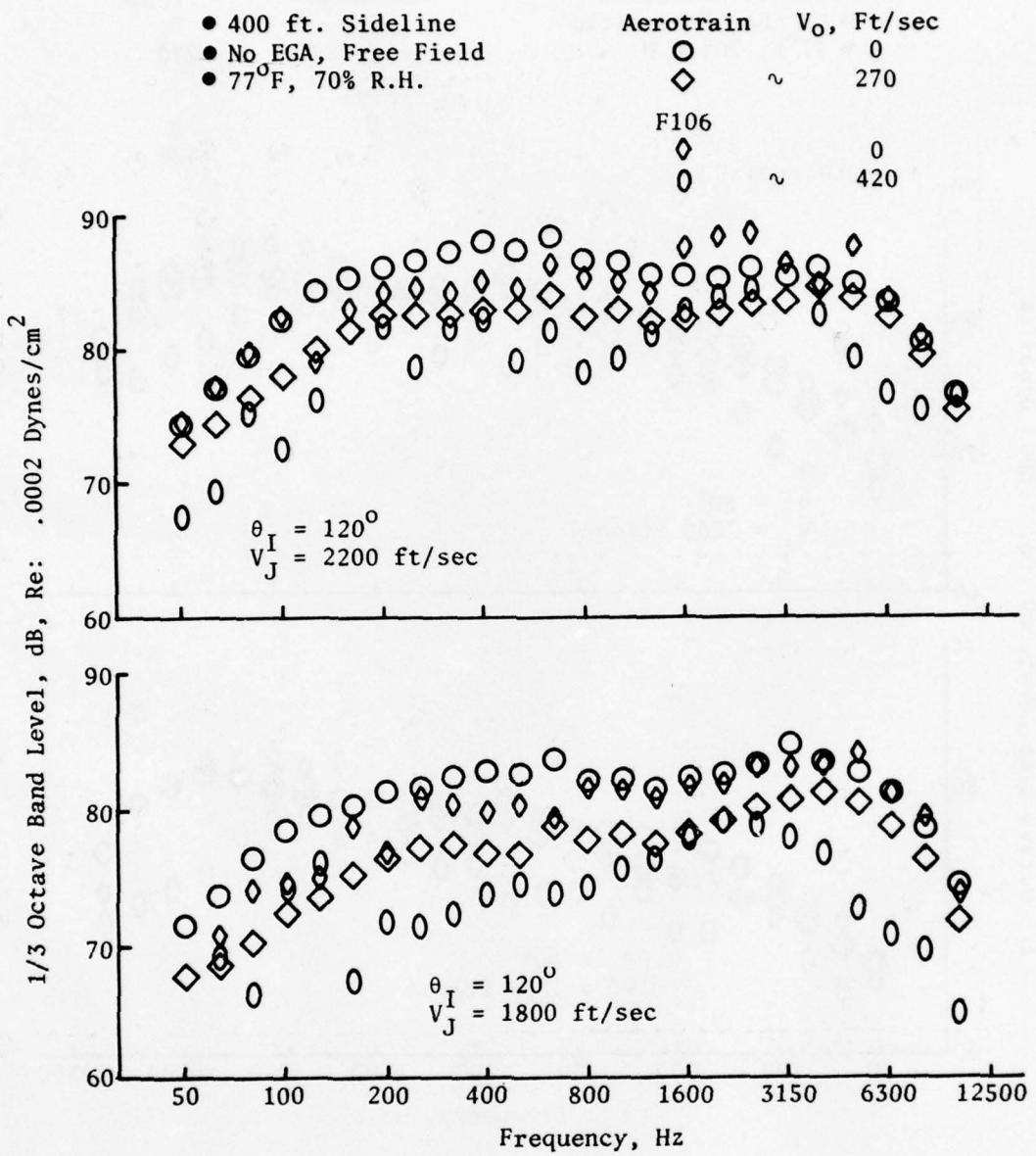


Figure 7-10. Comparison of Aerotrain and F-106 Data - 104-Tube Nozzle.

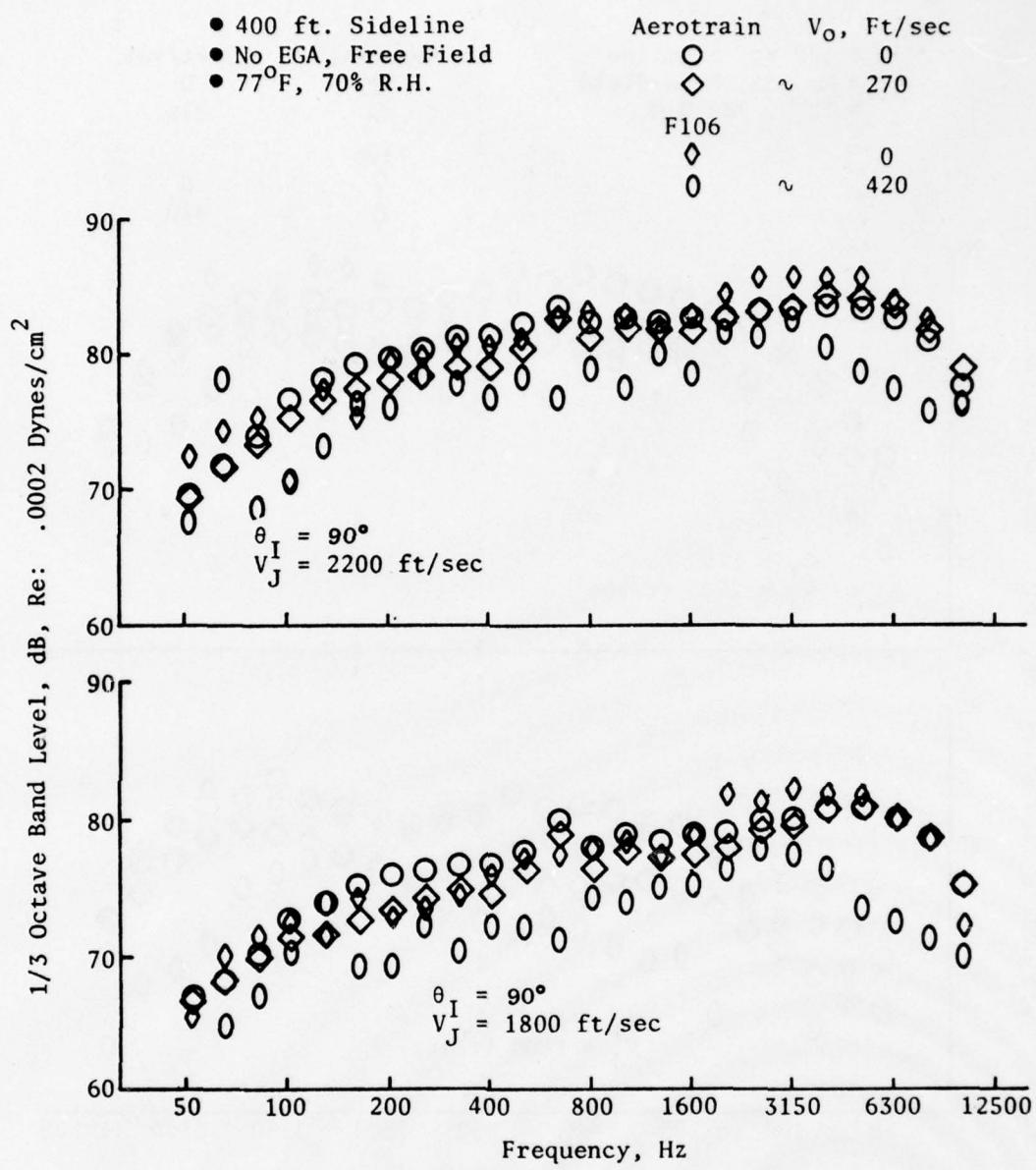


Figure 7-11. Comparison of Aerotrain and F-106 Data - 104-Tube Nozzle.

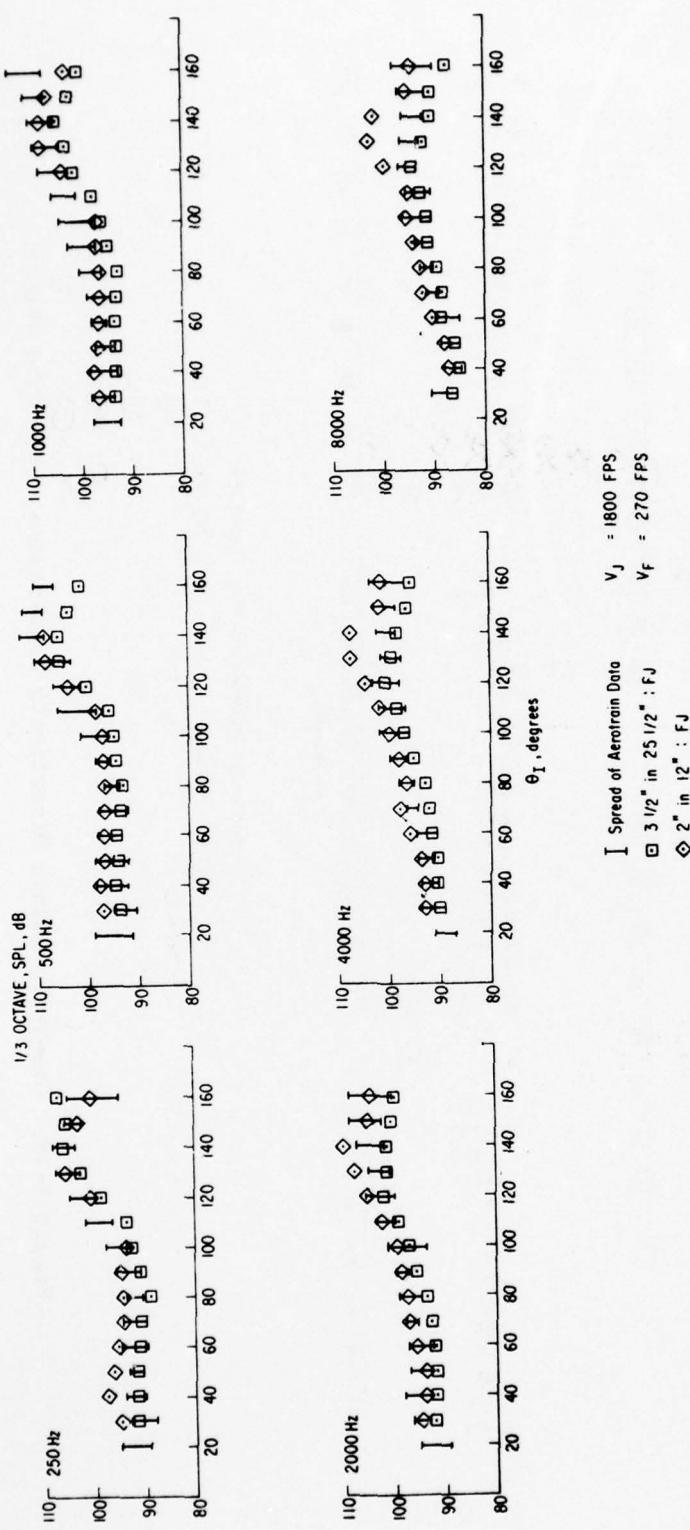


Figure 7-12. One-Third-Octave Directivity Comparisons - Conical Nozzle.

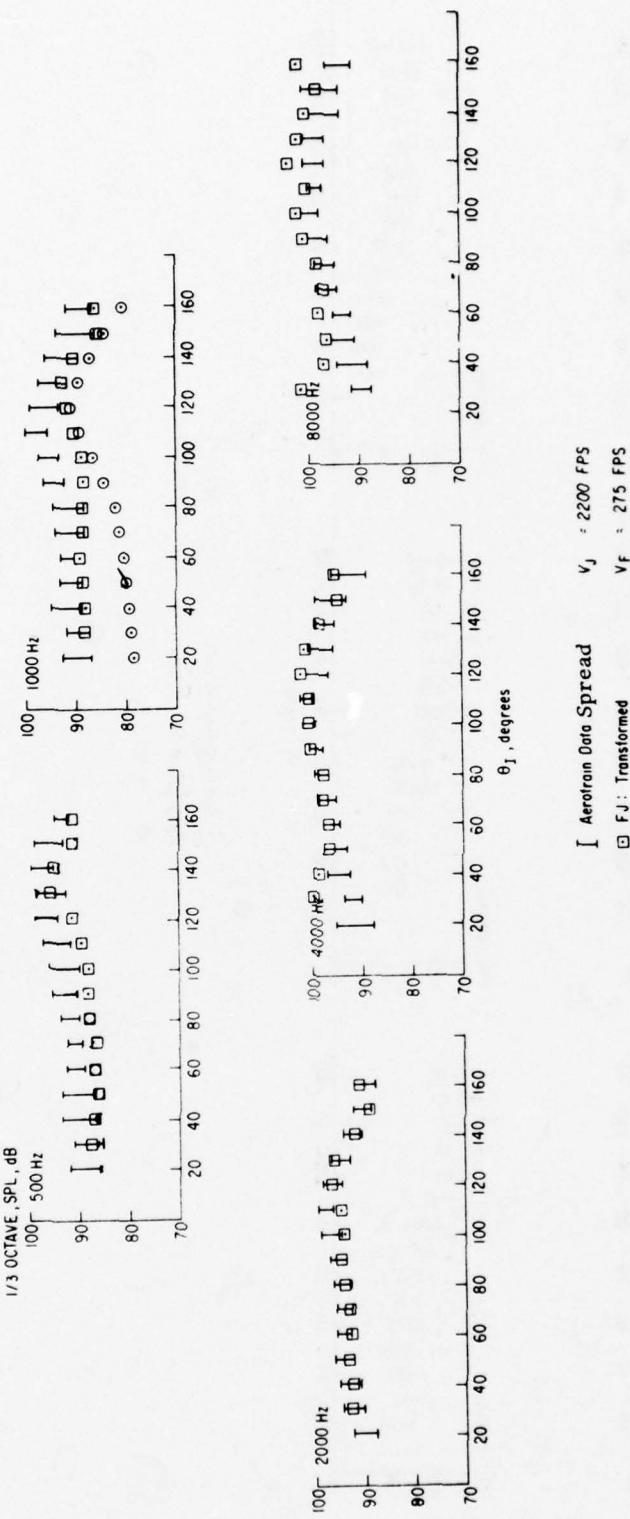


Figure 7-13. One-Third-Octave Directivity Comparisons - 104-Tube Nozzle.

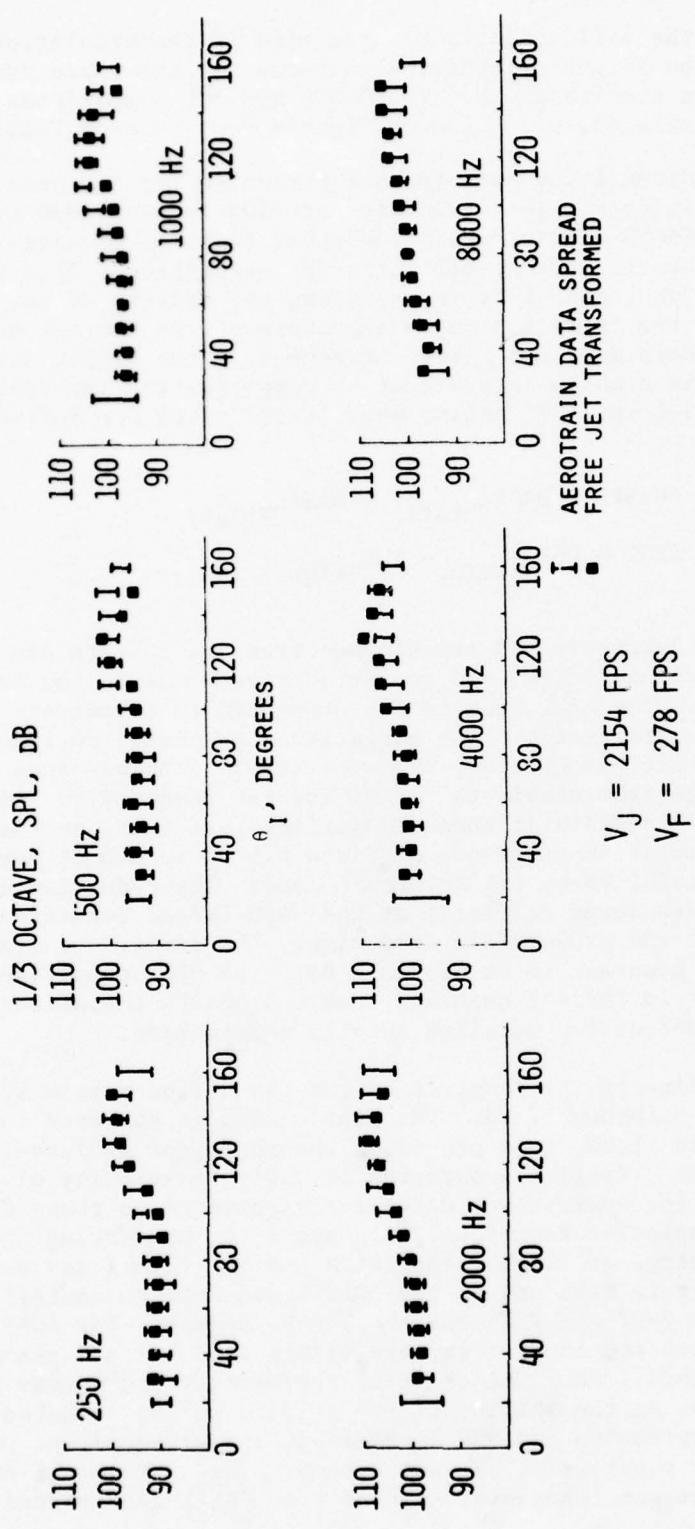


Figure 7-14. One-Third-Octave Directivity Comparisons - 8-Lobe Nozzle.

The next phase in the validation is to determine if the simulation procedure can predict the flight directivity patterns for the three configurations evaluated on the Aerotrain. The OASPL and PNL comparisons for the baseline conical nozzle are presented on Figures 7-15 through 7-20.

The PNL and OASPL directivity patterns are presented for the static and 270-ft/sec flight velocities for jet velocities of 1400 ft/sec, 1800 ft/sec, and 2200 ft/sec. The JENOTS static data is observed to be on the order of 3 dB below the Aerotrain static data at all three jet velocities. This static data bias provides an added complexity in assessing the ability of the simulation to determine the in-flight noise signature of the conical nozzle because, if the static data does not agree, agreement of the flight data cannot be expected. This problem is overcome by comparing the Aerotrain and flight results on a Δ OASPL and Δ PNL basis, where these terms are defined as follows:

- Δ OASPL = OASPL_{Static} - OASPL_{Flight}
- Δ PNL = PNL_{Static} - PNL_{Flight}

Comparisons of the Aerotrain and transformed free jet results are presented on Figures 7-21 and 7-22. All comparisons are made on the basis of both Δ PNL and Δ OASPL. The Δ PNL results are presented to accentuate any frequency-dependent characteristics. The comparisons presented on Figures 7-17 and 7-18 indicate that, in general, the simulation technique does indeed predict the change from static to flight for the range of jet velocities evaluated. Specific results of these comparisons are that, on the basis of Δ OASPL, the simulation technique predicts 0.5 dB to 3.0 dB more reduction at 90° than exhibited by the Aerotrain data. The reduction at the 150° acoustic angle is predicted correctly at the 1400-ft/sec condition, but overpredicted by 5 dB at the 2200-ft/sec condition. The forward-quadrant deltas are observed, in general, to be within 1 dB. The Δ PNL comparisons demonstrate more scatter in the aft quadrant than the Δ OASPL comparisons indicated and provide impetus for detailed spectra examination.

The OASPL and PNL directivity comparisons for the 8-lobe nozzle are presented on Figures 7-23 through 7-26. The static data is observed to agree, in general, within ± 1 dB, thus providing the basis for absolute-level comparisons of the flight directivity patterns at a flight velocity of 270 ft/sec. Comparisons of the appropriate directivity patterns on these figures demonstrate that the simulation technique, in general, is predicting the correct trends for the range of flight velocities and jet velocities evaluated. To further illustrate this point, the Δ OASPL and Δ PNL characteristics are presented on Figures 7-27 and 7-28 for the 8-lobe nozzle. The Δ OASPL comparisons at 2200 ft/sec and 1800 ft/sec are within 2 dB for all cases and, in general, are within 1 dB. The shape of the directivity curves are the same, thus demonstrating the ability of the transformation technique to predict aft-quadrant suppression and the increase in forward-quadrant noise levels for this moderate suppression exhaust system. The Δ PNL comparisons (Figure 7-28) exhibit the same characteristic as the Δ OASPL comparisons.

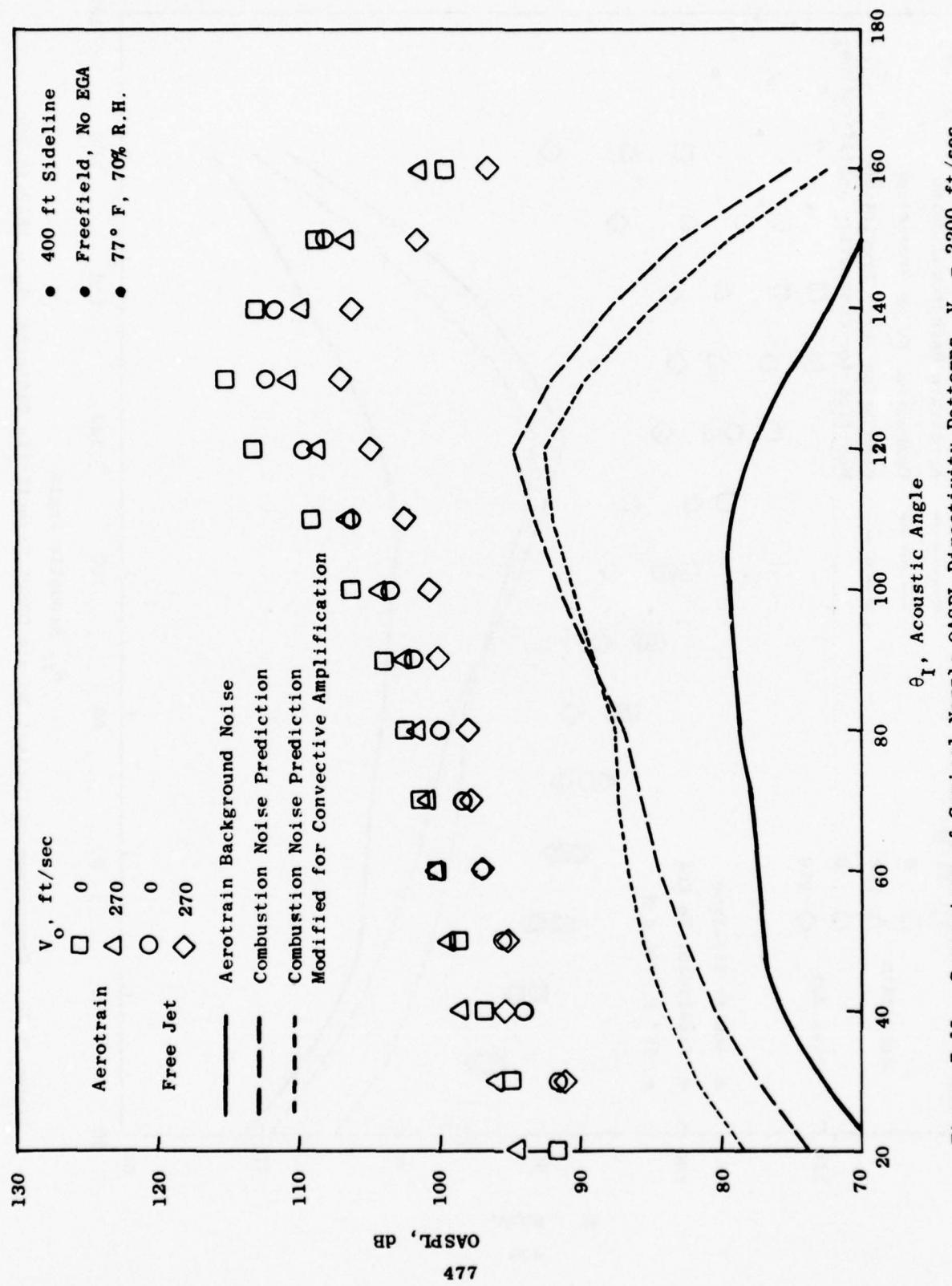


Figure 7-15. Comparison of Conical Nozzle OASPL Directivity Patterns, $V_J = 2200$ ft/sec.

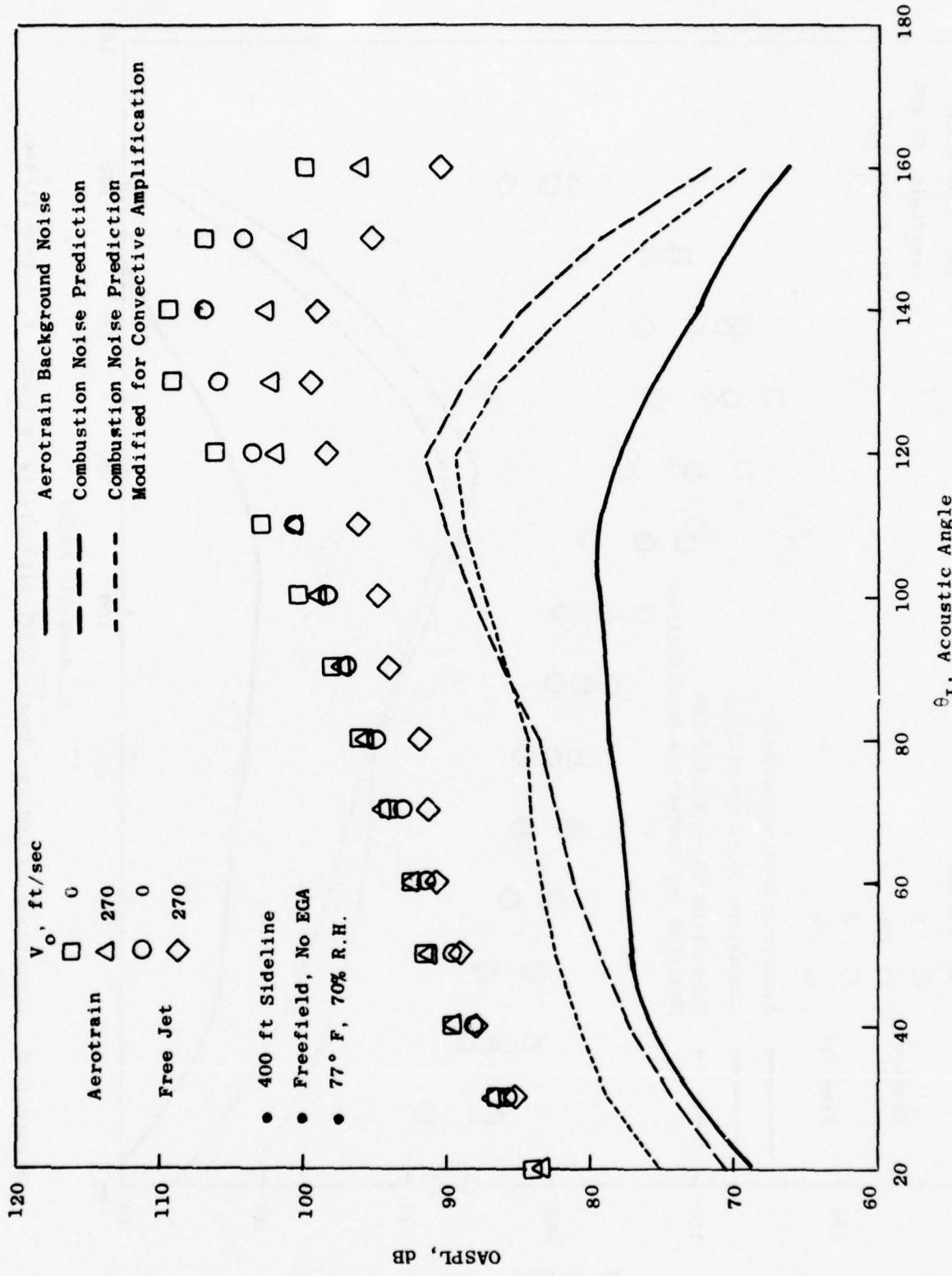


Figure 7-16. Comparison of Conical Nozzle OASPL Directivity Patterns, $V_J = 1800$ ft/sec.

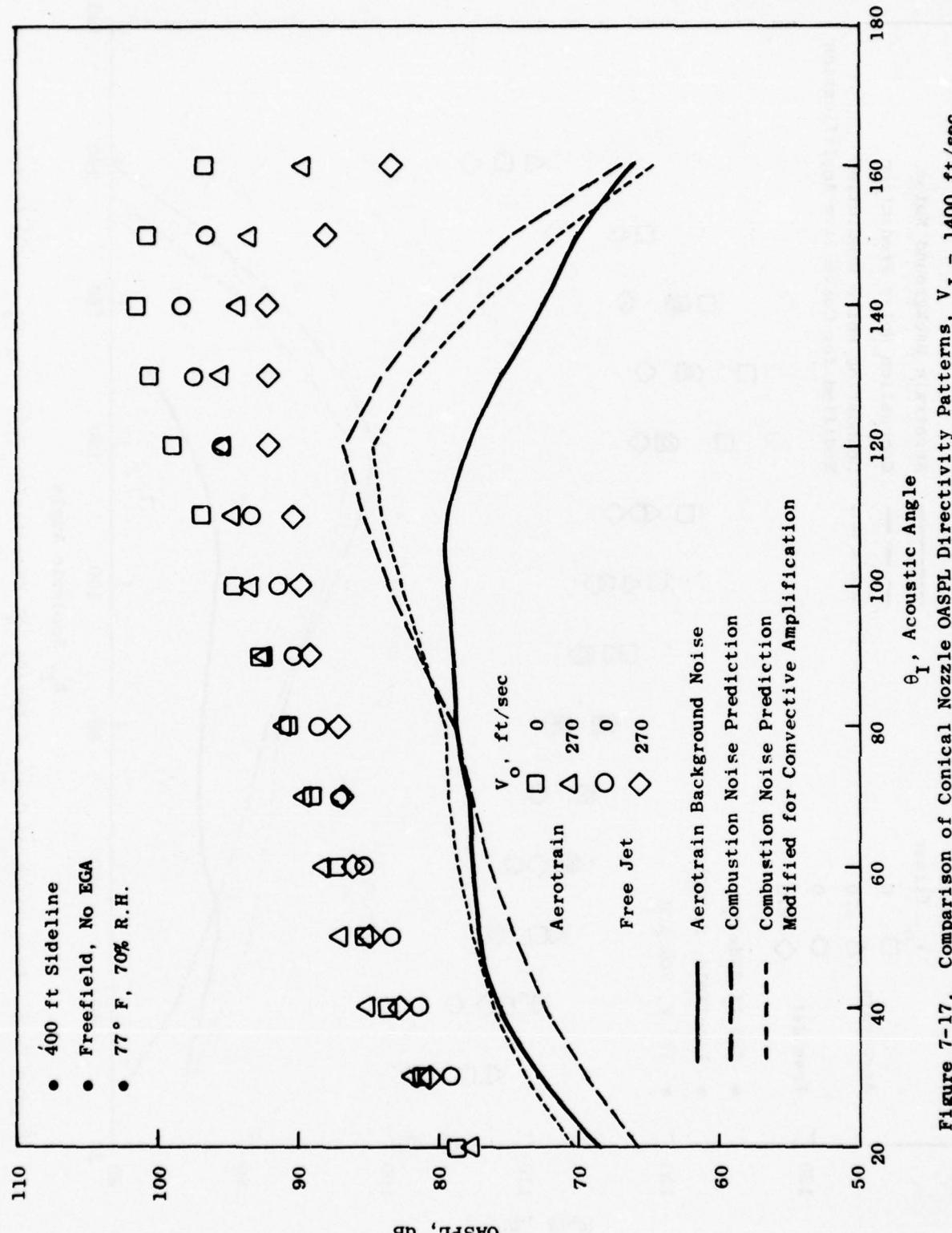


Figure 7-17. Comparison of Conical Nozzle OASPL Directivity Patterns, $V_J = 1400$ ft/sec.

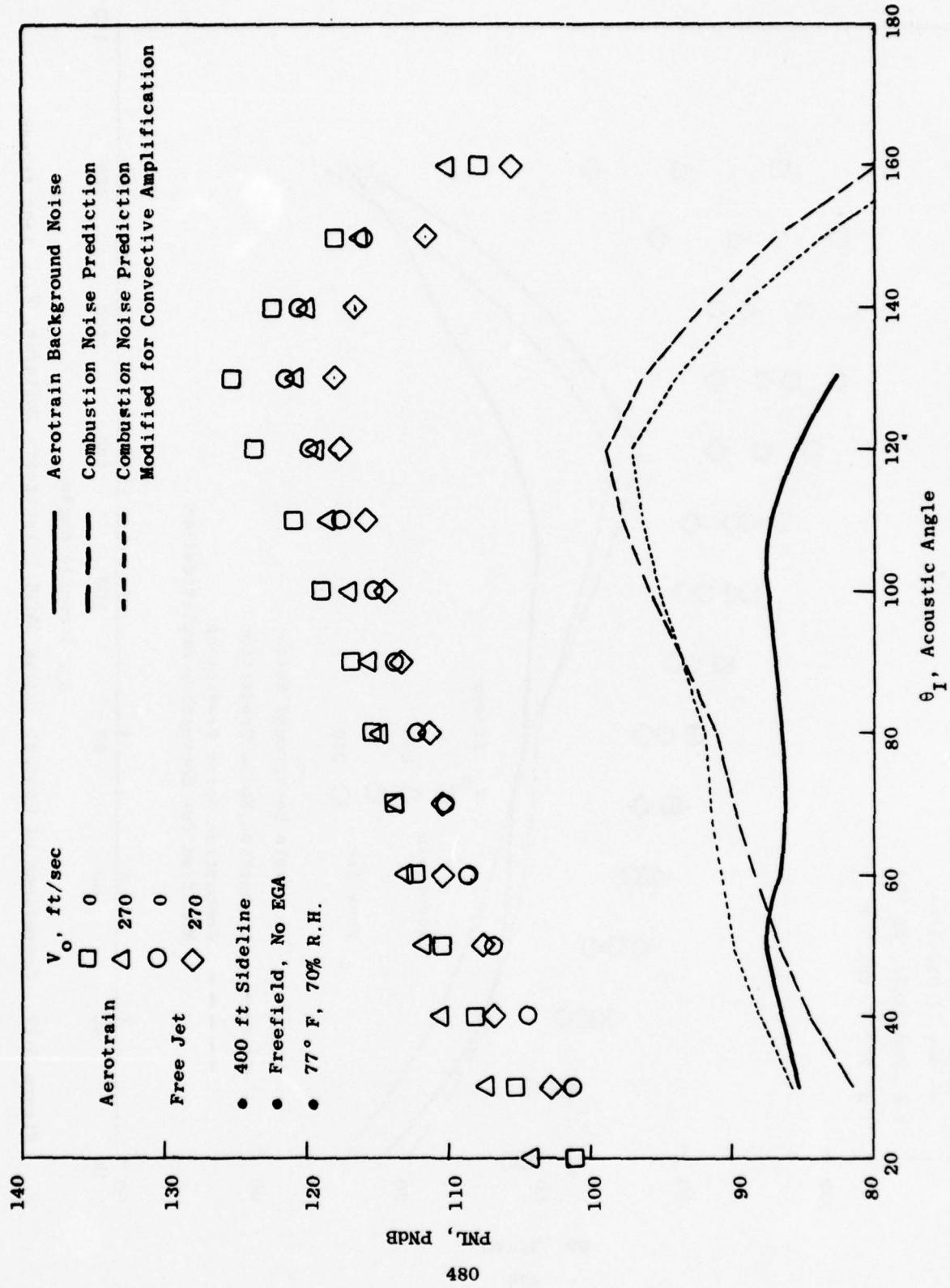


Figure 7-18. Comparison of Conical Nozzle PNL Directivity Patterns, $V_J = 2200$ ft/sec.

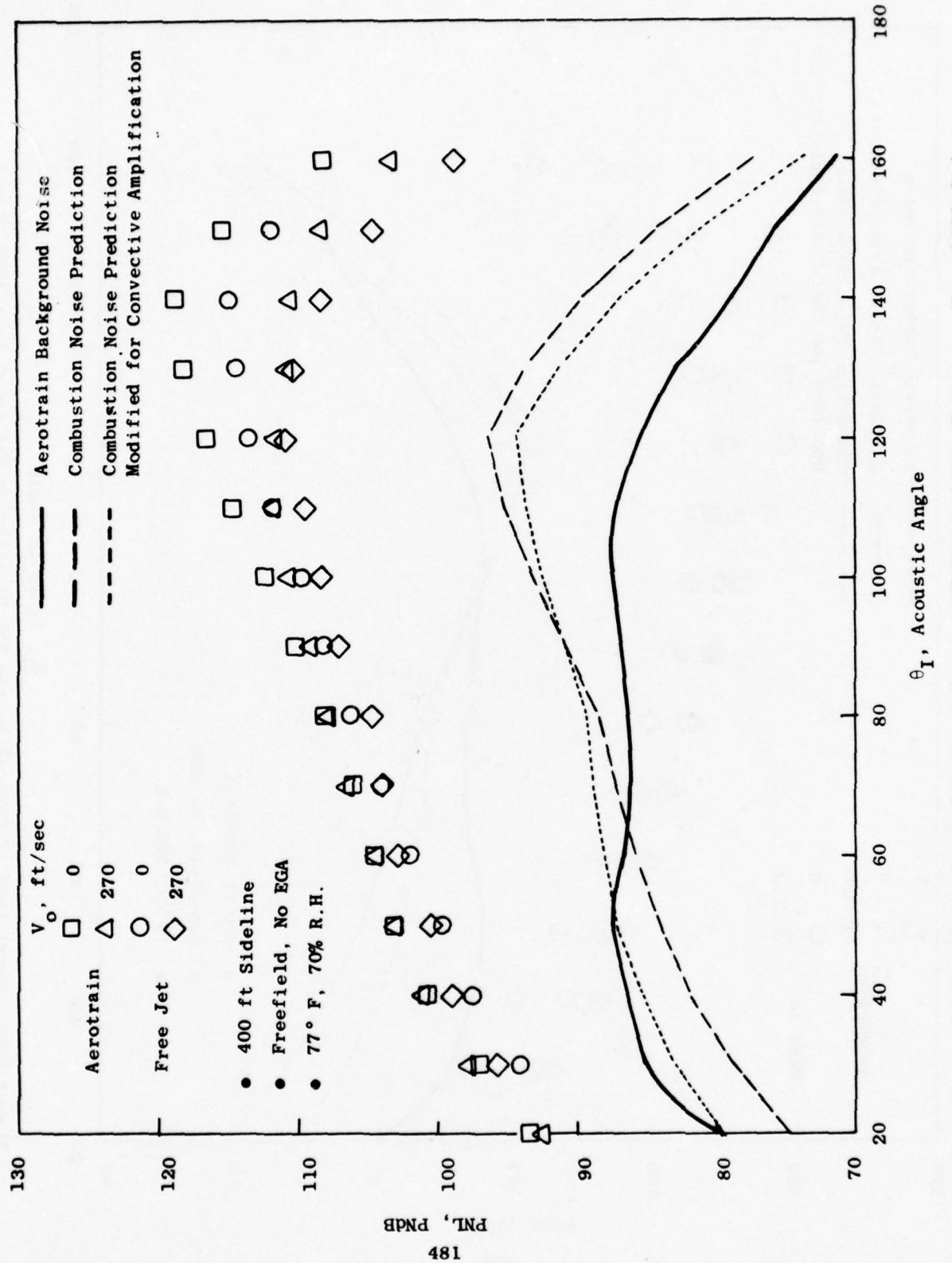


Figure 7-19. Comparison of Conical Nozzle PNL Directivity Patterns, $V_J = 1800$ ft/sec.

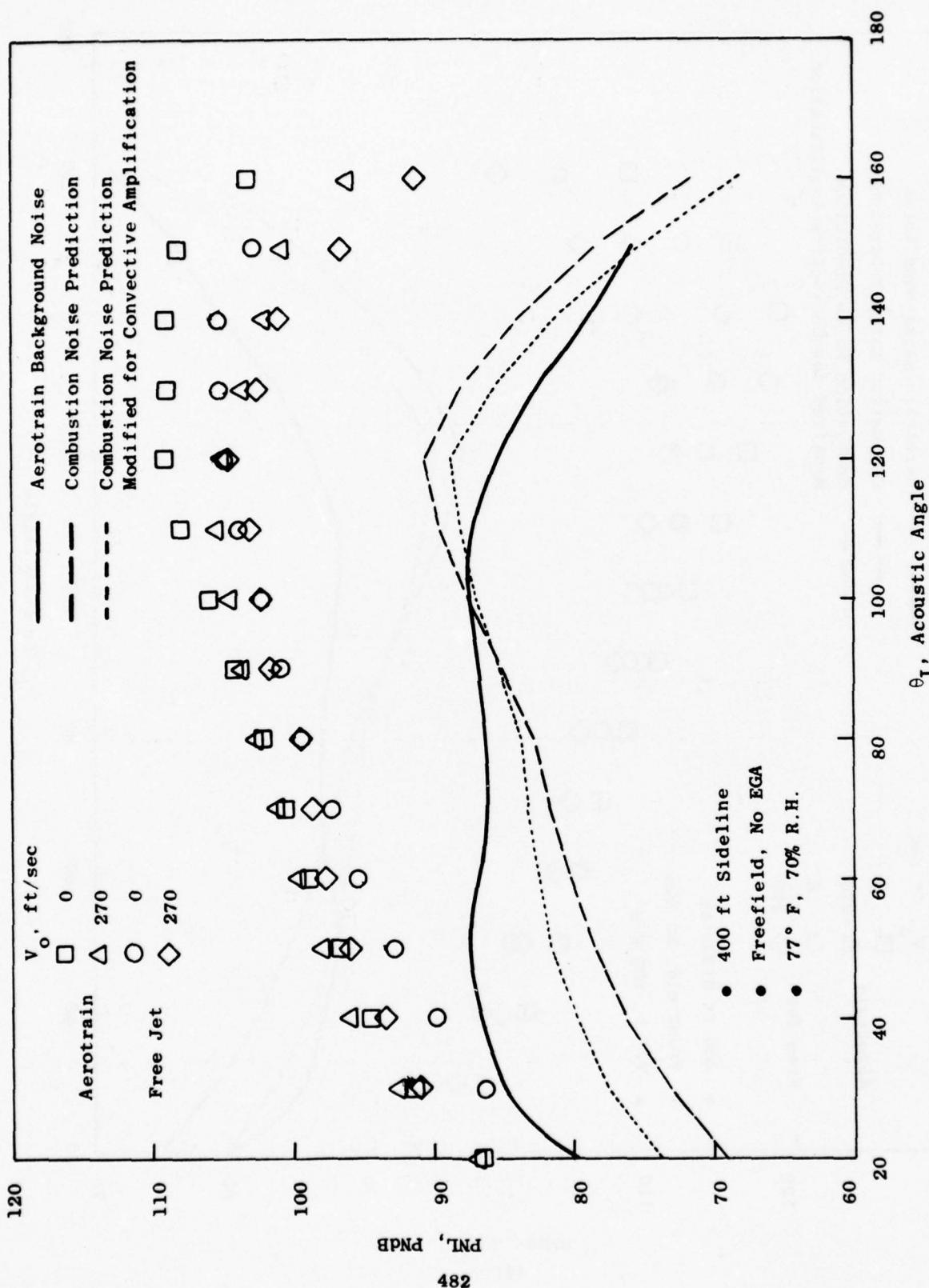


Figure 7-20. Comparison of Conical Nozzle PNL Directivity Patterns, $V_J = 1400$ ft/sec.

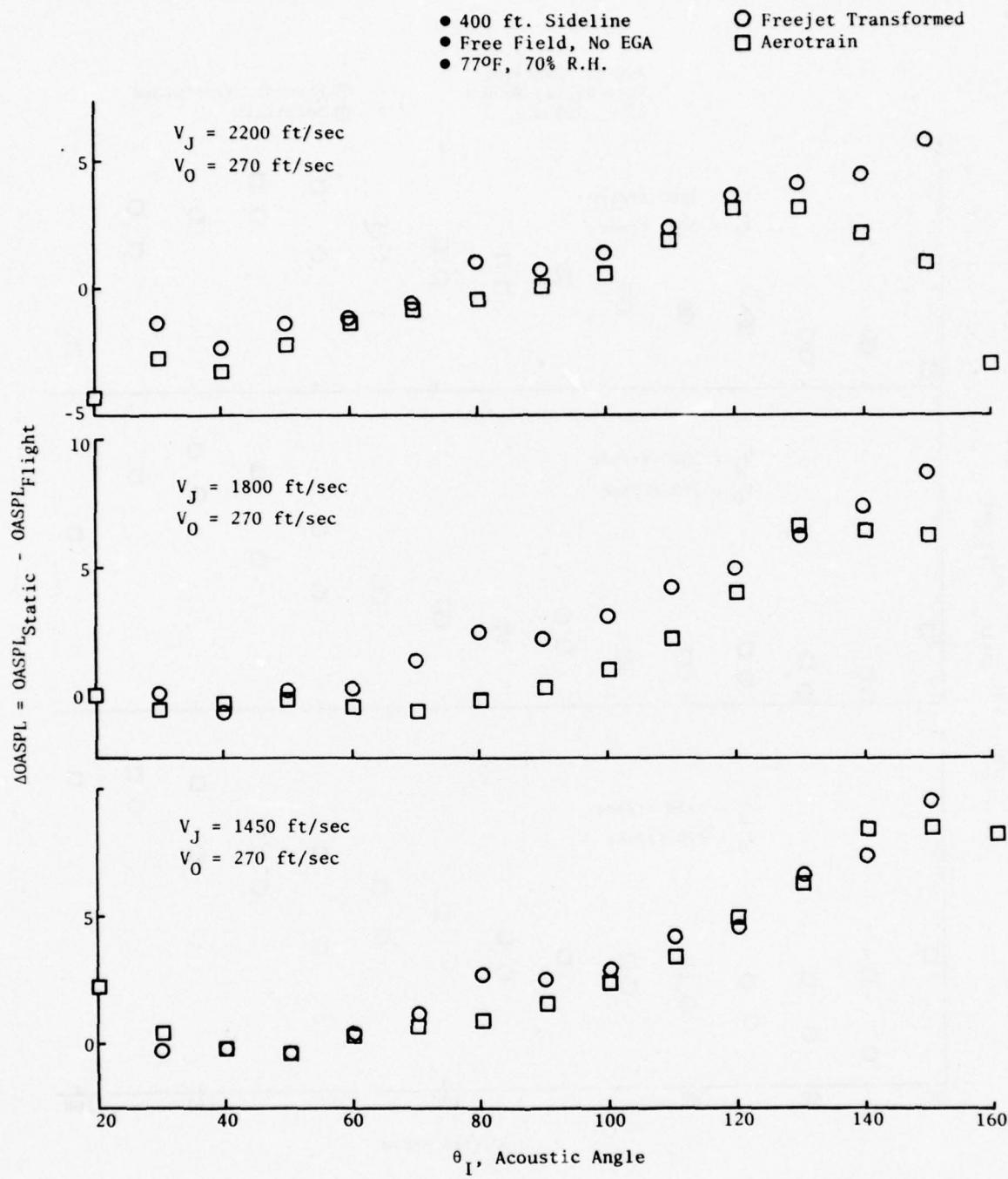


Figure 7-21. Comparison of Conical Nozzle ΔOASPL Directivity Patterns.

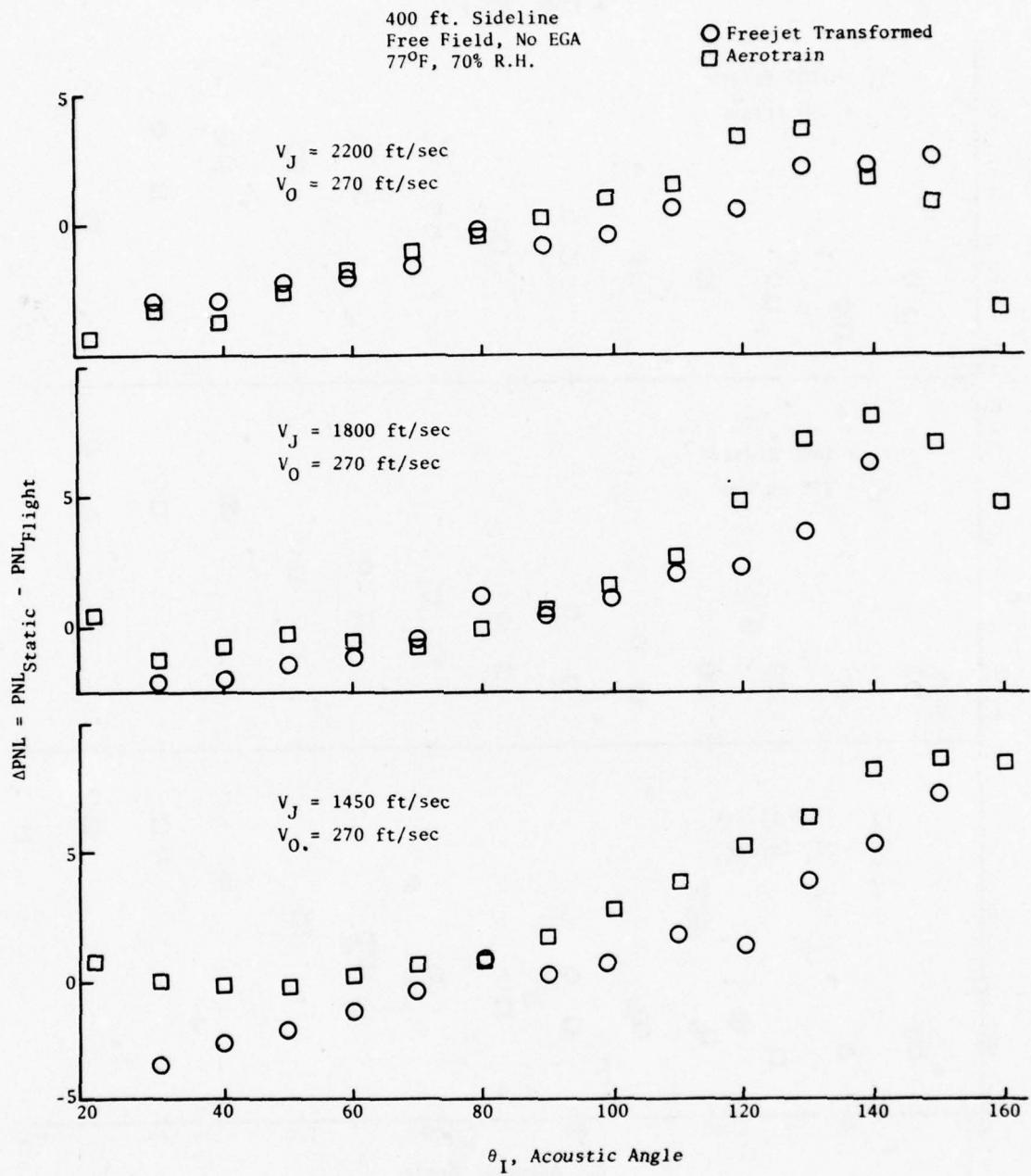


Figure 7-22. Comparison of Conical Nozzle ΔPNL Directivity Patterns.

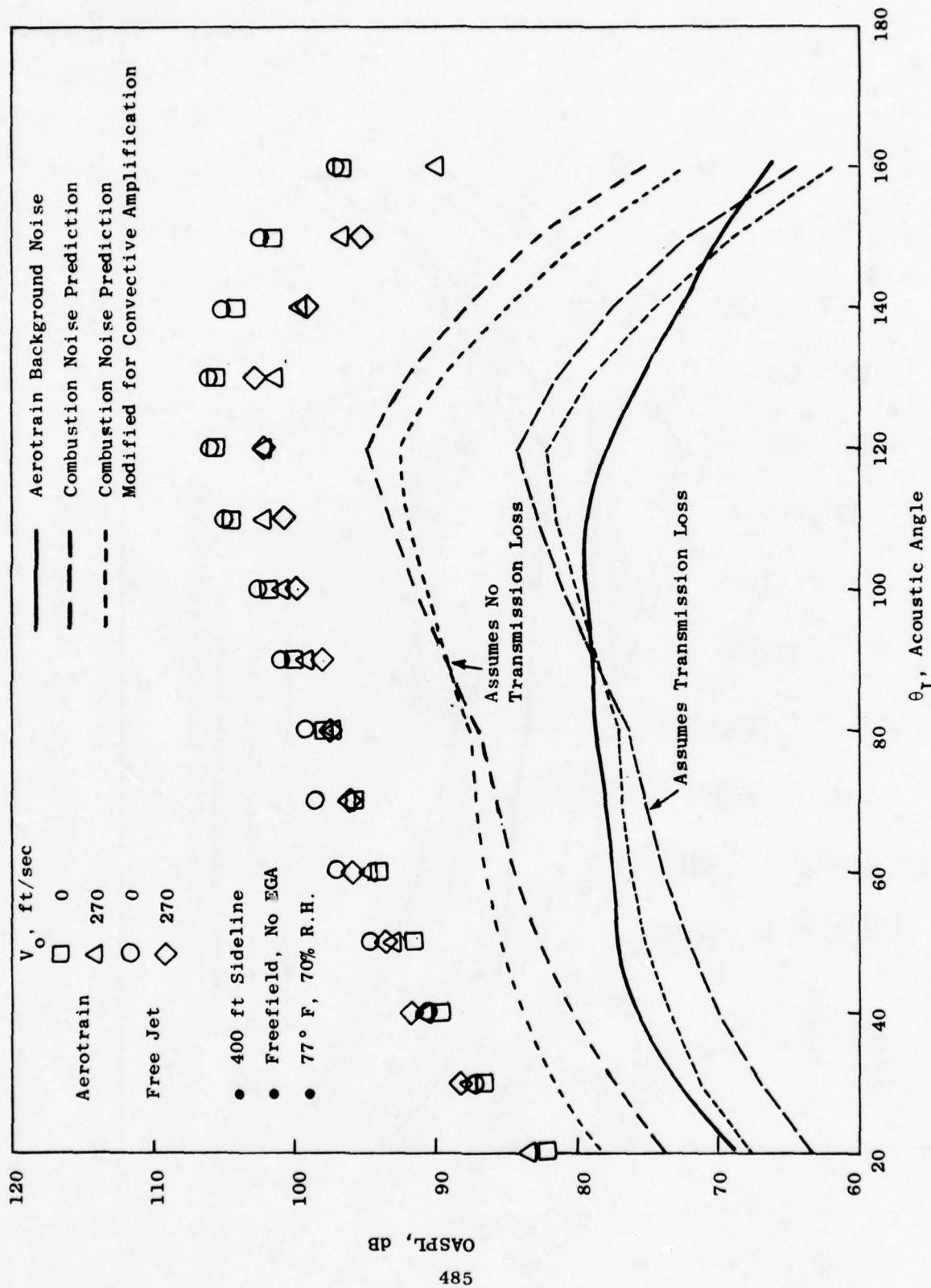


Figure 7-23. Comparison of 8-Lobe Nozzle OASPL Directivity Pattern, $V_J = 2200$ ft/sec.

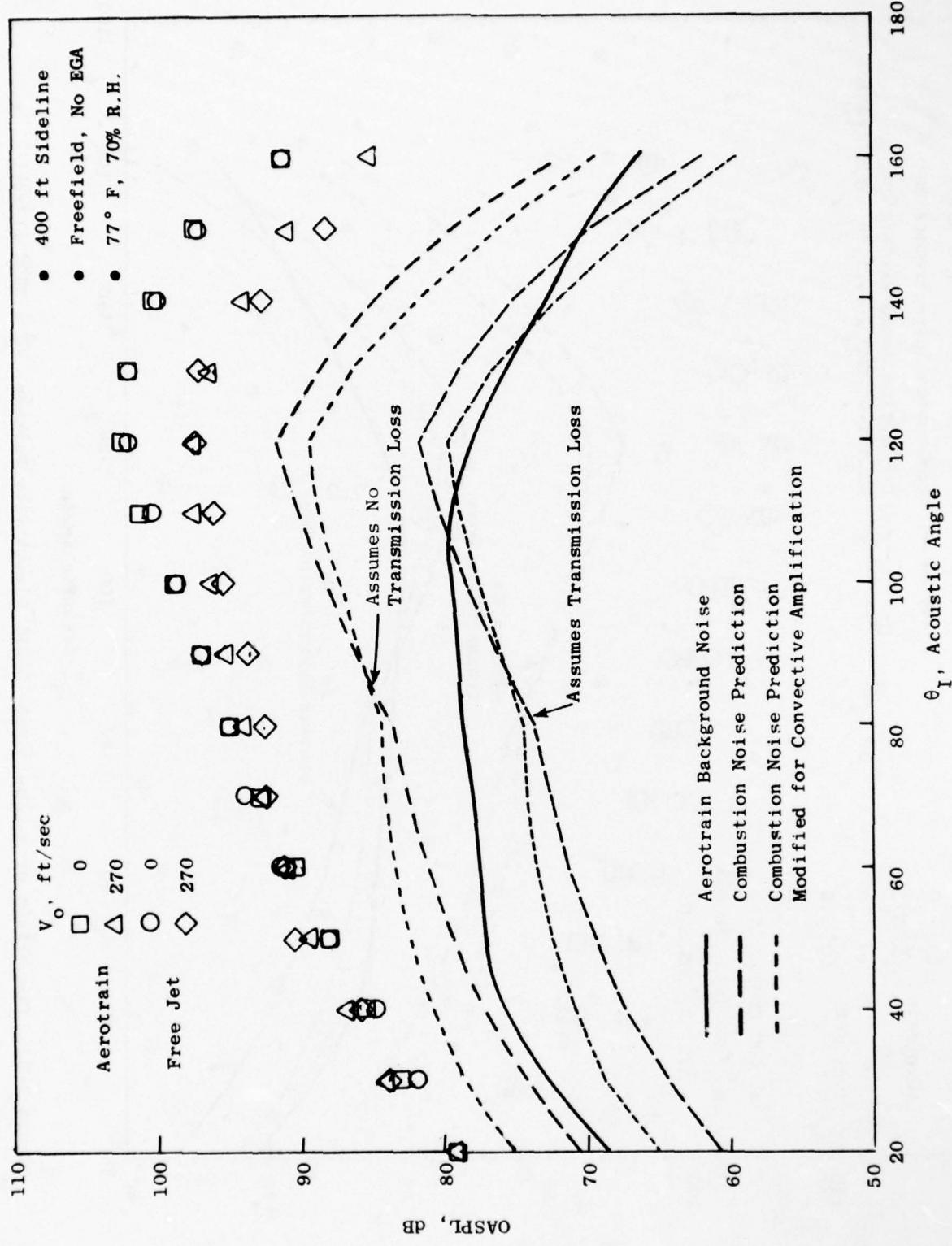


Figure 7-24. Comparison of 8-Lobe Nozzle OASPL Directivity Patterns, $V_J = 1800$ ft/sec.

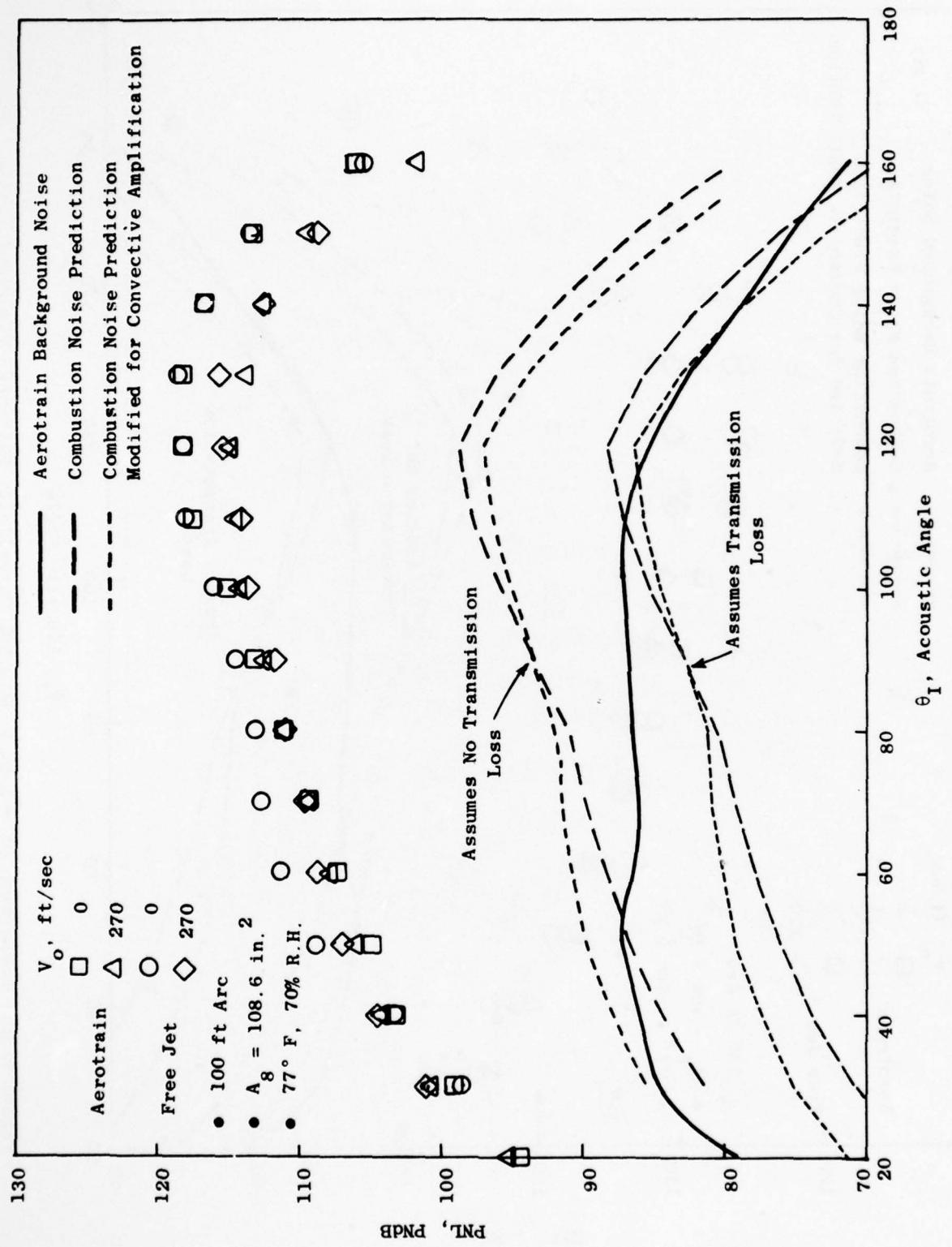


Figure 7-25. Comparison of 8-Lobe Nozzle PNL Directivity Patterns, $V_J = 2200 \text{ ft/sec}$.

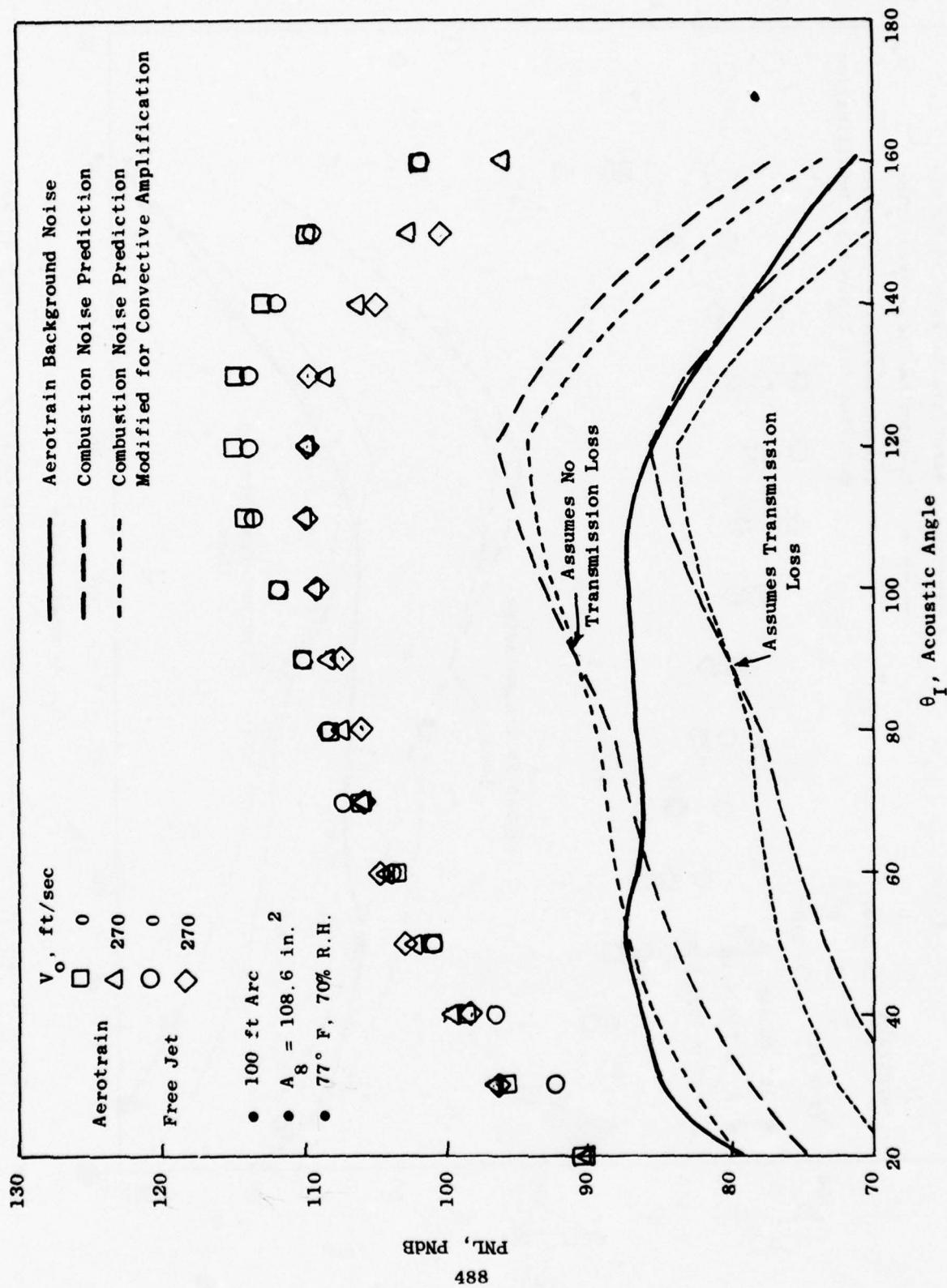


Figure 7-26. Comparison of 8-Lobe Nozzle PNL Directivity Patterns, $V_J = 1800 \text{ ft/sec.}$

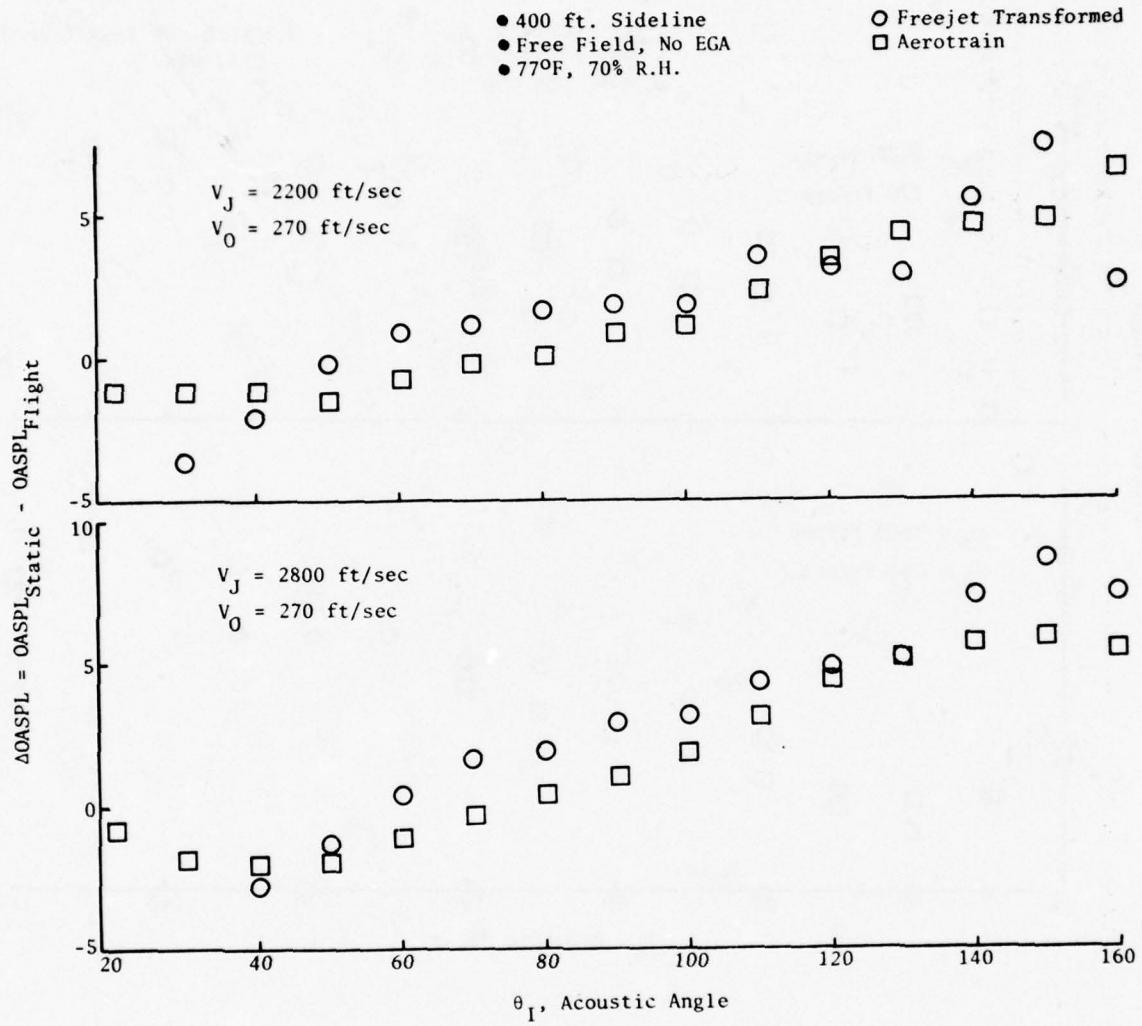


Figure 7-27. Comparison of 8-Lobe Nozzle $\Delta OASPL$ Directivity Patterns.

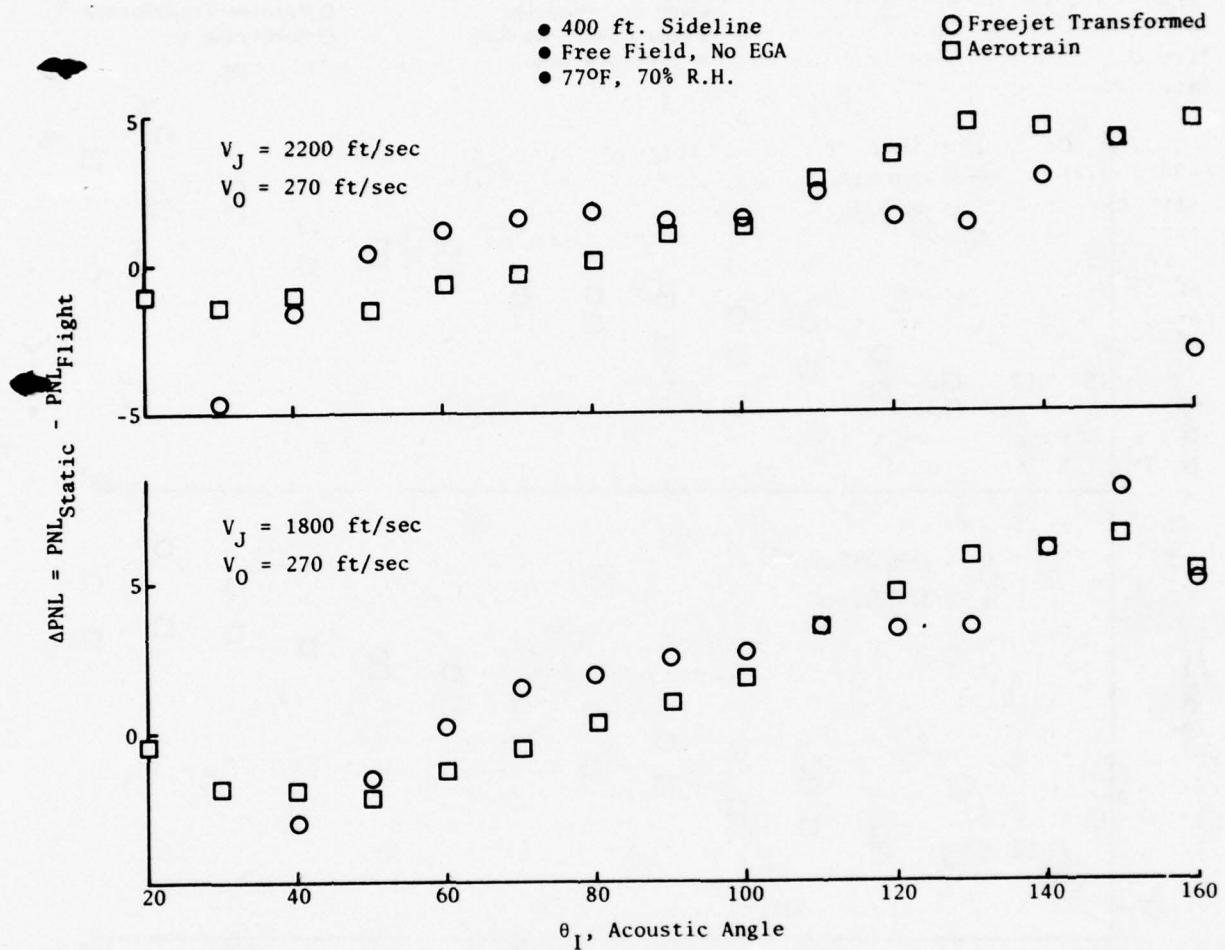


Figure 7-28. Comparison of 8-Lobe Nozzle $\Delta PN L$ Directivity Patterns.

The OASPL and PNL directivity patterns for the 104-tube nozzle are presented on Figures 7-29 through 7-32. The comparisons are only presented at jet velocities of 2200 ft/sec and 1800 ft/sec because the 1400-ft/sec Aerotrain static data is contaminated by the background noise of the test vehicle. The static comparisons show that the Aerotrain and JENOTS data agree within 2 dB except in the extreme forward quadrant where some contamination due to vehicle background noise has been observed. The flight directivity shapes of both the Aerotrain and the scaled, transformed, free-jet data are the same. Since the in-flight simulation depends on the validity of diametric scaling, as well as transforming the measured free jet data, the agreement is considered excellent.

The Δ OASPL and Δ PNL characteristics are presented on Figures 7-33 and 7-34 for the 104-tube nozzle. The comparisons of the increments predicted, using the in-flight simulation technique and the Aerotrain results, are generally within 1 dB except at the extreme angles of the acoustic envelope where background noise has been observed to have significant influence. The influence of background noise at the extreme forward quadrant angles (20° through 40°) is accentuated more strongly by the Δ PNL comparisons.

In summary, except in regions where background noise contamination is obvious the simulation technique correctly predicts the in-flight directivity characteristics of the 104-tube nozzle for the range of jet velocities and flight velocities studied.

The final phase in the assessment of the in-flight simulation technique is selected spectra comparisons for the conical, 8-lobe, and 104-tube nozzles. These comparisons are made at acoustic angles of 120° , 90° , and 50° .

Conical nozzle static and flight spectra are compared on Figures 7-35 through 7-37. The 120° spectra comparisons indicate that the in-flight simulation technique tends to predict less high frequency and more low frequency reduction than that demonstrated by the Aerotrain results. The 90° spectra show less dramatic low frequency reduction than the 120° angles with the simulation technique predicting more reduction due to flight than that demonstrated by the Aerotrain data. The comparisons at the 50° acoustic angle show extremely similar trends on an increment basis. The JENOTS conical nozzle does not show the same strong influence of shock noise observed for the Aerotrain conical nozzle.

The spectra comparisons for the 8-lobe nozzle are presented on Figures 7-38 through 7-40. The comparisons at the 120° acoustic angle show, in general, that the simulation technique again predicts more low frequency reduction, approximately 2 to 3 dB, than exhibited by the Aerotrain results. A similar low frequency difference is observed for the 90° acoustic angle. The comparisons at the 50° acoustic angle show no consistent differences between the Aerotrain and predicted results. In general, the predicted and Aerotrain data agree within ± 2 dB.

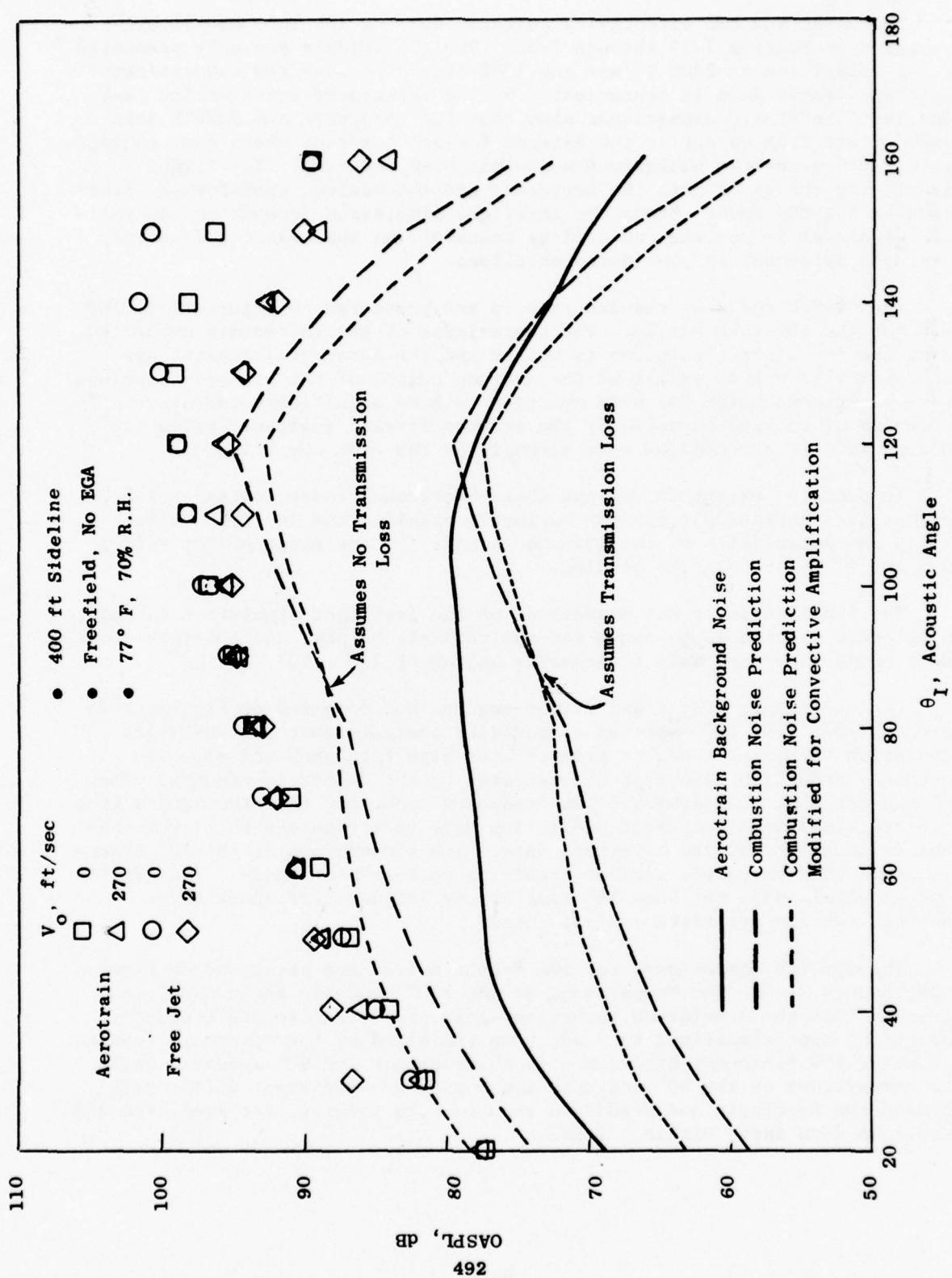


Figure 7-29. Comparison of 104-Tube Nozzle OASPL Directivity Patterns, $V_J = 2200$ ft/sec.

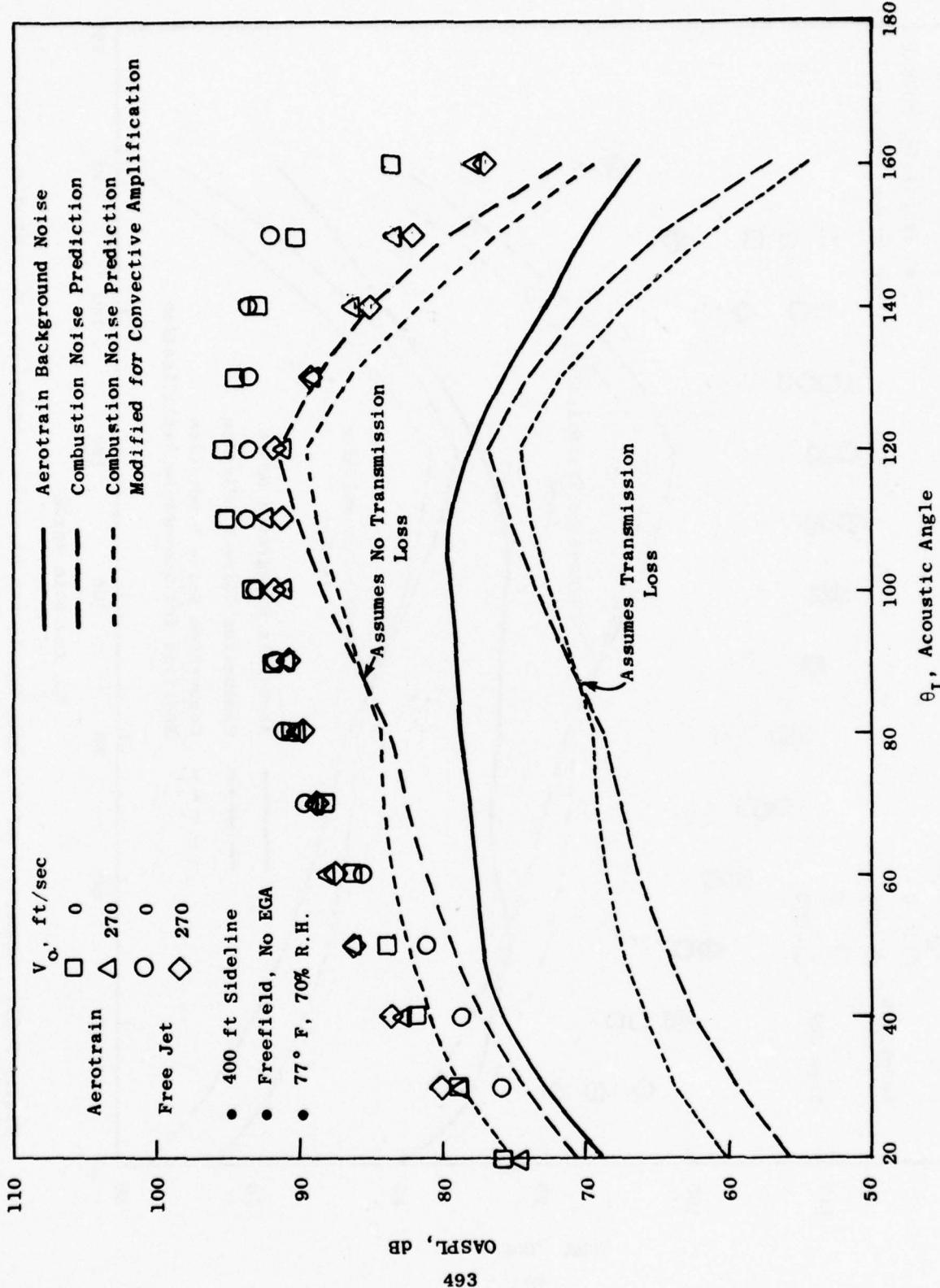


Figure 7-30. Comparison of 104-Tube Nozzle OASPL Directivity Patterns, $V_J = 1800$ ft/sec.

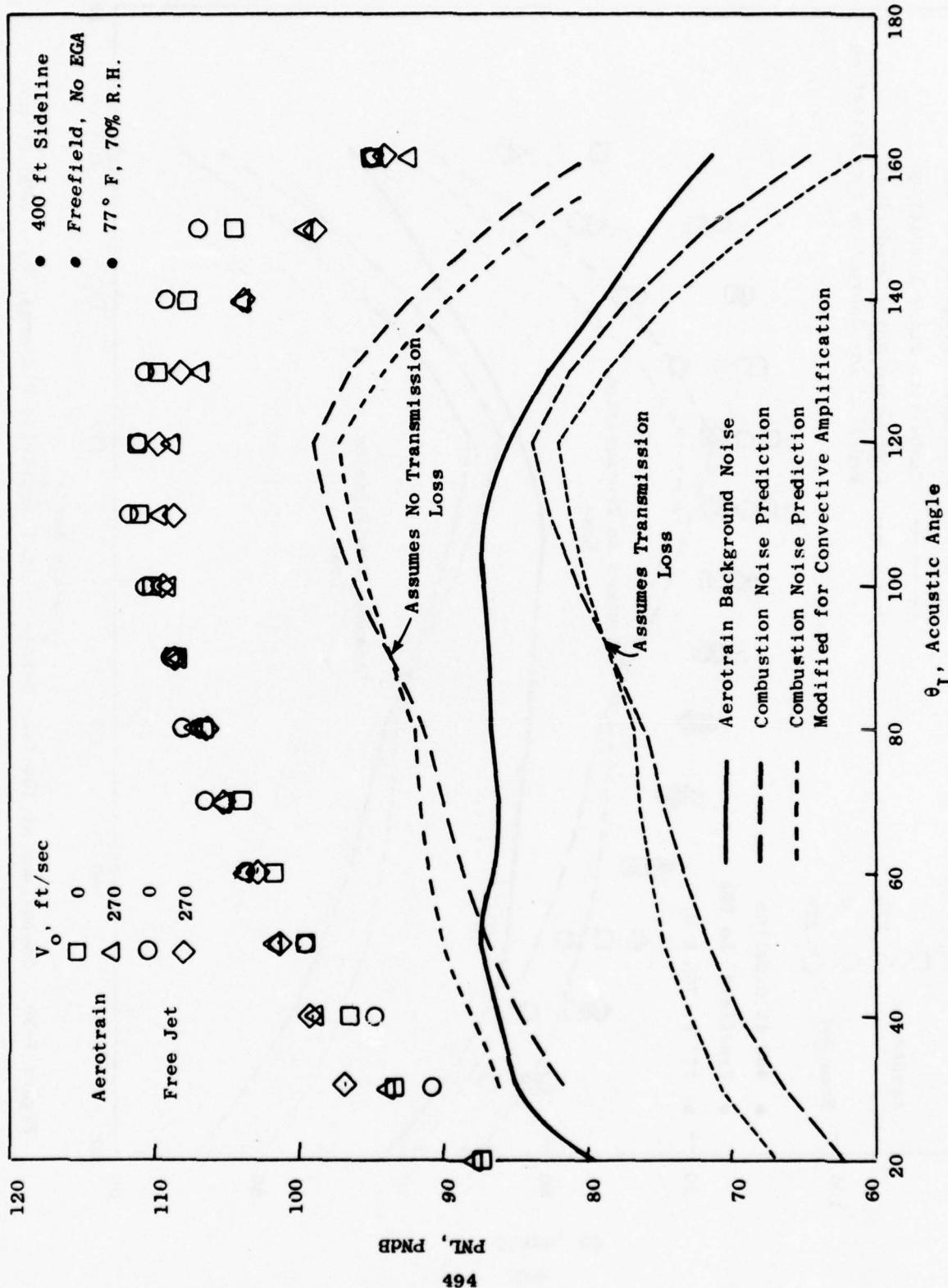


Figure 7-31. Comparison of 104-Tube Nozzle PNL Directivity Patterns, $V_J = 2200$ ft/sec.

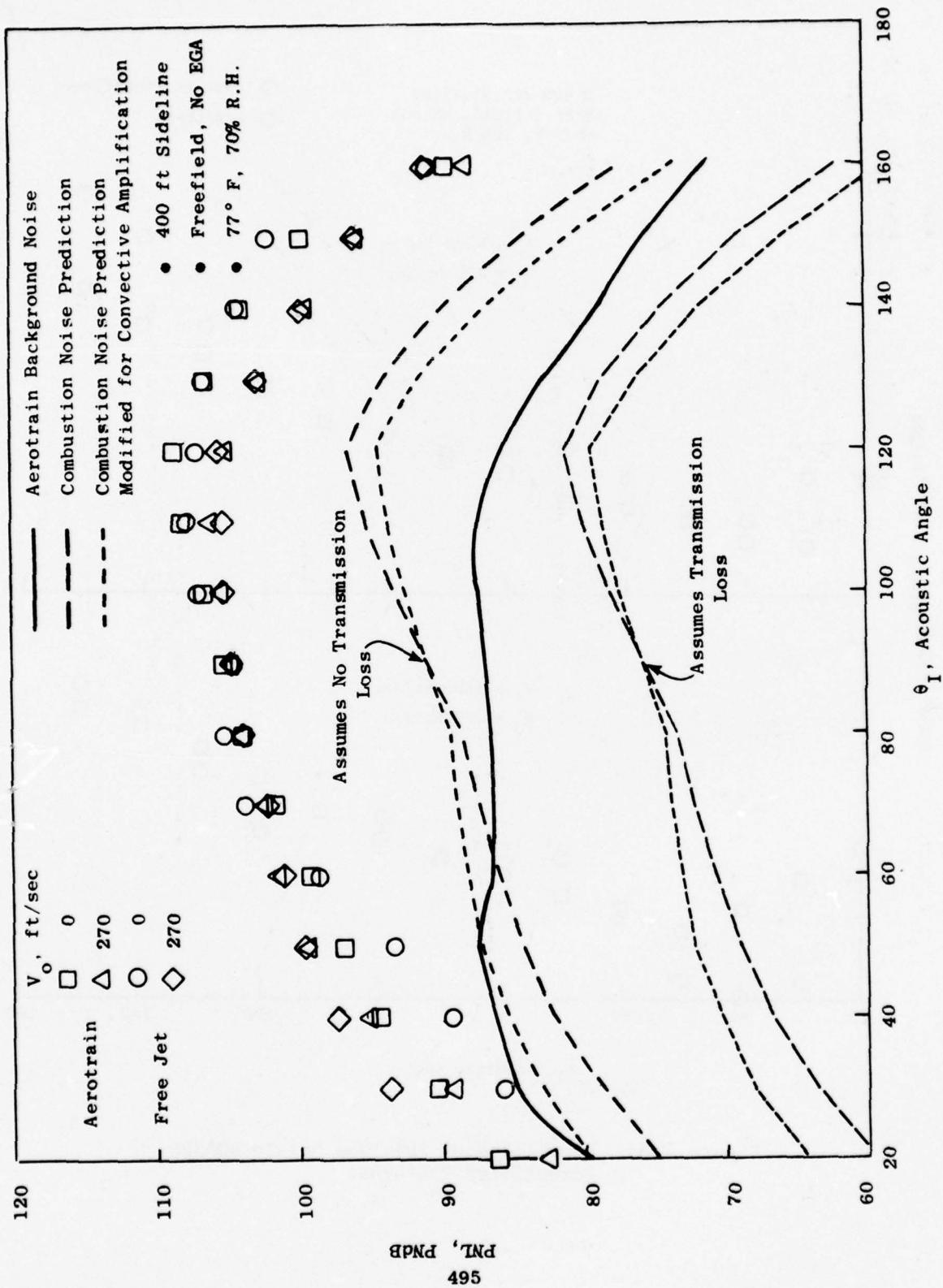


Figure 7-32. Comparison of 104-Tube Nozzle PNL Directivity Patterns, $V_J = 1800$ ft/sec.

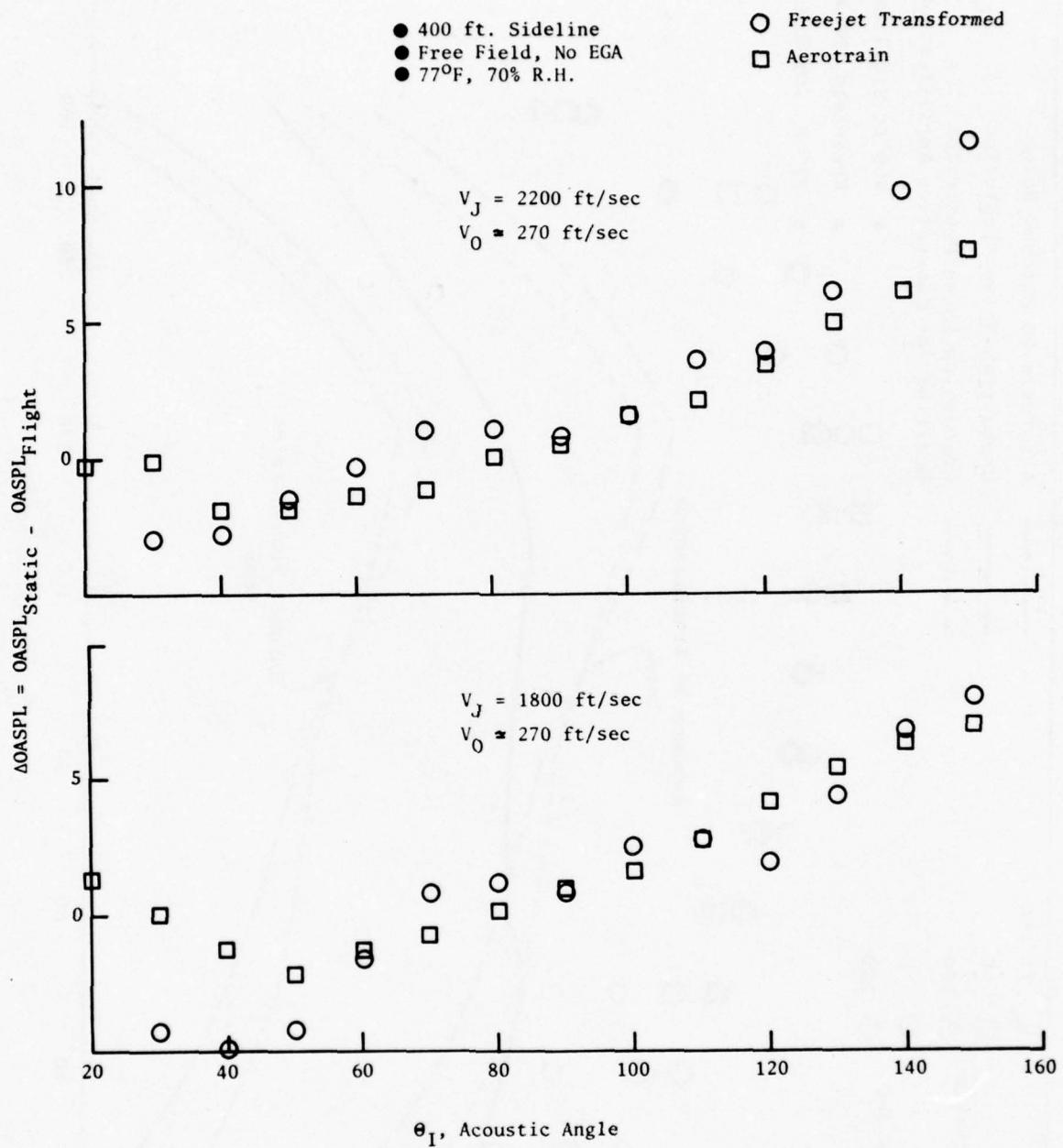


Figure 7-33. Comparison of 104-Tube Nozzle $\Delta OASPL$ Directivity Patterns.

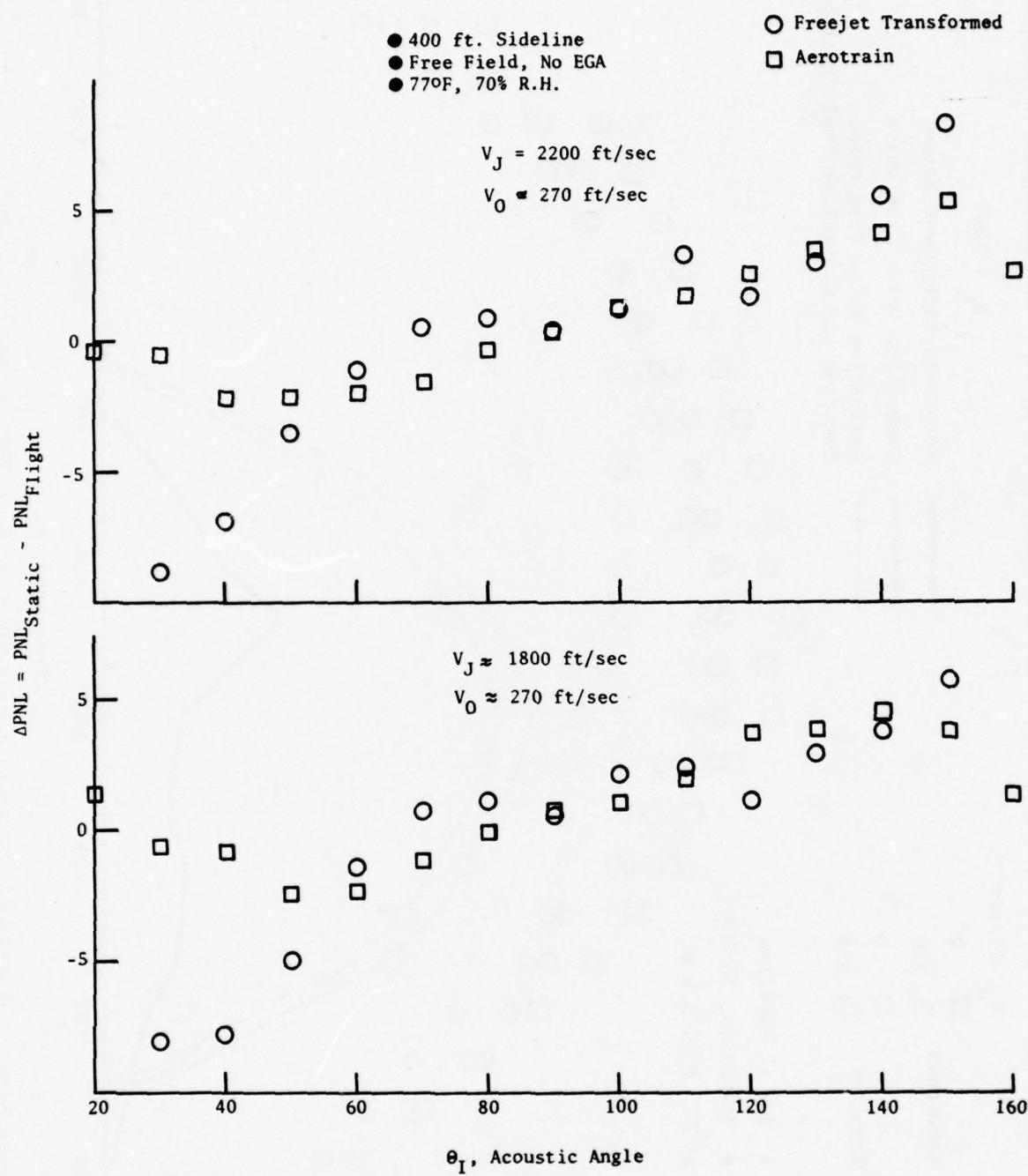


Figure 7-34. Comparison of 104-Tube Nozzle ΔPNL

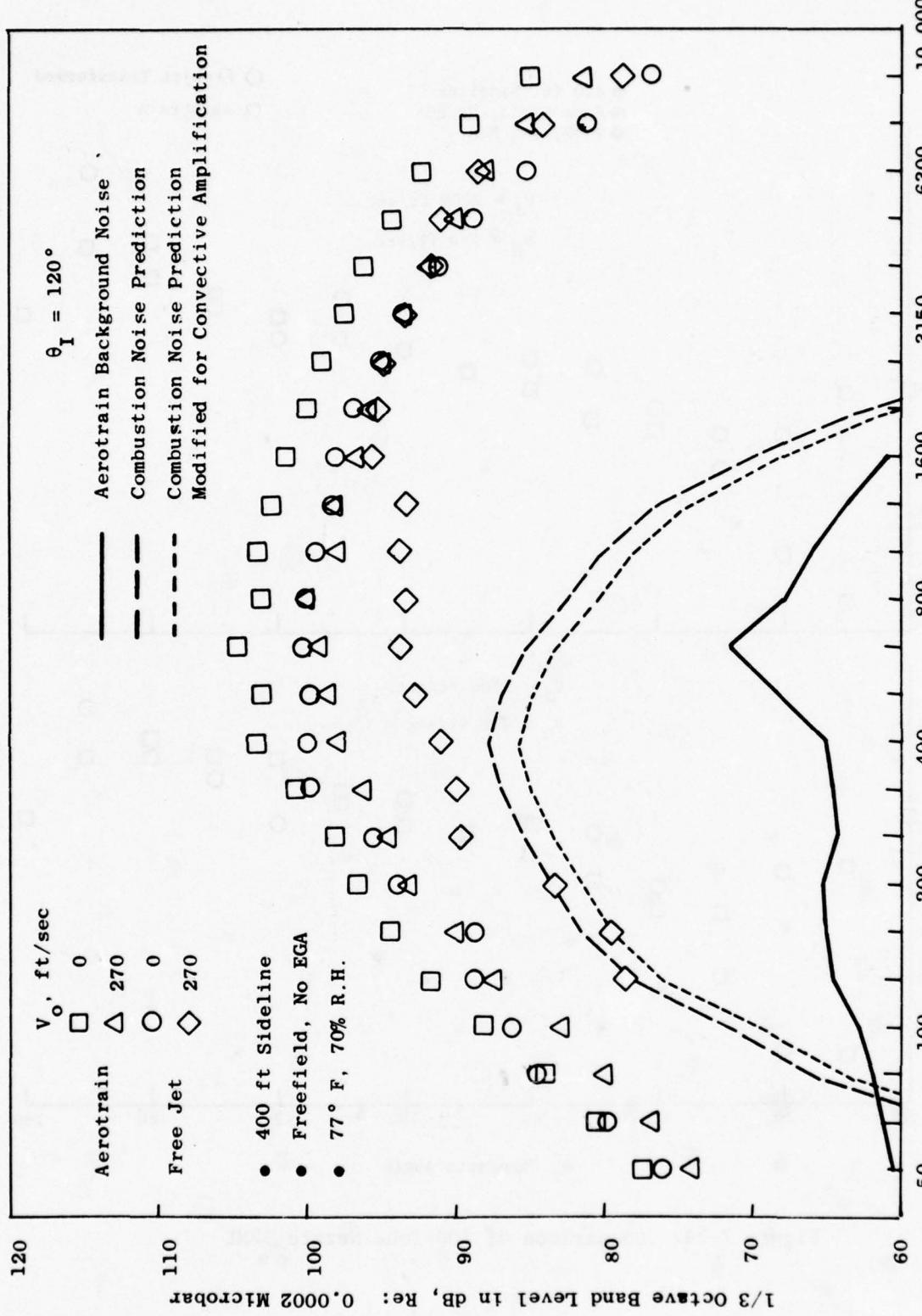


Figure 7-35. Comparison of Conical Nozzle Spectra, $V_J = 2200 \text{ ft/sec}$, $\theta_1 = 120^\circ$.

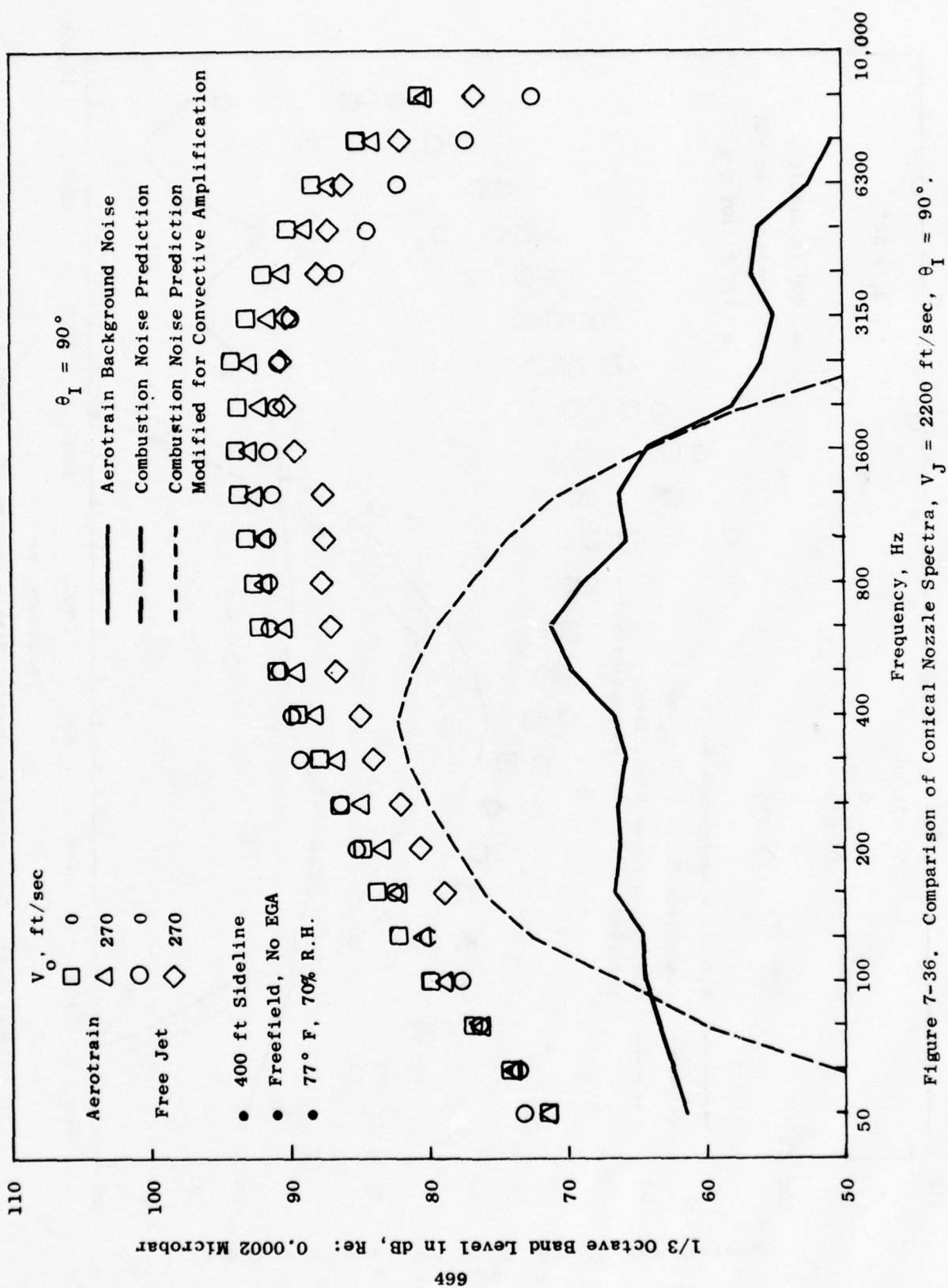


Figure 7-36. Comparison of Conical Nozzle Spectra, $V_J = 2200$ ft/sec, $\theta_1 = 90^\circ$.

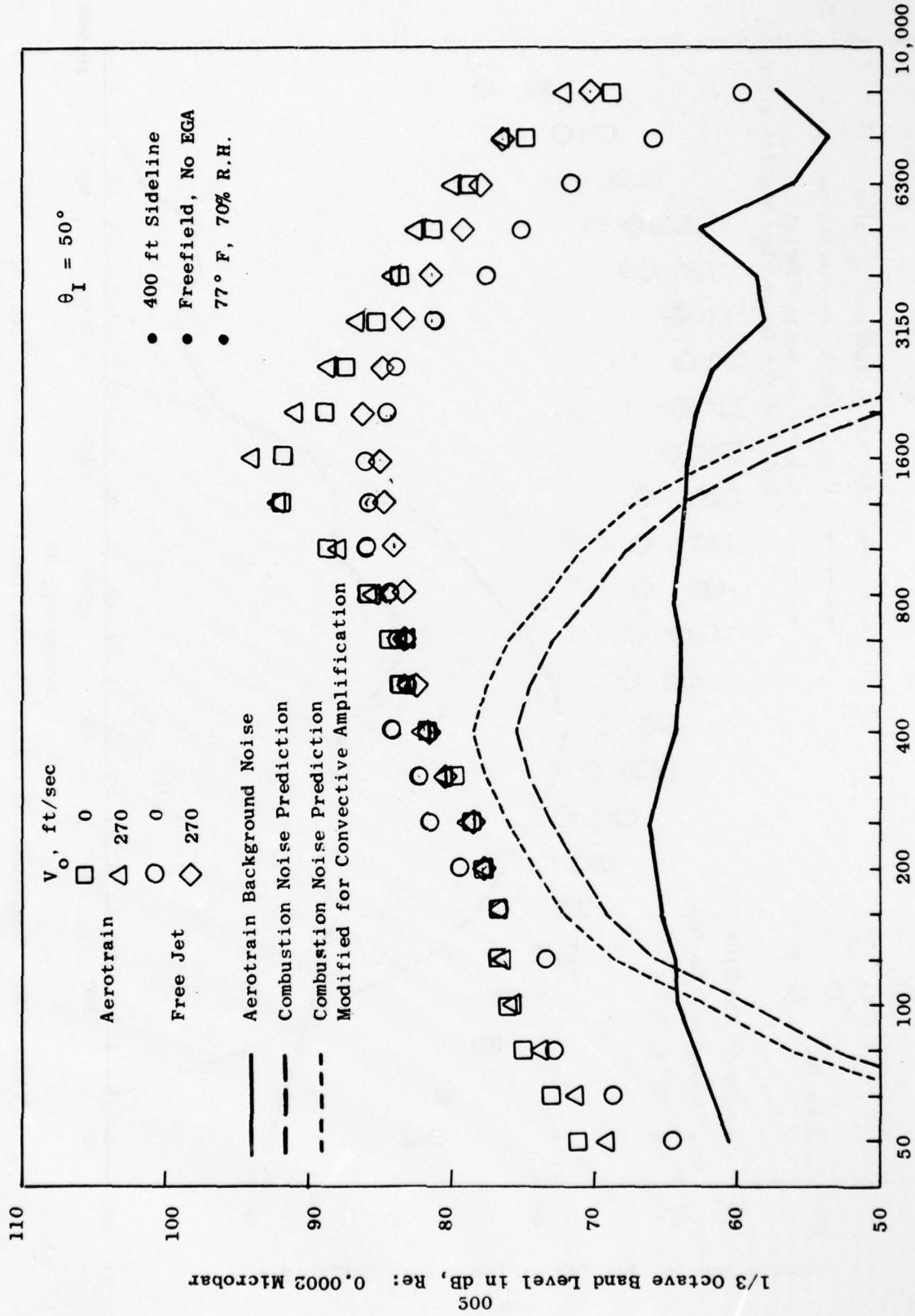


Figure 7-37. Comparison of Conical Nozzle Spectra, $V_J = 2200 \text{ ft/sec}$, $\theta_1 = 50^\circ$.

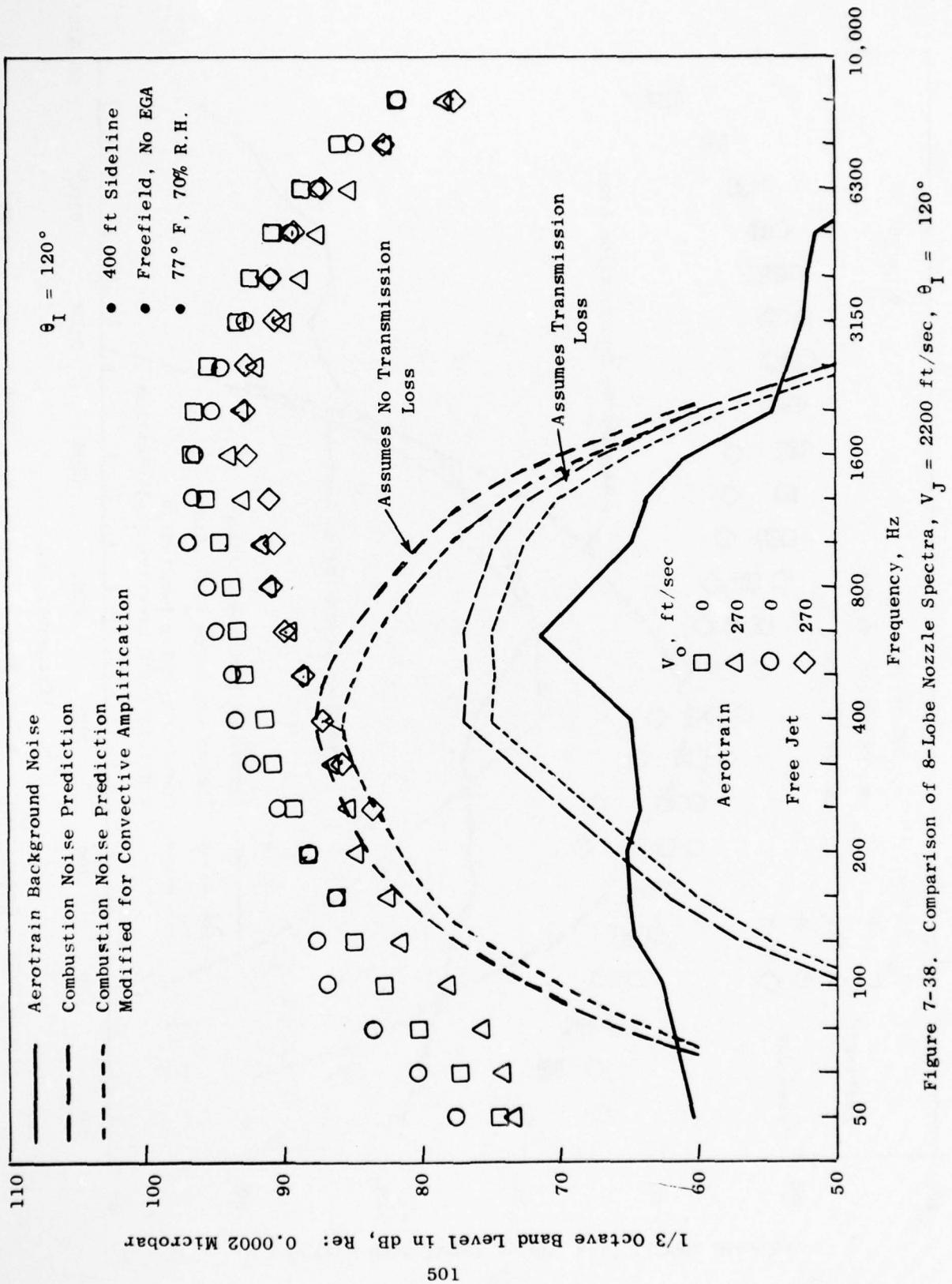


Figure 7-38. Comparison of 8-Lobe Nozzle Spectra, $V_J = 2200$ ft/sec, $\theta_1 = 120^\circ$

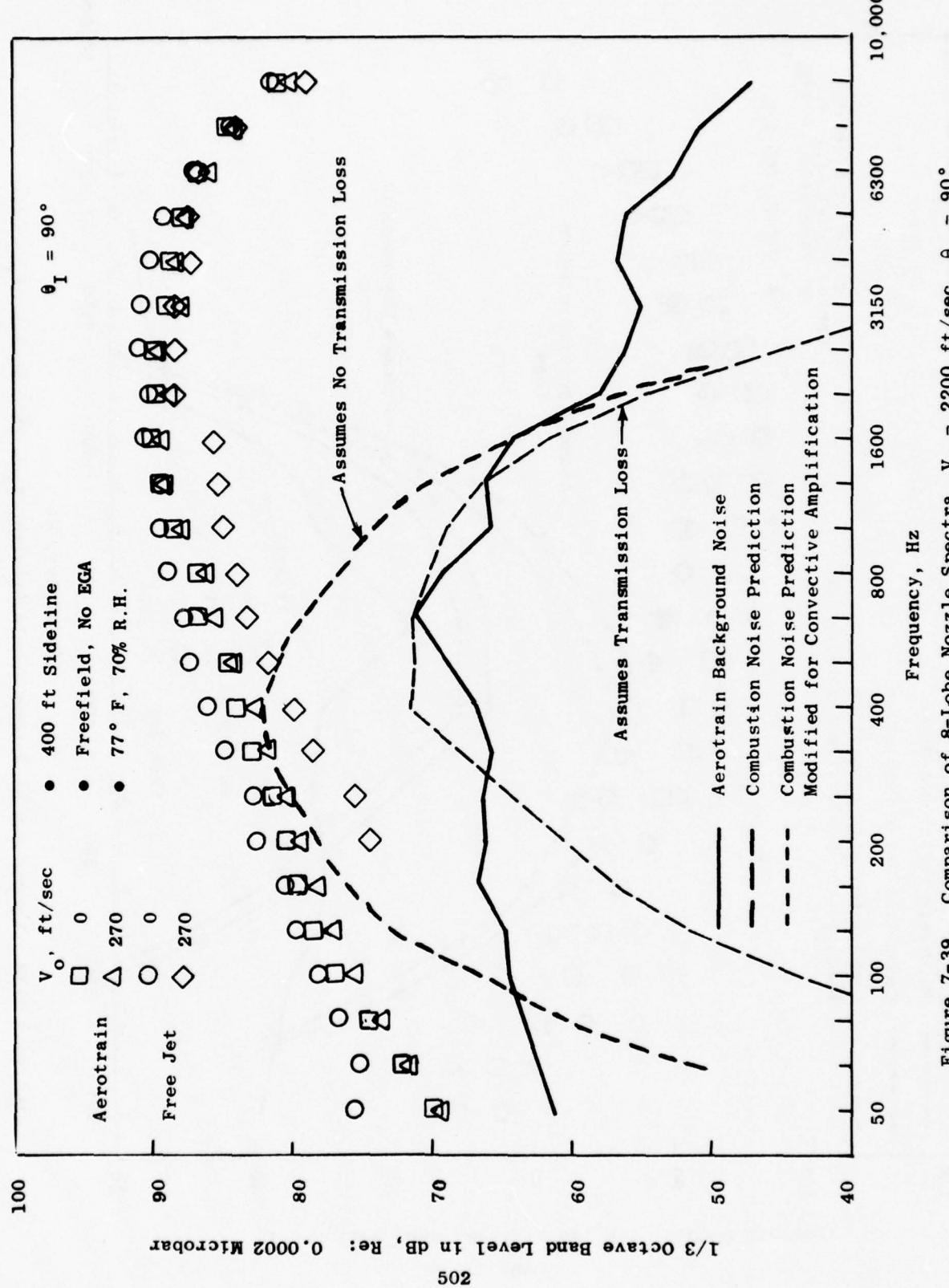


Figure 7-39. Comparison of 8-Lobe Nozzle Spectra, $V_J = 2200$ ft/sec, $\theta_1 = 90^\circ$.

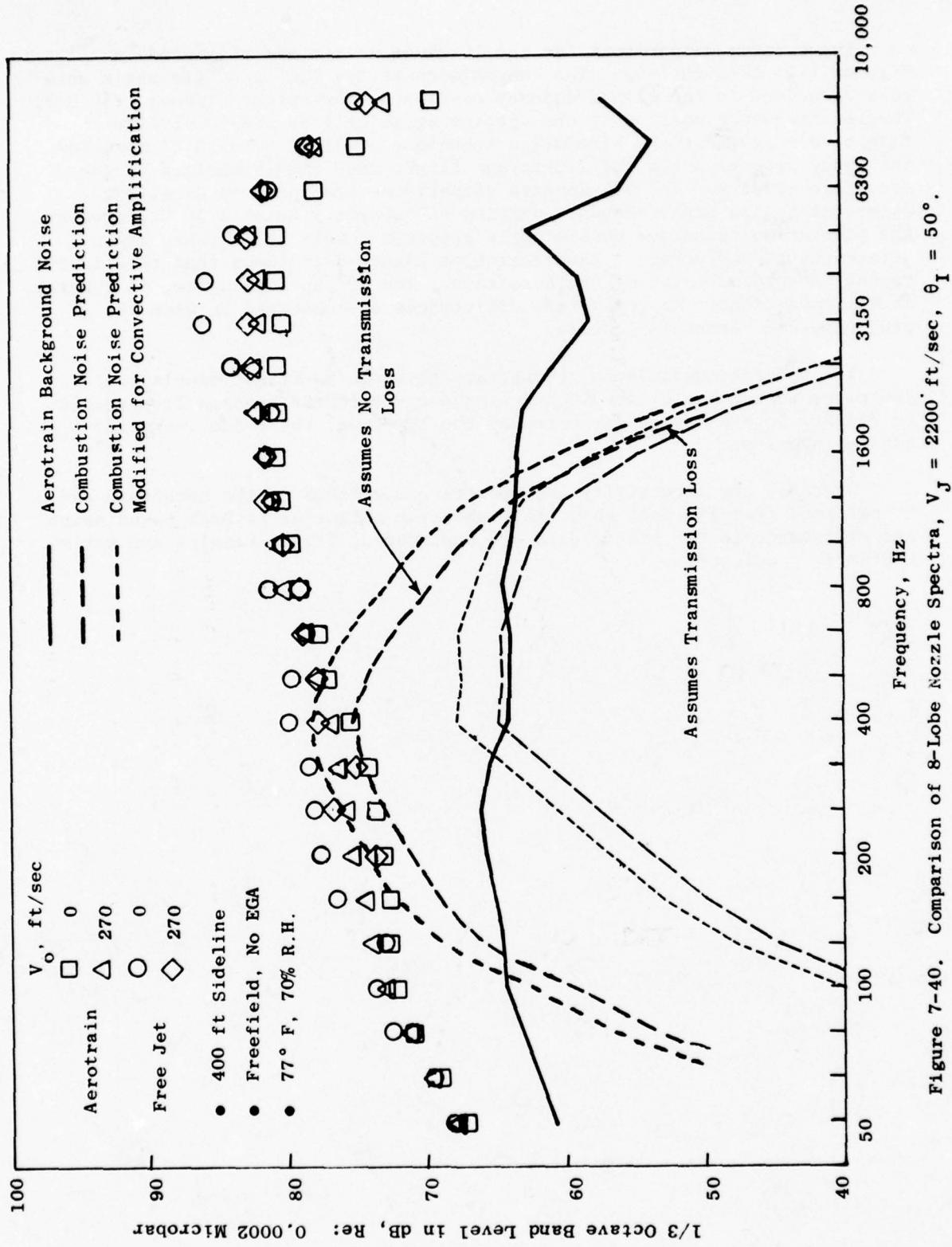


Figure 7-40. Comparison of 8-Lobe Nozzle Spectra, $V_J = 2200$ ft/sec, $\theta_I = 50^\circ$.

The spectra comparisons for the 104-tube nozzle are presented on Figures 7-41 through 7-43. The comparisons at the 120° acoustic angle show good agreement in the high frequency portion of the spectra (above 1250 Hz). The low frequency portion of the spectra agree well at the 150-ft/sec flight velocity, but the simulation technique predicts 5 to 10 dB more low frequency reduction for the 270-ft/sec flight case than exhibited by the Aerotrain results. The 90° spectra comparisons are again in excellent agreement in the high frequency portion of spectra. Below 1250 Hz, however, the simulation technique consistently predicts levels below those demonstrated by the Aerotrain. Examination of Figure 6-14 shows that this is due to the background noise of the Aerotrain. The 50° spectra agree, in general, at all conditions: no consistent differences are observed between the predicted and Aerotrain results.

The spectra comparisons demonstrate that the in-flight simulation technique is capable of predicting frequency-dependent changes from static to flight, such as those exhibited by the 104-tube, the 8-lobe, and the conical nozzles.

Overall, the directivity and spectra comparisons of the Aerotrain and transformed free jet data show that, when the influence of background noise and difference in the static data are considered, flight results are satisfactorily predicted.

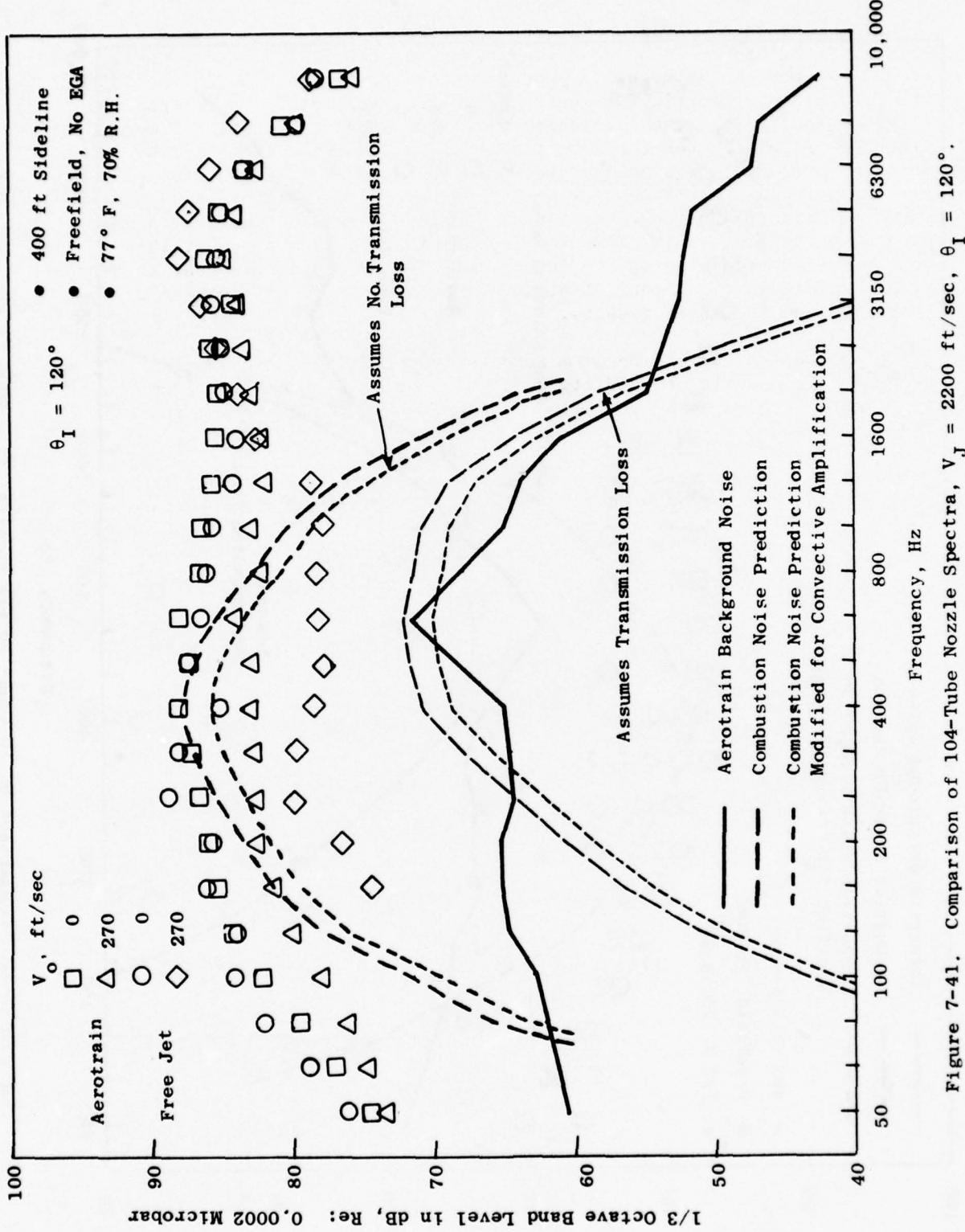


Figure 7-41. Comparison of 104-Tube Nozzle Spectra, $V_J = 2200 \text{ ft/sec}$, $\theta_1 = 120^\circ$.

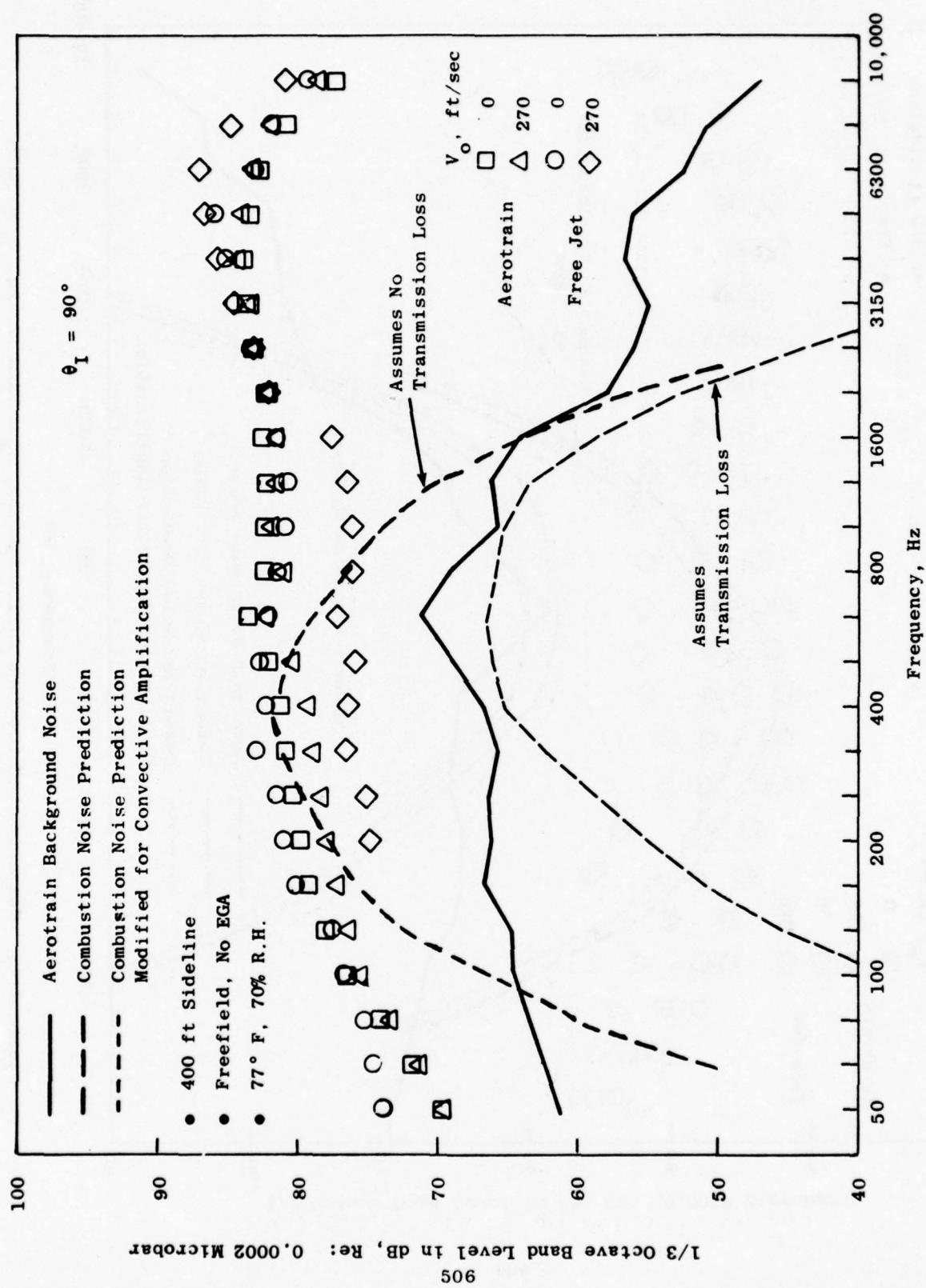


Figure 7-42. Comparison of 104-Tube Nozzle Spectra, $V_J = 2200$ ft/sec, $\theta_1 = 90^\circ$.

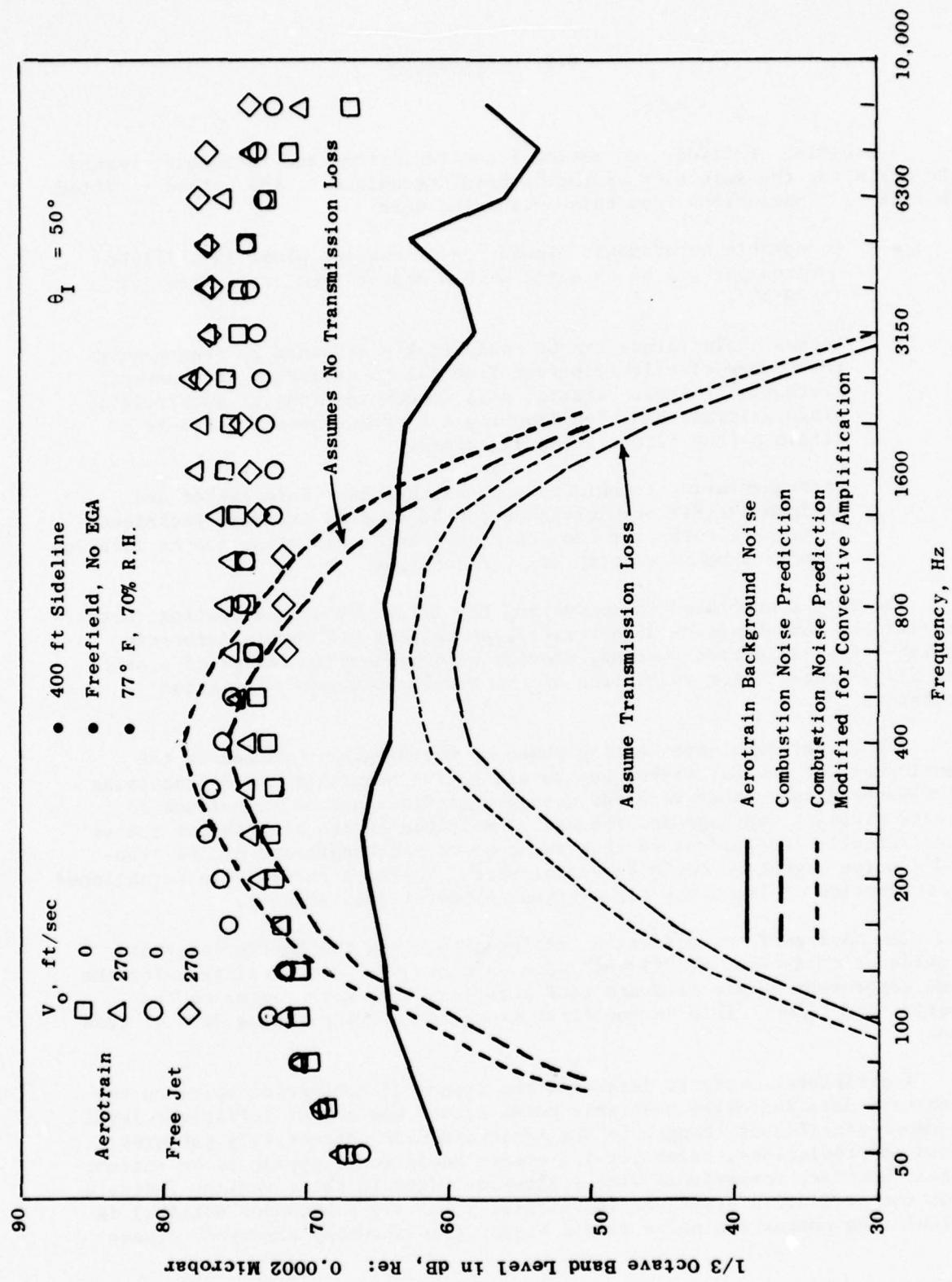


Figure 7-43. Comparison of 104-Tube Nozzle Spectra, $V_J = 2200$ ft/sec, $\theta_1 = 50^\circ$.

8.0 CONCLUSIONS

Evaluation of fixed- and moving-frame facilities and techniques formed the basis for the selection of the "hybrid" technique as the method verified in Task 4. Conclusions from this evaluation were:

- Acceptable aerodynamic simulation of the jet plume in a flight environment can be obtained with a modest area ratio free jet ($\approx 40-50$).
- Acoustic similitude can be analytically attained by transposing the source distribution from free jet to quiescent environment, synthesizing these "static" data to combinations of uncorrelated singularities, and then imposing the proper dynamic effects to attain a true flight noise signature.
- Instrumentation techniques such as the Laser Velocimeter and Ellipsoidal Mirror microphone can be used as standard techniques to measure turbulent flow characteristics and noise source location changes associated with simulated flight.

The data accumulated in conducting the flight assurance testing (Gates/Learjet and NASA-Lewis F-106 Aircraft), as well as the Bertin Aerotrain moving-frame validation testing, provide a comprehensive series of static and flight results for validation of the hybrid in-flight simulation technique.

The flight assurance testing phase of the program resulted in the development of several techniques to aid in the acquisition and processing of flyover data. These were the ground null/fiber optics techniques to locate aircraft overhead and the use of multiple height microphones spaced statistically independent so that an accurate representation of the free-field noise signature could be established. Variance curves were established as a function of frequency for a given number of data samples.

The moving-frame validation test program using the Bertin Aerotrain provided a unique set of "flight" data on a ground-based facility using the same suppressor nozzle hardware configurations that were tested on the Learjet and F-106. This is the first known set of comparative data of this type.

A peripheral study to determine the impact of combustion noise on the Aerotrain data indicated that this noise source was not of sufficient level to cause significant changes in the Aerotrain OASPL directivity patterns. Based on predictions, selective 1/3-octave bands would appear to be contaminated; however, comparisons with scale-model data in these regions indicate that the prediction procedure (particularly for the suppressor nozzles) is calculating combustion noise levels higher than actually observed. These

comparisons have indicated that current combustion noise prediction methodology should be modified to account for the change in impedance caused by the exhaust nozzle geometry.

Aerotrain background noise was found to significantly contaminate the 104-tube nozzle flight data at the lower power setting conditions. Contamination was not a problem for the conical nozzle; however, in future moving-frame test vehicle designs, background noise should be considered since it may be the limiting factor in determining the in-flight noise signature of high suppression exhaust nozzle systems.

Comparison of flight assurance and moving-frame results for the conical, 8-lobe, and 104-tube nozzles indicate that directivity and spectra characteristics exhibit similar trends when different flight velocity effects are accounted for. The trends are:

- The effect of flight on the aft quadrant noise levels is to cause significant reduction relative to the static data for both the baseline and suppressor nozzles.
- Little or no change is observed at the 90° angle for the range of flight velocities and jet velocities evaluated.
- The effect of flight on the forward quadrant noise levels causes the noise levels to be slightly less than, or slightly greater than the static levels (depending on the configuration and condition being examined).
- The effect of flight on spectral characteristics appears to be strongly configuration dependent.

The JENOTS free jet test series provided a unique set of scale-model test data to be scaled, transformed, and compared with the Aerotrain results to assess the validity of the in-flight simulation technique.

The laser velocimeter measurements conducted at JENOTS demonstrate the ability of the LV to detect flow field differences among the three exhaust nozzle configurations with varied levels of free-stream velocity. The effect of external flow was apparent in a lengthened potential core and less rapid velocity decay for circular nozzles. The effect on multielement suppressor nozzles was much less pronounced.

The ellipsoidal mirror microphone (EM) measurements verified that this technique can detect differences in jet noise source axial distributions among different nozzle configurations with variations in free-stream velocity.

The analytical screening study has demonstrated that any transformation procedure applied to free jet data must account for noise source composition, refraction of sound by the free jet, and turbulence scattering.

Comparison of the Aerotrain and the transformed free jet directivity patterns, on the basis of absolute levels as well as static-to-flight increments, indicates satisfactory agreement for all configurations except in those regions where the Aerotrain data was contaminated. Spectra comparisons show no consistent differences in the high frequency regions; however, the in-flight simulation technique tends, in general, to overpredict the low frequency reduction from static to flight.

The hybrid technique has been established to determine the in-flight noise signature of any arbitrary exhaust nozzle system in a cost-effective manner. The technique is flexible in that existing diagnostic tools, such as the laser velocimeter and ellipsoidal mirror, may be used to establish why the noise source generation characteristics of exhaust nozzle systems differ significantly in the static and flight operating environments.

9.0 RECOMMENDATIONS FOR FUTURE WORK

- Utilize the hybrid in-flight simulation technique in executing Task 5 - Investigation of "Inflight" Aero-Acoustic Effects on Suppressed Exhaust Systems.
- The success of the in-flight simulation technique (over the velocity and engine cycle range investigated) with exhaust nozzles indicative of simple to increasingly more complex geometries strongly suggests it is a viable means of estimating the in-flight noise signature of any arbitrary scale-model suppressor configuration. Further corroboration of this conclusion could be accomplished by testing a scale model of the F-106 baseline configuration on the free jet facility and transforming the results for comparison with the F-106 flyover results.
- A direct procedure should be evolved wherein the refractive correction required to translate measured free jet data to its equivalent "static" counterpart can be quantified and used in the calculation procedure of the in-flight simulation technique. This would be especially useful for the high frequency shallow angle (zone of silence) regime.
- Additional test data should be obtained on multielement suppressor configurations to further assess the ability of the in-flight simulation technique to predict the low frequency portion of the spectra.
- Strong consideration should be given to exploring the potential of mounting alternate propulsion systems on the Bertin Aerotrain which are indicative of future Advanced Technology Aircraft/Engine systems.
 - A corollary to this would be further substantiation that the in-flight simulation technique is, in fact, independent of nozzle flow upstream (engine cycle) conditions as well as nozzle geometry.
- The question of core noise (combustor plus any flow-induced noise contribution) contaminating forward flight noise results should also be further addressed. The exhaust systems evaluated in Task 4 could be subjected to a thorough diagnostic series of tests on the Aerotrain at low power setting conditions.
 - Consideration should be given to modifying the existing turbomachinery treatment section with some of the more exotic low frequency acoustic treatment designs recently shown to be effective in reducing core noise.

- Coherence-type analyses could be performed by utilizing fluctuating pressure data from judiciously installed pressure transducers, such as cooled Kulites, just upstream of the exhaust nozzle to extract the contribution (if any) of core noise in the far field.
- A program should be formulated utilizing a variety of engine cycles to investigate whether nozzle exit geometry does (as predicted by classical theory) reduce the transmissivity of low frequency noise, hence minimizing contamination of far field noise by core noise.

REFERENCES

1. Bender, J., et. al., "Aero-Acoustic Research in Wind Tunnels: A Status Report," Pennsylvania State University, Report No. N73-20277, February 1973.
2. Noiseux, D.V., "Study of Porous Strip Microphones for Acoustic Measurements in Wind Tunnels," NASA CR-114593, 1973.
3. Bies, D.A., "Investigation of the Feasibility of Making Model Acoustic Measurements in the NASA-Ames 40 by 80-Foot Wind Tunnel," prepared under Contract NASR-6206 by Bolt, Beranek, and Newman, Inc.
4. Atencio, A., and Soderman, P., "Comparisons of Aircraft Noise Measured in Flight Test and in the NASA-Ames 40 by 80-Foot Wind Tunnel," AIAA Paper No. 73-1047.
5. Atencio, A., "Wind Tunnel Measurements of Forward Speed Effects on Jet Noise from Suppressor Nozzles and Comparison with Flight Test Data," AIAA Paper No. 75-870.
6. Abramovich, G.N., "Turbulent Freejets of Liquid and Gas," Gosenergoigdat, Moscow, (1948).
7. Savell, C.T., "High Velocity Jet Noise Source Location and Reduction, Task 1 - Activation of Facilities and Validation of Source Location Techniques," Final Report, FAA-RD-76-79, I and Ia.
8. Hoch, R.G., Duponchel, D.P., Cocking, B.J., and Bryce, W.D., "Studies of the Influence of Density on Jet Noise," J.S.V. Vol. 28, No. 4, 1973.
9. Stone, J.R., "Interim Prediction Method for Jet Noise," NASA TMX-71618, 1974.
10. SAE, "Jet Exhaust Noise Prediction Procedure Proposed Revision of AIR 876," September, 1974.
11. Harris, C.M., "Absorption of Sound in Air in the Audio-Frequency Range," JASA, Volume 35, 1963.
12. Knesner, H.O., "Interpretation of the Anomalous Sound Absorption in Air and Oxygen in Terms of Molecular Collisions," JASA, Volume 5, 1933.
13. Bass, H.R., Bauer, H.J., and Evans, L.B., "Atmospheric Absorption of Sound: Analytical Expression," Journal of Acoustic Society of America, Volume 52, 5 (Part 2), 1972.
14. Von Glahn, U., and Goodykoontz, J., "Forward Velocity Effects on Jet Noise with a Dominant Internal Noise Source," NASA TMX-071438.

15. Keith, J.S., Ferguson, D.R., and Heck, P.H., "Analytical Method for Predicting the Pressure Distribution about a Nacelle at Transonic Speeds," NASA CR-112239, December 1972.
16. Bendot, J.S., and Piersol, A.G., "Measurement and Analysis of Random Data," Wiley, 1966.
17. Scheppe, F.C., "Uncertain Dynamic Systems," Prentice-Hall, 1973.
18. Amiet, R.K., "Correction of Open Jet Wind-Tunnel Measurements for Shear Layer Refraction," AIAA Paper No. 75-532, 1975.
19. Jacques, J.R., "The Noise from Moving Aircraft; Some Relevant Models," Ph.D. Thesis, University of Cambridge, U.K., August 1975.
20. General Electric Company, Viewgraph presentation on "High Velocity Jet Noise Source Location and Reduction," DOT Contract No. DOT-OS-30034, September 25, 1974, at Lockheed Corporation, Marietta, Ga.
21. Ribner, H.S., "Refraction, Transmission and Amplification of Sound by a Moving Medium," Journal of the Acoustical Society of America, 29, No. 4, pp. 435-441, 1975.
22. Miles, J.W., "On the Reflection of Sound at an Interface of Relative Motion," Journal of the Acoustical Society of America, 29, No. 2, pp. 226-228, 1957.
23. Packman, A.B., Ng, K.W., and Paterson, R.W., "Effect of Simulated Forward Flight on Subsonic Jet Exhaust Noise," AIAA Paper No. 75-869, 1975.
24. Harper-Bourne, M., and Fisher, M.J., "The Noise from Shock Waves in Supersonic Jets," AGARD CPP-131, September 1973.
25. Knott, P.R., et. al., "Supersonic Jet Exhaust Noise Investigation," Final Report, AFAPL-TR-76-68.
26. Knott, P.R., et. al., "Supersonic Jet Exhaust Noise Investigation," Interim Report, AFAPL-TR-74-25, June 1974.
27. Benzakein, M.J., and Knott, P.R. (editors), "Supersonic Jet Exhaust Noise," Final Report, AFAPL-TR-72-52, August 1972.
28. Peters, C.E., Chriss, D.E., and Pault, R.A., "Turbulent Transport Properties in Subsonic Coaxial Free Mixing Streams," AIAA Paper 69-681, June 1969.
29. Schubert, "Numerical Study of Sound Refraction by a Jet Flow II Wave Acoustics," Journal of the Acoustical Society of America, September 1971.

30. Atvars, Schubert, Grande, and Ribner, "Refraction of Sound by Jet Flow and Jet Temperature," NASA CR-494.
31. Crow, S.C., "Viscoelastic Character of Fine Grained Isotropic Turbulence," Physics of Fluids, 10(7), July 1967.
32. Balsa, T., "The Farfield of High Frequency Convected Singularities in Sheared Flows with an Application to Jet Noise Prediction," Journal of Fluid Mechanics (1176) Vol. 74 Part 2 pp. 193-208.
33. Schlinker, R.H., Petersen, R.A., and Kaplan, R.E., "Enhancement of Directional Microphone Measurements," AIAA Paper 73-1040, October 1973.
34. Hanson, R.J., and Lawson, C.L., "Solving Least Squares Problems," Prentice-Hall 1974.
35. Takaku, I., and Horiuchi, T., "Attenuation of Low-Frequency Sound in a Turbulent Duct," Journal of Acoustical Society of America, Vol. 58, No. 4, October 1975.
36. Burley, Richard R., "Flight Velocity Effects on the Jet Noise of Several Variations of a 104-Tube Suppressor Nozzle," NASA TMX-3049, July 1974.
37. Beulke, M.R., and Clapper, W.S., "A Forward Speed Effects Study on Jet Noise from Several Suppression Nozzles in NASA 40' x 80' Wind Tunnel," NASA CR-114741, May 1974.
38. Brooks, J.R., and Woodrow, R.J., "The Effects of Forward Speed on a Number of Turbojet Exhaust Silencers," AIAA Paper 75-506, 1975.
39. Stone, J., "On Effects of Flight on Jet Engine Exhaust Noise," NASA TMX-71819.
40. Motsinger, R.E., and Emmerling, J.J., "Review of Theory and Methods for Combustion Noise Prediction," AIAA Paper 7-541.
41. Hoch, R.G., Berthelot, "Use of the Bertin Aerotrain for the Investigation of Flight Effects on Aircraft Engine Exhaust Noise," AIAA Paper No. 76-534.
42. Levine, H., and Schwinger, J., "On The Radiation of Sound from an Unflanged Circular Pipe," Physical Review, Volume 73, Number 4, February 15, 1948.
43. Jubelin, B., and Thomas, P., "Localisation Des Sources Acoustiques D'un Jet Par Une Methode D'Interferences Par Reflexion Sur Un Plan," Communication présentée au 8 eme Congress International d'Acoustique, Londres, 23-31, Juillet 1974.

Preceding Page BLANK - ^{NOT} FILMED

APPENDIX

LISTING OF FLIGHT TRANSFORMATION COMPUTER PROGRAM

SUMMARY OF FLTRANS INPUT

DIAMJT - Equivalent diameter of nozzle being investigated
$$\text{DIAMJT} = \sqrt{4 A_{\text{flow}} / \pi}$$

Where A_{flow} is the nozzle flow area.

FLTVEL - Velocity of the free jet, ft/sec

ANGLE - Acoustic angles at which acoustic data is available, an array of 19 elements

NANG - Number of acoustic angles for which data are available

NFREQ - Number of frequencies for which SPL data are input

SCFACT - Scale factor, defined as the full-scale diameter divided by the scale-model diameter
Note: This allows the transforming of scaled or unscaled free-jet data

IREFRC - Option to omit refraction correction
(Yes = Correction, No = No Correction)

ITURBC - Option to omit turbulence absorption correction
(Yes = Correction, No = No Correction)

IPLOT - Option to plot data

Note: Actual free-jet data in form of 1/3-octave band SPL's versus frequency for the specified range of acoustic angles are read for magnetic tape. This input SPL array is called TSPL, with dimensions 33 X 19. The output SPL array is called TSPL1, with dimensions 33 X 19.

```

100000*#RUN *=;/NRB/FLTRANC(BCD,NOGO)
100010C
100020C 15475ES/NRB/FLTRANS
100030C
100040C MAIN PROGRAM FOR FLTRANS.
100050C USES THE FEIHE PROGRAM FROM SCHENECTADY (MANI) TO
100060C CALCULATE FLIGHT TRANSFORMATIONS FROM SPL SPECTRA.
100070C THE RESULTING SPL SPECTRA WILL BE WRITTEN ON
100080C DATAPLOT TAPES.
100090C
100100      COMMON /BLKCON/ BLANK,FREQ(33),IBLANK,IPDFIL,
100110      & IFREQ(33),INFILE,IPLOT,IPRNT,IREFRC,ITURBC,
100112      & NBCDI,NBCDO,NO,PI,SPDSND
100120      COMMON /FEI/ EM,FP,LIE,NP,SPL1(10),SPLF(10),
100130      & THETD(10)
100140C
100150      DIMENSION ANGLE(19),FPAR(33),SP(5),SPID(2),
100160      & SPLFLT(19,33)
100170      DIMENSION KEY(11),KODE(11)
100180      DIMENSION TSPL(627),TSPL1(33,19)
100190      DIMENSION ISPLZ(19,33),SPLDS(19,33)
100200      DIMENSION DOPCON(6),IDSHFT(6)
100210C
100220      EQUIVALENCE (KEY(1),SP(1)),(KEY(6),SPID(1))
100230      EQUIVALENCE (TSPL(1),TSPL1(1,1))
100240      EQUIVALENCE (ISPLZ(1,1),SPLDS(1,1))
100250C
100260      INTEGER SP
100270      LOGICAL FOUND
100280C
100290      DATA DOPCON / .56,.71,.89,1.12,1.47,1.78 /
100300      DATA IDSHFT / 3,2,1,0,-1,-2 /
100310      DATA KODE / 7*1,4*0 /
100320      DATA RPD / 1.7453293E-2 /
100322C
100324 1000 FORMAT (1H1/55X,"FLIGHT TRANSFORMATION SPECTRA"//
100326      & 62X,2A6/55X,5I5//)
100328      & 55X,"ACOUSTIC ANGLE FROM INLET"//
100329      & 3X,"FREQ",1X,17(3X,F4.0)//)
100331 1010 FORMAT (2X,15,1X,17(1X,F6.2))
100332 1020 FORMAT (1H0,31X,"MODEL/FULL SIZE SCALE FACTOR",5X,
100333      & "FREE JET VELOCITY",5X,"FREE JET DIAMETER"/
100334      & 43X,3,22X,F6.2,16X,F6.2//)
100336      & 8X,REFRACTION CORRECTION - ",A3,5X,
100338      & "TURBULANCE CORRECTION - ",A3)
100340C
100342      NAMELIST /INPUT/ ANGLE,DIAMJT,FLTVEL,
100350      & IPLOT,IPRNT,IREFRC,ITURBC,NANG,NFREQ,
100360      & SCFACT,SP,SPID,SPDSND
100370      NAMELIST /NLIST/ TSPL
100380C
100390 8000 FORMAT (1H0,"ERROR READING NAMELIST INPUT")
100400 8100 FORMAT (1H0,"DATA RECORD CANNOT BE FOUND ON DATAPLOT FILE",
100410      & 2X,"SP=",5I5,2X,"SPID=",2A6)
100420C
100430      CALL FNREW (INFILE)
100435      IF (IPLOT.EQ.NO) GO TO 100
100440      CALL FNREW (IPDFIL)
100450C
100460C READ NAMELIST INPUT
100470 100 NFREQ=0
100480      DO 110 I=1,11

```

```

100490 110 KEY(I)=IBLANK
100500 READ (NBCDI,INPUT,END=900,ERR=800)
100510C
100520C INITIALIZE ZERO SPL INDICATORS TO ZERO
100530 DO 120 I=1,NANG
100540 DO 120 J=1,NFREQ
100550 120 ISPLZ(I,J)=0
100560C
100570C READ SPL DATA FROM A DATAPLOT TAPE
100580 CALL FMFILE (INFILE,KEY,KODE,NLIST,0,.FALSE.,FOUND)
100590 IF (.NOT.FOUND) GO TO 810
100630C
100640C TEST NFREQ AND SET JDEL
100650 JDEL=33
100660 IF (NFREQ) ,140
100670 NFREQ=24
100680 JDEL=24
100690C
100700C CALCULATE MACH NUMBER AND FREQUENCY PARAMETERS
100710 140 EM=FLTVEL/SPDSND
100720 CONST=(PI*DIAMJT*SCFACT)/(12.0*SPDSND)
100730 DO 150 J=1,NFREQ
100740 150 FPAR(J)=FREQ(J)*CONST
100750C
100770C TEST FOR ZERO OR BLANK SPL VALUES
100780 DO 260 I=1,NANG
100790 IND=JDEL*(I-1)
100800 INDLST=IND+JDEL
100810 DO 250 J=1,NFREQ
100820 IND=IND+1
100830 IF (TSPL(IND)-.00001) 200,200,
100840 IF (TSPL(IND)-BLANK) 260,,260
100850 200 IF (IND-INDLST) ,220,220
100860 IND1=IND+1
100870 JF=J
100880 DO 210 INXT=IND1,INDLST
100890 JF=JF+1
100900 IF (TSPL(INXT)-.00001) 210,210,
100910 IF (TSPL(INXT)-BLANK) 230,,230
100920 210 CONTINUE
100930 220 TSPL(IND)=TSPL(IND-1)
100940 GO TO 250
100950 230 IF (J-1) ,240
100960 TSPL(IND)=TSPL(INXT)
100970 GO TO 250
100980 240 DIV=INXT-IND+1
100990 TSPL(IND)=TSPL(IND-1)+(TSPL(INXT)-TSPL(IND-1))/DIV
101000 250 CONTINUE
101010 260 CONTINUE
101030C
101040C SET THETD ARRAY FOR REAR QUADRANT ANGLES
101050 IR=NANG
101060 I=1
101070 300 IF (ANGLE(IR)-89.0) 310,,
101080 THETD(I)=180.0-ANGLE(IR)
101090 IR=IR-1
101100 I=I+1
101110 GO TO 300
101120 310 NP=I-1
101130 NA=IR+1
101140C
101150C FLIGHT TRANSFORMATION FOR REAR QUADRANT, ALL FREQUENCIES

```

```

101160      LIE=1
101170      IND=JDEL*(NANG-1)
101180      DO 390 J=1,NFREQ
101190      IND=IND+1
101200      INDJ=IND
101210      FP=FPAR(J)
101220C     SET SPL1 ARRAY FROM TSPL
101240      DO 350 I=1,NP
101250      SPL1(I)=TSPL(INDJ)
101260      INDJ=INDJ-JDEL
101270      350 CONTINUE
101290C     CALCULATE FLIGHT TRANSFORMATION
101310      CALL FEIHE
101330C     STORE SPLF SPECTRA IN SPLFLT ARRAY
101350      K=NP+1
101360      DO 370 I=NA,NANG
101370      K=K-1
101380      SPLFLT(I,J)=SPLF(K)
101390      370 CONTINUE
101410C     390 CONTINUE
101420      390 CONTINUE
101430C     SET THETD ARRAY FOR FORWARD QUADRANT ANGLES
101450      IR=NA
101460      I=1
101470      400 THETD(I)=180.0-ANGLE(IR)
101480      IF (IR-1) 410,410,
101490      IR=IR-1
101500      I=I+1
101510      GO TO 400
101520      410 NP=I
101530      NA=I
101540C     FLIGHT TRANSFORMATION FOR FORWARD QUADRANT, ALL FREQUENCIES
101560      LIE=2
101570      IND=JDEL*(NA-1)
101580      DO 490 J=1,NFREQ
101590      IND=IND+1
101600      INDJ=IND
101610      FP=FPAR(J)
101620C     SET SPL1 ARRAY FROM TSPL
101640      DO 450 I=1,NP
101650      SPL1(I)=TSPL(INDJ)
101660      INDJ=INDJ-JDEL
101670      450 CONTINUE
101690C     CALCULATE FLIGHT TRANSFORMATION
101710      CALL FEIHE
101730C     STORE SPLF SPECTRA IN SPLFLT ARRAY
101750      K=NP+1
101760      DO 470 I=1,NP
101770      K=K-1
101780      SPLFLT(I,J)=SPLF(K)
101790      470 CONTINUE
101810C     490 CONTINUE
101820      490 CONTINUE
101900C

```

```

101910C DOPPLER SHIFT
101920      DO 580 I=1,NANG
101940      DOPFAC=1.0/(1.0-EM*COS(ANGLE(I)*RPO))
101950      DO 530 K=1,6
101960      IF (DOPFAC-DOPCON(K)) .NE. 530,530
101970      IFLAG=IDSHFT(K)
101980      GO TO 540
101990 530 CONTINUE
102000      IFLAG=-3
102010 540 DO 580 J=1,NFREQ
102020      JJ=J+IFLAG
102030      IF (JJ-1) .NE. 550,550
102040      SPLDS(I,J)=SPLFLT(I,1)-3.0*FLOAT(1-JJ)
102050      GO TO 560
102060 550 IF (JJ-24) 570,570,
102070      SPLDS(I,J)=SPLFLT(I,24)-3.0*FLOAT(JJ-24)
102080 560 IF (SPLDS(I,J)) .NE. 580,580
102090      SPLDS(I,J)=0.0
102100      GO TO 580
102110 570 SPLDS(I,J)=SPLFLT(I,JJ)
102120 580 CONTINUE
102130C
102140C PRINT FLIGHT TRANSFORMED SPECTRUM, SPLDS
102150      IF (IPRNT.EQ.NO) GO TO 600
102152      WRITE (NBCDO,1000) SPID,SP,(ANGLE(I),I=1,NANG)
102151      DO 590 J=1,NFREQ
102154      WRITE (NBCDO,1010)
102156      & IFREQ(J),(SPLDS(I,J),I=1,NANG)
102157 590 CONTINUE
102158      WRITE (NBCDO,1020) SCFACT,FLTVEL,DIAMJT,IREFRC,ITURBC
102160CC
102170C WRITE SPLDS ON A DATAPLOT TAPE
102180 600 IF (IPLOT.EQ.NO) GO TO 100
102190      DO 610 I=1,NANG
102200      DO 610 J=1,NFREQ
102210 610 TSPL1(J,I)=SPLDS(I,J)
102220 640 CALL FILE (IDPFIL,KEY,7,NLIST,0,0,0,0)
102230      GO TO 100
102240C
102250C ERROR RETURNS
102260 800 WRITE (NBCDO,8000)
102270      GO TO 900
102280C
102290 810 WRITE (NBCDO,8100) SP,SPID
102300      GO TO 100
102310C
102315 900 IF (IPLOT.EQ.NO) GO TO 910
102320      CALL FNWEF (IDPFIL)
102330 910 STOP
102340      END
110000C
110010C
110020C BLOCK DATA SUBROUTINE FOR FLTTRANS
110030C
110040      BLOCK DATA
110050C
110060      COMMON /BLKCON/ BLANK,FREQ(33),IBLANK,IDPFIL,
110070      & IFREQ(33),INFILE,IPLOT,IPRNT,IREFRC,ITURBC,
110072      & NBCDI,NBCDO,NO,PI,SPDSND
110080C
110090      DATA IBLANK /"      "
110100      DATA IDPFIL /12/

```

```
110110      DATA IFREQ /50,63,80,100,125,160,200,250,315,400,500,  
110120      & 630,800,1000,1250,1600,2000,2500,3150,4000,5000,6300,  
110130      & 8000,10000,12500,16000,20000,25000,31500,40000,50000,  
110140      & 63000,80000/  
110150      DATA INFILE /10/  
110160      DATA IPLOT /"YES"/  
110170      DATA IPRNT /"NO"/  
110172      DATA IREFRC /"YES"/  
110174      DATA ITURBC /"YES"/  
110180      DATA NBCDI /05/  
110190      DATA NBCDO /06/  
110200      DATA NO /"NO"/  
110210C  
110220      DATA BLANK /037777777777/  
110230      DATA FREQ /50.,63.,80.,100.,125.,160.,200.,250.,315.,  
110240      & 400.,500.,630.,800.,1000.,1250.,1600.,2000.,2500.,3150.,  
110250      & 4000.,5000.,6300.,8000.,10000.,12500.,16000.,20000.,  
110260      & 25000.,31500.,40000.,50000.,63000.,80000./  
110270      DATA PI /3.1415926/  
110280      DATA SPDSND /1116.0/  
110290      END
```

```

200000*#RUN *=;/NRB/FEIHEC(BCD,NOGO)
200010C
200020C 15475ES/NRB/FEIHE
200030C
200040C SUBROUTINE FROM PROGRAM FEIHE
200050C ORIGINAL PROGRAM CAME FROM RAMANI MANI,
200060C RESEARCH LABS, SCHENECTADY
200070C
200080      SUBROUTINE FEIHE
200090C
200100      COMMON /BLKCON/ BLANK,FREQ(33),IBLANK,IPDFIL,
200110      & IFREQ(33),INFILE,IPILOT,IPRNT,IREFRC,ITURBC,
200120      & NBCDI,NBCDO,NO,PI,SPDSND
200130      COMMON /FEI/ EM,FP,LIE,np,SPL1(10),SPLF(10),
200140      & THETD(10)
200150      DIMENSION A(10,10),B(10),CORR(10),ERROR(10),
200160      & F(10,10),F1(10),FF(10,10),G(10),GF(10),GP(10),
200170      & IJVAL(10),IND(10),INDEX(10),SPL(10),SPLP(10),
200180      & THET(10),W(10),X(10),Y(10),YY(10),Z(10)
200190C
200200      DATA CEM /1.0/
200210C
200220 IF (NP .GE. 6) GO TO 120
200230 WRITE (02,116)
200240 116 FORMAT (/35H PROGRAM REQUIRES AT LEAST 6 POINTS)
200250 GO TO 5000
200260 120 NSST=3-LIE
200270 DO 1737 MCASE=NSST,5
200280 MAX=MCASE+1
200290 TOPI2=(2./PI)**2
200300 EMM=CEM*EM
200310 THETO=ATAN(SQRT(2.*EMM+EMM**2))
200320 THETOD=THETO*180./PI
200330 DO 157 I=1,np
200340 TH=THETD(I)*PI/180.
200350 CTH=COS(TH)
200360 QQ=(1.-EMM*CTH)**2
200370 STH=SIN(TH)
200380 CTH2=CTH*CTH
200390 XP=FP*STH
200400 YP=FP*SQRT(ABS(CTH2-(1.-EMM*CTH)**2))
200410 SCHUB=.26*EMM*(30.7*FP-4.35)
200420 SCHUB1=41.67*EMM
200430 IF(SCHUB.GT.SCHUB1)SCHUB=SCHUB1
200432 CORR(I)=0
200434 IF (IREFRC.EQ.NO) GO TO 562
200440 IF (FP.GT.3.) GO TO 462
200450 CALL BESLJY(XP,FJ0X,FJ1X,FY0X,FY1X)
200460 IF (THETD(I).GT.THETCD) GO TO 150
200470 CALL BESLI(YP,F10Y,F11Y)
200480 RBOTO=YP*FI1Y*FJ0X+XP*FI0Y*QQ*FJ1X
200490 AIBOTO=YP*FI1Y*FY0X+XP*FI0Y*QQ*FY1X
200500 GO TO 153
200510 150 CALL BESLJ(YP,FJ0Y,FJ1Y)
200520 RBOTO =YP*FJ1Y*FJ0X-XP*FJ0Y*QQ*FJ1X
200530 AIBOTO=YP*FJ1Y*FY0X-XP*FJ0Y*QQ*FY1X
200540 153 CRR=TOPI2/(RBOTO**2+AIBOTO**2)
200550 CORR(I)=-4.34295* ALOG(CRR)
200560 GO TO 157
200570 462 IF (LIE.EQ.2) GO TO 467
200580 IF (ABS(THETD(I)-20.).LT.1.) CORR(I)=SCHUB

```

```

200590 IF(ABS(THETD(I)-30.)<LT.1.) CORR(I)=SCHUB/2.
200600 IF(ABS(THETD(I)-40.)<LT.1.) CORR(I)=SCHUB/4.
200610 IF(ABS(THETD(I)-50.)<LT.1.) CORR(I)=SCHUB/6.
200620 IF(ABS(THETD(I)-60.)<LT.1.) CORR(I)=SCHUB/8.
200630 IF((THETD(I)-60.)>5.) CORR(I)=0.0
200640 GO TO 562
200650 467 CORR(I)=4.34295*ALOG(QQ)
200660 562 IF (FP.LT.30.) GO TO 157
200662      IF (ITURBC.EQ.N0) GO TO 157
200670 TAC90=2.*EMM/.25)**2*FP/38.4
200680 IF (TAC90.GT.6.) TAC90=6.
200690 IF (LIE.EQ.2) GO TO 578
200700 TAC=TAC90+2.*((1.5-THETD(I))/60.)
200710 IF (TAC.GT.6.) TAC=6.
200720 CORR(I)=CORR(I)+TAC
200730 GO TO 157
200740 578 TAC=TAC90*((2.8-THETD(I))/50.)
200750 IF (TAC.LT.0.) TAC=0.
200760 CORR(I)=CORR(I)+TAC
200770 157 CONTINUE
200780 DO 170 I=1,NP
200790 THET(I)=THETD(I)*PI/180.
200800 SPL(I)=SPL1(I)+CORR(I)
200810 170 CONTINUE
200820 SPMIN=SPL(1)
200830 DO 188 I=1,NP
200840 IF (SPL(I).LT.SPMIN) SPMIN=SPL(I)
200850 188 CONTINUE
200860 DO 220 I=1,NP
200870 XX=.1*(SPL(I)-SPMIN)
200880 G(I)=10.*XX
200890 220 CONTINUE
200900 APB=2*(MAX-1)+1
200910 IEX=4*(MAX-1)
200920 C=GAMF(APB)*2.**IEX
200930 DO 248 I=1,MAX
200940 AA=2*(MAX-I)+1
200950 BB=2*(I-1)+1
200960 TA=4*(MAX-I)+1
200970 TB=4*(I-1)+1
200980 TERM=GAMF(TA)*GAMF(1B)/(C*GAMF(AA)*GAMF(BB))
200990 YY(I)=SQRT(TERM)
201000 248 CONTINUE
201010 DO 400 I=1,NP
201020 TH=THET(I)
201030 Q=ABS(THETD(I)-90.)
201040 IF (Q.GT. 1.) GO TO 580
201050 F(MAX,I)=1./YY(MAX)
201060 MAX1=MAX-1
201070 DO 570 J=1,MAX1
201080 F(J,I)=0.
201090 570 CONTINUE
201100 GO TO 400
201110 580 CTH2=COS(TH)**2
201120 STH2=SIN(TH)**2
201130 DO 620 J=1,MAX
201140 F(J,I)=CTH2**((MAX-J)*STH2**((J-1)/YY(J))
201150 620 CONTINUE
201160 400 CONTINUE
201170 DO 1030 I=1,MAX
201180 IJVAL(I)=I
201190 1030 CONTINUE

```

```

201200 DO 1160 I=1,NP
201210 B(I)=G(I)
201220 1160 CONTINUE
201230 DO 1250 I=1,NP
201240 DO 1240 J=1,MAX
201250 A(I,J)=F(J,I)
201260 1240 CONTINUE
201270 1250 CONTINUE
201280 CALL NNLS(A,10,NP,MAX,B,X,RNORM,W,Z,INDEX,MODE)
201290 DO 2140 J=1,MAX
201300 Y(J)=X(J)/YY(J)
201310 2140 CONTINUE
201320 DO 2400 I=1,MAX1
201330 DO 2390 J=1,I
201340 JJ1=MAX+J-I
201350 FF(I,J)=1.E+06
201360 DO 2310 JJ=J,JJ1
201370 T1=MAX+1-I
201380 T2=JJ-J+1
201390 T3=T1-T2+1.
201400 TERM=Y(JJ)*GAMF(T2)*GAMF(T3)/GAMF(T1)
201410 IF (TERM .LT. FF(I,J)) FF(I,J)=TERM
201420 IF (ABS(FF(I,J)) .LE. 1.0E-06) FF(I,J)=0.
201430 2310 CONTINUE
201440 DO 2380 JJ=J,JJ1
201450 T1=MAX+1-I
201460 T2=JJ-J+1
201470 T3=T1-T2+1.
201480 TERM=GAMF(T1)/(GAMF(T2)*GAMF(T3))
201490 Y(JJ)=Y(JJ)-FF(I,J)*TERM
201500 2380 CONTINUE
201510 2390 CONTINUE
201520 2400 CONTINUE
201530 DO 2430 J=1,MAX
201540 FF(MAX,J)=Y(J)
201550 2430 CONTINUE
201560 DO 2680 I=1,NP
201570 GF(I)=0.
201580 GP(I)=0.
201590 CTH2=COS(THET(I))*2
201600 STH2=SIN(THET(I))*2
201610 CAF=1./(1.+EM*COS(THET(I)))*2
201620 DO 2670 J=1,MAX
201630 JJ=IJVAL(J)
201640 GP(I)=GP(I)+X(JJ)*F(JJ,I)
201650 CAFJ=CAF**J
201660 IF (ABS(THETD(I)-90.) .GT. 1.) GO TO 2658
201670 GF(I)=GF(I)+FF(J,J)
201680 GO TO 2670
201690 2658 SUM=0.
201700 DO 2665 JJ=1,J
201710 SUM=SUM+(CAFJ*FF(J,JJ)*CTH2** (J-JJ)*STH2** (JJ-1))
201720 2665 CONTINUE
201730 GF(I)=GF(I)+SUM
201740 2670 CONTINUE
201750 2680 CONTINUE
201760 DO 2730 I=1,NP
201770 IF (GP(I) .LE. 0.) GP(I)=1.0E-20
201780 IF (GF(I) .LE. 0.) GF(I)=1.0E-20
201790 SPLP(I)=SPMIN+4.34295* ALOG(GP(I))
201800 SPLP(I)=SPLP(I)-CORR(I)
201810 SPLF(I)=SPL(I)+4.34295* ALOG(GF(I)/GP(I))

```

```

201820 IF (LIE.EQ.1.AND.I.EQ.NP) GO TO 2730
201830 ERROR(I)=ABS(SPLP(I)-SPL1(I))
201840 2730 CONTINUE
201850 IF (LIE.EQ.1) NP1=NP-1
201860 IF (LIE.EQ.2) NP1=NP
201870 FNP1=NP1
201880 ESUM=0.0
201890 EMAX=ERROR(1)
201900 DO 1906 I=1,NP1
201910 ESUM=ESUM+ERROR(I)
201920 IF (ERROR(I).GT.EMAX) EMAX=ERROR(I)
201930 1906 CONTINUE
201940 AVERR=ESUM/FNP1
201950 TERR=AVERR+EMAX
201960 IF (AVERR.LT.2.) GO TO 1739
201970 1737 CONTINUE
201980 1739 CONTINUE
201990 5000 RETURN
202000 END
210000C
210010C
210020 FUNCTION GAMF(X)
210030 N=X-.9
210040 IF (N.EQ.0) N=1
210050 ANS=1.
210060 DO 60 I=1,N
210070 FI=I
210080 ANS=ANS+FI
210090 60 CONTINUE
210100 GAMF=ANS
210110 RETURN
210120 END
220000C
220010C
220020 *      SUBROUTINE NNLS (A,MDA,M,N,B,X,RNORM,W,ZZ,INDEX,MODE)
220030 *      C.L.LAWSON AND R.J.HANSON, JET PROPULSION LABORATORY, 1973 JUNE 15
220040 *      TO APPEAR IN 'SOLVING LEAST SQUARES PROBLEMS', PRENTICE-HALL, 1974
220050 *
220060 *          ***** NONNEGATIVE LEAST SQUARES *****
220070 *
220080 *      GIVEN AN M BY N MATRIX, A, AND AN M-VECTOR, B, COMPUTE AN
220090 *      N-VECTOR, X, WHICH SOLVES THE LEAST SQUARES PROBLEM
220100 *
220110 *          A * X = B SUBJECT TO X .GE. 0
220120 *
220130 *      A(),MDA,M,N      MDA IS THE FIRST DIMENSIONING PARAMETER FOR THE
220140 *                          ARRAY, A(). ON ENTRY A() CONTAINS THE M BY N
220150 *                          MATRIX, A.      ON EXIT A() CONTAINS
220160 *                          THE PRODUCT MATRIX, Q*A , WHERE Q IS AN
220170 *                          M BY M ORTHOGONAL MATRIX GENERATED IMPLICITLY BY
220180 *                          THIS SUBROUTINE.
220190 *      B()      ON ENTRY B() CONTAINS THE M-VECTOR, B.  ON EXIT B() CON-
220200 *                          TAINS Q*B.
220210 *      X()      ON ENTRY X() NEED NOT BE INITIALIZED.  ON EXIT X() WILL
220220 *                          CONTAIN THE SOLUTION VECTOR.
220230 *      RNORM    ON EXIT RNORM CONTAINS THE EUCLIDEAN NORM OF THE
220240 *                          RESIDUAL VECTOR.
220250 *      W()      AN N-ARRAY OF WORKING SPACE.  ON EXIT W() WILL CONTAIN
220260 *                          THE DUAL SOLUTION VECTOR.  W WILL SATISFY W(I) = 0.
220270 *                          FOR ALL I IN SET P AND W(I) .LE. 0.  FOR ALL I IN SET Z
220280 *      ZZ()      AN M-ARRAY OF WORKING SPACE.
220290 *      INDEX()    AN INTEGER WORKING ARRAY OF LENGTH AT LEAST N.

```

```

220300 *          ON EXIT THE CONTENTS OF THIS ARRAY DEFINE THE SETS
220310 *          P AND Z AS FOLLOWS..
220320 *
220330 *          INDEX(1) THRU INDEX(NSETP) = SET P.
220340 *          INDEX(IZ1) THRU INDEX(IZ2) = SET Z.
220350 *          IZ1 = NSETP + 1 = NPP1
220360 *          IZ2 = N
220370 *      MODE   THIS IS A SUCCESS-FAILURE FLAG WITH THE FOLLOWING
220380 *          MEANINGS.
220390 *          1     THE SOLUTION HAS BEEN COMPUTED SUCCESSFULLY.
220400 *          2     THE DIMENSIONS OF THE PROBLEM ARE BAD.
220410 *          EITHER M .LE. 0 OR N .LE. 0.
220420 *          3     ITERATION COUNT EXCEEDED. MORE THAN 3*N ITERATIONS.
220430 *
220440      SUBROUTINE NNLS (A,MDA,M,N,B,X,RNORM,W,ZZ,INDEX,MODE)
220450      DIMENSION A(MDA,N), B(M), X(N), W(N), ZZ(M)
220460      INTEGER INDEX(N)
220470      ZERO=0.
220480      ONE=1.
220490      TWO=2.
220500      FACTOR=0.01
220510 *
220520      MODE=1
220530      IF (M.GT.0.AND.N.GT.0) GO TO 10
220540      MODE=2
220550      RETURN
220560      10 ITER=0
220570      ITMAX=3*N
220580 *
220590      INITIATE THE ARRAYS INDEX() AND X().
220600 *
220610      DO 20 I=1,N
220620      X(I)=ZERO
220630      20 INDEX(I)=I
220640 *
220650      IZ2=N
220660      IZ1=1
220670      NSETP=0
220680      NPP1=1
220690 *          ***** MAIN LOOP BEGINS HERE *****
220700      30 CONTINUE
220710 *          QUIT IF ALL COEFFICIENTS ARE ALREADY IN THE SOLUTION.
220720 *          OR IF M COLS OF A HAVE BEEN TRIANGULARIZED.
220730 *
220740      IF (IZ1.GT.IZ2.OR.NSETP.GE.M) GO TO 350
220750 *
220760      COMPUTE COMPONENTS OF THE DUAL (NEGATIVE GRADIENT) VECTOR W().
220770 *
220780      DO 50 IZ=IZ1,IZ2
220790      J=INDEX(IZ)
220800      SM=ZERO
220810      DO 40 L=NPP1,M
220820      40      SM=SM+A(L,J)*B(L)
220830      50      W(J)=SM
220840 *          FIND LARGEST POSITIVE W(J).
220850      60      WMAX=ZERO
220860      DO 70 IZ=IZ1,IZ2
220870      J=INDEX(IZ)
220880      IF (W(J).LE.WMAX) GO TO 70
220890      WMAX=W(J)
220900      IZMAX=IZ
220910      70      CONTINUE

```

```

220920 *           IF WMAX .LE. 0. GO TO TERMINATION.
220930 *           THIS INDICATES SATISFACTION OF THE KUHN-TUCKER CONDITIONS.
220940     IF (WMAX) 350,350,80
220950   80 IZ=IZMAX
220960   J=INDEX(IZ)
220970 *           THE SIGN OF W(J) IS OK FOR J TO BE MOVED TO SET P.
220980 *           BEGIN THE TRANSFORMATION AND CHECK NEW DIAGONAL ELEMENT TO AVOID
220990 *           NEAR LINEAR DEPENDENCE.
221000   ASAVE=A(NPP1,J)
221010   CALL H12 (1,NPP1,NPP1+1,M,A(1,J),1,UP,DUMMY,1,1,0)
221020   UNORM=ZERO
221030   IF (NSETP.EQ.0) GO TO 100
221040     DO 90 L=1,NSETP
221050   90 UNORM=UNORM+A(L,J)**2
221060   100 UNORM=SQRT(UNORM)
221070   IF (DIFF(UNORM+ABS(A(NPP1,J))*FACTOR,UNORM)) 130,130,110
221080 *           COL J IS SUFFICIENTLY INDEPENDENT. COPY B INTO ZZ, UPDATE ZZ AND
221090 *           > SOLVE FOR ZTEST (= PROPOSED NEW VALUE FOR X(J)).
221100   110 DO 120 L=1,M
221110   120 ZZ(L)=B(L)
221120   CALL H12 (2,NPP1,NPP1+1,M,A(1,J),1,UP,ZZ,1,1)
221130   ZTEST=ZZ(NPP1)/A(NPP1,J)
221140 *           SEE IF ZTEST IS POSITIVE
221150 *           REJECT J AS A CANDIDATE TO BE MOVED FROM SET Z TO SET P.
221160 *           RESTORE A(NPP1,J), SET W(J)=0., AND LOOP BACK TO TEST DUAL
221170   IF (ZTEST) 130,130,140
221180 *           COEFFS AGAIN.
221190   130 A(NPP1,J)=ASAVE
221200   W(J)=ZERO
221210   GO TO 60
221220 *           THE INDEX J=INDEX(IZ) HAS BEEN SELECTED TO BE MOVED FROM
221230 *           SET Z TO SET P. UPDATE B, UPDATE INDICES, APPLY HOUSEHOLDER
221240 *           TRANSFORMATIONS TO COLS IN NEW SET Z, ZERO SUBDIAGONAL ELTS IN
221250 *           COL J, SET W(J)=0.
221260   140 DO 150 L=1,M
221270   150 B(L)=ZZ(L)
221280   INDEX(IZ)=INDEX(IZ1)
221290   INDEX(IZ1)=J
221300   IZ1=IZ1+1
221310   NSETP=NPP1
221320   NPP1=NPP1+1
221330   IF (IZ1.GT.IZ2) GO TO 170
221340     DO 160 JZ=IZ1,IZ2
221350     JJ=INDEX(JZ)
221360   160 CALL H12 (2,NSETP,NPP1,M,A(1,J),1,UP,A(1,JJ),1,MDA,1)
221370   170 CONTINUE
221380   IF (NSETP.EQ.M) GO TO 190
221390     DO 180 L=NPP1,M
221400   180 A(L,J)=ZERO
221410   190 CONTINUE
221420   W(J)=ZERO
221430 *           SOLVE THE TRIANGULAR SYSTEM.
221440 *           STORE THE SOLUTION TEMPORARILY IN ZZ().
221450   ASSIGN 200 TO NEXT
221460   GO TO 400
221470   200 CONTINUE
221480 *           ***** SECONDARY LOOP BEGINS HERE *****
221490 *           ITERATION COUNTER.
221500   210 ITER=ITER+1
221510   IF (ITER.LE.ITMAX) GO TO 220
221520   MODE=3
221530   PRINT 440

```

```

221540      GO TO 350
221550  220 CONTINUE
221560 *          SEE IF ALL NEW CONSTRAINED COEFFS ARE FEASIBLE.
221570 *          IF NOT COMPUTE ALPHA.
221580      ALPHA=TWO
221590      DO 240 IP=1,NSETP
221600      L=INDEX(IP)
221610      IF (ZZ(IP)) 230,230,240
221620  230      T=-X(L)/(ZZ(IP)-X(L))
221630      IF (ALPHA.LE.T) GO TO 240
221640      ALPHA=T
221650      JJ=IP
221660  240      CONTINUE
221670 *          IF ALL NEW CONSTRAINED COEFFS ARE FEASIBLE THEN ALPHA WILL
221680 *          STILL = 2.  IF SO EXIT FROM SECONDARY LOOP TO MAIN LOOP.
221690      IF (ALPHA.EQ.TWO) GO TO 330
221700 *          OTHERWISE USE ALPHA WHICH WILL BE BETWEEN 0. AND 1. TO
221710 *          INTERPOLATE BETWEEN THE OLD X AND THE NEW ZZ.
221720      DO 250 IP=1,NSETP
221730      L=INDEX(IP)
221740  250      X(L)=X(L)+ALPHA*(ZZ(IP)-X(L))
221750 *          MODIFY A AND B AND THE INDEX ARRAYS TO MOVE COEFFICIENT I
221760 *          FROM SET P TO SET Z.
221770      I=INDEX(JJ)
221780  260      X(I)=ZERO
221790      IF (JJ.EQ.NSETP) GO TO 290
221800      JJ=JJ+1
221810      DO 280 J=JJ,NSETP
221820      II=INDEX(J)
221830      INDEX(J-1)=II
221840      CALL G1 (A(J-1,II),A(J,II),CC,SS,A(J-1,II))
221850      A(J,II)=ZERO
221860      DO 270 L=1,N
221870      IF (L.NE.II) CALL G2 (CC,SS,A(J-1,L),A(J,L))
221880  270      CONTINUE
221890  280      CALL G2 (CC,SS,B(J-1),B(J))
221900  290      NPP1=NSETP
221910      NSETP=NSETP-1
221920      IZ1=IZ1-1
221930      INDEX(IZ1)=I
221940 *          SEE IF THE REMAINING COEFFS IN SET P ARE FEASIBLE.  THEY SHOULD
221950 *          BE BECAUSE OF THE WAY ALPHA WAS DETERMINED.
221960 *          IF ANY ARE INFEASIBLE IT IS DUE TO ROUND-OFF ERROR.  ANY
221970 *          THAT ARE NONPOSITIVE WILL BE SET TO ZERO
221980 *          AND MOVED FROM SET P TO SET Z.
221990      DO 300 JJ=1,NSETP
222000      I=INDEX(JJ)
222010      IF (X(I)) 260,260,300
222020  300      CONTINUE
222030 *          COPY B( ) INTO ZZ( ).  THEN SOLVE AGAIN AND LOOP BACK.
222040      DO 310 I=1,M
222050  310      ZZ(I)=B(I)
222060      ASSIGN 320 TO NEXT
222070      GO TO 400
222080  320      CONTINUE
222090      GO TO 210
222100 *          ***** END OF SECONDARY LOOP *****
222110 *
222120  330      DO 340 IP=1,NSETP
222130      I=INDEX(IP)
222140  340      X(I)=ZZ(IP)
222150 *          ALL NEW COEFFS ARE POSITIVE.  LOOP BACK TO BEGINNING.

```

```

222160      GO TO 30
222170 *          **** END OF MAIN LOOP ****
222180 *          COME TO HERE FOR TERMINATION.
222190 *          COMPUTE THE NORM OF THE FINAL RESIDUAL VECTOR.
222200 350 SM=ZERO
222210      IF (NPP1.GT.M) GO TO 370
222220      DO 360 I=NPP1,M
222230 360      SM=SM+B(I)**2
222240      GO TO 390
222250 370      DO 380 J=1,N
222260 380      W(J)=ZERO
222270 390 RNCRM=SQRT(SM)
222280      RETURN
222290 *          THE FOLLOWING BLOCK OF CODE IS USED AS AN INTERNAL SUBROUTINE
222300 *          TO SOLVE THE TRIANGULAR SYSTEM, PUTTING THE SOLUTION IN ZZ().
222310 400      DO 430 L=1,NSETP
222320      IP=NSETP+1-L
222330      IF (L.EQ.1) GO TO 420
222340      DO 410 II=1,IP
222350 410      ZZ(II)=ZZ(II)-A(II,JJ)*ZZ(IP+1)
222360 420      JJ=INDEX(IP)
222370 430      ZZ(IP)=ZZ(IP)/A(IP,JJ)
222380      GO TO NEXT, (200,320)
222390 440 FORMAT (35HO NNLS QUITTING ON ITERATION COUNT.)
222400 999 RETURN;END
230000C
230010C
230020 *          SUBROUTINE H12 (MODE,LPIVOT,L1,M,U,IUE,UP,C,ICE,ICV,NCV)
230030 *          C.L.LAWSON AND R.J.HANSON, JET PROPULSION LABORATORY, 1973 JUN 12
230040 *          TO APPEAR IN 'SOLVING LEAST SQUARES PROBLEMS', PRENTICE-HALL, 1974
230050 *          CONSTRUCTION AND/OR APPLICATION OF A SINGLE
230060 *          HOUSEHOLDER TRANSFORMATION..   Q = I + U*(U*T)/B
230070 *          MODE = 1 OR 2 TO SELECT ALGORITHM H1 OR H2 .
230080 *          LPIVOT IS THE INDEX OF THE PIVOT ELEMENT.
230090 *          L1,M IF L1 .LE. M THE TRANSFORMATION WILL BE CONSTRUCTED TO
230100 *          ZERO ELEMENTS INDEXED FROM L1 THROUGH M. IF L1 GT. M
230110 *          THE SUBROUTINE DOES AN IDENTITY TRANSFORMATION.
230120 *          U(),IUE,UP    ON ENTRY TO H1 U() CONTAINS THE PIVOT VECTOR.
230130 *          IUE IS THE STORAGE INCREMENT BETWEEN ELEMENTS.
230140 *          ON EXIT FROM H1 U() AND UP
230150 *          CONTAIN QUANTITIES DEFINING THE VECTOR U OF THE
230160 *          HOUSEHOLDER TRANSFORMATION. ON ENTRY TO H2 U()
230170 *          AND UP SHOULD CONTAIN QUANTITIES PREVIOUSLY COMPUTED
230180 *          BY H1. THESE WILL NOT BE MODIFIED BY H2.
230190 *          C()    ON ENTRY TO H1 OR H2 C() CONTAINS A MATRIX WHICH WILL BE
230200 *          REGARDED AS A SET OF VECTORS TO WHICH THE HOUSEHOLDER
230210 *          TRANSFORMATION IS TO BE APPLIED. ON EXIT C() CONTAINS THE
230220 *          SET OF TRANSFORMED VECTORS.
230230 *          ICE   STORAGE INCREMENT BETWEEN ELEMENTS OF VECTORS IN C().
230240 *          ICV   STORAGE INCREMENT BETWEEN VECTORS IN C().
230250 *          NCV   NUMBER OF VECTORS IN C() TO BE TRANSFORMED. IF NCV .LE. 0
230260 *          NO OPERATIONS WILL BE DONE ON C().
230270 *          SUBROUTINE H12 (MODE,LPIVOT,L1,M,U,IUE,UP,C,ICE,ICV,NCV)
230280 *          DIMENSION U(IUE,M), C(1)
230290 *          DOUBLE PRECISION SM,B
230300 *          ONE=1.
230310 *          IF (0.GE.LPIVOT.OR.LPIVOT.GE.L1.OR.L1.GT.M) RETURN
230320 *          CL=ABS(U(1,LPIVOT))
230330 *          IF (MODE.EQ.2) GO TO 60
230340 *          ***** CONSTRUCT THE TRANSFORMATION. *****
230350      DO 10 J=L1,M
230360 10      CL=AMAX1 (ABS(U(1,J)),CL)

```

```

230370      IF (CL) 130,130,20
230380      20 CLINV=ONE/CL
230390      SM=(DBLE(U(1,LPIVOT))*CLINV)**2
230400      DO 30 J=L1,M
230410      30 SM=SM+(DBLE(U(1,J))*CLINV)**2
230420 *           CONVERT DBLE. PREC. SM TO SNGL. PREC. SM1
230430      SM1=SM
230440      CL=CL*SQRT(SM1)
230450      IF (U(1,LPIVOT)) 50,50,40
230460      40 CL=-CL
230470      50 UP=U(1,LPIVOT)-CL
230480      U(1,LPIVOT)=CL
230490      GO TO 70
230500 *           ***** APPLY THE TRANSFORMATION I+U*(U**T)/B TO C. *****
230510      60 IF (CL) 130,130,70
230520      70 IF (NCV.LE.0) RETURN
230530      B=DBLE(UP)*U(1,LPIVOT)
230540 *           B MUST BE NONPOSITIVE HERE. IF B = 0., RETURN.
230550      IF (B) 80,130,130
230560      80 B=ONE/B
230570      I2=1-ICV+ICE*(LPIVOT-1)
230580      INCR=ICE*(L1-LPIVOT)
230590      DO 120 J=1,NCV
230600      I2=I2+ICV
230610      I3=I2+INCR
230620      I4=I3
230630      SM=C(I2)*DBLE(UP)
230640      DO 90 I=L1,M
230650      SM=SM+C(I3)*DBLE(U(1,I))
230660      90 I3=I3+ICE
230670      IF (SM) 100,120,100
230680      100 SM=SM*B
230690      C(I2)=C(I2)+SM*DBLE(UP)
230700      DO 110 I=L1,M
230710      C(I4)=C(I4)+SM*DBLE(U(1,I))
230720      110 I4=I4+ICE
230730      120 CONTINUE
230740      130 RETURN
230750      END
240000C
240010C
240020      SUBROUTINE G1 (A,B,COS,SIN,SIG)
240030 *           C.L.LAWSON AND R.J.HANSON, JET PROPULSION LABORATORY, 1973 JUN 12
240040 *           TO APPEAR IN 'SOLVING LEAST SQUARES PROBLEMS', PRENTICE-HALL, 1974
240050 *           COMPUTE ORTHOGONAL ROTATION MATRIX..
240060 *           COMPUTE.. MATRIX (C, S) SO THAT (C, S)(A) = (SQRT(A**2+B**2))
240070 *           (-S,C)          (-S,C)(B)   ( 0 )
240080 *           COMPUTE SIG = SQRT(A**2+B**2)
240090 *           SIG IS COMPUTED LAST TO ALLOW FOR THE POSSIBILITY THAT
240100 *           SIG MAY BE IN THE SAME LOCATION AS A OR B .
240110      ZERO=0.
240120      ONE=1.
240130      IF (ABS(A).LE.ABS(B)) GO TO 10
240140      XR=B/A
240150      YR=SQRT(ONE+XR**2)
240160      COS=SIGN(ONE/YR,A)
240170      SIN=COS*X
240180      SIG=ABS(A)*YR
240190      RETURN
240200      10 IF (6) 20,30,20
240210      20 XR=A/B
240220      YR=SQRT(ONE+XR**2)

```

```

240230      SIN=SIGN(ONE/YR,B)
240240      COS=SIN*XR
240250      SIG=ABS(B)*YR
240260      RETURN
240270      30 SIG=ZERO
240280      COS=ZERO
240290      SIN=ONE
240300      RETURN
240310      END
251000C
251010C
251020      SUBROUTINE G2    (COS,SIN,X,Y)
251030 *      C.L.LAWSON AND R.J.HANSON, JET PROPULSION LABORATORY, 1972 DEC 15
251040 *      TO APPEAR IN 'SOLVING LEAST SQUARES PROBLEMS', PRENTICE-HALL, 1974
251050 *      APPLY THE ROTATION COMPUTED BY G1 TO (X,Y).
251060      XR=COS*X+SIN*Y
251070      Y=-SIN*X+COS*Y
251080      X=XR
251090      RETURN
251100      END
252000C
252010C
252020      FUNCTION DIFF(X,Y)
252030 *      C.L.LAWSON AND R.J.HANSON, JET PROPULSION LABORATORY, 1973 JUNE 7
252040 *      TO APPEAR IN 'SOLVING LEAST SQUARES PROBLEMS', PRENTICE-HALL, 1974
252050      DIFF=X-Y
252060      RETURN
252070      END
260000C
260010C
260020 SUBROUTINE BESLI (X,B10,B11)
260030 T=X/3.75
260040 IF (X .GT. 3.75) GO TO 200
260050 T2=T**2
260060 A2=3.5156229
260070 A4=.0899424
260080 A6=1.2067492
260090 A8=.2659732
260100 A10=.0360768
260110 A12=.0045813
260120 AB1=((((A12*T2+A10)*T2+A8)*T2+A6)*T2+A4)*T2+A2)*T2+1.
260130 B10=AB1
260140 B2=.87890594
260150 B4=.51498869
260160 B6=.15084934
260170 B8=.02658733
260180 B10=.00301532
260190 B12=.00032411
260200 BBI=((((B12*T2+B10)*T2+B8)*T2+B6)*T2+B4)*T2+B2)*T2+.5
260210 B11=BBI*X
260220 GO TO 830
260230 200 TN=1./T
260240 C0=.39894228
260250 C1=.01328592
260260 C2=.00225319
260270 C3=-.00157565
260280 C4=.00916281
260290 C5=.02057706
260300 C6=.02635537
260310 C7=-.01647633
260320 C8=.00392377
260330 CB1=(((((C8*TN+C7)*TN+C6)*TN+C5)*TN+C4)*TN+C3)*TN+C2)*TN+C1

```

```

260340 &)*TN+C0
260350 BI0=CB1/SQRT(X)
260360 BI0=BI0*EXP(X)
260370 D0=.39894228
260380 D1=-.03988024
260390 D2=-.00362018
260400 D3=.00163801
260410 D4=-.01031555
260420 D5=.02282967
260430 D6=-.02895312
260440 D7=.01787654
260450 D8=-.00420059
260460 DBI=(((((D8*TN+D7)*TN+D6)*TN+D5)*TN+D4)*TN+D3)*TN+D2)*TN+D1)*
260470 & TN+D0
260480 BI1=DBI/SQRT(X)
260490 BI1=BI1*EXP(X)
260500 830 RETURN
260510 END
270000C
270010C
270020 SUBROUTINE BESLJY (X,BJ0,BJ1,BY0,BY1)
270030 PI=3.1415926
270040 IF (X .GT. 3.) GO TO 395
270050 X32=(X/3.)*2
270060 A2=-2.2499997
270070 A4=1.2656208
270080 A6=-.3163866
270090 A8=.0444479
270100 A10=-.0039444
270110 A12=.00021
270120 BJ0=((((A12*X32+A10)*X32+A8)*X32+A6)*X32+A4)*X32+A2)*X32+1.
270130 Y=(2./PI)*ALOG(X/2.)*BJ0
270140 Y0=.36746691
270150 Y2=.60559366
270160 Y4=-.74350384
270170 Y6=.25300117
270180 Y8=-.04261214
270190 Y10=.00427916
270200 Y12=-.00024846
270210 BY0=((((Y12*X32+Y10)*X32+Y8)*X32+Y6)*X32+Y4)*X32+Y2)*X32+Y0+Y
270220 H0=.5
270230 H2=-.56249985
270240 H4=.21093573
270250 H6=-.03954289
270260 H8=.00443319
270270 H10=-.00031761
270280 H12=-.1109E-04
270290 H1X=((((H12*X32+H10)*X32+H8)*X32+H6)*X32+H4)*X32+H2)*X32+H0
270300 BJ1=H1X*X
270310 D=(2./PI)*X*ALOG(X/2.)*BJ1
270320 D0=-.6366198
270330 D2=.2212091
270340 D4=2.1682709
270350 D6=-1.3164827
270360 D8=.3123951
270370 D10=-.0400976
270380 D12=.0027873
270390 Y1X=((((D12*X32+D10)*X32+D8)*X32+D6)*X32+D4)*X32+D2)*X32+D0+D
270400 BY1=Y1X/X
270410 GO TO 760
270420 395 X3=3./X
270430 C0=.79788456

```

```

270440 C1=-.77E-06
270450 C2=-.0055274
270460 C3=-.00009512
270470 C4=.00137237
270480 C5=-.00072805
270490 C6=.00014476
270500 F0=((((C6*X3+C5)*X3+C4)*X3+C3)*X3+C2)*X3+C1)*X3+C0
270510 T0=-.78539816
270520 T1=-.04166397
270530 T2=-.3954E-04
270540 T3=.00262573
270550 T4=-.00054125
270560 T5=-.00029333
270570 T6=.00013558
270580 THETA0=((((T6*X3+T5)*X3+T4)*X3+T3)*X3+T2)*X3+T1)*X3+T0+X
270590 BJ0=(1./SQRT(X))*F0*COS(THETA0)
270600 BY0=(1./SQRT(X))*FC*SIN(THETA0)
270610 E0=.79788456
270620 E1=.156E-05
270630 E2=.01659667
270640 E3=.00017105
270650 E4=-.00249511
270660 E5=.00113653
270670 E6=-.0002033
270680 F1=((((E6*X3+E5)*X3+E4)*X3+E3)*X3+E2)*X3+E1)*X3+E0
270690 G0=-2.35619449
270700 G1=.12499612
270710 G2=.565E-04
270720 G3=-.00637879
270730 G4=.00074348
270740 G5=.00079824
270750 G6=-.00029166
270760 THETA1=((((G6*X3+G5)*X3+G4)*X3+G3)*X3+G2)*X3+G1)*X3+G0+X
270770 BJ1=(1./SQRT(X))*F1*COS(THETA1)
270780 BY1=(1./SQRT(X))*F1*SIN(THETA1)
270790 760 RETURN
270800 END
280000C
280010C
280020 SUBROUTINE BESLJ (X,BJ0,BJ1)
280030 PI=3.1415926
280040 IF (X .GT. 3.) GO TO 395
280050 X32=(X/3.)**2
280060 A2=-2.2499997
280070 A4=1.2656208
280080 A6=-.3163866
280090 A8=.0444479
280100 A10=-.0039444
280110 A12=.00021
280120 BJ0=((((A12*X32+A10)*X32+A8)*X32+A6)*X32+A4)*X32+A2)*X32+1.
280130 H0=.5
280140 H2=-.56249985
280150 H4=.21093573
280160 H6=-.03954289
280170 H8=.00443319
280180 H10=-.00031761
280190 H12=.1109E-04
280200 H1X=((((H12*X32+H10)*X32+H8)*X32+H6)*X32+H4)*X32+H2)*X32+H0
280210 BJ1=H1X*X
280220 GO TO 760
280230 395 X3=3./X
280240 CO=.79788456

```

```

280250 C1=-.77E-06
280260 C2=-.0055274
280270 C3=-.00009512
280280 C4=.00137237
280290 C5=-.00072805
280300 C6=.00014476
280310 F0=((((C6*X3+C5)*X3+C4)*X3+C3)*X3+C2)*X3+C1)*X3+C0
280320 T0=-.78539816
280330 T1=-.04166397
280340 T2=-.3954E-04
280350 T3=.00262573
280360 T4=-.00054125
280370 T5=-.00029333
280380 T6=.00013558
280390 THETA0=((((T6*X3+T5)*X3+T4)*X3+T3)*X3+T2)*X3+T1)*X3+T0+X
280400 BJ0=(1./SQRT(X))*F0*COS(THETA0)
280410 E0=.79788456
280420 E1=.156E-05
280430 E2=.01659667
280440 E3=.00017105
280450 E4=-.00249511
280460 E5=.00113653
280470 E6=-.0002033
280480 F1=((((E6*X3+E5)*X3+E4)*X3+E3)*X3+E2)*X3+E1)*X3+E0
280490 G0=-2.35619449
280500 G1=.12499612
280510 G2=.565E-04
280520 G3=-.00637879
280530 G4=.00074348
280540 G5=.00079824
280550 G6=-.00029166
280560 THETA1=(((((G6*X3+G5)*X3+G4)*X3+G3)*X3+G2)*X3+G1)*X3+G0+X
280570 BJ1=(1./SQRT(X))*F1*COS(THETA1)
280580 760 RETURN
280590 END

```